University of London

University College, London

Department of Chemistry

Christopher Ingold Laboratories

London WC1H 0AJ

HALOGEN-BRIDGED MIXED-VALENCE COMPLEXES OF PLATINUM: SOLID-STATE NMR AND RESONANCE RAMAN SPECTROSCOPIC STUDIES

by

Elliot John Winston Austin

Thesis submitted in partial fulfilment of the requirements for the degree of Doctor of Philosophy of the University of London

1995

ACKNOWLEDGEMENTS

I am indebted to Dr. Patrick Barrie for collecting and processing the solid-state NMR spectra shown in this thesis, and for his help in discussing the results. Thanks are also due to his assistant, David Butler. I am very grateful to Dan Oprescu, who maintained the equipment in the Raman Room and kept it operational, and to Dr. Steve Best, who wrote the software to drive the Raman spectrometers; Dr. Best merits further thanks for his considered opinions on various aspects of this work. I wish to thank all those who gave technical support, particularly those who work in the Glassblowers', Microanalysis, Electronics or Workshop, and Marianne Odlyha (ULIRS thermal methods service) for recording the DSC measurements.

I am grateful for the support and friendship of all fellow inmates of Laboratory 201C, both current (Danny, Marcus, Dave, Suzanne, Jon and Joe) and past (Navjot, Phil, Adrianna, Slava, Rob, and Pete); special thanks are due to Adrianna Barbieri for her initial work on the ammine complexes. I wish to thank all my friends, particularly Rob, Bruce and Danny (again), and the UCL Football Club for keeping me entertained all this time. Most of all, I am totally indebted to Dr. Joanna Muffett for her patience over this last year, and to my parents for all their support and encouragement.

I am grateful to the Science and Engineering Research Council for funding and to Johnson Matthey plc for the loan of platinum starting materials. Finally, I wish to thank my supervisor Professor R. J. H. Clark for enabling the late submission of this thesis.

This thesis is dedicated to my late father, John Austin

Nov. 21st 1947 - Nov. 10th 1995

ABSTRACT

Solid-state NMR spectroscopy has been combined with resonance Raman spectroscopy in the study of platinum compounds belonging to the class known as Halogen-bridged Mixed-valence Metal Linear-Chain complexes (HMMCs). This class is characterised by the repeat unit of —[—X—$M^{IV}L_4$—X———$M^{II}L_4$——]—, where M is the metal (Ni, Pd or Pt), X is the halogen (Cl, Br or I) and L_4 represents the four equatorial metal - ligand bonds. The metals can bond to a combination of halogens and amines of varying denticity; the net charge of the chain is balanced by interstitial counterions. Much of the interesting chemistry of this class is associated with the intervalence charge transfer (IVCT: $M^{IV} \leftarrow M^{II}$), which gives rise to an intense, polarised absorption, usually in the visible region. Excitation within this band can couple with motion along the chain to enhance the intensity of the Raman active symmetric (X-M^{IV}-X) stretch, which is termed the ν_1 mode. The influence of metal or halogen on the properties of HMMCs is usually attributed to the degree of charge delocalisation that occurs on chain formation.

The application of solid-state NMR spectroscopy to the analysis of HMMCs has been investigated. Studies on $[Pt(2,3,2\text{-tet})][Pt(2,3,2\text{-tet})X_2](ClO_4)_4$ (2,3,2-tet = 3,7-diazanonane-1,9-diamine) show that it is possible to probe ^{15}N nuclei at natural abundance, although it is not very practical; subsequent solid-state ^{15}N NMR studies used ^{15}N-enriched ligands. Solid-state ^{15}N and ^{195}Pt NMR analyses of $[Pt(en)X_2][Pt(en)X_4]$ (en = ethylenediamine) show that, contrary to expectation, the effect of chain formation is small and is similar for Pt^{II} and Pt^{IV} nuclei alike.

The influence of counterions is examined in the study of the cationic chain complexes $[Pt(en)_2][Pt(en)_2X_2]Y_4$ ($Y = ClO_4^-$, BF_4^- or PF_6^-) and their monomers. The variation in ^{15}N chemical shift with Y is accounted for by the hydrogen-bonding strength of the counterion. For $Y = ClO_4^-$ or BF_4^-, the relationship between monomers and chain is similar to that observed in the neutral-chain systems, but for $Y = PF_6^-$ it is more complicated. The results of the analysis of the mixed-halide HMMCs $[Pt(en)_2][Pt(en)_2Cl_{2-2\alpha}Br_{2\alpha}](ClO_4)_4$ show that the number of [Cl-Pt^{IV}-Br] units in these species is close to that predicted for a purely random distribution,

and hence much larger than that assumed previously. Simulated vibrational spectra have been computed and are compared with Raman and infrared spectra to help determine the most likely distribution of halogens.

The unusual traits of some platinum ammine complexes have been examined. Solid-state ^{15}N NMR spectra demonstrate that there are two distinct forms of *cis*-$Pt(NH_3)_2Cl_2$, *cis*-$Pt(NH_3)_2Br_2$ and *trans*-$Pt(NH_3)_2Cl_2$, and that the properties of some tetraammine complexes are dependent on the preparative conditions (solvent, ratios of reagents, *etc.*). The HMMCs *cis*-$[Pt(NH_3)_2Br_2][Pt(NH_3)_2Br_4]$ and *cis*-$[Pt(NH_3)_2I_2][Pt(NH_3)_2I_4]$ are reported for the first time, but the complex thought to be *cis*-$[Pt(NH_3)_2Cl_2][Pt(NH_3)_2Cl_4]$ is shown to contain significant *trans* impurities.

A new kind of HMMC, made by treating $[Pt(opd)_2]^0$ (opd = *ortho*-phenylenediamine) with $[Pt(en)_2Cl_2](ClO_4)_2$, is reported. It contains many defects and its unusual vibrational spectra are discussed briefly.

CONTENTS

LIST OF FIGURES

Chapter 6 Linear-chain complexes containing platinum ammines

LIST OF TABLES

NOTATION

c	speed of light
ca.	*circa*
CCD	Charge Coupled Device
CDW	Charge Density Wave
CP	Cross Polarisation
dan	1,8-diaminonaphthalene
dcpd	4,5-dichloro-*o*-phenylenediamine
DMF	dimethylformamide
dmpd	4,5-dimethyl-*o*-phenylenediamine
δ_N	^{15}N chemical shift
δ_{Pt}	^{195}Pt chemical shift
DSC	Differential Scanning Calorimetry
e-h	electron-hole (pair)
en	ethylenediamine
e-p	electron-phonon (coupling)
ESR	Electron Spin Resonance
eV	electron Volt
FID	Fourier Induction Decay
FT	Fourier Transform
h	Planck's constant
HMMC	Halogen-bridged Mixed-valence Metal Linear-Chain (complex)
i.r.	infrared
IVCT	Intervalence Charge Transfer
J_{N-Pt}	Coupling between ^{15}N and ^{195}Pt nuclei
KE	Kinetic Energy
L or LL	amine ligand
LMTO	Linear Muffin Tin Orbital
M	metal (Ni, Pd or Pt)
MAS	Magic Angle Spinning
MFT	Mean Field Theory
MGS	Magnus Green Salt
MO	Molecular Orbital
MX	Metal-Halogen chain
NMR	Nuclear Magnetic Resonance
opd	*ortho*-phenylenediamine
OZ_α	vibrational model for $PtBr_\alpha$
phen	1,10-phenanthroline
PM	photomultiplier (tube)
$PtBr_\alpha$	$[Pt(en)_2][Pt(en)_2Cl_{2-2\alpha}Br_{2\alpha}](ClO_4)_4$
PtX	$[Pt(en)_2][Pt(en)_2X_2](ClO_4)_4$
rR	resonance Raman
RZ_α	vibrational model for $PtBr_\alpha$
σ	nuclear shielding
SDW	Spin Density Wave
STE	self-trapped electron
STX	self-trapped exciton
2,3,2-tet	3,7-diazanonane-1,9-diamine
TPA	*trans*-polyacetylene
ULCC	University of London Computing Centre
UPE	unpaired electron
UV	Ultra Violet
WR	Wolffram's Red
X	halogen (X = Cl, Br or I)
XPS	X-ray photoelectron spectroscopy
Y	counterion
ZB	zone boundary
ZC	zone centre

CHAPTER 1

INTRODUCTION

1.1 Mixed Valence Chemistry

1.1.1 Introduction

Platinum is one of over forty elements that can form compounds in which two (or more) formal oxidation states are present. Such compounds, termed mixed-valence by Robin and Day in preference to other equally suitable labels,[1] have been in existence for a considerable time; the iron(II) / iron(III) complex Prussian blue was first synthesised in 1704. The intense colour characteristic of many of these complexes encouraged great interest in these species. Although the conditions required for their formation were often appreciated, a full understanding of their precise composition did not follow swiftly. Indeed, it was not until early this century that the presence of two valences was suggested by Hofmann to account for the colour of the various iron cyanide complexes.[2] The subsequent proposition, that two such valences should not be uniquely fixed but that rapid valence oscillation should occur on each site, was used to explain the absorption of light in a mixed cerium/uranium oxide.[3] Although this was extended by Wells,[4] who drew comparisons between compounds of different metals, mixed-valence systems were generally viewed as singularities of particular elements, rather than a group of compounds with definable properties. Robin and Day were the first to classify mixed-valence complexes in 1967,[1] using a simple one-electron model based on ligand field theory.

1.1.2 Robin and Day classification

For two atomic species A and B, in oxidation states m and n (>m) respectively, and with N of the B species bonded to a single A species, the ground state wavefunction (zeroth order) is written as

$$\Psi'_0 = \psi_A^m \psi_{B_1}^n \cdots\cdots \psi_{B_N}^n \qquad [1.1.1]$$

The transfer of a single electron from A to B gives rise to N excited state functions,

$$\Psi_k = \psi_A^{m+1} \sum_i C_{ki} \psi_{B_1}^n \cdot\cdot \psi_{B_k}^{n-1} \cdot\cdot \psi_{B_N}^n \quad \text{(for k = 1 to N)} \qquad [1.1.2]$$

where C_{ki} are chosen both to normalise Ψ_k and to ensure that the latter transforms according to one of the representations of the appropriate symmetry point group. If one of the Ψ_k has the appropriate symmetry then it can mix with Ψ_0' to give a ground state of

$$\Psi_0 = \sqrt{(1-\alpha^2)}\Psi'_0 + \alpha\Psi_k \qquad [1.1.3]$$

By summing over all k, and then treating the system as one electron outside a closed shell, the ground state expression can finally be reduced to

$$\Psi_0 = \frac{\kappa}{R}\left(\sqrt{(1-\alpha^2)}\phi_A + \alpha \sum_i C_{ki}\phi_{B_i}\right) \qquad [1.1.4]$$

where κ is the product of all closed shell core functions, R is a normalising factor, and ϕ denotes the single electron wavefunction for the appropriate ψ. α is related to two quantities: E_k, the energy of Ψ_k above Ψ_0', and V, the mixing matrix element. If E_k is large or V is small, α approaches zero; if E_k is zero, α takes its maximum of $R/\sqrt{2}$. The classification of mixed-valence systems is based on the value of α and is shown below in Table 1.1.1.

Table 1.1.1 Robin and Day classification

Class	α	Metal ion symmetry	Delocalisation	Conductivity	Energy of intervalence transition
I	0	A, B very different	none	insulator	in ultra violet
II	> 0	A, B nearly identical	slight	semiconductor	in visible range
IIIA	$R/\sqrt{2}$	All identical	short range	insulator	in visible range
IIIB	$R/\sqrt{2}$	All identical	complete	metallic	edge in infrared

1.2 Halogen-bridged Mixed-valence Metal Linear-Chain complexes

1.2.1 Introduction

This work is concerned primarily with the chemistry of platinum compounds that belong to the group known as Halogen-bridged Mixed-valence Metal Linear-Chains (HMMCs). This lengthy nomenclature emphasises the important distinctive features of these species; namely that they contain metal atoms in more than one oxidation state that are linked by halogen atoms to form a straight chain. A typical structural representation is shown in Figure 1.2.1.

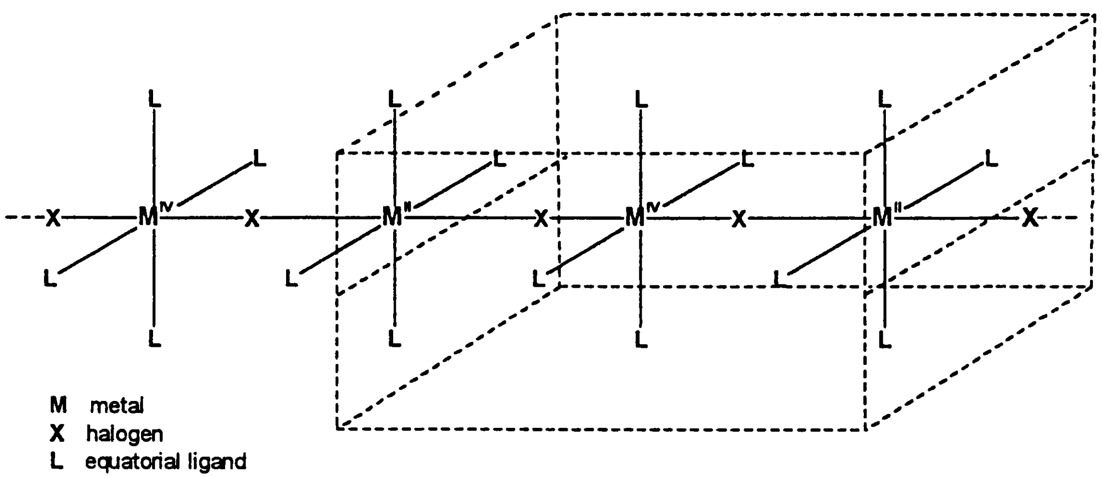

Figure 1.2.1 A representation of an HMMC complex, without counterions. The dashed lines enclose a unit cell.

The only metals (M) that can solely support such a system are nickel, palladium and platinum; others metals such as copper and gold may only be doped into platinum chains. Mixed-metal species that contain combinations of Ni, Pd and Pt, are known, with the more electropositive element filling preferentially the M^{IV} sites. The bridging halogens (X) may be chlorine, bromine or iodine, or mixtures of them. The metals are bonded to equatorial ligands (L), which can be a combination of amines (of various denticities) and halogens. The resultant net charge is balanced by that on interstitial counterions: anions, including X^-, ClO_4^-, BF_4^-, PF_6^-, HSO_4^- and SO_4^{2-}, and cations, such as K^+, Rb^+ and Cs^+.

Just as the nature of mixed-valence compounds was not appreciated until long after their initial discovery, so many years elapsed between the synthesis of Wolffram's Red (WR) salt $[Pt(etn)_4][Pt(etn)_4Cl_2]Cl_4.4H_2O$ [5] and the determination of HMMC structure. Brosset reported the first complete analysis in 1948, solving the crystal structure of the neutral chain complex *trans*-$[Pt(NH_3)_2Br_2][Pt(NH_3)_2Br_4]$.[6] Wolffram's Red itself was not analysed successfully until 1961.[7] HMMC species generally crystallise with sections of chain parallel to each other, settling into needle-like shapes. Two-dimensional order may be imposed by hydrogen-bonding ligand-counterion networks, but neither the platelets that this can produce, nor the more usual needles, are particularly suited to X-ray diffractometry. The difficulty of forming crystals of sufficient size and homogeneity means that the number of reliable published structures is not great (see section **1.3**).

Fortunately, HMMCs do lend themselves to study by numerous other techniques. The anisotropy in their macroscopic structure means that single-crystal studies are particularly valuable. A survey of experimental measurements is given in section **1.5**. Early studies of HMMCs concentrated on establishing general trends for metal, halogen, ligand and counterion, and involved the synthesis of most of the linear-chain complexes now known. More recently, the exact nature of the metal-halogen (MX) chain, notably its electronic structure and vibrational behaviour, has become the focus. Most of the attention has been paid to a relatively small number of linear-chain systems; the bulk of the experimental work has been carried out on the $[Pt(en)_2][Pt(en)_2X_2](ClO_4)_4$ (en = ethylenediamine, X = Cl, Br or I). The increasingly rigorous analysis that this has involved has uncovered the existence of various defect states, both intrinsic and induced. Assignment of these defects is essential for determining the processes that follow optical excitation of HMMCs (see section **1.4**). To exploit the expansion of the experimental field, theoretical modelling has become well established in the study of both electronic states and vibrational motions (see section **1.6**). As the balance of power in this field has shifted seamlessly from synthetic chemists through spectroscopists to physicists, so the terminology has moved with it to reflect the electronic and magnetic states of the linear chains. Complexes may be designated as Charge Density Waves (CDWs) or Spin Density Waves (SDWs); the charges and spin are those that appear on the metal centres. In the Robin and Day classification, these correspond to Class II and Class IIIB respectively. CDW species are divided into strong and weak types and they account for the majority of HMMCs, since the only SDW compounds are nickel linear-chain complexes containing 1R,2R-cyclohexanediamine.

1.2.2 Synthetic routes

There are three general methods for the formation of HMMC complexes:

(1) Partial oxidation of metal (II) species.

(2) Mixing of metal (II) and metal (IV) species (in equimolar amounts).

(3) Partial reduction of metal (IV) species.

The route that is the most effective depends on the exact nature of the HMMC, but a rough guide is given in Table 1.2.1. In some cases the description of the actual process occurring is a matter of semantics. For example, *trans*-$[Pd(NH_3)_2Cl_2][Pd(NH_3)_2Cl_4]$ is produced by the evaporation of a reaction mixture containing an excess of chlorine added to a suspension of *trans*-$Pd(NH_3)_2Cl_2$.[8] As such it is likely to involve the formation *in situ* of excess of palladium (IV), which is unstable to reduction in the absence of oxidant. Thus the process superficially follows route (1), but in reality may follow route (3).

Table 1.2.1 The various types of HMMC complexes and their synthetic routes

Metal (II)	Metal (IV)	Chain type	Route (1)	Route (2)	Route (3)
Ni or Pd	Pt	all		Only method	
Pt	Pt	ionic	For X = I only	For good crystals	Rare
		neutral	Reliable	Occasional use	Rare
Pd	Pd	all	Usual route		*in situ*
Ni	Ni	all	Only method		

The oxidising agent used most commonly in Method (1) is the corresponding halogen (X_2). Other reagents have been tried on occasion: ammonium persulphate has been used for making neutral chains,[9] while concentrated acids (sulphuric, perchloric or fluoroboric) have been employed in the synthesis of certain tetraammine species.[10-13] Simple crystallisation of solutions containing only a mixture of the constituent monomers of the HMMC is the usual form of method (2) when it is applied to neutral-chain complexes. In the syntheses of ionic chains, the counterion is usually present in excess in solution, added as either the acid or the salt.

1.2.3 Basic view of bonding and structure

The section on theoretical modelling (**1.6**) deals with the currently accepted views of the electronic structures of MX chains, but it is worth looking first at the simple atomic orbital interactions by way of introduction. The Group VIII metals (nickel, palladium or platinum) will be d^8 configuration for the M^{2+} state, and d^6 for the M^{4+} state. Figure 1.2.2 shows a crude approximation of the relative energies of the metal d orbitals, where the z-axis is taken as parallel to that of the chain.

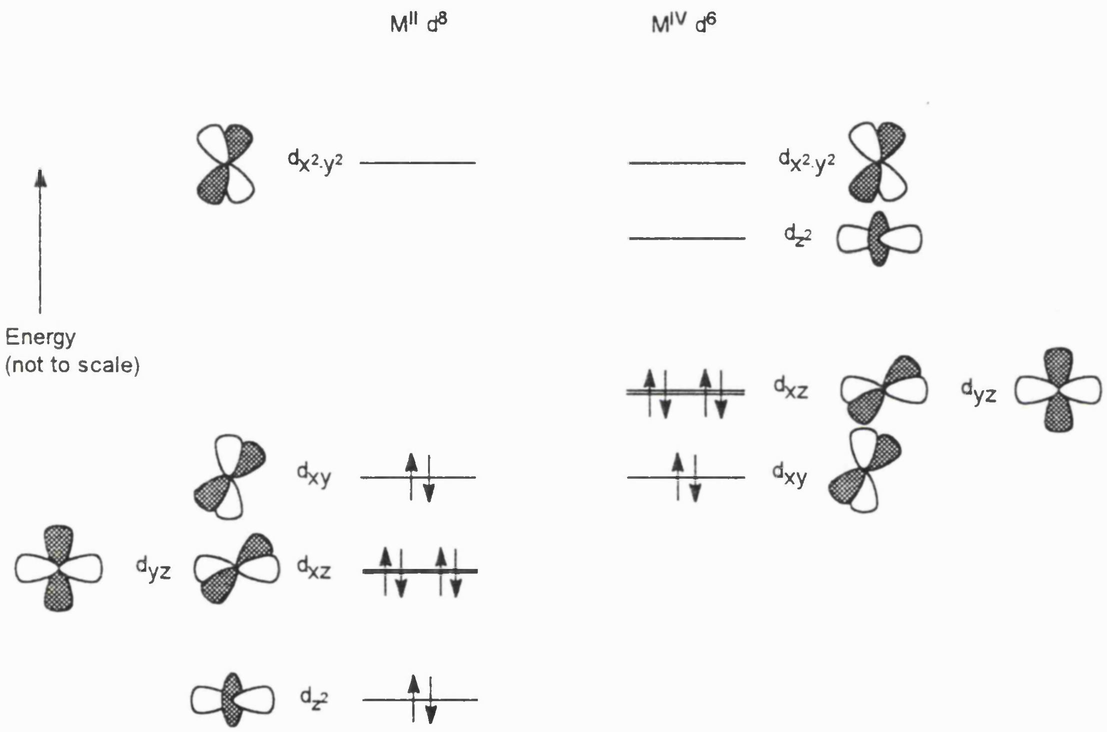

Figure 1.2.2 *Representation of the metal d orbitals. The metal (II) species has eight d electrons, and is square planar. The metal (IV) species has two electrons fewer, and has a distorted square planar structure. The d_{z^2} orbital is unoccupied in the oxidised species.*

The primary orbital overlap is between the d_{z^2} of the metals and the p_z of the halogens. In a unit cell of four chain atoms (see Figure 1.2.1), this corresponds to the interaction of three fully occupied orbitals (two p_z and one d_{z^2}) and one empty (M^{IV} d_{z^2}). The degree of bonding between the metal (II) site and the adjacent halogens is therefore assumed to be dependent on donation from the occupied M^{II} d_{z^2} to the empty M^{IV} d_{z^2}. In the Robin and Day classification the amount of donation corresponds to the value of α, *i.e.* the contribution to the ground state by the excited state following electron transfer. This ought to be reflected in the relative sizes of the bond lengths, r(M^{IV}-X) and r(M^{II}-X); the ratio of these values (ρ) has been used in the past as an indicator of the extent of charge delocalisation along the MX chain. To demonstrate the variation of ρ, there is a survey of structural data of HMMC complexes in section **1.3**.

1.3 Structural properties of HMMC complexes

1.3.1 X-ray crystallography

The HMMC crystal structures that have been published have helped to establish the main features of linear-chain complexes.[14] Most HMMCs can only crystallise in one form, either monoclinic or orthorhombic. There are a few complexes, *e.g.* $[Pt(en)_2][Pt(en)_2X_2](ClO_4)_4$ (X = Cl or Br), which exhibit two phases, with the one favoured depending on pressure [15] or temperature.[16] The ML_4 segments (see Figure 1.2.1) usually stack in an eclipsed conformation with no relative rotation. The net charge of the chain unit is determined by the identity of the equatorial ligands (L). If the net charge is zero there are no counterions and the structure is fairly simple (see Figure 1.3.1);[17] this chain type is termed neutral.

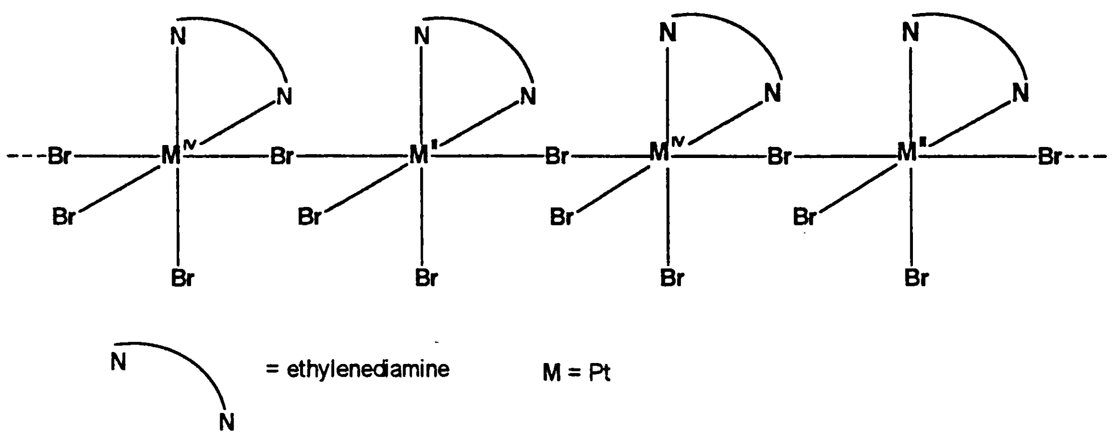

Figure 1.3.1 Representation of the structure of $[Pt(en)Br_2][Pt(en)Br_4]$

Little work has been done on the anionic chains (negative net charge), which have alkali metals as counterions. Most of the complexes that have been analysed are cationic chains, where the position and orientation of the negative counterions are dependent on the identity of the counterion and the ligand. For instance, perchlorate ions do not bond in the same manner to macrocyclic ligands as they do to ethylenediamine (en),[18-20] while the interactions of ClO_4^-, PF_6^- and HSO_4^- with en are all markedly different.[21] Some degree of two- or three-dimensional order can be imposed when these ions hydrogen-bond to more than one chain.

1.3.2 Trends in HMMCs

The effects of changing the components of HMMCs have been investigated and from them certain trends have been deduced.[14] These trends are based on the data of only a few complete series (change of metal, halogen, *etc.*), and on data that are not always reproducible; significant discrepancies have been observed on the reanalysis of some compounds. This is true for species that are hard to prepare, such as *trans*-$[Pt(NH_3)_2Br_2][Pt(NH_3)_2Br_4]$,[6,22,23] and for well-known entities, like $[Pt(en)_2][Pt(en)_2X_2](ClO_4)_4$ (X = Cl, Br or I).[16,24-27] There is no doubt as to the approximate structure of each HMMC, but the metal-halogen distance along the chain can vary from analysis to analysis, and so the size of ρ, which equals $r(M^{IV}\text{-}X)/r(M^{II}\text{-}X)$, is not uniquely defined. Despite the small sample size for two of the chain types, it is generally accepted that the distance $r(M^{II}\text{-}M^{IV})$ increases in the order:

cationic chain < neutral chain < anionic chain [14]

From the results known, the variation in ρ with halogen (X), metal (M) or counterion (Y) is plotted in Figures 1.3.2, 1.3.3 and 1.3.4 respectively.

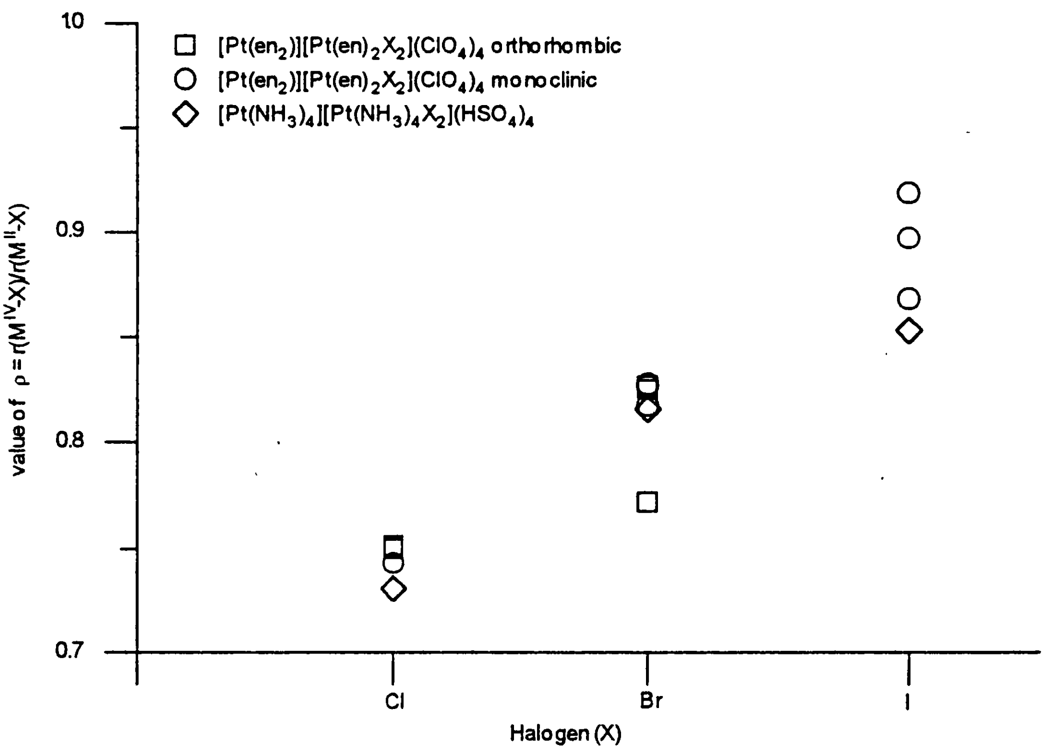

Figure 1.3.2 *A plot showing the variation in the value of ρ with halogen (X). There are only a few complete sets of data, and in some cases, several values of ρ have been reported. $[Pt(en)_2][Pt(en)_2I_2](ClO_4)_4$ only forms monoclinic crystals. Data are taken from references 10, 16, 21, 24, 25 and 28.*

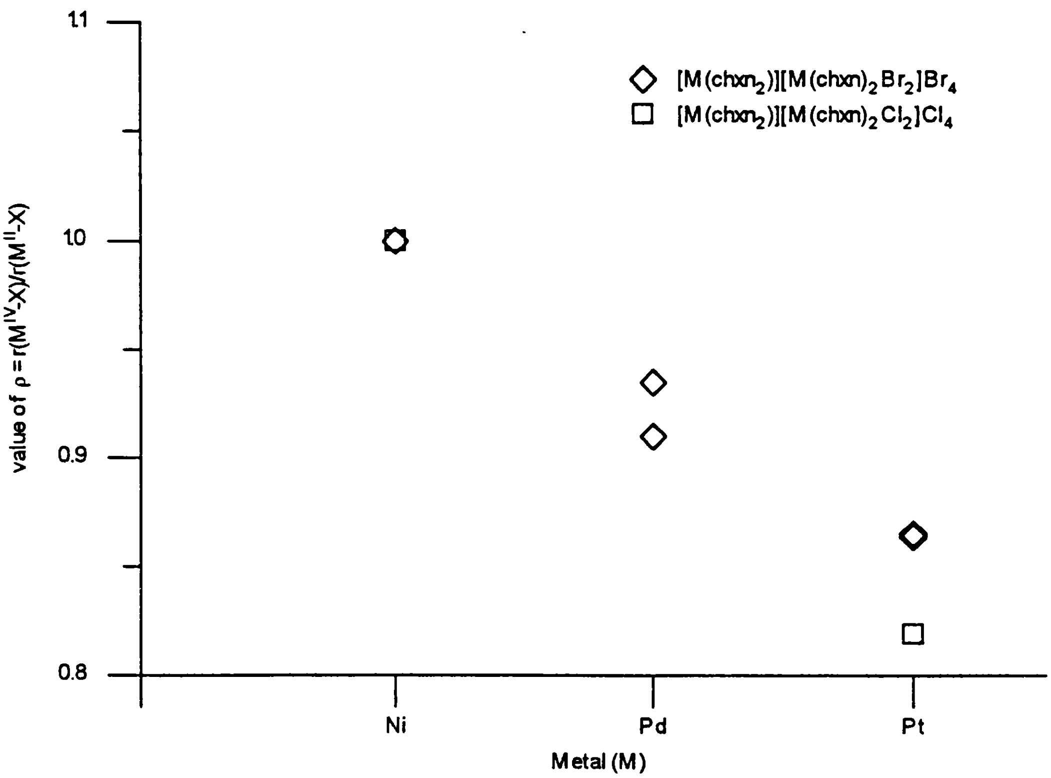

Figure 1.3.3 *A plot showing the variation in ρ with metal (M). Very few complexes of nickel or palladium have been analysed successfully by X-ray crystallography. Data are taken from references 29-32.*

Although few complete data sets exist for variation in metal or halogen, it can be stated that the value of ρ increases as M is changed from Ni → Pd → Pt or as X is changed from Cl → Br → I. The patterns seen in Figures 1.3.2 and 1.3.3 have often been equated with an increase in valence delocalisation in the order Pt < Pd < Ni for the metal and Cl < Br < I for the halogen.[14] Likewise the variation in ρ with counterion, depicted in Figure 1.3.4, has been tentatively ascribed to a change in the effective oxidation states of the metal centres.[33] The reasoning behind this is not clear. There is a hydrogen-bond interaction between counterions and ligands, and it depends on the identity of the L-Y pair, not just the counterion. The hydrogen-bonding may affect the physical structure of the chain without altering the electron distribution along the chain. Therefore delocalisation cannot be inferred solely from the value of the structural parameter ρ.

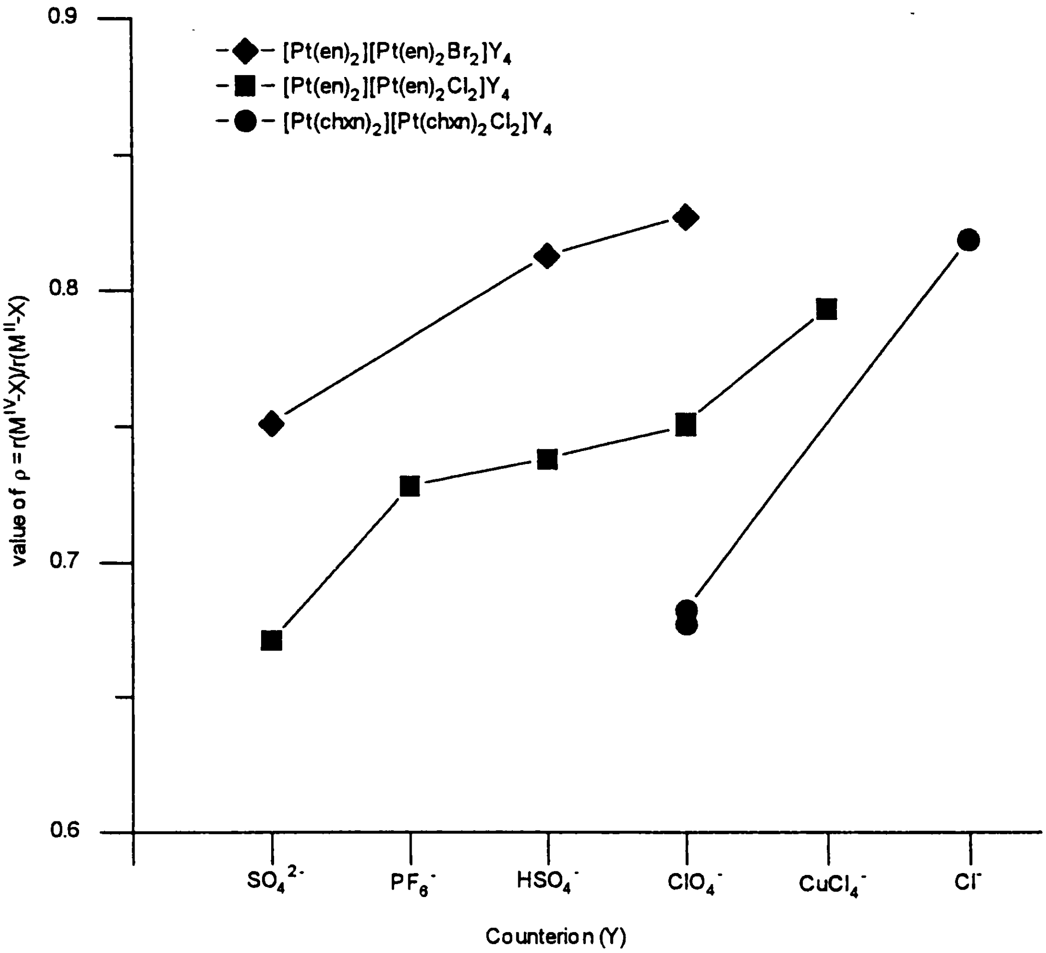

Figure 1.3.4 *A plot showing the variation in the value of ρ with counterion (Y) for three particular MX chain types. ρ is dependent on the interaction of Y with the ligands. Data are taken from references 21, 32 and 33.*

The supposed charge delocalising strengths of metals and bridging halogens can also be questioned. The scatter plot in Figure 1.3.5, which surveys the bond lengths $r(M^{IV}\text{-}X)$ and $r(M^{II}\text{-}X)$ in cationic chains containing Pt^{IV} sites, highlights several key points. The $r(M^{IV}\text{-}X)$ distance is reasonably constant for a given halogen, but there is wide variation in the $r(M^{II}\text{-}X)$ distance. Thus the ligand / counterion interaction affects only the position of the metal (II) site. The $r(M^{IV}\text{-}X)$ distance seems independent of the identity of the metal (II) site. $(M^{IV}\text{-}X)$ bonds in HMMCs are longer than those in the Pt^{IV} monomers, but the difference is similar for all halogens. Altering X alone changes $r(M^{IV}\text{-}X)$, but by an amount that can be related simply to the change in size of the halogen, rather than to any additional lengthening of the bond. By comparison, the mean value of $r(M^{II}\text{-}X)$ is not altered much by change of halogen, but the spread about the mean increases notably in the order I < Br < Cl. No direct relation between structure and delocalisation can be deduced from these observations.

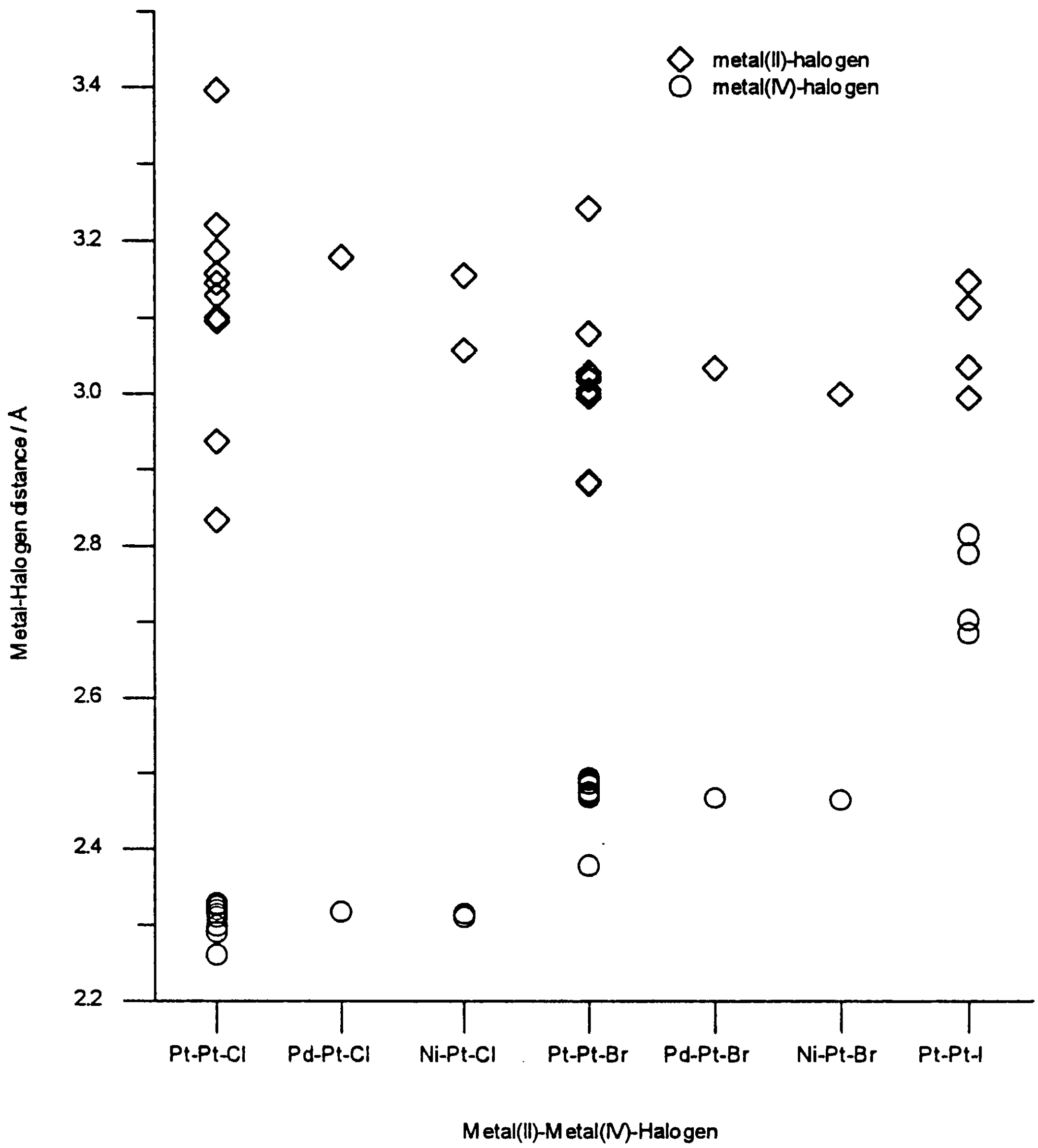

Figure 1.3.5 *A plot showing M^{II}-X (squares) and M^{IV}-X (circles) bond lengths for cationic chain complexes containing platinum (IV) sites. Data are drawn from references 10, 14, 16, 21, 24, 25, 29-31, and 33-35.*

1.3.3 Pressure, temperature and phase changes

The data displayed in section **1.3.2** are for samples grown and analysed at ambient pressure and temperature. The complex $[Pt(en)_2][Pt(en)_2Br_2](ClO_4)_4$ was found to crystallise in either monoclinic or orthorhombic form,[27] depending on the temperature of crystallisation.[36]

Subsequent investigations into this compound and into $[Pt(en)_2][Pt(en)_2Cl_2](ClO_4)_4$ have shown that the phase changes occur at around 29 °C and 19 °C respectively.[37,38] Above the given temperature, the complex will form orthorhombic crystals, below it monoclinic. The analogous iodide complex is found only in the monoclinic form.[15,24,25] Crystals of the bromide complex have been grown at high pressure to give a monoclinic product.[15] $r(M^{IV}\text{-}X)$ is smaller and $r(M^{II}\text{-}X)$ larger than in samples grown at ambient pressure, with a net reduction of $r(M^{II}\text{-}M^{IV})$ and hence of the b axis length (parallel to the chain). The a axis and c axis lengths are reduced by a greater amount, because the counterions pack more symmetrically at higher pressures. There has been report of a third phase in $[Pt(en)_2][Pt(en)_2Cl_2](ClO_4)_4$ which coexists with the normal CDW phase at pressures between 3 and 6 GPa.[39] It is thought to contain solitons (see section **1.4**), although this has not been confirmed. These structural results have an important bearing on experimental procedures. When complexes that exhibit a phase change are analysed by a technique sensitive to crystal structure (such as solid-state NMR spectroscopy), it is important to ensure that measurements are made at a temperature well away from a phase boundary.

1.4 Chain defects and excitation processes

1.4.1 Defect types

For the sake of simplicity, the ground-state charge distribution for the metal atoms along the chain is assumed to alternate between the values of +2 and +4. Certain defects, either mobile through the chain or trapped on a particular site may exist at higher energies. The simplest types are depicted in Figure 1.4.1, where halogens and bonds are ignored for brevity. They are split into two classes: simple charge alteration to a site (known as a polaron), and charge alteration followed by a change in phase (known as a kink). These are the basic units; all other defects are combinations of them.

②④②④②④②④②④	ground state	GS	④	metal with formal oxidation state
			❷	metal site out of sequence with 2-4 alternation

Polaron defects			Kink defects		
②④②④❸④②④②④	hole polaron	h^+	②④②④②❸❹❷❹❷	neutral kink	S^0
②④②④❹④②④②④	hole bipolaron	h^{2+}	②④②④②❷❹❷❹❷	negative kink	S^-
②④②④②❸②④②④	electron polaron	e^-	②④②④❹❷❹❷❹❷	positive kink	S^+
②④②④②❷②④②④	electron bipolaron	e^{2-}			

Figure 1.4.1 *The simplest types of defects are represented by showing the formal oxidation states of the metal centres. The black circles with white numbers denote states that are out of sequence with the periodic alternation between +2 and +4.*

1.4.2 Excitation process

The excitation process is concerned with Intervalence Charge Transfer (IVCT). A simple picture of this transition is shown in Figure 1.4.2. An electron is assumed to pass from the occupied d_{z^2} orbital of an M^{II} centre to the empty d_{z^2} orbital of an adjacent M^{IV} site, probably *via* the p_z of the bridging halogen atom. The excited state has an electron polaron and hole polaron next to each other, known as an "electron-hole" (e-h) pair. While this is not an exact description of what occurs (see section **1.6**), it emphasises one important point. The transition is polarised parallel to the chain; *i.e.* there is a net flow of charge along the chain axis. Hence linear-chain crystals will exhibit polarised behaviour in measurements relating to the IVCT process (see section **1.5**).

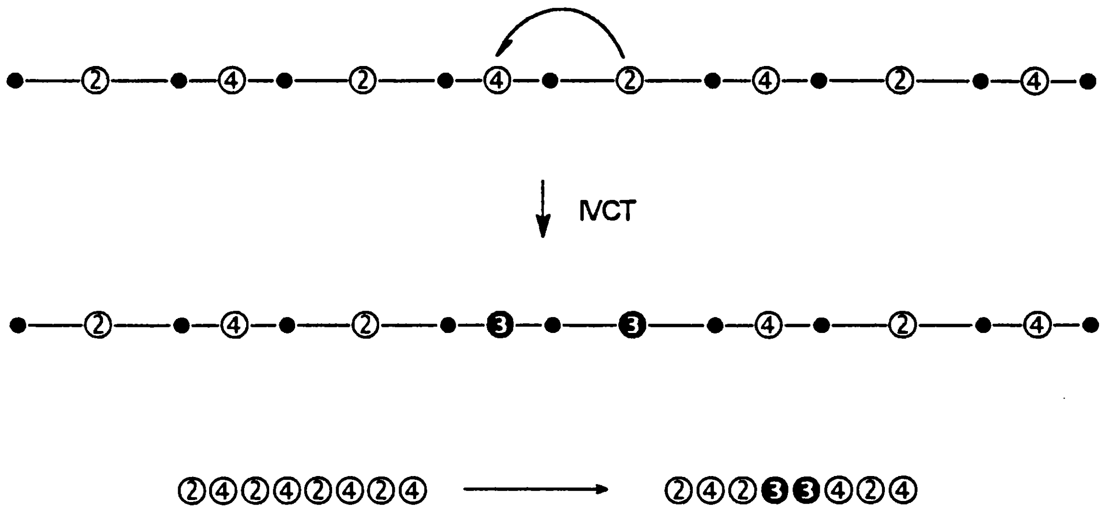

Figure 1.4.2 *A simple diagram showing intervalence charge transfer (IVCT). An electron is assumed to pass from the metal (II) site to the metal (IV) site via the p_z orbital of the interposed halogen.*

The real excitation process will be more complicated than this, because the molecular orbitals in HMMCs are predicted to be arranged in bands of energy (see section **1.6**). Promotion of an electron from a bonding orbital to an excited state is expected to produce a wave-like e-h pair that traverses the chain. The electron and hole have a mean separation that is governed by competition between inter-site like-charge repulsions and charge transfer integrals (see section **1.6.2**).[40] This "exciton" will relax to a self-trapped state by a distortion to the MX chain structure, which creates a new excited state at lower energy. The mean separation of electron and hole is now determined by competition between inter-site repulsions and electron-phonon coupling. When the former is dominant, the electron and hole are attracted so strongly that they will be adjacent, a state known as a "self-trapped exciton" (STX). An STX is luminescent and decays to the ground state releasing energy predicted to be about half that used to form the e-h pair.[40] Some non-linear relaxation processes for the STX that have been proposed are depicted in Figure 1.4.3.[41-43] In all of them, the electron density will fluctuate until the defect separation lowers the system to an optimum energy. The new configurations will give characteristic spectroscopic signals once they are "trapped" (see section **1.5**). For example, absorptions corresponding to further excitation from a trapped state will be observed in the optical spectrum. Excitons that form a separated electron-hole pair instead of an STX behave in a more straightforward manner. Once the lattice has relaxed, they become simple polaron pairs; no soliton formation is expected.

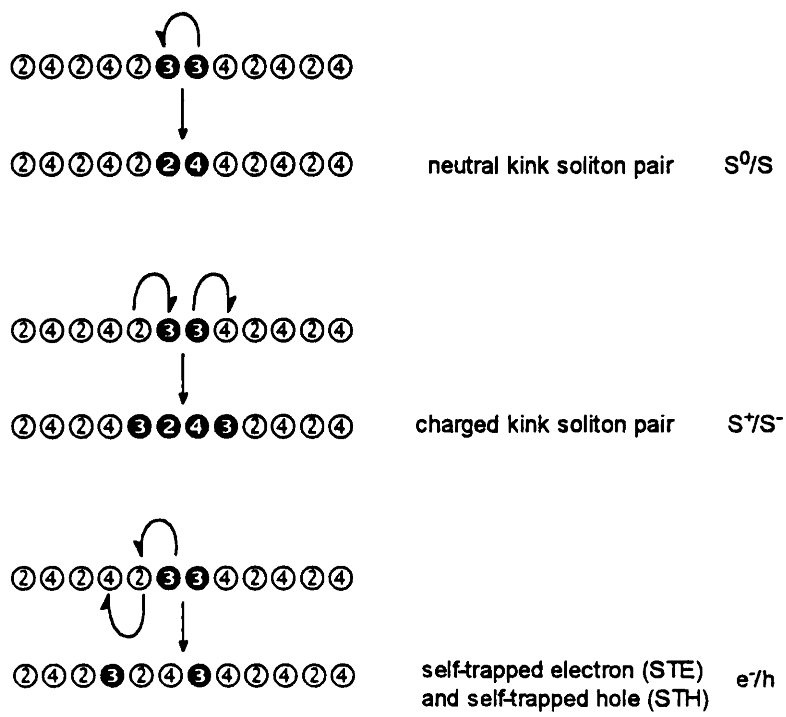

Figure 1.4.3 *Three possible non-linear relaxation processes for the self-trapped exciton (STX). The arrows represent the movement of single electrons.*

1.4.3 Defect occurrence and creation

A large amount of effort has gone into assigning the spectroscopic signals of the various possible defects. This is so that the ones that occur as a result of intervalence transfer can be determined, and so the excitation and relaxation processes of the HMMCs might be better understood. Even highly crystalline linear-chain complexes will contain naturally a small number of defects. The concentration has been related to crystal segment length. In $[Pt(en)_2][Pt(en)_2I_2](ClO_4)_4$ it was found to be about 1 in 10^4, which represents a mean separation of defects of about 10 μm, roughly the same as the segment length found in the crystal.[44] There are established techniques for the artificial creation of defects. An obvious method is photoexcitation, given the processes involved in relaxation. The energy of the exciting line will determine the separation of single defects, and therefore the most likely method of decay. At high energies, excited states with large numbers of defects might be produced. An alternative method is chemical induction of defects. In theory, this can be achieved by changing any of the HMMC components, although only substitution of metal or halogen has been tried. Gold (III) has been introduced in small concentrations into a PtCl chain to give a compound that has absorptions in the visible range corresponding to defect excitation signals that are greatly enhanced.[45] Neither copper-doped complexes, in which the amount of dopant is much higher than in the gold system,[46-48] nor the M_a^{II}-M_b^{IV} HMMC species (M_a = Ni or Pd, M_b = Pt) where the ratio of M_a to M_b is 1 : 1,[34,35,49-53] have been investigated in this regard. Mixed-halide compounds have been studied extensively. Experiment and theory have been applied to the complexes $[Pt(en)_2][Pt(en)_2X_{2-2\alpha}X'_{2\alpha}](ClO_4)_4$ ($X \neq X'$). It has been suggested that the chains are made up of phases containing only one type of halogen.[38,54-56] It is predicted that a given defect will be sited preferentially in one of the two phase types (MX or MX') depending on its charge.[57-61] The largest charge separation across phase boundaries is predicted for X = Cl, X' = I.[62,63] The study of the influence of counterions and ligands has previously been limited to the template effect described in section **1.3**. A further method for defect creation involves the infusion of halogen gas (chlorine or iodine) into crystals, causing extra hole polarons.[64]

1.5 Experimental methods and results

A large variety of analytical techniques have been applied to HMMC complexes, with those of greatest interest probing some property of the excited state. The following sections summarise the majority of the results recorded for systems similar to those examined in this thesis, namely cationic or neutral platinum HMMCs.

1.5.1 Electronic spectroscopy

HMMC complexes are intensely coloured, unlike their constituent monomers, and so optical absorption studies have long been an area of interest. Many of them have been analysed either by diffuse reflectance from powdered samples [65-67] or by transmission through pressed discs.[14,68] More recently, samples have been analysed as single crystals in preference to powders, because absorption polarised perpendicular to the chain has sufficient intensity to mask the position of the IVCT signal.[66,69] The first polarised single crystal absorption spectrum recorded was that of $[Pt(NH_3)_4][Pt(NH_3)_4Cl_2]Cl_4.4H_2O$.[66] Assignments of the major signals were made from the complexes $[Pt(en)_2][Pt(en)_2X_2](ClO_4)_4$ (X = Cl or I).[69] For incident light perpendicular to the chain axis ($E \perp b$), there are three main peaks, Q, α and β where $E_Q < E_\alpha < E_\beta$. Q is in the same range as the broad peak originally attributed to the IVCT in disc samples, but it is now assigned as $Pt^{IV}(d_{z^2}) \leftarrow Pt^{II}(d_{xz}, d_{yz})$. For E // b, the main absorption edge (P) has energy E_{CT} and is ascribed to intervalence charge transfer (IVCT). The P edge is usually in the visible range, so the widely held association between the colour of HMMCs and the IVCT is justified (see section **1.4**). To the high energy side of E_{CT} there is a very broad band, and this is thought to be due to mixing between the exciton level and the electron-hole continuum.[70] The P-edge energy values from various single-crystal studies are shown in Figure 1.5.1. The onset of the absorption edge is sharper at lower temperatures. E_{CT} increases as the temperature is reduced or as the halogen is changed from I to Br to Cl. Applying hydrostatic pressure to crystals during measurement shifts the P edge to lower energies. The relation between E_{CT} and counterion does not reflect the value of ρ.

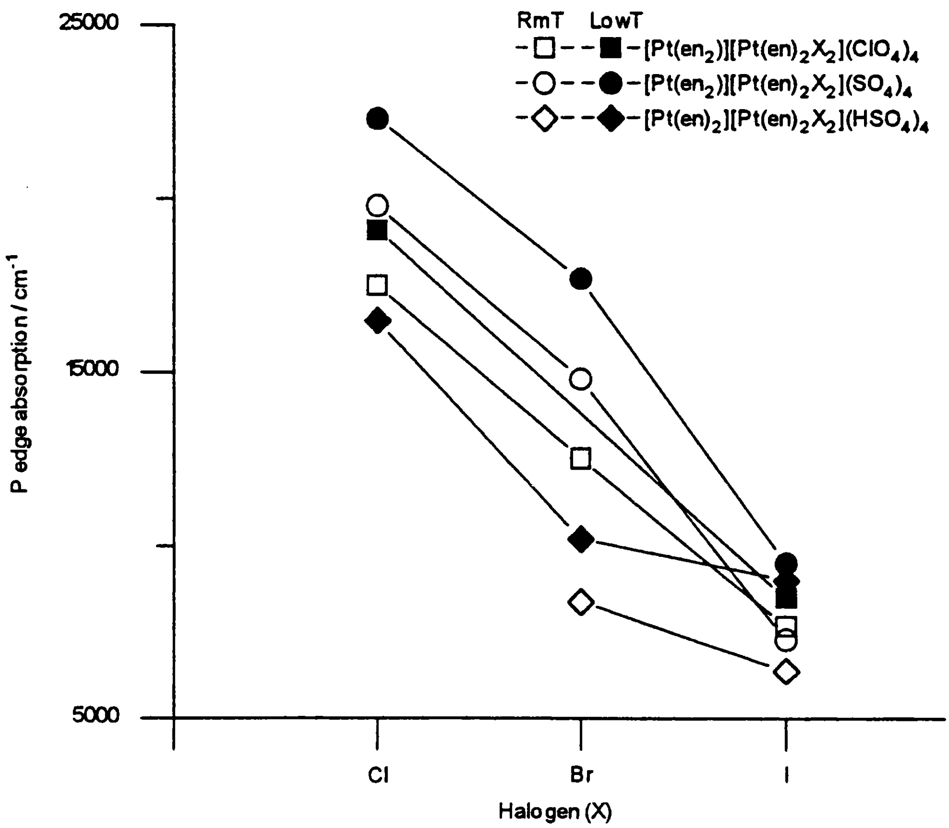

Figure 1.5.1 *A plot showing the observed P edge absorption energies for three MX systems. The low temperature data (filled shapes) were recorded at temperatures between 2 and 5 K. RmT refers to room temperature data (open shapes). Results are taken from references 21, 69, 71 and 72.*

There are four weak signals that can appear on the low energy side of the P edge. They have been assigned the labels A to D, inclusive, in order of discovery (but not in order of energy since $E_C < E_A < E_B < E_D$). The A and B bands occur at about 70 % and 85 % of the IVCT energy respectively, and A has the greater intensity. Both bands are more prominent in gold (III)-doped complexes,[45,73] or halogen-doped crystals,[64] than in uncontaminated chains. The A and B bands are enhanced by photolysis, with size increasing linearly with length of radiation time for small values, before tending to a limit;[74,75] recently the dependence of the peak intensities has been determined as $\sqrt{N}$ (where N is the number of photons).[76] A and B decay after photolysis ceases unless the irradiated sample is kept at a temperature low enough to make the defects fairly stable. The defects can be reversibly destroyed and created by annealing (warming) and irradiating, respectively. Defect creation requires a wavelength with energy greater than E_{CT}; the larger the energy, the more intense A and B become.[74,75] The C band is much weaker and is in the near infrared region.[76,77] The energy of the D band lies between E_B and E_{CT} but it is so weak that it is often smothered by the IVCT signal.[73,78,79] The identity of the defect state(s) that cause the A and B absorptions has remained unresolved. There have been two proposals. The first attributes these peaks to the excitation of solitons, formed as a result of exciton relaxation.[45,80] The energy of the neutral kink species is predicted to fall in the appropriate range,[81] and the defect was shown to be uncharged by a recent photoconduction experiment.[79] The second model was developed because the A and B have different intensities,[74] which is thought to require a defect with spin and charge.[75] Solitons have either one or the other but not both, and so A, B and C have been explained quantitatively with a polaron model. The absorptions for electron and hole types differ slightly in energy.[77] An ultrafast optical response study appears to confirm this analysis.[82] Reflectance measurements have been less extensive, although some single-crystal studies have been undertaken.[66,83,84] Reflectance has been more usefully employed in the far infrared region, where phonon modes occur, than in the visible.[65]

1.5.2 Conductivity

The conductivities of HMMCs have been measured in two ways. Polycrystalline pellets [85,86] or single crystals (four-point analysis) have been analysed.[62] Platinum linear-chain complexes are semiconductors, typical of Class II mixed-valence species. Conductivity along the chain, $\sigma_{//}$, is generally two to three orders of magnitude greater than that perpendicular to it, $\sigma_{\perp}$. $\sigma_{//}$ follows similar trends to the IVCT edge energy regarding change of halogen or metal.[85] Application of pressures in excess of 100 kbar has been shown to increase chain conductivity by as much as 10^9, but $\sigma_{//}$ tends to a limit so that the chains do not reach a metallic state.[86] Doping halogen molecules into crystals can enhance conductivity along the chain, but it has far more effect on $\sigma_{\perp}$, so much so that it becomes greater than $\sigma_{//}$.[62] The drift mobilities for hole and electron polarons have shown that the halogen acts as an inter-chain bridge for holes alone.[87]

1.5.3 Luminescence

The self-trapped exciton (STX) described in section **1.4** is luminescent. A polarised single-crystal study on the emission band it produces (L band) was carried out first on Wolffram's Red.[67] Luminescence is z-polarised and is known to result from a localised interaction because the shape of the observed peak is Gaussian. The energy of the L band is only about 50 % of that of the IVCT edge, but it has similar metal and halogen dependencies.[88] The intensity of the L band falls away with increase in pressure,[89] because the energy required for the exciton to separate, and thereby relax by some other route, is reduced. The energy of the exciting radiation is known to alter both peak position and intensity.[16,90] As the excitation wavelength is shortened, the L band gains intensity and moves to higher energy, tending to a limit in both cases. Time-resolved studies have shown the lifetime of the luminescent state to be of the order of 100 ps for PtCl complexes.[91,92] Because this is significantly shorter than that calculated for a free (untrapped) exciton, non-radiative processes must determine the rate of decay of the excited state. There is a separate, broad unstructured emission (the B band, unrelated to the B absorption) which occurs at higher energy than the L band, and has an associated lifetime of less than 7 ps.[92] This band is produced as a result of the recombination of electron and hole as the excited free state relaxes to the STX.

1.5.4 Resonance Raman spectroscopy

In luminescence experiments there are discrete emission peaks in addition to the L and B bands that occur at energies approaching that of the exciting radiation.[67] When the energy of this radiation is greater than E_{CT}, these peaks form a progression of evenly spaced signals whose intensity increases towards the exciting line. The lifetime of the excited state that causes them is less than 7 ps, *i.e.* much shorter than that for the STX.[91] Resonance Raman (rR) theory indicates that they arise from decay of the excited state to various vibrational levels of the electronic ground state.[93] Strong enhancement is predicted for totally symmetric modes within the threshold of the rR condition. The high energy emission lines are z-polarised, so it is generally accepted that the periodic signals seen in HMMC complexes are due to the fundamental breathing mode (v_1) and its overtones.[14]

HMMCs have been studied by resonance Raman techniques in their own right for several years.[14] As for other analytical methods, the single crystal has become the preferred state for the analysed sample instead of a polycrystalline substrate. The improvement in resolution that came with single-crystal analysis (and the use of chilled samples) enabled the true structure of the ν_1(PtCl) mode to be revealed (see section **1.5.5**).[94] ν_1 is dependent on the exciting line, ν_0, when in resonance, both in its structure and in its wavenumber.[95,96] The dispersion of ν_1 over a given range of excitation energy increases in the order Cl < Br < I. Excitation profiles have been measured for disc samples by determining the intensity of the ν_1 mode against that of an internal standard,[95-99] but attempts to correlate them with electronic spectra of powders have failed because of the erroneous assignment of the IVCT band in the latter.[66,69] Overtone progressions in the spectra of pellets extend further and are more intense than in those of single crystals. Therefore even comparisons of ν_1 values between complexes containing the same metal and halogen are not particularly useful. The effect of changing the bridging halogen or the metal is even more complicated, because the dynamics of the chain will be affected primarily by the alteration of masses and related force constants (see section **1.6.5**). Characteristic frequency ranges can be determined for particular metal-halogen combinations, but no relation to delocalisation can be deduced.[14] The value of ν_1 is affected by temperature, but not pressure. ν_1 is shifted to larger wavenumber by increasing the temperature,[100] while a hydrostatic pressure study has found little change in ν_1 up to 3 GPa.[79] Where a phase boundary is crossed, there is often a discontinuity in the ν_1 value.[37-39]

The electronic spectra of HMMCs contain several peaks besides the P absorption edge. The bands A-D are distinct from this edge and provide a separate range of excitation frequencies through which linear-chains show resonant behaviour. For example, there are three peaks in $[Pt(en)_2][Pt(en)_2Cl_2](ClO_4)_4$ which are enhanced by exciting lines in this range (see Figure 1.5.2).[101-103] They have been assigned provisionally to the localised vibrations of three polaron defects: electron polarons (e^- or p^-) at 263 cm^{-1}, electron bipolarons (e^{2-} or p^{2-}) at 272 cm^{-1} and hole polarons (h^+ or p^+) at 287 cm^{-1}. Similar defects have been observed in $[Pt(en)_2][Pt(en)_2Br_2](ClO_4)_4$, although only electron polarons and bipolarons have been confirmed, at 150 cm^{-1} and 130 cm^{-1}, respectively.[48,104] Peaks found at 174 cm^{-1} and

182 cm^{-1} have been suggested for the hole polaron mode. Resonance Raman studies have shown that defects are more common in orthorhombic crystals of $[Pt(en)_2][Pt(en)_2Br_2](ClO_4)_4$ than they are in the monoclinic ones.[105]

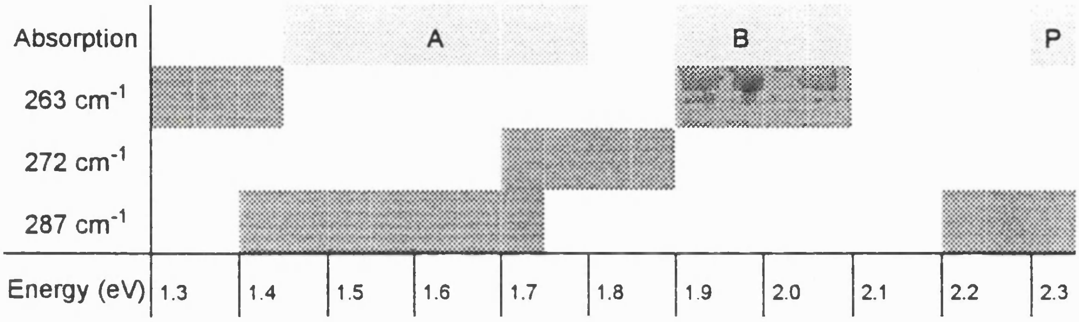

Figure 1.5.2 Representation of the enhancement ranges of the three defect modes compared with bands observed in the absorption spectra.[101-103]

Photolysis generally increases the intensity of defect modes, although if there is a high concentration of electron polarons they may combine to form bipolarons. Photolysed defects are not permanent and can be removed by annealing.[106] The models outlined in section **1.6** have been used to predict the positions of the polaron signals for HMMC species, with variable success. There are other weak modes that occur naturally in HMMC resonance Raman spectra besides polaron signals, and assignment of them has raised concerns over the purity of HMMC samples.[38,107] This is because the positions of the weak signals match some of the many bands found in the resonance Raman spectra of mixed-halide compounds.[46] Interest in the mixed-halide complexes has grown from the belief that they exist as block copolymers, with few units of $[BrPt^{IV}Cl]$ in the chain.[38,108] Photoabsorption is expected to result in charge separation across the phase boundary between halide segments.[55,58] Electron polarons are predicted to be located preferentially in the segment containing the halide with greater electronegativity, with hole polarons in the less electronegative section.[56,58,59]

1.5.5 Vibrational spectroscopy

Because there are so many peaks in some HMMC electronic spectra, it is a question of semantics whether Raman spectra are considered to be resonance or not. For a defect free chain, excitation energy smaller than E_{CT} will result in normal Raman scattering for the ν_1

mode. The nature of the splitting in ν_1 has been investigated both by Raman [109-111] and infrared [109,111,112] spectroscopies, and is considered in more detail in section **1.6.5**. Ligand modes exhibit normal scattering, and have been probed at low temperature. $[Pt(en)_2][Pt(en)_2Cl_2](ClO_4)_4$ has been analysed around its phase transition temperature,[113] with a large change in the ν(C-H) modes observed between orthorhombic and monoclinic phases; little alteration is seen in ν(M-N) or δ(N-C-C-N). This implies that phase transition mainly involves a modification of the methylene-perchlorate interactions. The hydrogen-bonding of the H-(N) atoms in certain HMMCs has been examined by infrared spectroscopy.[114] The separation of ν(N-H)-Pt^{II} and ν(N-H)-Pt^{IV} is found to correlate well with ρ. The C band can be observed in the near infrared range at around 3500 cm^{-1}.[115,116] Reflectivity experiments in the far infrared have revealed that in addition to the stretching modes ν_1, ν_2 (the asymmetric halogen stretch) and ν_3 (the anti-phase motion of $M^{IV}X_2$ units against the M^{II} centres), HMMCs exhibit chain-bending modes.[63,73,117-118]

1.5.6 Electron spin resonance spectroscopy

There should be no unpaired electrons in a "normal" chain with formal M^{II} and M^{IV} sites, but when there are defects present which possess spin, then a signal will be observed in the electron spin resonance (ESR) spectrum. Polarons and neutral solitons have spin, but charged solitons do not. Initial ESR studies of $[Pt(en)_2][Pt(en)_2X_2](ClO_4)_4$ (X = Cl, Br or I) indicated the presence of platinum $5d^7$ electrons.[44] The unpaired spin concentration varies from 1.1 x 10^{20} to 2.1 x 10^{20} mol^{-1} as X is changed from I to Cl, which equates to one unpaired electron (UPE) per 10^4 platinum atoms, or a mean separation of UPEs of 10 μm. Unlike conductivity, defect concentration is not temperature dependent, which means that the UPEs are trapped and play no part in conduction. Analysis of crystals has shown them to be composed of segments about 10 μm in length, and so the ESR results are consistent with defects occurring at the segment edges.

The structure of the ESR spectrum is dependent on the identity of the halogen. A single-line spectrum is seen when X = I or Br, although the bromide exhibits superhyperfine structure at 10 K.[76,105] The most complex spectrum is that of the chloride, which shows both hyperfine and superhyperfine couplings.[44,73,119] Neither coupling is due to ligand interactions, because samples containing pure $^{15}N_2$-ethylenediamine give spectra that are almost identical to those for pure $^{14}N_2$- ligand.[120] The hyperfine splitting is consistent with an unpaired electron spanning two platinum centres that have nuclear spins of I = 0, ½ or 1.[121] The bridging halogens cause the superhyperfine splitting.[120] To model the bromide spectrum, the UPE must be spread over ten or more Br atoms.[105] The UPE in $[Pt(en)_2][Pt(en)_2Cl_2](ClO_4)_4$ is more localised, and two possibilities have been offered for its structure. The first is a neutral soliton,[119,122] which will not contribute to the conductivity of the chain.[44] Two possible configurations arise as the electron moves along the chain (see Figure 1.5.3).

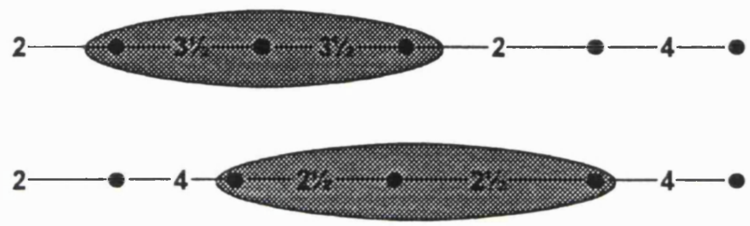

Figure 1.5.3 *Diagram showing the electron distributions of the neutral soliton, as deduced from ESR measurements. The black circles represent the halogen atoms, while the numbers denote the effective oxidation states of the metal sites in the chain.*

The alternative is an electron-hole pair,[120] suggested because the hole-rich complexes doped with halogen gas have a very similar ESR signal.[62] There are several possible distributions, all of which are spread over five metals and four halogens, with a node on the central platinum. The intensity of the signal is reduced when halogen doping is heavy,[62] and this is attributed to the production of spinless bipolarons.[76] Photolysis with energy greater than E_{CT} increases the ESR signal.[73,122] The extra UPEs produced are not stable at room temperature, although they can be maintained at 77 K.

1.5.7 Nuclear magnetic resonance spectroscopy

HMMC complexes decompose in solution. Solution Nuclear Magnetic Resonance (NMR) spectra contain peaks relating to the constituent monomers or monomeric ions alone, and so it has been used little, save to detect impurities.[38] Few complexes have been examined by solid-state NMR spectroscopy either. The ^{13}C nuclei in neutral-chain platinum complexes of thioureas were analysed in 1983,[123] and there have been two subsequent studies probing the same nuclei concerning the nickel or palladium HMMCs of 1R,2R-cyclohexanediamine.[30,124] ^1H relaxation time experiments have been carried out for the palladium compound. The only solid-state ^{15}N or ^{195}Pt NMR studies are those that appear in this work.[125-127] The solid-state NMR technique is considered more fully in Chapter **2**.

1.5.8 Other techniques

Many techniques have been employed in studies of HMMCs, several of which have been applied only rarely. Third-harmonic generation measurements are a recent innovation, probing the two-photon excitation that leads to the optically forbidden exciton.[128-130] X-ray photoelectron spectroscopy (XPS) has been used to examine the orbital energies of the metals in $[M^{II}(en)_2][Pt^{IV}(en)_2X_2](ClO_4)_4$.[131-133] For the $[Pt^{IV}Cl_2]$ segments, the energy of the $4f_{7/2}$ level is slightly lower in the chain than it is as a monomer for M = Pt, but not for M = Ni or Pd. For a given metal combination, the $4f_{7/2}$ binding energy in the chain decreases in the order Cl > Br > I. The same systems have been studied by EXAFS, to show that in the mixed-metal systems there are no Pt^{II}, Ni^{IV} or Pd^{IV} centres.[134] The structural phase changes in $[Pt(en)_2][Pt(en)_2X_2](ClO_4)_4$ (X = Cl or Br) have been analysed by Differential Scanning Calorimetry (DSC),[36,38,135] or pulsed neutron diffraction.[136]

1.6 Models of HMMC complexes

1.6.1 Early models

One of the simplest models of MX chain electronic structure is that described in the Robin and Day classification, outlined in section **1.1.2**. This was improved by Piepho, Krausz and Schatz (PKS) to create a vibronic coupling model,[137] with similar basic valence states, namely:

$$\Psi_a = \psi_A^m \psi_B^n \quad \text{and} \quad \Psi_b = \psi_A^n \psi_B^m \qquad [1.6.1]$$

These are used to define a pair of potential energy surfaces, $E_{1,2}$, such that:

$$E_{1,2} = h\nu[\tfrac{1}{2}q^2 \mp \sqrt{\varepsilon^2 + (\lambda q + W)^2}\,] \qquad [1.6.2]$$

where ε is the electronic coupling coefficient, W is the zero point energy difference between the two states, ν is the fundamental vibrational frequency associated with the normal coordinate q, and λ is proportional to the value d defined in Figure 1.6.1.

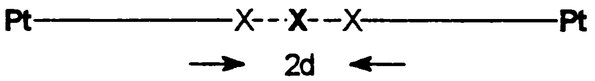

Figure 1.6.1 The distortion parameter, d, is defined as the distance between the real position of X and the theoretical midpoint position, ***X***.

This model has been used to study a theoretical single unit cell of Wolffram's red (WR), $[Pt(etn)_4][Pt(etn)_4Cl_2]Cl_4.4H_2O$.[138] WR is taken to be symmetrical, *i.e.* W = 0. The energy levels E_1 and E_2 are calculated and used to predict the resonance Raman spectrum. Experimental peaks can be reproduced qualitatively, but the values of λ and ε required make the calculated value of d (d_{calc}) too small. d_{calc} is only sufficiently large when W is non-zero, and even then no unique set of ε, λ and W can be defined. The PKS model is inadequate because it is based on discrete mixed-valence units. A more appropriate model is required for linear-chain complexes, such as that used by Whangbo, who perceived a similarity between transition metal polymers and organic ones such as *trans*-polyacetylene (TPA).[139] In the TPA model, each atom contributes one π electron, and adjacent pairs form the bonding (π) or antibonding (π^*) orbitals shown in Figure 1.6.2. Chain molecular orbitals (MOs) are then constructed from combinations of the π or π^* orbitals. There are two possible extremes, the alternant (A) and the regular (B) (see Figure 1.6.2).

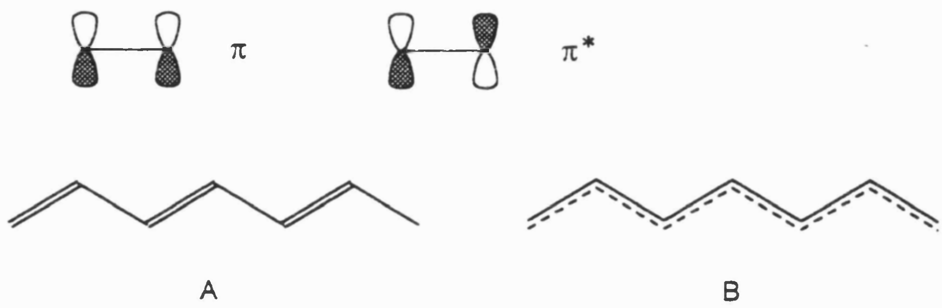

Figure 1.6.2 *A depiction of the bonding (π) and antibonding (π*) orbitals used to construct the π molecular orbitals of trans-polyacetylene, and the two theoretical extremes that result: the alternant system (A) and the regular system (B).*

In both systems, the energies of the MOs range from π all-in-phase up to π* all-in-phase. In the regular system the MOs form a continuous half-filled band, while in the alternant system there is a gap between the π and π* orbitals. The gap exists because the periodic electron density means that the difference between π and π* energies is greater than that between in-phase and out-of-phase pairs. The π band is full while the π* band is empty, and there is the possibility of electron transfer between the two across the energy gap. Representations of the MOs in the two systems are shown in Figure 1.6.3.

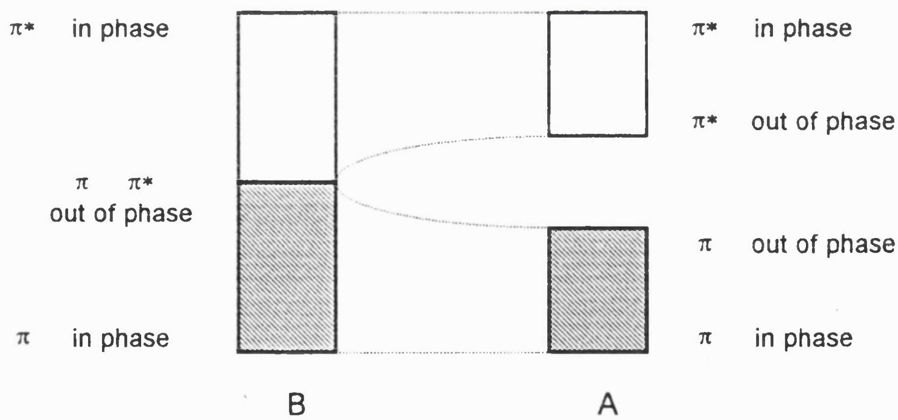

Figure 1.6.3 *A representation of the band orbitals for the alternant (A) and regular (B) chain systems. The shaded areas show the extent of electron population.*

Whangbo and Foshee managed to relate HMMCs to the alternant species (A), and applied a tight-binding scheme based on the extended Hückel method to an approximate model of the WR cation $[Pt(NH_3)_4][Pt(NH_3)_4Cl_2]^{4+}$.[140] The platinum d_{z^2} orbitals along the chain are combined in similar fashion to the carbon p orbitals in TPA. The HMMC equivalent of system B is constructed from unit cells of the d^7 ion $[Pt^{III}(NH_3)_4Cl]^{2+}$, which contribute one electron each. The energy levels of the molecular orbitals they form comprise a half-filled band like that in TPA. As in system A, this band is split into two by the periodic distortion along the chain. The upper band is mainly $d_{z^2}^{IV}$ in character with some $d_{z^2}^{II}$ mixed in and the lower band is complementary. Total energies for the model were calculated as a function of the parameter d. The minimum was at a value of d close to that found experimentally.

1.6.2 Nasu model

The simplest Nasu model is a one-dimensional metal, with N sites and N electrons, at absolute zero.[141] This is unstable to two interactions, which are considered separately at first. Electron-electron (e-e) repulsion makes electrons occupy different sites, which they will do with spins opposing, creating a Spin Density Wave (SDW). Electron-phonon (e-p) interaction creates a Peierls type lattice distortion, which raises and lowers the site energy alternately along the chain. Two electron occupancy of the low energy sites is then favoured, and a Charge Density Wave (CDW) results. Since both e-e and e-p effects coexist in real systems, it is important to determine which of the two density waves prevails under given conditions. A model Hamiltonian which takes both effects into account is generated for a one-dimensional crystal with N electrons and N lattice sites. This has the generalised form:

$$H = -T\sum_{k,\sigma}(C^*_{k,\sigma}C_{k+1,\sigma} + C^*_{k+1,\sigma}C_{k,\sigma}) + U\sum_{k} n_{k,\uparrow}n_{k,\downarrow} + V\sum_{k,\sigma,\sigma'} n_{k,\sigma}n_{k+1,\sigma'}$$

$$+\sqrt{S}\sum_{k,\sigma} Q_k n_{k,\sigma} + \tfrac{1}{2}\sum_{k}(-\omega^2\frac{\partial^2}{\partial Q_k^2} + Q_k^2) \qquad [1.6.3]$$

$$\text{where } n_{k,\sigma} = C^*_{k,\sigma}C_{k,\sigma}$$

In each summation, k denotes the number of the site. The factor $C_{k,\sigma}$ ($C^*_{k,\sigma}$) is the creation (annihilation) operator of an electron at site k with spin σ. Q_k represents the coordinate of a site-localised phonon mode with frequency ω; for HMMCs this is the symmetric stretch ν_1. The five terms and their energy coefficients are summarised in Table 1.6.1. The most important assumption made in assembling this Hamiltonian is that bond charge interactions, as opposed to on-site ones, are negligible. The inclusion of bond-bond and bond-site terms does not change significantly the predicted behaviour of the N-site systems.[142] Prior to the Nasu model there had been some discussion surrounding the omission of bond charge effects from Hubbard-type calculations.[143]

Table 1.6.1 Composition of the five terms in the Nasu Hamiltonian in Equation [1.6.3]

Term	Description	Factor	Description
First	KE of electron in unperturbed band	-T (<0)	Energy of transfer of electron between neighbouring sites
Second	Short-range intra-site e-e interaction	U (>0)	Intra-site repulsion energy
Third	Inter-site e-e interaction	V	Inter-site repulsion energy
Fourth	Short-range e-p interaction	S (>0)	e-p coupling energy
Fifth	Energy of Einstein phonons	-	-

Early work on the Nasu model [40,67,68,144,145] was confined to the limiting case of the adiabatic approximation, which allows the kinetic energy of the phonon to be ignored:

$$\omega << T, U, S \qquad [1.6.4]$$

The energy coefficients may be replaced with dimensionless equivalents: $h \equiv H/2T$, $u \equiv U/2T$, $v \equiv V/2T$, $s \equiv S/2T$. The phonon mode coordinate is also replaced: $q_k \equiv Q_k/\sqrt{S}$. The Hamiltonian is then rewritten as:

$$h = -\sum_{\sigma}\sum_{|j|\leq\pi} e_j C^*_{j,\sigma} C_{i,\sigma} + u\sum_{k} n_{k,\uparrow} n_{k\downarrow} + v\sum_{k,\sigma,\sigma'} n_{k,\sigma} n_{k+1,\sigma'} + s\sum_{k,\sigma} q_k n_{\sigma} + \tfrac{1}{2}s\sum_{k} q_k^2 \qquad [1.6.5]$$

$$\text{where } C_{j,\sigma} \equiv N^{-1/2}\sum_{k} e^{-ijk} C_{k,\sigma}, \quad e_k \equiv \cos(k)$$

The calculation may be further simplified by replacing the $n_{k,\sigma}$ and q_k terms with their mean values and fluctuations therefrom ($\delta n_{k,\sigma}$ and δq_k). When Mean Field Theory (MFT) is applied, the terms $\delta n_{k,\sigma}$ and δq_k are ignored so that new expressions are obtained for the energies of the CDW and SDW states, allowing the more stable to be determined for a particular S-T-U-V combination. V is always smaller than U, so it can be omitted to simplify the model further.[141] The favoured state for each ratio of S : T : U is displayed as an S-T-U triangle (see Figure 1.6.4). The relative sizes of S, T and U at any point are found from the lengths of the perpendiculars dropped from the point to the subtense of the corresponding vertices. The SDW-CDW boundary is essentially at U=S (*i.e.* the line TN). The phases SDW(CDW) and

CDW(SDW), formed by the boundaries TNP and TNS respectively, are metastable. That is to say in the case of SDW(CDW) the CDW forms a local minimum in a plot of energy against coordinate q, but SDW is the global minimum. An excited state containing an electron-hole pair can be mixed with the ground state by making a correction to the CDW calculation.[144] This raises the CDW energy causing the erosion by the SDW phase in the S-T-U triangle.

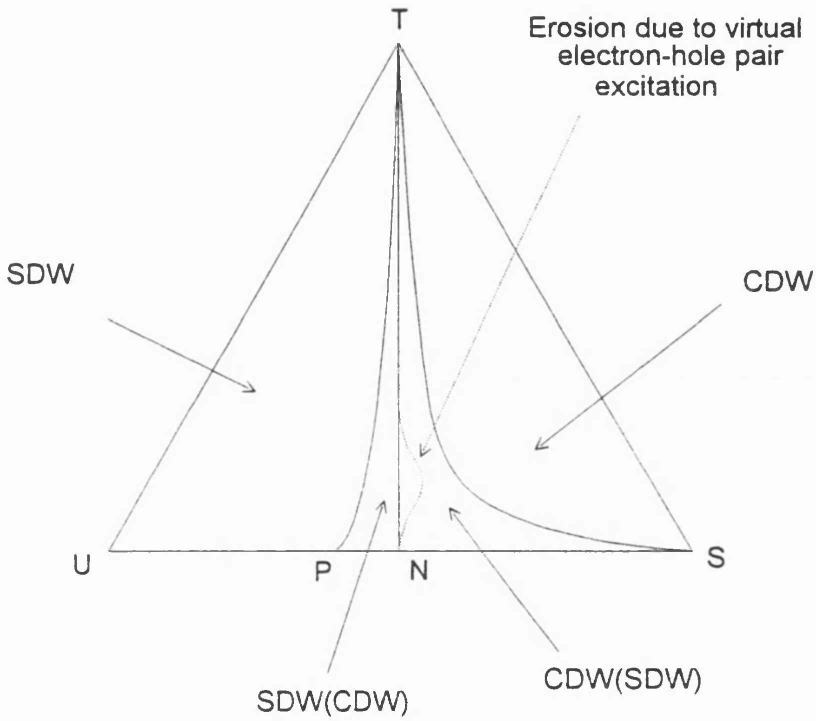

Figure 1.6.4 *A diagram showing the S-T-U triangle developed by Nasu. The dominant phase depends on the relative values of S, T and U.*

If V is not ignored, then the energy calculations can be used to construct an S-T-U-V tetrahedron, like that shown in Figure 1.6.5.[145] The plane TNL is created by the relation U = S + 2V and it divides the solid. The metastable phases are defined by the volumes TNLP and TNLS. Erosion of the CDW state will result from excited state mixing as it does in the S-T-U triangle, but it is not shown in the diagram.[68]

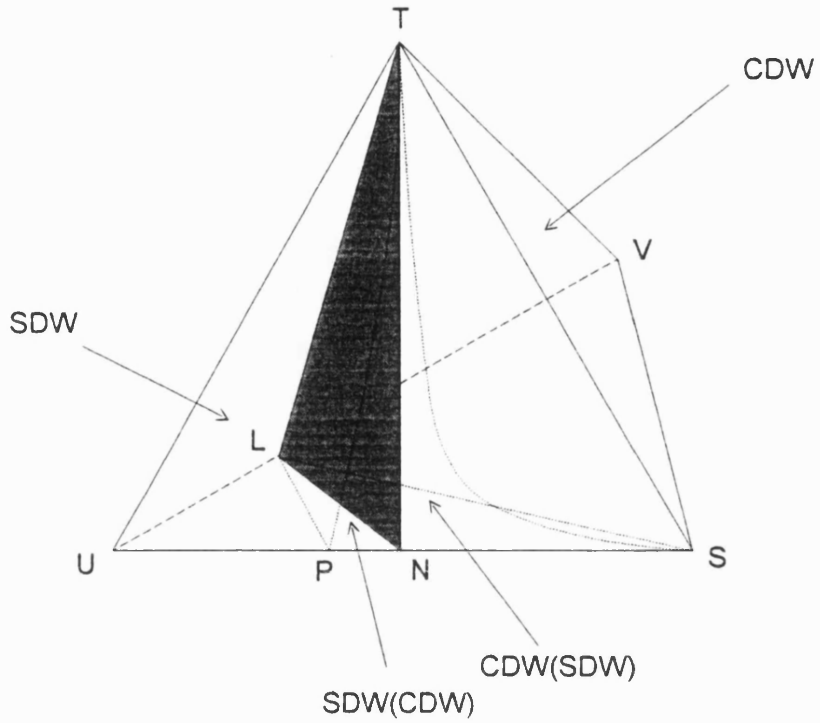

Figure 1.6.5 *A diagram showing the S-T-U-V tetrahedron. The relative values of S, T, U and V at any point are found from the lengths of the perpendiculars dropped from the point to the face opposite the particular vertex.*

The application of the Nasu model to HMMCs is straightforward, since the various energy coefficients may be related qualitatively to the constituents of the MX chain. The N sites are taken as the metal centres, with the N electrons they contribute forming a half-filled one-band orbital. While the halogen orbitals are not directly involved in the Nasu model, electron transfer between adjacent metals is assumed to occur *via* the p_Z orbital of the bridging atom, and the larger it is, the bigger T becomes. Of the other factors, U, the intra-site repulsion, decreases as the metal d_{z^2} gets more voluminous. V is much smaller and less sensitive than U, because of the large inter-site distance. S, the electron-phonon coupling, is related to the change of electrostatic potential of a metal-site electron due to the motion of the halogen. In the Nasu model, it depends solely on the excited (metallic) state distance, r(M^{III}-X), and therefore on the ground state metal-metal separation. For a given metal r(M^{II}-X) increases with halogen size (see section **1.3**), and *vice-versa*. r(M^{IV}-X) depends on the ligand-counterion interaction. The trends in S, T, U and V are related explicitly to metal and halogen in Table 1.6.2. All but a few HMMC complexes are CDW species. By relating their absorption spectra to the energy difference between CDW and SDW states, which is dictated by the size of (2S + 4V - U)/2T, values of approximately 1 eV are derived for each of U, S and 2T.[145] These values mean that the effective charge difference between metal (II) and metal (IV) sites is less than two, and so the sites are designated as $M^{II+\alpha}$ and $M^{IV-\alpha}$ respectively.

Table 1.6.2 HMMC variables and their effect on Nasu parameters

Variable	Alteration	S	T	U	V	Structure
Metal	Ni→Pd→Pt	small increase	negligible	decreases		more CDW-like
Halogen	Cl→Br→I	small increase	increases	negligible		more SDW-like
Ligand-counterion	M-M distance shortened	small decrease	negligible	negligible	negligible	slightly more SDW-like

The Nasu model has been applied to the study of the processes of optical excitation and relaxation, so that experimental observations made on HMMCs (see section **1.4**) might be explained.[40,68] Peaks due to exciton formation are expected to dominate the optical spectrum. The exciton energy level is calculated to be close enough to that of the electron-hole continuum for significant mixing to take place, with consequent broadening of signals.[68] The wavelike excited state that extends over the crystal has its mean electron-hole separation determined by competition between V and T (see Figure 1.6.6).[40]

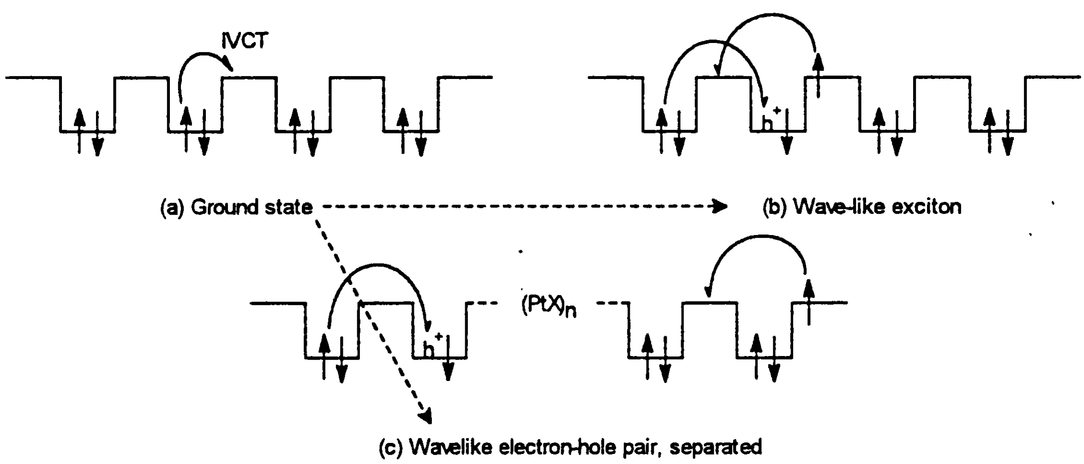

Figure 1.6.6 The diagram shows the two types of excitation from the ground state (a). Either a wave-like exciton (b) is formed, in which electron and hole are separated by the metal-metal distance, or the effective separation is greater and the wave-like electron-hole pair (c) is created.

After relaxation, a self-trapped state is formed in which the mean separation of electron and hole is governed by V and by a function of S. The electron and hole will be sited adjacently to give the luminescent STX when V is large (see Figure 1.6.7). A plot of potential energy against local distortion (δq_k) for $U \approx S \approx 2T$ correctly predicts the luminescence energy to be about half that of the band gap from ground state to exciton.[40] This result had previously defied explanation. The model can be extended to include non-adiabatic conditions,[121] where ω is no longer negligible, although V is ignored again for simplicity. In HMMC complexes, ω is less than 5 % of the size of S, and its omission from the model induces an error in the calculation of the energy gap of up to 10%. Non-linear relaxation of the exciton has also been examined, and two processes are shown in Figure 1.6.7.[41-43]

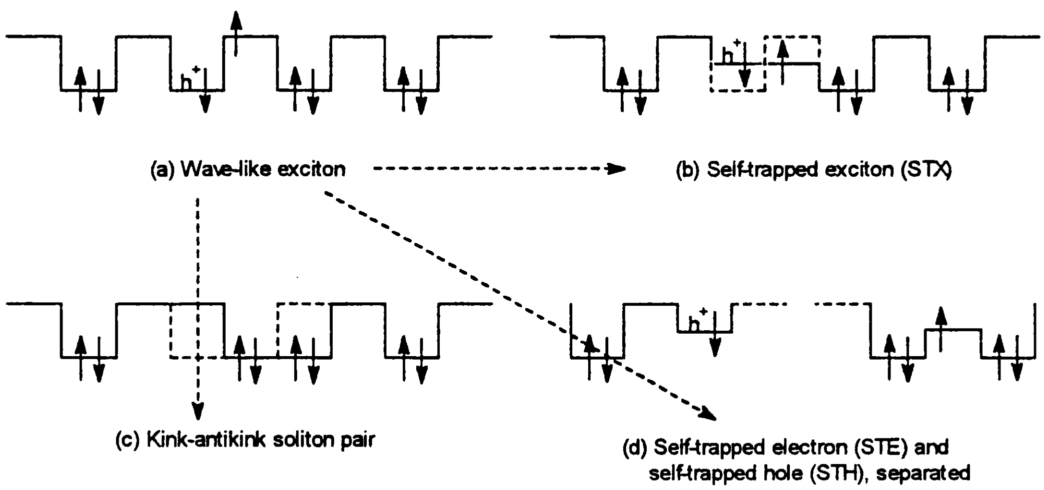

Figure 1.6.7 *Diagram showing the relaxation processes for the wave-like exciton (a). If the electron and hole sites are adjacent, then the luminescent self-trapped exciton (b) is formed. Alternatively, the electron and hole may be separated (d). A further possibility involves the transfer of a second electron to the adjacent site, giving the soliton pair (c). Dashed lines represent the ground state energy levels.*

The Nasu model has been used to determine whether excitation generates solitons or polarons. The band predicted for soliton excitation does not match any of those observed experimentally.[146,147] Instead, all four of the weak resonances found in optical spectra (C, A, B and D in order of increasing energy) can be shown to arise from relaxation *via* the polaron channel. More recently Nasu's work has involved the prediction of optical absorption peak profiles for HMMC compounds.[148,149] The charge transfer band most closely matches that calculated for strongly bound excitons. Although the spectral profiles of polarons and solitons were found, the peaks found in electronic spectra are too weak to allow assignment to be made from their shape. The Nasu model has undoubtedly increased the qualitative understanding of the interactions that govern HMMC properties. However, the initial N-site model involves only the orbitals and electrons of the metal and some direct involvement of the halogen p_z orbitals is expected; the involvement should depend strongly on the identity of the halogen. For this reason an adapted model was introduced by Bishop (see section **1.6.3**).

1.6.3 Bishop Model

Central to the inclusion of halogen orbitals in the description of HMMC complexes is the relationship that has been proposed between this class of compounds and the high-T_c superconductors, which are two- or three-dimensional.[150-152] The MX chains have been proposed as one-dimensional analogues of these species, in which the halogens in HMMCs correspond to the oxygen atoms in superconductors. The one-band model, which Bishop employed initially,[150,153,154] was therefore supplanted by a two-band approach.[155] For the same chain length as the Nasu model, Bishop *et al.* use 2N sites: N metal sites, contributing N electrons as before, and N halogens, supplying 2N electrons. The two bands of orbitals formed will be three-quarters filled; the bonding levels are full, while the antibonding band is half-filled. The model Hamiltonian shown in Equation [1.6.6] is applied mostly to the PtX system. It is generated from the terms depicted in Figure 1.6.8, and otherwise uses the same notation as Equation [1.6.1]. The Bishop formula differs from Equation [1.6.1] in the following ways. There is no V inter-site term; U is also set to zero on occasion. The adiabatic approximation removes the Einstein phonon energy. T, the electron transfer integral, is replaced by the expression $(t_0 - \alpha\Delta_k)$, which allows for transfer *via* the bridging halogen. The Nasu terms $\sqrt{S}Q_k$ that occur in the electron-phonon coupling expression are replaced by a sum containing the expressions $[(-1)^k e_0 - \beta(\Delta_k + \Delta_{k-1})]$. The bonds are modelled as springs, and two force constants are included to describe them, namely K_{MX} and K_{MM}, the latter representing the rigidity of the lattice. Different mathematical approximations have been used in solving the Hamiltonians generated to demonstrate the consistency of the results.[156]

$$H=\sum_{k,\sigma}(-t_0+\alpha\Delta_k)(C^*_{k,\sigma}C_{k+1,\sigma}+C^*_{k+1,\sigma}C_{k,\sigma})+U\sum_k n_{k,\uparrow}n_{k,\downarrow}$$
$$+\sum_{k,\sigma}[(-1)^k e_0-\beta_k(\Delta_k+\Delta_{k-1})]n_{k,\sigma}+\tfrac{1}{2}K_{MX}\sum_k \Delta_k^2+\tfrac{1}{2}K_{MM}\sum_k(\Delta_{2k}+\Delta_{2k+1})^2 \qquad [1.6.6]$$

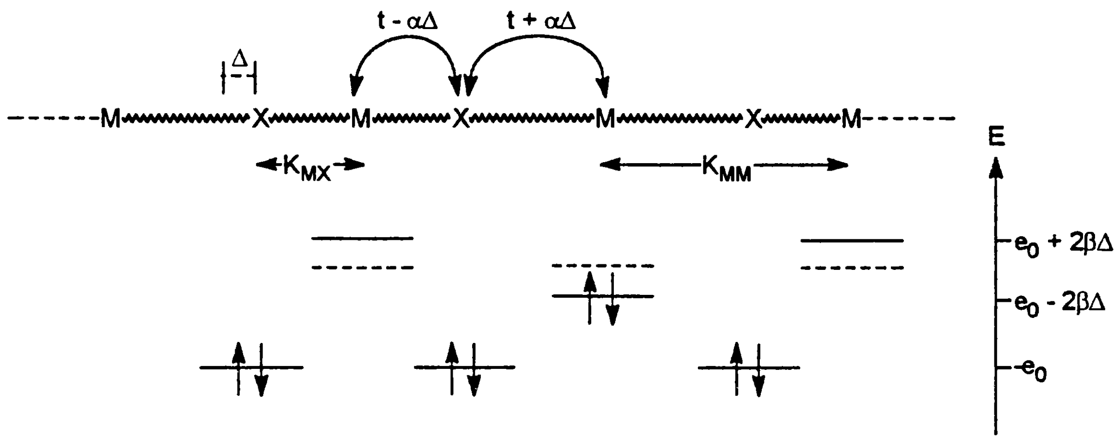

Figure 1.6.8 A diagram of the linear-chain model from which the terms in the Bishop Hamiltonian are derived. The energy levels of the interacting orbitals of all the chain atoms are represented, the halogens at $-e_0$, while the metals are at $e_0 \pm 2\beta\Delta$.

The Bishop model has significantly different properties to the Nasu model. It supports more ground states than just SDW or CDW. Bishop and co-workers have applied it to the question of chain periodicity, which is assumed to be four in the standard formulation of platinum HMMCs. If the value of β is sufficiently large, then charge can clump together, giving lattices with very long periods.[157,158] While the value of β required is too big for large lattice periods to become the ground state in MX species, they are expected to mix with the ground state of period four. The Bishop model introduces asymmetry into the electron-hole polaron system by having a two-band structure that is three-quarters filled.[75,158,159] Electron defects have different energies and intensities to hole defects, unlike in the one-band model where they are equal. This is the fundamental improvement made by Bishop *et al.*, and it has been used to emphasise the superiority of this model.[152,160] Inter-site e-e terms are omitted from the Bishop model so that the complexity of the calculations is reduced. On-site terms are also often neglected, with the result that the distortion, Δ, and the force constants, K_{MM}, have the greatest influence.[161] Δ has been used as a measure of delocalisation (see section **1.3**), and K_{MM} is linked to the identity of the metal and the halogen. When the e-e correlation varies significantly with either variable, then omission of U or V will distort the representation of the dependence of the chain on metal or halogen. The most generalised Hamiltonians cannot span the range of HMMCs without being liable to significant error.[152,160] This is particularly true for the strong CDW materials, *i.e.* PtCl chains, where the redistribution of charge around localised defects cannot be described adequately. Therefore, a more specific Hamiltonian is used for this class of compounds:[162,163]

$$H = \sum_{k,\sigma}(-t_0 + \alpha(x_{k+1} - x_k)(C^*_{k,\sigma}C_{k+1,\sigma} + C^*_{k+1,\sigma}C_{k,\sigma}) + \sum_k U_k n_{k,\uparrow} n_{k,\downarrow}$$
$$+ \sum_{k,\sigma}(-1)^k e_0 n_{k,\sigma} + \sum_{k,\sigma} V_c \frac{(n_{k,\sigma} - Z_k)(n_{k+1,\sigma} - Z_{k+1})}{R_{k,k+1}} + \sum_k \frac{\mu}{R^v_{k,k+1}} \qquad [1.6.7]$$
$$+ \sum_k [\frac{p_k^2}{2M_k} + \frac{1}{2}K_k(x_{k+1} - x_{k-1})^2]$$
$$\text{where } R_{k,k+1} = \sqrt{(x_{k+1} - x_k + \langle r(Pt-Cl)\rangle)^2 + (y_{k+1} - y_k)^2}$$

Distortion of the chain is no longer constrained to one dimension. The terms x_k represent atomic positions parallel to the chain, while y_k is the distance perpendicular to this axis. Any deviation from linearity will cause a small, but not insignificant change to the value of $R_{k,k+1}$. The value of β is set to zero, as is K_{MX}. The fourth summation is a nearest neighbour Coulombic expression and the fifth is an electrostatic repulsion, with $(-v)^{th}$ power dependence. The Raman and optical spectra derived from this equation fit the experimental data for PtCl chains much more closely than does the earlier model.[80,100] Significantly, to account for the wavenumbers of four defects (e^-, e^{2-}, S^0 and S^-), the chain is required to buckle.[163] Equation [1.6.7] can be applied without correction to weaker CDWs, but the increase in accuracy over the simpler equation is not great, and so the latter is still used for the SDW nickel complexes.[164]

1.6.4 LMTO Calculations

Several Linear Muffin-Tin Orbital (LMTO) calculations have been carried out the last ten years by Albers.[165-170] One complex alone has been studied, the neutral chain species *trans*-$[Pt(NH_3)_2Br_2][Pt(NH_3)_2Br_4]$. Calculations are carried out for both the observed dimerised PtBr chain and the theoretical symmetrical state. This is not an ideal complex to study because three inconsistent crystal structures have been reported [6,22-23] and few other relevant spectroscopic data exist. It was chosen because it has no long range electrostatic effects due to counterions and because ammonia is the simplest amine ligand contained by HMMCs. The first complete all-electron full-potential description showed the role played by equatorial ligands.[166] When they are absent, non-bonding platinum orbitals are present at the Fermi level, which prevents dimerisation by the Peierls mechanism. Computations on the ligandless system using an expanded lattice indicated that there is no inter-chain coupling. Further work has shown that spin magnetic moments are small.[167] Various terms in the Bishop model have been derived.[166,168,169] For instance, the metal intra-site repulsion is found to be three times the inter-site hopping integral. Occupation of the halogen p orbitals is thought to be incomplete.[170]

1.6.5 Vibrational Models

Sporadic attempts have been made at modelling the vibrational spectra of HMMCs in general, and those of $[Pt(en)_2][Pt(en)_2X_2](ClO_4)_4$ (X = Cl or Br) in particular. Until recently, few of these had involved any appreciation of the atomic motions in terms of chain dynamics. Instead, earlier work concerned a simple four-atom unit cell, using harmonic force constant parameters similar to those shown in Figure 1.6.9.

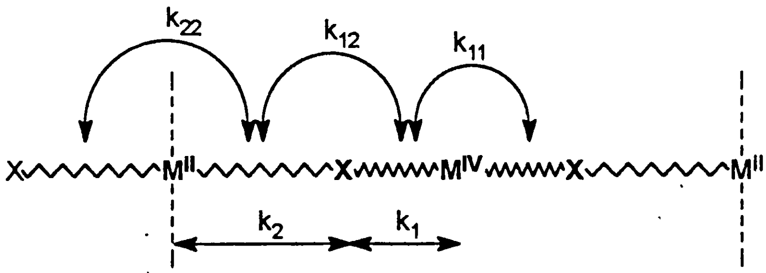

Figure 1.6.9 *Diagram showing the four atom unit cell used in early vibrational modelling attempts. Five force constants are defined. The force-force interactions were often set to zero, since only two vibrational modes were originally assigned. M and X both have a single isotope.*

Four in-chain vibrational modes are derived from this model, of which three are represented in Figure 1.6.10. The IR and Raman inactive acoustic mode (ν_4) is not shown. The symmetric stretch, $\nu(M^{IV}\text{-}X)$, is labelled ν_1 and is the only Raman-active mode, although it is IR inactive.

There are two IR-active modes: the asymmetric halogen stretch, ν_2, and the anti-phase motion of $M^{IV}X_2$ units against the M^{II} centres, ν_3.

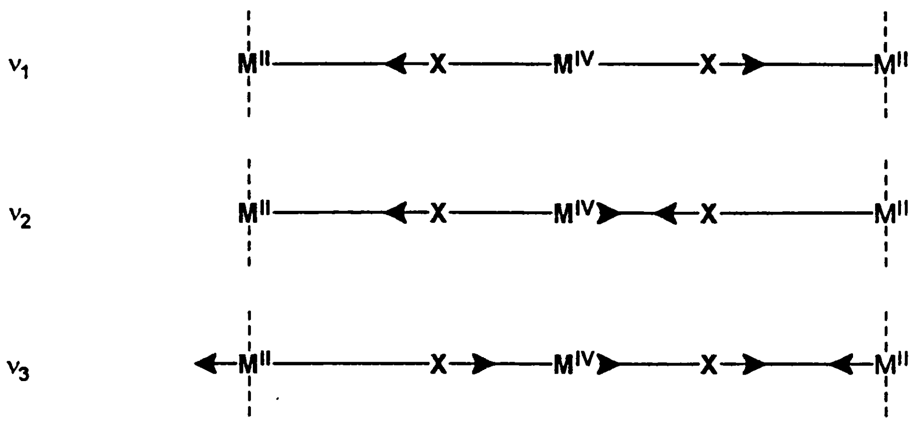

Figure 1.6.10 *A diagram showing three of the four vibrational modes of the four atom unit cell; the acoustic translation is omitted. The dashed lines denote the cell boundaries, and the cell atoms are in bold type.*

Originally, only ν_1 and ν_2 were observed directly, and so three of the force constants had to be assumed, leaving two unknowns. Barraclough *et al.* took k_2 as 10 N m^{-1}, k_{12} as 5 N m^{-1} and k_{22} as zero in their analysis of $[Pt(en)_2][Pt(en)_2Cl_2](ClO_4)_4$.[171] This gave a k_1 value *ca.* 15% smaller than the equivalent ones in the related Pt^{IV} monomers, a negligible k_{11}, and ν_3 equal to 50 cm^{-1}. Pavaskeraidis *et al.* [172] and Allen *et al.* [173] each made all stretch-stretch interactions zero. The former took the combined mass of ligands and platinum atom for the mass of the metal centre,[172] while the latter found that vibrational frequencies derived from the four-atom model are not sensitive to the mass used.[173] Far IR studies on $[Pt(en)_2][Pt(en)_2X_2](ClO_4)_4$ (X = Cl, Br or I) yielded information on the out-of-chain modes, prompting the explicit inclusion of ligands into the model of Degiorgi *et al.* (see Figure 1.6.11).[63] ν_1 and ν_2 are dependent on the values of $(k_1 \pm k_2)$ and $(k'_1 \pm k'_2)$.[65] k_2 is about 80% of k_1, k'_1 is of a similar magnitude to k_2, and k'_2 is very small. The model was expanded to include an electron polaron defect.[117]

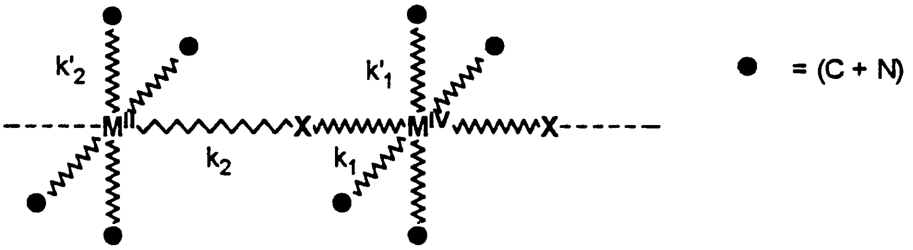

Figure 1.6.11 A depiction of the twelve atom unit cell, used by Degiorgi et al.. The black circles represent a combined mass of one carbon atom and one nitrogen atom.

None of the models based around a single unit cell will reflect accurately the vibrational properties of HMMCs. The dynamics of one-dimensional chains have long been of theoretical interest, because they act as a starting point for analyses of higher-dimensional systems such as ionic crystals. The 1-d chains involve simpler calculations, yet still display some of the properties of the more complex species. The most primitive models are equidistant point masses joined by common nearest-neighbour forces. Much of the early work was concerned with the development of mathematical techniques to determine the behaviour of such chains, and in particular the effect of mass substitution and disorder.[174-181] Equations of motion are set up for the N atoms. Cyclic boundary conditions, where atoms 1 and N are regarded as neighbouring, are used universally in preference to fixing the chain between rigid "walls" or leaving the ends untethered. For large N, results are not greatly dependent on the boundary,[182] and the cyclic condition means that no special equations are needed for the terminal atoms. Solution of the equations leads to the relationship between the frequencies of the normal modes (ω_n) and the position of atom p (x_p) (for n=1 to N):

$$\omega_n^2 = \frac{4f}{m}\sin^2\frac{n\pi}{N} \qquad [1.6.8]$$

$$\text{and } x_p = \exp[i(\pm\frac{2n\pi p}{N} + \omega_n t)] \qquad [1.6.9]$$

m is the atomic mass, and f is the force between atoms. The expression ($n\pi/N$) is replaced by the wavevector, k, and the range of n is altered so that $-\frac{1}{2}\pi < k \leq \frac{1}{2}\pi$. This defines the Brillouin zone, and the equation:

$$\omega = 2\sqrt{\frac{f}{m}}|\sin k| \quad (-\tfrac{1}{2}\pi < k \leq \tfrac{1}{2}\pi) \qquad [1.6.10]$$

is the dispersion relation.[182] ω may be plotted against k, or a frequency spectrum g(ω) may be derived, where g(ω)δω is the fraction of normal mode frequencies in the range ω to ω+δω.

Chains of greater complexity may be analysed by considering them to be composed of unit cells, rather than individual atoms. A unit cell containing two atoms with mass m and M ($m < M$) respectively will have two bands of normal modes (see Figure 1.6.12). The lower band contains the acoustic modes, in which the two atoms in the unit cell move in the same direction. When $k = 0$ (the "zone centre"), all the atoms in the chain move in phase. This is a simple translation of zero vibrational energy. The "top" acoustic mode, in which neighbouring units move in opposing directions along the chain, occurs at $k = \frac{1}{2}\pi$ ("zone boundary"). The optic band is separated from the acoustic band by the "gap". In the optic modes, the masses m and M within each unit cell move in opposition to each other. The highest energy mode in the optic band is at zone centre, with the lowest at the zone boundary. These are the only non-degenerate modes. For a system of N heavy atoms and N light ones, there will be a further N-2 modes in each band, all of them doubly degenerate.

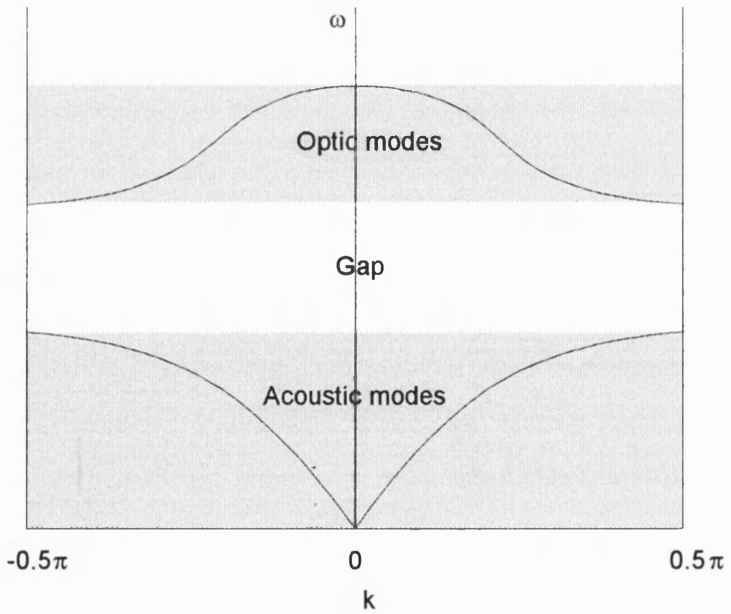

Figure 1.6.12 A representation of the dispersion relation for a diatomic chain with masses m and M (where $M > m$). The frequency is plotted against the wavevector k. The maximum energy of the acoustic band is $\sqrt{(2f/M)}$. The maximum and minimum energies of the optic band are $\sqrt{(2f(M+m)/Mm)}$ and $\sqrt{(2f/m)}$, respectively.

A four-atom unit cell similar to that in Figure 1.6.10 is used to model the HMMC system. At this stage only the masses m and M are included and only nearest-neighbour interactions are considered, so isotopic effects and forces perpendicular to the chain are ignored. The unit cell has four vibrational modes and so four bands of modes are created in the chain. The symmetric stretch within the unit cell (ν_1) is Raman active, and is most intense at the zone centre. As the wavevector is increased (or decreased), the modes will have less Raman intensity, but more infrared intensity. A similar pattern is found for the infrared intensity of the symmetric stretch, ν_2. In reality, vibrations in HMMCs are more complicated than this, because there are different isotopes of both metal and halogen, and because there are forces that extend over more than one bond. Occasionally, the new force constants will alter the dispersion of the individual bands so much that individual bands may be inverted, or that bands overlap. Within the simple diatomic model it is possible to predict the qualitative effect of changing one of the masses in the chain (or alternatively one of the force constants).[183] There are four scenarios, depending on whether a light or heavy mass is changed, and whether the new mass is heavier or lighter than the one replaced. The possibilities are summarised in Table 1.6.3.

Table 1.6.3 The four possible single mass defects and the new separate modes that are created by them

Mass replaced	New mass	No. defect modes	Origin	New location of mode
m	m' < m	One	Optic band	Above optic band
m	m' > m	One	Optic band	In gap
M	M' < M	Two	Optic band Acoustic band	Above optic band In gap
M	M' > M	None	-	-

The modes that separate from the main bands are centred on the defect and are highly localised. Other vibrations that involve motion of the impurity are distorted slightly so that the two-fold degeneracy of the normal chain is lifted. The ratio of m' : m (or M' : M) determines how great the effect of substitution is on the vibrational modes; it is at its greatest when the ratio is either very large or very small. The frequency spectrum becomes more distorted as the number of defects is increased. In chain modelling terminology, this moves into the area of "mixed crystals",[183,184] which include compounds such as mixed alkali halides and certain mixtures of atoms from Group IIIb, IVb or Vb. These have been modelled as chain species of the form AB_xC_{1-x},[184-187] where the distribution is --AYAYAYAY-- (where Y is B or C, and A is the heaviest atom). Vibrations relate to domains of --AB.....AB-- bounded at each end by a C atom (and *vice-versa*) which act as discrete chains with differing boundary conditions. The shape of the frequency spectrum depends on the relative masses of B and C, and the forces in the bonds AB and AC. If these are chosen so that the single defect mode of C in an AB chain occurs at a sufficiently different energy from that found for B in AC, then two-mode behaviour is observed. This produces a gap between the B and C vibrations in which no modes appear, regardless of the relative concentrations of B and C. In one-mode behaviour there is no gap, and the distribution of frequencies is continuous throughout AB_xC_{1-x} species.

Chain modelling has been applied to HMMCs to explain the form of the vibrational spectra of $[Pt(en)_2][Pt(en)_2X_2](ClO_4)_4$ (X = Cl, Br or I),[110,112] in particular the isotopic structure of Raman spectrum for X = Cl. One-mode behaviour is expected because the ratio of atomic masses is small; however it is more appropriate to consider pairs of halogens around the Pt^{IV} centres rather than individual atoms because the chain is dimerised. There are three combinations of isotopes (^{35}Cl-^{35}Cl, ^{35}Cl-^{37}Cl and ^{37}Cl-^{37}Cl) and three sets of vibrational modes. This is the same as for a simple monomer, but the number of modes in each set will not conform to the expected 9 : 6 : 1 ratio. Each chain segment consists of a run of N of the same unit U, which has a probability p_u, terminated at each end by a unit other than U. Such a segment has probability of $(1-p_u)(p_u)^N(1-p_u) = (1-p_u)^2(p_u)^N$. The summation of this geometric series for N = 1 to ∞, will give approximate weightings for the three bands of vibrations (this assumes that each run gives the same intensity of signal, which may not be the case). The ratio for 35-35 : 35-37 : 37-37 is then 21 : 26 : 5, which is a more accurate reflection of the observed Raman spectra than the monomeric distribution.[173] A simple monomeric model can predict correctly the peak ratios seen in the infrared spectra,[112] because the dispersion of IR modes is much less than that of Raman modes. To account for the differing behaviour of IR and Raman vibrations, Bishop *et al.* introduced extra force constants (see Figure 1.6.13).[112]

The forces k_3, k_4 and k_5 replace the stretch-stretch interactions, k_{mn} of Figure 1.6.9. The use of more than two force constants was only practical after ν_3 was assigned (at 120 cm^{-1}),[63] since it allowed a more thorough investigation of k_1 and k_2.[188] Calculated values of, ν_1, ν_2, and ν_3 were shown to be reasonably constant irrespective of the value of k_2 / k_1, so k_1 and k_2 could not be uniquely defined. The most important of the new forces is k_5, because the Raman-active ν_1 mode involves no metal displacement (for a pure isotopic chain), while the M^{II} and M^{IV} atoms move out of phase in the infrared-active ν_2 mode. Increasing k_5 will raise the energy of the zone-boundary ν_2 phonon, reducing the dispersion, and will decouple adjacent unit cells, which localises the ν_2 motion. The size of k_5 required to reproduce all spectra exactly is larger than that derived on a purely ion-ion repulsion basis.[112] The reason for this may be the inadequacy of the model, which lacks metal-ligand interactions, or it may reflect the strength of hydrogen-bonding between the ligands and the counterions.

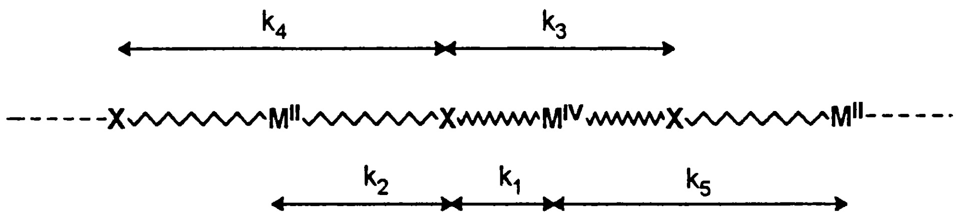

Figure 1.6.13 A diagram showing the force constants required to fit both infrared and Raman spectroscopic results.

CHAPTER 2

EXPERIMENTAL METHODS

2.1 Raman and Resonance Raman Spectroscopy

2.1.1 Introduction

As the title of this thesis suggests, resonance Raman spectroscopy is one of the two techniques that have been employed the most in this study of HMMC complexes. For this reason, a brief theoretical treatment of the subject is given in this section. It is not intended as an intense mathematical undertaking, merely as a reflection of the general approach that is commonly used in the analysis of Raman or resonance Raman data.[93] Complementary to this is a description of the experimental set-up used for the accumulation of all the spectra reported herein. Pertinent to both is an understanding of the basic properties of Raman scattering.

In the vibrational Raman process, a monochromatic beam of electromagnetic radiation, of frequency ν_0 and irradiance $\mathcal{I}_0$, is considered as it is directed onto a sample. Providing this excitation energy does not fall within the contour of an electronic transition, then most of the radiation is simply absorbed or transmitted. Nevertheless, some of the incident photons are destroyed, creating transient excited states in the molecules with which they interact. The excited states decay and new photons are emitted spontaneously in all directions. Since the majority of molecules relax back to their initial state, most of these photons have the same energy as the incident ones. This radiation is termed Rayleigh scattering, and has an intensity of about $10^{-5}\,\mathcal{I}_0$. Occasionally, the relaxation will be to a state other than the initial one. The photons emitted will have different energies from the Rayleigh photons. They account for about a thousandth of the intensity of the scattered radiation and comprise what is known as Raman scattering. Their energies are measured relative to the energy of the Rayleigh photons as the basis of Raman spectroscopy. Because discrete peaks are observed in Raman spectra, only certain transitions from the excited states are allowed. These transitions are examined in section **2.1.2**, where the Raman process is considered in greater detail.

2.1.2 Theory of Raman scattering

The incident radiation has a time-dependent electric field component, **E**, which induces an oscillating dipole moment, μ, in the molecules in the sample. Ignoring small terms, the two quantities are related by the equation:

$$\mu = \alpha \mathbf{E} + \tfrac{1}{2}\beta \mathbf{E}^2 \qquad [2.1.1]$$

where α and β are tensors representing polarisability and hyperpolarisability, respectively. The magnitude of α is typically some 10^{10} times that of β, so unless the electric field is very strong only the first term on the right hand side of Equation [2.1.1] is important. The tensor α is real and symmetric under most conditions; resonance Raman scattering is one of the exceptions (*vide infra*).[189] The components of the tensor are labelled $\alpha_{\rho\sigma}$, where ρ and σ denote the axes of the coordinate system used. For a transition between two vibrational levels, m and n, in the same electronic ground state, g, the intensity of the Raman scattering at 90 $^{\circ}$ to the incident radiation for a bulk sample of randomly oriented molecules is given by:

$$\mathcal{I}_{\pi/2} = \kappa \mathcal{I}_0 (\nu_0 \pm \nu_{gn,gm})^4 \sum_{\rho,\sigma} [\alpha_{\rho\sigma}]_{gn,gm} [\alpha_{\rho\sigma}]^*_{gn,gm} \qquad [2.1.2]$$

where κ is a constant, $\nu_{gn,gm}$ is the frequency of the vibrational Raman transition, and $[\alpha_{\rho\sigma}]_{gn,gm}$ is the $\rho\sigma$ th element in the transition polarisability tensor. The asterisk denotes the complex conjugate. The transition is assumed to pass through the vibrational level v in the excited electronic state, e. Each of the elements $[\alpha_{\rho\sigma}]_{gn,gm}$ can be expressed by the Kramers-Heisenberg dispersion formula as:[190,191]

$$[\alpha_{\rho\sigma}]_{gn,gm} = \frac{1}{hc} \sum_{e,v} \left[\frac{[\mu_\rho]_{gn,ev} [\mu_\sigma]_{ev,gm}}{\nu_{ev,gm} - \nu_0 + i\Gamma_{ev}} + \frac{[\mu_\sigma]_{gn,ev} [\mu_\rho]_{ev,gm}}{\nu_{ev,gn} + \nu_0 + i\Gamma_{ev}} \right] \qquad [2.1.3]$$

where $[\mu_p]_{gn,ev}$ is the transition dipole moment for the process $|gn\rangle \leftarrow |ev\rangle$. Since this cannot be evaluated precisely, the Born-Oppenheimer approximation is invoked.[192] This allows the electronic and vibrational states of the molecule to be treated separately, so that the three states entered during the Raman process may be written as:

$$|gm\rangle = |g\rangle|m\rangle, \quad |ev\rangle = |e\rangle|v\rangle \text{ and } |gn\rangle = |g\rangle|n\rangle \qquad [2.1.4]$$

$[\mu_p]_{gn,ev}$ is then cast as:

$$[\mu_p]_{gn,ev} = \langle n|[\mu_p]_{ge}|v\rangle, \text{ where } [\mu_p]_{ge} = \langle g|\mu_p|e\rangle \qquad [2.1.5]$$

$[\mu_p]_{ge}$ is the pure electronic transition moment for $|g\rangle \leftarrow |e\rangle$. The Born-Oppenheimer approximation means that two additional adjustments can be made. Firstly, because the dependence of $[\mu_p]_{ge}$ on the normal coordinates of the system (Q_k) is small, all terms of higher than first order can be ignored. Therefore:

$$[\mu_p]_{ge} = [\mu_p]^0_{ge} + \sum_k \left(\frac{\partial [\mu_p]_{ge}}{\partial Q_k} \right)_0 Q_k = [\mu_p]^0_{ge} + \sum_k [\mu_p]'_{ge} Q_k \qquad [2.1.6]$$

Secondly, the expressions for transition dipole moment can be written with the electronic and vibrational components separate, once the new values of $[\mu_p]_{ge}$ have been introduced:

$$\begin{aligned} \langle n|[\mu_p]^0_{ge}|v\rangle &= [\mu_p]^0_{ge}\langle n|v\rangle \\ \langle n|[\mu_p]'_{ge}|v\rangle &= [\mu_p]'_{ge}\langle n|Q_k|v\rangle \end{aligned} \qquad [2.1.7]$$

and so:

$$[\mu_p]_{gn,ev} = [\mu_p]^0_{ge}\langle n|v\rangle + \sum_k [\mu_p]'_{ge}\langle n|Q_k|v\rangle Q_k \qquad [2.1.8]$$

When the values from Equation [2.1.8] are substituted into Equation [2.1.3], a basic expression for $[\alpha_{\rho\sigma}]_{gn,gm}$ is derived which can be applied to Raman scattering and, with the inclusion of vibronic coupling, to resonance Raman scattering.

2.1.3 Raman scattering

Non-resonance (or "normal") Raman scattering requires the energy of the incident photons to be far from that required for transition to an excited electronic state. This leads to three simple approximations, the first two being a consequence of the large size of the denominators in Equation [2.1.3].

1. The damping factor $i\Gamma_{ev}$ is so much smaller than $(\nu_{ev,gm} - \nu_0)$ or $(\nu_{ev,gn} + \nu_0)$ that it can be ignored.

2. The denominators have little dependence on m, n or v, and so $\nu_{ev,gm}$ or $\nu_{ev,gn}$ may be approximated by a single value, ν_e.

3. The vibrational states of the excited state form a complete orthonormal set, *i.e.*:

$$\sum_{v} |v\rangle\langle v| = 1 \qquad [2.1.9]$$

The vibrational levels of the ground state are orthonormal as well, so:

$$\sum_{v} \langle n|v\rangle\langle v|m\rangle = \langle n|m\rangle = \delta_{n,m} \qquad [2.1.10]$$

and

$$\sum_{v} \langle n|Q_k|v\rangle\langle v|m\rangle = \langle n|Q_k|m\rangle = \delta_{n,m\pm1} \qquad [2.1.11]$$

where $\delta_{n,m}$ is the Kronecker delta function, which has zero value except when n and m are equal. The transition polarisability can then be rewritten finally as the sum of three terms.

$$\begin{aligned}[\alpha_{\rho\sigma}]_{gn,gm} = &\frac{1}{hc}\sum_{v}\frac{2\nu_e}{(\nu_e^2 - \nu_0^2)}[\mu_\rho]^0_{ge}[\mu_\sigma]^0_{eg}\langle n|m\rangle \\ &+\frac{1}{hc}\sum_{v}\sum_{k}\frac{2\nu_e}{(\nu_e^2 - \nu_0^2)}\left([\mu_\rho]'_{ge}[\mu_\sigma]^0_{eg} + [\mu_\rho]^0_{ge}[\mu_\sigma]'_{eg}\right)\langle n|Q_k|m\rangle \\ &+\frac{1}{hc}\sum_{v}\sum_{k,k'}\frac{2\nu_e}{(\nu_e^2 - \nu_0^2)}\left([\mu_\rho]'_{ge}[\mu_\sigma]'_{eg}\right)\langle n|Q_kQ_{k'}|m\rangle\end{aligned} \qquad [2.1.12]$$

The first term has zero value unless n = m, and so only contributes to Rayleigh scattering. The second term has two conditions that make it non-zero: n = m+1, which is Stokes Raman scattering, and n = m-1, which is anti-Stokes Raman scattering. The intensities of first overtone modes (k = k') and of binary combination modes ($k \neq k'$) are derived from the third term, but they are usually small.

2.1.4 Resonance Raman scattering

None of the approximations applied to normal Raman scattering is valid when the excitation energy is within the contour of an electronic transition. Moreover, there is vibronic coupling between excited states and so the electronic transition moment of Equation [2.1.6] is no longer correct. According to the Herzberg-Teller perturbation description, vibronic coupling results from variation of the Hamiltonian with respect to the normal coordinates, and is quantified by:[193]

$$h^k_{es} = \langle e|\frac{\partial H}{\partial Q_k}|s\rangle_{Q_k=0} \qquad [2.1.13]$$

where s refers to the coupled excited state. The moment $[\mu_\rho]_{ge}$ is then given by:

$$[\mu_\rho]_{ge} = [\mu_\rho]^0_{ge} + \sum_s \sum_k [\mu_\rho]^0_{gs} \frac{h^k_{es}}{\Delta\nu_{es}} Q_k \qquad [2.1.14]$$

where $\Delta\nu_{es} = \nu_{ev,gm} - \nu_{sv,gm}$. This expansion is only valid for weak vibronic coupling, *i.e.* when $\frac{h^k_{es}}{\Delta\nu_{es}}$ is small. It can be substituted into the expression for the transition polarisability *in lieu* of Equation [2.1.6] to give a complicated series of summations. Under the resonance condition, $(\nu_{ev,gm} - \nu_0)$ is so small for one particular excited state that only one term need be considered in each summation over the excited electronic states. $[\alpha_{\rho\sigma}]_{gn,gm}$ may be written as the sum of four contributions, known as the A, B, C and D-terms, *i.e.*:

$$[\alpha_{\rho\sigma}]_{gn,gm} = A + B + C + D \qquad [2.1.15]$$

Each term may be expressed in a compact form by introducing the following abbreviations: $F_{\alpha\beta,\gamma\delta} = [\mu_\rho]^0_{\alpha\beta}[\mu_\sigma]^0_{\gamma\delta}$, $\nu_{den} = \nu_{ev,gm} - \nu_0 + i\Gamma_{ev}$ and $G_{\theta\phi} = \langle n|Q_\theta|v\rangle\langle v|Q_\phi|m\rangle$, except for θ or ϕ equal to zero, when Q has no contribution, *e.g.* $G_{0,0} = \langle n|v\rangle\langle v|m\rangle$. Then:

$$A = \left(\frac{1}{hc}\right) F_{ge,eg} \sum_v \frac{G_{0,0}}{\nu_{den}} \qquad [2.1.16A]$$

$$B = \left(\frac{1}{hc}\right)^2 \sum_{s\neq e} F_{gs,eg} \frac{h^k_{se}}{\Delta\nu_{se}} \sum_v \frac{G_{k,0}}{\nu_{den}} + \left(\frac{1}{hc}\right)^2 \sum_{s\neq e} F_{ge,sg} \frac{h^k_{es}}{\Delta\nu_{es}} \sum_v \frac{G_{0,k}}{\nu_{den}} \qquad [2.1.16B]$$

$$C = \left(\frac{1}{hc}\right)^2 \sum_{s\neq g} F_{se,eg} \frac{h^k_{gs}}{\Delta\nu_{gs}} \sum_v \frac{G_{k,0}}{\nu_{den}} + \left(\frac{1}{hc}\right)^2 \sum_{s\neq g} F_{ge,es} \frac{h^k_{sg}}{\Delta\nu_{sg}} \sum_v \frac{G_{0,k}}{\nu_{den}} \qquad [2.1.16C]$$

$$D = \left(\frac{1}{hc}\right)^3 \sum_{s,s'\neq e} F_{gs,s'g} \frac{h^k_{es}h^k_{es'}}{\Delta\nu_{es}\Delta\nu_{es'}} \sum_v \frac{G_{k,k'}}{\nu_{den}} \qquad [2.1.16D]$$

The A-term (Equation [2.16A]) is the most important, but it will only be non-zero if $G_{0,0} (= \langle n|v\rangle\langle v|m\rangle)$ is non-zero for at least one v and $F_{ge,eg} (= [\mu_\rho]^0_{ge}[\mu_\sigma]^0_{eg})$ is non-zero. This requires the electronic transition to be electric-dipole allowed and the removal of the orthogonality of the vibrational wavefunctions of ground and excited states. To achieve this, either the potential energy minimum must be displaced along the normal coordinate, or the shape of the potential energy surface must be altered, during excitation. The former is usually the more effective way of increasing the A-term contribution, although it is not significant for modes that are not totally symmetric unless there is a change of molecular symmetry between ground and excited state. A-term scattering can give rise to intense overtone progressions (*i.e.* n > m+1). Likewise, D-term scattering may provide intensity for first overtones (k = k') or binary combination modes (k ≠ k'), but it is only significant when A = 0. The C-term is negligible, probably because the energy gap between the two coupled states is so great. Like the A-term, B-term scattering requires the excitation to be electric-dipole allowed, but the vibronic coupling factors make it less intense. It also requires the transition from the ground state to the coupled level to be electric-dipole allowed, so $|e\rangle$ and $|s\rangle$ must have the same symmetry.[194,195] B-term scattering is responsible for the Raman intensity of non-totally symmetric modes.

2.1.5 Application of Raman spectroscopy to HMMC complexes

Raman spectroscopy is a valuable tool for studying inorganic complexes, whether the excitation satisfies the resonance condition or not. "Normal" Raman scattering, which occurs when the incident radiation does not fall within the contour of an electronic transition, gives the signals of the pure vibrational modes, from which structural and physical properties of the ground state can be determined.[196,197] Resonance Raman (rR) scattering involves the creation of an intermediate excited electronic state and so rR spectroscopy may be used to study properties of the excited state.[198-200] Mixed-valence complexes have been classified on the basis of their resonance Raman spectra.[201] Resonance Raman theory has been used successfully to simulate the spectra of small molecules that undergo totally symmetric vibrations and where transitions take place between simple electronic states.[93] A similar theoretical treatment might seem appropriate for HMMCs because of the spectra they exhibit when analysed as pressed discs. When the excitation energy lies within the contour of the IVCT band, the fundamental symmetric stretch mode (ν_1) is greatly enhanced and a long overtone progression is observed. While this behaviour is typical of Raman intensities due to A-term scattering, it is not the case here. In contrast to small discrete molecules, the vibrations in HMMCs are governed by chain dynamics, so vibrations along the MX axis are not totally symmetric and there are many closely spaced vibrational levels for each electronic state. The fine structure of the ν_1 mode, which was not observed clearly until the first single-crystal study,[94] is a consequence of this. The metal-halogen stretching mode has many more components than the three expected from isotopic splitting, both in PtCl chains,[98] and to a lesser degree in PtBr chains.[96] In addition, the excited electronic states in HMMCs are numerous and closely spaced and many are of the same symmetry. Therefore the transitions do not come within the threshold of weak vibronic coupling, and the Herzberg-Teller expression is not valid for HMMC complexes.

The dispersion of the symmetric mode ν_1 is an important feature of HMMC complexes. If the energy of the incident radiation is greater than E_{CT}, then as its wavelength is reduced, the energies of the ν_1 peaks are increased.[96,99] Precise assessment of dispersion is difficult because of the complicated isotopic structure of the mode and because the shape of the peak varies with exciting line. It has been proposed that the ν_1 signal has many components each of which has its own excitation profile and a fixed position.[96,99] Attempts to prove this have foundered because the resolution of recorded spectra has not been sufficient to allow accurate peak deconvolution. The numbers of peaks, their positions, shapes and widths have been assigned almost arbitrarily, and they do not account for the sharp P absorption edge seen in electronic spectra. It has been suggested that the amount by which a peak can be dispersed depends on the identity of the bridging halogen,[95] and that it increases as X is changed from Cl $\rightarrow$ Br $\rightarrow$ I. However, this is not reasonable because the complexes analysed by Clark *et al.* were compared over a range of excitation energies measured absolutely, rather than relative to their respective absorption edges. For instance, little dispersion was observed for the chloride complexes but this was because they were examined in a region below the P edge energy, and so they were not in resonance. To find possible explanations for dispersion, it is necessary to look carefully at the excitation process. There are two factors that can reduce the energy of the emitted radiation and thereby make the vibrational energies appear to be larger. If the potential well of the final electronic state is steeper than that of the initial state, then its vibrational levels will be less closely spaced. This could be caused by a structural change that occurs while the electron is in the excited electronic state, *e.g.* displacement of the minimum energy position of the halogen. The second factor is dissipation of energy by the excited state prior to emission, which may result from mixing with an excited state of similar energy. To account for dispersion, as the energy of the incident radiation is increased up to a certain limit, the effect must be more pronounced; either the structural change is greater or more energy is dissipated in the excited state.

In summary, these observations mean that results of resonance Raman studies of HMMCs must be treated with some caution. That is not to say that such spectra are not of any value, but that it is important to appreciate that their behaviour is more complicated than was originally supposed.[14] Theoretical predictions are bound to be inaccurate, and the treatment used for small molecules is not valid. Resonance Raman spectroscopy may be used for the analysis of localised defects, and for determining the effects of halogen doping, and "normal" Raman spectroscopy remains a useful tool for examining the dynamics of the chain vibrational modes.

2.2 The Raman experiment

2.2.1 Introduction

A synopsis of the Raman experimental procedure followed in the accumulation of all the spectra in this thesis is given below. This is to clarify the uses and limitations of the technique in the study of HMMCs. A schematic diagram showing the arrangement of lasers and spectrometers is shown in Figure 2.2.1.

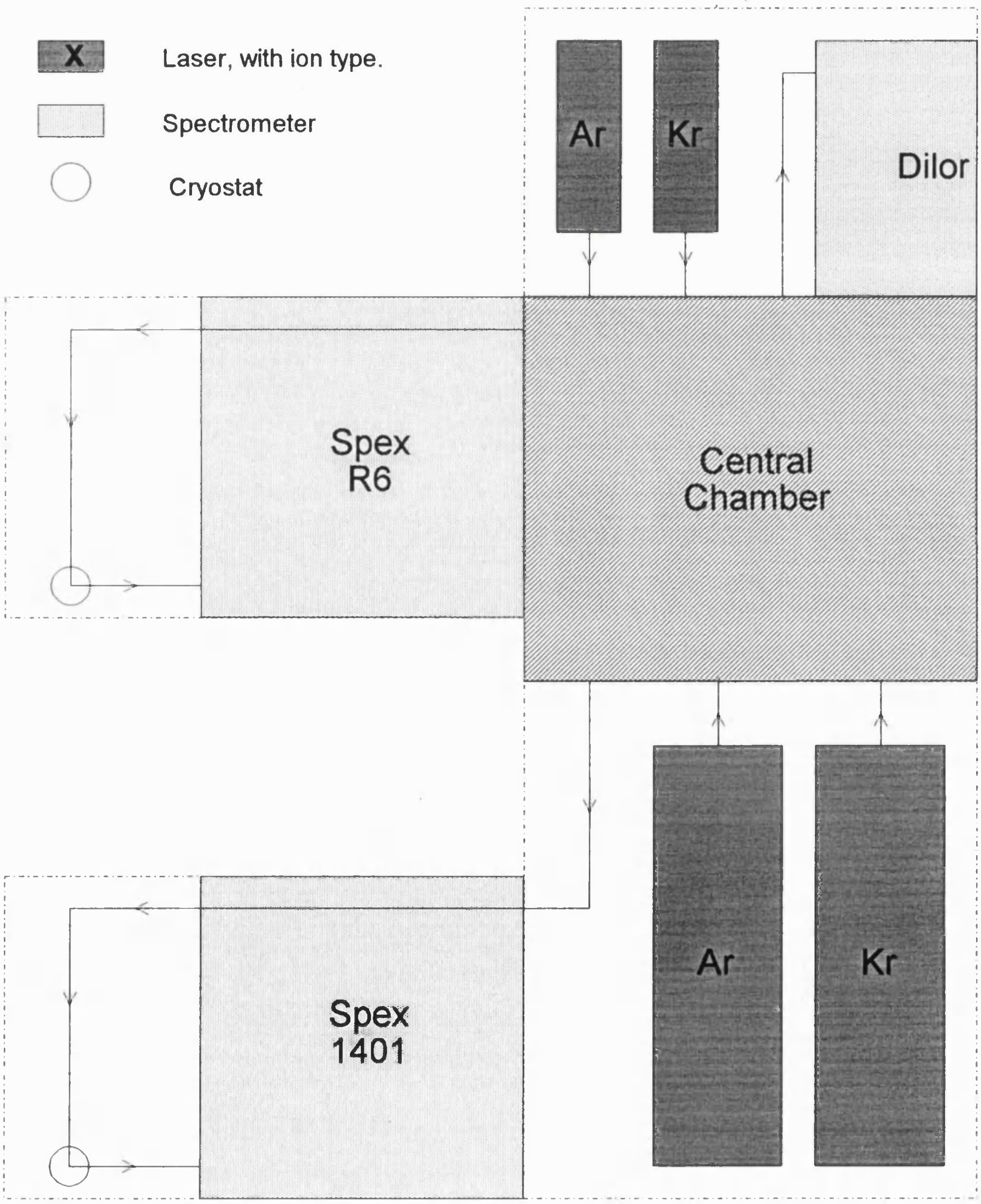

Figure 2.2.1 *Schematic plan view of the Raman experimental set-up. The dotted lines represent the table boundaries, the arrowed lines the optical paths. The Pellin-Broca prisms are mounted in the central chamber.*

There are two key points to note in the diagram: each laser can be directed to any of the spectrometers, and the equipment is mounted on a single table base to minimise vibrations. The Nicolet Fourier Transform (FT) Raman spectrometer is not shown. It does not have a usable cryostat, the 1064 nm Nd:YAG laser with which it is fitted is too powerful to focus on HMMCs at room temperature and small crystal samples cannot be aligned accurately with the laser. While the FT Raman technique may prove to be of some value to linear-chain study in the future, no results collected with this machine are reported here. The Dilor Raman microscope has a very short spectral response range, and it is not specially adapted for work at low temperature. However, crystals or particular surfaces of a crystal can be examined easily using the microscope, and the accumulation time of the machine is very fast. It offers the best means for checking the uniformity of large samples of crystals (see section **4.4**), because crystals can simply be scattered onto a glass slide and analysed very quickly.

All the spectra reported in this thesis were recorded on one of the two scanning spectrometers. The Spex 14018/R6 (usually abbreviated as R6) double monochromator, with Jobin-Yvon holographic gratings (1800 line mm^{-1}), was used with 406.7 nm excitation since it is the more sensitive of the two instruments in the blue part of the visible spectrum. The majority of the spectra were recorded on the Spex 1401 double monochromator, with Bausch and Lomb gratings (1200 line mm^{-1}). The Spex 1401 has good response over a large range, and furthermore it is equipped with a Charged Coupled Device (CCD) camera, which makes alignment of small crystals much easier than it is on the R6.

2.2.2 Optical path

The exciting radiation necessary to promote Raman scattering comes from one of four different lasers. In theory this should have made a large number of possible wavelengths available, but the age and unreliability of the apparatus meant that not all were possible (the large argon ion laser fell into disrepair). The lasers, and the excitation lines from each that were used, are listed in Table 2.2.1.

Table 2.2.1 Lasers and the wavelengths that are used in this work

Colour	Krypton ion		Argon ion	
	CR-3000K	CR-52	CR-18	I-70
blue	406.7 468.0 476.2			
turquoise			488.0	
green	530.9		497.0	488.0 497.0 514.5
yellow	568.2			
red	647.1 676.4 752.5	647.1 676.4		

CR = Coherent Radiation, I = Innova.

The radiation emitted by lasers is coherent and virtually monochromatic, and polarised in the same vertical plane. The radiation from any laser can be directed into the central chamber (see Figure 2.2.1) where it is be aligned with a Pellin-Broca prism; the prism diverts plasma lines from the optical path. The beam is reflected by a series of mirrors, which are adjusted so that it is exactly vertical as it enters the cryostat. Crystals or pressed discs are mounted on a sample block made of copper, which has its face set at 30 ^{o} to the vertical. The block is in thermal contact with a reservoir containing liquid nitrogen. The cryostat is kept under vacuum to prevent water from condensing on the windows through which the beam passes. The laser beam is filtered to provide the requisite intensity and is focused onto the sample with an adjustable lens. Any light emitted by the sample passes through a vertical window to be collected by a second lens, and focused by it onto the slits of the spectrometer. The optical paths within the instrument are designed so that this should result in near maximum intensity at the detector. The set-up of the cryostat and lens is shown in Figure 2.2.2. The detectors are GaAs photomultiplier (PM) tubes (type RCA31034), which are thermoelectrically cooled. They give a signal that is relayed to a DPC2 digital photometer. Each scanning or data collection operation is driven by computer programme (written by Dr. S. P. Best) run on a personal computer (PC). The spectral data collected in this way are calibrated against the Rayleigh emission line. The signal is usually optimised for each sample by finding the maximum intensity for a known peak, by adjusting the various lens foci and mirror orientations. The whole process of obtaining a good signal is simplified by the CCD camera mounted inside the spectrometer (this only applies to the Spex 1401). CCD alignment involves diverting the light entering the slits to the camera along a path length identical to the slit-detector distance. The image that is seen reproduces exactly the signal that arrives at the detector. It is also possible to see the contours of the sample, which is particularly useful for single crystal studies.

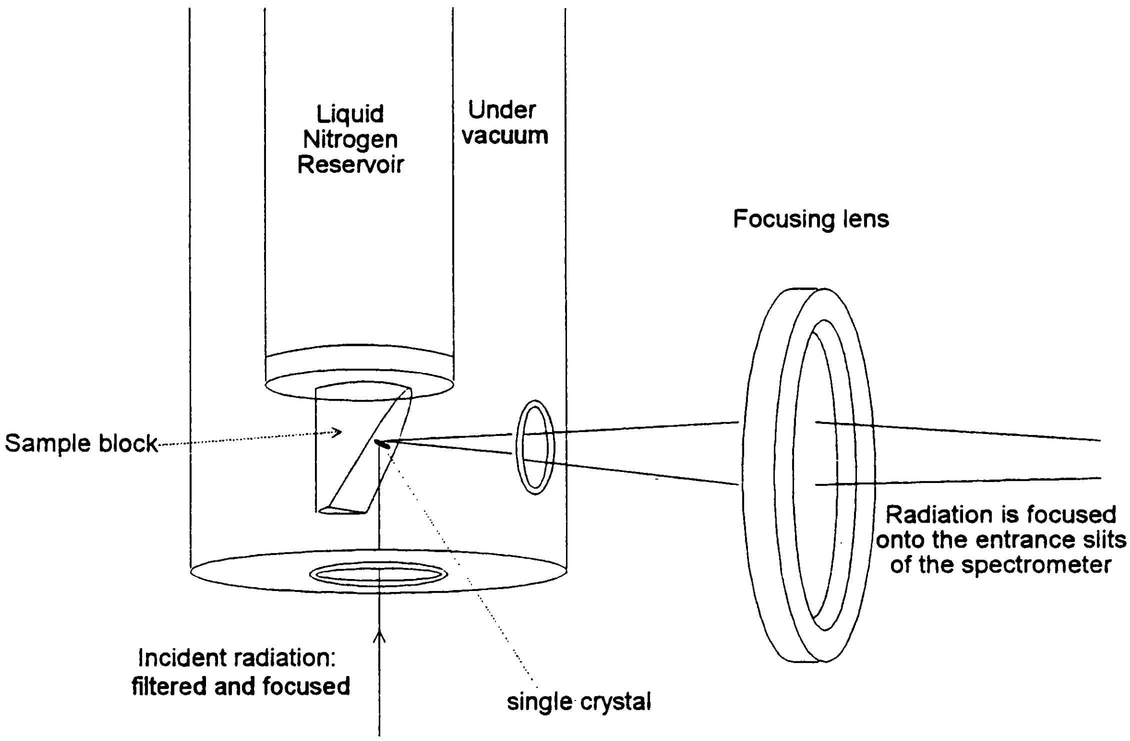

Figure 2.2.2 *A representation of the cryostat, with sample block, and the path taken by the laser beam. A single HMMC crystal is shown. It is mounted so that the electric part of the electromagnetic wave oscillates along the chain axis.*

2.3 Solid-State NMR spectroscopy

2.3.1 Introduction

Chemical shifts are determined by two contributions. The diamagnetic part results from the motion of paired electrons, particularly those in the core orbitals, and is therefore largely independent of the outer electrons. Other atoms may have an effect on it if they have significant electron donating or withdrawing character. The paramagnetic contribution arises from the modification of electronic wavefunctions by the applied magnetic field, and will vary considerably with nuclear environment. For mixed-valence compounds, for each type of atom there should be as many sets of chemical shift patterns as there are valences in the system. HMMC complexes contain four nuclei that are probed routinely in solution. The amine ligands contain three isotopes with nuclear spin of I = ½: namely ^{1}H, ^{13}C and ^{15}N. The fourth, and the sole chain component is ^{195}Pt. HMMC complexes that are soluble are decomposed into their constituent monomers in solution,[202] and so meaningful NMR analysis of these complexes can only be achieved in the solid state.

2.3.2 NMR and the solid state

A nucleus with non-zero spin (I > 0) has angular momentum (J) and 2I + 1 possible values for the angular momentum quantum number (m_I). It therefore has an associated magnetic moment (μ) which is related to J by the gyromagnetic ratio (γ) such that $\mu = \gamma J$. Interaction of the moment μ with a static magnetic field **B** will split the nuclear energy term into 2I + 1 levels. By convention, the field is z-directed, such that $\mathbf{B} = B_0 k$. The energy levels are then:

$$E = -\gamma \hbar m_I B_0 \qquad [2.3.1]$$

and the energies of the observed transitions are given by:

$$\Delta E = |\gamma \hbar B_0| \qquad [2.3.2]$$

In addition, **B** exerts a torque on μ that makes it precess about **B** with an angular frequency ω_L, where $\omega_L = \gamma B_0$. This is known as the Larmor frequency and corresponds to the frequency gap between the spin levels. These relations are equally true for N nuclei of the same type, with the net effect being resultant magnetisation aligned with the field; this is shown in Figure 2.3.1.

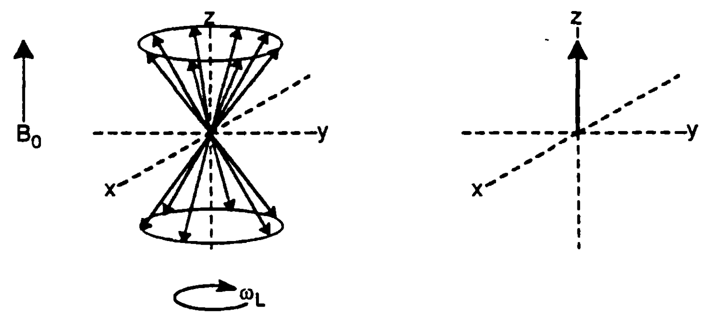

Figure 2.3.1 ***(a) A representation of the precession of nuclear spins in a static magnetic field for a nucleus with half-spin and (b) the net magnetisation.***

This motion of nuclear spins occurs within a stationary frame of reference, the "laboratory frame". If this frame is rotated at the Larmor frequency, then the nuclei will appear to be static and coincident with the applied field, B_0. This is the rotating frame, with axes denoted by x', y' and z', and it has a bulk magnetisation vector, $\mathbf{M} = M_x\,\mathbf{i} + M_y\,\mathbf{j} + M_z\,\mathbf{k}$, where $M_x = M_y = 0$ and $M_z = M_0$. In pulse NMR, an electromagnetic wave is directed along the z-axis, so that the magnetic component oscillates along the x-axis. If a wave with the Larmor frequency is used, then the x'-axis rotates at ω_L, while the magnetic field appears stationary and directed along the x'-axis. The vector **M** is then acted on by the pulsed field, B_1, and is made to precess about the x'-axis with a frequency $\omega = \gamma B_1$. If the pulse is turned on for a time τ, **M** will precess through an angle $\alpha = \gamma B_1 \tau$ (see Figure 2.3.2). B_1 and τ are usually chosen so that $\alpha = 90^o$ or 180^o, leaving **M** in the z = 0 plane or inverted, respectively. When the pulse wave has finished, the system is acted on by B_0 alone and the vector **M** will initially rotate in the x-y plane of the laboratory frame with frequency ω_L. A measurable current of the same frequency may then be induced in coils parallel to the x- and y-axes, and this acts as the source of the NMR signal. The pulse time is very short so **M** is momentarily given by:

$$\mathbf{M} = M_0 \sin\alpha\mathbf{j} + M_0 \cos\alpha\mathbf{k} \qquad [2.3.3]$$

The net magnetic moment is unstable in the field B_0 and the signal will undergo free induction decay (FID) which is measured and converted to a frequency spectrum by Fourier transform.

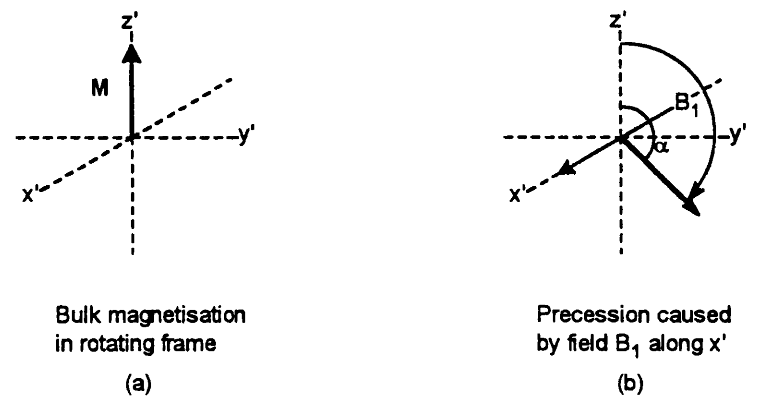

Figure 2.3.2 *Diagram (a) shows the resultant magnetisation of Figure 2.3.1b as seen in the rotating frame, which spins about the z-axis at the Larmor frequency. Diagram (b) shows the effect of directing an electromagnetic pulse of Larmor frequency along the z-axis so that its magnetic part oscillates along the x-axis. In the rotating frame, the net x'-directed magnetisation causes **M** to precess around the x'-axis.*

The signal will decay *via* one of two mechanisms. Spin-lattice relaxation re-establishes the spin populations aligned with the field directly, increasing $M_{z'}$. After the pulse, the distribution of spins is equivalent to a high Boltzmann temperature, and spins relax to the lower level by dissipating energy into the lattice. Alternatively, in spin-spin relaxation the net signals seen in the x' and y' directions ($M_{x'}$ and $M_{y'}$) are reduced by the gradual dephasing of spins that precess at fractionally different rates. The relaxation processes have associated time factors, T_1 and T_2 respectively, which govern the rate of decay:

$$(M_z - M_0)_t = (M_z - M_0)_0 \, e^{-t/T_1} \qquad [2.3.4a]$$

$$(M_{y'})_t = (M_{y'})_0 \, e^{-t/T_2} \qquad [2.3.4b]$$

Once $M_{z'}$ has relaxed back to its initial value, there will be no net magnetisation in the x'-y' plane, but $M_{y'}$ can reach zero before $M_{z'}$ has relaxed back completely. Therefore T_1 is always greater than, or equal to, T_2.

In NMR terms, solids differ from liquids in three important ways. Firstly, dipole-dipole interactions cannot be ignored in the solid state. Consideration of nuclear pairs i and j, with gyromagnetic ratios γ_i and γ_j, that are separated by the vector r_{ij}, which makes an angle θ_{ij} with a magnetic field **B'**, shows the dipolar interaction Hamiltonian to be of the form:[203]

$$H_D = \sum_{i<j} \tfrac{1}{2}\gamma_i\gamma_j\hbar^2 r_{ij}^{-3}\,(I_i.I_j - 3I_{iz}I_{jz})(3\cos^2\theta_{ij} - 1) \qquad [2.3.5]$$

In solution, rapid isotropic motion allows ($3\cos^2\theta_{ij}$-1) to be replaced by the integrated average of zero. For a solid, the action of rotation on a nuclear pair may be depicted as in Figure 2.3.3.

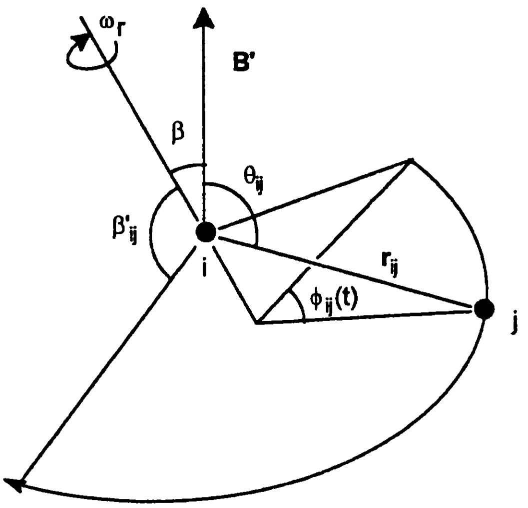

Figure 2.3.3 *A representation of a pair of nuclei, i and j, that are rotated at an angle β to the applied magnetic field, B'.*

θ_{ij} may be expressed in terms of the other angles in the system:

$$\cos\theta_{ij} = \cos\beta\cos\beta'_{ij} + \sin\beta\sin\beta'_{ij}\cos(\omega_r t + \phi_{ij}(0)) \qquad [2.3.6]$$

Substituting this expression for $\cos\theta_{ij}$ into Equation [2.3.6] makes H_D time-dependent, but H_D can be rearranged to separate a constant value from the time-dependent part that is periodic with a mean value of zero. The constant term has the same form as the original Hamiltonian (Equation [2.3.5]), but is reduced a factor of $|\frac{1}{2}(3\cos^2\beta-1)|$:

$$\tilde{H}_D = \tfrac{1}{2}(3\cos^2\beta - 1)\sum_{i<j}\tfrac{1}{2}\gamma_i\gamma_j\hbar^2 r_{ij}^{-3}(I_i.I_j - 3I_{iz}I_{jz})(3\cos^2\beta_{ij} - 1) \qquad [2.3.7]$$

Chemical shift anisotropy is the second factor that distinguishes solid state studies from solution ones. The chemical shift (σ) is a second rank tensor, but for any atom i (as in Figure 2.3.3) orthogonal axes may be chosen so that it has just three on-diagonal elements. In solution, rapid tumbling means that an averaged value is seen for σ, but this is not the case in the solid state. If the Hamiltonian is expressed as:

$$H_s = \hbar\sum_i (I_i.\sigma_i.B') \qquad [2.3.8]$$

then only the z-directed components, σ_{izz}, will be significant, so that:

$$H_s = \hbar\sum_i(\gamma_i\sigma_{izz}B_0) \text{ where } \sigma_{izz} = \sum_{n=1}^{3}\lambda_{in}^2\sigma_{in} \qquad [2.3.9]$$

σ_{in} are the principal values of σ, and λ_{in} are their respective direction cosines relative to **B'**. If the solid is spun, as in Figure 2.3.3, then the principal values behave like $\mathbf{r_{ij}}$, with λ_{in} being equivalent to θ_{ij}. The Hamiltonian is then time-dependent, with a periodic component, which gives rise to spinning sidebands, and a mean constant value derived from the time-averaged shift tensor:

$$\tilde{\sigma}_{izz} = \tfrac{1}{3}\sigma \sin^2\beta + \tfrac{1}{2}(3\cos^2\beta - 1)\sum_{n=1}\sigma_{in}\cos^2\beta_{in} \qquad [2.3.10]$$

This will result in a broadened spectrum for all values of β where $3\cos^2\beta \neq 1$.

The rates of the spin relaxation processes are the third area of difference between liquids and solids under NMR conditions. T_1 and T_2 are of comparable size in solution, but in the solid state the spin-lattice mechanism is normally inefficient for all but the smallest most mobile of atoms (*i.e.* hydrogen), and so T_1 is much greater than T_2. To avoid saturation, the spins must be allowed to relax back before the next pulse is sent, which requires a delay several times as long as T_1. A combination of this and the large number of scans that are needed to obtain a spectrum from the weak FID signals means that acquisition times become impractically long.

2.3.3 Optimising Solid-State NMR spectra

The problems that cause broad signals and long acquisition times in solid-state NMR can be diminished. There are three routine procedures that make it possible to record high-resolution spectra for many of the spin-half nuclei. They are magic angle spinning (MAS) which is universally applicable, high-power decoupling, which is useful only for nuclei attached to protons, and cross-polarisation (CP) which also requires protons near to the probed nuclei. MAS makes use of the fact that the expressions for broadening caused by dipole-dipole interactions and chemical shift anisotropy both contain the same factor, $(3\cos^2\beta\text{-}1)$. β is under experimental control (see Figure 2.3.3), and when it is equal to 54° 44', $(3\cos^2\beta\text{-}1)$ is zero. The principle of MAS is to spin the sample at precisely the "magic" angle of 54° 44' fast enough for θ_{ij} to be averaged quickly. If this is achieved then H_D is reduced to zero and $\tilde{\sigma}_{izz}$ becomes equal to the isotropic value σ. H_S has an ω_r dependence, so unless the spinning speed is very fast, spinning sidebands will be observed. In practice, the spinning speeds that can be attained are sufficiently quick to remove dipolar coupling for all nuclei other than hydrogen and fluorine. High-power decoupling will help to remove unwanted broadening. When the protons are irradiated with a strong pulse at the proton frequency during the acquisition of the spectrum, their spins change so rapidly that the time-averaged magnetic moment is zero. CP solves the problem of long relaxation times It involves the exchange of magnetisation between protons and the nuclei of interest, which is why nearby protons are needed for it to work. The CP process involves a series of pulses, which are depicted in Figures 2.3.4 (a)-(e).

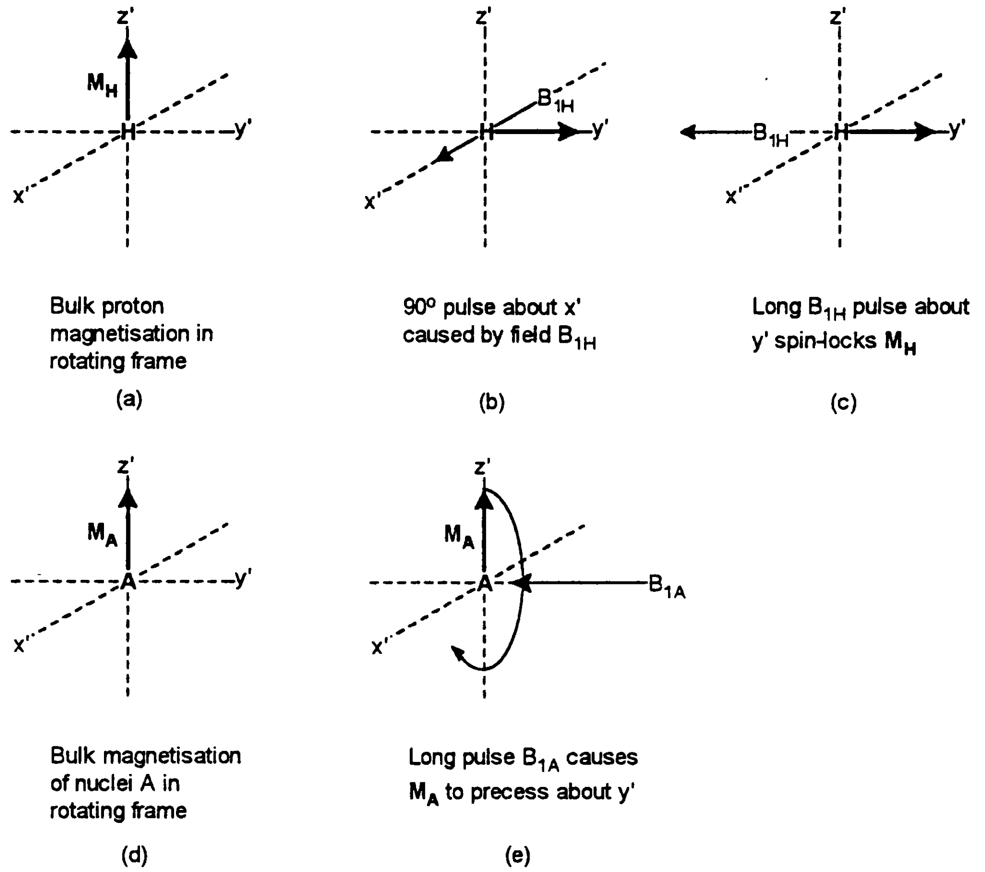

Figure 2.3.4 *The diagram shows the stages leading up to cross-polarisation. The proton magnetisation in (a) is processed by 90° by a pulse B_{1H} so that it lies along y' (b), and locked by a long pulse along y' (c). The bulk magnetisation of the other nuclei (d) is made to precess around y' by a long pulse (c), so that it has no net magnetisation along the y'-axis.*

The proton magnetic moment is spin-locked along the y'-axis by a $90^o{}_{x'}$ pulse followed by a long pulse along the y'-axis. The magnetic moment for nuclei A is made to precess about y' by the contact pulse B_{1A}. The y'-axis is the quantisation axis for the magnetisation of both nuclei. Spin populations along y' are unstable, because B_{1H} is too small to sustain the proton distribution set up by B_0, while for nuclei A there is no net magnetisation, which equates to an infinite Boltzmann temperature. These population levels are represented in Figure 2.3.5.

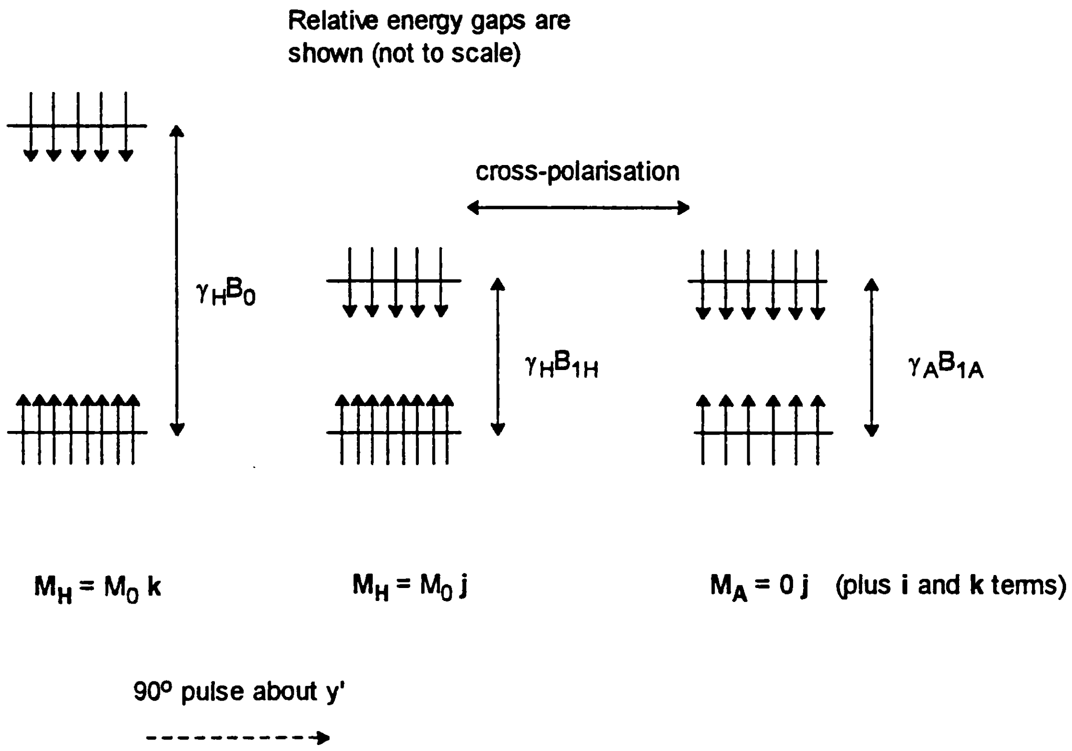

Figure 2.3.5 A diagram representing the spin populations of the nuclei H and A just before cross-polarisation magnetisation transfer takes place.

The Hartmann-Hahn matching condition is:

$$\gamma_{1A}B_{1A} = \gamma_{1H}B_{1H} \qquad [2.3.11]$$

and when this is fulfilled then there is highly efficient energy transfer between the two sets of nuclei. The excess proton magnetisation is exchanged rapidly, creating a large population difference in the A nuclei, which increases its signal by a factor of γ_H/γ_A. Furthermore, the magnetisation of A that occurs during the contact time depends on M_H, since the delay time between scans needs to be large enough only for proton relaxation to occur. Proton relaxation is usually fairly quick, and so many more scans can be carried out using CP than would otherwise be the case.

2.3.4 HMMC complexes and Solid-State NMR spectroscopy

There are four nuclei contained by HMMCs that can be probed by solid-state NMR spectroscopy, and they are listed in Table 2.3.1, along with their sensitivities relative to ^{1}H.

Sensitivity is measured on equal numbers of atoms and is a function of the nuclear moment. The natural sensitivity is the product of the sensitivity and the natural abundance. Both sensitivity measurements are quoted relative to ^{1}H. The resonant frequency is proportional to the gyromagnetic ratio.

Table 2.3.1 Major nuclei found in HMMCs with spin I = ½ [204]

Atom	Isotope	Sensitivity	Natural abundance (%)	Natural sensitivity	NMR frequency at 7.05 T (MHz)
hydrogen	^{1}H	1.00	99.98	1.00	301.130
carbon	^{13}C	1.59×10^{-2}	1.108	1.76×10^{-4}	75.468
nitrogen	^{15}N	1.04×10^{-3}	0.37	3.85×10^{-6}	30.424
platinum	^{195}Pt	9.94×10^{-3}	33.8	3.36×10^{-3}	64.497

The reason for using solid-state NMR spectroscopy to study HMMCs is to probe the oxidation state of the metal. This can be done directly in chains that contain platinum, which is the only metal that has spin of a half. However, solid-state ^{195}Pt NMR analysis is not necessarily a good probe of platinum oxidation state, because the paramagnetic contribution to the chemical shift is very large and can dominate other influences. The small amount of work that has been carried out in the solid state has been limited to platinum (IV) compounds.[205,206] Platinum nuclei with large chemical shift anisotropies give spectra which contain many intense spinning sidebands. Platinum (IV) complexes are usually isotropic enough to give a small number of sidebands that can be removed by fast spinning, but platinum (II) species are often highly anisotropic, and so many scans are required before an adequate signal-to-noise ratio can be reached. Unambiguous assignment of the isotropic chemical shifts involves recording spectra at three different spinning speeds and then determining which resonances are unshifted. Therefore solid-state ^{195}Pt NMR studies of Pt^{II} nuclei are very time consuming. Some solution studies have been reported which mainly concern platinum (II) species, but they are usually coupled to ^{15}N NMR analyses.[207,208]

Of the three nuclei that yield information about the platinum oxidation states indirectly, the least useful are protons. Solid-state ^{1}H NMR spectra are impractically broad because of the large dipole-dipole coupling interactions involved. The presence of ^{1}H sites is beneficial to the study of the other nuclei because cross-polarisation may be applied. ^{13}C analysis of ligands bound to HMMCs has shown that the difference between $\delta(^{13}C_{N-M^{II}})$ and $\delta(^{13}C_{N-M^{IV}})$ is either small [124] or insignificant.[123] The metal is expected to have a greater influence on the nitrogen nuclei in the amine ligands, because there is a direct bond between them. Although solution studies of ^{15}N nuclei are routine, solid-state ^{15}N NMR is not widely employed. ^{15}N nuclei are thought to be useful probes of electron densities and charge delocalisation,[209] and to be sensitive to metals to which they are bound.[210] The interaction with ^{195}Pt, which gives a measurable coupling constant, $J_{^{15}N-^{195}Pt}$, has aroused significant interest.[211-214] It has been demonstrated that the *J* coupling in the *cis-* / *trans-* isomers of square-planar platinum (II) complexes depends on the substituents and their relative positions.[211] In addition, discrete ranges have been observed for the values of $J_{^{15}N-Pt^{II}}$ and $J_{^{15}N-Pt^{IV}}$ in compounds containing diamine ligands.[214] There is coupling between ^{14}N and ^{195}Pt nuclei, but the $J_{^{14}N-^{195}Pt}$ coupling constants are not usually measured and are not of interest in this thesis. The terms J_{N-Pt}, $J_{N-Pt^{II}}$ and $J_{N-Pt^{IV}}$ are used in this work, but they refer exclusively to couplings between ^{15}N and ^{195}Pt nuclei.

2.4 Initial investigations by Solid-State NMR spectroscopy

2.4.1 Natural abundance ^{15}N studies of platinum linear-chain complexes

Solid-state NMR studies were initially focused on the ^{15}N sites in HMMCs. Platinum was chosen as the metal in the MX chain for three reasons. First, its linear-chains exhibit the strongest charge density waves and so they should have the widest separation between $N\text{-}M^{II}$ and $N\text{-}M^{IV}$ signals, making their spectra the easiest to resolve. Second, there are few stable amine, or ammine, compounds of palladium (IV) or nickel (IV), so the effect of chain formation on $N\text{-}M^{IV}$ chemical shifts in NiX or PdX systems cannot be assessed. Third, because ^{195}Pt is a spin-half nucleus, satellite peaks are observed from which $J_{^{15}N\text{-}Pt}$ coupling constants can be derived, which are a useful aid to the determination of the oxidation state of the platinum.

The first complexes analysed were $[Pt(2,3,2\text{-tet})][Pt(2,3,2\text{-tet})X_2](ClO_4)_4$ (X = Cl (**201**), Br (**202**) or I (**203**)), where 2,3,2-tet is 3,7-diazanonane-1,9-diamine, a tetradentate macrocycle (see Figure 2.4.1). They were chosen because the samples available from their recent characterisation [215,216] were large enough to enable solid-state NMR analysis, even with ^{15}N at natural abundance. 2,3,2-tet has both primary and secondary nitrogens and so the behaviour of the two types may be compared.

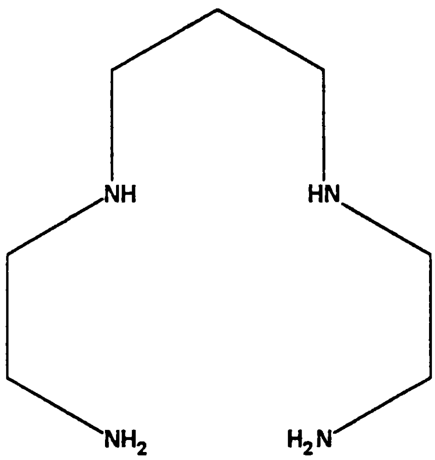

Figure 2.4.1 Structure of the tetradentate ligand 2,3,2-tet ($C_7H_{20}N_4$). The abbreviated name refers to the number of carbon atoms separating successive nitrogens, and the denticity of the ligand.

All samples were examined under CP / MAS conditions and spun at 4 kHz, which is fast enough to remove all spinning sidebands. Proton relaxation measurements set the recycle delay at 6 s. Accumulation of spectra was very slow because of the low ^{15}N abundance. For instance, $[Pt(2,3,2\text{-tet})][Pt(2,3,2\text{-tet})Cl_2](ClO_4)_4$ was scanned *ca.* 40000 times, which took more than sixty hours. The spectra recorded for the three HMMCs exhibit the important features common to all the solid-state ^{15}N NMR spectra (see Figure 2.4.2). The chloride-chain complex contains four major peaks, two each for the primary and secondary nitrogens. Each large peak has a pair of satellites due to ^{15}N-^{195}Pt coupling. The combined integrated intensity of a pair of satellites is about half that of the corresponding unsplit resonance, which is consistent with the ratio of 1 : 4 : 1 predicted from the 33.8 % abundance of the spin-half ^{195}Pt nuclei. The size of the $J_{^{15}N\text{-}^{195}Pt}$ coupling constant reveals the oxidation state of the Pt centres bound to the nitrogen atoms. In solution, $J_{N\text{-}Pt}$ has a discrete range of values for each of N-Pt^{II} and N-Pt^{IV}; $J_{N\text{-}Pt^{IV}}$ lies between 247 and 275 Hz, $J_{N\text{-}Pt^{II}}$ between 302 and 411 Hz.[214] The primary and secondary nitrogens are assigned by referring to the solution ^{15}N NMR spectrum of the ligand $(H_2NCH_2CH_2NHCH_2)_2$ (2,2,2-tet), in which the primary nitrogens appear upfield of the secondary by *ca.* 13 ppm.[217] The chemical shifts and coupling constants of the assigned peaks are listed in Table 2.4.1.

Table 2.4.1 **^{15}N chemical shifts and $J_{N\text{-}Pt}$ coupling constants for the HMMCs $[Pt(2,3,2\text{-tet})][Pt(2,3,2\text{-tet})X_2](ClO_4)_4$ (X = Cl, Br or I) [a]**

X	Label	Nitrogen type	N-Pt^{II}		N-Pt^{IV}		$\lvert\Delta\delta_N\rvert$
			δ / ppm	*J* / Hz	δ / ppm	*J* / Hz	/ ppm
Cl	**201**	primary	-389.6	305	-372.5	230	17.1
		secondary	-364.7	330	-344.3	245	20.4
Br	**202**	primary	-386.3	-	-378.4	-	7.9
		secondary	-360.2	335	-348.9	-	11.3
I	**203**	primary	-390.9	-	-387.1	-	3.8
		secondary	*-358.8*	*310*	*-358.8*	-	*0*

[a] *Chemical shifts are accurate to ± 0.5 ppm; coupling constants have an error of ± 20 Hz.*

The gap between the N-Pt^{II} and N-Pt^{IV} positions ($\Delta\delta_N$) of the primary nitrogens, decreases from 17.1 to 7.9 to 3.8 ppm in the order Cl > Br >I, while $\Delta\delta_N$ for the secondary nitrogens drops from 20.4 ppm in the chloride to almost nothing in the iodide. In the primary nitrogens, the bridging halogen has little influence on $\delta_{N\text{-}Pt^{II}}$, so the variation in $\Delta\delta_N$ reflects changes in $\delta_{N\text{-}Pt^{IV}}$. In the secondary nitrogens, there is a small concerted change in $\delta_{N\text{-}Pt^{II}}$. The relation between $\Delta\delta_N$ and bridging halogen is in consistent with the influence of X outlined in section **1.5**. The effect of chain formation was investigated by analysing the monomers [Pt^{II}(2,3,2-tet)]Cl_2 **(204)** and [Pt^{IV}(2,3,2-tet)Cl_2]Cl_2 **(205)**. The spectra of these complexes are shown in Figure **2.4.3** (a)-(b), and the peak positions and coupling constants are summarised in Table 2.4.2. They confirm the assignments of oxidation states in the HMMCs. $\Delta\delta_N$ is smaller in the monomers than it is in the chloride HMMC, but this is probably because the counterions are different. It would be better to compare the solid-state NMR spectra of the HMMCs with those of the perchlorate salts [Pt(2,3,2-tet)]$(ClO_4)_2$ and [Pt(2,3,2-tet)Cl_2]$(ClO_4)_2$, but these complexes were not analysed.

Table 2.4.2 **^{15}N chemical shifts and $J_{N\text{-}Pt}$ coupling constants for [Pt(2,3,2-tet)]Cl_2 and [Pt(2,3,2-tet)Cl_2]Cl_2 [a]**

M	Label	M-NH$_2$		M-NHR	
		δ / ppm	*J* / Hz	δ / ppm	*J* / Hz
Pt^{II}	**204**	-382.6	310	-362.5	315
Pt^{IV}	**205**	-368.7	230	-343.4	225

[a] *Chemical shifts are accurate to ± 0.5 ppm; coupling constants have an error of ± 20 Hz.*

2.4.2 ^{195}Pt NMR analysis

The solid-state ^{195}Pt NMR spectra of the HMMCs of 2,3,2-tet were recorded, but the results were poor. When X = Cl, there is a broad expanse of evenly spaced spinning sidebands that stretches for more than 5000 ppm. When X = I, the peaks are in two bands *ca.* 1500 ppm wide that almost overlap. The sidebands are spaced out at a distance equivalent to the rotor speed, which at 5.4 kHz was the maximum possible at the time, although this was subsequently improved (see Chapter **3**). Isotropic chemical shift values were not obtained because spectra would have to be collected at two other spinning speeds to determine them accurately.

2.4.3 Discussion and conclusions

The initial solid-state NMR studies were carried out so that the potential of the technique could be evaluated and the direction of further work might be determined. The results of the ^{15}N analysis show that probing ^{15}N nuclei in natural abundance is possible, but not very practical. Acquisition times are too great for it to be considered for routine use, but where ^{15}N-enrichment is impossible good spectra can still be obtained if enough sample is available. This contributed to the decision to ignore the perchlorate monomeric salts and to continue instead with a study of enriched samples, in which compounds without counterions were probed first so that the factors influencing ^{15}N chemical shifts and $J_{N\text{-}Pt}$ coupling constants might be properly understood. The results of the ^{195}Pt analysis were less promising, although matters were not helped by the low spinning speed attainable at the time. Judgement was reserved until more work had been done. The individual results cannot be commented on to any great depth. Although the $\Delta\delta_N$ values appear to show that there is greater delocalisation as X is changed from Cl $\rightarrow$ Br $\rightarrow$ I, it will be shown later that this is misleading. Early indications of this are that $\Delta\delta_N$ is larger for the monomers than it is in the HMMC, and that the bridging halogen has little effect on $J_{N\text{-}Pt^{II}}$.

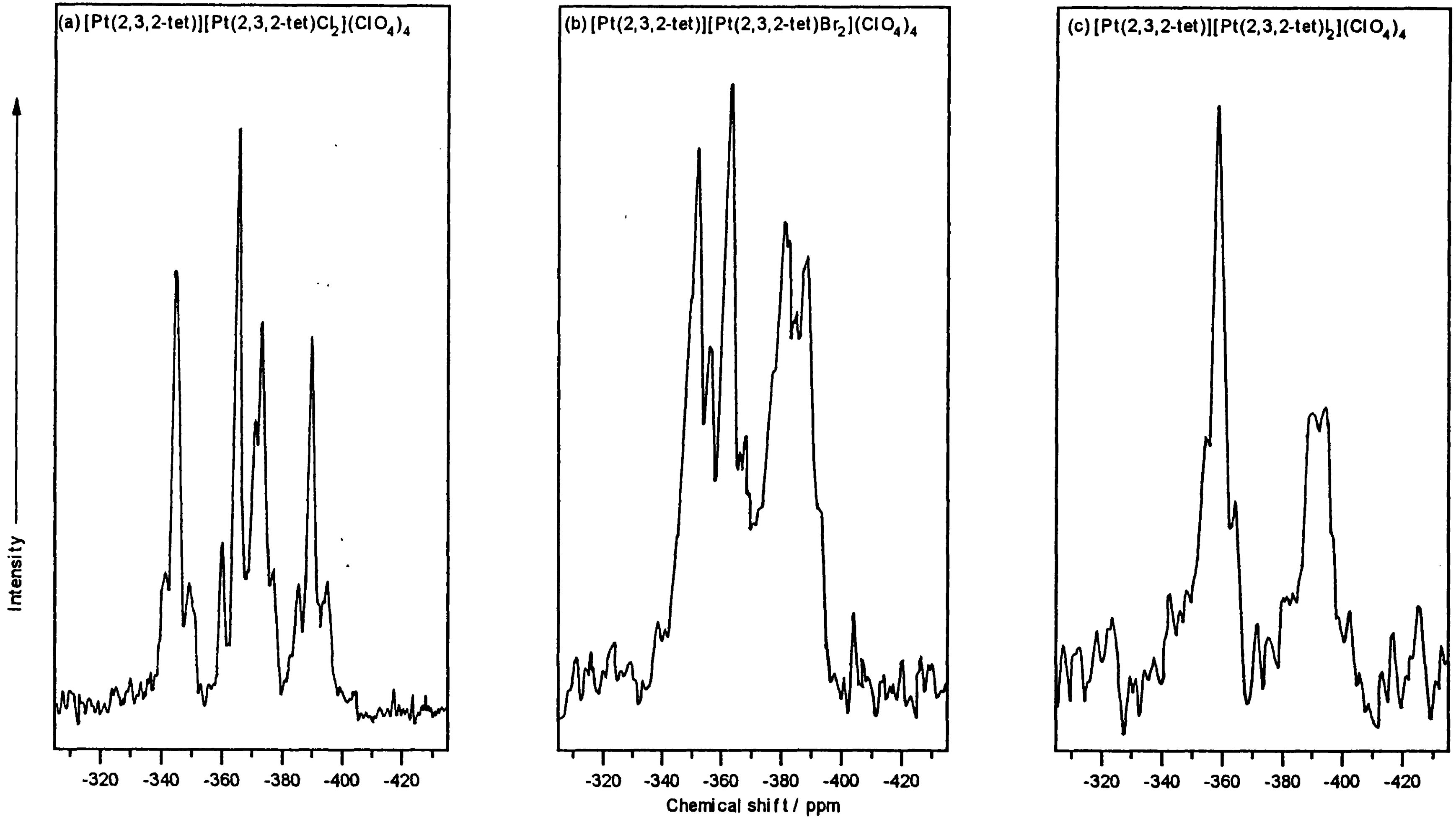

Figure 2.4.2 *Solid-state* ^{15}N *NMR spectra of the HMMCs* $[Pt(2,3,2\text{-}tet)][Pt(2,3,2\text{-}tet)X_2](ClO_4)_4$*, where (a) X = Cl, (b) X = Br or (c) X = I.*

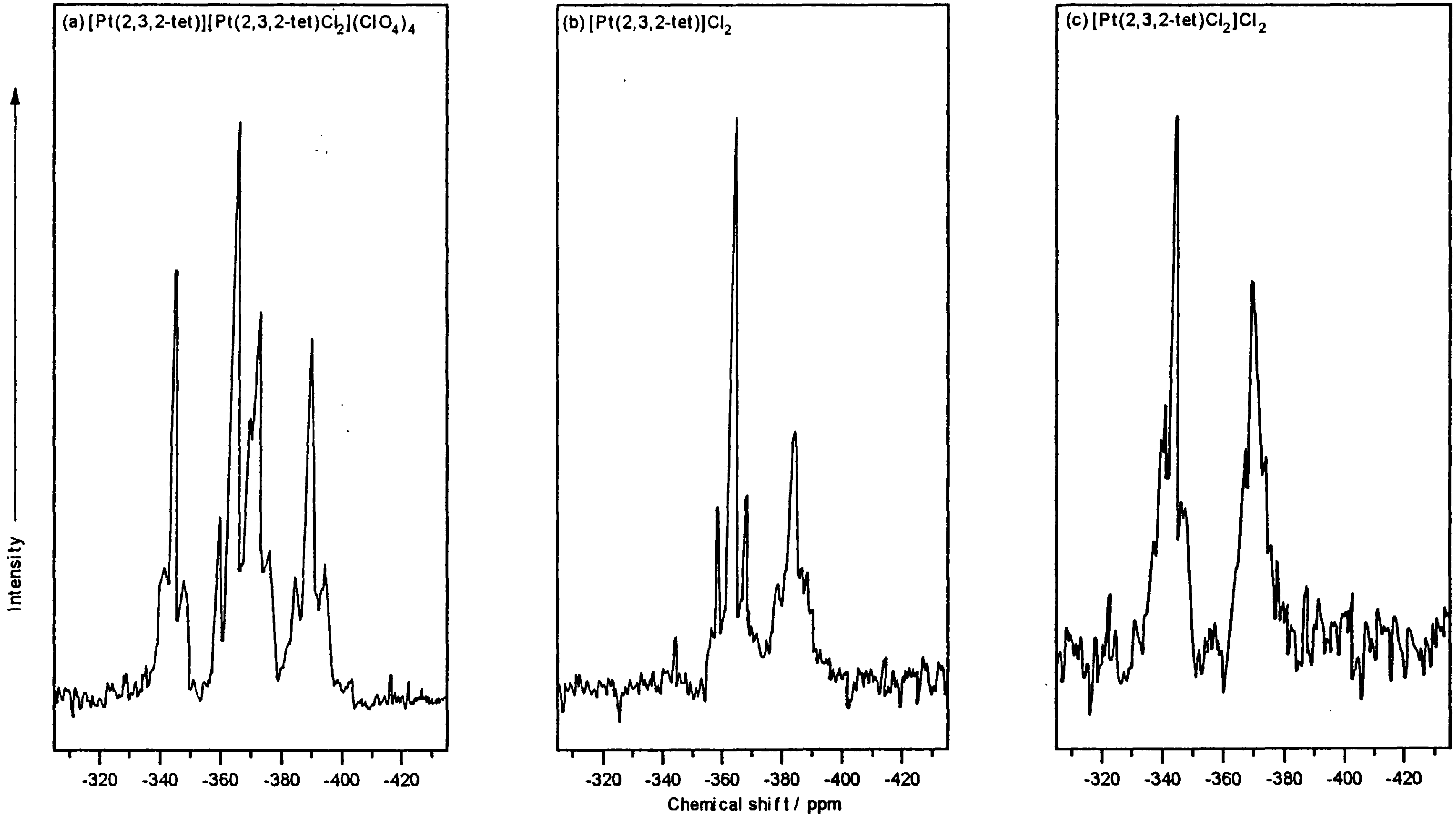

Figure 2.4.3 *Solid-state ^{15}N NMR spectra of (a) [Pt(2,3,2-tet)][Pt(2,3,2-tet)Cl_2](ClO_4)$_4$, (b) [Pt(2,3,2-tet)]Cl_2 and (c) [Pt(2,3,2-tet)Cl_2]Cl_2.*

2.4.4 Experimental details

(a) Syntheses

[Pt(2,3,2-tet)]Cl$_2$ was prepared by heating to 90 °C a stirred solution containing potassium tetrachloroplatinate and a slight excess of amine. The reaction proceeded *via* the insoluble intermediate [Pt(2,3,2-tet)][PtCl$_4$] to a colourless solution. The white solid was recovered by evaporating the solution to minimum volume and then recrystallising from water.

[Pt(2,3,2-tet)Cl$_2$]Cl$_2$ was made from [Pt(2,3,2-tet)]Cl$_2$ by a standard oxidation method.[218]

[Pt(2,3,2-tet)][Pt(2,3,2-tet)X$_2$](ClO$_4$)$_2$ (X = Cl, Br or I) was synthesised [215,219] by a method analogous to those of Bekaroglu *et al.*,[220] employing the starting materials listed above.

(b) Solid-State NMR

Solid-state ^{15}N NMR spectra were recorded using a Bruker MSL-300 spectrometer at 30.42 MHz using cross-polarisation, proton dipolar decoupling, and magic-angle spinning. The CP condition was set on a sample of doubly ^{15}N-enriched ammonium nitrate. Spinning speeds of 4.2-4.5 kHz were employed, sufficient to eliminate virtually all spinning sidebands for these complexes. The contact time was 10 ms, acquisition times were 25-70 ms and the recycle delay between scans was 6 s. The typical 90 ° pulse length for protons was 7 μs. All spectra were recorded at room temperature (296 K). Typically, measurements were carried out on sample sizes of 150-300 mg of natural abundance material and total scan times were *ca.* 60 h. Chemical shifts are quoted relative to external liquid nitromethane using solid NH_4NO_3 as a secondary reference: the ammonium peak was taken to resonate at -358.4 ppm.[217] Observed chemical shifts were not corrected for the change in magnetic susceptibility between samples.

2.5 Aims

The aims of this thesis are split into three broad areas. The first contains the principal objectives, which are to determine (a) how useful solid-state NMR spectroscopy is for studying HMMCs and (b) the factors that influence the solid-state NMR spectra of HMMCs. These are covered in the first half of Chapter **3** and of Chapter **4**. The relative merits of probing ^{15}N or ^{195}Pt nuclei are assessed in Chapter **3**, where the neutral-chain HMMCs $[Pt(en)X_2][Pt(en)X_4]$ (X = Cl, Br or I) and their constituent monomers are examined. The results of these studies also enable the influence of the halogen (axial or equatorial), oxidation state or chain formation to be evaluated in the absence of any counterions. The influence of the counterions on the nuclear environments is covered in Chapter **4** where the HMMCs $[Pt(en)_2][Pt(en)_2X_2]Y_4$ (X = Cl, Br or I, Y = ClO_4^-, BF_4^- or PF_6^-) and their constituent monomers are analysed.

The second area of interest concerns the application of the findings of the principal objectives to specific problems. The results of Chapters **3** and **4** are applied to two main studies. The nature of mixed-halide HMMCs is examined, both in Chapter **3** where the reaction of $[Pt(en)Cl_2][Pt(en)Cl_4]$ with HBr is explored, and in Chapter **4** where the HMMC species $[Pt(en)_2][Pt(en)_2X_{2-2\alpha}X'_{2\alpha}](ClO_4)_4$ (X = Cl, X' = Br) are analysed. In Chapter **5**, various platinum ammine complexes are studied. The unusual behaviour shown by some of these complexes in the solid state is reviewed, and the factors which control HMMC formation are investigated.

The third area is composed of various resonance Raman studies. In Chapters **3** and **4** the mixed-halide complexes are examined by resonance Raman spectroscopy. A vibrational model is constructed in Chapter **4** to explain some of the bands that are observed in these Raman spectra. The large number of defect modes that are exhibited by these species prompted the work in Chapter **6**. This concerns HMMCs that contain aromatic ligands and which also have many inherent defects. The structure of the thesis is shown graphically in Figure 2.5.1, which shows how the various studies are interrelated.

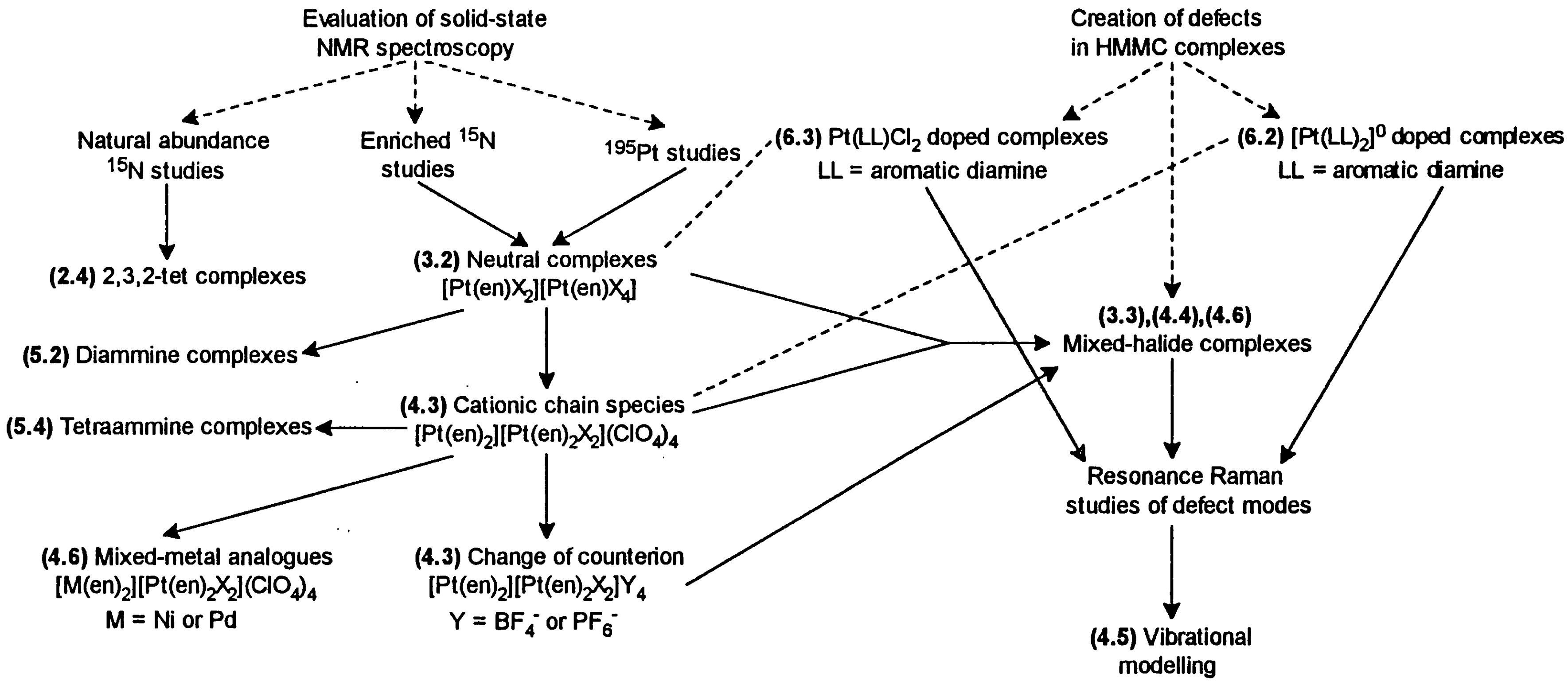

Figure 2.5.1 *Diagram showing the structure of the thesis. Numbers in bold refer to the number of the section in which they appear. A dotted line with arrow denotes a constituent part of the main heading, a solid line with arrow denotes the progression of work, and a plain dotted line shows which areas of work are related.*

CHAPTER 3

NEUTRAL-CHAIN COMPLEXES OF ETHYLENEDIAMINE

3.1 Introduction

The solid-state ^{15}N NMR analysis of the HMMCs of 2,3,2-tet highlights the limitations of working with nitrogen in natural abundance and the problems caused by counterions. It also establishes three criteria for the next system to be chosen for study by this technique. (1) The amine ligand must be readily available in an ^{15}N-enriched state, either commercially or by simple synthesis.[221,222] (2) The chain systems must be neutral so that counterion effects can be avoided. (3) It must be possible to synthesise most, if not all, of the M^{II} and M^{IV} monomers, so that the effect of chain formation can be analysed. The family of complexes that best fulfils these requirements contains the linear-chain species $[Pt(en)X_2][Pt(en)X_4]$, where en is ethylenediamine ($C_2H_8N_2$). $^{15}N_2$-en.2HCl is manufactured by MSD isotopes. The monomers $Pt^{II}(en)X_2$ and $Pt^{IV}(en)X_4$ (X = Cl, Br or I) are all simple to prepare.[223,224] The neutral-chain chloride, $[Pt(en)Cl_2][Pt(en)Cl_4]$, has long been known,[9,225,226] and synthetic routes for it and the related bromide and iodide are well established.[223,227] The mixed-valent character of these compounds was recognised soon after their initial synthesis,[227] and was confirmed by X-ray crystallographic analysis of the bromide.[17] Although the general structure is well known (see Figure 3.1.1), the Pt^{IV}-X and Pt^{II}-X distances for X = Cl or I have not been defined unambiguously. The en ligands are in the eclipsed conformation.[228,229] Only one monomeric complex, $Pt(en)Cl_2$, has had its crystal structure published.[230] The planar $Pt(en)Cl_2$ molecules form stacks similar to those in the HMMCs save that each unit is rotated successively by 180 °.

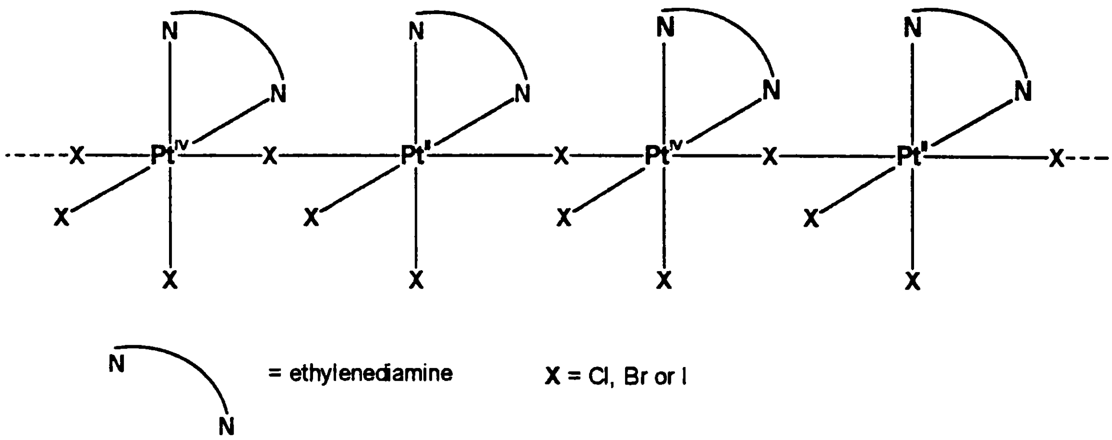

Figure 3.1.1 A representation of the structure of [Pt(en)X$_2$][Pt(en)X$_4$]

Two enantiomeric forms of Pt(en)X$_2$ arise because of the positions of the carbon atoms relative to the PtN$_2$X$_2$ plane (see Figure 3.1.2). Only one of the pair is usually present in a given crystal, although it is not known whether there is any variation throughout a polycrystalline sample.[229] The spectral properties of the chain compounds are known and they are typical of the HMMCs discussed in Chapter 1.[14]

Figure 3.1.2 Enantiomeric forms of the ligand ethylenediamine in its coordination to a platinum (II) centre.

The work in this chapter is primarily concerned with the preparation of ^{15}N-enriched samples of the neutral complexes for study by solid-state ^{15}N NMR spectroscopy, and a complementary solid-state ^{195}Pt NMR analysis of unenriched species. Subsequently there is an investigation of the reaction between [Pt(en)Cl$_2$][Pt(en)Cl$_4$] and HBr to determine the effect of bromide impurities on resonance Raman and solid-state NMR spectra.

3.2 Solid-State NMR Spectroscopy of Haloamine complexes

3.2.1 ^{15}N analysis of $[Pt(en)X_a]$ (X = Cl, Br or I; a = 2, 3 or 4)

The neutral complex $Pt(en)Cl_2$ (**301**) was made by a standard route,[224] except that enough ^{15}N-enriched en.2HCl was used to ensure a minimum concentration of 25 % ^{15}N sites in the sample. $Pt(en)Cl_4$ (**302**) was prepared from $Pt(en)Cl_2$ by a standard oxidation method,[218] and the linear-chain $[Pt(en)Cl_2][Pt(en)Cl_4]$ (**303**) was produced from the reaction of the two monomers. The corresponding bromide (**304-306**) and iodide (**307-309**) species were made by analogous routes. The solid-state ^{15}N NMR spectra were recorded for the nine complexes with empirical formula $[Pt(en)X_a]$ (X = Cl, Br or I; a = 2, 3 or 4), using about 50 mg of sample in each analysis (see Figures 3.2.1-3). ^{15}N-^{195}Pt coupling constants ($J_{N\text{-}Pt}$) are found easily for the three chloride complexes, but not for the corresponding bromides or iodides. When X = Br or I, there is more overlap between the satellites and the main resonance, partly because the coupling values are smaller, but mainly because the peaks are much broader. All halogen isotopes are quadrupolar; some have nuclear spin of $^3/_2$, *e.g.* ^{35}Cl, ^{37}Cl, ^{79}Br or ^{81}Br, while ^{127}I has a nuclear spin of $^5/_2$. This is thought to cause ^{15}N-X dipolar interactions that increase in the order Cl < Br < I, and which are not wholly removed by MAS.[231] The peaks in the chloride species are so well resolved that the ratios of intensity of satellites to main resonance can be evaluated; they are in the correct range for Pt-bound ^{15}N nuclei. ^{15}N chemical shifts and $J_{N\text{-}Pt}$ values for the nine spectra are listed in Table 3.2.1.

In the mixed-valence complexes, the magnitude of $\Delta\delta_N$, which is the difference between the shifts of the unsplit resonances, decreases in the order Cl > Br >I. Where assignments can be made, the same also seems to be true for the difference in coupling constant values. These trends imply that the Pt^{II} and Pt^{IV} centres become more similar to each other as the halogen is changed from Cl $\rightarrow$ Br $\rightarrow$ I. Although this is consistent with the accepted picture of charge delocalisation, comparison of HMMCs with their constituent monomers proves otherwise. For instance, in the case of $[Pt(en)Cl_2][Pt(en)Cl_4]$, the N-Pt^{II} and the N-Pt^{IV} chemical shifts are both 1.4 ppm upfield of the position in the corresponding monomer, so the separation of the peaks (*i.e.* $\Delta\delta_N$) is not altered by chain formation. The coupling constants, $J_{N\text{-}Pt^{II}}$ and $J_{N\text{-}Pt^{IV}}$, are both reduced on chain formation but are still well within the ranges associated with each particular oxidation state. In effect, the platinum environments have not changed relative to each other. Similar behaviour is exhibited in the analogous bromide system. The HMMC spectra in all cases can be approximated by superimposing those of the constituent molecules, and then applying a small shift upfield.

Simple trends are observed for the monomers. The main resonance in $Pt^{II}(en)X_2$ occurs further downfield as X is changed from Cl → Br → I, corresponding to a reduction in shielding around the nitrogen atoms. The reverse is true for $Pt^{IV}(en)X_4$, where the nitrogen atoms are more shielded when the halogens are larger. The net effect is that the $\delta_{N\text{-}Pt^{II}}$ and $\delta_{N\text{-}Pt^{IV}}$ values are more similar in the bromides than they are in the chlorides. In the iodide complexes, the N-Pt^{II} resonance is downfield of the N-Pt^{IV} resonance. It is likely that this relationship is maintained for $[Pt(en)I_2][Pt(en)I_4]$, although in principle the peaks in the iodide linear-chain can be assigned either way round. Selective enrichment of $[Pt(en)I_2][Pt(en)I_4]$ was attempted; $Pt(en)I_2$ was treated with $Pt(^{15}N_2\text{-en})I_4$, and $Pt(^{15}N_2\text{-en})I_2$ with $Pt(en)I_4$, giving a bronze product in either case. However, the spectra recorded are too similar for any conclusions to be made.

Table 3.2.1 **^{15}N chemical shifts and $J_{N\text{-}Pt}$ coupling constants for the species $[Pt(en)X_a]$ [a]**

^{15}N site probed:			H_2N-Pt^{II}		H_2N-Pt^{IV}		$\lvert\Delta\delta_N\rvert$
Complex	Crystal colour	Label	δ / ppm	J / Hz	δ / ppm	J / Hz	/ ppm
$Pt(en)Cl_2$	yellow	**301**	-382.8	390			
$Pt(en)Cl_4$	yellow	**302**			-355.9	260	
$[Pt(en)Cl_2][Pt(en)Cl_4]$	red	**303**	-384.2	350	-357.3	250	26.9
$Pt(en)Br_2$	yellow	**304**	-376.7	335			
$Pt(en)Br_4$	orange	**305**			-360.0	240	
$[Pt(en)Br_2][Pt(en)Br_4]$	green	**306**	-377.8	325	-362.1	245	15.7
$Pt(en)I_2$	yellow	**307**	-366.2	-			
$Pt(en)I_4$	mauve	**308**			-368.9	-	
$[Pt(en)I_2][Pt(en)I_4]$	copper	**309**	-369.5	-	-371.0	-	1.5

[a] *Chemical shifts are accurate to ± 0.3 ppm, coupling constants to ± 15 Hz, with the exception of $Pt(en)Br_2$, which is to ± 50 Hz.*

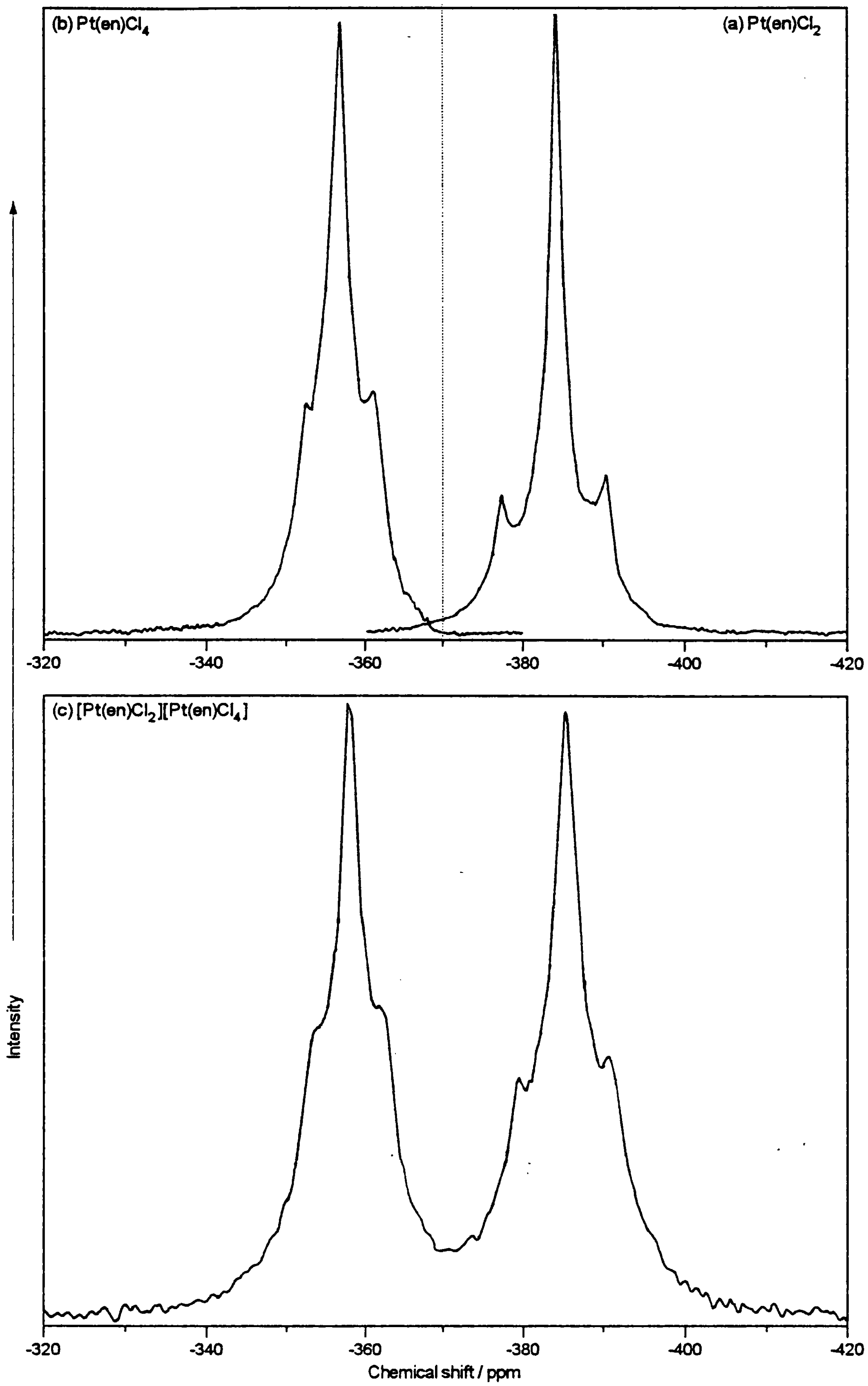

Figure 3.2.1 *Solid-state ^{15}N NMR spectra of (a) Pt(en)Cl_2, (b) Pt(en)Cl_4 and (c) [Pt(en)Cl_2][Pt(en)Cl_4].*

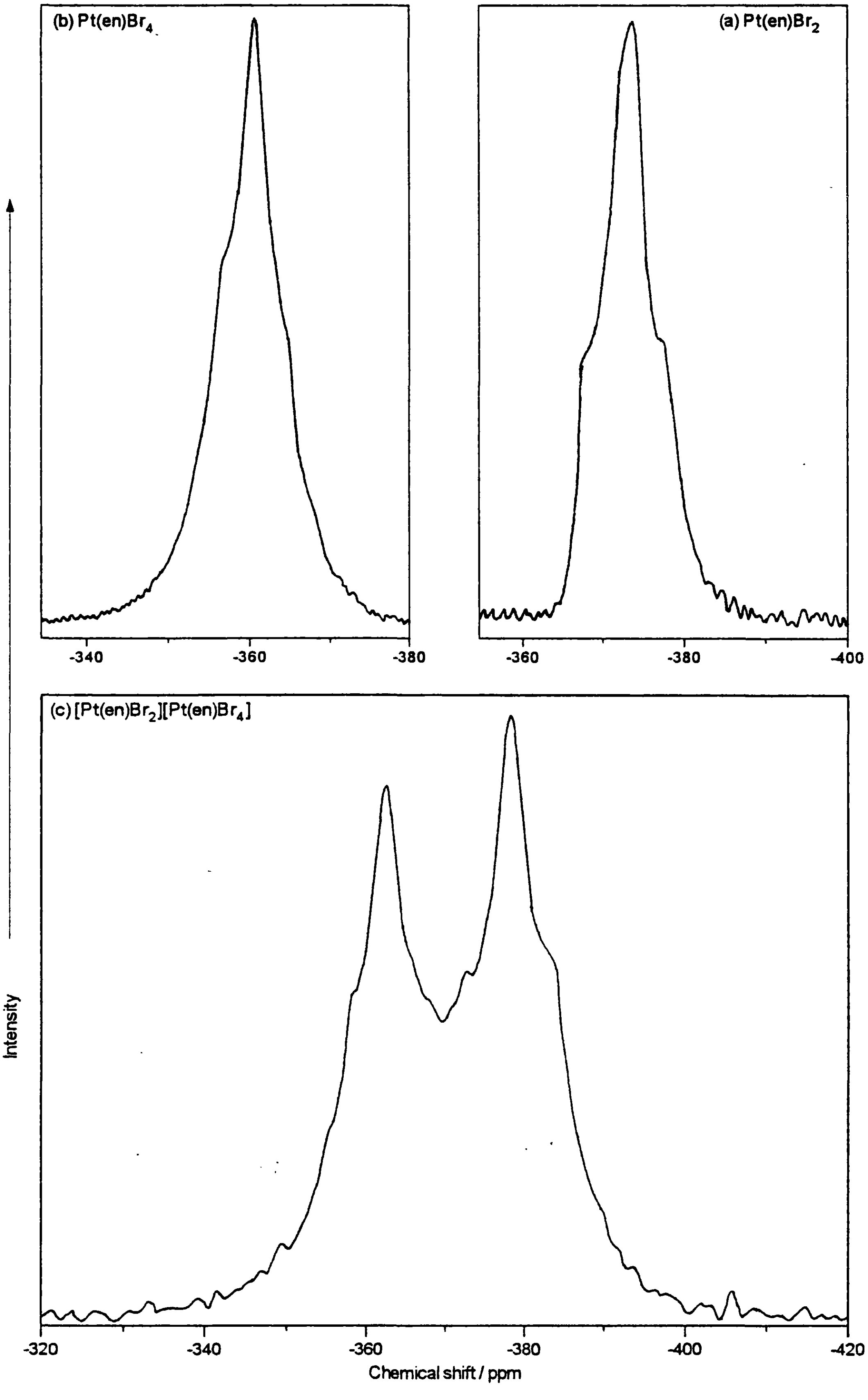

Figure 3.2.2 *Solid-state ^{15}N NMR spectra of (a) $Pt(en)Br_2$, (b) $Pt(en)Br_4$ and (c) $[Pt(en)Br_2][Pt(en)Br_4]$.*

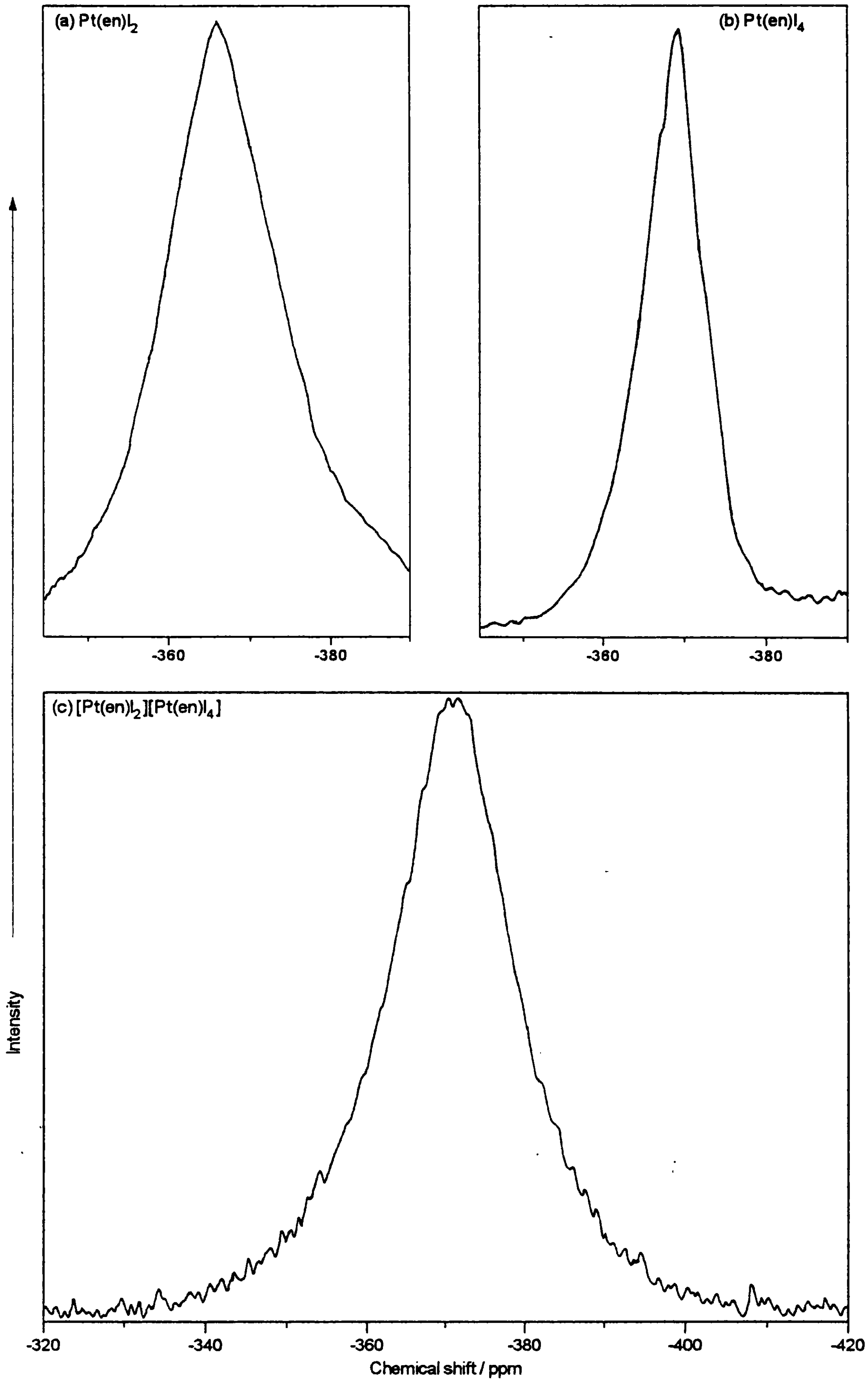

Figure 3.2.3 *Solid-state ^{15}N NMR spectra of (a) $Pt(en)I_2$, (b) $Pt(en)I_4$ and (c) $[Pt(en)I_2][Pt(en)I_4]$.*

3.2.2 ^{15}N analysis of [Pt(en)X_2][Pt(en)I_4] (X = Cl, Br or I)

To verify the assignments of the peaks in [Pt(en)I_2][Pt(en)I_4], the complexes [Pt(en)X_2][Pt(en)I_4] (X = Cl (**310**)or Br(**311**)) were synthesised. [Pt(en)Br_2][Pt(en)I_4] was made from Pt(en)Br_2 and Pt(en)I_4 by the reported method,[227] and [Pt(en)Cl_2][Pt(en)I_4] by an analogous route. The bronze-coloured products were analysed by solid-state ^{15}N NMR spectroscopy. Each spectrum contains two main peaks, one for the [Pt^{II}(en)X_2] units and one for the [Pt^{IV}(en)I_4] units; the ^{15}N chemical shifts alone are listed in Table 3.2.2, since coupling constants could not be determined accurately. There is no clear evidence in the spectra that scrambling of the X and I ligands occurs. Comparison with Table 3.2.1 shows that the positions of resonances for the [Pt^{II}(en)Cl_2] and [Pt^{II}(en)Br_2] segments are very similar to those in their respective single-halide linear-chains. There is greater variation in $\delta_{N\text{-}Pt^{IV}}$ for the [Pt^{IV}(en)I_4] unit, with the value in [Pt(en)Cl_2][Pt(en)I_4] being downfield of that in Pt(en)I_4. The position of the Pt^{IV} peak in [Pt(en)Br_2][Pt(en)I_4] occurs at high enough field to be near that assigned as the Pt^{IV} resonance in [Pt(en)I_2][Pt(en)I_4]. This provides additional support for the relative positions of the Pt^{II} and Pt^{IV} peaks in the iodide species, as indicated in Table 3.2.1.

Table 3.2.2 ^{15}N chemical shifts for the complexes [Pt(en)X_2][Pt(en)I_4] (X = Cl, Br or I) [a]

Complex	Crystal colour	Label	H_2N-Pt^{II}	H_2N-Pt^{IV}
			δ / ppm	δ / ppm
Pt(en)I_2	yellow	**307**	-366.2	
Pt(en)I_4	mauve	**308**		-368.9
[Pt(en)Cl_2][Pt(en)I_4]	copper	**310**	-383.9	-366.7
[Pt(en)Br_2][Pt(en)I_4]	copper	**311**	-377.4	-372.6
[Pt(en)I_2][Pt(en)I_4]	copper	**309**	-369.5	-371.0

[a] *Chemical shifts are accurate to ± 0.3 ppm.*

3.2.3 ^{195}Pt analysis of [Pt(en)X_a]

^{195}Pt MAS NMR spectra were recorded for the complexes [Pt(en)X_a] (X = Cl, Br or I, a = 2, 3 or 4). Samples were made with ligands containing naturally abundant nitrogen nuclei so that complications from ^{195}Pt-^{15}N coupling were avoided. The large sample size required for analysis would have made ^{15}N-enrichment far too expensive in any case. Scanning time was upwards of forty hours for all complexes except $Pt(en)Cl_4$. The difficulty in producing good quality solid-state ^{195}Pt NMR spectra has several causes. Platinum relaxation times are not known accurately, while the size of the dwell time between scans leads to a loss of data points. A wide spectral range must be excited, which requires a pulse that is potentially too short to excite a large enough number of nuclei. In addition, the direct bonding between the Pt nuclei and the quadrupolar halogens means that there is strong coupling that may not be totally removed, even under MAS conditions with high power decoupling.[232,233] With the exception of the nearly isotropic $Pt(en)Cl_4$, the neutral complexes give ^{195}Pt NMR spectra with many spinning sidebands, covering a range of about 8000 ppm in the worst case. Isotropic peaks were determined by pinpointing the resonance(s) unshifted by change of spinning speed. Two different rotor speeds, *ca.* 12 kHz and *ca.* 15 kHz, were generally sufficient to do this unambiguously. The spectra for the compounds $[Pt(en)Cl_a]$ (a = 2 or 3) and $[Pt(en)I_a]$ (a = 2 or 4) are shown in Figures 3.2.4-5, and the values extracted from them are shown in Table 3.2.3. There are certain terms in the table that are not encountered in the ^{15}N analysis and need to be defined. δ_{iso} is the isotropic chemical shift and refers to peaks that are not moved by change in the rotor speed. If spinning speeds were fast enough to remove all the spinning sidebands then peaks would only be seen at the δ_{iso} values. The isotropic shift is related to the three principle components of the ^{195}Pt shielding tensors (σ_{11}, σ_{22} and σ_{33}) by:

$$\sigma_{iso} = -\delta_{iso} = \tfrac{1}{3}(\sigma_{11} + \sigma_{22} + \sigma_{33}) \qquad [3.1.1]$$

$$\text{where } |\sigma_{33} - \sigma_{iso}| > |\sigma_{11} - \sigma_{iso}| > |\sigma_{22} - \sigma_{iso}| \qquad [3.1.2]$$

η is the asymmetry parameter. For Pt^{II} sites it is assumed to be zero, while for Pt^{IV} sites it is calculated from the expression:

$$\eta = (\sigma_{22} - \sigma_{11})/(\sigma_{33} - \sigma_{iso}) \qquad [3.1.3]$$

$\Delta\sigma$ is frequently termed the shielding anisotropy and is calculated as follows:

$$\Delta\sigma = \sigma_{33} - \tfrac{1}{2}(\sigma_{11} + \sigma_{22}) \qquad [3.1.4]$$

For the Pt^{IV} sites, $\Delta\sigma$ is obtained from the static spectra, giving an error of ± 40 ppm. The error in $\Delta\sigma$ for the Pt^{II} sites is ± 200 ppm, since the values are estimated from fast spinning results.

The set of results is not complete because some of the complexes do not give sufficient signal intensity in their solid-state ^{195}Pt NMR spectra. For instance, $[Pt(en)I_2][Pt(en)I_4]$ was prepared and analysed several times without success. The measurements that are obtained are consistent with the observations of the ^{15}N NMR studies. ^{195}Pt chemical shifts are particularly sensitive to the number and nature of adjacent ligands, yet chain formation barely affects δ_{iso} for $Pt(en)Cl_2$ or for $Pt(en)Cl_4$, and deshields both metal centres. $\Delta\sigma$ is also affected little by chain formation. Both $\Delta\sigma$ values for $[Pt(en)Cl_2][Pt(en)Cl_4]$ are greater than those in the respective monomers. The relative values of δ_{iso} for $Pt(en)I_2$ and for $Pt(en)I_4$ are the reverse of those for the corresponding chloride species, which mirrors the pattern for their δ_N values.

Table 3.2.3 **^{195}Pt MAS spectral results for the complexes $[Pt(en)X_a]$ (a = 2, 3 or 4 for X = Cl or I, or a = 2 for X = Br) [a]**

Complex	Pt^{II}			Pt^{IV}		
	δ_{iso} / ppm	$\Delta\sigma$ / ppm	η	δ_{iso} / ppm	$\Delta\sigma$ / ppm	η
$Pt(en)Cl_2$ [b]	-2154	-8100	0			
$Pt(en)Cl_4$				-374	-380	0.14
$[Pt(en)Cl_2][Pt(en)Cl_4]$ [b]	-1924	-7300	0	-328	+230	0.10
$[Pt(en)Br_2][Pt(en)Br_4]$	-	-	-	-1429	-	-
$Pt(en)I_2$	-3288	-6500	0			
$Pt(en)I_4$				-3605	-2180	0.33
$[Pt(en)I_2][Pt(en)I_4]$	Signal too weak			Signal too weak		

[a] *δ_{iso} values are accurate to ± 8 ppm, and are relative to 1 M aqueous Na_2PtCl_6. The estimated error in $\Delta\sigma$ is ± 40 ppm for the Pt^{IV} centres, and ± 200 ppm for the Pt^{II} centres.*

[b] *δ_{iso} values have been adjusted from those in Figure 3.2.4, which show chemical shifts relative to $PtCl_4^{2-}$ rather than to $PtCl_6^{2-}$.*

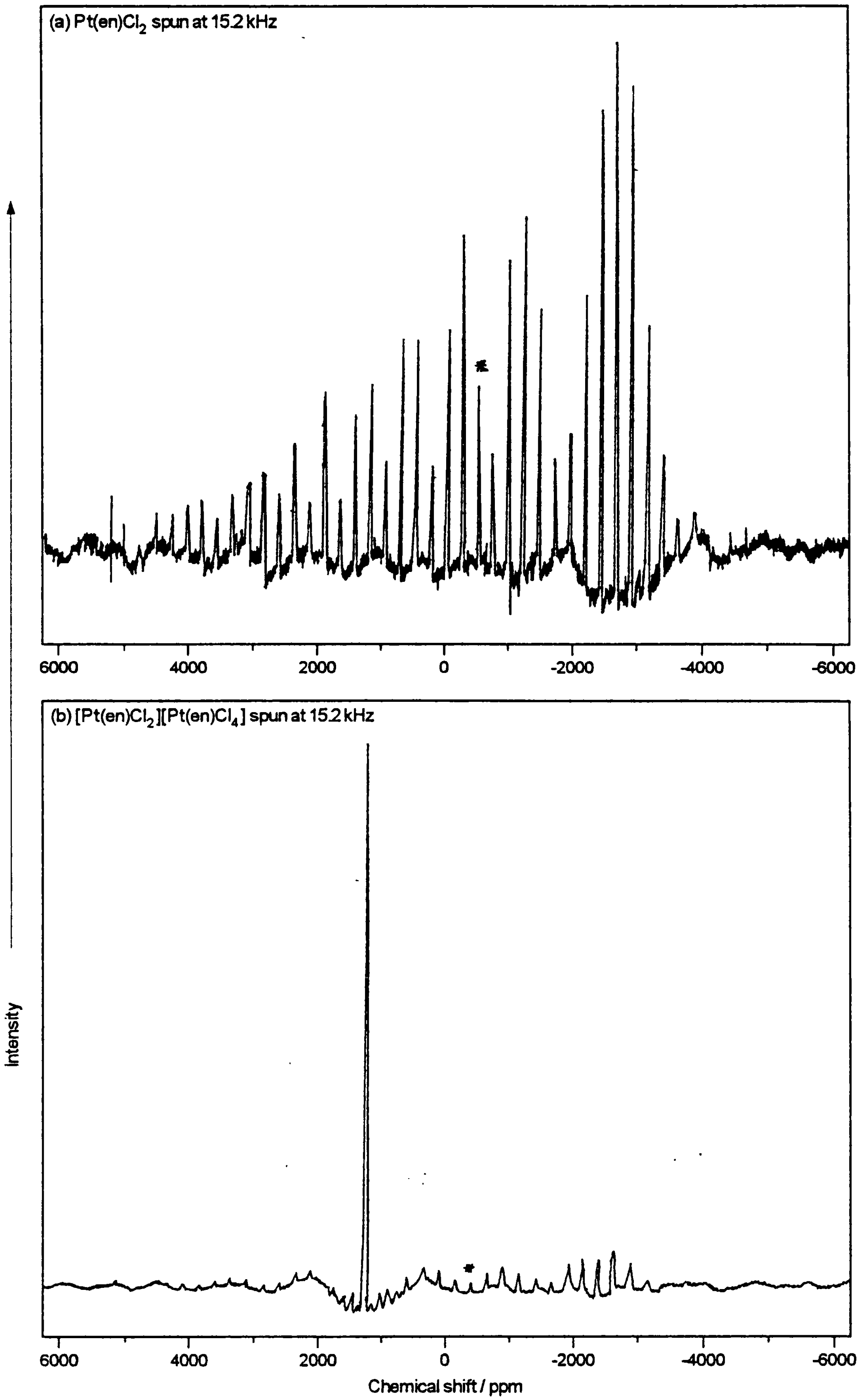

Figure 3.2.4 *Solid-state ^{195}Pt NMR spectra recorded at one spinning speed for (a) $Pt(en)Cl_2$ and (b) $[Pt(en)Cl_2][Pt(en)Cl_4]$. Isotropic peaks are starred.*

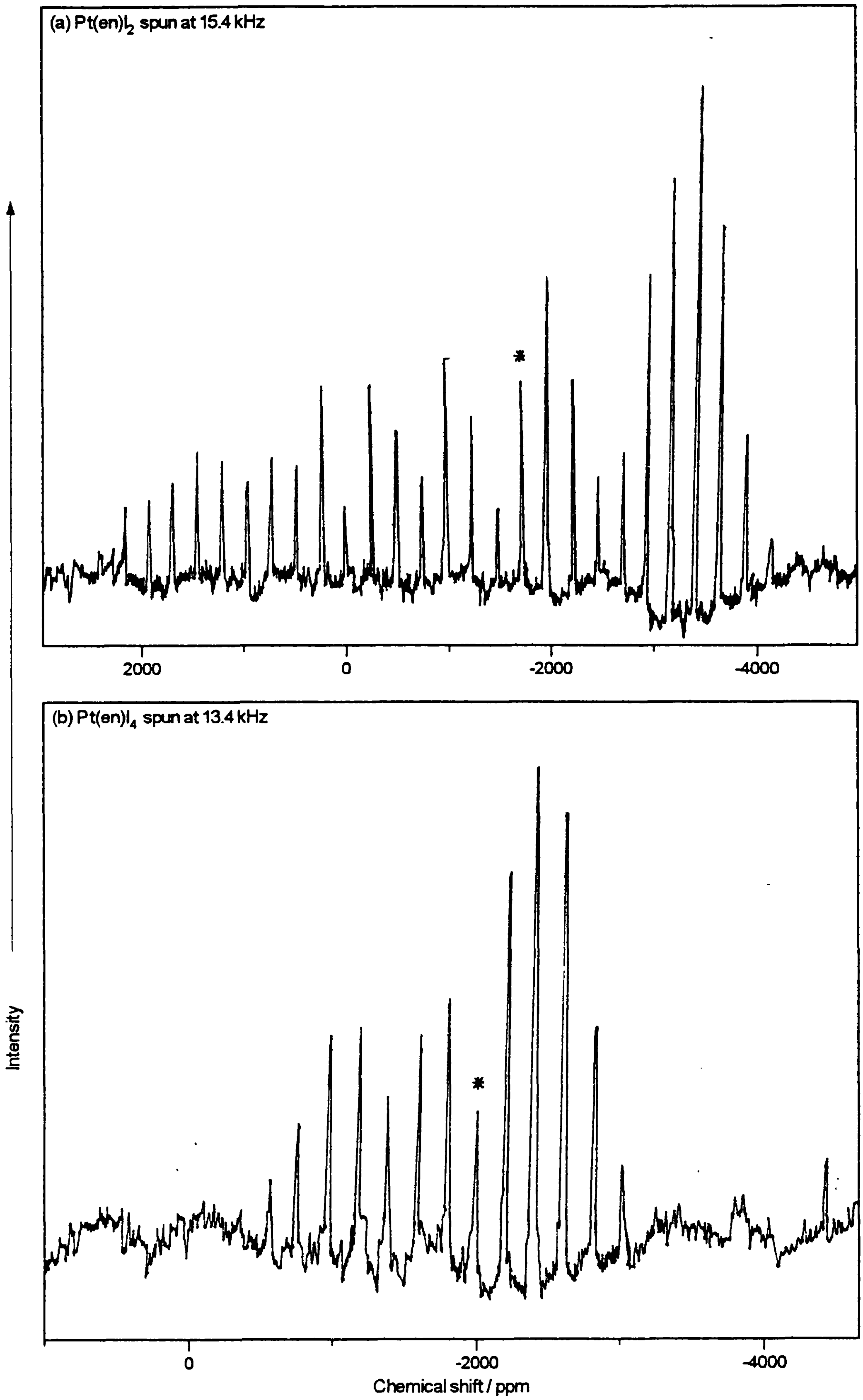

Figure 3.2.5 *Solid-state ^{195}Pt NMR spectra recorded at one spinning speed for (a) $Pt(en)I_2$ and (b) $Pt(en)I_4$. Isotropic peaks are starred.*

3.2.4 Discussion of the solid-state NMR results

The aim of this work is to understand the influence of certain properties of the platinum complexes so that the trends in chemical shift (δ_N or δ_{Pt}) or coupling constant ($J_{N\text{-}Pt}$) can be explained. There are three factors that have to be taken into account: the identity of the halogens coplanar with en, the identity of the axial substituents and the effect of chain formation. Because there have been few solid-state NMR spectroscopic studies on either ^{15}N or ^{195}Pt nuclei, it is difficult to find data with which to make direct comparisons. Both nuclei have been examined extensively in solution, but the effect of chain formation is necessarily peculiar to the solid state. Reference is made to the solution studies by necessity, but this is not done without reservation since there are solid state effects that cannot be quantified. Solution NMR theory has not advanced sufficiently to allow the ^{15}N or ^{195}Pt NMR spectra of even the simplest compounds to be reproduced theoretically, nor indeed for the effect on chemical shift of substituent change to be predicted accurately.[213] The solid-state NMR study is limited to the appreciation of trends, rather than to the explanation of individual results.

The influence of the halogens coplanar with ethylenediamine can be determined from the solid-state NMR spectra of $Pt^{II}(en)X_2$. In the graphs below, data from these spectra are compared with those from the solution NMR spectra of *cis*-$Pt^{II}(NH_3)_2X_2$ (X = Cl, Br or I).[213] There is good correlation between the two sets of compounds, both for δ_N (Figure 3.2.6), and for δ_{Pt} (Figure 3.2.7). Therefore the arguments used to account for the *cis*-diammine results may be applied to the solid-state NMR data with some confidence. In mixed-valence systems, the charge associated with the metal centres is of interest. For metals the dominant factor in the magnetic shielding is the local paramagnetic contribution, σ_p.[202,234] σ_p depends on three properties of the system: the asymmetry of the outer shell electronic distribution (the platinum 5d and 6p orbitals), the mean inverse cube of the distance of these electrons from the nucleus, and the size of the ligand field transition energy (ΔE). If changes in the first two are small, then there should be a strong correlation between ^{195}Pt chemical shift and ΔE, but this has not been observed,[235,236] nor have attempts to include other contributions such as 5d orbital contraction been successful. In studies on the complexes *trans*-$Pt(H)ZL_2$ ($L = PEt_3$), the shielding around the metal has been related to the covalency of the Pt-Z bond.[237] When the coordinating nucleus in Z is large and has orbital energies matching those of the Pt_{5d} shell then the metal will be better shielded; this is the "heavy-atom effect".[235,236]

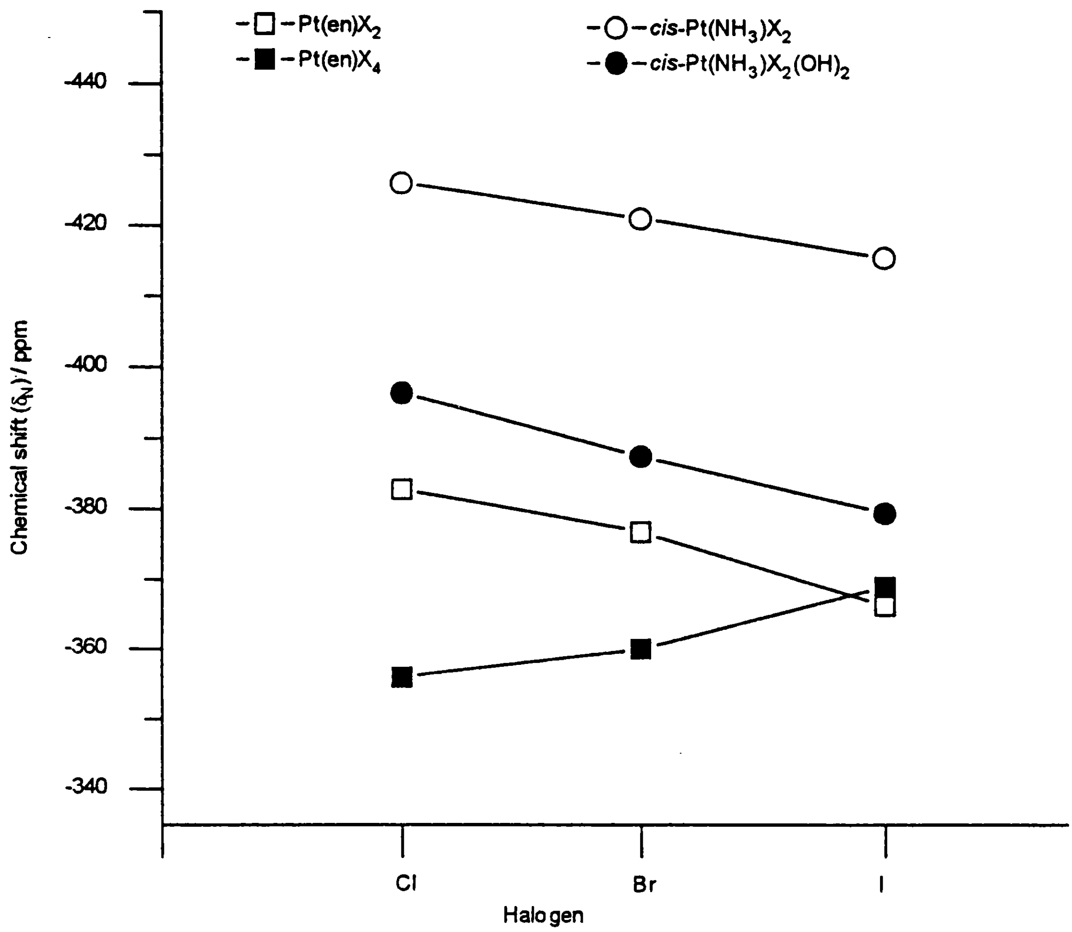

Figure 3.2.6 *A graph displaying the solid-state δ_N values for Pt(en)X_2 and Pt(en)X_4 and the solution δ_N values for* cis-*Pt(NH_3)$_2X_2$ and* cis-*Pt(NH_3)$_2X_2$(OH)$_2$ (X = Cl, Br or I). The squares represent solid-state data taken from Table 3.2.1, and the circles represent solution data.[213] All chemical shifts are referenced externally to nitromethane.*

Theoretical analysis of the hydride chemical shift (δ_H) in the same system has shown that motion of the metal electrons that increases the shielding around the platinum will in turn deshield the hydrogen atom.[238,239] The influence of Z on δ_H is related to changes in the paramagnetism of the metal. There has been no equivalent theoretical treatment for ^{15}N chemical shifts (δ_N). δ_N has been linked to effective charge in simple free amines in the same way that ^{13}C or ^{17}O shifts have been in other ligands,[240] and it has a linear relationship with the stretching frequency ν_{NH} in saturated primary amines.[241] Few patterns have been established for δ_N values for amine ligands coordinated to platinum, although variation of δ_N in *cis*-$Pt(NH_3)_2X_2$ has been discussed in similar terms to that of δ_H in *trans*-Pt(H)ZL_2.[213] By analogy, in the solid state, the shielding around the nitrogen atoms is expected to decrease as the halogen is changed from Cl → Br → I. The "heavy atom" effect, whereby the larger halogens have better orbital overlap with the metal, is responsible for the change in δ_{Pt}.[213] No value of δ_{Pt} was recorded for Pt(en)Br_2, but the platinum atom is much more shielded in Pt(en)I_2 than it is in Pt(en)Cl_2.

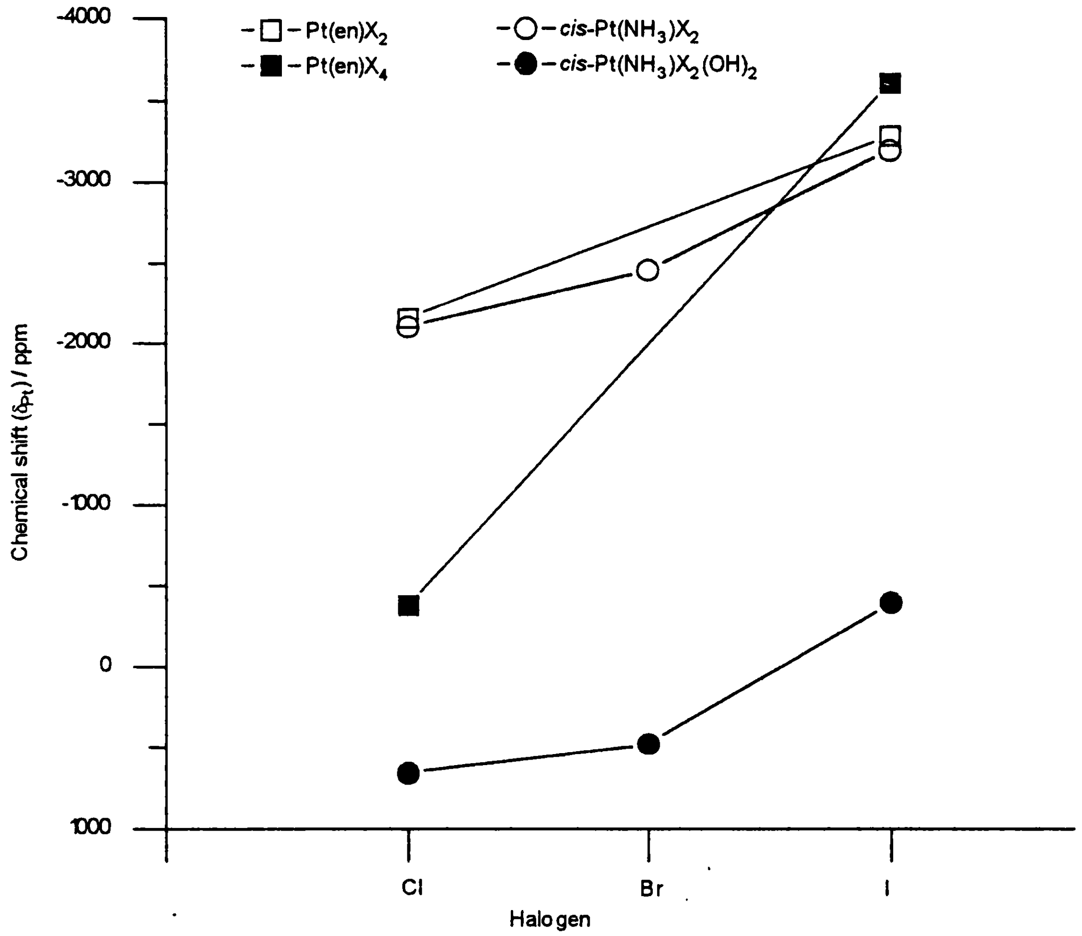

Figure 3.2.7 *A graph displaying the solid-state δ_{Pt} values for Pt(en)X_2 and Pt(en)X_4 and the solution δ_{Pt} values for* cis-*$Pt(NH_3)_2X_2$ and* cis-*$Pt(NH_3)_2X_2(OH)_2$ (X = Cl, Br or I). The squares represent solid-state data taken from Table 3.2.3, and the circles represent solution data.[213] Aqueous Na_2PtCl_6 is the reference for all data.*

There is a *cis* and a *trans* contribution to δ_N. Appleton *et al.* evaluated them by analysing the two ^{15}N chemical shifts for $[Pt^{II}(NH_3)_3X]^+$ (X = Cl, Br or I).[213] They are shown in Table 3.2.4

where they are quoted relative to those for $[Pt(NH_3)_4]^{2+}$ ions. The *trans* shifts are some three times greater than the *cis* shifts, and act in the opposite direction as a direct result of the paramagnetism around the metal atom. Thus the ligand *trans* to the nitrogen atom analysed is the main influence on δ_N in *cis*-$Pt(NH_3)_2X_2$, and hence on δ_N in $Pt(en)X_2$.

Table 3.2.4 Solution NMR results for $[Pt^{II}(NH_3)_3X]^+$ (X = Cl, Br or I) [a]

X	$\Delta(\delta_{Pt})$ / ppm	$\Delta(\delta_{N_{cis}})$ / ppm	$\Delta(\delta_{N_{trans}})$ / ppm	$\Delta(J_{cis})$ / Hz	$\Delta(J_{trans})$ / Hz
Cl	+227	-2.9	+0.9	+44	-6
Br	+88	+3.7	-1.5	+32	-11
I	-239	+16.6	-5.3	+2	-18

[a] *Chemical shifts and coupling constant values are quoted relative those found for $[Pt(NH_3)_4]^{2+}$ ions. All data are taken from reference 213.*

The interpretation of the one-bond coupling constant $J_{^{15}N-^{195}Pt}$ is better established than that of any of the chemical shifts. Although there are several possible contributions to the value of the coupling constant, the most important is the Fermi contact terms which in solution is:[211]

$$\left|{}^1J_{^{15}N-^{195}Pt}\right| \propto \alpha_{Pt}^2\alpha_N^2\left|\psi_{Pt_{6s}}(0)\right|^2\left|\psi_{N_{2s}}(0)\right|^2 \qquad [3.2.1]$$

The α^2 terms represent the proportion of s character of the hybrid orbital used in the Pt-N bond by each atom. The $|\psi|^2$ wavefunctions are the electron density of the subscripted orbital at the relevant nucleus, and are taken at the atom centre, *i.e.* zero coordinate. Variation in J_{N-Pt} is normally attributed to a change in α_{Pt}^2, the Pt_{6s} contribution to the Pt-N bond. Chemical shifts are related to properties of the Pt_{5d} orbitals. As a crude approximation, the hybridised orbitals are assumed to be dsp^2 for Pt^{II} and d^2sp^3 for Pt^{IV}, which equates to an *s*-orbital contribution of one quarter and one sixth respectively. If all other terms are assumed to be invariant, then the J_{N-Pt} coupling will be about 50 % bigger in the platinum (II) complex. Coupling constants for the peak positions depicted in Figure 3.2.6 are shown in Table 3.2.5. J_{N-Pt} is significantly smaller for $Pt(en)Br_2$ than it is for $Pt(en)Cl_2$, which suggests that the Pt_{6s} contribution to its Pt-N bond is smaller. The coupling for *cis*-$Pt(NH_3)_2I_2$ in solution does not fit this pattern, because it is larger than that for *cis*-$Pt(NH_3)_2Br_2$, probably due to steric crowding of the iodide ions.[213] Little else can be deduced from the platinum (II) results alone, nor can the greater variation of J_{N-Pt} values for $Pt(en)X_2$ be explained simply.

Table 3.2.5 Comparison of the coupling constants for Pt(en)X$_2$ or Pt(en)X$_4$ (this work) with those for *cis*-Pt(NH$_3$)$_2$X$_2$ or *cis*-Pt(NH$_3$)$_2$X$_2$(OH)$_2$ [213]

X	Pt(en)X$_2$	Pt(en)X$_4$	Ratio	*cis*-Pt(NH$_3$)$_2$X$_2$	*cis*-Pt(NH$_3$)$_2$X$_2$(OH)$_2$	Ratio
	$J_{^{15}N\text{-}Pt}$ / ppm	$J_{^{15}N\text{-}Pt}$ / ppm		$J_{^{15}N\text{-}Pt}$ / ppm	$J_{^{15}N\text{-}Pt}$ / ppm	
Cl	390	260	1.50	326	271	1.20
Br	335	240	1.40	310	247	1.26
I	-	-	-	311	199	1.56

The axial substituents are the second influence on nuclear environments. The effect of oxidation state change can be gauged by comparing *cis*-Pt^{IV}(NH$_3$)$_2$X$_2$(OH)$_2$ with *cis*-Pt(NH$_3$)$_2$X$_2$ (X = Cl, Br or I), where the hydroxyl groups in the Pt^{IV} complexes are in the axial position (see Figures 3.2.6-7).[213] Irrespective of the equatorial halogen, the shielding around the metal for a given Pt^{IV} complex is less than that in the related *cis*-Pt(NH$_3$)$_2$X$_2$. This is thought to be due to the contraction of the Pt$_{5d}$ orbital that occurs as the positive charge is increased. Results suggest that X has a slightly greater influence in the higher oxidation state,[213] since the change in δ_N or δ_{Pt} with X is about 25 % larger in the Pt^{IV} complexes. The solid-state NMR data for Pt(en)X$_4$ are also shown in Figures 3.2.6-7. They follow trends that are the opposite of those observed in Pt(en)X$_2$, *cis*-Pt(NH$_3$)$_2$X$_2$ or *cis*-Pt^{IV}(NH$_3$)$_2$X$_2$(OH)$_2$. For example, the nitrogen nuclei are more shielded as X is changed from Cl $\rightarrow$ Br $\rightarrow$ I, so much so that the shifts in Pt(en)I$_4$ appear on the "wrong" side of those for Pt(en)I$_2$; δ_N is at higher field, and δ_{Pt} at lower field, for Pt(en)I$_4$. The relationship between Pt(en)X$_2$ and Pt(en)X$_4$ is less straightforward than that between *cis*-Pt(NH$_3$)$_2$X$_2$ and *cis*-Pt^{IV}(NH$_3$)$_2$X$_2$(OH)$_2$. In Pt(en)X$_4$, the inductive effect of the axial halogens has more influence on the electronic environments of platinum or nitrogen nuclei than the heavy atom effect of the equatorial halogens. If this means that the Pt-N bonds in Pt(en)I$_4$ are more covalent than those in Pt(en)I$_2$, then the Pt^{IV} nuclei will be more shielded at the expense of the N nuclei, and the formal oxidation states of +2 or +4 will not be applicable to Pt(en)I$_2$ or Pt(en)I$_4$. The coupling constants for Pt(en)X$_4$ obey the theoretical relationship to the Pt(en)X$_2$ values, although there is little correlation between them and the solution values of the *cis*-diammines. The ratio of $J_{N\text{-}Pt^{II}}$ to $J_{N\text{-}Pt^{IV}}$ is exactly 1.5 when X = Cl and slightly lower when X = Br, which is consistent with the relative values of α^2_{Pt}.

The main objective of this work is the analysis of HMMCs under the same conditions as their constituent monomers. The most important and surprising discovery is that the act of chain formation has little effect on either the coupling constants or the chemical shifts. Although the reduction in $J_{N\text{-}Pt}$ for the $[Pt(en)Cl_2]$ unit, from 390 Hz in $Pt(en)Cl_2$ to 350 Hz in $[Pt(en)Cl_2][Pt(en)Cl_4]$, equates to the s-orbital contribution falling from 25 % to 22 % (in terms of the simple model in Equation [3.2.1]) this is not a significant result. The coupling for the $[Pt(en)Cl_4]$ segment, which is assumed to have a minimum of s character in the monomer, is also reduced. In addition, the couplings for the bromide constituents are unaltered by chain formation, within experimental error. The effect of chain formation on ^{15}N chemical shift is to move δ_N upfield consistently throughout by a very small amount, which means that the nitrogen nuclei are better shielded in the HMMCs than in the monomers. This is mirrored by the ^{195}Pt chemical shifts. Each δ_{Pt} for $[Pt(en)Cl_2][Pt(en)Cl_4]$ is downfield of the corresponding values in $Pt(en)Cl_2$ and $Pt(en)Cl_4$, and so the metals are less shielded. The effect of chain formation on $\Delta\sigma$ is comparable for Pt^{II} and Pt^{IV} centres. Unfortunately, there are insufficient data with which to discuss the effect of chain formation on δ_{Pt} for X = Br or I. Discussion of solid-state NMR results must be tempered by the knowledge that there are intermolecular forces in addition to intramolecular ones, and that the chemical shift might not be determined by atoms within each molecule alone. But to a first approximation, where no counterions are present, intermolecular effects are assumed to be the same for related chains and monomers. Using this assumption it may be stated that these results are contrary to the normal image of HMMC production, in which net charge transfer occurs between M^{II} and M^{IV} centres, *i.e.* charge delocalisation. Instead, the shielding around all Pt nuclei decreases, while that around N nuclei increases, and so there is no change to the Pt^{II} and Pt^{IV} environments relative to one another. This is taken to imply that there is no net transfer of charge between metal sites as a result of chain formation, and so the fact that charge appears to be more delocalised in $[Pt(en)I_2][Pt(en)I_4]$ than in $[Pt(en)Cl_2][Pt(en)Cl_4]$ merely reflects the relative differences in effective oxidation state between $Pt(en)I_2$ and $Pt(en)I_4$ and between $Pt(en)Cl_2$ and $Pt(en)Cl_4$.

3.3 A study of the reaction of [Pt(en)Cl2][Pt(en)Cl4] with HBr

3.3.1 Introduction

Raman spectra were collected for the samples of $[Pt(en)X_2][Pt(en)X_4]$ which had been synthesised for the NMR investigation. By no means is this new work, since the infrared and Raman spectra of all three linear-chain complexes have been reported. $[Pt(en)Cl_2][Pt(en)Cl_4]$ and $[Pt(en)Br_2][Pt(en)Br_4]$ were analysed in 1978,[242] $[Pt(en)I_2][Pt(en)I_4]$ in 1981.[243] The resonance Raman spectra are typical of those of HMMCs since they are dominated by the ν_1 mode, the symmetric ($X-Pt^{IV}-X$) stretch, and its overtones. Also typical is the exhibition of other weaker modes, particularly in the case of the chloride complex. Not all of these are due to vibrations that exist in the simple chain models (see section **1.6**). Some have remained unattributed to any mode, while others have been assigned intuitively rather than analytically. The lack of assignments has not been perceived as a problem previously because the ν_1 mode has always been of greatest interest, but recent work has suggested that many preparations of $[Pt(en)_2][Pt(en)_2X_2](ClO_4)_4$ (X = Cl or Br) and related complexes might produce halogen impurities in the MX chains.[38] In the case of $[Pt(en)_2][Pt(en)_2Cl_2](ClO_4)_4$, there are two areas of the spectrum that cause concern. There is a weak signal at *ca.* 210 cm^{-1}, which occurs in most MX chains, and is normally thought to relate to the bending mode $\delta(PtN_2)$, and either one or two small bands that are observed at *ca.* 180 cm^{-1} but have rarely been ascribed to any mode. There are large peaks in the same regions in the spectra of the mixed-halide complexes $[Pt(en)_2][Pt(en)_2Cl_{2-2\alpha}Br_{2\alpha}](ClO_4)_4$ which are attributed to a $\nu(Br-Pt^{IV}-Cl)$ vibration and the $\nu_1(Br-Pt^{IV}-Br)$ symmetric stretch, respectively.[38,55] There is no identifiable cause for widespread bromine contamination of chloride-chain species, but the correlation of these peaks does suggest that it is a possibility. One-dimensional models that are used to assign impurity modes are very simple, and cannot account for all the modes that give rise to Raman bands. This includes vibrations that involve motion of the equatorial ligands or of chain atoms away from the main axis. Asymmetry is inherent in HMMCs and is caused by simple physical defects such as terminations, or by electronic defects (see section **1.5**), or by isotopic effects. It means that chain vibrations are rarely truly symmetric, and so modes that are expected to be Raman-inactive will possess some Raman activity.

This section concerns the reaction of [Pt(en)Cl$_2$][Pt(en)Cl$_4$] with different proportions of hydrobromic acid. The effect on the Raman spectra of the HMMC of introducing bromine atoms into the chlorine chain is investigated to show whether the weak signals in the Raman spectra of [Pt(en)Cl$_2$][Pt(en)Cl$_4$] or [Pt(en)Br$_2$][Pt(en)Br$_4$] are due to halogen impurities. A standard solution of HBr was prepared and four reagent systems were made by adding 0.2, 1.0, 2.0 or 4.0 molar equivalents of Br^- ions to [Pt(en)Cl$_2$][Pt(en)Cl$_4$] (see Table 3.3.1). The crystalline products (**312a - 312d**) ranged in colour from red-brown, through blue, to green. Chemical analysis was used to determine the amounts of chlorine and bromine present in each case, which are expressed in terms of atoms per unit cell.

Table 3.3.1 Reaction mixtures of [Pt(en)Cl$_2$][Pt(en)Cl$_4$] and HBr

Label	Crystal colour	Molar equivalents of HBr added	Maximum % of Br atoms in chain	No. of atoms per unit cell [a]	
				Cl	Br
303	red	-	0	6	0
312a	red-brown	0.2	10	5.8	0.2
312b	blue	1.0	50	5.0	1.0
312c	grey	2.0	100	4.1	1.9
312d	green	4.0	100	2.4	3.6
306	green	-	100	0	6

[a] *found by chemical analysis.*

3.3.2 Solid-state ^{15}N NMR results

Solid-state ^{15}N NMR spectroscopy is sensitive enough to distinguish between nitrogen nuclei in related complexes. The difference between the ^{15}N chemical shifts of Pt(en)Cl$_2$ and Pt(en)Br$_2$ is sufficient for the composition of partially brominated [Pt(en)Cl$_2$][Pt(en)Cl$_4$] to be determined qualitatively. The solid-state ^{15}N NMR spectra of the six HMMC samples, including [Pt(en)Cl$_2$][Pt(en)Cl$_4$] and [Pt(en)Br$_2$][Pt(en)Br$_4$], are shown in Figures 3.3.1-2.

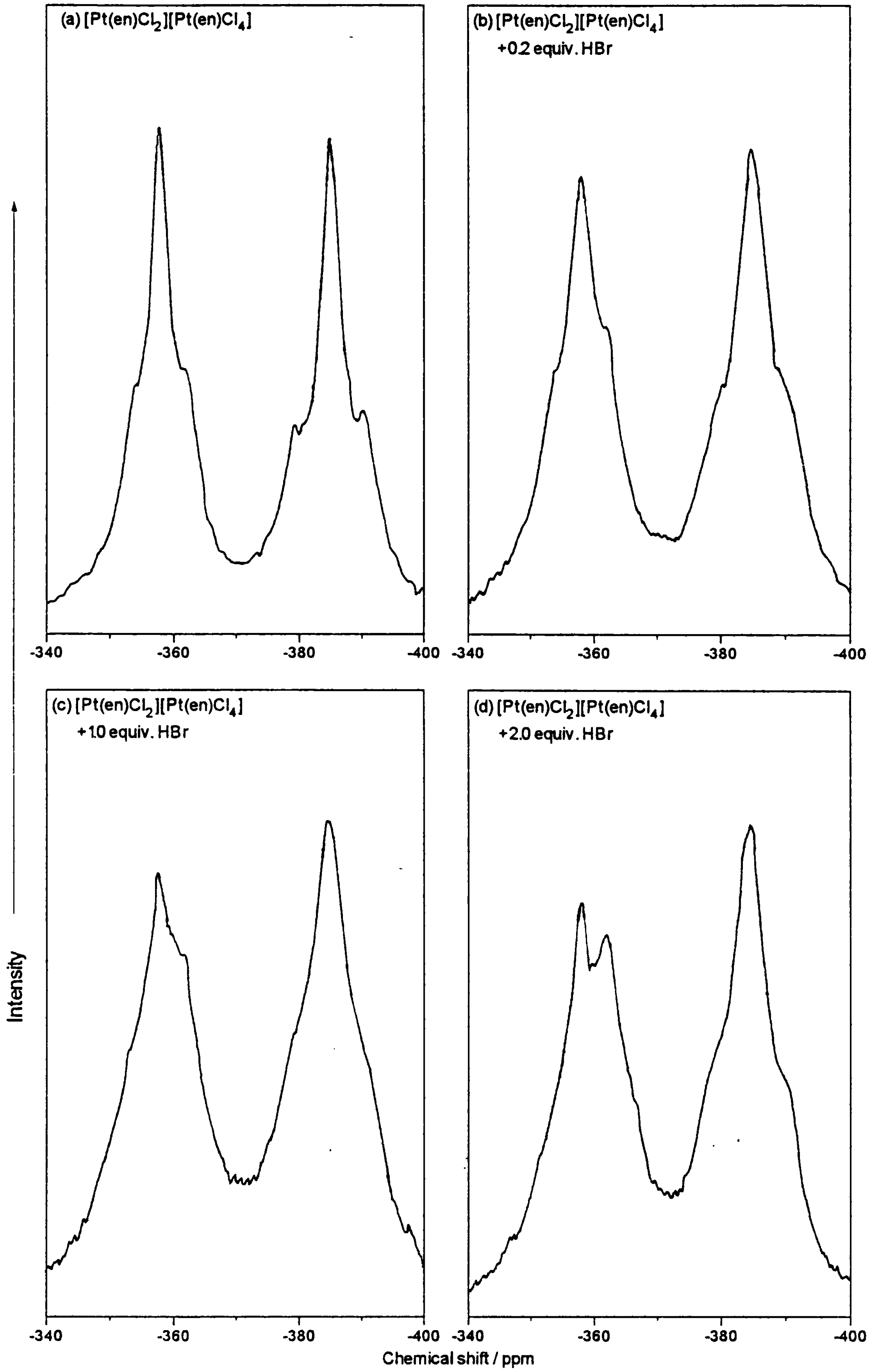

Figure 3.3.1 *Solid-state ^{15}N NMR spectra of (a) $[Pt(en)Cl_2][Pt(en)Cl_4]$ and of the mixed-halide complexes (b)* ***312a****, (c)* ***312b*** *and (d)* ***312c****.*

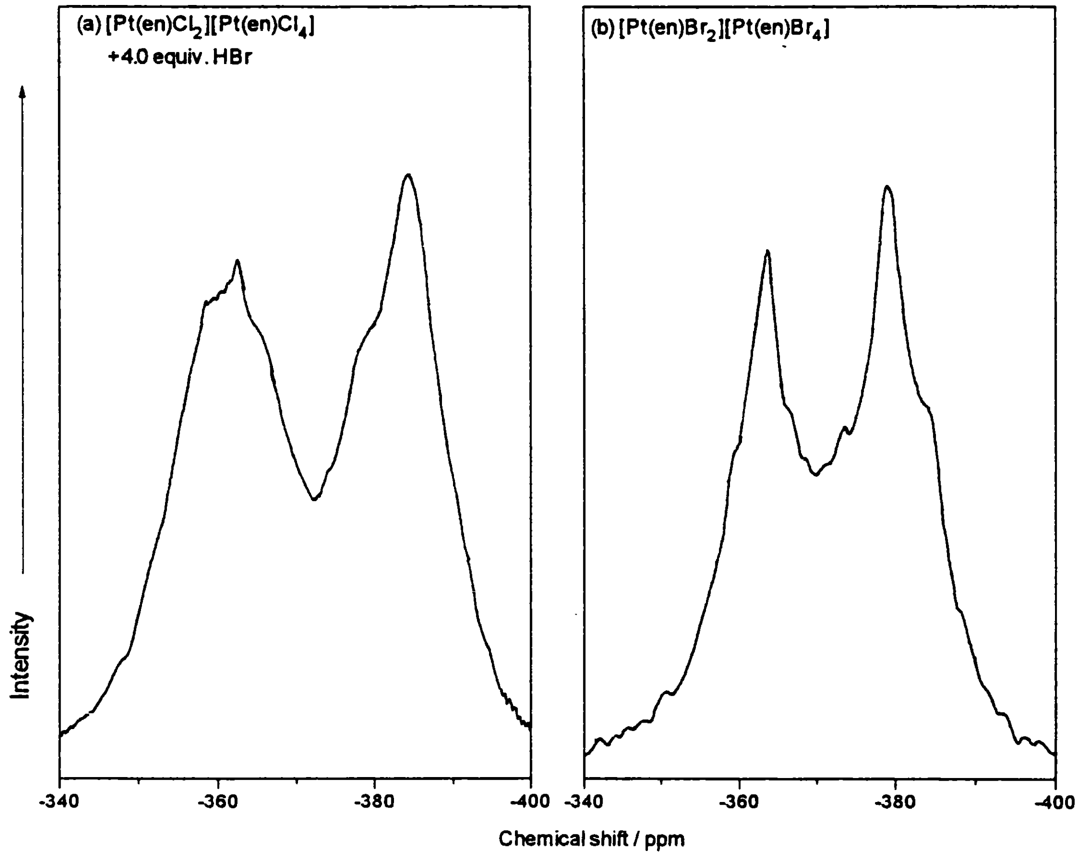

Figure 3.3.2 *Solid-state ^{15}N NMR spectra of (a) the mixed-halide complex **312d** and (b) [Pt(en)Br$_2$][Pt(en)Br$_4$].*

The shapes of the spectra indicate that bromination does not affect the N-Pt^{II} and N-Pt^{IV} resonances in the same way. No great change was expected in the N-Pt^{II} region, but the peak broadens on its low field side as the bromine proportion increases, resulting in a distinct signal at around -378 ppm in **312d**. Deconvolution of the NMR spectra has shown that there are many peaks in the N-Pt^{IV} region of the brominated species, but only three are strong enough to be resolved by the naked eye. At low bromine concentrations a signal appears at about -361 ppm, which is on the high field side of the resonance for the [Pt^{IV}(en)Cl$_4$] unit. It gains in intensity as the bromide proportion is increased so that in **312d** it is the larger of the two. The [Pt^{IV}(en)Cl$_4$] signal falls away as bromination is continued until it is absent from the spectrum of [Pt(en)Br$_2$][Pt(en)Br$_4$]. The peak at -361 ppm does not dominate immediately though, because a second new resonance emerges at still higher field (near -368 ppm), most prominently for **312d**. In the N-Pt^{IV} region of the spectrum of [Pt(en)Br$_2$][Pt(en)Br$_4$], the -361 ppm signal is the only one present.

3.3.3 Discussion of the solid-state NMR results

The three partially brominated products **312a - 312c** were expected to have the formula [Pt(en)Cl$_2$][Pt(en)Cl$_2${Cl$_{2-2\alpha}$Br$_{2\alpha}$}], where the {} brackets signify chain halogens, and α has the value 0.1, 0.5 or 1.0 respectively. However, the signal at around -378 ppm gets more intense as the bromine content increases, which changes the shape of the N-Pt^{II} region. The N-Pt^{II} signal for [Pt(en)Br$_2$][Pt(en)Br$_4$] is at -377.8 ppm; the two peaks for the mixed-halide unit [Pt^{II}(en)ClBr] are probably at *ca.* -384 and -377 ppm, respectively.[213] Therefore some of the equatorial chlorine ligands at Pt^{II} sites must be replaced by bromine ligands. The degree of replacement can be evaluated approximately from the relative intensities of the peaks within the N-Pt^{II} signal. For instance, in **312c** the N-Pt^{II} signal can be deconvoluted into two parts in which the peak at *ca.* -384 ppm contributes about 80 % of the total intensity. So roughly 20 % of the chlorine atoms in the bulk population of [Pt^{II}(en)Cl$_2$] are replaced randomly by bromine. There is no reason to suppose that bromine substitution of the Pt^{IV} equatorial Cl atoms will not occur as well. For the sake of argument, the fraction of halogens replaced is assumed to be the same. Therefore, of the four equatorial chlorine atoms in any subunit, an average of 0.8 will be replaced when [Pt(en)Cl$_2$][Pt(en)Cl$_4$] is treated with two equivalents of HBr. This means that of the two equivalents of bromine atoms added, a maximum of 1.2 will enter the chain, which equates to 60 % replacement.

The Pt^{IV} centres have two sorts of ligand (axial and equatorial), and so there are nine possible types of Pt^{IV} nuclei. The chemical shifts of two are known: [Pt(en)Cl$_4$] at -357.3 ppm, and [Pt(en)Br$_4$] at -362.1 ppm. It is possible to determine approximate shift values for the other Pt^{IV} nuclei. $\delta_{N\text{-}Pt^{II}}$ for [Pt(en)Cl$_2$][Pt(en)Cl$_4$] is 6.4 ppm upfield of that for [Pt(en)Br$_2$][Pt(en)Br$_4$]. If the influence of the equatorial ligands on $\delta_{N\text{-}Pt^{IV}}$ is the same (in reality it might be larger), then the value of -362.1 ppm for $\delta_{N\text{-}Pt^{IV}}$ for the [Pt(en)Br$_2${Br$_2$}] unit means $\delta_{N\text{-}Pt^{IV}}$ = -368.5 ppm for [Pt^{IV}(en)Cl$_2${Br$_2$}] and, by interpolation, $\delta_{N\text{-}Pt^{IV}}$ = -362.9 ppm for [Pt(en)Cl$_2${BrCl}]. There are five other Pt^{IV} types, but these three are sufficient for discussing the shapes of the spectra. Although there will be substitution at the equatorial positions, the major first product of bromination is [Pt(en)Cl$_2$][Pt(en)Cl$_2${BrCl}], which has an N-Pt^{IV} resonance at *ca.* -363 ppm. This is converted to [Pt(en)Cl$_2$][Pt(en)Cl$_2${Br$_2$}] when more bromide ions are present, leading to the third peak at -368 ppm for **312d**. Once all the equatorial halogens are substituted, then only the [Pt(en)Br$_2${Br$_2$}] resonance is seen, which coincidentally gives a signal near that for the [Pt(en)Cl$_2${BrCl}] unit. That is why intensity at *ca.* -362 ppm rises, falls, and then rises again as more bromide is added. This simplified picture takes no account of the equatorial substitutions since replacement of the chain halogens is expected to occur more rapidly; at low bromine concentrations only a few equatorial chlorine ligands will be replaced. For example, the signal predicted to be at lowest field (δ_N = *ca.* -351 ppm) is due to the [Pt^{IV}(en)Cl$_2${Br$_2$}] unit, but this should be very rare. Complications arise when a single equatorial chlorine is replaced because two signals will be seen thanks to the *cis* and *trans* influences being different. The dominant pattern of the N-Pt^{IV} signals will remain unaffected though, since it is largely determined by the identity of the chain halogens.

3.3.4 Resonance Raman spectroscopy

Raman spectra were recorded for all the complexes analysed by solid-state NMR spectroscopy. The crystals that made up the samples were generally too small for successful alignment by eye and the CCD camera (see section **2.2**) had not yet been installed, so the HMMCs were examined as pressed discs. The Raman spectra of [Pt(en)Cl$_2$][Pt(en)Cl$_4$] (**303**), [Pt(en)Br$_2$][Pt(en)Br$_4$] (**306**) and the mixed-halide products **312a - 312d**, recorded at four different exciting lines, are shown in Figures 3.3.3 - 8. Some spectra of single crystals of [Pt(en)Cl$_2$][Pt(en)Cl$_4$] were recorded later and are shown in Figure 3.3.9. All the spectra are plotted over the same range of 100 - 400 cm^{-1}, which contains all the signals that are of interest here. The major peaks observed in this range are listed in Tables 3.3.3 - 9. Intensities are quoted relative to the ν_1(Cl-Pt-Cl) stretch ("ν_{1c}"), except for [Pt(en)Br$_2$][Pt(en)Br$_4$], where the intensity of the ν_1(Br-Pt-Br) mode ("ν_{1b}") is used as the standard. Analysis of the spectra is complicated by the dispersion and enhancement ranges of the individual peaks. To simplify matters, for each exciting line the spectral range is split into ten separate regions (labelled A - J) which correspond to areas in which peaks are observed; more than one band can appear in a given region. Dispersion means that the absolute energies of the section boundaries vary with excitation energy. The regions are divided into four types according to which complexes exhibit peaks therein: (1) only the mixed-halide species, (2) all compounds save **306**, (3) all compounds save **303**, and (4) all (six) compounds. In Table 3.3.2 the regions are listed with their type number and descriptions of vibrations likely to have the appropriate wavenumber. There are four kinds of vibration listed in the table: chain modes, defect modes, equatorial modes and terminal modes. The chain modes are the only ones that are predicted by simple models of HMMCs (see section **1.6**). The charge defect modes are simple localised motions that have short enhancement ranges. The equatorial modes are not enhanced, and have little intensity. The terminal modes occur at the chain ends, which are created naturally during synthesis or artificially due to fracturing, and are the most difficult to model. There is no attempt to assign the individual Raman peaks specifically because it is too difficult a task with the available data. This is done for the vibrational spectra of the mixed-halide complexes [Pt(en)$_2$][Pt(en)$_2$Cl$_{2-2\alpha}$Br$_{2\alpha}$](ClO$_4$)$_4$ in section **4.5**, but only with the aid of vibrational modelling.

The changes in the Raman spectra that occur as bromine content is increased are mostly predictable. The intensities of the PtCl vibrations fall away, most notably in the case of ν_{1c}, while those of the corresponding bromide vibrations grow. There are no signals in the regions F, G or I in [Pt(en)Br$_2$][Pt(en)Br$_4$], nor in regions D or H in [Pt(en)Cl$_2$][Pt(en)Cl$_4$]. Peaks are only seen in A, E or J when both chlorine and bromine are present in the system. The intensity in J comes from a combination mode containing ν_{1m}, but the peaks in A and E may be due to single-halide polaron modes which result from charge separation in the mixed-halide species. The regions that are central to the determination of the purity of [Pt(en)Cl$_2$][Pt(en)Cl$_4$] are B and C, where most spectra have peaks. The intensities of these signals are very small in [Pt(en)Cl$_2$][Pt(en)Cl$_4$] and [Pt(en)Br$_2$][Pt(en)Br$_4$]. Moreover, the dispersions and enhancement ranges of the signals observed in the mixed-halide species do not match those for the single-chloride chains. No peaks are observed in region B of the single-crystal spectra of [Pt(en)Cl$_2$][Pt(en)Cl$_4$], and the signals in region C have smaller relative intensities than those in the pressed disc spectra.

Table 3.3.2 Spectral regions and the assignment of selected bands

Region	Type	Labels	Vibration	Comments
A	1	ν_{db}	ν_d(Br-Pt^{III}-Br)	Electron polaron
B	4	ν_{1b}	ν_1(Br-Pt^{IV}-Br)	Symmetric chain stretch
		δ_c	$\delta(PtCl_2)$	Bending motion of equatorial chlorine atoms
		ν_{3c}	ν_3(Cl-Pt^{IV}-Cl)	Chain mode, weakly Raman active
C	4	δ_N	$\delta(PtN_2)$	Bending motion of Pt(en)
		ν_{1m}	ν_1(Br-Pt^{IV}-Cl)	Breathing mode of mixed-halide unit, strongly Raman active
D	3	ν_{2b}	ν_2(Br-Pt^{IV}-Br)	Asymmetric chain stretch
E	1	ν_{d1c}	ν_d(Cl-Pt^{II}-Cl)	Electron polaron
		ν_{em}	$\nu(Br_{eq}$-Pt-$Cl_{eq})$	Equatorial stretching mode
F	2	ν_{d2c}	ν_d(Cl-Pt^{III}-Cl)	Hole polaron
G	2	ν_{1c}	ν_1(Cl-Pt^{IV}-Cl)	Symmetric chain stretch
		ν_{2m}	ν_2(Br-Pt^{IV}-Cl)	Asymmetric motion of mixed-halide unit, weakly Raman active
		ν_{ec}	$\nu(Cl_{eq}$-Pt-$Cl_{eq})$	Equatorial stretching mode
H	3	$2\nu_{1b}$		Overtone mode
I	2	ν_{2c}	ν_2(Cl-Pt^{IV}-Cl)	Asymmetric chain stretch
J	1	$(\nu_{1b} + \nu_{1m})$		Combination mode

Table 3.3.3 Wavenumbers / cm^{-1}, and relative intensities of the bands in the Raman spectra of $[Pt(en)Cl_2][Pt(en)Cl_4]$ (303) [a]

Region	488 nm	514 nm	647 nm	676 nm
B	$180^{0.04}$	$178^{0.08}$	$164^{0.03}$	$163^{0.02}$
C	$213^{0.03}$	$212^{0.03}$	$207^{0.01}$	$208^{0.01}$
F			$283^{0.15}$	$279^{0.16}$
G	$300^{0.10}$	$298^{0.16}$	$291^{0.16}$	$291^{0.20}$
G	$308^{0.82}$	$307^{0.75}$	$301^{0.75}$	$301^{0.72}$
G	$319^{0.08}$	$315^{0.09}$	$312^{0.09}$	$313^{0.08}$
I	$353^{0.04}$	$348^{0.07}$	$345^{0.05}$	$345^{0.02}$

Table 3.3.4 **Wavenumbers / cm^{-1}, and relative intensities of the bands in the single-crystal Raman spectra of $[Pt(en)Cl_2][Pt(en)Cl_4]$ (303) [a]**

Region	514 nm	568 nm	647 nm
C	216 $^{0.05}$	211 $^{0.02}$	205 $^{0.02}$
G	299 $^{0.10}$	298 $^{0.13}$	292 $^{0.11}$
G	308 $^{0.80}$	305 $^{0.79}$	301 $^{0.81}$
G	322 $^{0.10}$	319 $^{0.08}$	315 $^{0.08}$
H	353 $^{0.03}$	350 $^{0.03}$	343 $^{0.02}$

Table 3.3.5 **Wavenumbers / cm^{-1}, and relative intensities of the bands in the Raman spectra of 312a [a]**

Region	488 nm	514 nm	647 nm	676 nm
A			147 $^{0.01}$	weak
B	184 $^{0.03}$	178 $^{0.08}$	168 $^{0.35}$	166 $^{0.30}$
C	215 $^{0.17}$	212 $^{0.40}$	204 $^{0.42}$	205 $^{0.30}$
E	265 $^{0.01}$	260 $^{0.03}$	256 $^{0.01}$	weak
F			281 $^{0.11}$	283 $^{0.16}$
G		300 $^{0.11}$	294 $^{0.20}$	293 $^{0.17}$
G	310 $^{0.80}$	306 $^{0.65}$	301 $^{0.62}$	302 $^{0.62}$
G	320 $^{0.20}$	316 $^{0.24}$	313 $^{0.18}$	313 $^{0.21}$
H	hidden	hidden	337 $^{0.05}$	334 $^{0.04}$
I	354 $^{0.04}$	349 $^{0.08}$	344 $^{0.05}$	341 $^{0.03}$
J			377 $^{0.01}$	weak

Table 3.3.6 **Wavenumbers / cm^{-1}, and relative intensities of the bands in the Raman spectra of 312b [a]**

Region	488 nm	514 nm	647 nm	676 nm
A	142 ^{wk}		142 $^{0.01}$	145 $^{0.04}$
B	180 $^{0.06}$	178 $^{0.18}$	169 $^{1.15}$	164 $^{1.28}$
C	213 $^{0.44}$	210 $^{0.71}$	202 $^{0.78}$	202 $^{1.14}$
D	234 ^{wk}	234 ^{wk}	225 ^{wk}	226 ^{wk}
E	261 $^{0.03}$	257 $^{0.04}$	252 $^{0.03}$	250 $^{0.06}$
F			280 $^{0.08}$	281 $^{0.07}$
G	299 $^{0.08}$	296 $^{0.08}$	291 $^{0.19}$	289 $^{0.20}$
G	309 $^{0.68}$	306 $^{0.65}$	301 $^{0.55}$	301 $^{0.48}$
G	321 $^{0.24}$	317 $^{0.27}$	312 $^{0.26}$	311 $^{0.32}$
H	353 $^{0.06}$	351 $^{0.10}$	339 $^{0.27}$	337 $^{0.27}$
J		weak	378 $^{0.08}$	376 $^{0.06}$

Table 3.3.7 Wavenumbers / cm^{-1}, and relative intensities of the bands in the Raman spectra of 312c [a]

Region	488 nm	514 nm	647 nm	676 nm
A			$143^{\mathbf{0.03}}$	$143^{\mathbf{0.10}}$
B	$180^{\mathbf{0.11}}$	$178^{\mathbf{0.74}}$	$169^{\mathbf{4.88}}$	$164^{\mathbf{8.50}}$
C	$212^{\mathbf{0.49}}$	$209^{\mathbf{1.14}}$	$202^{\mathbf{1.25}}$	$201^{\mathbf{2.00}}$
D	$235^{\mathbf{wk}}$	$234^{\mathbf{wk}}$	$226^{\mathbf{0.02}}$	$225^{\mathbf{wk}}$
E	$258^{\mathbf{0.02}}$	$255^{\mathbf{0.05}}$	$250^{\mathbf{0.05}}$	$251^{\mathbf{wk}}$
F	$289^{\mathbf{wk}}$	$286^{\mathbf{wk}}$	$284^{\mathbf{sh}}$	
G	$298^{\mathbf{sh}}$	$297^{\mathbf{sh}}$	$293^{\mathbf{0.12}}$	$291^{\mathbf{0.14}}$
G	$309^{\mathbf{0.64}}$	$307^{\mathbf{0.59}}$	$309^{\mathbf{0.88}}$	$304^{\mathbf{0.86}}$
G	$319^{\mathbf{0.36}}$	$316^{\mathbf{0.41}}$		
H	$352^{\mathbf{0.03}}$	$351^{\mathbf{0.17}}$	$335^{\mathbf{1.60}}$	$332^{\mathbf{2.16}}$
J	$389^{\mathbf{0.01}}$	$385^{\mathbf{0.05}}$	$374^{\mathbf{0.27}}$	$372^{\mathbf{0.53}}$

Table 3.3.8 Wavenumbers / cm^{-1}, and relative intensities of the bands in the Raman spectra of 312d [a]

Region	488 nm	514 nm	647 nm	676 nm
A			$147^{\mathbf{0.15}}$	$144^{\mathbf{0.15}}$
B	$181^{\mathbf{0.90}}$	$179^{\mathbf{1.67}}$	$165^{\mathbf{23.3}}$	$164^{\mathbf{27.0}}$
C	$212^{\mathbf{1.20}}$	$210^{\mathbf{1.34}}$	$202^{\mathbf{1.85}}$	$202^{\mathbf{1.50}}$
D	$233^{\mathbf{0.05}}$	$235^{\mathbf{0.05}}$	$225^{\mathbf{0.10}}$	$228^{\mathbf{0.10}}$
E	$255^{\mathbf{0.10}}$	$254^{\mathbf{0.10}}$	$249^{\mathbf{wk}}$	$248^{\mathbf{wk}}$
G	$311^{\mathbf{0.54}}$	$309^{\mathbf{0.50}}$	$309^{\mathbf{1.00}}$	$310^{\mathbf{1.00}}$
	$320^{\mathbf{0.46}}$	$316^{\mathbf{0.50}}$		
H	$355^{\mathbf{0.21}}$	$352^{\mathbf{0.50}}$	$332^{\mathbf{8.80}}$	$332^{\mathbf{8.90}}$
J	$389^{\mathbf{0.06}}$	$386^{\mathbf{0.25}}$	$373^{\mathbf{1.20}}$	$371^{\mathbf{0.60}}$

Table 3.3.9 Wavenumbers / cm^{-1}, and relative intensities of the bands in the Raman spectra of [Pt(en)Br$_2$][Pt(en)Br$_4$] (306) [a]

Region	514 nm	647 nm	676 nm
B	$177^{\mathbf{1.00}}$	$165^{\mathbf{1.00}}$	$163^{\mathbf{1.00}}$
C	$209^{\mathbf{0.01}}$	$206^{\mathbf{wk}}$	$200^{\mathbf{0.01}}$
D	$229^{\mathbf{0.06}}$	$227^{\mathbf{wk}}$	$222^{\mathbf{wk}}$
H	$349^{\mathbf{0.44}}$	$336^{\mathbf{0.42}}$	$331^{\mathbf{0.48}}$

[a] *the figures in superscripted bold type denote intensity relative to ν_{1c} (ν_{1b} in Table 3.3.9); wk = < 0.01 . Raman signals have been corrected for spectral response.*

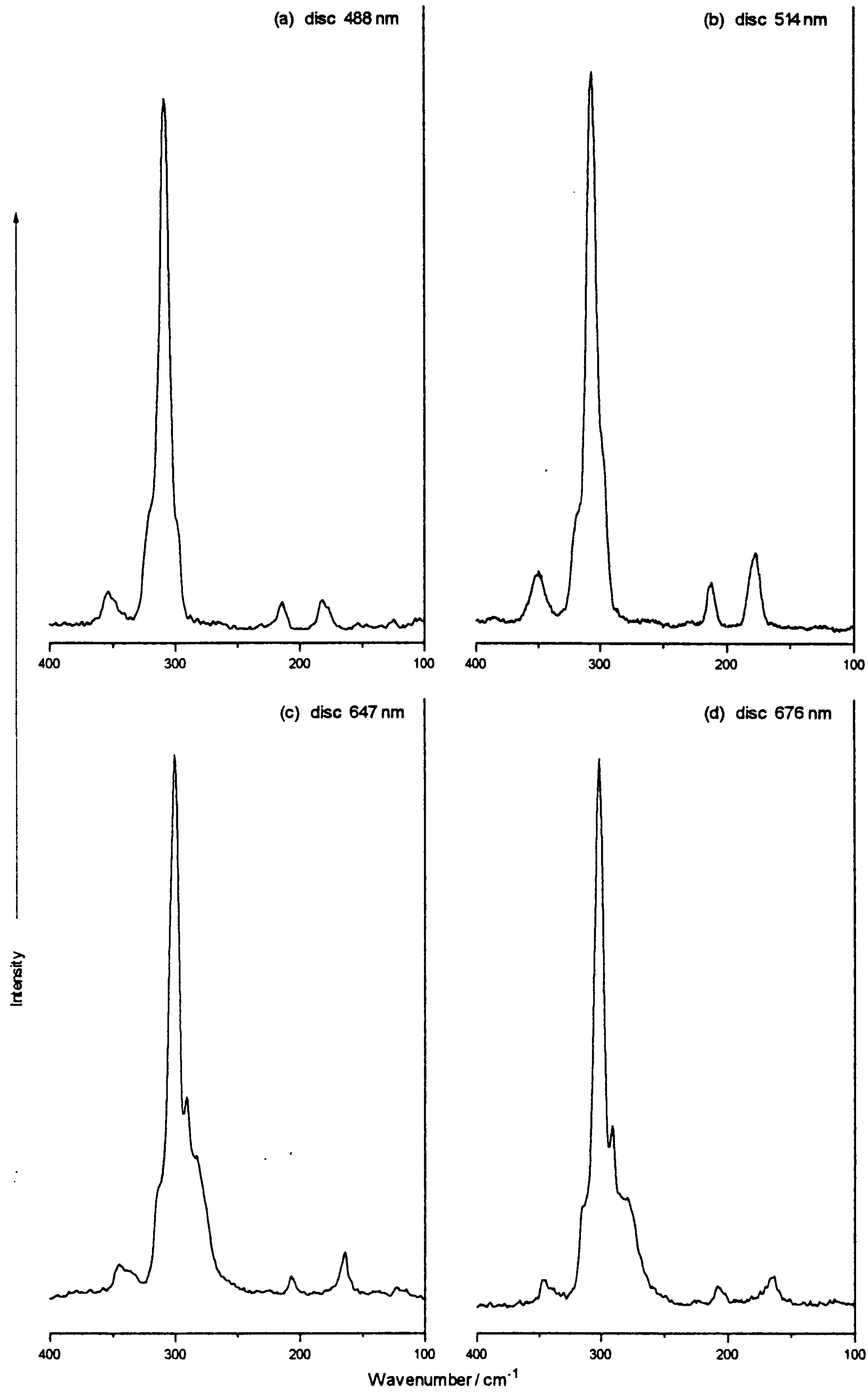

Figure 3.3.3 *Raman spectra of $[Pt(en)Cl_2][Pt(en)Cl_4]$ recorded at the excitation wavelengths (a) 488 nm, (b) 514 nm, (c) 647 nm and (d) 676 nm.*

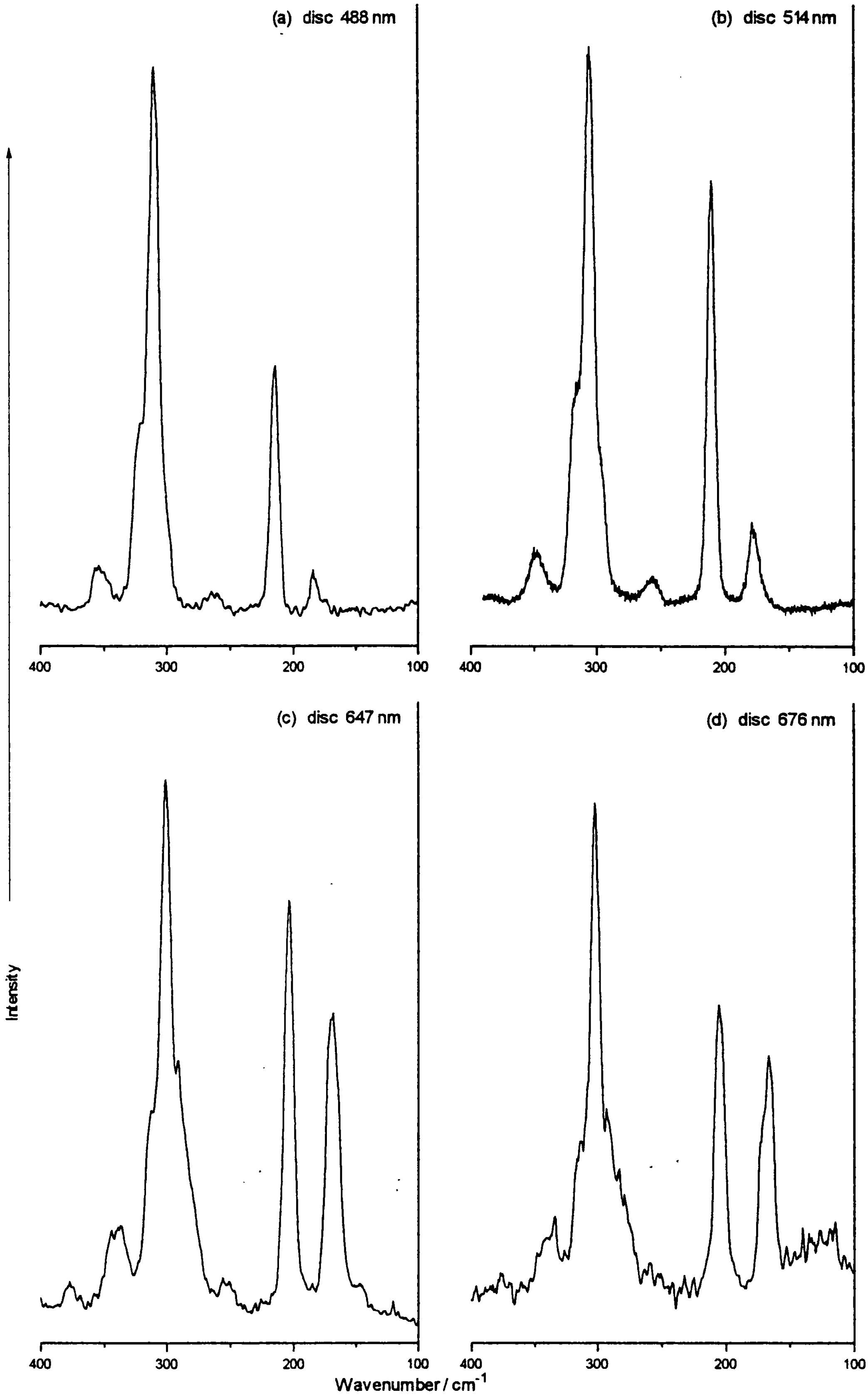

Figure 3.3.4 *Raman spectra of **312a** recorded at the excitation wavelengths (a) 488 nm, (b) 514 nm, (c) 647 nm and (d) 676 nm.*

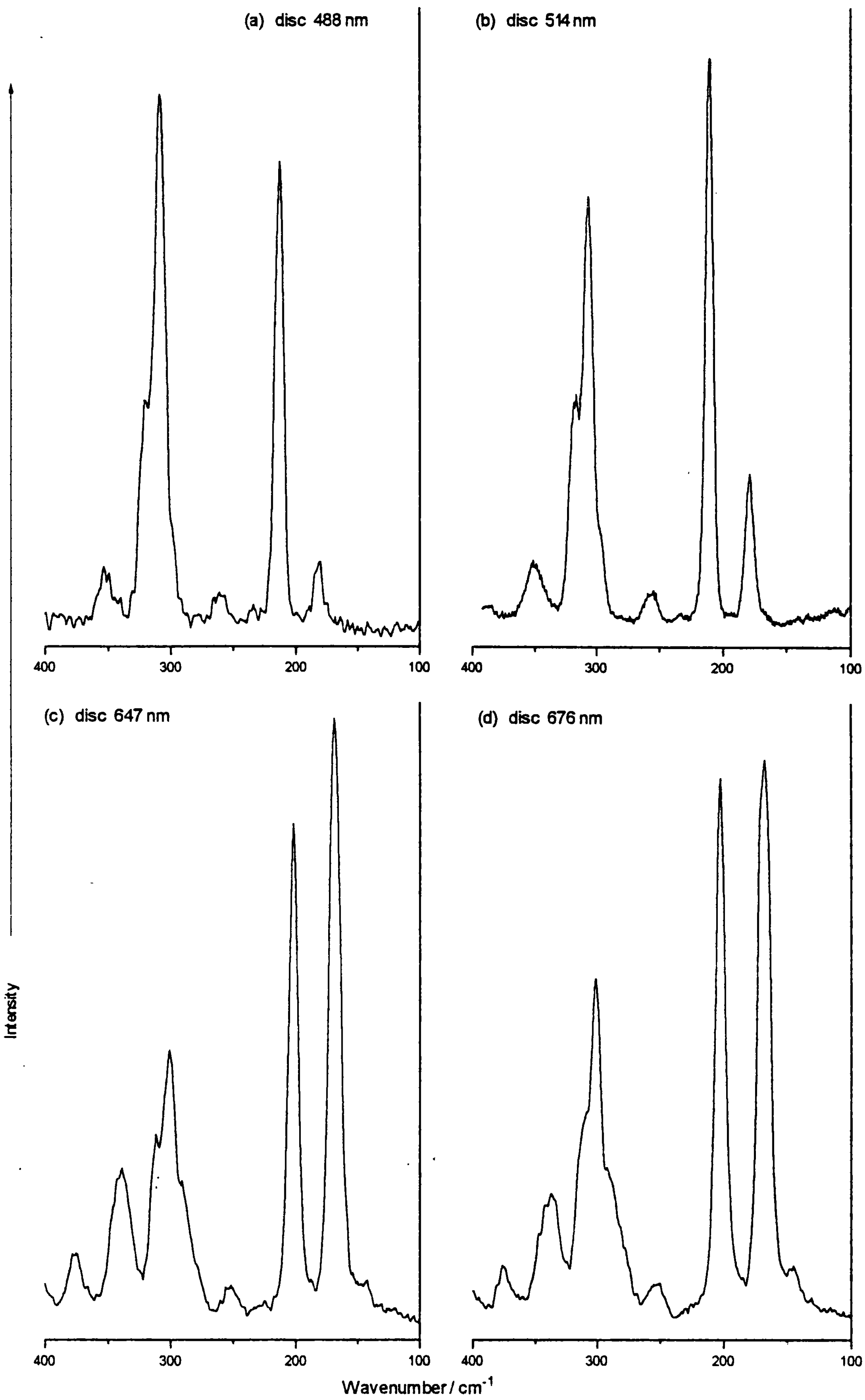

Figure 3.3.5 *Raman spectra of **312b** recorded at the excitation wavelengths (a) 488 nm, (b) 514 nm, (c) 647 nm and (d) 676 nm.*

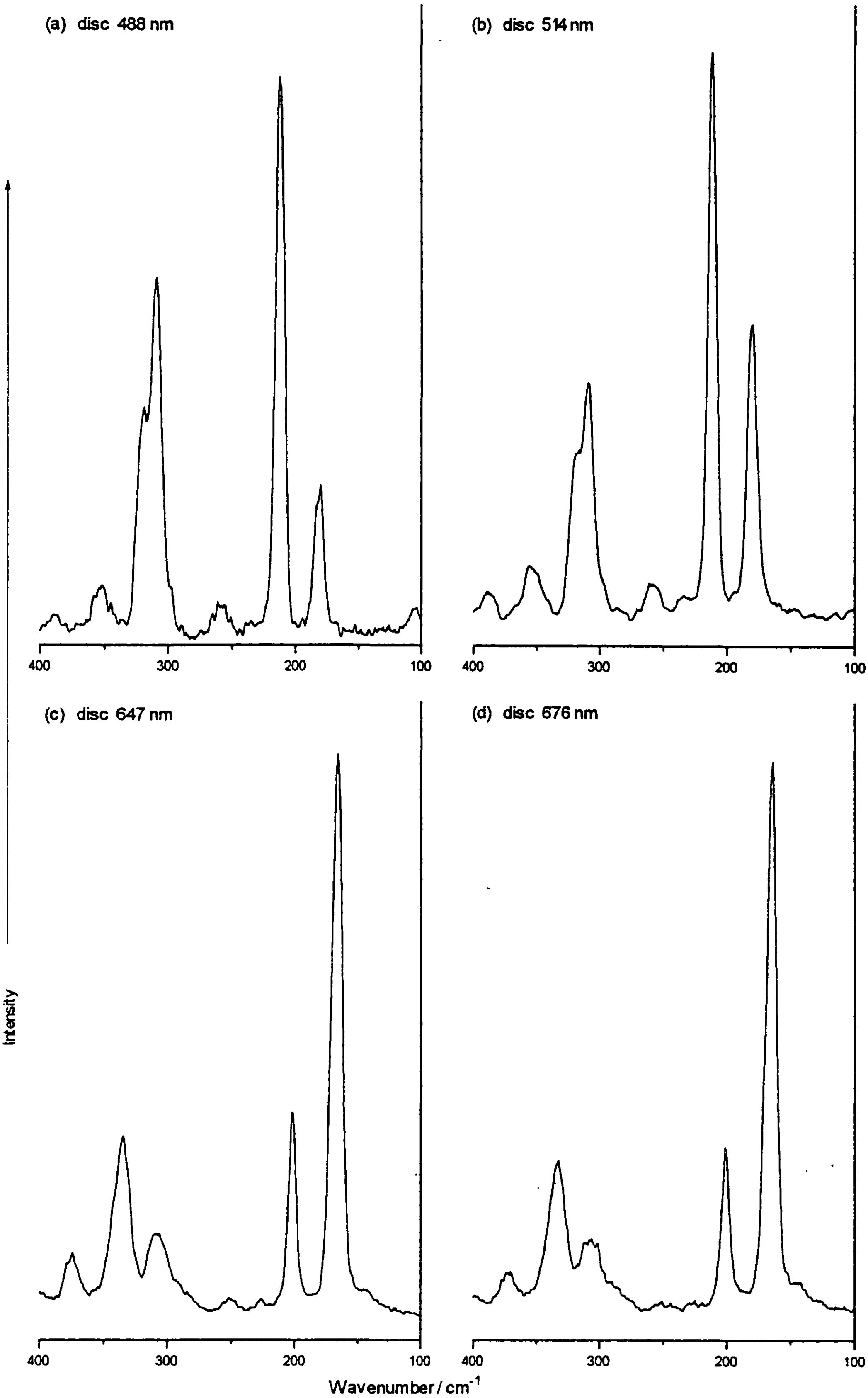

Figure 3.3.6 *Raman spectra of **312c** recorded at the excitation wavelengths (a) 488 nm, (b) 514 nm, (c) 647 nm and (d) 676 nm.*

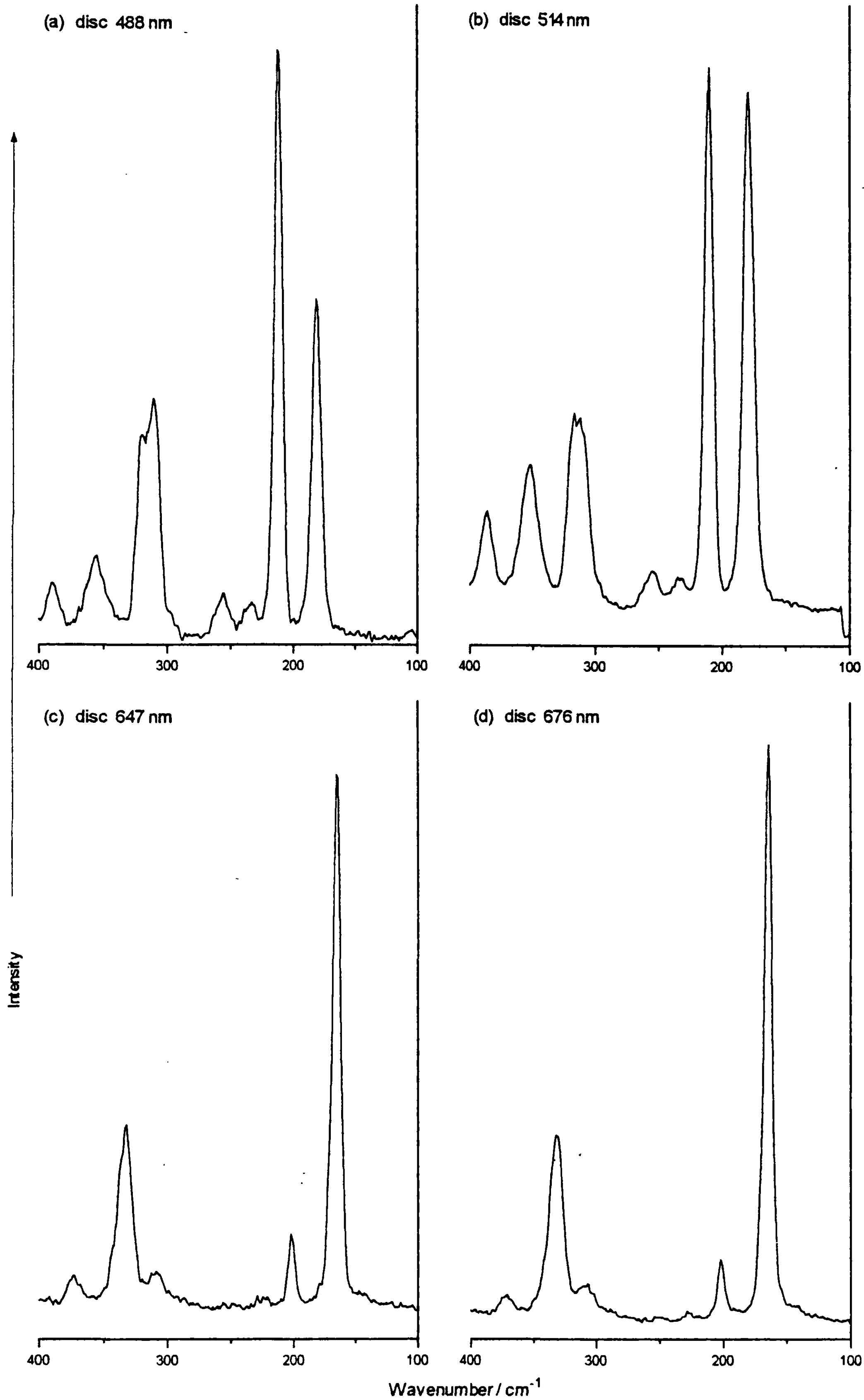

Figure 3.3.7 *Raman spectra of **312d** recorded at the excitation wavelengths (a) 488 nm, (b) 514 nm, (c) 647 nm and (d) 676 nm.*

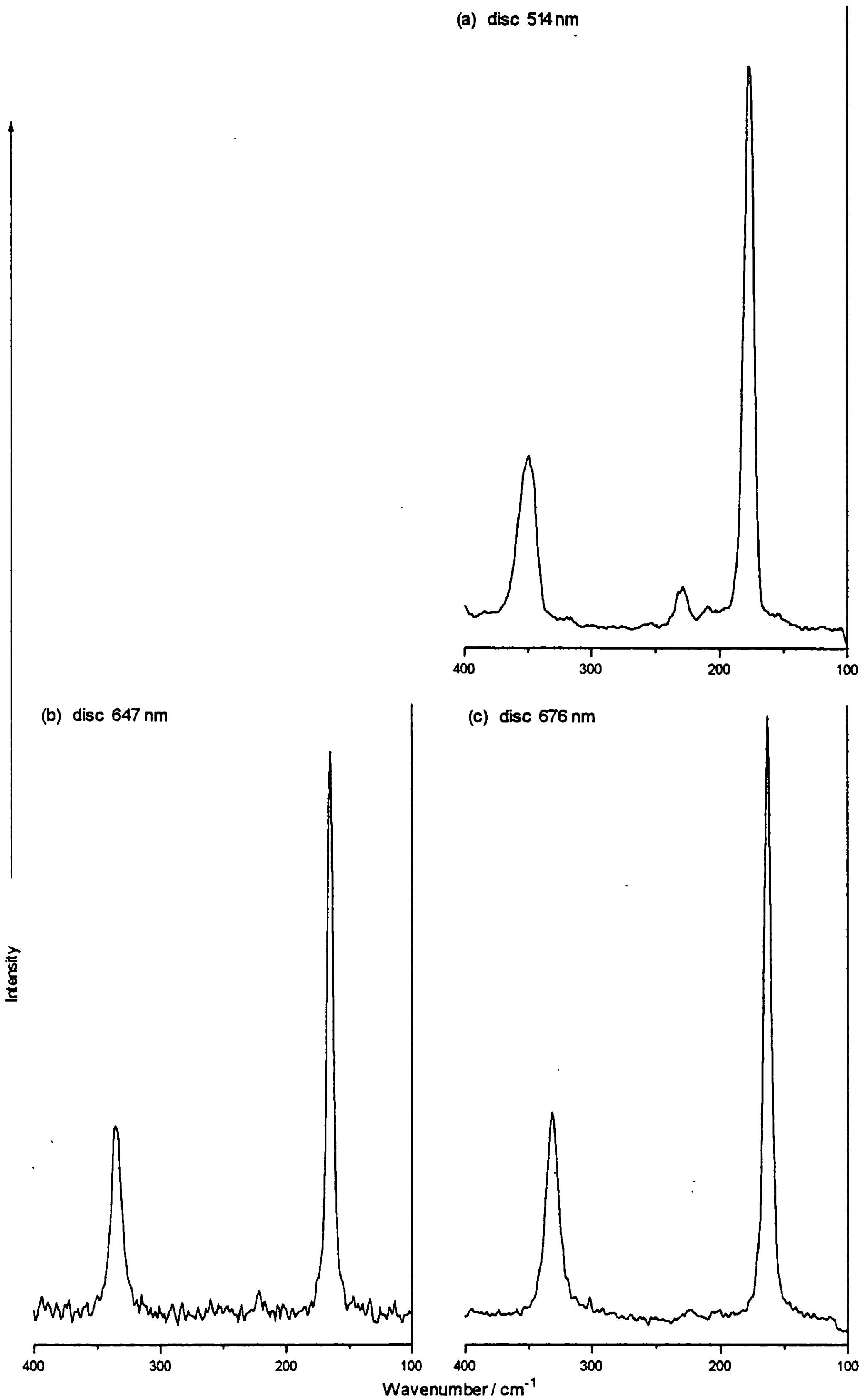

Figure 3.3.8 *Raman spectra of [Pt(en)Br2][Pt(en)Br4] recorded at the excitation wavelengths (a) 514 nm, (b) 647 nm and (c) 676 nm.*

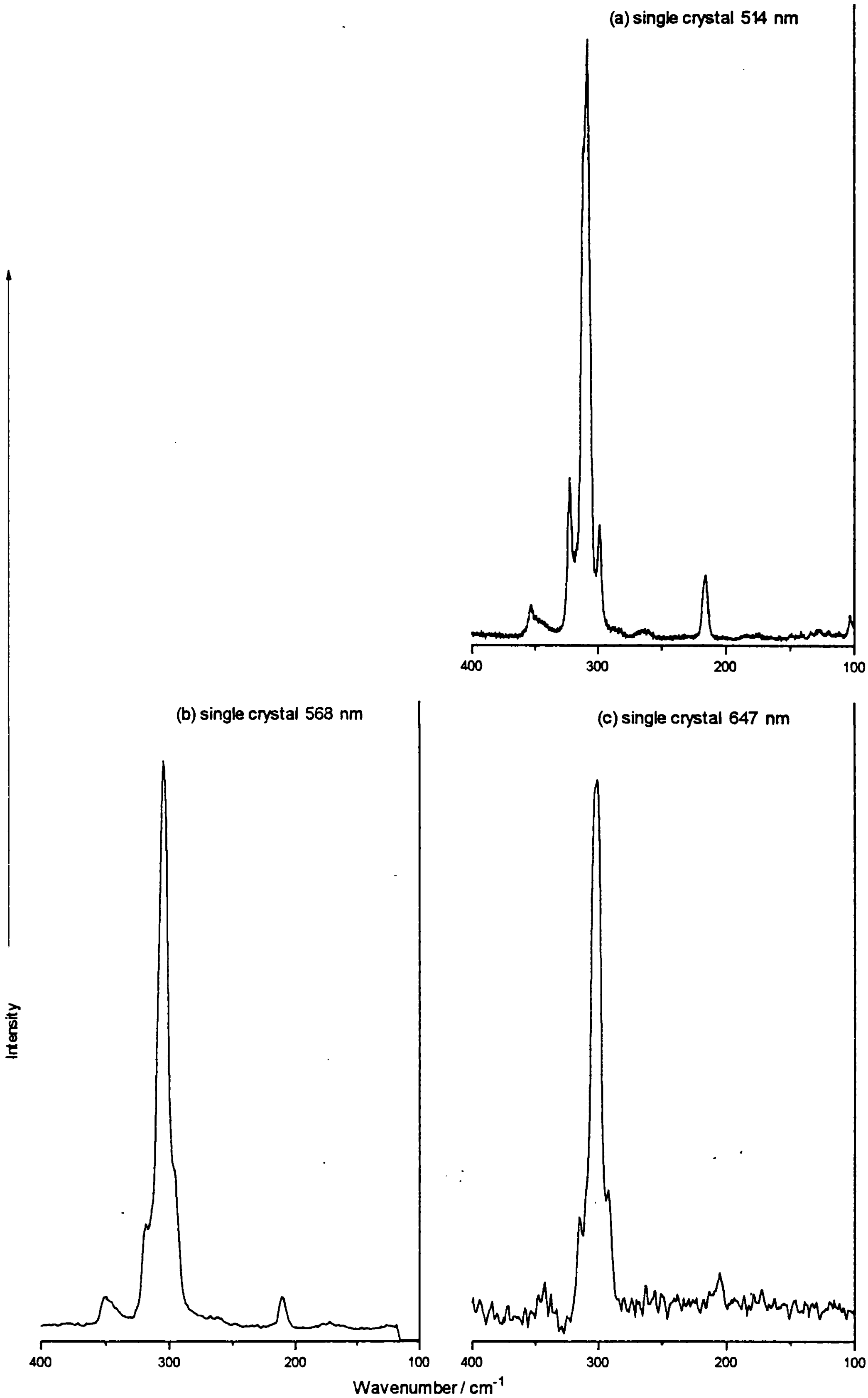

Figure 3.3.9 *Single-crystal Raman spectra of $[Pt(en)Cl_2][Pt(en)Cl_4]$ recorded at the excitation wavelengths (a) 514 nm, (b) 647 nm and (c) 676 nm.*

3.3.5 Discussion of the vibrational spectra

The assignments of the peaks in regions B and C are central to the resonance Raman analysis. The signal in region C in $[Pt(en)Cl_2][Pt(en)Cl_4]$ is at *ca.* 210 cm^{-1} and shows little dispersion or enhancement when the excitation energy is altered; similar behaviour is seen for $[Pt(en)Br_2][Pt(en)Br_4]$. This is in complete contrast to the ν_{1m} mode, which dominates this region in the spectra of the mixed-halides, **312a-312d**. The complementary ν_{2m} signal, which could confirm the presence of ν_{1m} in $[Pt(en)Cl_2][Pt(en)Cl_4]$, is not observed clearly in any of the HMMCs because it falls within the contour of the ν(PtCl) vibrational modes. Instead, the peaks in region C for $[Pt(en)X_2][Pt(en)X_4]$ (X = Cl or Br) are usually attributed to the $\delta(PtN_2)$ bending mode because it is fairly independent of the halogen identity.[95,96] This is the most reasonable assignment that can be derived from a conventional model of the HMMC system. Alternative explanations are hard to prove or involve too many assumptions. For instance, the termini of chains will give rise to defect modes, but the way in which chains terminate has never been addressed, probably because such sites will make only a small contribution to the vibrational spectra. In theory, the terminal atom can be Pt^{II}, Pt^{IV} or $X(-Pt^{IV})$. If it is platinum, then the identity of the neighbouring halogen might not have much influence on the vibrational energy.

The assignment of ν_{1b} for the signals in region B can be discounted for the following reasons. There is no intensity in region B of the single-crystal spectra of $[Pt(en)Cl_2][Pt(en)Cl_4]$, the excitation energy dependence of the signal in the disc spectra is different to that of ν_{1b} in the brominated HMMCs, and there are no peaks assigned either to $2\nu_{1b}$ or to ν_{1m}. The peak in region I has a different relationship to excitation energy from that of $2\nu_{1b}$, and it is present in single-crystal spectra that have no intensity in region B, and so it is attributed to the weakly Raman-active asymmetric vibration, ν_{2c}. The lack of a ν_{1m} signal is significant because mixed-halide units are produced in the reaction between Br^- and $[Pt(en)_2Cl_2]^{2+}$ ions,[244] and so there should be some correlation between the intensities of ν_{1b} and of ν_{1m}. These results mean that certain observations that appear to support the assignment of the signal in region B to the ν_{1b} mode can be ignored. For instance, the peak itself has a dispersion similar to that shown by ν_{1b} in the spectra of $[Pt(en)Br_2][Pt(en)Br_4]$, and the spectrum of $[Pt(en)Cl_2][Pt(en)Cl_4]$ has peaks in region I, which is near to the position associated with $2\nu_{1b}$, and in region C, where the ν_{1m} signal occurs in the mixed-halide species. There are alternative explanations for the peak region B. The bending mode $\delta(PtCl_2)$ has been proposed,[242] but weak signals have been found in this region for complexes that have no equatorial halogen atoms (see section **4.4**). In addition, there is little or no intensity in this region in single-crystal spectra, and the related mode $\delta(PtBr_2)$ has not been assigned. Of the more conventional vibrations, ν_{3c} is a suitable candidate. A suggested assignment for it in $[Pt(en)_2][Pt(en)_2Cl_2](ClO_4)_4$ is *ca.* 165 cm^{-1},[110,112] although this has not been confirmed. ν_{3c} should have little Raman intensity, particularly in more uniform crystal structures, but the presence of terminations might reduce the asymmetry of the mode and increase its Raman activity. Other possibilities are connected with the terminal modes that were discussed in relation to the vibration in region C. Support for them is derived from comparisons of the spectra for samples analysed as pressed discs and as single-crystals. The greater intensity in the B region of the disc spectra may be due to the larger number of chain fractures in the discs.

Infrared spectroscopy is often a source of results complementary to Raman studies, but the FT-infrared spectra of the neutral-chain HMMCs do not contribute any significant data to this work. They were recorded at room temperature and so they are not well resolved. Selected spectra are displayed in Figure 3.3.10. The peaks pertinent to this discussion are those due to the modes ν_{2b}, ν_{2m} and ν_{1m}. ν_{2b} is probably the large signal at *ca.* 225 cm^{-1} in the spectrum of **312d**; approximate wavenumbers are known for ν_{2m} and ν_{1m} from their Raman signals. Unfortunately, there are ligand modes and equatorial modes that obscure the regions of the spectrum in which ν_{1m} or ν_{2m} appear, and it is difficult to tell whether there is any intensity at *ca.* 225 cm^{-1} for $[Pt(en)Cl_2][Pt(en)Cl_4]$.

All assignments for the mixed-valence species must be tempered by the knowledge that $[Pt(en)Cl_2][Pt(en)Cl_4]$ has been doped imperfectly with HBr. From the solid-state ^{15}N NMR results it has been shown that up to about 40 % of the bromine ions added exchange with the equatorial chlorine atoms. None of the axial modes is expected to be affected significantly by this and only one extra mode is thought to occur as a result of equatorial substitution, namely the weak signal in region E. The purpose of the bromination experiment was to determine whether any of the peaks in the Raman spectra of $[Pt(en)Cl_2][Pt(en)Cl_4]$ are due to bromide impurities. The synthesis of [Pt(en)Cl_2][Pt(en)Cl_4] does not involve directly any bromine or bromide ions, but the ease with which heavy halogens replace light ones in HMMCs means that contamination can result from a very small amount of impurity. Bromine atoms are known to replace bridging chlorine atoms in HMMCs readily in solution or even when the solid linear-chain is ground with a bromide salt.[14] The starting materials (Pt(en)Cl_2 or en.2HCl) are possible sources of contamination. However, the results in this section show that the weak signals in the spectra of [Pt(en)Cl_2][Pt(en)Cl_4] are not consistent with ν_{1m} or ν_{1b}, and so the chloride samples are assumed to be uncontaminated.

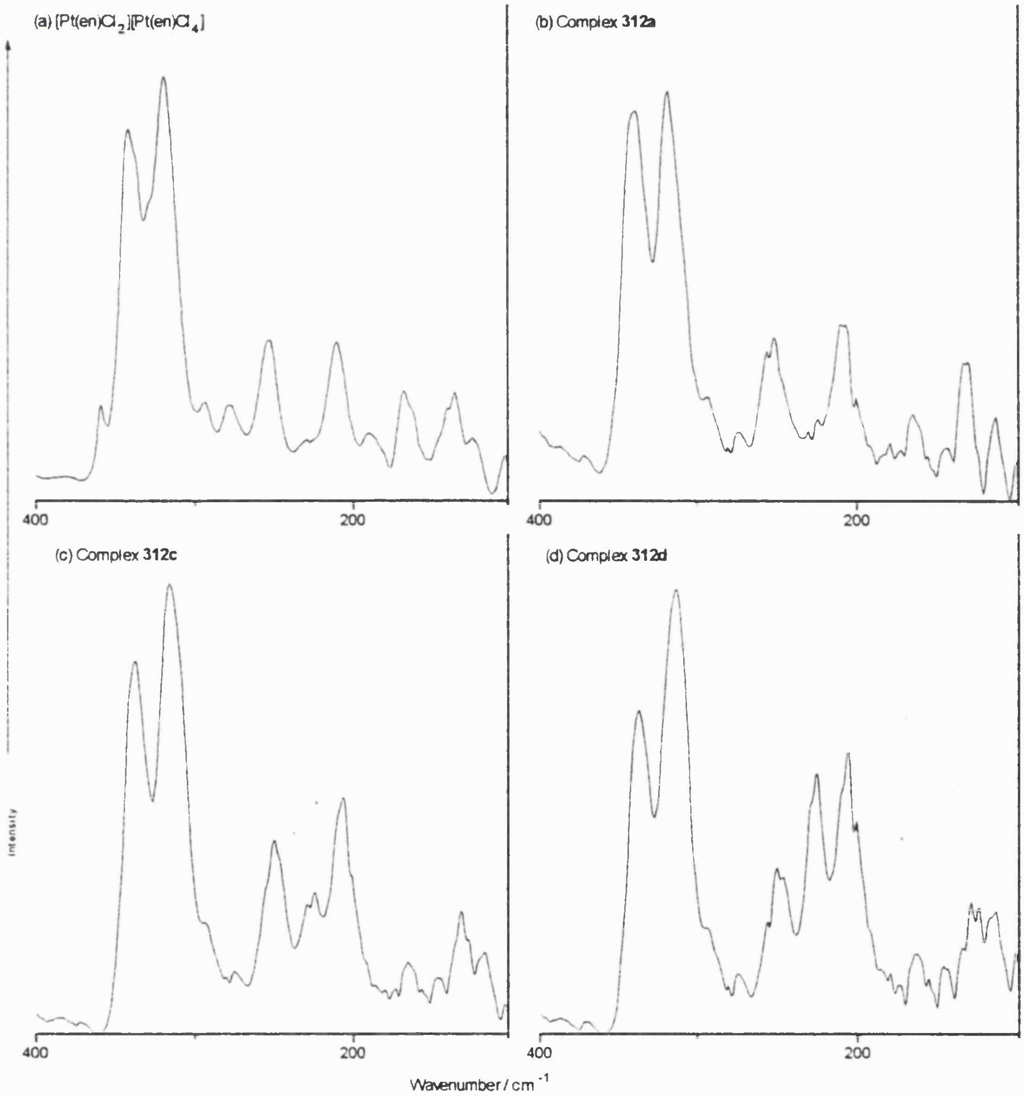

*Figure 3.3.10 FT-infrared spectra for (a) [Pt(en)Cl_2][Pt(en)Cl_4], (b) **312a**, (c) **312c** and (d) **312d**.*

3.4 Conclusions

There are a number of conclusions that can be drawn from the studies made on the neutral-chain complexes. These are both the specific, relating to the explanation of particular observations or the analysis of certain trends, and the general, encompassing the use of experimental techniques. The latter category is headed by the application of solid-state NMR spectroscopy to the study of HMMC complexes. In this chapter, it has been demonstrated that this technique has great value as a tool for analysis of both monomeric and linear-chain species. Of the nuclei that can be probed, ^{15}N sites are the most useful, because they are more sensitive to oxidation state than ^{13}C nuclei and are easier to study than ^{195}Pt nuclei. It is unfortunate that the study of ^{195}Pt sites is not very practical since it would provide a more direct analysis of the platinum oxidation state. Some samples, notably linear-chain ones, fail to give a solid-state ^{195}Pt NMR signal large enough for detection, and most platinum (II) sites that can be probed are so anisotropic that they give many spinning sidebands even at the fastest rotor speeds. Accumulation times are very long and the determination of isotropic peaks requires data from two or more spinning speeds. In solid-state ^{15}N NMR spectroscopy it is fair to say that studies on the nuclei at natural abundance levels do not give particularly good results. Therefore, all the ^{15}N NMR spectra in this chapter are from samples in which at least 25 % of the nitrogen atoms are ^{15}N ones. While this involves extra expense, it is offset by the smaller sample sizes, which reduce the amount of platinum required. The biggest obstacle to overcome in applying this technique is therefore acquiring the ligand in ^{15}N-enriched form.

There are a number of conclusions to be drawn from the solid-state ^{15}N or ^{195}Pt NMR studies. Generally, for the monomeric complexes Pt(en)X$_2$ and Pt(en)X$_4$, the trends in δ_N, δ_{Pt}, and $J_{N\text{-}Pt}$ follow those found in the solution NMR analysis of related species. These trends can be explained in terms of the contribution of the equatorial and axial halogens. The apparent reversal of the relative chemical shift values for Pt(en)I$_2$ and Pt(en)I$_4$ can be accounted for in this way. More interesting discoveries were made in the analysis of linear-chain compounds. Although the nuclei associated with the nominal Pt^{II} and Pt^{IV} centres become more similar as the halogen is changed from Cl $\rightarrow$ Br $\rightarrow$ I, this merely reflects the nature of these sites in the respective monomeric species. Regardless of the oxidation state, chain formation reduces the shielding around the platinum nuclei while increasing it around the nitrogen nuclei, but by a small amount in each case. Where the $J_{N\text{-}Pt}$ coupling constant is altered, it is smaller in the linear-chain complexes, for both N-Pt^{II} and N-Pt^{IV} sites. The solid-state NMR results provide no real evidence for the charge delocalisation that is normally assumed to occur as a result of chain formation.[14] Instead, the relative charge densities in linear-chain compounds do not appear to differ significantly from those in the monomeric forms.

Certain key points are established as a result of the bromination experiment. From the solid-state NMR studies, it is clear that substitution of chlorine atoms by bromine ones occurs on equatorial sites as well as axial ones. While replacement of the chain atoms is evidently favoured, a significant proportion of the equatorial ones will be exchanged as well. If a unit cell of [Pt(en)Cl$_2$][Pt(en)Cl$_2${Cl$_2$}] (axial atoms in {}) is reacted with two bromide ions, the average unit produced is thought to be [Pt(en)Cl$_{1.6}$Br$_{0.4}$][Pt(en)Cl$_{1.6}$Br$_{0.4}${Cl$_{0.8}$Br$_{1.2}$}]. Raman studies on a range of mixed-halide species confirm the purity of the HMMC [Pt(en)Cl$_2$][Pt(en)Cl$_4$]. The spectra of the complex contain certain weak signals in regions normally associated with impurity modes, but in each case there is an alternative explanation that involves motions of pure [Pt(en)Cl$_2$][Pt(en)Cl$_4$] alone. It is noted that even in **312d**, which was made by treating [Pt(en)Cl$_2$][Pt(en)Cl$_4$] with four equivalents of HBr, ν_{1c} and ν_{1m} signals are observed in the Raman spectra. Complete substitution of the axial chlorine atoms cannot be effected simply, and will not occur before a significant proportion of the equatorial chlorine atoms has been replaced.

3.5 Experimental Details

3.5.1 Syntheses

Platinum (II) monomers

$Pt(en)Cl_2$ was prepared by a standard route.[224] It was enriched to approximately 25 % ^{15}N by treating fully 4 equiv. of potassium tetrachloroplatinate (K_2PtCl_4) with 1 equiv. of fully enriched en.2HCl before treating with a further 3 equiv. of an unenriched sample of en.2HCl.

$Pt(en)Br_2$ was prepared both by Johnson's method [224] adapted for the use of K_2PtBr_4, or by the reaction of $Pt(en)Cl_2$ with KBr.[223]

$Pt(en)I_2$ was synthesised from $Pt(en)Cl_2$ using the method of Watt and McCarley.[223]

Platinum (IV) monomers

$Pt(en)Cl_4$ was prepared from $Pt(en)Cl_2$ by the chlorine oxidation method of Basolo *et al.*.[218]

$Pt(en)Br_4$ was initially prepared by the oxidation of $Pt(en)Br_2$, using conditions similar to those of Chugaev and Chernyaev,[9] but with double the amount of persulphate and free halide they used. Subsequent preparations involved similar methods to those outlined above, but with the linear-chain complex as starting material.

$Pt(en)I_4$ was usually synthesised by methods analogous with those for $Pt(en)Br_4$. An alternative path followed the route outlined by Watt and McCarley,[223] which involved the reaction of free ligand with potassium tetraiodide.

Platinum linear-chain complexes $[Pt(en)X_2][Pt(en)X_4]$ (X = Cl, Br or I)

$[Pt(en)Cl_2][Pt(en)Cl_4]$ was made by an adaptation of the method of Chugaev and Chernyaev,[9] half the specified amount of persulphate being used. It was also prepared by treating equimolar amounts of the Pt^{II} and Pt^{IV} monomers in the presence of HCl.

$[Pt(en)Br_2][Pt(en)Br_4]$ was synthesised by analogous routes to those used for the preparation of the chloride complex.

$[Pt(en)I_2][Pt(en)I_4]$ was initially synthesised by similar routes to those used for the preparation of the other linear-chains. A more suitable method involves the mixing of equimolar dimethylformamide (DMF) solutions of the Pt^{II} and Pt^{IV} monomers, followed by immediate precipitation of the complex upon the addition of water.

Platinum linear-chain complexes [Pt(en)X$_2$][Pt(en)I$_4$] (X = Cl or Br)

Both compounds were made by methods analogous with that for the preparation in DMF of [Pt(en)I$_2$][Pt(en)I$_4$]. In each case, solutions of Pt(en)X$_2$ and Pt(en)I$_4$ were prepared in a minimum of warm DMF. These were then mixed, and the desired product precipitated by the addition of water.

Platinum linear-chain complexes [Pt(en)Cl$_2$][Pt(en)Cl$_2${Cl$_{2-2\alpha}$Br$_{2\alpha}$}]

The mixed-halide species were made by the crystallisation of a solution containing [Pt(en)Cl$_2$][Pt(en)Cl$_4$] and the appropriate amount of a known solution of hydrobromic acid. Chemical analyses for the four products (**312a - 312 d**) are shown in Table 3.5.1, along with the approximate halogen composition for the unit cell of each HMMC.

Table 3.5.1 Chemical analyses of the complexes 312a - 312d

Label	Percentage by mass / %					No. atoms per unit cell	
	C	H	N	Cl	Br	Cl	Br
312a	6.90	1.80	7.29	27.84	2.53	5.8	0.2
312b	6.67	1.89	7.15	23.97	10.54	5.0	1.0
312c	6.59	1.93	6.92	18.44	19.62	4.1	1.9
312d	6.30	1.70	6.60	10.00	34.20	2.4	3.6

3.5.2 Solid-State NMR spectroscopy

^{15}N analysis

Solid-state ^{15}N NMR spectra were recorded using a Bruker MSL-300 spectrometer at 30.42 MHz using cross-polarisation (CP), proton dipolar decoupling, and magic-angle spinning (MAS). The CP condition was set on a sample of doubly ^{15}N-enriched ammonium nitrate. Spinning speeds of 4.2-4.5 kHz were employed, sufficient to eliminate virtually all spinning sidebands for these complexes. The contact time was 0.5 ms, acquisition times were 20-100 ms and the recycle delay between scans was 1 s. The typical 90 ° pulse length for protons was 7 μs. All spectra were recorded at room temperature (296 K). Typically, measurements were carried out on sample sizes of 40-100 mg of 25-100 % enriched material with total scan times of up to 1 h. Chemical shifts are quoted relative to that of external liquid nitromethane using solid NH_4NO_3 as a secondary reference: the ammonium peak was taken to resonate at -358.4 ppm.[217] Observed chemical shifts were not corrected for the change in magnetic susceptibility between samples.

^{195}Pt analysis

Solid-state ^{195}Pt NMR spectra were recorded using a Bruker MSL-300 spectrometer at 64.42 MHz. Spinning speeds of 12.0-15.3 kHz were employed. High-power decoupling was used during the acquisition time (1-2 ms). The recycle delay between scans was 5 s. High power r.f. pulses of 1 μs were used (equivalent to a 45 ° flip angle) to ensure reasonably uniform excitation of the wide spectral width under investigation (1 MHz). All spectra were recorded at room temperature (296 K). Measurements were carried out on sample sizes of greater than 200 mg of natural abundance material. Total scan times varied from about 1 h for Pt(en)Cl_4 to over 60 h for [Pt(en)Cl_2][Pt(en)Cl_4]. Chemical shifts are quoted relative to that of 1 mol l^{-1} aqueous Na_2PtCl_6 solution.

3.5.3 Resonance Raman spectroscopy

Spectra were recorded using Spex 1401 or 14018/R6 double spectrometers, with Bausch and Lomb gratings (1200 line mm^{-1}) and Jobin-Yvon holographic gratings (1800 line mm^{-1}), respectively. Appropriate exciting lines were provided by Kr^+ (CR-52) and Ar^+ lasers (I-70). Samples were analysed as pressed discs at liquid-nitrogen temperature.

CHAPTER 4

LINEAR-CHAIN COMPLEXES CONTAINING PLATINUM *BIS*-ETHYLENEDIAMINE

4.1 Introduction

The linear-chain complexes $[Pt(en)_2][Pt(en)_2X_2]Y_4$ (Y is the counterion, X = Cl, Br or I) are the most extensively studied of all the HMMCs. Most of the work has concentrated on the perchlorate variety ($Y = ClO_4^-$), as can be seen from the experimental review (see section **1.5**). Solid-state NMR analysis of the HMMCs based around the platinum *bis*-ethylenediamine unit is logically the next stage on from the work on $[Pt(en)X_2][Pt(en)X_4]$. The complexes $[Pt(en)_2][Pt(en)_2X_2]Y_4$ fulfil two of the three requirements laid out at the beginning of Chapter **3**, since they contain a ligand available in an ^{15}N-enriched state, and most of the constituent monomers can be synthesised. All the varieties of $[Pt^{II}(en)_2]Y_2$ and $[Pt(en)_2X_2]Y_2$ (X = Cl or Br) can be made, although problems surround the preparation of $[Pt(en)_2I_2]Y_2$. The third criterion is not met because the chains in these HMMCs have a net (positive) charge that is balanced by counterions. In Chapter **3** the effect of chain formation on solid-state NMR spectra was established, and this may be taken into account so that the influence of the counterions can be determined more accurately. The species $[Pt(en)_2][Pt(en)_2X_2]Y_4$ are ideal for studying the properties of mixed-halide complexes because they do not contain any equatorial halogen atoms and so halogen exchange will only occur along the MX chain. In addition, a number of mixed-metal complexes are known.

In keeping with the bulk of the reported work on HMMCs, the first part of this chapter concerns the linear-chains $[Pt(en)_2][Pt(en)_2X_2](ClO_4)_4$. The solid-state ^{15}N NMR spectra of them and their constituent monomers are discussed. This is followed by an examination of the mixed-halide complexes, $[Pt(en)_2][Pt(en)_2X_{2-2\alpha}X'_{2\alpha}][ClO_4]_4$ (X and X' are different halogens). Solid-state NMR studies are combined with resonance Raman analyses to help determine the distribution of halogens throughout the chain. Vibrational modelling is used as an aid to the interpretation of the Raman spectra. Much of the work is repeated for the HMMCs with fluoroborate (BF_4^-) or hexafluorophosphate (PF_6^-) counterions to determine the influence of the counterion on solid-state NMR or Raman spectra. The final stage involves a brief survey of mixed-metal complexes, $[M(en)_2][Pt(en)_2X_2](ClO_4)_4$ (M = Ni or Pd).

4.2 Solid-State ^{15}N NMR spectroscopy of monovalent platinum complexes.

4.2.1 Introduction

The most important single-valence platinum complexes in this study are the constituent monomers; for the HMMCs $[Pt(en)_2][Pt(en)_2X_2]Y_4$ they are $[Pt^{II}(en)_2]Y_2$ and $[Pt^{IV}(en)_2X_2]Y_2$. A significant part of the solid-state NMR work involves making comparisons between the nuclear environments of HMMCs and monomers. This is more complicated for ionic systems than it is for neutral compounds because the bonding of the counterions in the HMMCs is liable to be significantly different from that in the monomers. Surprisingly, the constituent monomers are rarely used to synthesise linear-chain complexes; the starting materials are normally halide salts. For X = Cl or Br, $[Pt(en)_2]Cl_2$ and $[Pt(en)_2Cl_2]Cl_2$ are mixed together in the presence of the relevant acid, HY, and with excess of HBr if the bromide is required.[220] For X = I, $[Pt(en)_2]Cl_2$ is oxidised with iodine in a solution of HY. The purity of samples produced by such methods have been questioned.[38] HMMCs prepared by mixing equimolar amounts of constituent monomers will have fewer sources of impurity, and so this technique was employed in this work wherever possible. The counterion salts were made from the halide complexes by recrystallising with the appropriate acid. In the following sections, solid-state NMR results for all the monomeric species are reported. Also shown are the spectra of the Magnus Salt-type complexes, $[Pt(en)_2][PtX_4]$. They are composed of stacks of alternating $[Pt(en)_2]^{2+}$ and $[PtX_4]^{2-}$ units and are treated with free ethylenediamine to produce the corresponding salt $[Pt(en)_2]X_2$.

4.2.2 Halide complexes and Magnus salts

The standard preparation of halide salts involves the reaction of K_2PtCl_4 with a fivefold excess of free ethylenediamine.[220] This is impractical for a study using ^{15}N-enriched en, and so an excess of "natural" ligand was treated with ^{15}N-enriched samples of either $Pt(en)X_2$ or $[Pt(en)_2][PtX_4]$ (see section **4.8**). Solid-state ^{15}N NMR analysis of the products showed that for a given X the same spectrum is observed regardless of the starting material. The spectrum of $[Pt(en)_2]Cl_2$ **(401)** is the most clearly resolved and has four sharp peaks (see Figure 4.2.1a). They correspond to two main resonances and to four satellite peaks, which arise from coupling between ^{15}N and ^{195}Pt nuclei, but the overlap of each main peak with a satellite of the other means that only four signals are observed. The spectrum is consistent with the presence of two kinds of nitrogen in the system in equal abundance. Since the starting material has no influence on the resonances observed, the two nitrogen sites that are distinct must be within each ligand. The main peaks are at -376.9 and -380.2 ppm respectively, compared with -382.8 ppm for the signal in $Pt(en)Cl_2$. Two peaks can also be observed in the high-resolution spectra of the other halide salts $[Pt(en)_2]X_2$, (X = Br (**402a**) or I (**403**)) (see Figure 4.2.1b, c). At normal resolution, only one main peak is seen in each case, but even when dipole-dipole interactions are taken into account the signal is broader than would be expected for a single resonance. The halide salts are normally white, but many years ago a blue form of $[Pt(en)_2]Br_2$ was reported by Hantzsch and Rosenblatt.[245] A sample of this blue complex (**402b**) was generated accidentally in a solid mixture of white $[Pt(en)_2]Br_2$ and en.2HBr. Its solid-state ^{15}N NMR spectrum has a peak at -377.7 ppm, which is about 2 ppm upfield of that for uncontaminated white $[Pt(en)_2]Br_2$, and a coupling constant typical of a $J_{N\text{-}Pt^{II}}$ value. All the spectra of the Magnus Salt-type complexes $[Pt(en)_2][PtX_4]$ (X = Cl (**404**), Br (**405**) or I (**406**)) contain sharp, well-resolved peaks, and show no evidence of dipole-dipole broadening (see Figure 4.2.1d-f). Two signals are seen in each case, with their separation decreasing in the order X = Cl > Br > I. Changing X from Cl → Br → I causes the mean position of the signals to drift to lower field in halides and Magnus Salts. The influence of X is much smaller than it is in the neutral complexes where the halogens and nitrogens are bonded to the same metal centre. The coupling constants all lie between 290 and 320 Hz, which is a much smaller range than is observed for $Pt^{II}(en)X_2$.

Each halide salt $[Pt(en)_2]X_2$ was treated with the corresponding halogen (X_2) to make the Pt^{IV} salt $[Pt(en)_2X_2]X_2$. The oxidation was successful in two cases, giving a yellow solid for X = Cl (**407**) or Br (**408**). The solid-state ^{15}N NMR spectra of these Pt^{IV} species display two distinct nitrogen types like the corresponding $[Pt(en)_2]X_2$ (see Figure 4.2.1g, h), but the mean chemical shifts of the N-Pt^{IV} nuclei are downfield. Coupling constants can be determined for $[Pt(en)_2Cl_2]Cl_2$, and they are smaller than the $J_{N\text{-}Pt^{II}}$ values for $[Pt(en)_2]X_2$. The spectrum of $[Pt(en)_2Br_2]Br_2$ is too poorly resolved for $J_{N\text{-}Pt^{IV}}$ to be calculated. The oxidation of $[Pt(en)_2]I_2$

with iodine produced a shiny grey material **(409)** entirely unlike that expected for a Pt^{IV} complex. Its solid-state ^{15}N NMR spectrum is very sharply defined with a single peak, and well-resolved satellites (see Figure 4.2.1i). The coupling constant is much larger than normal $J_{N-Pt^{IV}}$ values, but it is consistent with that for N-Pt^{II} nuclei.

Table 4.2.1 **^{15}N chemical shifts and J_{N-Pt} coupling constants for halide complexes and Magnus Salt-type compounds, (X = Halogen) [a]**

X	$[Pt^{II}(en)_2]X_2$			$[Pt^{II}(en)_2][PtX_4]$			$[Pt^{IV}(en)_2X_2]X_2$		
	Label	δ / ppm	J_{N-Pt} / Hz	Label	δ / ppm	J_{N-Pt} / Hz	Label	δ / ppm	J_{N-Pt} / Hz
Cl	**401**	-376.9 -380.2	290 295	**404**	-379.8 -386.6	320 -	**407**	-363.4 -367.9	*ca.* 250 *ca.* 250
Br	**402a** **402b**	-375.9 -377.3	- -	**405**	-379.0 -384.5	- -	**408**	-371.0	-
I	**403**	-375.2	-	**406**	-380.5 -382.0	- 320	***409***	*(-378.1)*	*(310)*

[a] *Chemical shifts are accurate to ± 0.4 ppm. Coupling constants are accurate to ± 20 Hz.*

4.2.3 Salts containing HMMC counterions

The HMMCs studied in this chapter have the general formula $[Pt(en)_2][Pt(en)_2X_2]Y_4$, where Y = ClO_4^-, BF_4^- or PF_6^-. The salts $[Pt^{II}(en)_2]Y_2$ and $[Pt(en)_2X_2]Y_2$ (X = Cl or Br) were prepared, so that suitable comparisons could be made between monomers and HMMCs. The syntheses are very simple, involving the recrystallisation of the appropriate halide complex from a dilute solution of the required acid, HY. The progress of each reaction was followed by analysing the solid-state ^{15}N NMR of the extracted solid. This is particularly useful for removing concerns over the purity of HMMCs and their precursors,[38] and it cannot be done satisfactorily by any other technique. A good example of this process is the preparation of $[Pt^{II}(en)_2](ClO_4)_2$ **(410)** in which $[Pt(en)_2]Cl_2$ is treated with perchloric acid (see Figure 4.2.2). The spectrum of $[Pt(en)_2]Cl_2$ has two main peaks at -376.9 and -380.2 ppm respectively, while that of the purified perchlorate has just one at -387.4 ppm. The pure $[Pt(en)_2](ClO_4)_2$ was only obtained after three extractions with perchloric acid. Because the difference between the chemical shifts of the two salts is so great, purity can be gauged easily at any stage. A similar number of recrystallisations were needed to isolate pure samples of the other Pt^{II} salts,

$[Pt(en)_2](BF_4)_2$ (**411**) and $[Pt(en)_2](PF_6)_2$ (**412**). The fluoroborate salt has a single peak in its solid-state ^{15}N NMR spectrum at -390.6 ppm, some 3 ppm upfield of that for the perchlorate (see Figure 4.2.5a). The spectrum of the hexafluorophosphate species has two resonances, but it is not symmetrical like that of $[Pt(en)_2]Cl_2$, because the coupling constants for the two nitrogen types are inequivalent (see Figure 4.2.6a). The value of $J_{N\text{-}Pt^{II}}$ does not vary much from 300 Hz, even in $[Pt(en)_2](PF_6)_2$.

It is equally important to produce pure samples of the Pt^{IV} monomers, but the proximity of axial halogens broadens the NMR signals and diminishes the influence of the counterion on N-Pt^{IV} chemical shifts, so purity is harder to determine. Pt^{IV} salts are harder to purify if the Pt^{IV} state is unstable, because oxidising halogen must be present in solution and this can result in halide impurities in the crystal lattice. $[Pt(en)_2I_2]^{2+}$ species could not be isolated, while $[Pt(en)_2Br_2]^{2+}$ ions became reduced, even in the solid state; the conversion of $[Pt(en)_2Cl_2]Cl_2$ is the only one that proceeds smoothly. A single main peak is observed in the spectrum of each purified Pt^{IV} complex. The N-Pt^{IV} peaks in $[Pt(en)_2Cl_2]Y_2$ (Y = ClO_4^- (**413**), BF_4^- (**414**) or PF_6^- (**415**)) are *ca.* 20 ppm downfield of the respective N-Pt^{II} signals in $[Pt(en)_2]Y_2$, while the N-Pt^{IV} peaks in $[Pt(en)_2Br_2]Y_2$ (Y = ClO_4^- (**416**) or BF_4^- (**417**)) are less than 15 ppm downfield (see Figures 4.2.3-6). $J_{N\text{-}Pt^{IV}}$ cannot be determined accurately because the peaks are so broad, but it does not differ greatly from 240 Hz in any Pt^{IV} complex, and so it is significantly smaller than $J_{N\text{-}Pt^{II}}$ in each case. ^{15}N chemical shifts and $J_{N\text{-}Pt}$ values are listed in Table 4.2.2.

Table 4.2.2 **^{15}N chemical shifts and $J_{N\text{-}Pt}$ coupling constants of the "counterion" salts of platinum *bis*-ethylenediamine (Y = counterion) [a]**

Y	$[Pt^{II}(en)_2]Y_2$			$[Pt^{IV}(en)_2Cl_2]Y_2$			$[Pt^{IV}(en)_2Br_2]Y_2$		
	Label	δ / ppm	$J_{N\text{-}Pt}$ / Hz	Label	δ / ppm	$J_{N\text{-}Pt}$ / Hz	Label	δ / ppm	$J_{N\text{-}Pt}$ / Hz
ClO_4^-	**410**	-387.4	305	**413**	-367.6	235	**416**	-374.9	250
BF_4^-	**411**	-390.6	300	**414**	-369.2	240	**417**	-375.9	240
PF_6^-	**412**	-390.0 -393.9	280 290	**415**	-370.0	235			

[a] *Chemical shifts are accurate to ± 0.4 ppm. Coupling constants are accurate to ± 20 Hz for the platinum (II) complexes, ± 40 Hz for the platinum (IV) complexes.*

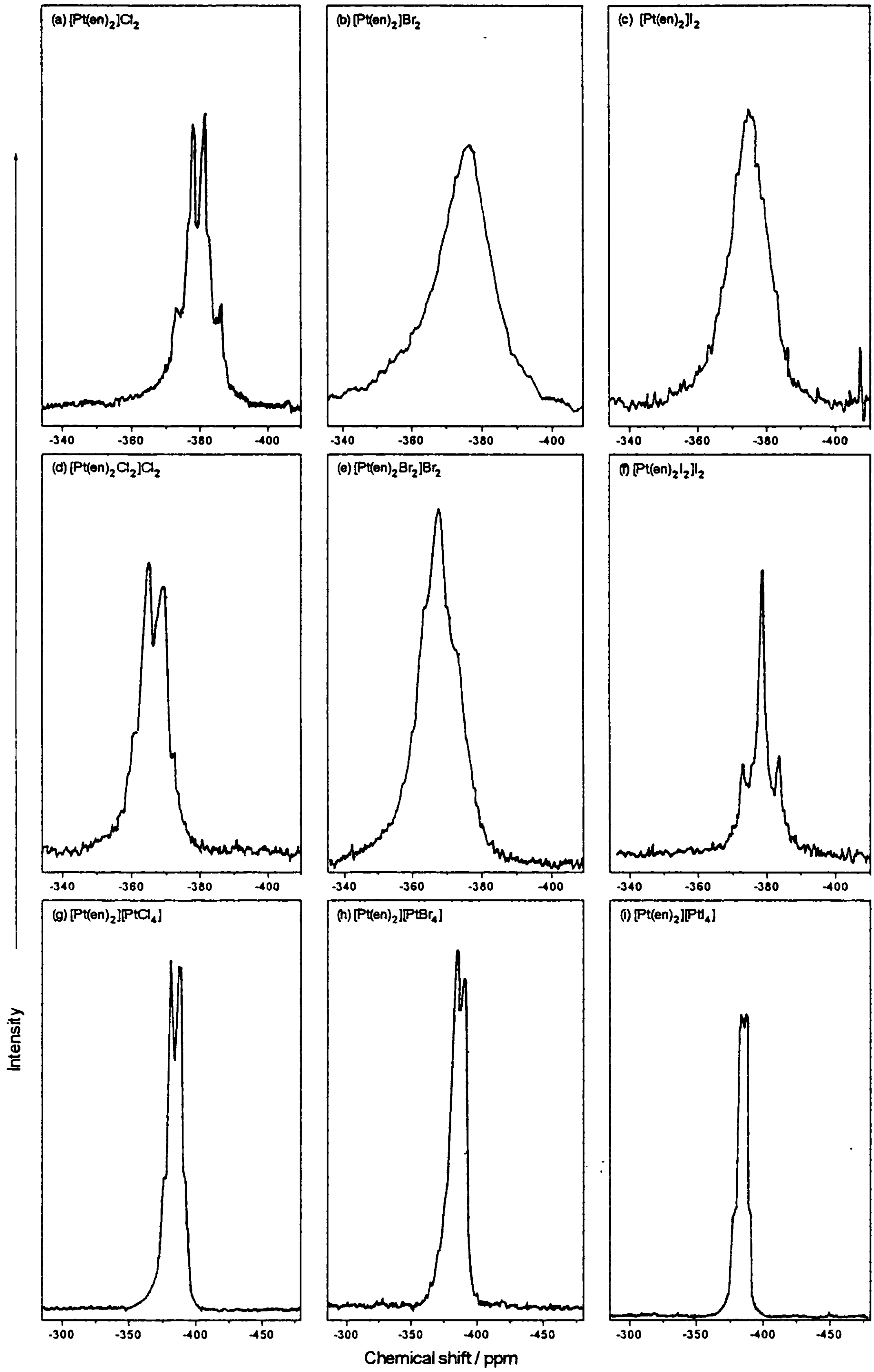

Figure 4.2.1 Solid-state ^{15}N NMR of: (a)-(c) [Pt(en)$_2$]X$_2$, (d)-(f) [Pt(en)$_2$X$_2$]X$_2$ and (g)-(i) [Pt(en)$_2$][PtX$_4$], where X = Cl, Br or I, respectively.

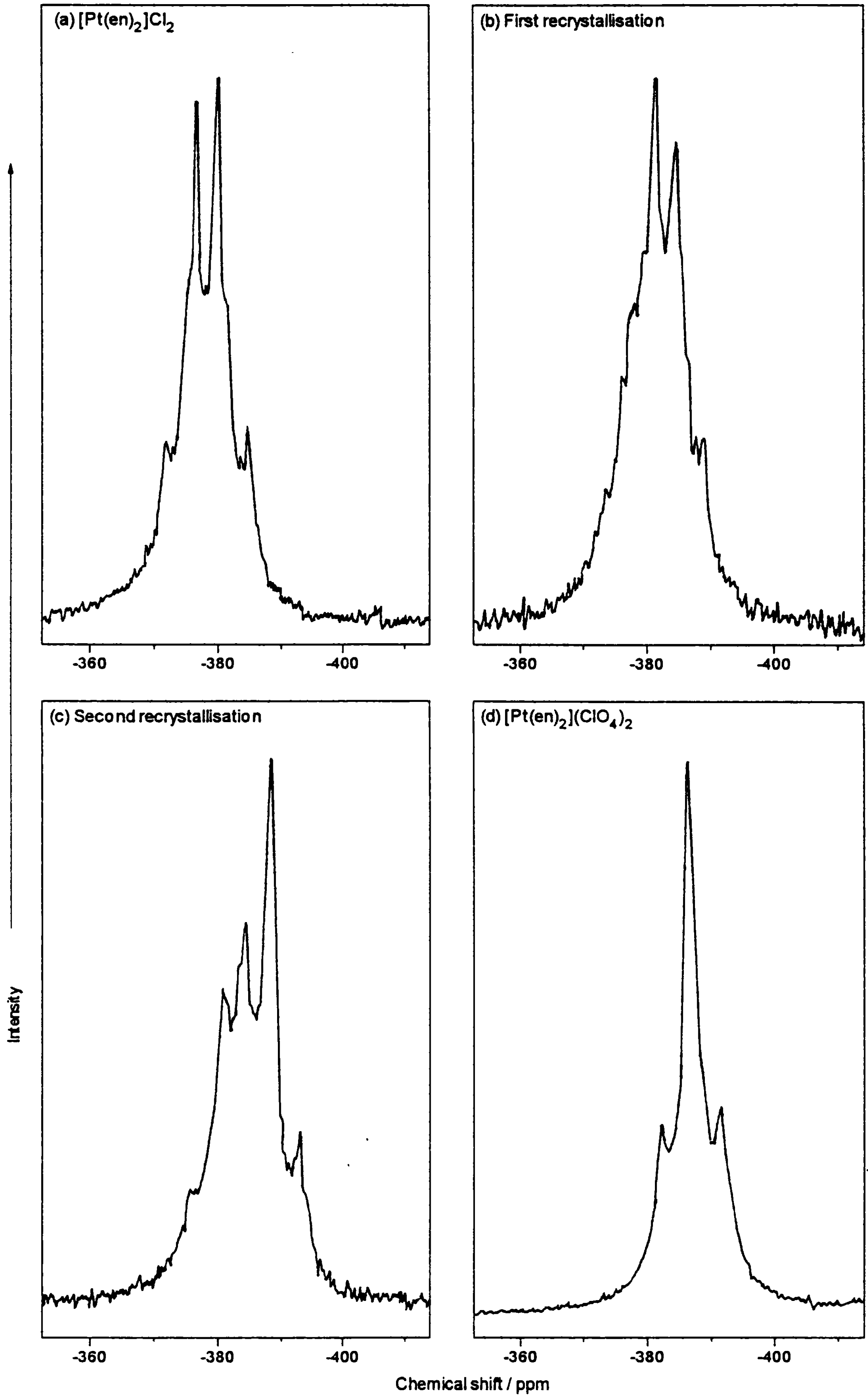

Figure 4.2.2 *Solid-state ^{15}N NMR spectral analysis of the reaction of $[Pt(en)_2]Cl_2$ with $HClO_4$ to produce $[Pt(en)_2](ClO_4)_2$.*

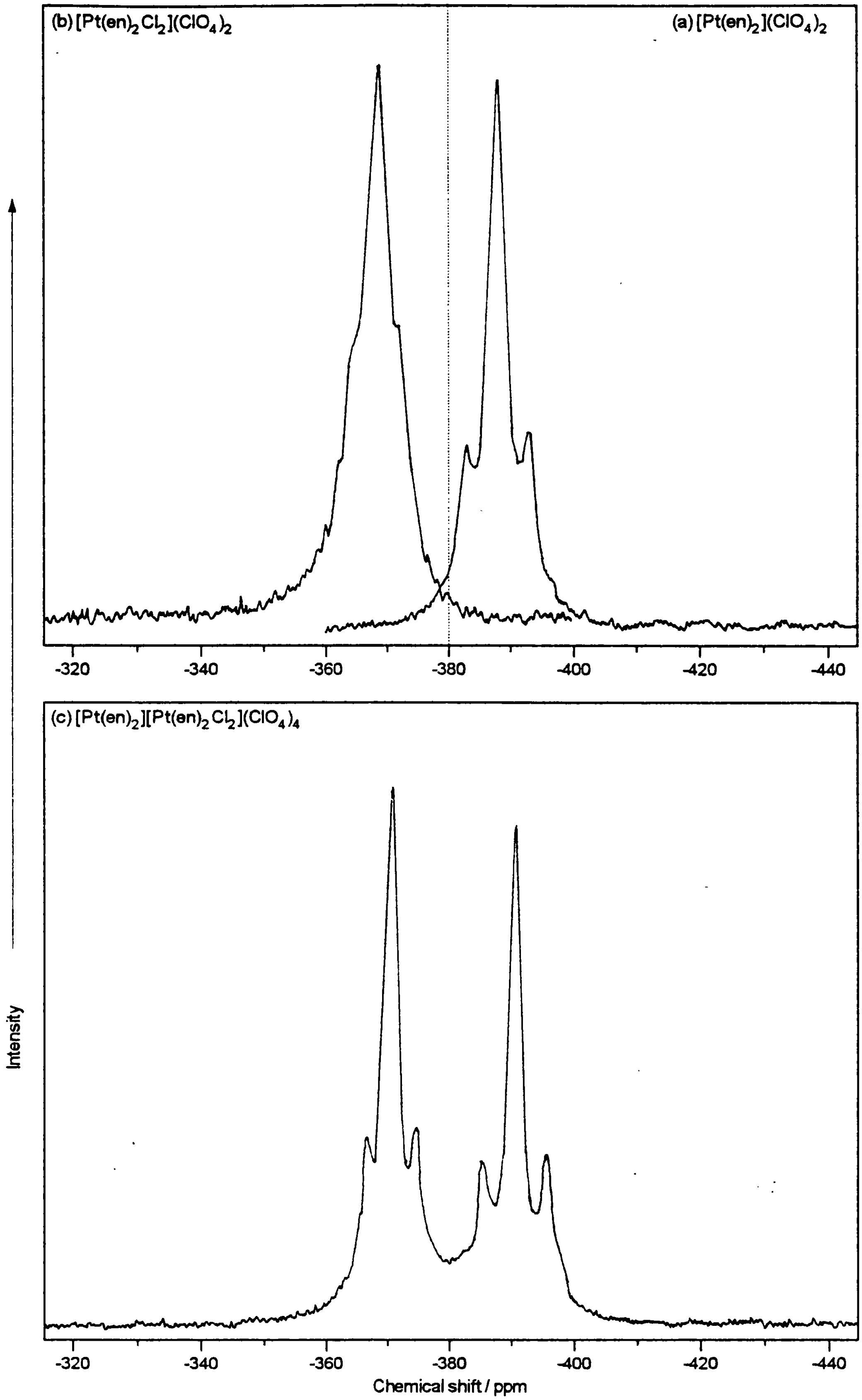

Figure 4.2.3 Solid-state ^{15}N NMR spectra of (a) $[Pt(en)_2](ClO_4)_2$, (b) $[Pt(en)_2Cl_2](ClO_4)_2$ and (c) $[Pt(en)_2][Pt(en)_2Cl_2](ClO_4)_4$.

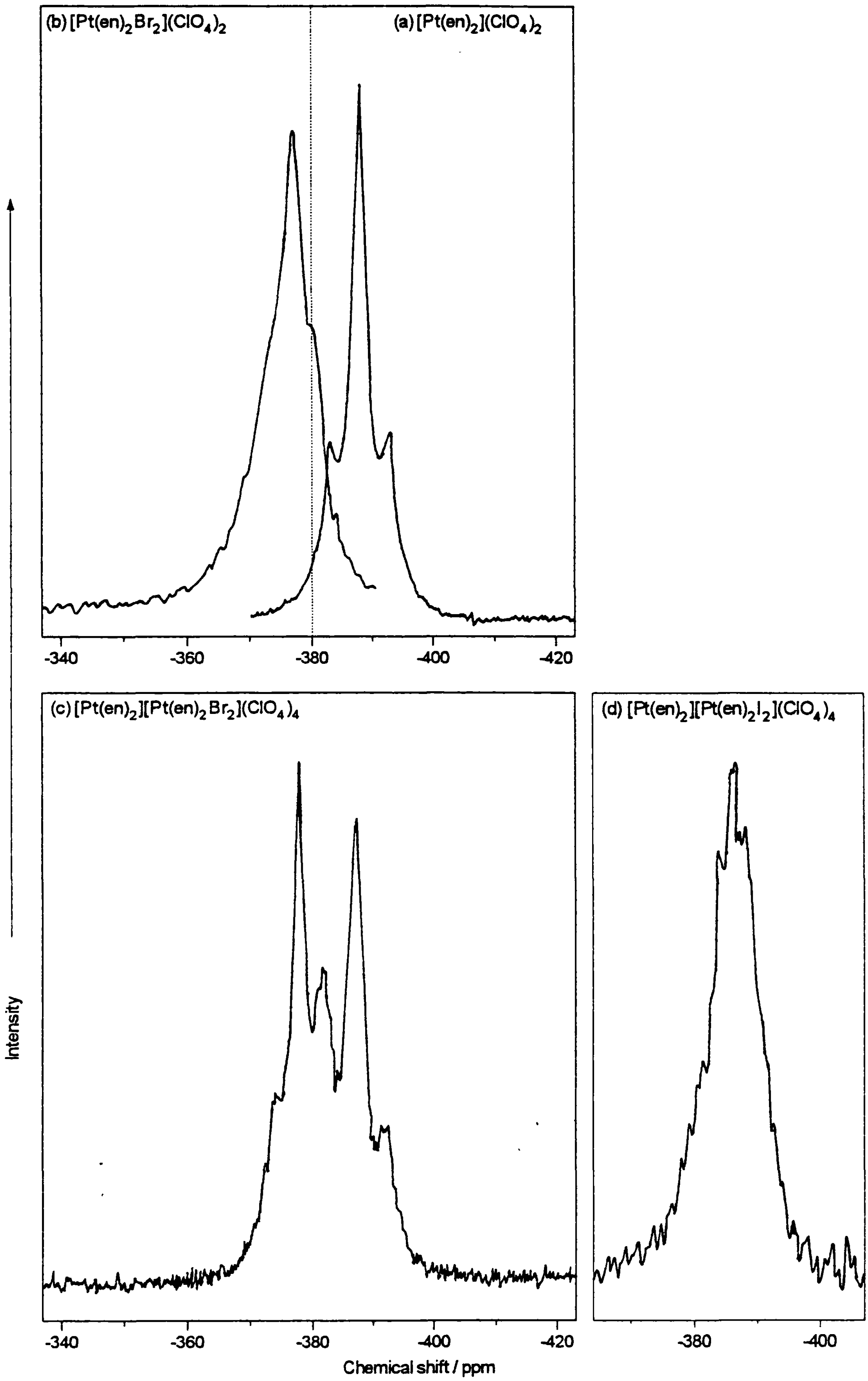

Figure 4.2.4 *Solid-state ^{15}N NMR spectra of (a) $[Pt(en)_2](ClO_4)_2$, (b) $[Pt(en)_2Br_2](ClO_4)_2$, (c) $[Pt(en)_2][Pt(en)_2Br_2](ClO_4)_4$ and (d) $[Pt(en)_2][Pt(en)_2I_2](ClO_4)_4$.*

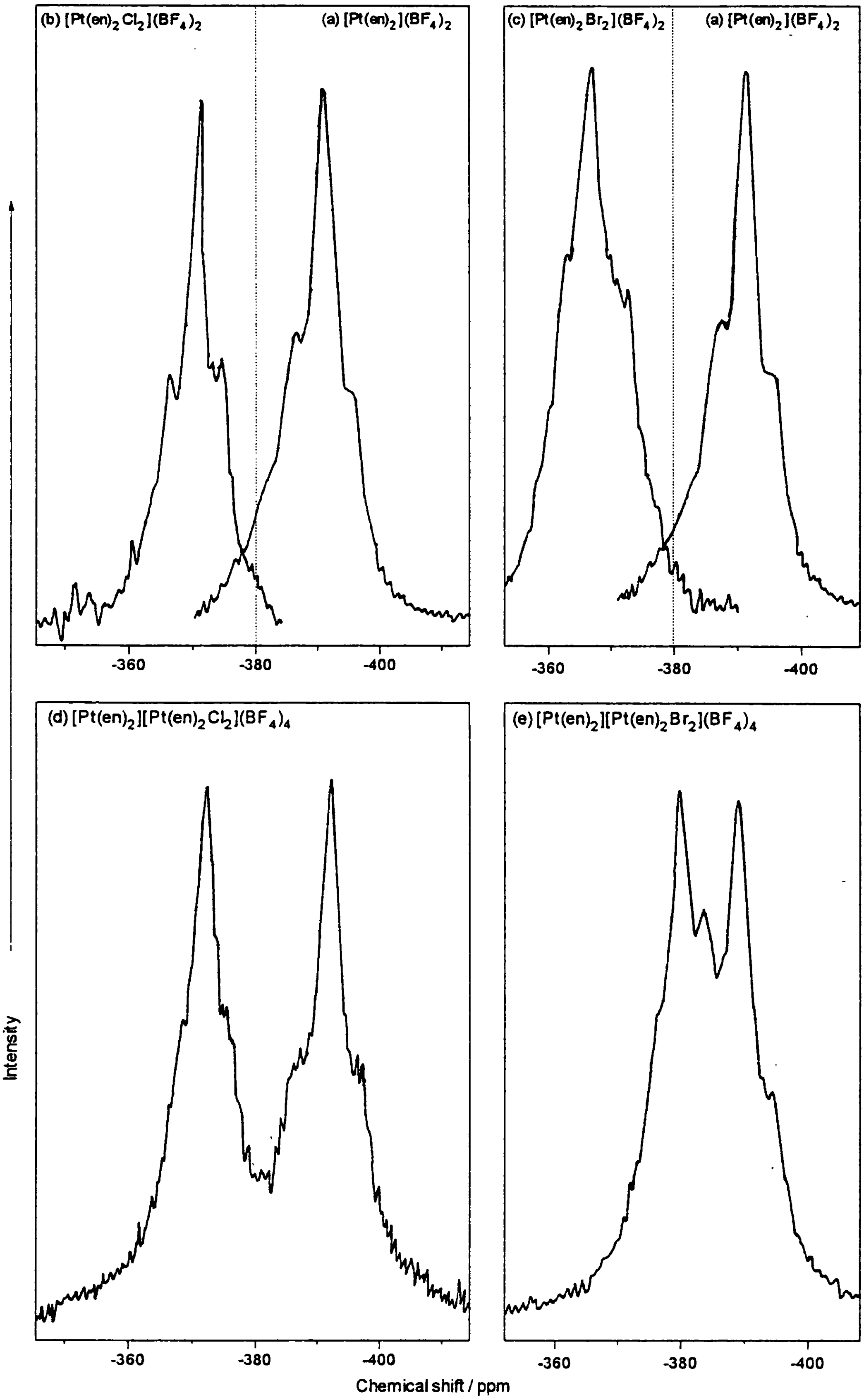

Figure 4.2.5 Solid-state ^{15}N NMR spectra of (a) $[Pt(en)_2](BF_4)_2$, (b) $[Pt(en)_2Cl_2](BF_4)_2$, (c) $[Pt(en)_2Br_2](BF_4)_2$, (d) $[Pt(en)_2][Pt(en)_2Cl_2](BF_4)_4$ and (e) $[Pt(en)_2][Pt(en)_2Br_2](BF_4)_4$.

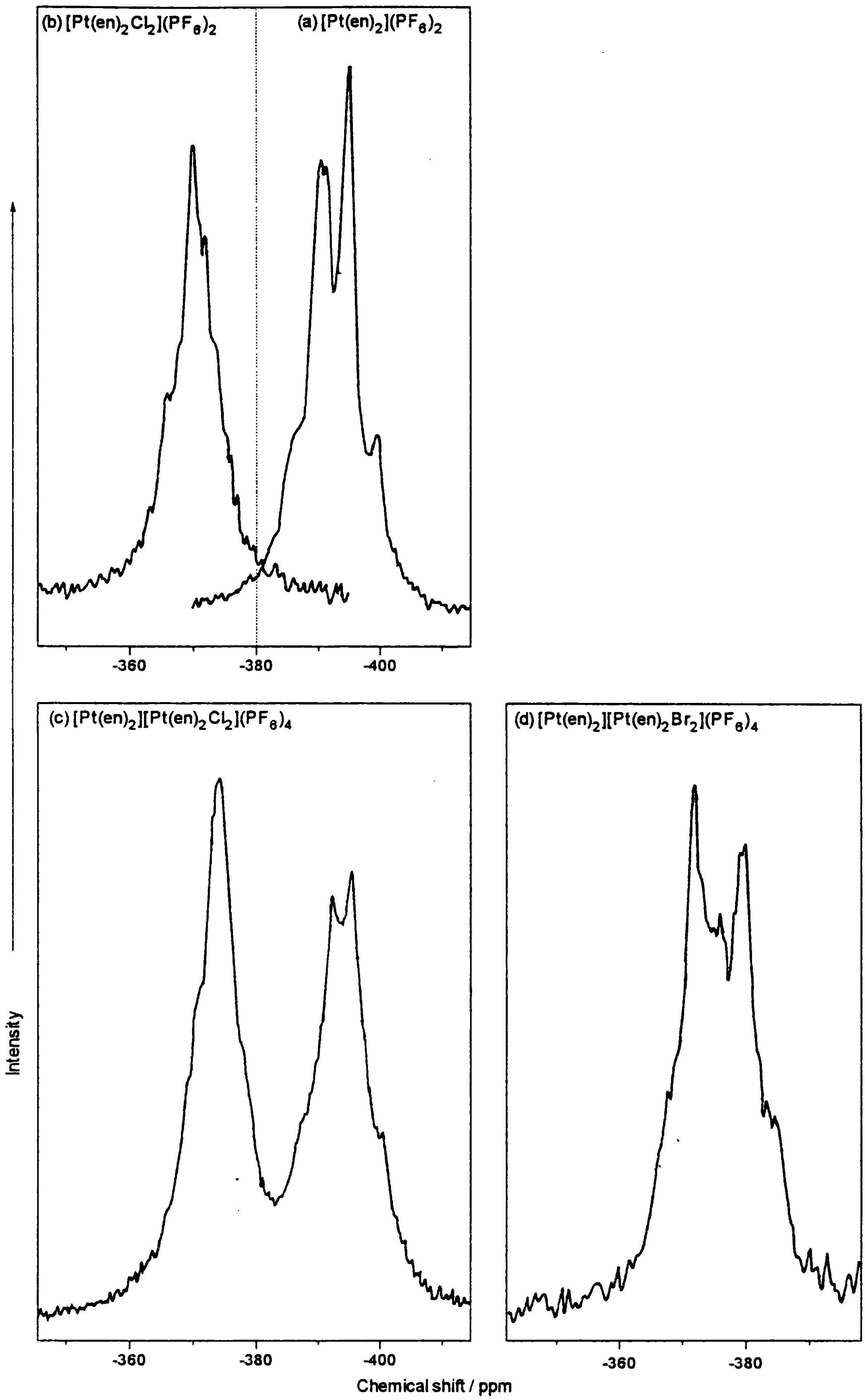

Figure 4.2.6 Solid-state ^{15}N NMR spectra of (a) [Pt(en)$_2$](PF$_6$)$_2$, (b) [Pt(en)$_2$Cl$_2$](PF$_6$)$_2$, (c) [Pt(en)$_2$][Pt(en)$_2$Cl$_2$](PF$_6$)$_4$ and (d) [Pt(en)$_2$][Pt(en)$_2$Br$_2$](PF$_6$)$_4$.

4.2.4 Discussion

The influence of the counterions on ^{15}N chemical shifts cannot be quantified absolutely, so direct comparison of δ_N for $[Pt(en)_2]X_2$ and $Pt(en)X_2$ (X = Cl, Br or I) is not appropriate. The $J_{N\text{-}Pt^{II}}$ values are significantly smaller in the ionic species. In terms of Equation [3.2.1], this relates to a reduction in either the s character in the Pt-N bond (*i.e.* smaller α^2_{Pt}) or in the electron density of the Pt_{6s} orbital at the platinum nucleus (*i.e.* smaller $|\Psi_{Pt_{6s}}(0)|^2$). If the hybrid orbitals are assumed to be the same in both systems, then the smaller $J_{N\text{-}Pt}$ in $[Pt(en)_2]X_2$ corresponds to a lower effective platinum oxidation state. This can be attributed to the replacement of the halogen atoms in $Pt(en)X_2$ by less electronegative nitrogen atoms. A more significant difference between the two species is in the number of distinct types of nitrogen they contain. While there is only one in each neutral complex ($Pt(en)X_2$ or $Pt(en)X_4$), there are two in each halide salt (*i.e.* $[Pt(en)_2]X_2$ or $[Pt(en)_2X_2]X_2$) or Magnus salt ($[Pt(en)_2][PtX_4]$). The crystal structure of $[Pt(en)_2]Cl_2$ has been resolved.[246] Only the *gauche* conformer is observed; it has one δ and one λ ligand in each ion (see Figure 3.1.2). The atomic positions show that for each ligand there are two N sites, which are distinguished by their Pt-N or N-Cl^- distances. Although the two r(Pt-N) distances are similar (2.039 and 2.046 Å), the ^{15}N chemical shift is very sensitive to environment. Of the three "counterion complexes", only $[Pt(en)_2](PF_6)_2$ has two main resonances in its solid-state ^{15}N NMR spectrum. Few structural results are known for the monomers so the factors that control the number of nitrogen types present cannot be determined. The crystal structure of $[Pt(en)_2Cl_2](ClO_4)_2$ shows just one Pt-N distance,[247] which is consistent with the single main peak seen in its spectrum. It may be coincidence that X^- and PF_6^- ions have a centre of symmetry and have two N types in their salts, while the salts of tetrahedral ions have only one type of nitrogen. The interaction of the anion with the hydrogens attached to the N atoms may be influential, or the conformation of the PtN_4 plane may be important.

The interpretation of the solid-state NMR spectra of the neutral complexes deals with intramolecular effects alone, and is derived from published solution NMR work with little compromise (see Chapter 3). An approximate relation for the diamagnetic contribution to the shielding of nuclei in solution, which depends on the neighbouring nuclear charges and the inverse of their distances, was proposed by Ramsey.[248] In the solid state, the identity of the halogen in $[Pt(en)_2]X_2$ (X = Cl, Br or I) has little influence on the mean chemical shift of the N-Pt^{II} nuclei, so the diamagnetic contribution must be small. For example, the N-Cl^- distance in *cis*-$[Pt(en)_2Cl_2]Cl_2$ (*sic*) [249] or $[Pt(en)_2]Cl_2$ [246] is *ca.* 0.2 Å longer than the N-O distance in $[Pt(en)_2Cl_2](ClO_4)_2$,[247] and yet perchlorate ions shield the nitrogen atoms better. The dominant influence on δ_N is probably the ability of the counterion to form a hydrogen bond to the NH_2 groups in the ligands. The stronger the bond, the greater the shielding of the nitrogen atoms. The counterions may be arranged in order of increasing hydrogen-bonding strength on the basis of the observed ^{15}N chemical shifts:

$$I^- < Br^- < Cl^- < ClO_4^- < BF_4^- < PF_6^- \qquad [4.2.1]$$

An important property of solid-state ^{15}N NMR spectroscopy is its suitability for analysing the composition of salts. It means that the progress of recrystallisations can be followed, particularly when there is a large difference between the chemical shifts of starting material and product. The technique is therefore most readily applied to the conversion of $[Pt(en)_2]Cl_2$ to $[Pt(en)_2]Y_2$ (Y = ClO_4^-, BF_4^- or PF_6^-), but it can be used to determine the completion point for reactions of $[Pt(en)_2Cl_2]Cl_2$ or $[Pt(en)_2Br_2]Br_2$, even though the peaks are much broader. In the case of $[Pt(en)_2](ClO_4)_2$, the spectra of partially converted $[Pt(en)_2]Cl_2$ can be deconvoluted to reveal two discrete resonances that relate to a hybrid complex. The signals have roughly equal intensity, and one of them is coincident with one the peaks for $[Pt(en)_2]Cl_2$. It is logical to assign them to $[Pt(en)_2](Cl)(ClO_4)$, *i.e.* $[Pt(en)_2]^{2+}$ units that have one Cl^- and one ClO_4^- as the nearest two anions (see Figure 4.2.2 and Table 4.2.3).

Table 4.2.3 Chemical shifts and coupling constants for $[Pt(en)_2](Y)(Y')$ [a]

Counterions		Label	First peak	Second peak	Couplings
Y	Y'		δ / ppm	δ / ppm	$J_{N\text{-}Pt}$ / Hz
Cl	Cl	**401**	-376.9	-380.2	290
Cl	ClO_4	***418***	-380.0	-383.5	305
ClO_4	ClO_4	**410**	-387.4		305

[a] *Chemical shifts are accurate to ± 0.4 ppm.*

There are two spectra that do not follow the patterns established by the majority. The first is that of the blue bromide salt, $[Pt(en)_2]Br_2$ (**402b**) which has a single main peak 3.4 ppm upfield of that for the normal white form of $[Pt(en)_2]Br_2$. The second is the spectrum of the species termed $[Pt^{IV}(en)_2I_2]I_2$ (**409**), which was the product of the reaction of $[Pt(en)_2]I_2$ with iodine. This has a single peak 2.9 ppm upfield of that for $[Pt^{II}(en)_2]I_2$, but the coupling constant value of 310 Hz is too large for a Pt^{IV} complex. The Raman spectrum of complex **409** has a single resonance at *ca.* 111 cm^{-1} at 752 nm excitation. This is a much lower wavenumber than is normally found for $\nu_s(I\text{-}Pt^{IV}\text{-}I)$, or for the ν_1 mode in cationic PtI chains, but it is in the right range for the ν_1 mode in I_3^-. The properties of both **402b** and **409** are consistent with those of a Pt^{II} complex that has some impurity doped into its crystal lattice that increases the shielding around the nitrogen nuclei. Possible impurities include X_3^- ions (at X^- sites) and X_2 molecules.

4.3 Solid-State ^{15}N NMR studies of HMMC complexes

4.3.1 Introduction

Cationic HMMCs of the form [Pt(en)$_2$][Pt(en)$_2$X$_2$]Y$_4$ are formed readily when $[Pt(en)_2]^{2+}$ and $[Pt(en)_2Cl_2]^{2+}$ ions are mixed in the presence of the anion Y^-. The Pt^{II} and Pt^{IV} species do not have to be present in equimolar quantities, although that would improve yield and purity of the product, and they can be generated *in situ* if required. Because they are not difficult to synthesise, the first method published for the preparation of HMMCs remained the accepted route for many years.[220] More recently, there has been criticism of this technique because of the level of purity of its products.[38] Where possible, the HMMCs studied by solid-state NMR spectroscopy were prepared in a variety of ways. For X = Cl or Br, the most efficient method is to mix equimolar amounts of [Pt(en)$_2$]Y$_2$ and [Pt(en)$_2$X$_2$]Y$_2$ that are known to be pure from their solid-state ^{15}N NMR spectra in the presence of HY. For X = I, the chloride (or bromide) HMMC can be converted with iodide ions, or [Pt(en)$_2$]Y$_2$ can be partially oxidised with excess of iodine. The latter is more likely to give non-stoichiometric mixtures of Pt^{II} and Pt^{IV} centres in the product.

The complexes [Pt(en)$_2$][Pt(en)$_2$X$_2$](ClO$_4$)$_4$ have been studied so often in recent years that they are usually abbreviated as PtX in the literature. Most of the work in this Chapter is concerned with the perchlorate HMMCs, partly because so much is known about them, and partly because they give better quality solid-state ^{15}N NMR spectra than HMMCs do with Y = BF_4^- or PF_6^-. The fluorine atoms in these counterions broaden the observed peaks slightly and reduce the resolution, possibly because of residual dipolar coupling of ^{15}N to ^{19}F. Analysis of the perchlorate complexes is not without problems, because in [Pt(en)$_2$][Pt(en)$_2$Cl$_2$](ClO$_4$)$_4$ and [Pt(en)$_2$][Pt(en)$_2$Br$_2$](ClO$_4$)$_4$ there is a crystallographic phase transition close to room temperature (see section **1.3**). Solid-state NMR analysis was therefore carried out at several temperatures to check that change of phase does not alter the spectra significantly.

4.3.2 Studies on [Pt(en)$_2$][Pt(en)$_2$X$_2$](ClO$_4$)$_4$ (X = Cl, Br or I)

Several samples of each HMMC were prepared to check the reproducibility of the solid-state NMR spectra. Red crystals of [Pt(en)$_2$][Pt(en)$_2$Cl$_2$](ClO$_4$)$_4$ **(419)** were best made by mixing $[Pt(en)_2](ClO_4)_2$ and $[Pt(en)_2Cl_2](ClO_4)_2$ in dilute $HClO_4$, while an analogous reaction gave green crystals of $[Pt(en)_2][Pt(en)_2Br_2](ClO_4)_4$ (**420**). Either complex can be treated with iodide ions to give the bronze-coloured $[Pt(en)_2][Pt(en)_2I_2](ClO_4)_4$ (**421**), but a sample of better quality was obtained by oxidising of $[Pt(en)_2](ClO_4)_2$ with iodine. The solid-state ^{15}N NMR spectra of $[Pt(en)_2][Pt(en)_2X_2](ClO_4)_4$ (X = Cl, Br or I) are shown in Figures 4.2.3-4. Temperature was found to have little effect on the spectra of the chloride or bromide. At high temperatures the N-Pt^{II} and N-Pt^{IV} peaks are slightly closer together, but by an amount within experimental error. The HMMC $[Pt(en)_2][Pt(en)_2Cl_2](ClO_4)_4$ was also analysed by solid-state ^{195}Pt NMR spectroscopy. A sample was scanned for over sixty hours, but the signal was not strong enough to justify a second spinning speed to be tried, or for any of the other HMMCs to be analysed.

The spectra of the cationic HMMCs follow similar trends to those of the neutral-chain systems. There is one main peak for each oxidation state in the HMMC, except for $[Pt(en)_2][Pt(en)_2I_2](ClO_4)_4$ where two signals cannot be resolved. The peaks corresponding to ^{15}N-Pt^{II} and ^{15}N-Pt^{IV} get closer together as the bridging halogen is changed from Cl to Br to I, until are coincident in the iodide. The chemical shift of the N-Pt^{II} resonance is nearly the same for all three HMMCs, so the trend in $\Delta\delta_N$ is correlated with δ_N for the N-Pt^{IV} peak (see Table 4.3.1). A close approximation of the shape of the solid-state ^{15}N NMR spectrum of $[Pt(en)_2][Pt(en)_2Cl_2](ClO_4)_4$ can be achieved by superimposing the signals of $[Pt(en)_2](ClO_4)_2$ and $[Pt(en)_2Cl_2](ClO_4)_2$. Chain formation causes a shift of about 2 ppm upfield for both nitrogen types. For the bromide linear chain, the N-Pt^{IV} resonance appears in the expected position, *i.e.* upfield of the monomeric species, but the platinum (II) centre behaves differently. $[Pt(en)_2I_2](ClO_4)_2$ was not isolated, so no comment can be made on the N-Pt^{IV} chemical shift for $[Pt(en)_2][Pt(en)_2I_2](ClO_4)_4$. Coupling constants are not greatly affected by chain formation. $J_{N\text{-}Pt^{II}}$ and $J_{N\text{-}Pt^{IV}}$ are slightly larger for $[Pt(en)_2][Pt(en)_2Cl_2](ClO_4)_4$ than they are for the respective monomers, whereas for $[Pt(en)_2][Pt(en)_2Br_2](ClO_4)_4$ both values are smaller. Chemical shifts and coupling constants are given in Table 4.3.1, alongside those of the constituent monomers.

Table 4.3.1 **^{15}N chemical shifts and coupling constants for the linear-chain complexes [Pt(en)$_2$][Pt(en)$_2$X$_2$](ClO$_4$)$_4$ (X = Cl, Br or I), and their constituent monomers [a]**

Complex	Label	Crystal colour	H$_2$N-Pt^{II}		H$_2$N-Pt^{IV}		|Δδ$_N$|
			δ / ppm	J / Hz	δ / ppm	J / Hz	/ ppm
[Pt(en)$_2$](ClO$_4$)$_2$	**410**	colourless	-387.4	305			
[Pt(en)$_2$Cl$_2$](ClO$_4$)$_2$	**413**	yellow			-367.6	235	*(19.8)*
[Pt(en)$_2$][Pt(en)$_2$Cl$_2$](ClO$_4$)$_4$	**419**	red	-389.4	320	-369.5	245	19.9
[Pt(en)$_2$Br$_2$](ClO$_4$)$_2$	**416**	yellow			-374.9	250	*(12.5)*
[Pt(en)$_2$][Pt(en)$_2$Br$_2$](ClO$_4$)$_4$	**420**	green	-386.7	300	-377.6	230	9.1
[Pt(en)$_2$][Pt(en)$_2$I$_2$](ClO$_4$)$_4$	**421**	gold	*-386.3*	-	*-386.3*	-	-

[a] *Chemical shifts are accurate to ± 0.4 ppm. N-Pt^{II} coupling constants are accurate to ± 20 Hz. N-Pt^{IV} coupling constants are accurate to ± 40 Hz.*

4.3.3 Studies on [Pt(en)$_2$][Pt(en)$_2$X$_2$](BF$_4$)$_4$ (X = Cl or Br)

HMMCs containing BF$_4^-$ counterions have been largely ignored in comparison to the perchlorate complexes, even though they have similar properties (see section **1.4**), are easy to synthesise, and exhibit only one crystal phase. Unfortunately, the presence of fluorine atoms in BF$_4^-$ leads to dipole-dipole interactions that broaden the NMR signals of fluoroborate complexes in the solid state (see section **2.3**). Only two fluoroborate HMMCs were prepared, the red [Pt(en)$_2$][Pt(en)$_2$Cl$_2$](BF$_4$)$_4$ (**422**) and the green [Pt(en)$_2$][Pt(en)$_2$Br$_2$](BF$_4$)$_4$ (**423**). The iodide was neglected because it is not likely to give useful results. The overlap between N-Pt^{II} and N-Pt^{IV} signals and the broadening caused by the fluorines means that there will be little peak definition. In any case there is no [Pt(en)$_2$I$_2$](BF$_4$)$_2$ with which to make comparisons.

The solid-state ^{15}N NMR spectra of [Pt(en)$_2$][Pt(en)$_2$X$_2$](BF$_4$)$_4$ (X = Cl or Br) are shown in Figure 4.2.5. They are not as well resolved as those of the corresponding perchlorates, but the trends displayed are largely the same. Two peaks are observed which are closer together when X = Br than when X = Cl, and whose separation |Δδ$_N$| is almost independent of the identity of the counterion. The influence of the bridging halogen on the chemical shifts is also little affected by the counterion. The N-Pt^{II} peak moves 3.0 ppm downfield, and the N-Pt^{IV} peak 7.4 ppm upfield, as X is changed from Cl to Br. The corresponding values for Y = ClO$_4^-$ are

2.7 and 8.1 ppm. Chemical shifts are slightly altered by chain formation. Coupling constants are difficult to determine in some cases because of the signals are broad, but they are similar in chain and monomeric species. The chemical shifts and coupling constants of [Pt(en)$_2$][Pt(en)$_2$X$_2$](BF$_4$)$_4$ and their constituent monomers are listed in Table 4.3.2.

Table 4.3.2 ^{15}N chemical shifts and coupling constants for the linear-chain complexes [Pt(en)$_2$][Pt(en)$_2$X$_2$](BF$_4$)$_4$ (X = Cl or Br), and their constituent monomers [a]

Complex	Label	Crystal colour	H$_2$N-Pt^{II}		H$_2$N-Pt^{IV}		$\|\Delta\delta_N\|$
			δ / ppm	J / Hz	δ / ppm	J / Hz	/ ppm
[Pt(en)$_2$](BF$_4$)$_2$	**411**	colourless	-390.6	300			
[Pt(en)$_2$Cl$_2$](BF$_4$)$_2$	**414**	yellow			-369.2	240	*(21.4)*
[Pt(en)$_2$][Pt(en)$_2$Cl$_2$](BF$_4$)$_4$	**422**	red	-391.8	300	-372.0	240	19.8
[Pt(en)$_2$Br$_2$](BF$_4$)$_2$	**417**	yellow			-375.9	240	*(14.7)*
[Pt(en)$_2$][Pt(en)$_2$Br$_2$](BF$_4$)$_4$	**423**	green	-388.8	300	-379.4	240	9.4

[a] *Chemical shifts are accurate to ± 0.4 ppm. N-Pt^{II} coupling constants are accurate to ± 30 Hz. N-Pt^{IV} coupling constants are accurate to ± 50 Hz.*

4.3.4 Studies on [Pt(en)$_2$][Pt(en)$_2$X$_2$](PF$_6$)$_4$ (X = Cl or Br)

HMMCs containing the hexafluorophosphate (PF$_6^-$) counterion have rarely been studied. They are not as easy to synthesise as the HMMCs with tetrahedral anions, and the crystals they form are not usually of sufficient quality to make X-ray diffractrometric analysis worthwhile. The only [Pt(en)$_2$][Pt(en)$_2$X$_2$](PF$_6$)$_4$ crystal structure that has been reported is for X = Cl.[21] Samples of [Pt(en)$_2$][Pt(en)$_2$Cl$_2$](PF$_6$)$_4$ (**424**) were made by mixing [Pt(en)$_2$](PF$_6$)$_2$ and [Pt(en)$_2$Cl$_2$](PF$_6$)$_2$ in a solution of HPF$_6$. This results in crystals that are orange and cuboid rather than red and needle-like. [Pt(en)$_2$][Pt(en)$_2$Br$_2$](PF$_6$)$_4$ was not made by this method because [Pt(en)$_2$Br$_2$](PF$_6$)$_2$ could not be isolated. Instead it was prepared by treating a solution of the chloride complex with excess of bromide ions, to give a sample of dark green crystals (**425**). The solid-state ^{15}N NMR spectra of the HMMCs [Pt(en)$_2$][Pt(en)$_2$X$_2$](PF$_6$)$_4$ (X = Cl or Br) are shown in Figure 4.2.6. They are quite unlike those for the other two HMMC systems studied. In the spectrum of [Pt(en)$_2$][Pt(en)$_2$Cl$_2$](PF$_6$)$_4$ there are two peaks in the

N-Pt^{II} region, and although only one peak can be resolved in the spectrum of the bromide analogue, the N-Pt^{II} resonance is broad enough to contain more than one signal. The mean value of $\Delta\delta_N$ is slightly smaller than it is for the other HMMCs, but for the chloride the close relationship between chain and monomeric resonances is maintained. The effect of changing the bridging halogen is different for $[Pt(en)_2][Pt(en)_2X_2](PF_6)_4$, since the N-Pt^{IV} peak moves relatively little, so that the size of $\Delta\delta_N$ is reflected in the position of the N-Pt^{II} resonance. ^{15}N chemical shifts and $J_{N\text{-}Pt}$ coupling constants are listed in Table 4.3.3.

Table 4.3.3 ^{15}N chemical shifts and coupling constants for the linear-chain complexes $[Pt(en)_2][Pt(en)_2X_2](PF_6)_4$ (X = Cl or Br), and their constituent monomers [a]

Complex	Label	Crystal colour	$H_2N\text{-}Pt^{II}$		$H_2N\text{-}Pt^{IV}$		$\|\Delta\delta_N\|$
			δ / ppm	*J* / Hz	δ / ppm	*J* / Hz	/ ppm
$[Pt(en)_2](PF_6)_2$	**413**	colourless	-390.0 -393.9	280 290			
$[Pt(en)_2Cl_2](PF_6)_2$	**416**	yellow			-370.0	235	*(20.0)* *(23.9)*
$[Pt(en)_2][Pt(en)_2Cl_2](PF_6)_4$	**424**	orange	-391.3 -394.8		-373.6	240	17.7 21.2
$[Pt(en)_2][Pt(en)_2Br_2](PF_6)_4$	**425**	olive	-379.3		-370.9		8.4

[a] *Chemical shifts are accurate to ± 0.4 ppm. N-Pt^{II} coupling constants are accurate to ± 30 Hz. N-Pt^{IV} coupling constants are accurate to ± 50 Hz.*

4.3.5 Discussion

The solid-state ^{15}N NMR spectra of the HMMC complexes can be viewed from three perspectives: the effect of chain formation, the influence of the counterion (Y) and the influence of the bridging halogen (X). The first can only be determined in systems where the HMMC and both its constituent monomers have been analysed, *i.e.* Y = ClO_4^-, BF_4^- or PF_6^- for X = Cl, and Y = ClO_4^- or BF_4^- for X = Br. The presence of ions in these complexes was expected to complicate the solid-state NMR study, but the cationic HMMCs show similar behaviour to the neutral chain complexes. For X = Cl, the separation of the N-Pt^{II} and N-Pt^{IV} peaks ($|\Delta\delta_N|$) is not greatly affected by chain formation. $|\Delta\delta_N|$ is smaller in the HMMC than in the monomers when X = Br, which might be misinterpreted as evidence of increased charge delocalisation.

However, the effect of chain formation is to move the N-Pt^{IV} peaks 2 ppm upfield independent of the identity of X, and so the reduction of $|\Delta\delta_N|$ is related to the position of the N-Pt^{II} resonance, which may be upfield or downfield of its position in the monomer. Such a change in N-Pt^{II}, which is unaccompanied by any great difference in $J_{N\text{-}Pt}$, is probably due to an alteration in the hydrogen-bonding between the ligand and the anion. The conformations of the ethylenediamine ligands are known to be $\delta\lambda$ in the monomer $[Pt(en)_2]Cl_2$ and $\delta\delta$ in the HMMC $[Pt(en)_2][Pt(en)_2Cl_2](ClO_4)_4$.[246]

The counterion has little influence on the value of $J_{N\text{-}Pt}$, but it can have a substantial effect on the ^{15}N chemical shifts. $\Delta\delta_N$, which is the mean separation of the N-Pt^{II} and N-Pt^{IV} resonances, can be evaluated for the HMMCs to give a measure of the similarity of the two metal oxidation states. There is not much variation in $\Delta\delta_N$ for X = Cl, nor for X = Br, except that $\Delta\delta_N$ is noticeably smaller when Y = PF_6^-. The parameter ρ, which is the ratio of r(M^{IV}-X) to r(M^{II}-X), depends on the counterion as well as the other HMMC components, and has traditionally been thought of as a reliable gauge of delocalisation. For a given combination of metal, halogen and ligand, ρ is smaller for the hexafluorophosphate HMMC than it is for Y = ClO_4^- or BF_4^-, which means that it should be the least delocalised. There is therefore no direct correlation between the values $\Delta\delta_N$ and ρ. It is more likely that ρ reflects the physical structure imposed by the counterions, rather than the electronic distribution along the chain.

In examining the influence of the counterion on absolute ^{15}N chemical shift positions, it is simpler to consider the tetrahedral ions on their own at first, because the complexes formed by the octahedral PF_6^- exhibit markedly different behaviour. The δ_N values for all the complexes with Y = ClO_4^- or BF_4^- are shown graphically in Figure 4.3.1. There is a simple relationship between the two sets of compounds, with the peaks in BF_4^- species occurring at *ca.* 1-3 ppm higher field. This means that nitrogen nuclei are better shielded in the fluoroborate complexes than in the perchlorates, which reflects directly the stronger hydrogen bonds formed by the BF_4^- ion.

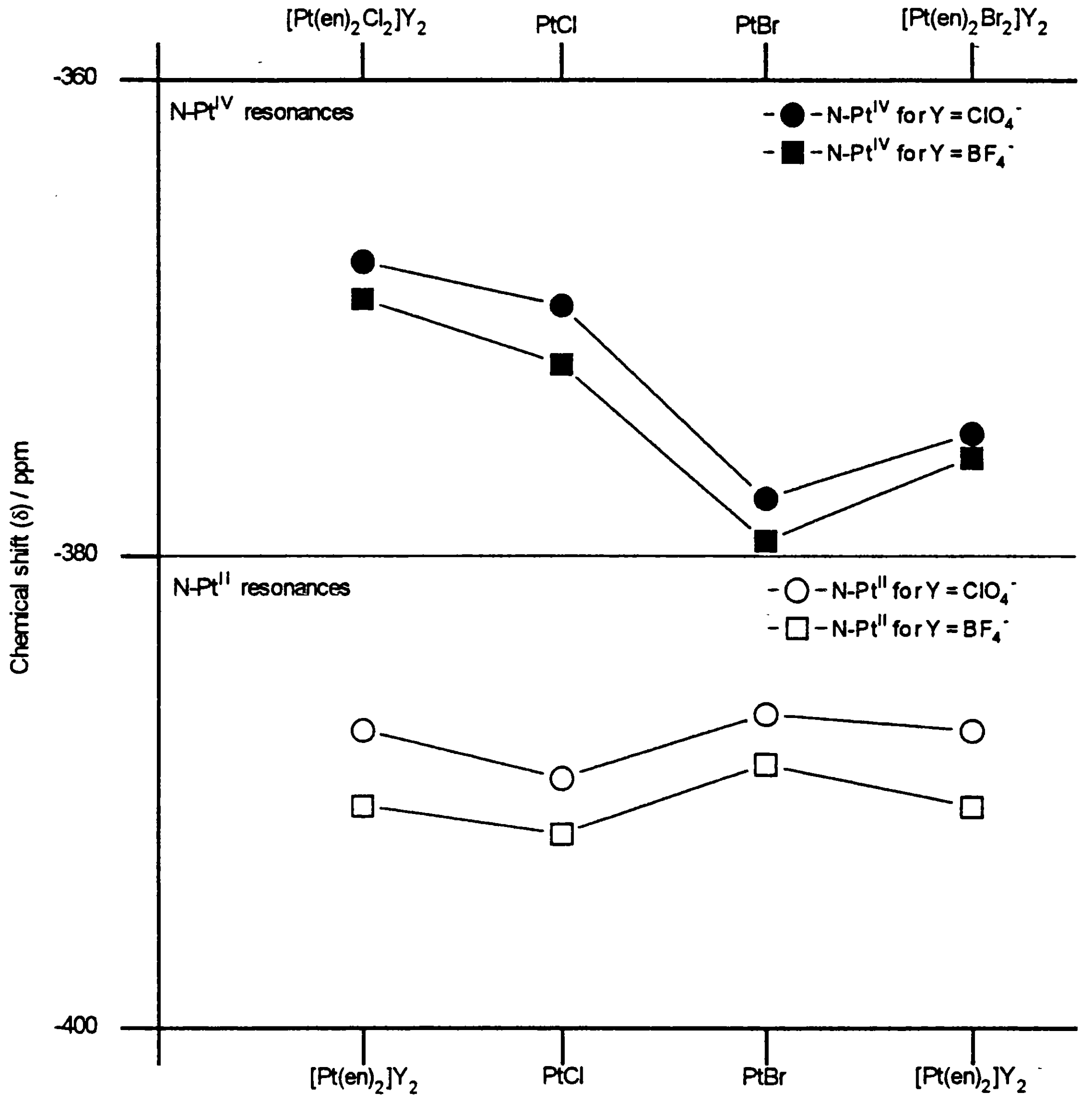

Key	PtCl	$[Pt(en)_2][Pt(en)_2Cl_2]Y_4$
	PtBr	$[Pt(en)_2][Pt(en)_2Br_2]Y_4$
	Y	ClO_4^- or BF_4^-

Figure 4.3.1 *Graph showing the ^{15}N chemical shifts for complexes containing fluoroborate or perchlorate counterions.*

The solid-state ^{15}N NMR spectrum of $[Pt(en)_2][Pt(en)_2Cl_2](PF_6)_4$ contains two main N-Pt^{II} peaks separated by *ca.* 3.5 ppm, which is a larger difference than any change resulting from chain formation. A recent analysis of the crystal structure of $[Pt(en)_2][Pt(en)_2Cl_2](PF_6)_4$ confirms that there are two different types of nitrogen atom attached to the platinum (II) centres.[21] The spectrum of the bromide analogue, $[Pt(en)_2][Pt(en)_2Br_2](PF_6)_4$, cannot be explained so easily. The positions of its peaks relative to those of the chloride do not follow the patterns observed for other HMMCs. The N-Pt^{IV} resonance is in almost the same position, but the solitary N-Pt^{II} signal occurs well downfield. Unfortunately, $[Pt(en)_2Br_2](PF_6)_2$ was not isolated, and the crystal structure of $[Pt(en)_2][Pt(en)_2Br_2](PF_6)_4$ has not been solved, so the significance of these results cannot be established. It is likely that there is a large difference between the structures of the chloride- and bromide-chain complexes.

Changing the bridging halogen might alter the hydrogen-bonds between counterions and ligands, particularly if it results in a different crystal phase. The distortion this causes to the chemical shifts is small enough not to disrupt the trends established in Chapter 3. Therefore the influence of the halogen in cationic HMMCs may be viewed in similar terms to those used for the neutral-chain species. The reduction in the separation of the N-Pt^{II} and N-Pt^{IV} signals that occurs as X is changed from Cl $\rightarrow$ Br $\rightarrow$ I reflects the relative oxidation states of the sites in their monomeric forms. It does not imply that the extent of charge delocalisation is any greater in the linear-chain species.

4.4 Mixed-halide HMMC complexes $[Pt(en)_2][Pt(en)_2X_{2-2\alpha}X'_{2\alpha}](ClO_4)_4$

4.4.1 Introduction

The mixed-halide complexes are written as $[Pt(en)_2][Pt(en)_2X_{2-2\alpha}X'_{2\alpha}](ClO_4)_4$, where X and X' are different halogens. All three combinations of X-X' are known: Cl-Br, Cl-I and Br-I. Mixed-halide HMMCs contain a natural high concentration of charge defects, and can support many more under photolysis, and are therefore of particular interest.[38,54-6] For a time these compounds were believed to be block copolymers, *i.e.* composed of long segments of MX and MX' chains, with few interfaces.[57,58] In this superlattice structure, hole polarons are predicted to be in the MX segments and electron polarons in the MX' segments, where X is more electronegative than X'.[61] Peierls-Hubbard models based on these structures have been used to predict optical absorptions,[250] and Raman and resonance Raman spectra have been interpreted likewise.[57-60] The block copolymer model is not derived from experimental observations, but has probably developed from the false assumption that the halogens in $[Pt(en)_2X_2]^{2+}$ ions are not labile.[90,251] *Trans*-$[Pt(en)_2X_2]^{2+}$ is known to undergo exchange with free halide (X'^-) in solution,[244] at a rate that is first-order with respect to $[Pt^{II}]$, $[Pt^{IV}]$ and $[X'^-]$.[252] Even though the "mixed unit", $[Pt(en)_2ClBr]^{2+}$, has been observed in a solution ^1H NMR analysis of a mixed-halide HMMC, its concentration in the solid is still thought to be small.[38] The only major concession has been that long segments of MX or MX' (greater than ten unit cells) are thought to be rare.[108,111] This study investigates the distribution of halogens throughout a mixed-halide HMMC.

4.4.2 Solid-State ^{15}N NMR spectroscopy

The mixed-halide study was limited to the Cl-Br case, because both spectrometer time and ^{15}N-enriched ligand were in limited supply. The peaks in $[Pt(en)_2][Pt(en)_2I_2](ClO_4)_4$ are not sufficiently resolved to make examination of the Cl-I or Br-I mixed-halide species worthwhile. The mixed-halide HMMCs were prepared by mixing solutions of $[Pt(en)_2][Pt(en)_2Cl_2](ClO_4)_4$ and $[Pt(en)_2][Pt(en)_2Br_2](ClO_4)_4$ in the required proportions and allowing crystals to form. The products have the formula $[Pt(en)_2][Pt(en)_2Cl_{2-2\alpha}Br_{2\alpha}](ClO_4)_4$, which is abbreviated in this text as $PtBr_\alpha$, reflecting the proportion of bromine atoms in the chain. Three reaction mixtures were prepared in which the ratio of $PtBr_{0.0}$ to $PtBr_{1.0}$ was chosen to produce mixed-halide complexes with α = 0.25 (**426a**), 0.5 (**426b**) or 0.75 (**426c**). The crystals isolated were blue, grey or green in colour, respectively. The true α values are estimated from the solid-state ^{15}N NMR spectra (*vide infra*), but are little different to the theoretical ones. Elemental analysis was used only as a means to verify these values, since it is not an accurate method for evaluating the quantities of two halogens within the same system. The phase transition of each complex was followed by Differential Scanning Calorimetry (DSC). The onset temperatures lie in the range 18 - 27 °C, with peaks occurring some 2 °C higher in each case. So that any effect of the phase changes could be identified, solid-state ^{15}N NMR spectra were collected both at room temperature and at 318 K. The spectra shown in Figure 4.4.1 are those recorded at 318 K, since all HMMCs have the same crystal lattice structure at this temperature. Satellite peaks due to ^{15}N-^{195}Pt coupling complicate all of these spectra, but the chemical shifts of the unsplit peaks can still be determined. The position of the main ^{15}N-Pt^{II} resonance appears to vary continuously with proportion of bromide (or chloride) in the chain, but this is misleading. The ^{15}N-Pt^{IV} signals are composed of three main peaks whose relative intensities depend on the Cl : Br ratio, but which are at fixed positions. The chemical shift of the peak at highest or lowest field is similar to that of the N-Pt^{IV} signal for $[Pt(en)_2][Pt(en)_2Cl_2](ClO_4)_4$ or $[Pt(en)_2][Pt(en)_2Br_2](ClO_4)_4$ respectively. The middle peak is at *ca.* -373.5 ppm, and is logically assigned to the "mixed unit", *i.e.*$[Pt^{IV}(en)_2ClBr]$. No more than five peaks are seen in the N-Pt^{IV} region, because all but two of the satellites overlap with the unsplit signals. The separation of satellites and unsplit resonances is related to the size of the applied magnetic field, and so overlaps occur purely by chance. The variation of N-Pt^{II} chemical shift can also be explained in terms of the influence of the nearest pair of chain halogens. The chemical shifts of the units $[Pt^{II}(en)_2Cl_2]$, $[Pt^{II}(en)_2ClBr]$ and $[Pt^{II}(en)_2Br_2]$ are similar to each other, so one large resonance is observed instead of three discrete peaks. The position of the signal changes with the intensities of the three closely spaced peaks, so that its chemical shift is nearest to that of the unit with the greatest population. The chemical shifts of the observed peaks are listed in Table 4.4.1, and are taken from the spectra shown in Figure 4.4.1. Both the main unsplit resonances (U) and the satellites (S) are assigned for the N-Pt^{II} and N-Pt^{IV} regions. The subscripted halogens are the pair nearest to the metal centre.

Table 4.4.1. ^{15}N chemical shifts and probable assignments for the mixed-halide HMMCs $[Pt(en)_2][Pt(en)_2Cl_{2-2\alpha}Br_{2\alpha}](ClO_4)_4$ [a]

Chemical shift / ppm					Peak assignment
$PtBr_{0.0}$	$PtBr_{0.25}$	$PtBr_{0.5}$	$PtBr_{0.75}$	$PtBr_{1.0}$	(S = satellite, U = unsplit peak, X-X' = neighbouring halogens)
419	**426a**	**426b**	**426c**	**420**	
-365.5	-365.5				S^{IV}_{Cl-Cl}
-369.6	-369.2	-369.8	-370.4		U^{IV}_{Cl-Cl}, S^{IV}_{Cl-Br}
-373.7	-373.2	-373.4	-373.9	-373.9	S^{IV}_{Cl-Cl}, U^{IV}_{Cl-Br}, S^{IV}_{Br-Br}
	-376.8	-377.3	-377.6	-377.6	S^{IV}_{Cl-Br}, U^{IV}_{Br-Br}
		-382.3	-381.2	-381.6	S^{IV}_{Br-Br}, S^{II}_{Br-Br}
	-382.8	-383.2	-382.0		S^{II}_{Cl-Br}
-384.4	-384.2				S^{II}_{Cl-Cl}
-389.8	-389.3	-387.9	-387.2	-386.7	U^{II}_{Cl-Cl}, U^{II}_{Cl-Br}, U^{II}_{Br-Br}
			-391.6	-391.5	S^{II}_{Br-Br}
	-392.8	-393.2	-392.5	-392.3	S^{II}_{Cl-Br}
-394.7	-393.8				S^{II}_{Cl-Cl}

[a] *Chemical shift positions are accurate to ± 0.4 ppm.*

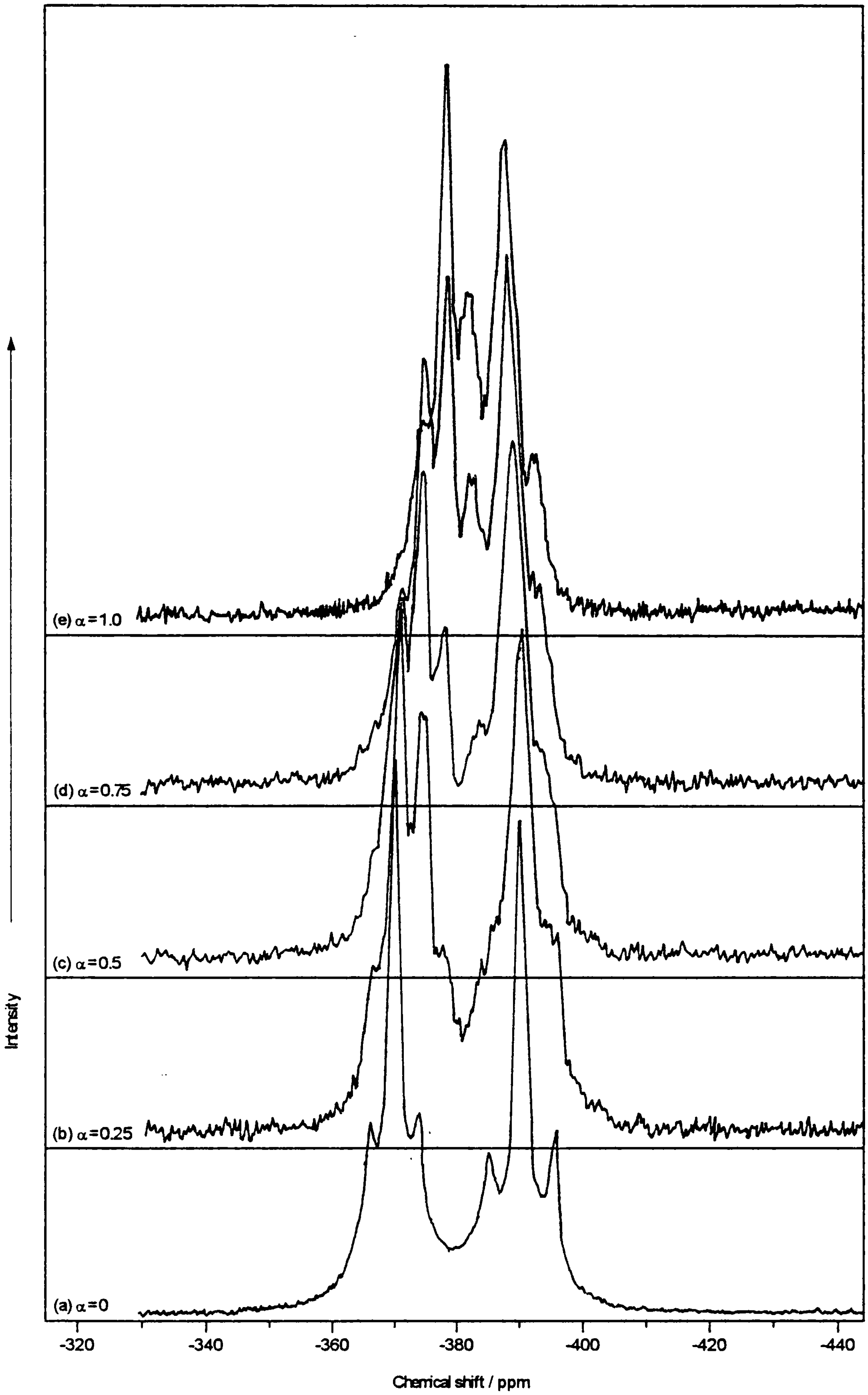

Figure 4.4.1 *Solid-state ^{15}N NMR spectra of the HMMCs [Pt(en)$_2$][Pt(en)$_2$Cl$_{2-2\alpha}$Br$_{2\alpha}$](ClO$_4$)$_4$, where (a) α = 0, (b) α = 0.25, (c) α = 0.5, (d) α = 0.75 or (e) α = 1.0.*

The solid-state ^{15}N NMR spectra may be used to determine the ratio of chlorine to bromine in each mixed-halide chain. All five of the spectra in Figure 4.4.1 can be reproduced very closely with plots constructed from only eight peaks. Five peaks of fixed chemical shifts are used to represent the N-Pt^{IV} resonances: three main signals (which contain some overlapped satellite intensity) and two *J*-coupling satellites. Three peaks are combined to produce the N-Pt^{II} signal; their positions vary because individual components due to each unit type are not modelled. The cross-polarisation rates for all types of ^{15}N site are expected to be nearly equal, which means that signal intensity should be directly proportional to the number of ^{15}N nuclei present. This is crucial, since it allows the relative populations of the three kinds of unit to be determined by calculating the areas under the peaks in the model spectra. The amount of chain bromine deduced from the solid-state NMR results are shown in Table 4.4.2, alongside the values found from elemental analyses. An example of a modelled spectrum is given in Figure 4.4.2 where the plot constructed for $[Pt(en)_2][Pt(en)_2Cl_{1.0}Br_{1.0}](ClO_4)_4$ is shown.

Table 4.4.2 Calculated populations of Pt^{IV} units in mixed-halide complexes

Mixed-halide complex	Label	Percentages of Pt^{IV} subunits (calc.).			% of bromine found in chain	
		Cl-Pt^{IV}-Cl	Cl-Pt^{IV}-Br	Br-Pt^{IV}-Br	Solid-state NMR [a]	Elemental analysis
$PtBr_{0.0}$	**419**	100			0	1
$PtBr_{0.25}$	**426a**	59	31	10	26.5	27
$PtBr_{0.5}$	**426b**	26	40	33	53	50
$PtBr_{0.75}$	**426c**	8	30	62	77	74
$PtBr_{1.0}$	**420**			100	100	99

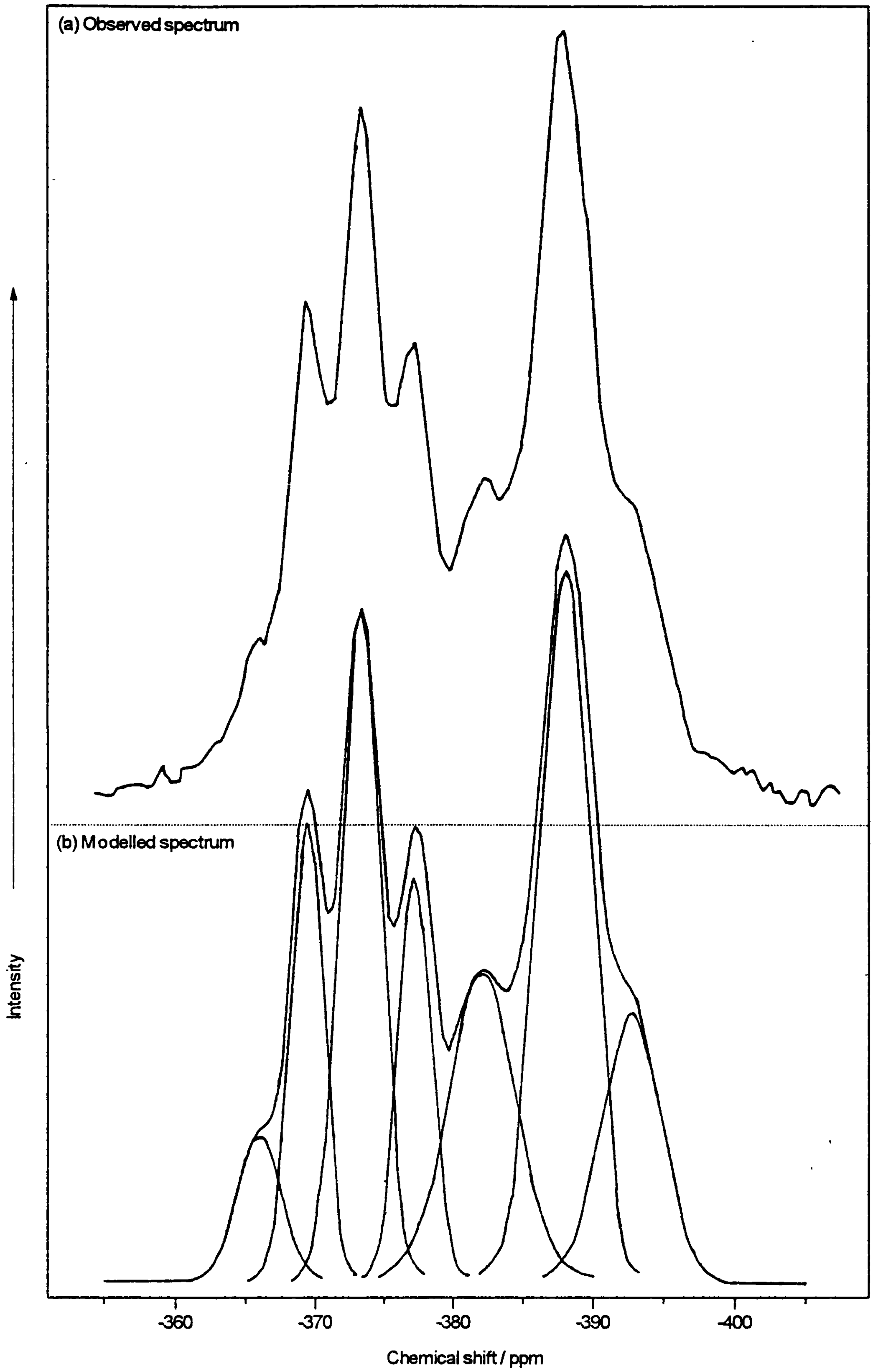

Figure 4.4.2 *Comparison between the modelled and observed spectra of the mixed-halide complex [Pt(en)$_2$][Pt(en)$_2$Cl$_{1.0}$Br$_{1.0}$](ClO$_4$)$_4$.*

4.4.3 Resonance Raman studies

Raman spectra were recorded for all five of the samples that were analysed by solid-state ^{15}N NMR spectroscopy. The mixed-halide species have many vibrational modes, each with its own excitation profile, so for any given excitation line there might be one or more peaks in resonance. All the spectra in this chapter are termed Raman for simplicity, although there is usually at least some part of each spectrum in resonance. Individual peaks may be identified as being resonant as the need arises. Samples taken from HMMC material prior to its analysis by solid-state ^{15}N NMR spectroscopy were examined both as pressed discs and as single-crystals. The mixed-halide HMMCs were not recrystallised since this would have altered the composition of the crystals and invalidated the study. The single-crystal spectra are better resolved than the disc spectra as expected, but they also differ in other ways. The spectra of single crystals have fewer, weaker overtone or combination modes for a given excitation energy, and contain a smaller number of charge defect modes. The single-crystal and disc spectra of $[Pt(en)_2][Pt(en)_2Cl_2](ClO_4)_4$ collected at three excitation lines are compared in Figure 4.4.3 as an example. The most significant difference is at excitation energies well below that of the P-edge. The ν_1 mode should not be in resonance at 568 nm or 647 nm. In the single-crystal spectra the first overtone is very weak, which is typical of a simple Raman combination mode. But in the disc spectra there are several overtones, with the first being very strong, and the ν_1 mode is accompanied by a strong signal at *ca.* 288 cm^{-1}, which corresponds to an electronic defect. In addition, the wavenumber and dispersion of the ν_1 mode depend on whether the sample is analysed as a single-crystal or a pressed disc. The results are consistent with the P-edge energy in the disc samples being smaller than in the crystals. This could be due to grinding or compression, which occurs during disc formation, that fractures the chains in the sample. For this reason the spectra of the pressed discs are ignored, so only the data from the single-crystal studies are reported.

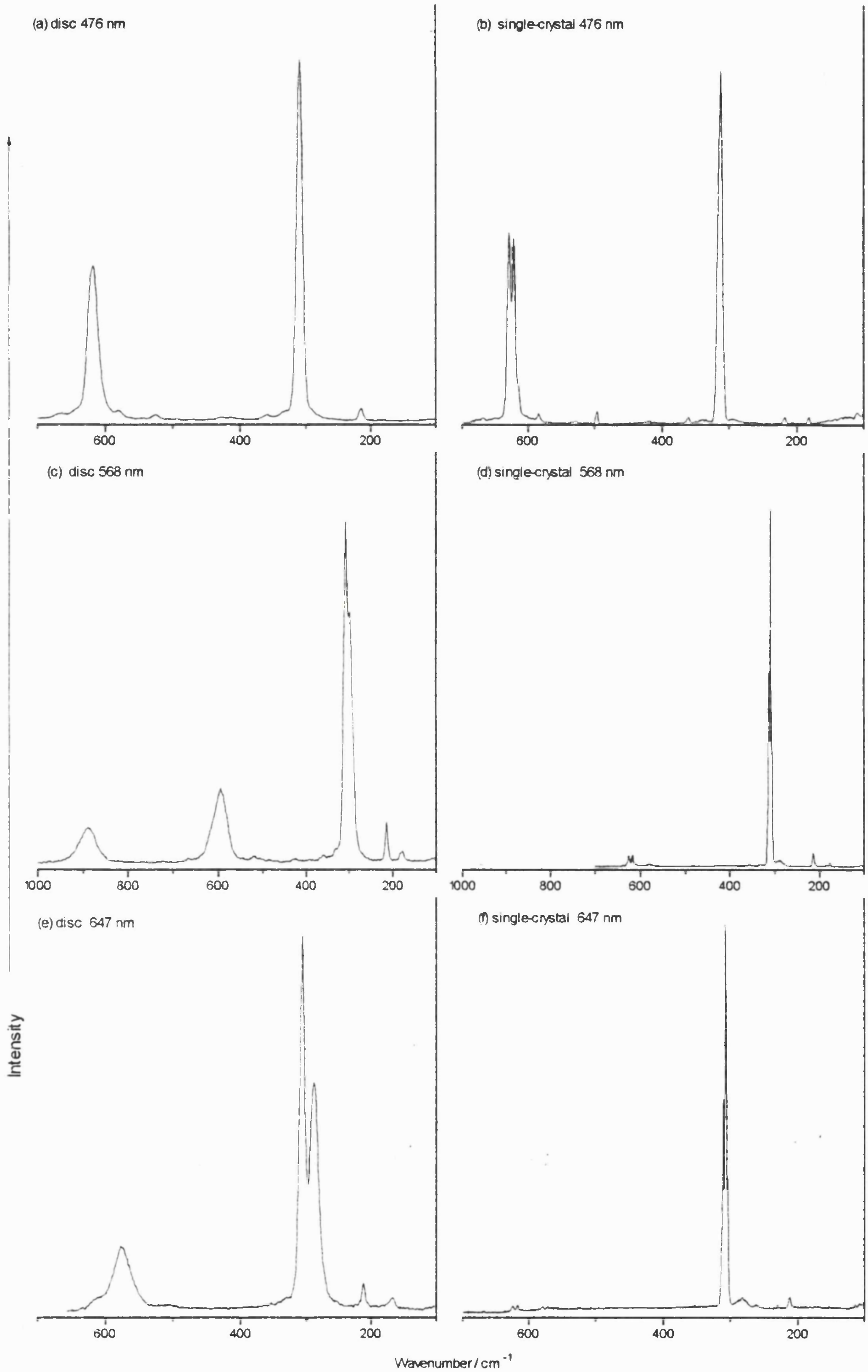

Figure 4.4.3 *Comparison between the spectra of $[Pt(en)_2][Pt(en)_2Cl_2](ClO_4)_4$ examined as a compressed disc (left) and as a single-crystal (right).*

The Raman spectra of $[Pt(en)_2][Pt(en)_2Cl_2](ClO_4)_4$ have been reported several times, but it is still worth emphasising certain points. The structure of the ν_1 mode has aroused much interest in the past, and it is supposed to vary considerably with excitation line.[99] It can be resolved more easily than the ν_1 signal in $[Pt(en)Cl_2][Pt(en)Cl_4]$ because the cationic chains lack the equatorial modes that appear at *ca.* 320 cm^{-1} in the neutral species. The ν_1 profile at five different incident wavelengths is shown in Figure 4.4.4. The structure of the signal does not vary much even over a large range of excitation energies (15000 - 24500 cm^{-1}), although the peaks are less well resolved at shorter wavelengths. In the chain length correlation model for dispersion, the shorter segments will be more enhanced at higher excitation energies.[96,253] In this case the isotopic pattern should be closer to the 9 : 6 : 1 found in Pt^{IV} complexes, but this is not observed. The spectra show that dispersion in $[Pt(en)_2][Pt(en)_2Cl_2](ClO_4)_4$ is much greater than had previously been suggested.[95] At 407 nm excitation, the main component of the ν_1 band is at *ca.* 320 cm^{-1}, which is 11 cm^{-1} higher than at 568 nm.

The single-crystal spectra of $[Pt(en)_2][Pt(en)_2Cl_{2-2\alpha}Br_{2\alpha}](ClO_4)_4$ (α = 0, 0.25, 0.5, 0.75 or 1.0) are shown in Figures 4.4.5 - 9. Peak positions and assignments are listed in Tables 4.4.3 - 7, where certain abbreviations are employed. ν_{1x} and ν_{2x} denote the symmetric and asymmetric chain stretches for the units [Cl-Pt^{IV}-Cl] (x = c), [Br-Pt^{IV}-Br] (x = b) or [Cl-Pt^{IV}-Br] (x = m). The terms ν_{dx} represent defect stretching modes for the same segments, while ν_T is a general expression for terminal vibrations. Only signals occurring at less than 450 cm^{-1} are detailed for the mixed-halide species because the peaks at higher energy are usually broad and noisy and are overtone or combination modes that are difficult to assign with certainty. Even at low wavenumber there are complications due to combination modes. For instance in the spectra of $PtBr_{50}$ (**426b**) the signals due to ν_{2m} and (ν_{1b} + ν_{db}) overlap. The latter dominates at 647 nm excitation, but both have significant intensity at shorter wavelengths. The main purpose of this work is to determine the distribution of halogens in a mixed-halide chain, and this is best done by considering the variation in the fundamental chain modes. Some very small peaks that appear rarely have not been assigned, nor have some background signals that are observed in some complexes at less than 150 cm^{-1}.

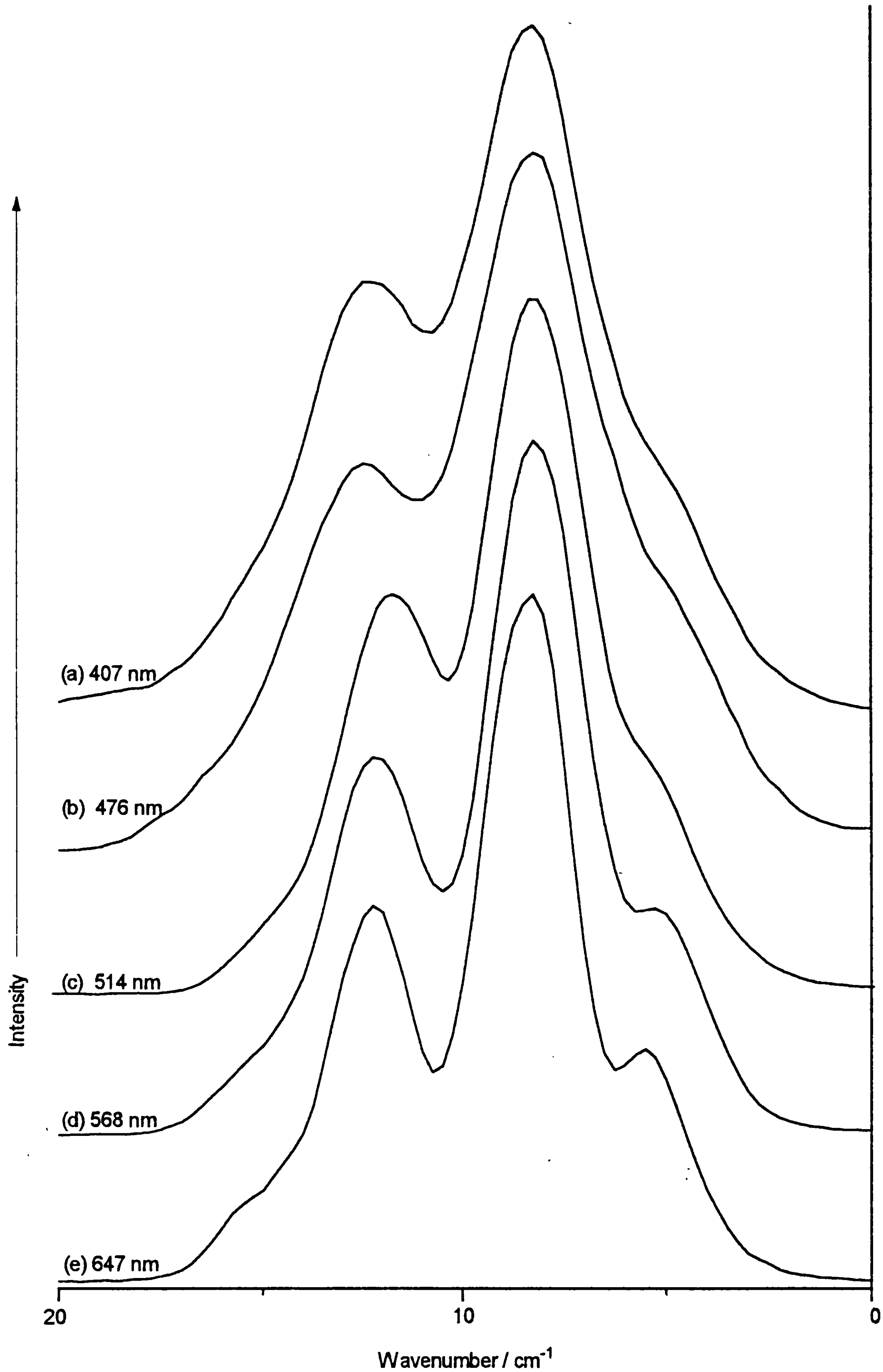

Figure 4.4.4 *The influence of the excitation line on the profile of the ν_1 mode in the single-crystal spectra of $[Pt(en)_2][Pt(en)_2Cl_2](ClO_4)_4$. The ν_1 profiles are shown over a 20 cm^{-1} window, and are calibrated so that the largest peak in each spectrum appears at the same wavenumber.*

The spectra of the single-halide complexes $[Pt(en)_2][Pt(en)_2X_2](ClO_4)_4$ (X = Cl or Br) are similar to those of the neutral complexes $[Pt(en)X_2][Pt(en)X_4]$. Each exhibits a strong ν_1 mode, a weak ν_2 signal and a small peak at *ca.* 210 cm^{-1}, which is assigned to the $\delta(PtN_2)$ bending mode or to a ν_T type vibration. The spectra of the chloride-chain show weak signals at *ca.* 180 cm^{-1} that may result from the ν_{3c} vibration, a terminal mode or even an out-of-chain PtX_2 bending motion. Defect modes are observed at *ca.* 20 cm^{-1} below the lowest energy part of the ν_{1c} signal. Unlike $[Pt(en)Cl_2][Pt(en)Cl_4]$, the spectra of $[Pt(en)_2][Pt(en)_2Cl_2](ClO_4)_4$ have no intensity due to equatorial ν(PtCl) modes in the ν_{1c} region, and so it is easier to gauge the effect on ν_{1c} of increasing the chain bromine content. The mixing of chain halogens has three consequences; the position and structure of the fundamental modes in $PtBr_{0.0}$ or $PtBr_{1.0}$ and altered, defect signals are enhanced, and new vibrational modes that involve the mixed-unit [Cl-Pt^{IV}-Br] are observed. Neither ν_{2c} nor ν_{2b} has enough Raman activity to be seen in the mixed-halide complexes; ν_{2c} occurs at roughly the same wavenumber as the intense $2\nu_{1b}$. ν_{1c} and ν_{1b} are observed in $PtBr_{0.25}$, $PtBr_{0.5}$ and $PtBr_{0.75}$ but they appear at higher energies than in the respective $[Pt(en)_2][Pt(en)_2X_2](ClO_4)_4$. This is because the segments of each unit type are much shorter, and the vibrations are more localised and higher in energy. For ν_{1c}, this means that the isotopic pattern tends towards the 9 : 6 : 1 spread predicted for wholly decoupled vibrations. The defect modes are probably all at their strongest when Cl and Br are in equal proportions in the chain, *i.e.* in $[Pt(en)_2][Pt(en)_2Cl_{1.0}Br_{1.0}](ClO_4)_4$. Defect signals are identified at *ca.* 20 cm^{-1} below the lowest energy peak in ν_{1c}, and at *ca.* 10 cm^{-1} below ν_{1b}. The wavenumber of ν_{dc} corresponds to that of the hole polaron in PtCl,[102] ν_{db} to that of the electron polaron in PtBr.[105] There are probably other defects, such as on the [Cl-Pt^{IV}-Br] unit, but they are not clearly resolved. In particular the structure of ν_{2m} is more complicated than is expected for the asymmetric stretch of the mixed-halide unit. The dispersion of ν_{1m} or ν_{2m} is much the same in each of $PtBr_{0.25}$, $PtBr_{0.5}$ and $PtBr_{0.75}$, and so each mode is probably highly localised. ν_{1m} and ν_{2m} are enhanced by excitation energies between those that enhance ν_{1c} and ν_{1b}.

Table 4.4.3 Wavenumbers / cm^{-1}, relative intensities and assignments for the bands in the Raman spectra of $[Pt(en)_2][Pt(en)_2Cl_2](ClO_4)_4$ [a]

407 nm	476 nm	514 nm	568 nm	647 nm	Assignment
	182.0 $^{0.01}$	179.5 $^{0.01}$	177.0 ^{wk}		ν_{3c}, ν_T or bend
			183.5 ^{wk}		ν_{3c}, ν_T or bend
226.0 ^{wk}	218.0 $^{0.01}$	217.5 $^{0.02}$	214.5 $^{0.02}$	211.5 $^{0.02}$	$\delta(PtN_2)$ or ν_T
301.5 ^{wk}		292.5 $^{0.02}$	288.5 $^{0.01}$	281.5 ^{wk}	ν_{dc}
317.0 $^{0.07}$	310.0 $^{0.05}$	310.0 $^{0.03}$	305.0 $^{0.10}$	304.0 $^{0.14}$	ν_{1c}
320.5 $^{0.63}$	313.5 $^{0.76}$	312.0 $^{0.65}$	309.0 $^{0.67}$	307.0 $^{0.58}$	ν_{1c}
324.5 $^{0.30}$	317.5 $^{0.19}$	315.5 $^{0.32}$	313.0 $^{0.23}$	311.0 $^{0.28}$	ν_{1c}
345.0 ^{wk}			329.5 ^{wk}		ν_a
368.5 $^{0.01}$	361.0 $^{0.01}$	358.0 $^{0.01}$	356.5 $^{0.01}$	353.0 ^{wk}	ν_{2c}
	496.0 $^{0.02}$	487.0 $^{0.02}$			
590.5 $^{0.02}$	584.0 $^{0.02}$	583.0 $^{0.02}$	581.0 $^{0.01}$	579.0 $^{0.01}$	ν(Pt-N)
	614.5 $^{0.36}$	614.5 $^{0.06}$	611.5 ^{wk}	610.0 ^{wk}	$2\nu_{1c}$
630.5 $^{0.30}$	621.0 $^{0.34}$	619.5 $^{0.06}$	617.5 $^{0.02}$	617.0 $^{0.02}$	$2\nu_{1c}$
636.5 $^{0.45}$	627.0 $^{0.05}$	626.5 $^{0.02}$	625.0 $^{0.02}$	624.0 $^{0.02}$	$2\nu_{1c}$

Table 4.4.4 Wavenumbers / cm^{-1}, relative intensities and assignments for the bands in the Raman spectra of 426a [a]

407 nm	476 nm	514 nm	568 nm	647 nm	Assignment
		165.0 ^{wk}	161.0 $^{0.06}$	154.0 $^{0.73}$	ν_{db}
		180.0 $^{0.06}$	177.5 $^{0.20}$	172.0 $^{4.17}$	ν_{1b}
189.0 ^{wk}	187.5 $^{0.09}$	186.0 $^{0.68}$	182.0 $^{1.23}$	177.5 $^{1.88}$	ν_{1b}
227.0 $^{0.07}$	218.5 $^{0.74}$	214.0 $^{1.61}$	210.0 $^{1.38}$	206.5 $^{2.33}$	ν_{1m}
			223.0 ^{wk}	219.0 ^{wk}	
		242.0 ^{wk}	238.5 ^{wk}	236.0 ^{wk}	ν_{2b}
		282.5 ^{wk}			
300.5 $^{0.01}$	293.0 $^{0.10}$	292.0 $^{0.25}$	287.5 $^{0.01}$	285.0 $^{0.32}$	ν_{dc}
321.5 $^{0.66}$	313.0 $^{0.55}$	312.5 $^{0.50}$	309.0 $^{0.66}$	307.0 $^{0.66}$	ν_{1c}
325.0 $^{0.34}$	316.0 $^{0.45}$	315.0 $^{0.50}$	312.0 $^{0.34}$	310.0 $^{0.34}$	ν_{1c}
			322.0 $^{0.04}$	317.5 $^{0.12}$	ν_{2m}
	331.5 $^{0.11}$	328.5 $^{0.32}$	325.0 $^{0.25}$	321.5 $^{0.31}$	ν_{2m}
343.0 $^{0.01}$	337.5 $^{0.06}$	335.0 $^{0.10}$	332.5 $^{0.07}$	330.5 $^{0.12}$	ν_a
	360.0 $^{0.01}$	357.5 $^{0.03}$	353.0 $^{0.23}$	347.0 $^{1.49}$	$2\nu_{1b}$
367.5 $^{0.01}$	370.0 $^{0.02}$	369.0 $^{0.17}$	362.5 $^{0.57}$	357.0 $^{0.49}$	$2\nu_{1b}$
	399.0 ^{wk}	397.0 $^{0.13}$	391.5 $^{0.49}$	386.5 $^{0.43}$	$(\nu_{1b} + \nu_{1m})$
434.0 $^{0.04}$	430.0 $^{0.16}$	423.5 $^{0.45}$	418.0 $^{0.50}$	415.0 $^{0.18}$	$2\nu_{1m}$

Table 4.4.5 **Wavenumbers / cm^{-1}, relative intensities and assignments for the bands in the Raman spectra of 426b [a]**

407 nm	476 nm	514 nm	568 nm	647 nm	Assignment
		139.0 $^{0.02}$			
			158.0 $^{0.03}$	153.0 $^{0.36}$	ν_{db}
			177.0 $^{1.31}$	168.5 $^{5.75}$	ν_{1b}
195.5 $^{0.08}$	187.5 $^{0.27}$	183.5 $^{0.44}$	181.5 $^{1.31}$	176.5 $^{0.81}$	ν_{1b}
226.5 $^{1.00}$	216.5 $^{1.00}$	211.0 $^{1.00}$	210.0 $^{1.00}$	206.5 $^{1.00}$	ν_{1m}
			241.5 $^{0.01}$	230.5 ^{wk}	ν_{2b}
278.0 ^{wk}			274.5 $^{0.01}$		
299.0 $^{0.08}$	292.0 $^{0.13}$	290.5 $^{0.12}$	289.5 $^{0.12}$	286.0 $^{0.09}$	ν_{dc}
322.5 $^{2.80}$	314.5 $^{0.35}$	312.5 $^{0.18}$	309.0 $^{0.21}$	307.0 $^{0.21}$	ν_{1c}
325.5 $^{1.40}$	317.5 $^{0.28}$	315.0 $^{0.19}$			ν_{1c}
			321.0 $^{0.07}$	317.5 $^{0.07}$	ν_{2m}
				321.0 $^{0.39}$	$(\nu_{db} + \nu_{1b})$
	330.0 $^{0.15}$	326.5 $^{0.20}$	325.0 $^{0.14}$		ν_{2m}
343.0 $^{0.35}$	336.0 $^{0.10}$	333.0 $^{0.07}$	332.5 $^{0.05}$		ν_a
			344.5 $^{0.21}$		$2\nu_{1b}$
		357.0 $^{0.02}$	351.0 $^{0.60}$	339.0 $^{1.82}$	$2\nu_{1b}$
367.0 $^{0.03}$	370.5 $^{0.04}$	365.0 $^{0.09}$	360.0 $^{0.33}$	345.0 $^{0.30}$	$2\nu_{1b}$
			385.5 $^{0.17}$	381.5 $^{0.04}$	$(\nu_{1b} + \nu_{1m})$
	398.0 $^{0.08}$	395.0 $^{0.08}$	390.5 $^{0.30}$	387.0 $^{0.03}$	$(\nu_{1b} + \nu_{1m})$
439.5 $^{0.12}$	427.0 $^{0.29}$	421.5 $^{0.31}$	419.0 $^{0.14}$	413.0 ^{wk}	$2\nu_{1m}$

Table 4.4.6 Wavenumbers / cm^{-1}, relative intensities and assignments for the bands in the Raman spectra of 426c [a]

407 nm	476 nm	514 nm	568 nm	647 nm	Assignment
			156.5^{wk}	$153.0^{0.05}$	ν_{db}
	$177.0^{0.18}$	$179.0^{0.21}$	$176.0^{0.30}$	$166.0^{1.00}$	ν_{1b}
$194.0^{1.00}$	$186.5^{0.82}$	$184.5^{0.79}$	$180.5^{0.70}$		ν_{1b}
$226.0^{2.07}$	$214.5^{2.49}$	$212.5^{1.23}$	$209.5^{0.21}$	$206.0^{0.07}$	ν_{1m}
$252.0^{0.02}$	$244.0^{0.01}$	$241.0^{0.01}$	$237.0^{0.01}$		ν_{2b}
	$262.5^{0.01}$				
		282.0^{wk}	$273.5^{0.01}$		
$299.5^{0.53}$	$293.0^{0.15}$	$291.0^{0.15}$	$288.5^{0.03}$	$286.0^{0.02}$	ν_{d1c}
$323.5^{4.48}$	$314.0^{0.41}$	$313.0^{0.22}$	$309.5^{0.01}$		ν_{1c}
	$316.0^{0.41}$				ν_{1c}
$334.5^{0.27}$	$330.0^{0.18}$	$327.0^{0.19}$	$319.0^{0.14}$		ν_{2m}
$342.5^{0.14}$	$336.0^{0.08}$	$334.0^{0.05}$	$323.5^{0.08}$	$321.5^{0.04}$	ν_a
			$345.5^{0.23}$		$2\nu_{1b}$
		$353.0^{0.05}$	$349.5^{0.28}$		$2\nu_{1b}$
	$368.0^{0.22}$	$365.0^{0.19}$	$356.5^{0.12}$	$336.0^{0.61}$	$2\nu_{1b}$
			$385.0^{0.07}$		$(\nu_{1b} + \nu_{1m})$
$400.0^{0.21}$	$395.0^{0.32}$	$393.5^{0.21}$	$390.0^{0.06}$	$381.5^{0.07}$	$(\nu_{1b} + \nu_{1m})$
$435.5^{0.32}$	$424.5^{0.53}$	$421.0^{0.22}$	$419.0^{0.02}$		$2\nu_{1m}$

Table 4.4.7 Wavenumbers / cm^{-1}, relative intensities and assignments for the bands in the Raman spectra of $[Pt(en)_2][Pt(en)_2Br_2](ClO_4)_4$ [a]

407 nm	476 nm	514 nm	568 nm	647 nm	Assignment
	$174.0^{0.35}$	$173.0^{0.69}$	$168.5^{0.69}$	$164.0^{1.00}$	ν_{1b}
	$182.0^{0.47}$	$179.5^{0.31}$	$172.0^{0.31}$		ν_{1b}
	$186.0^{0.18}$				ν_{1b}
no	$215.5^{0.14}$	$214.5^{0.05}$	$209.5^{0.03}$	207.0^{wk}	$\delta(PtN_2)$ or ν_T
peaks	$244.0^{0.03}$	$242.5^{0.02}$		$229.5^{0.01}$	ν_{2b}
observed	$262.5^{0.03}$				
	$281.0^{0.02}$				
	$348.5^{0.27}$	$341.0^{0.19}$			$2\nu_{1b}$
	$358.5^{0.29}$	$352.0^{0.30}$	$344.5^{0.30}$	$333.0^{0.50}$	$2\nu_{1b}$

[a] *the figures in bold type are the intensities (wk = < 0.01) corrected for spectral response and are relative to ν_{1c} ($PtBr_{0.0}$ and $PtBr_{0.25}$), ν_{1m} ($PtBr_{0.5}$) or ν_{1b} ($PtBr_{0.75}$ and $PtBr_{1.0}$).*

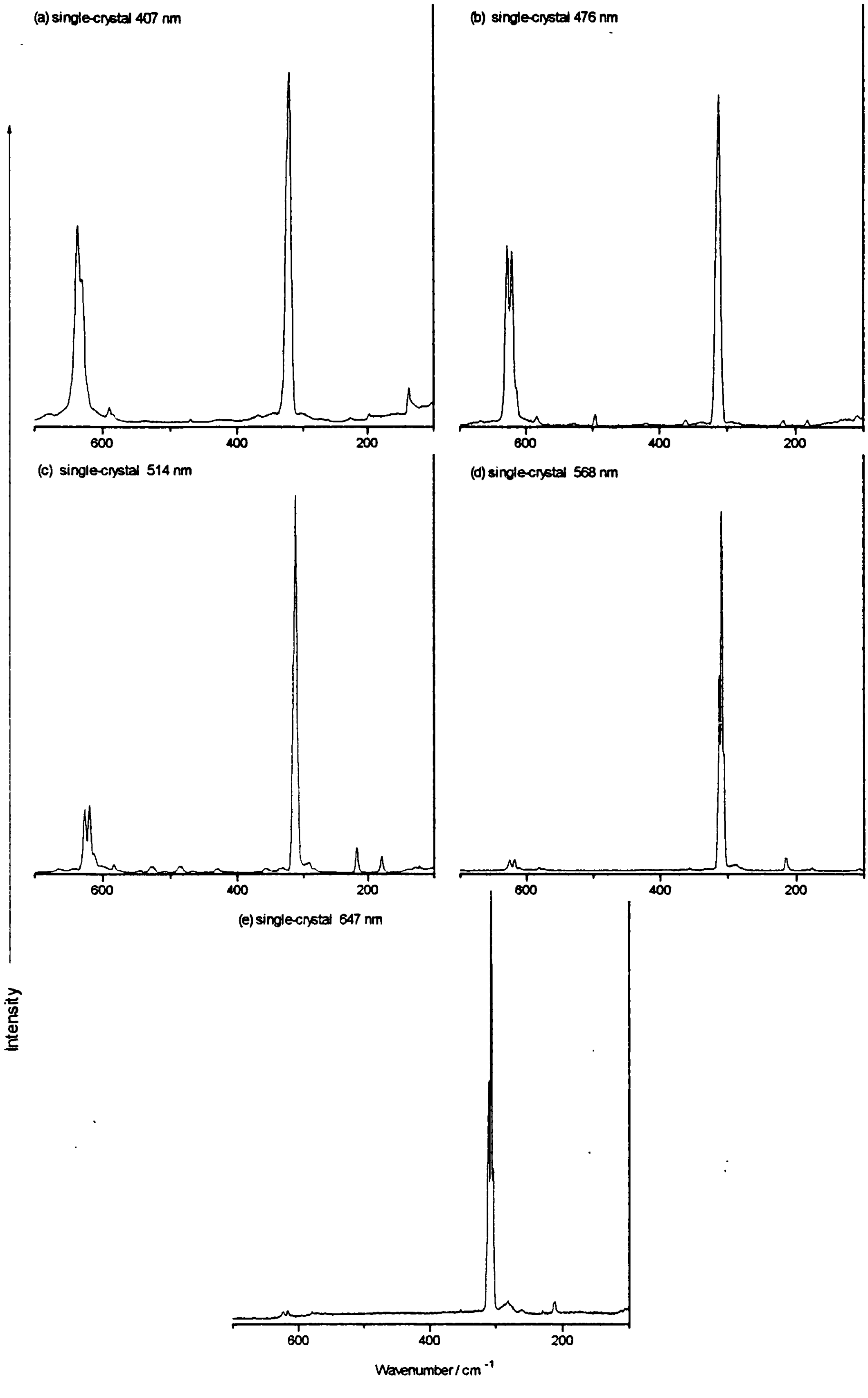

Figure 4.4.5 *Raman spectra of* $[Pt(en)_2][Pt(en)_2Cl_2](ClO_4)_4$ *recorded at excitation wavelengths of (a) 407 nm, (b) 476 nm, (c) 514 nm, (d) 568 nm and (e) 647 nm.*

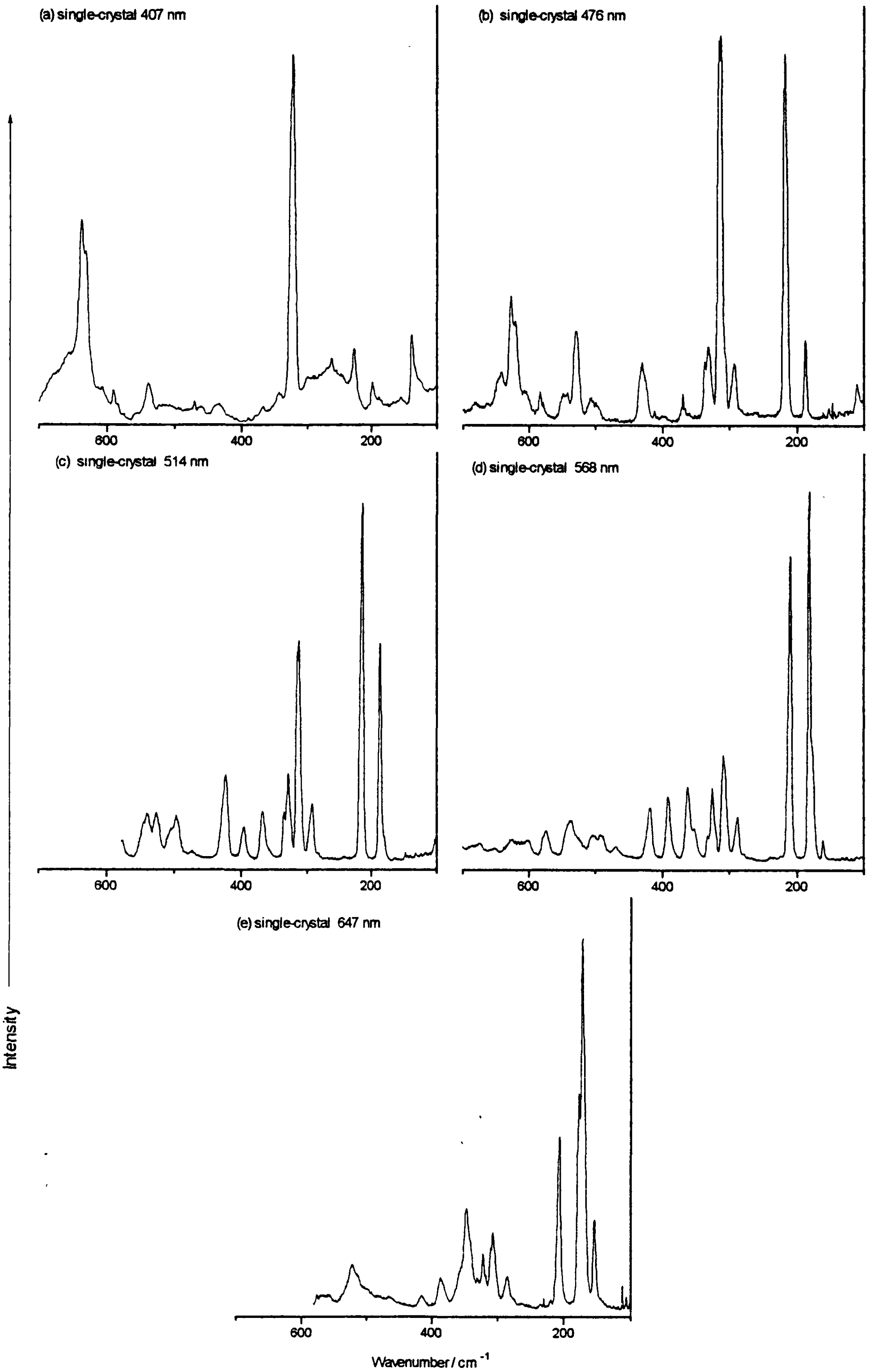

Figure 4.4.6 Raman spectra of $[Pt(en)_2][Pt(en)_2Cl_{1.5}Br_{0.5}](ClO_4)_4$ recorded at excitation wavelengths of (a) 407 nm, (b) 476 nm, (c) 514 nm, (d) 568 nm and (e) 647 nm.

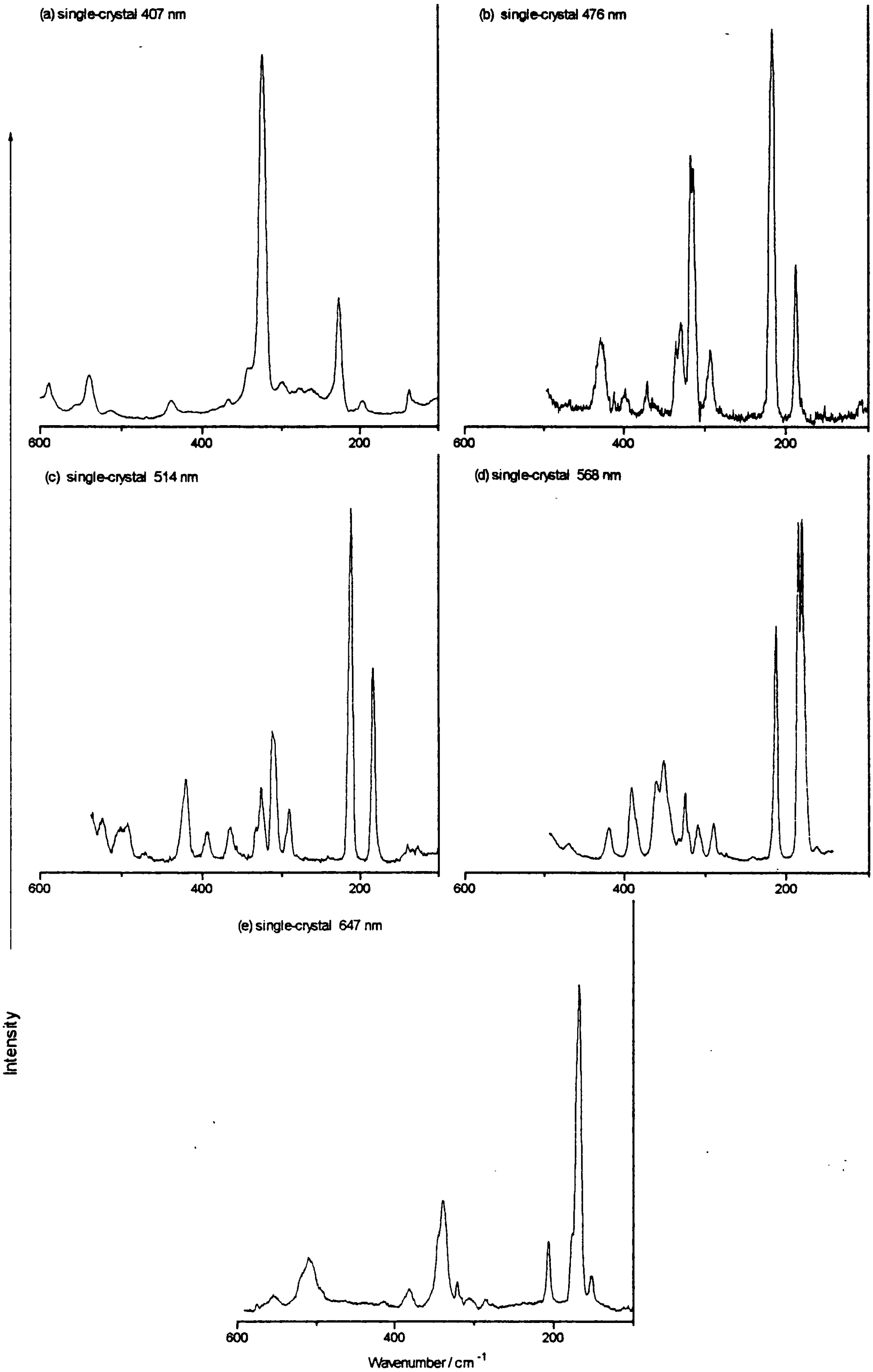

Figure 4.4.7 *Raman spectra of $[Pt(en)_2][Pt(en)_2Cl_{1.0}Br_{1.0}](ClO_4)_4$ recorded at excitation wavelengths of (a) 407 nm, (b) 476 nm, (c) 514 nm, (d) 568 nm and (e) 647 nm.*

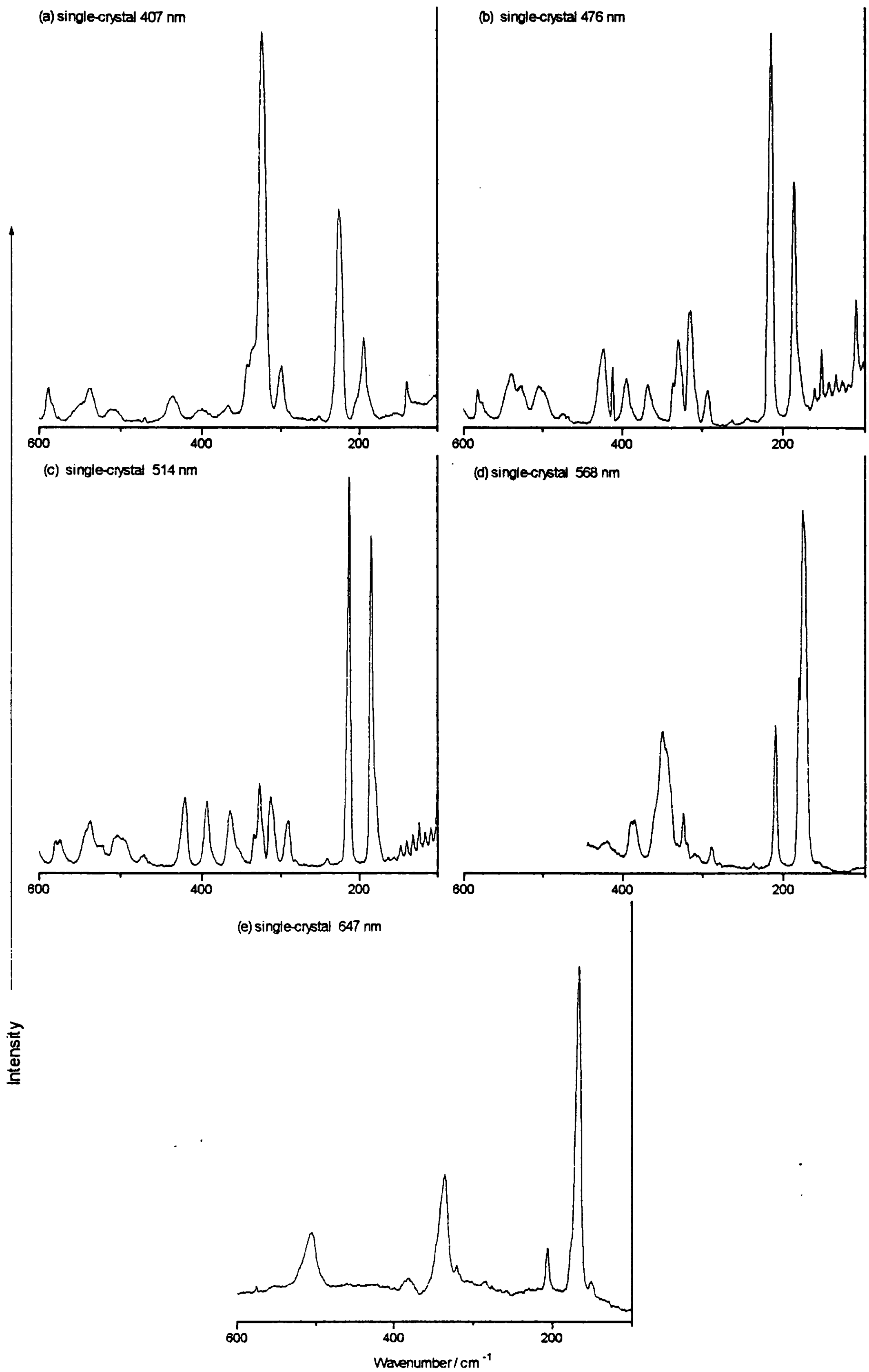

Figure 4.4.8 *Raman spectra of $[Pt(en)_2][Pt(en)_2Cl_{0.5}Br_{1.5}](ClO_4)_4$ recorded at excitation wavelengths of (a) 407 nm, (b) 476 nm, (c) 514 nm, (d) 568 nm and (e) 647 nm.*

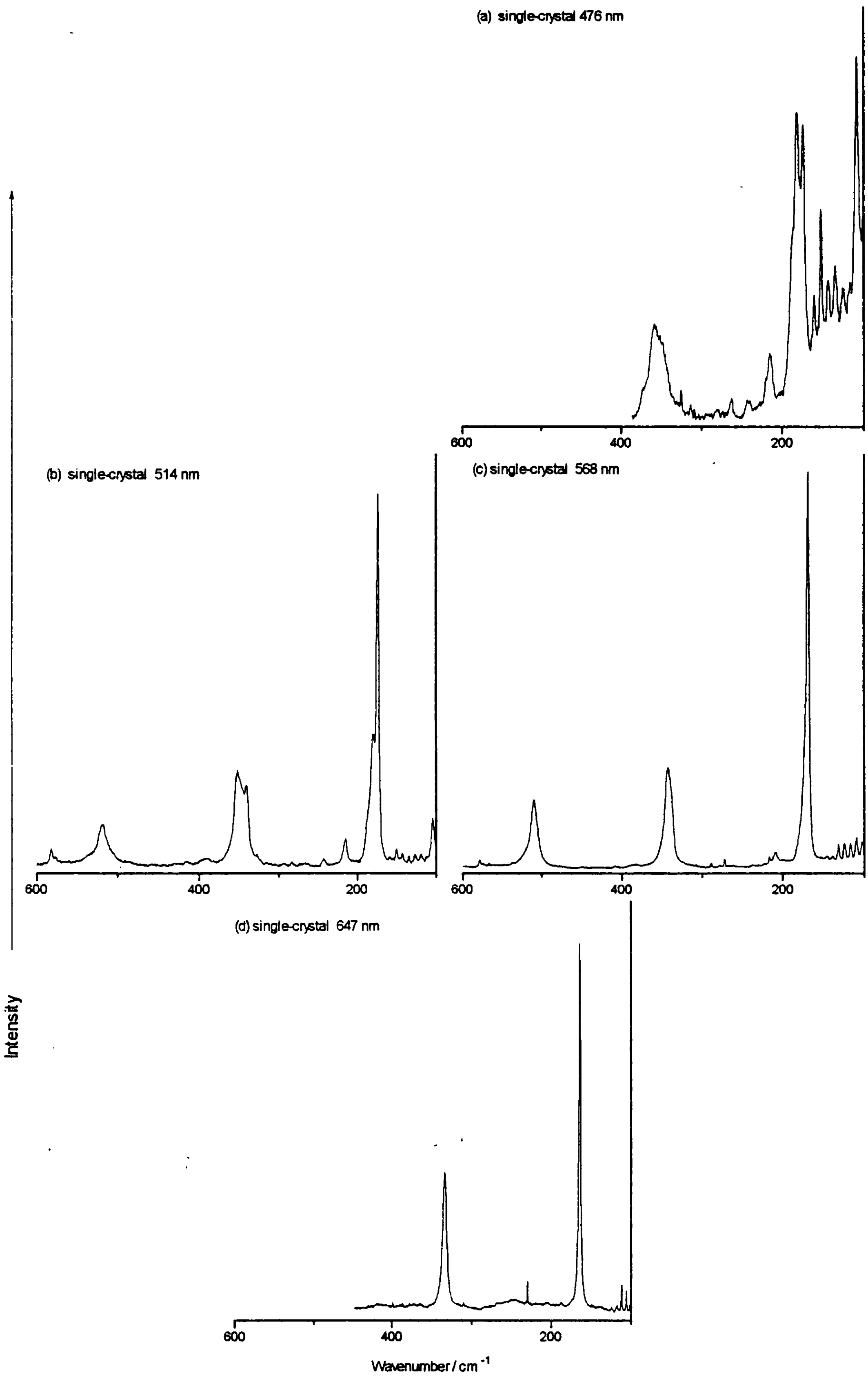

Figure 4.4.9 *Raman spectra of [Pt(en)$_2$][Pt(en)$_2$Br$_2$](ClO$_4$)$_4$ recorded at excitation wavelengths of (a) 476 nm, (b) 514 nm, (c) 568 nm and (d) 647 nm. The spectrum at 407 nm excitation is omitted as it contains no Raman signals of note.*

4.4.4 Fourier Transform infrared studies

The infrared spectra should provide information that is complementary to the Raman data, but so many of the ligand or counterion modes have significant intensity that it is difficult to assign chain vibrations unambiguously. The species $PtBr_\alpha$ were analysed as pressed polythene discs, not as single crystals; the physical state of the sample is not thought to be significant,[112] presumably because the infrared active modes are very localised. The spectra are shown in Figure 4.4.10 and peak positions and rough assignments for the range 100-400 cm^{-1} are given in Table 4.4.8. The peaks are not as well resolved as the signals seen in the Raman spectra, mainly because the FT-IR spectra were recorded at room temperature, whereas the Raman spectra were collected at liquid nitrogen temperature. This means that the wavenumbers of peaks that appear in both types of spectra may not match exactly. The FT-IR spectra contain intense ν_2 modes. ν_{2c} is coincident with a ligand mode, so its position cannot be determined exactly, but ν_{2b} is more clearly defined. Neither ν_{2b} nor ν_{1m} has any intensity in $PtBr_{0.0}$. The peak at 165.1 cm^{-1} in $PtBr_{0.0}$ has been assigned to a bending mode, or to the ν_{3c} stretch.[112] The ν_{2m} signals are hidden by ring bending modes.

Table 4.4.8 Wavenumbers / cm^{-1}, intensities and assignments for bands in the FTIR spectra of $[Pt(en)_2][Pt(en)_2Cl_{2-2\alpha}Br_{2\alpha}](ClO_4)_4$ in the range 100 - 400 cm^{-1}

$PtBr_{0.0}$	$PtBr_{0.25}$	$PtBr_{0.5}$	$PtBr_{0.75}$	$PtBr_{1.0}$	Assignment
	113.9 m	118.2 w	117.2 m	117.2 m	
138.1 m	134.0 m	135.6 m	134.8 m	138.5 w	
153.8 m	147.4 m	151.8 w	145.1 w		
165.1 m	165.2 m		167.9 w		ν_{3c}, PtCl bend
180.0 m	179.2 m	173.1 s,br	173.7 m	172.9 br	
	191.4 w		191.0 w		
	210.4 w	215.7 w	210.8 w		ν_{1m}
	240.2 sh	238.2 s	237.8 s	237.3 vs	ν_{2b}
253.3 s	255.5 vs	254.6 vs	256.4 vs	256.0 s	in plane $\delta(PtN_2)$
290.2 s	290.6 s	289.1 s	290.0 s	288.5 m	in plane $\delta(PtN_2)$
				296.9 m	
325.5 w	326.0 m	325.0 m	324.8 m	323.8 w	ring bends, ν_{2m}
357.8 vs	355.7 s	354.5 ms	355.0 ms	354.5 ms	ν_{2c}, ligand mode
		372.2 w			

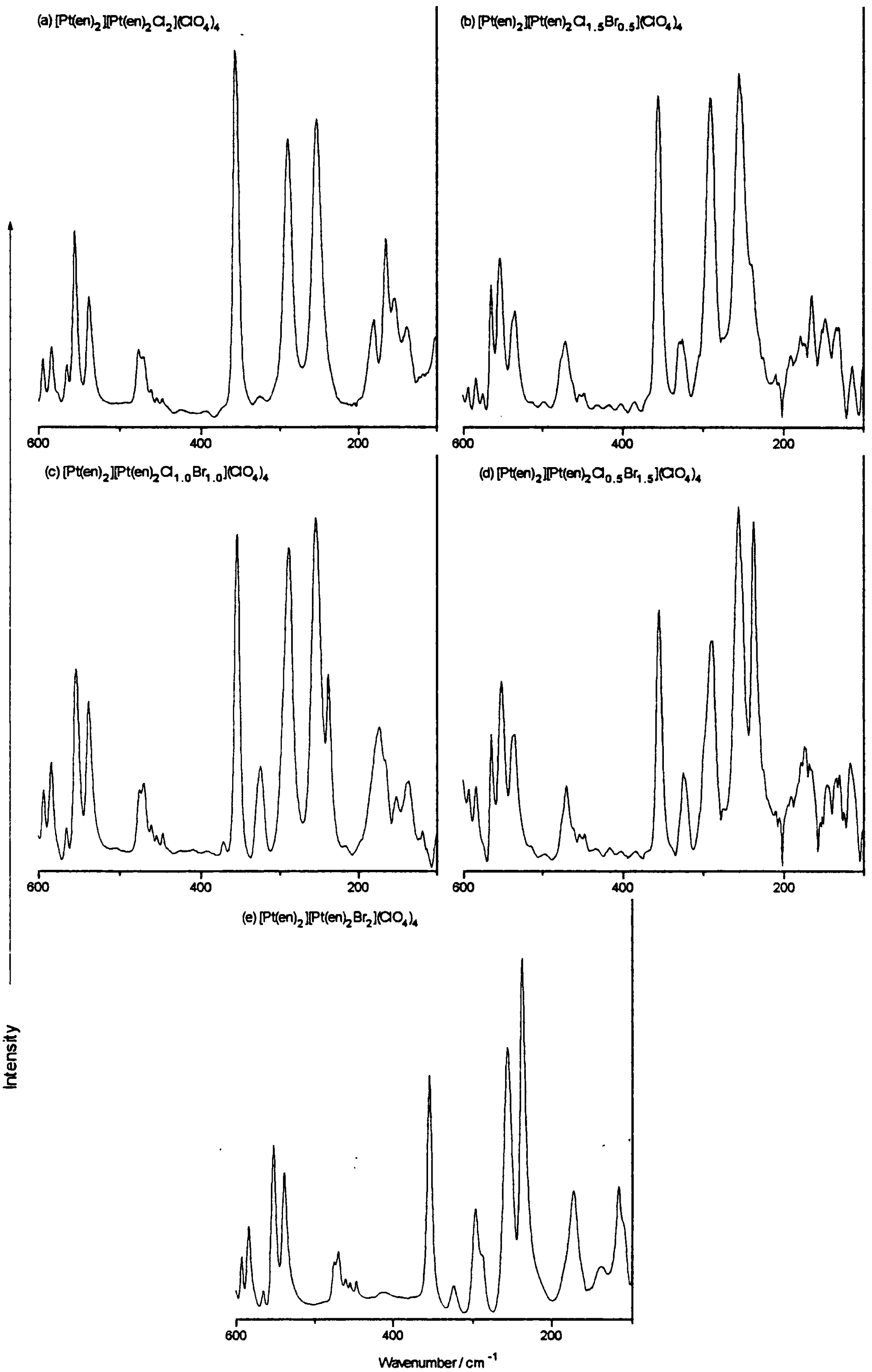

Figure 4.4.10 *Fourier Transform infrared spectra of $[Pt(en)_2][Pt(en)_2Cl_{2-2\alpha}Br_{2\alpha}](ClO_4)_4$, where (a) α = 0, (b) α = 0.25, (c) α = 0.5, (d) α = 0.75 and (e) α = 1.0.*

4.4.5 Discussion

Together, the results of the solid-state NMR and vibrational spectroscopic studies confirm the presence of significant populations of [Cl-Pt^{IV}-Br] units in the mixed-halide complexes. The proportions of the three unit types estimated from the solid-state ^{15}N NMR data in section **4.4.2** reveal what fraction (α) of chain halogens is bromine. If the distribution of halogen atoms about the Pt^{IV} centres is random, then the predicted relative intensities of the three units are $(1-\alpha)^2$ for [Cl-Pt^{IV}-Cl], $2\alpha(1-\alpha)$ for [Cl-Pt^{IV}-Br] and α^2 for [Br-Pt^{IV}-Br] (see Table 4.4.9). In all three mixed-halides, there are fewer [Cl-Pt^{IV}-Br] units, and more [Cl-Pt^{IV}-Cl] and [Br-Pt^{IV}-Br] units, than would be the case if the distribution of halogen atoms was entirely random.

Table 4.4.9 Calculated populations of Pt^{IV} units in mixed-halide complexes

Mixed-halide complex	Label	Calculated bromine %	Percentages of Pt^{IV} subunits			
			Source	Cl-Pt^{IV}-Cl	Cl-Pt^{IV}-Br	Br-Pt^{IV}-Br
$PtBr_{0.25}$	**426a**	26.5	Measured	59	31	10
			Predicted	56	38	7
$PtBr_{0.5}$	**426b**	53.0	Measured	26	40	33
			Predicted	22	50	28
$PtBr_{0.75}$	**426c**	77.0	Measured	8	30	62
			Predicted	5	35	59

When Poë investigated the equilibria shown in Equations [4.5.1-2], he found the ratio of $K_1 : K_2$ to be about 2.7 in solution, compared with the value of 4.0 expected for random distribution.[244]

$$[Pt(en)_2Cl_2]^{2+} + Br^- \xrightleftharpoons{K_1} [Pt(en)_2ClBr]^{2+} + Cl^- \qquad [4.5.1]$$

$$[Pt(en)_2ClBr]^{2+} + Br^- \xrightleftharpoons{K_2} [Pt(en)_2Br_2]^{2+} + Cl^- \qquad [4.5.2]$$

The effective ratio of $K_1 : K_2$ in the mixed-halide complexes lies in the range 1.6 to 1.9, and so is only slightly smaller than that in solution. The kinetics of the halogen-exchange reaction have been studied, and it is believed to proceed *via* a bridging-halogen transition state; the rate of reaction is first order in [Pt^{II}], [Pt^{IV}] and [X^-].[254] At the start of the synthesis of a mixed-halide complex, there are four ions present: $[Pt(en)_2]^{2+}$, $[Pt(en)_2Cl_2]^{2+}$, $[Pt(en)_2Br_2]^{2+}$

and ClO_4^-. The concentration of halide ions is likely to be very small, and so the scrambling of halogens should occur slowly. The amount of scrambling that takes place may be greater when the ions are allowed to remain in solution for a longer time or are heated to higher temperatures. To determine whether halogen exchange occurs when there are no Pt^{II} ions, a solution containing equimolar amounts of $[Pt(en)_2Cl_2](ClO_4)_2$ and $[Pt(en)_2Br_2](ClO_4)_2$ was prepared. A yellow crystalline material was extracted from it, and its infrared and Raman spectra were collected and compared with those of the starting materials (see Figure 4.4.11). The asymmetric stretches, ν_{as}(X-Pt^{IV}-X') (X = X', or X ≠X'), are observed in the former, the symmetric stretches, ν_s(X-Pt^{IV}-X'), in the latter. The wavenumbers of these modes are listed in Table 4.4.10, along with those of the corresponding chain vibrations for $PtBr_{0.0}$, $PtBr_{0.5}$ and $PtBr_{1.0}$. The spectra of the species $[Pt(en)_2ClBr](ClO_4)_2$ contain all the peaks that appear in the spectra of $[Pt(en)_2Cl_2](ClO_4)_2$ or $[Pt(en)_2Br_2](ClO_4)_2$, although the exact wavenumbers of some modes are slightly different, presumably because of crystallisation effects. There are additional resonances due to motions of the [Cl-Pt^{IV}-Br] unit at 236.5 cm^{-1} in the Raman spectrum and at 346.3 cm^{-1} in the infrared spectrum. The relationships between these resonances and the chain modes ν_{1m} and ν_{2m} are consistent with those observed in $PtBr_{0.0}$ or $PtBr_{1.0}$ between ν_1 and ν_s, or between ν_2 and ν_{as}. The two new modes are assigned to the "symmetric" and "asymmetric" stretches of the mixed-halide unit [Cl-Pt^{IV}-Br], and they indicate that halogen scrambling does occur even when Pt^{II} ions are absent or in low concentration.

Table 4.4.10 Wavenumbers / cm^{-1} of the ν_s and ν_{as} bands in the Pt^{IV}monomers

Complex	ν_s(X-Pt^{IV}-X) / cm^{-1}	ν_1 chain mode / cm^{-1}	ν_{as}(X-Pt^{IV}-X) / cm^{-1}	ν_2 chain mode / cm^{-1}
$[Pt(en)_2Cl_2](ClO_4)_2$	356.0 360.0	304.0 307.0 311.0	372.3	357.3
$[Pt(en)_2Br_2](ClO_4)_2$	210.5	164.0	243.9	237.3
$[Pt(en)_2Cl_{1.0}Br_{1.0}](ClO_4)_2$	236.5	206.5	346.3	325.0

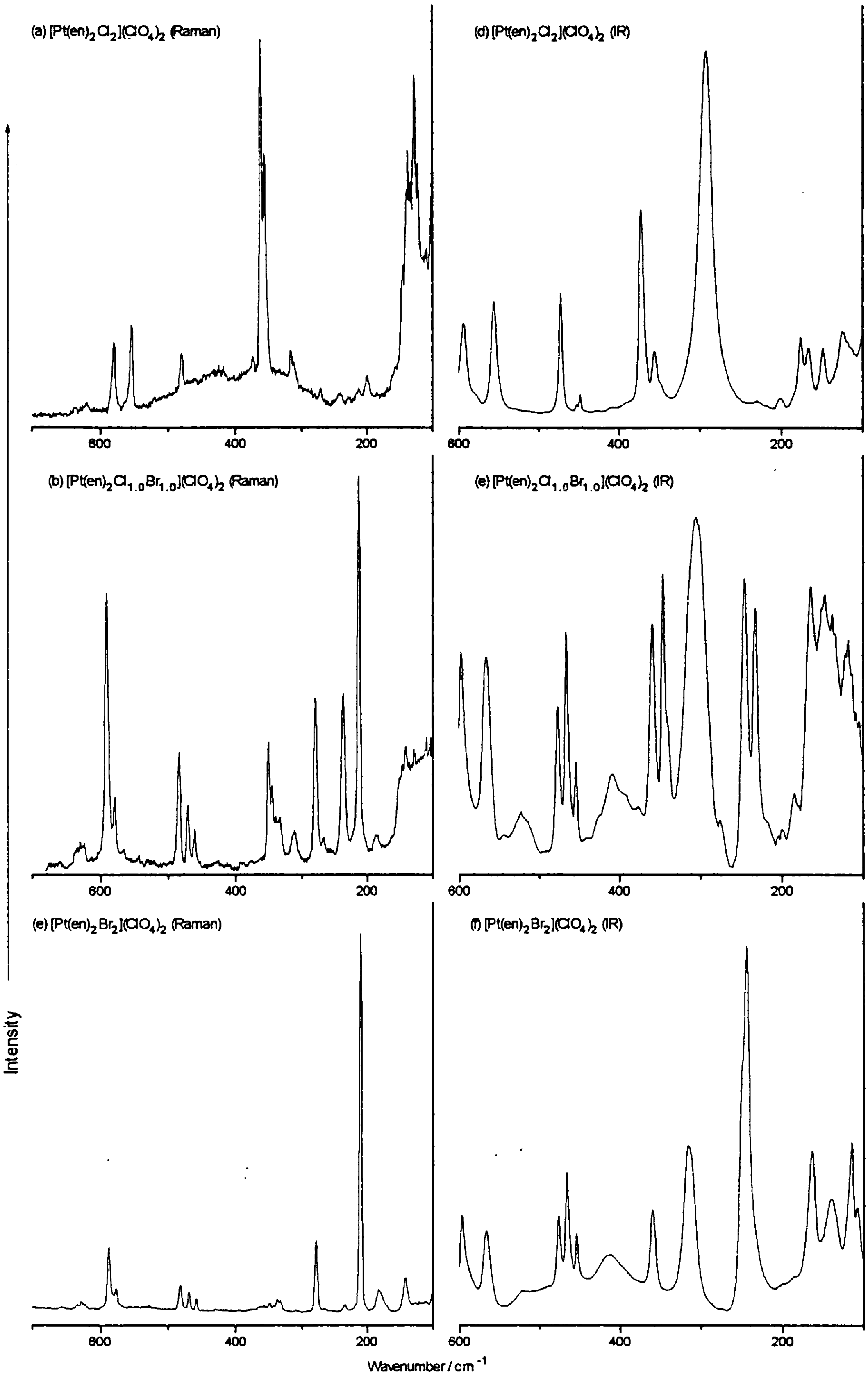

Figure 4.4.11 *Comparison of the Raman (left column) and infrared (right column) spectra of [Pt(en)$_2$Cl$_2$](ClO$_4$)$_2$ and [Pt(en)$_2$Br$_2$](ClO$_4$)$_2$ with those of the mixed-halide complex with empirical formula [Pt(en)$_2$ClBr](ClO$_4$)$_2$*

The Raman spectra of the mixed-halide HMMCs contain two peaks (ν_{1m} and ν_{2m}) which relate to the vibrations of [Cl-Pt^{IV}-Br] units. ν_{1m} is observed in the FT-IR spectra, though it has little intensity, but ν_{2m} overlaps with a ligand mode and cannot be resolved. The vibrational spectra confirm the purity of the single-halide HMMCs $PtBr_{0.0}$ and $PtBr_{1.0}$. ν_{1m} is not seen in the FT-IR spectrum of either chain. The dispersion of ν_{1m} is the same for all the mixed-halide HMMCs, but the signal that appears at *ca.* 210 cm^{-1} in the Raman spectra of $PtBr_{0.0}$ or $PtBr_{1.0}$ shows entirely different behaviour. The Cl : Br ratio has a much greater influence on ν_{1c} or ν_{1b} than it does on ν_{1m}. As the proportion of X is reduced, the ν_1(X-Pt^{IV}-X) signal moves to larger wavenumber, which is consistent with the lengths of the $[X\text{-}Pt^{IV}\text{-}X\text{-}Pt^{II}]_n$ segments being reduced (*i.e.* n is smaller). If chains were composed of long sections of one unit then the chloride isotopic structure observed in $PtBr_{0.0}$ would be maintained in the spectra of $PtBr_{0.25}$. The ν_{1m} signal changes only in its intensity, which may mean that [Cl-Pt^{IV}-Br] segments are short or that the ν_{1m} mode is very localised.

Electronic defects are an important feature of mixed-halide HMMCs. The FT-IR spectra of the mixed-halide species yield little information about them, probably because the signals they give are too weak to be observed. Two modes are observed clearly in the Raman spectra. They are labelled ν_{db} and ν_{dc} and have been assigned to the electron polaron in PtBr and the hole polaron in PtCl, respectively.[102,105] It has been suggested that an electron polaron centred on the [Cl-Pt^{IV}-Br] unit gives rise to a mode at *ca.* 196 cm^{-1},[57] but this has not been confirmed. There may be other regions of the spectrum where defect modes are concealed, for instance in the high energy part of the ν_{1b} peak. There are further difficulties in the Raman analysis because the structure of electronic defects in mixed-halide species is not clear. ESR results (see section **1.5.6**) indicate that UPEs in PtCl or PtBr are delocalised over several nuclei. But the segments of each type of Pt^{IV} unit are likely to be very short in the mixed-halide HMMCs, so defect vibrations may well be more localised than in PtCl or PtBr.

The signals in the Raman spectra cannot be assigned accurately using intuition alone. Therefore, in the next section chain modes are simulated using a vibrational modelling computer program to help determine the origin of some of the signals observed.

4.5 Vibrational modelling

4.5.1 Introduction

The relative bulk populations of the units $[BrPt^{IV}Br]$, $[BrPt^{IV}Cl]$ and $[ClPt^{IV}Cl]$ in the mixed-halide HMMCs $[Pt(en)_2][Pt(en)_2Cl_{2-2\alpha}Br_{2\alpha}](ClO_4)_4$ were calculated from the intensities of the N-Pt^{IV} peaks in the solid-state ^{15}N NMR spectra (see section **4.4.2**). The N-Pt^{II} region is less well resolved, and the halogen distribution about Pt^{II} centres cannot be determined in the same way, but the fact that only one peak is observed rather than two discrete signals means that $[ClPt^{II}Cl]$ and $[BrPt^{II}Br]$ are not the only Pt^{II} units present. The proportions of $[BrPt^{II}Br]$, $[BrPt^{II}Cl]$ and $[ClPt^{II}Cl]$ may be a simple function of the solution concentrations of the $[XPt^{IV}X']$ units. Solid-state ^{15}N NMR results show that Pt^{II} environments are not greatly affected by the identity of the neighbouring halogens, so it is possible that during chain formation all terminal Pt^{II} atoms "look" the same to free Pt^{IV} ions. The NMR data are not inconsistent with a picture of random distribution of Pt^{IV} units, but halogen distribution in mixed-halide chains cannot be determined unambiguously from solid-state NMR data alone. In this section the vibrational spectra recorded for the complexes are compared with theoretical spectra derived from model chains. The chains are constructed with the $[XPt^{IV}X']$ units in the proportions determined in the solid-state ^{15}N NMR study (see Table 4.4.2). Three different models are investigated in which: (R) the three kinds of Pt^{IV} unit are distributed randomly, (O) there is a small degree of order imposed by allowing only $[ClPt^{II}Cl]$ and $[BrPt^{II}Br]$ units at the Pt^{II} sites, and (B) the probability of successive Pt^{IV} units being the same type is so high that block copolymers are formed.

4.5.2 The vibrational modelling process

Vibra90, a program installed on the ULCC Convex system and accessed remotely from the UCL timeshare (ts) facility, was used to generate all the theoretical vibrational spectra; details of the program and computing procedures are given in section **4.8**. The program acts upon computer files that contain the atomic coordinates, atomic masses, a set of internal coordinates and the forces acting along them, to produce output files consisting of vibrational frequencies and atomic displacements. The complexity of the modelled chains is limited by the capabilities of Vibra90. It supports a maximum of 50 atoms and 150 internal coordinates.

Therefore models that include equatorial atoms [65,117] will have too few unit cells (*i.e.* four) for proper analysis. Simple one-dimensional chains composed of 48 atoms (*i.e.* twelve subunits) are normally used instead. The cyclic boundary conditions that are used in most cases require the number of subunits to be whole.

In this study, the simplest model of an MX chain uses the six force constants depicted in Figure 4.5.1. Trial runs using only the five constants employed by Swanson *et al.* [112] showed that ν_1 and ν_2 for $[Pt(en)_2][Pt(en)_2Br_2](ClO_4)_4$ cannot be reproduced simultaneously. Addition of the sixth constant enables greater control over the difference in wavenumber between ν_1 and ν_2. Vibra90 requires the definition of an internal coordinate for each force, and so a total of 108 internal coordinates are needed to model a 48-atom chain with the force constants k_1 - k_6. Under cyclic boundary conditions there are 48 interatomic bonds, 48 vectors covering two bonds, and 12 long distance Pt^{IV} - Pt^{IV} interactions.

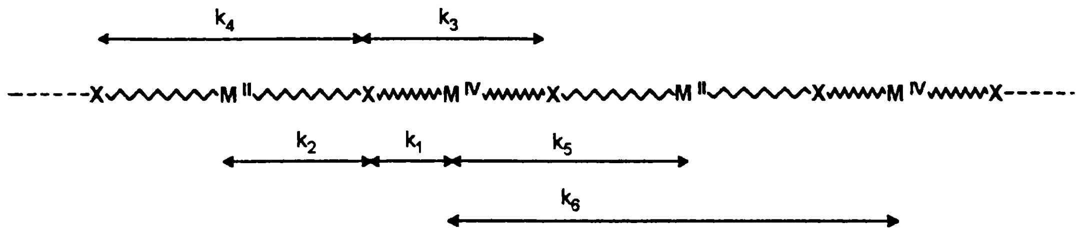

Figure 4.5.1 *Diagram showing the six force constants used for the modelling of linear-chain complexes containing one type of halogen.*

Although the vibrational spectra of $[Pt(en)_2][Pt(en)_2X_2](ClO_4)_4$ (X = Cl, Br or I) have been recorded on many occasions, not all chain modes have been identified in them. For instance, no signal due to the infrared-active ν_3 mode has been located with certainty, even for X = Cl. Knowledge of ν_1 and ν_2 alone is not helpful, because if they can be reproduced simultaneously using k_1 and k_2 alone, then there will be an infinite number of solutions,[188] and the addition of extra force constants merely adds to the complexity. Vibrational analysis of isotopic effects in $[Pt(en)_2][Pt(en)_2Cl_2](ClO_4)_4$ has provided the data needed to produce a more specific answer to the problem.[110,112] Raman spectra show that the chain vibration $\nu_1(Pt^{35}Cl)$ is at 311.0 cm^{-1}, while the localised defect mode $\nu_1(^{37}Cl\text{-}Pt\text{-}^{35}Cl)$ is at 308.4 cm^{-1}. Infrared spectra yield the corresponding ν_2 modes: $\nu_2(^{35}Cl\text{-}Pt^{IV}\text{-}^{35}Cl)$ is at 359.1 cm^{-1}, $\nu_2(^{35}Cl\text{-}Pt^{IV}\text{-}^{37}Cl)$ is at

356.5 cm^{-1}.[110] The first objective of this work is to match these values as closely as possible using Vibra90. This is done by finding the energies of the zone centre (ZC) and zone boundary (ZB) modes of the four vibrational bands in a Pt^{35}Cl chain, and of the localised defect modes in a chain in which one of the ^{35}Cl atoms is replaced by a ^{37}Cl atom. The six force constants are adjusted until the appropriate matches with experimental results are made. The influence of each force constant should be appreciated. The starting point is a basic model in which all force constants are set to zero except for k_1 and k_2, which are 1.8 and 0.2 N m^{-1}, respectively. A small increase is applied to each force constant in turn, and its effect on the four vibrational bands is recorded (see Tables 4.5.1 - 3); a reduction of the same constant has an opposite, usually unequal effect. All four vibrational modes are analysed, but there are only reliable vibrational data for ν_1 and ν_2. The most important result is that it is very difficult to tune the energies of the ν_1 and ν_2 bands correctly unless both k_5 and k_6 are included in the model. k_1 and k_2 control the zone centre energies for ν_1 and ν_2, but they have little effect on the dispersion of either band or on the energy of defects relative to ZC. k_3 and k_4 are less influential, but they can be used to tune individual bands selectively since k_3 does not affect ν_2 nor does k_4 affect ν_1. The dispersion of the bands can only be altered significantly by k_5 or k_6. Both forces are necessary to produce the correct dispersions simultaneously for ν_1 and ν_2, because k_5 affects both ν_1 and ν_2, whereas k_6 only affects the ν_2 modes. Many of the relations between force constants and vibrational bands may be deduced logically. For instance, k_6 acts between two M^{IV} centres and so it has no influence on ν_1 because none of the M^{IV} centres moves in the totally symmetric mode. Likewise the M^{IV} - M^{IV} distance is constant when the M^{IV} centres move in phase in the ZC ν_2 mode. However, the ZB ν_2 mode involves a large variation in $r(M^{IV} - M^{IV})$, so k_6 has a large influence on the dispersion of ν_2. Similar arguments relating to the $r(M^{II} - M^{IV})$ distance show that k_5 does not affect the zone centre modes of ν_1 or ν_2. The results shown in the tables are for a PtCl chain, but the principles are the same for all HMMCs.

Table 4.5.1 Effect of change of individual force constants on the chain mode, ν_2

Vibrational modes with initial values / cm^{-1}		Zone Centre	Zone Boundary	Dispersion	Defect mode	Zone centre - defect
Force constant	Change / $N\ m^{-1}$	355.14	354.84	0.30	351.63	3.51
k_1	+ 0.10	+ 9.14	+ 9.16	- 0.02	+ 9.07	+ 0.07
k_2	+ 0.10	+ 5.61	+ 5.25	+ 0.36	+ 5.34	+ 0.27
k_3	+ 0.02	nil	nil	nil	+ 0.03	- 0.03
k_4	+ 0.02	+ 0.10	+ 0.12	-0.02	+ 0.11	- 0.01
k_5	+ 0.04	nil	+ 4.20	- 4.20	+ 1.57	- 1.57
k_6	+ 0.30	nil	+ 3.66	- 3.66	+ 1.42	- 1.42

Table 4.5.2 Effect of change of individual force constants on the chain mode, ν_1

Vibrational modes with initial values / cm^{-1}		Zone Centre	Zone Boundary	Dispersion	Defect mode	Zone centre - defect
Force constant	Change / $N\ m^{-1}$	311.45	312.03	0.58	307.11	4.34
k_1	+ 0.10	+ 7.69	+ 7.65	- 0.04	+ 7.57	+ 0.12
k_2	+ 0.10	+ 7.69	+ 8.33	+ 0.64	+ 7.84	- 0.15
k_3	+ 0.02	+ 3.10	+ 3.08	- 0.02	+ 3.03	+ 0.07
k_4	+ 0.02	nil	nil	nil	+ 0.01	- 0.01
k_5	+ 0.04	+ 0.58	+ 5.59	+ 5.01	+ 2.21	- 1.63
k_6	+ 0.30	nil	nil	nil	+ 0.03	- 0.03

Table 4.5.3 Effect of change of individual force constants on the chain modes, ν_3 and ν_4

		ν_3					ν_4
Vibrational modes with initial values / cm^{-1}		Zone Centre	Zone Boundary	Disp^n	Defect mode	(ZC - DM) separation	Zone Boundary
Force constant	Change / $N\ m^{-1}$	75.38	55.87	19.51	55.86	19.52	49.12
k_1	+ 0.10	+ 0.13	+ 0.15	- 0.02	+ 0.16	- 0.03	+ 0.08
k_2	+ 0.10	+ 15.51	+ 10.77	+ 4.74	+ 10.77	+ 4.73	+ 10.17
k_3	+ 0.02	nil	+ 0.06	- 0.06	+ 0.07	- 0.07	nil
k_4	+ 0.02	+ 4.06	+ 3.02	+ 1.04	+ 3.03	- 1.03	+ 2.65
k_5	+ 0.04	nil	nil	nil	nil	nil	+ 8.32
k_6	+ 0.30	nil	nil	nil	nil	nil	+ 52.10

4.5.3 Fitting the Raman results for [Pt(en)$_2$][Pt(en)$_2$X$_2$](ClO$_4$)$_4$ (X = Cl or Br).

Although isotopic defect modes have been located for PtCl, the force constants used in the model still outnumber the vibrational frequencies observed. The situation is worse for PtBr, because only the zone centre energies of ν_1 and ν_2 are known, and there are no isotopic data from which to benefit. No unique solution can be found for the force constants of either complex, so one force has to be assumed and the others calculated from it. k_2, the strength of the Pt^{II}-X interaction, is chosen for this purpose and is given the values of 0.2, 0.4 or 0.6 N m^{-1}. The force constants are given subscripts to denote the halogens involved, so k_{2b} refers to Pt^{II}-Br and k_{2c} refers to Pt^{II}-Cl. The spectrum of PtCl is fitted by first using k_{2c} = 0.2 N m^{-1}. The ν_{1c} and ν_{2c} bands are tuned roughly by changing k_{1c}, and the zone centre modes in each band are fine tuned by altering k_{3c} and k_{4c}. The wavenumbers of the isotopic defect modes are then matched by adjusting k_{5c} and k_{6c}. For the remaining values of k_{2c}, both k_{5c} and k_{6c} are kept the same to calculate the new values for k_{1c}, k_{3c}, k_{4c} (see Table 4.5.4).

Table 4.5.4 Force constants determined for the model of [Pt(en)$_2$][Pt(en)$_2$Cl$_2$](ClO$_4$)$_4$

Force constant	Internal coordinate	Force constant set		
		A / N m^{-1}	B / N m^{-1}	C / N m^{-1}
k_{2c}	M^{II}-Cl	0.2	0.4	0.6
k_{1c}	M^{IV}-Cl	1.844	1.718	1.579
k_{3c}	Cl-M^{IV}-Cl	0.010	-0.038	-0.090
k_{4c}	Cl-M^{II}-Cl	-0.035	-0.024	-0.002
k_{5c}	M^{IV}-Cl-M^{II}	-0.02	-0.02	-0.02
k_{6c}	M^{IV}-M^{IV}	0.30	0.30	0.30

A model of PtCl was constructed to test these values. It consists of fifty PtCl chains of forty-eight atoms in which the chlorine isotopes are randomly distributed. The chains are generated by a FORTRAN77 program ("GENERA"; see section **4.8**). Vibra90 determines the frequency and atomic displacements associated with each chain vibration. These values are fed into a second FORTRAN77 program ("INTENS"; see section **4.8**) which calculates infrared or Raman intensities. Infrared intensity is derived from the dipole moment, which is estimated by assuming simple point charges of +2 or +4 for platinum and -1 for the halogens. Raman intensity is approximated by making polarisability change proportional to the mean change in

Pt^{IV}-Cl bond length.[112] The wavenumbers are rounded to the nearest 0.1 cm^{-1}, the intensities at each point summed and then Gaussian broadened to give the theoretical spectra. The amount of broadening applied was determined empirically from the ν_{1c} signal in the Raman spectrum. The ν_{1c} signal generated with force constant set A is shown in Figure 4.5.2 with five different peak broadening values ranging from 0.1 - 0.5 cm^{-1}. 0.4 cm^{-1} Gaussian broadening gives the best match with experimental data, so it is used in all subsequent plots. The theoretical Raman ν_{1c} signals generated using each of the three force constant sets are compared with the single-crystal Raman spectrum of PtCl (647 nm excitation) in Figure 4.5.3. Although the data used to find the force constants were gathered under different conditions to this Raman spectrum, every model reproduces the shape of the ν_1 profile closely, so that the best value of k_2 cannot be ascertained. The observed Raman peaks are broad and are composed of many discrete signals that can be distinguished in the 0.1 cm^{-1} broadened theoretical plot (see Figure 4.5.2a). The more prominent peaks have been labelled (A to H); apostrophes denote unresolved shoulders. The structure of the ν_{1c} signal is explained by considering the chain as a sequence of individual segments each made up of only one type of unit cell.[112] Effectively there are only three unit types, -cc-, -cC-, and -CC-, where -cC- represents [^{35}Cl-Pt^{IV}-^{37}Cl]. Each segment of N units gives rise to four bands of vibrational modes (ν_{1c} - ν_{4c}), with N modes in each. The zone centre mode has the greatest Raman intensity of those in the ν_{1c} band. Statistically, most of the ν_{1c} Raman intensity arises from motions which span segments of five, or fewer, unit cells. By analysing the atomic displacements in the Vibra90 output files, the peaks labelled in Figure 4.5.2a can be related to the vibration of certain segments. For instance, the solitary units -CC-, -cC- and -cc- contribute to the signals A, C' and H respectively. Of the larger peaks, B contains modes from segments such as -cC-cC-, -Cc-cC- or -cC-cC-cC-, while C has a large component due to -cC-xx-cC- or -cC-xx-Cc- (x = c or C). Peaks D - H relate to vibrations of blocks of -cc- units. Generally, for a given unit, higher energy signals are due to shorter sequences, but they also contain some intensity resulting from the non-zone centre modes of longer segments.

Bromine has two isotopes, ^{79}Br and ^{81}Br, that exist at roughly 50 % natural abundance. No isotopic structure is seen in the Raman spectrum of PtBr, nor have isotopic defect modes been identified as they were for PtCl. Therefore, there are no constraints over the values that the six force constants k_{1b} - k_{6b} can take. For the sake of simplicity, k_{4b}, k_{5b} and k_{6b} are made equal to the corresponding k_{4c}, k_{5c} and k_{6c} for each three value of k_{2b}. PtBr is modelled by tuning k_{1b} and k_{3b} alone; the three sets of force constants derived are listed in Table 4.5.5. k_{1b} is significantly smaller than k_{1c}. k_{3b} has a large negative value that reflects the difference between the zone centre wavenumbers of the ν_1 and ν_2 modes. (ν_{2c} - ν_{1c}) is 48 cm^{-1}, or 15 % of the absolute value of ν_{1c}; (ν_{2b} - ν_{1b}) is over 72 cm^{-1}, or more than 40 % of the size of ν_{1b}.

Table 4.5.5 Force constants determined for the model of $[Pt(en)_2][Pt(en)_2Br_2](ClO_4)_4$

Force constant	Internal coordinate	Force constant set		
		A / N m^{-1}	B / N m^{-1}	C / N m^{-1}
k_{2b}	M^{II}-Br	0.2	0.4	0.6
k_{1b}	M^{IV}-Br	1.303	1.246	1.166
k_{3b}	Br-M^{IV}-Br	-0.075	-0.150	-0.240
k_{4b}	Br-M^{II}-Br	-0.035	-0.024	-0.002
k_{5b}	M^{IV}-Br-M^{II}	-0.02	-0.02	-0.02
k_{6b}	M^{IV}-M^{IV}	0.30	0.30	0.30

The sets of force constant values are tested on a model of PtBr in which the halogen isotopes are randomly distributed. The ν_{1b} Raman profile does not depend greatly on which k_{2b} is used. The atomic displacements of the ν_{1b} motions show that the lack of structure is because the vibrations are not highly localised but are spread over long segments of chain. In PtCl when adjacent units are not identical then there is a discontinuity in the vibrational character of the chain, but the difference between the vibrational energies of -bb- and -BB- (notation as above) is small enough to avoid this.

N.B. human error led to incorrect fitting of the ν_{2b} peaks. In PtCl the highest energy vibration is the ZC mode, and the same was mistakenly assumed to be true for PtBr. The error was noticed too late for the mixed-halide data to be rerun, so the results reported above are the original force constants. k_{1b} and k_{3b} are the only modes affected. Estimates of the correct values are given for information. (A) k_{1b} = 1.42 N m^{-1}, k_{3b} = -0.15 N m^{-1}, (B) k_{1b} = 1.32 N m^{-1}, k_{3b} = -0.20 N m^{-1} and (C) k_{1b} = 1.22 N m^{-1}, k_{3b} = -0.30 N m^{-1}.

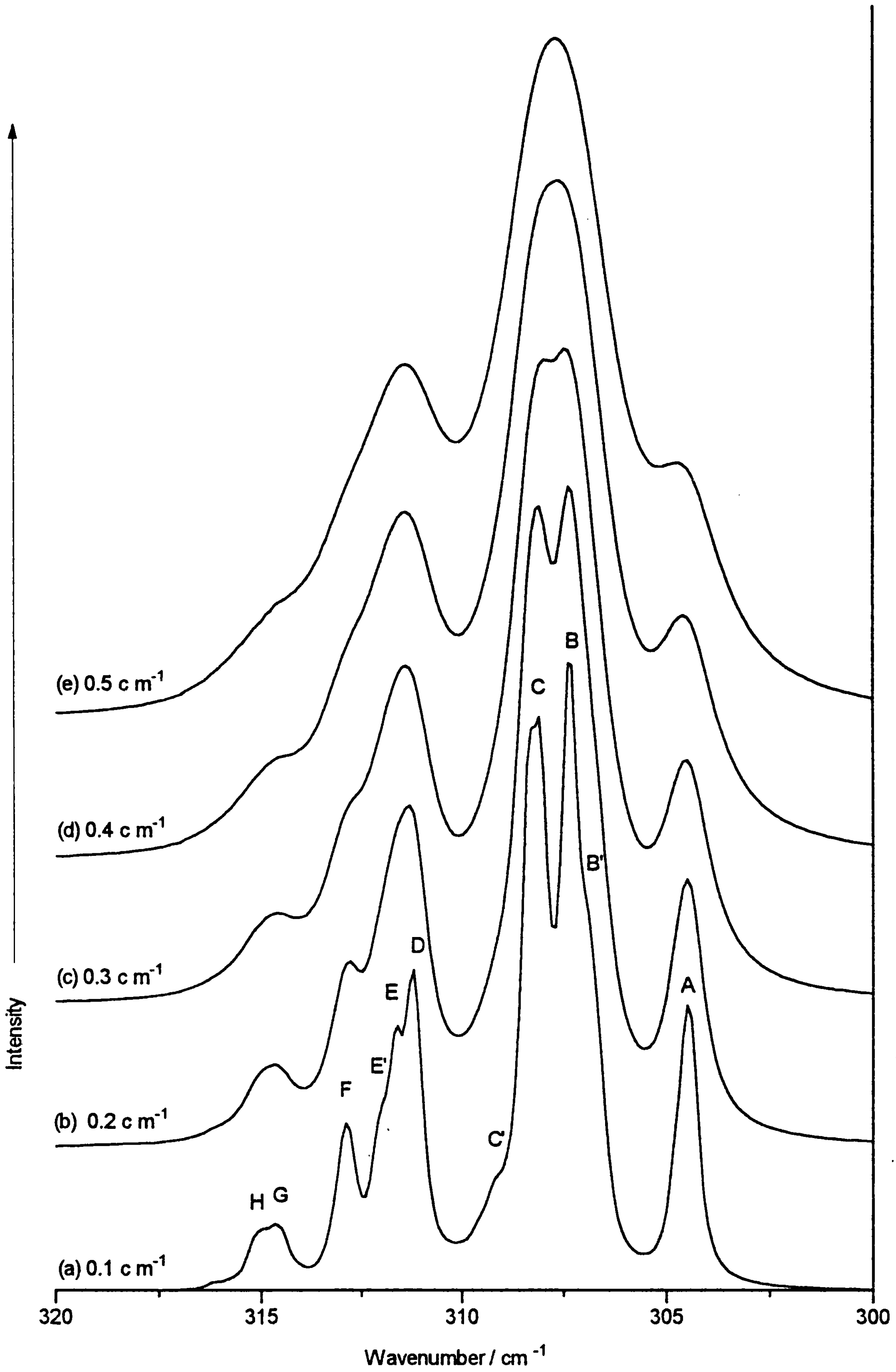

Figure 4.5.2 *The effect of the size of peak broadening on the ν_{1c} region of the theoretical Raman spectrum of $[Pt(en)_2][Pt(en)_2Cl_2](ClO_4)_4$.*

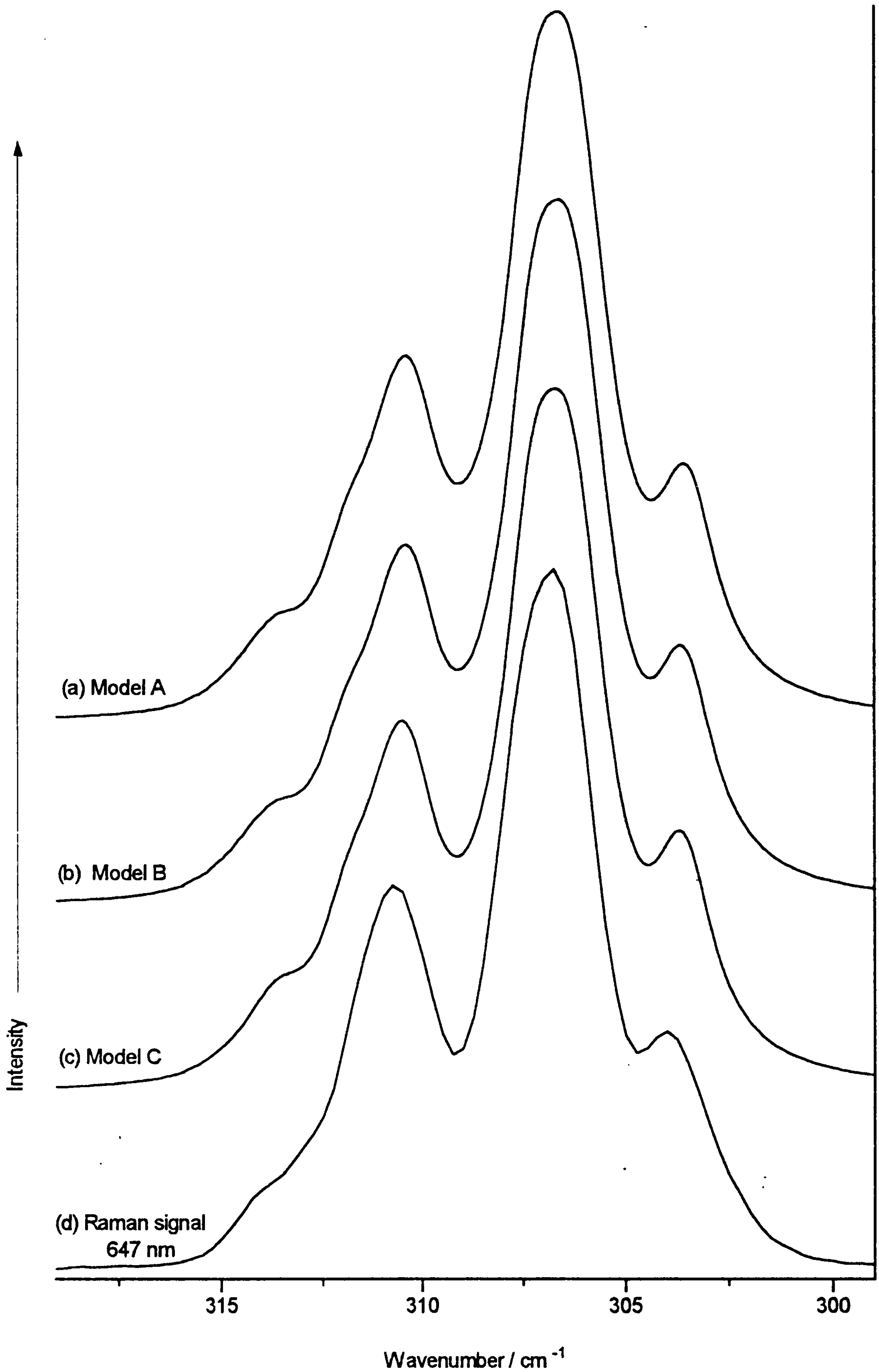

Figure 4.5.3 *Calculated Raman spectra (0.4 cm^{-1} Gaussian broadened) compared with a single-crystal sample examined at 647 nm excitation.*

4.5.4 Extension of the model to mixed-halide HMMCs

The analysis of mixed-halide HMMCs is restricted to two main objectives. Firstly, the assignment of peaks that appear only in the spectra of mixed-halide HMMCs and an accurate description of the chain motion to which they relate. Secondly, an assessment of which model and set of force constants reproduces the observed spectra most closely. Only qualitative results can be derived because so many assumptions are made in producing the simulated plots. For instance, the relative intensities of the peaks in the simulated spectra will not be accurate. Raman intensities in the model are calculated from changes in bond distances. This is a reasonable approximation for a single-halide chain, but not for a system containing three different types of unit cell that do not have the same excitation profile.

Where possible, the force constants derived in the analysis of $[Pt(en)_2][Pt(en)_2X_2](ClO_4)_4$ (X = Cl or Br) are retained in the modelling of the mixed-halide spectra, although three new forces have to be defined (see Figure 4.5.4). For simplicity, only cases where k_{2b} and k_{2c} are equal are considered. The remaining force constants k_{nb} and k_{nc} (n = 1, 3 - 6) take the values listed in Tables 4.5.4 - 5. Since $k_{nc} = k_{nb}$ for n = 4, 5 or 6, k_{4m} and k_{6m} are given the same values as k_{4c} and k_{6c} respectively. The model was tested with k_{3m} equal to either k_{3c} or k_{3b}, but the calculated spectra did not appear to differ significantly, so k_{3m} is defined as the mean of k_{3c} and k_{3b}. The sets of force constants derived for each value of k_2 are listed in Table 4.5.6.

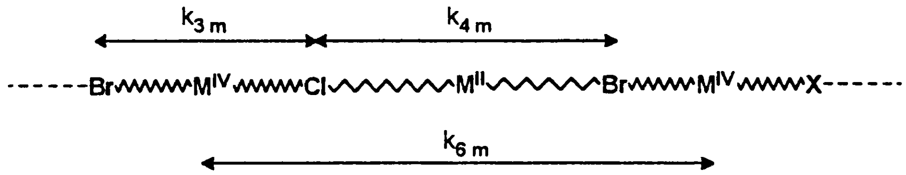

Figure 4.5.4 Diagram showing the three extra force constants defined for the mixed-halide model.

Three computer-generated HMMCs are investigated in this section. $PtBr_{0.5}$ is modelled as a random (R) or an ordered (O) chain, while $PtBr_{0.25}$ is modelled only as a random chain. The models are termed TZ_α, where T is the type (R, O or B), Z is the force constant data set (A, B or C) and α relates to the complex $PtBr_\alpha$ that is represented. The models of $PtBr_{0.5}$ are composed of fifty chains of forty-eight atoms that are constructed by the program GENERA using the unit cell probabilities determined in the solid-state ^{15}N NMR study; the models of $PtBr_{0.25}$ contain just twenty-five chains. Each model was submitted to Vibra90 to obtain the vibrational frequencies and atomic displacements, which were processed by the program INTENS to give theoretical infrared or Raman spectra. The infrared spectra are not of great interest, because the experimental results are too poor to allow useful comparisons, and only the ν_1 and ν_2 modes are evaluated in the Raman spectra.

Table 4.5.6 Force constants used in modelling the mixed-halide complexes [Pt(en)$_2$][Pt(en)$_2Cl_{2-2\alpha}Br_{2\alpha}$](ClO$_4$)$_4$

Force constant	Previous label	Internal coordinate	Modelling run		
			A / N m^{-1}	B / N m^{-1}	C / N m^{-1}
K_2	k_{2c}	M^{II}-Cl	0.2	0.4	0.6
K_4	k_{2b}	M^{II}-Br	0.2	0.4	0.6
K_1	k_{1c}	M^{IV}-Cl	1.844	1.718	1.579
K_3	k_{1b}	M^{IV}-Br	1.303*	1.246*	1.166*
K_5	k_{3c}	Cl-M^{IV}-Cl	0.010	-0.038	-0.090
K_7	k_{3b}	Br-M^{IV}-Br	-0.075*	-0.150*	-0.240*
K_6	k_{3m}	Br-M^{IV}-Cl	-0.033	-0.104	-0.165
K_8	k_{4c} k_{4b} k_{4m}	Cl-M^{II}-Cl Br-M^{II}-Br Br-M^{II}-Cl	-0.035	-0.024	-0.002
K_9	k_{5c} k_{5b}	M^{IV}-Cl-M^{II} M^{IV}-Br-M^{II}	-0.02	-0.02	-0.02
K_{10}	k_{6c}, k_{6b}, k_{6m}	M^{IV}-M^{IV}	0.30	0.30	0.30

** the values of k_{1b} and k_{3b} are known to be incorrect (see text).*

The Raman spectra calculated for the three models are displayed over the range 150-400 cm^{-1} in Figures 4.5.6-8. They have some general features in common with each other. There are large signals in only four areas, significantly fewer than in real spectra. The resonances at 165-175 cm^{-1} and 305-315 cm^{-1} correspond to the ν_{1b} and ν_{1c} modes respectively. The atomic displacements associated with the peaks in the other two regions show that they involve vibrations of the mixed-halide unit, [ClPt^{IV}Br]. The signals at *ca.* 200 cm^{-1} result from the breathing mode, ν_{1m}, while the asymmetric vibration ν_{2m} gives the peaks at 330-340 cm^{-1}. The relative amplitudes of the atoms in a single [ClPt^{IV}Br] unit for each mode are depicted in Figure 4.5.5. The d terms represent atomic displacements given by

Vibra90; the subscripts denote the vibration (1 for ν_1, 2 for ν_2) and the atom (c = Cl, b = Br and m = metal). ν_{1m} mostly involves motion of bromine atoms. d_{1b} is roughly 1.8 - 2.0 times the size of d_{1c} when k_2 = 0.2 N m^{-1}, and a further 10 % bigger when k_2 = 0.6 N m^{-1}. By contrast the ν_{2m} mode involves almost no movement of the bromine atom since d_{2b} is about a tenth of d_{2c}, and only a third of d_{2m}. The movements of the atoms account for the isotopic structure of the two resonances. The ν_{2m} signal consists of two peaks that relate directly to the two chlorine isotopes: the $\nu_2[^{35}Cl\text{-}Pt^{IV}\text{-}Br]$ peak is roughly three times more intense than the $\nu_2[^{37}Cl\text{-}Pt^{IV}\text{-}Br]$ peak, and is at more than 6 cm^{-1} higher wavenumber. ν_{1m} shows no more isotopic structure than ν_{1b} does in $[Pt(en)_2][Pt(en)_2Br_2](ClO_4)_4$ since it involves relatively little movement of the chlorine atoms.

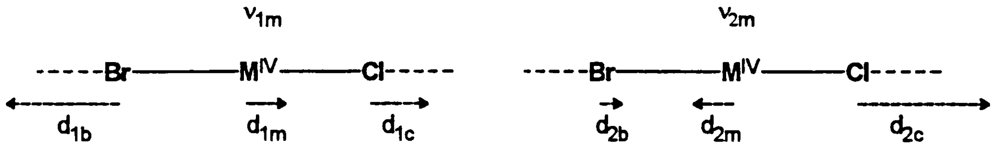

Figure 4.5.5 *Examples of ν_{1m} and ν_{2m} modes for single units of $[BrPt^{IV}Cl]$. The dashed arrowheads represent approximate relative atomic displacements and are not to scale with the bond lengths.*

The influence of the force constant k_2 on the structure or wavenumber of a given peak depends on which atoms have the greatest amplitude in the vibration to which it relates. Modes in which chlorine atoms are the more mobile are largely unaffected by k_2, so neither ν_{1c} nor ν_{2m} varies much when the force constant set is changed. In contrast, ν_{1b} and ν_{1m} separate into two or even three peaks as k_2 is increased. For instance, when k_2 = 0.6 N m^{-1}, the approximate positions of the zone centre ν_{1b} modes for segments of one, two or three units are 173, 170 and 167 cm^{-1}, respectively. These wavenumbers differ sufficiently for individual peaks to be distinguished in the simulated spectra.

There are so few differences between the spectra calculated for $RZ_{0.5}$ and $OZ_{0.5}$ for all Z that it is hard to favour one model over the other. The ν_{1c} resonance has more of its intensity in the high energy region in $OZ_{0.5}$ than it does in $RZ_{0.5}$, but the distinctions between their ν_{1b} modes are more significant, particularly when k_2 = 0.4 or 0.6 N m^{-1}. $RC_{0.5}$ has two prominent peaks at *ca.* 170 and 173 cm^{-1}, whereas $OC_{0.5}$ has most of its ν_{1b} intensity at *ca.* 166 cm^{-1} with only a weak signal at *ca.* 173 cm^{-1}. This pattern is repeated for $RB_{0.5}$ and $OB_{0.5}$, although the highest energy peak is at *ca.* 170 cm^{-1} because of the smaller dispersion.

The influence of the bromine content on the calculated spectra can be seen by comparing the results for $RZ_{0.5}$ and $RZ_{0.25}$. Neither ν_{1m} nor ν_{2m} changes much in profile as the proportion of bromine is increased, but ν_{1c} and ν_{1b} are significantly different. ν_{1c} for $RZ_{0.25}$ has similar shape to ν_{1c} for PtCl (or $RZ_{0.0}$ for that matter), but the isotopic pattern for ν_{1c} in $RZ_{0.5}$ is closer to the 9 : 6 : 1 associated with Pt^{IV} complexes. $RZ_{0.25}$ contains few $[BrPt^{IV}Br]$ units, so long segments of PtBr are rare and the most intense peak in the ν_{1b} region is that at highest wavenumber for k_2 = 0.4 or 0.6 N m^{-1}.

All four of the major resonances seen in the theoretical spectra of the mixed-halide HMMCs are observed in real Raman spectra, although the wavenumbers of some peaks do not match up precisely, mainly because of the effects of dispersion (see section **4.5.7**). However, the wavenumbers predicted for ν_{1m} are too low while those for ν_{2m} are too high, even when dispersion is taken into account. The energy of ν_{1m} can be raised by increasing the value of k_{3m}, but it is more difficult to adjust the energy of ν_{2m} as it requires the k_1 and k_2 terms to be reworked from first principles. The experimental spectra contain other peaks for which the models fail to account. The majority of these are overtone or combination modes, but three of the peaks in the range 100-350 cm^{-1} result from fundamentals. They are labelled ν_{db}, ν_{dc} and ν_a in the tables in section **4.4**.

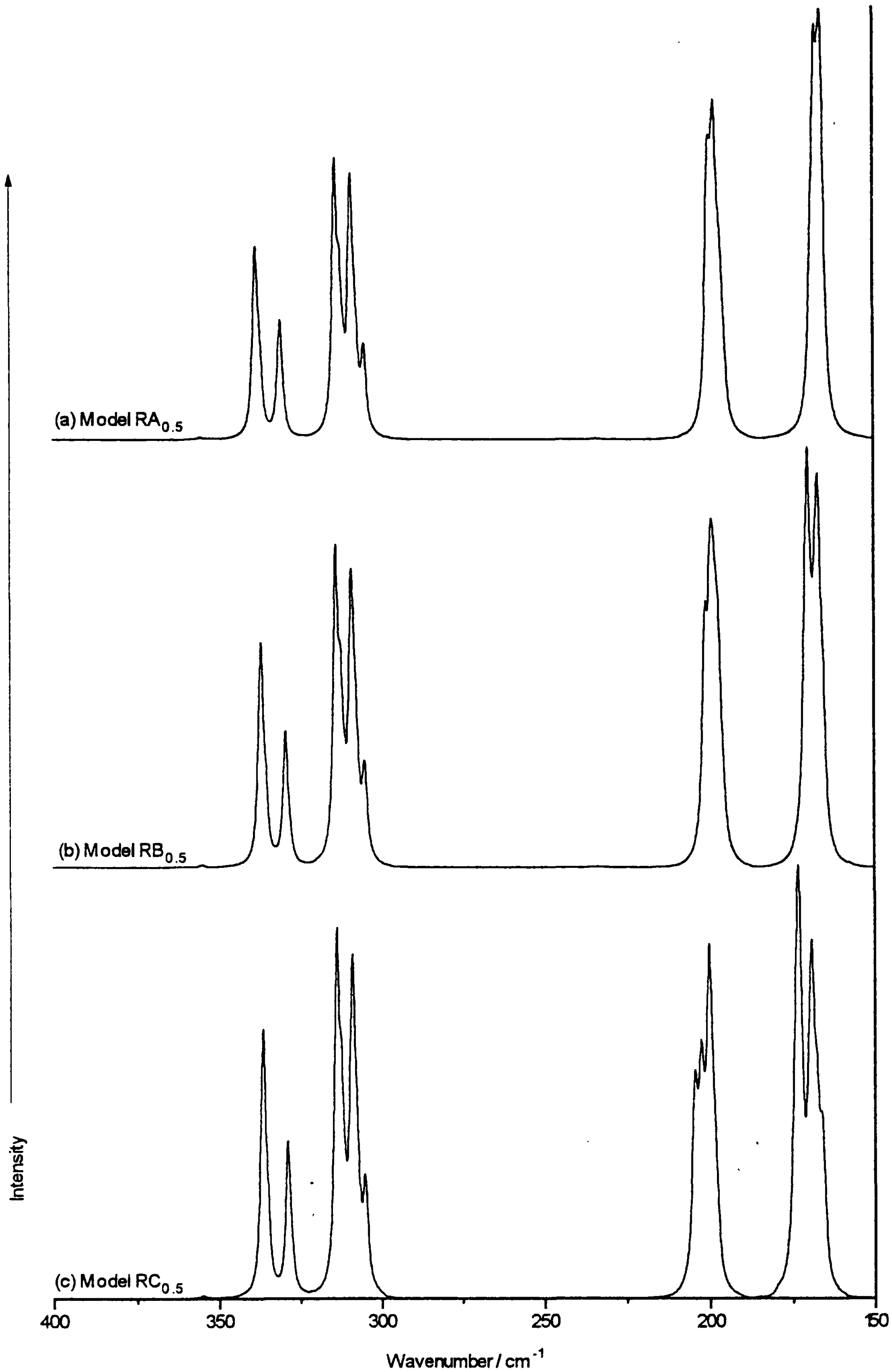

Figure 4.5.6 *Theoretical Raman spectra for $PtBr_{0.5}$ using the models (a) $RA_{0.5}$, (b) $RB_{0.5}$ and (c) $RC_{0.5}$.*

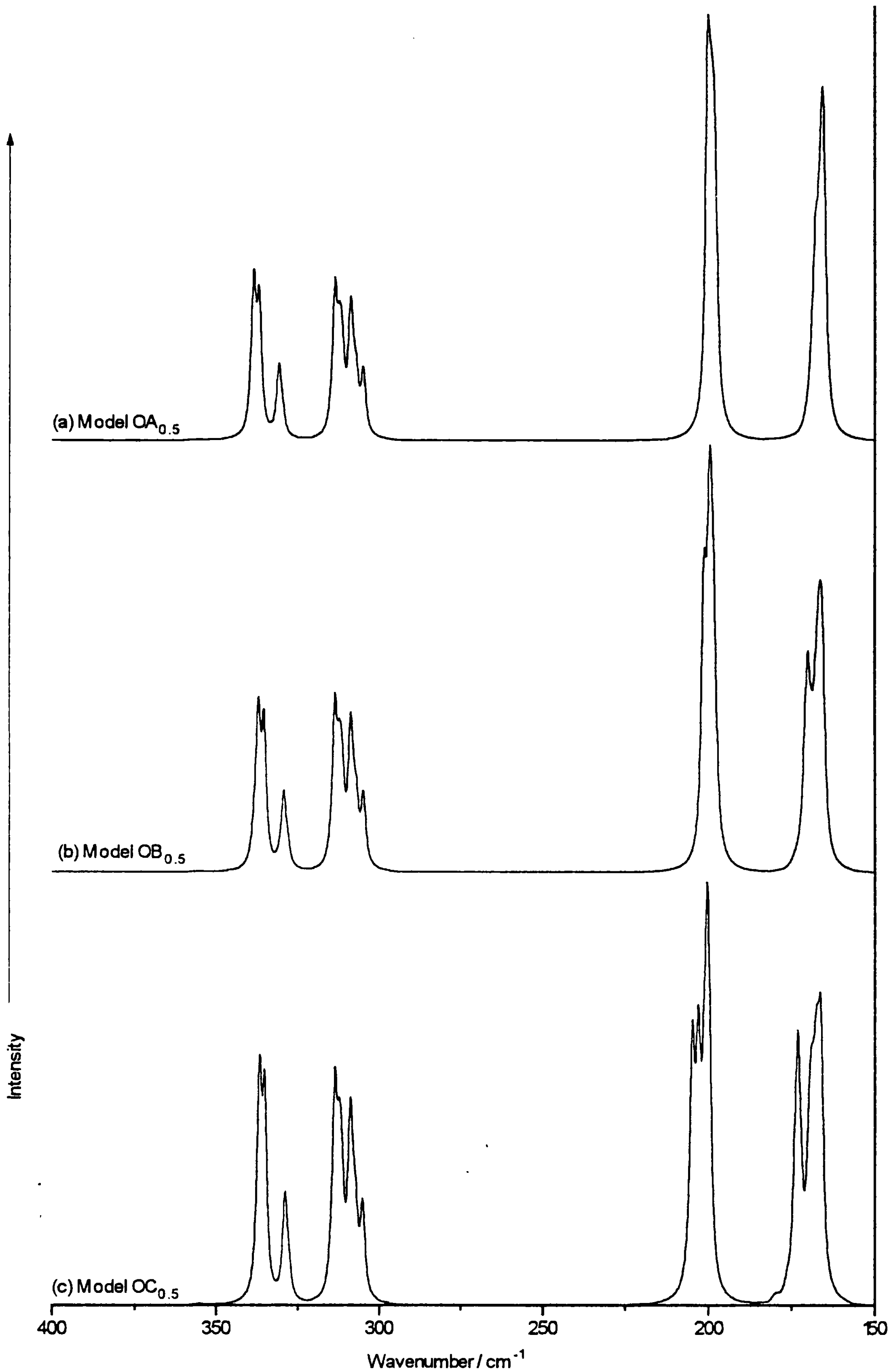

Fgure 4.5.7 Theoretical Raman spectra for $PtBr_{0.5}$ using the models (a) $OA_{0.5}$, (b) $OB_{0.5}$ and (c) $OC_{0.5}$.

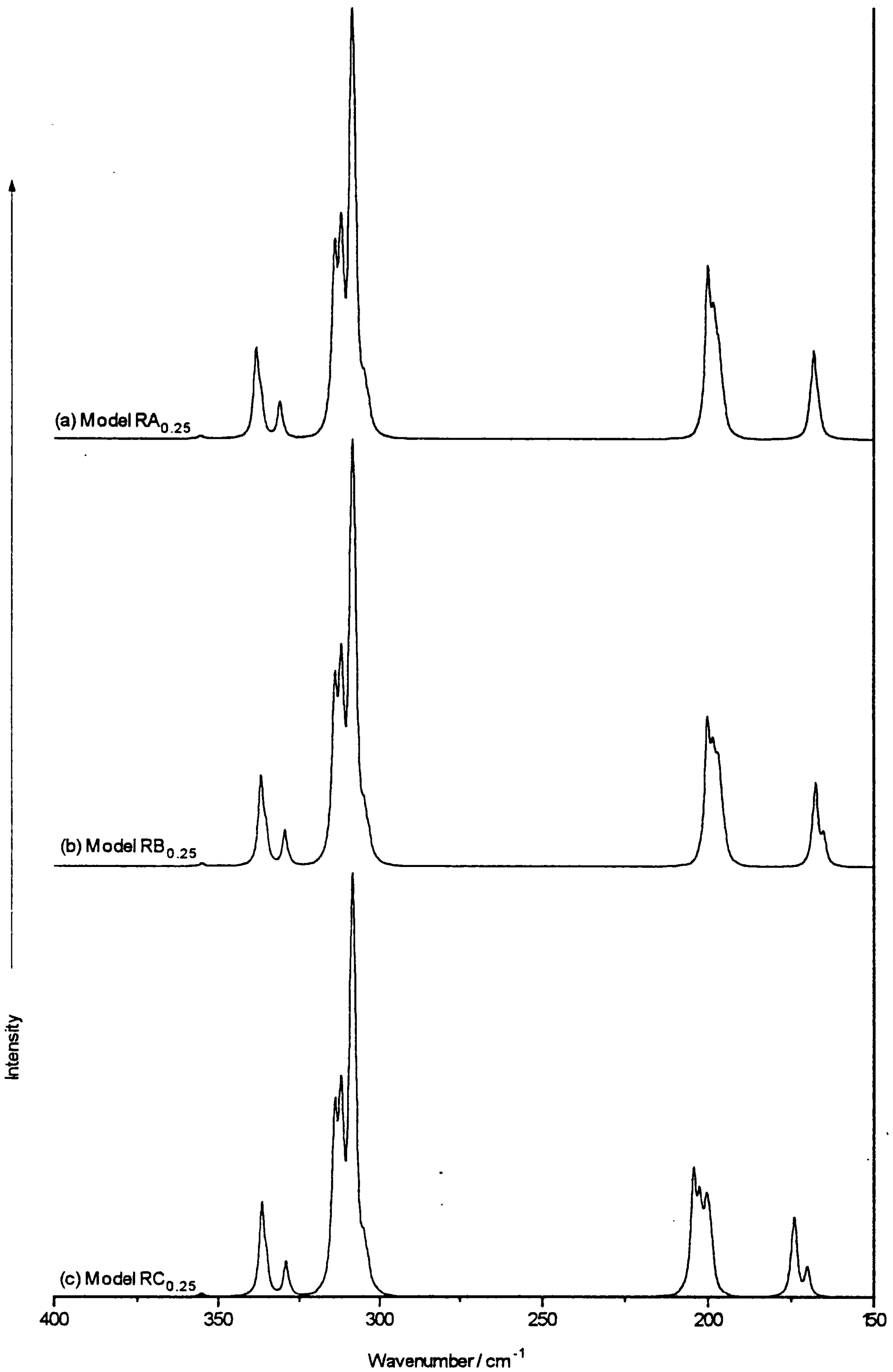

Figure 4.5.8 *Theoretical Raman spectra for $PtBr_{0.25}$ using the models (a) $RA_{0.25}$, (b) $RB_{0.25}$ and (c) $RC_{0.25}$.*

4.5.5 The modelling of electronic defects.

The limitations of the simple vibrational modelling technique are exposed by the analysis of electronic defects. The difficulties in creating vibrational models to fit the experimental data for polaron modes have resulted in their abandonment in favour of model Hamiltonians in which the vibrational energy of the HMMC is one component.[100,163] Nevertheless, it is still necessary to assume that the chain buckles when an electron polaron is formed in PtCl so that its vibrational frequency is lower than that of the hole polaron. In this section polarons are modelled as point charges by inserting a Pt^{III} centre into an existing chain (only PtCl and PtBr are examined). A Pt^{IV} centre is replaced to give an electron polaron (e^-), whilst a Pt^{II} centre is replaced to give a hole polaron (h^+). For the analyses to be carried out, the Pt^{III}-X bond length and certain new force constants (see Figure 4.5.9) must be defined. The long range forces that are the equivalents of k_6 (not shown) are given the same value as k_6 in all cases, and both k_9 and k_{10} are set equal to k_5. k_5 has the same value in PtCl and PtBr, as does k_6, but k_8 is defined as the mean of k_{3c} and k_{4c} or k_{3b} and k_{4b}, depending on which HMMC is analysed. The only parameter that is free to be varied is k_7, the strength of the Pt^{III}-X bond.

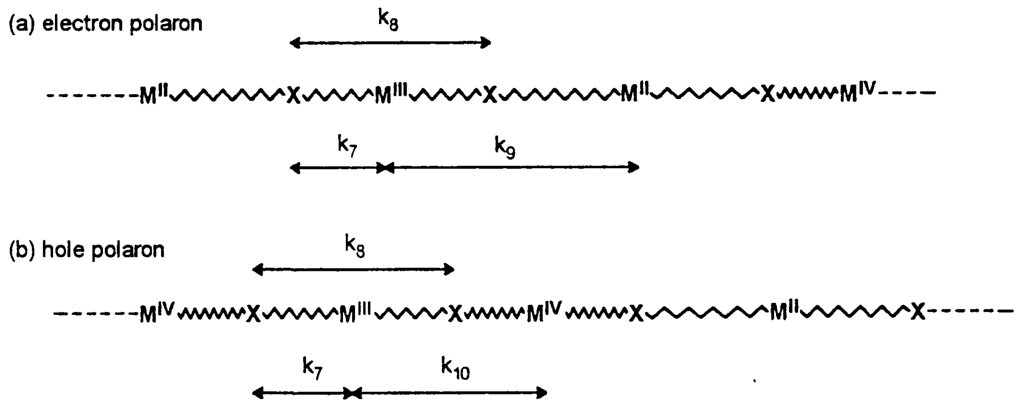

Figure 4.5.9 A diagram showing the new force constants that need to be defined for modelling polaron defects.

PtCl is easier to study than PtBr because its defect modes are better understood and because the excitation wavelengths that enhanced them are more accessible with the available lasers. A Pt^{III}-Cl distance of 2.66 Å is assumed, a value taken from a previous study.[102] The experiment models are very simple and involve a single polaron in a long segment of "normal" chain. The electron polaron is thought to occur at *ca.* 265 cm^{-1} and the hole polaron at *ca.* 285 cm^{-1},[57,102] but no value of k_{7c} will produce the correct wavenumber for the latter. The hole polaron produces four modes because the two [$ClPt^{IV}Cl$] units within the segment [$ClPt^{IV}Cl$-Pt^{III}-$ClPt^{IV}Cl$] can vibrate symmetrically or asymmetrically, and can be either in phase or out of phase with each other. When $k_{7c} \sim (k_{1c} + k_{2c})/2$, the Raman-active symmetric stretches have a vibrational wavenumber in the range 320-340 cm^{-1}. The two asymmetric stretch modes are at 40-100 cm^{-1} higher wavenumber and have a greater dependence both on k_{7c} and on k_{2c}. There are only two vibrational modes associated with the electron polaron. The energy of the symmetric stretch can be adjusted to the proposed value of *ca.* 265 cm^{-1} by making k_{7c} roughly 62 - 70 % (depending on k_{2c}) of the size of k_{1c}. If k_{7c} is made to be 76 - 82 % of the size of k_{1c}, then the defect mode falls at *ca.* 285 cm^{-1}.

The hole polaron modes in $[Pt(en)_2][Pt(en)_2Br_2](ClO_4)_4$ have not been located, but peaks have been assigned to electron polarons (*ca.* 150 cm^{-1}) and electron bipolarons (*ca.* 130 cm^{-1}). k_{7b} can be tuned for each set of force constants to give the required energy for the symmetric stretch of the electron polaron defect mode, and the value found for it can be used to calculate the likely positions of the hole polaron modes. Some examples of this analysis are shown in Table 4.5.7. Significantly, the lowest energy hole defect mode (the most Raman-active) falls in the region where ν_{1b} occurs. ν_{1b} has a large dispersion and so in any given spectrum there may be considerable overlap between the two signals.

Table 4.5.7 Examples of electron and hole polaron defect modes calculated for $[Pt(en)_2][Pt(en)_2Br_2](ClO_4)_4$ for a given value of k_{7b}

Model	k_{2b} / N m^{-1}	k_{1b} / N m^{-1}	k_{7b} / N m^{-1}	Electron polaron (p^-)		Hole polaron (p^+)	
				ν_s / cm^{-1}	ν_{as} / cm^{-1}	ν_s / cm^{-1}	ν_{as} / cm^{-1}
A	0.2	1.303	1.00	148.7	207.7	188.3 199.8	248.1 257.6
B	0.4	1.226	0.95	150.3	210.4	176.1 194.9	239.8 250.3
C	0.6	1.166	0.80	152.0	206.5	157.4 187.4	240.1 *uncertain*

Bipolaron defects are modelled by replacing a Pt^{IV} centre with a Pt^{II} centre, or *vice versa*, and so the only new force constants that need consideration are the longer range ones, which for simplicity can be assigned the same values as in the "normal" chains. The electron bipolaron for PtBr is calculated to give a Raman signal at (A) 89.5, (B) 134.0 or (C) 164.6 cm^{-1} for the three force constant sets. The corresponding values for PtCl are: (A) 125.2, (B) 193.4 or (C) 246.5 cm^{-1}.

4.5.6 The modelling of edge defects

Although edge defects are expected to be rare in HMMCs, and to contribute little Raman intensity, their existence may help explain the presence in the spectra of PtCl of certain weak modes. Two models of chain termination are suggested: (1) the chain is suspended between two very heavy masses, (2) the chain is cyclic with a very large force between the two terminal atoms. The chains are made symmetric about the midpoint for simplicity. Three atoms could be the terminal species: Pt^{II}, Pt^{IV} or Cl-(Pt^{IV}). The two possible models with Pt^{IV} atoms as the termini are shown in Figure 4.5.10; they give the best results. For model (1) the breathing mode of the edge defect has a vibrational wavenumber of 140 cm^{-1}; the corresponding vibration in model (2) is at *ca.* 180 cm^{-1}. Both values are marginally bigger when force constant set C is used instead of set A. When Cl-(Pt^{IV}) atoms are the termini, a defect mode occurs with model (2), although its wavenumber is only *ca.* 100 cm^{-1}. For all these models there are weakly Raman-active asymmetric modes that have vibrational wavenumbers in the range 320-345 cm^{-1}. Pt^{II} termini give rise to no significant defect modes.

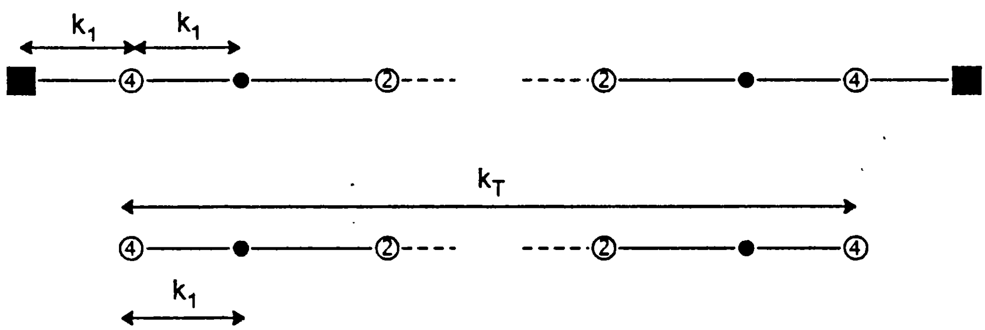

Figure 4.5.10 Depiction of the two types of edge defect model with terminal Pt^{IV} atoms. The black squares represent very heavy masses, and k_T >> k_1.

4.5.7 Discussion

The vibrational modelling experiments were carried out to help determine the origin of the peaks seen in the Raman spectra of HMMCs. The extent of the study is limited by the size of the models used and the accuracy of the experimental data. Vibra90 supports molecular simulations involving fifty atoms or fewer, so it is impractical to analyse anything other than simple one-dimensional chains. Infrared spectra are of little value because most of the signals that are of interest overlap with ligand or counterion modes, and in some cases are obscured by them. The Raman spectra recorded for $PtBr_{0.0}$ and $PtBr_{1.0}$ are of good quality, but the peaks in the spectra of mixed-halide HMMCs are often poorly defined. An additional complication is the dispersion of modes in the Raman spectra of HMMCs. However, the analysis of ν_{1c} modes is straightforward because they are not in resonance at wavelengths longer than 500 nm. To obtain equivalent results for ν_{1b} requires excitation energies much lower than those possible with the lasers available. The FT-Raman spectrometer has a 1064 nm Nd : YAG laser, but it lacked the apparatus for low temperature analysis of crystals.

Vibrational modelling has been applied successfully to the analysis of the ν_1 and ν_2 modes for the HMMC $[Pt(en)_2][Pt(en)_2Cl_2](ClO_4)_4$. The simulation of the ν_{1c} signal is almost exact with any one of the three sets of force constants used (see Figure 4.5.3). The models show that ν_{2c} appears in Raman spectra as a weak resonance at *ca.* 355 cm^{-1} owing to the asymmetric stretch of the mixed-isotope unit -Cc-. It is harder to be confident about the results of modelling the spectra of $[Pt(en)_2][Pt(en)_2Br_2](ClO_4)_4$ because of the lack of suitable data. The wavenumbers for ν_{1b} and ν_{2b} at 647 nm excitation can be reproduced, but there is no simple explanation for the structure of the ν_{1b} mode at shorter excitation wavelengths. *N.B.* The major error caused by the miscalculation of k_1 and k_3 is in the wavenumber of ν_{2b} which is wrong by a maximum of 5 cm^{-1}; neither k_1 nor k_3 has much influence on the dispersion of ν_1 or ν_2. There are other small peaks in the single-crystal Raman spectra of PtCl or PtBr, which relate to the modes ν_T (*et al.*), ν_a, $\delta(PtN_2)$, ν_{dc} and ν_{db} (see Table 4.4.3). The models of chain terminations may provide assignments for the first three. It is possible to create a breathing mode for an edge defect with a wavenumber of *ca.* 180 cm^{-1}, matching that of ν_T. The corresponding asymmetric mode has some Raman activity and is observed at *ca.* 330 cm^{-1}

(*i.e.* close to that for ν_a) whichever model is used. Alternatives to ν_T are given in Table 4.4.3, but the model used in this work gives ν_{3c} a much lower wavenumber, while chain bending cannot be modelled with Vibra90. It is possible that the peak at *ca.* 210 cm^{-1} is also due to a termination mode, but its relative intensity does not vary much with excitation energy nor does it increase when the sample has been pressed to form a disc. The standard assignment of $\delta(PtN_2)$ is accepted in the absence of better options.

Simple vibrational modelling fails to account for the bands assigned to the defect modes in PtCl. ν_{dc} has been attributed to the symmetric stretching mode of a hole polaron,[102] but the model will not predict such a low energy for this vibration for any reasonable value of k_{7c}. In contrast, k_{7b} can be adjusted for each value of k_{2b} so that the wavenumber of the electron polaron is close to 150 cm^{-1}. The corresponding hole polarons are then predicted to occur at slightly higher wavenumbers than ν_{1b}, which may therefore be the reason for the structure of that mode. The only way to have a defect peak in the range 280-290 cm^{-1} for PtCl using this vibrational model is to assign it to the electron polaron. The value of k_{7c} this requires will make the hole polaron appear at *ca.* 330 cm^{-1}, which is the wavenumber of the mode ν_a. However, there is no evidence to support this possibility. A further weakness of these models is that they can give very low wavenumbers for the electron bipolaron Raman modes. A value of 130 cm^{-1} can be derived for PtBr, which matches a suggested assignment for the mode,[105] but for PtCl the bipolaron vibrations are thought to be of similar energy to the related polaron modes.[163] The problems encountered in modelling defect modes for PtCl appear to be due to the ionic nature of the HMMC. It is surprising that the use of a point charge model has more success for PtBr than for PtCl because the charge is more delocalised in the former.

The main part of the discussion concerns the spectra of mixed-halide HMMCs. They differ from a superposition of the spectra of PtCl and PtBr in two important ways: the structures of the ν_{1c} and ν_{1b} signals, and the presence of peaks due to the modes ν_{1m} and ν_{2m}. The ν_{1c} resonance for $[Pt(en)_2][Pt(en)_2Cl_2](ClO_4)_4$ has a distinctive shape that is changed by the introduction of bromine atoms into the chain. The ν_{1c} signals for $PtBr_{0.5}$ at 514 or 568 nm excitation are compared with those predicted for the models $RC_{0.5}$ and $OC_{0.5}$ in Figure 4.5.11 (the simulated plots are very similar for all three force constant sets). The peaks do not match each other exactly because the experimental signals are weak, broad and poorly resolved. Thus it is difficult to favour one type of model over another, although the block copolymer (B) may be discounted. It has a ν_{1c} signal very similar in structure to that for PtCl.

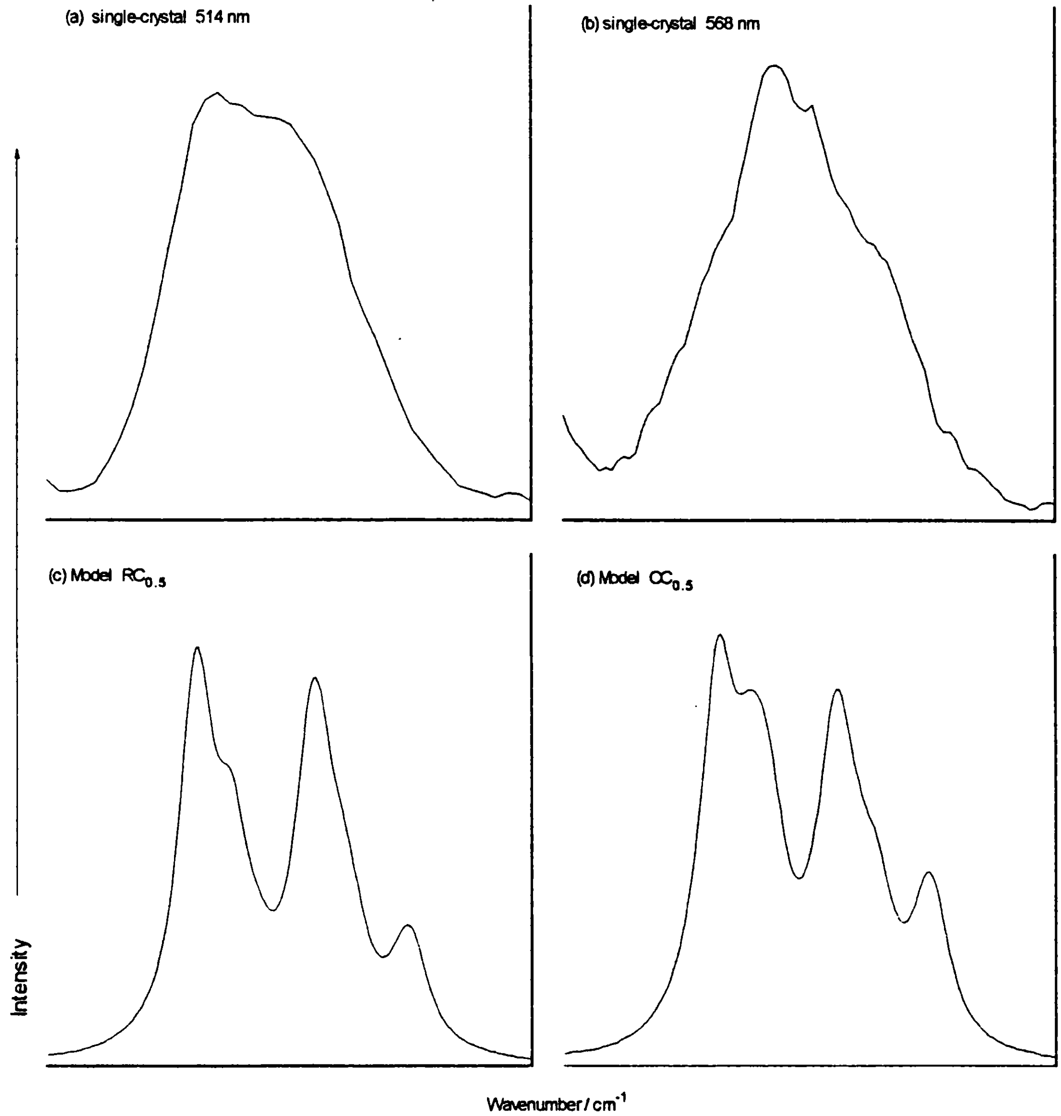

Figure 4.5.11 *Comparison of ν_{1c} Raman signals over a 20 cm^{-1} range: observed for (a), (b) $PtBr_{0.5}$ and predicted for (c) $RC_{0.5}$ and (d) $OC_{0.5}$.*

The variation in the structure of the ν_{1b} signal with exciting line makes it difficult to tell which model has the closest fit (see Figure 4.5.12). The results suggest that k_2 must be larger than 0.4 N m^{-1} (*i.e.* not set A) to account for the peak separation observed at 568 nm excitation. None of the models gives a shoulder at the high wavenumber end of the ν_{1b} signal, and so the spectrum at 647 nm excitation indicates the presence of other modes, such as defect modes.

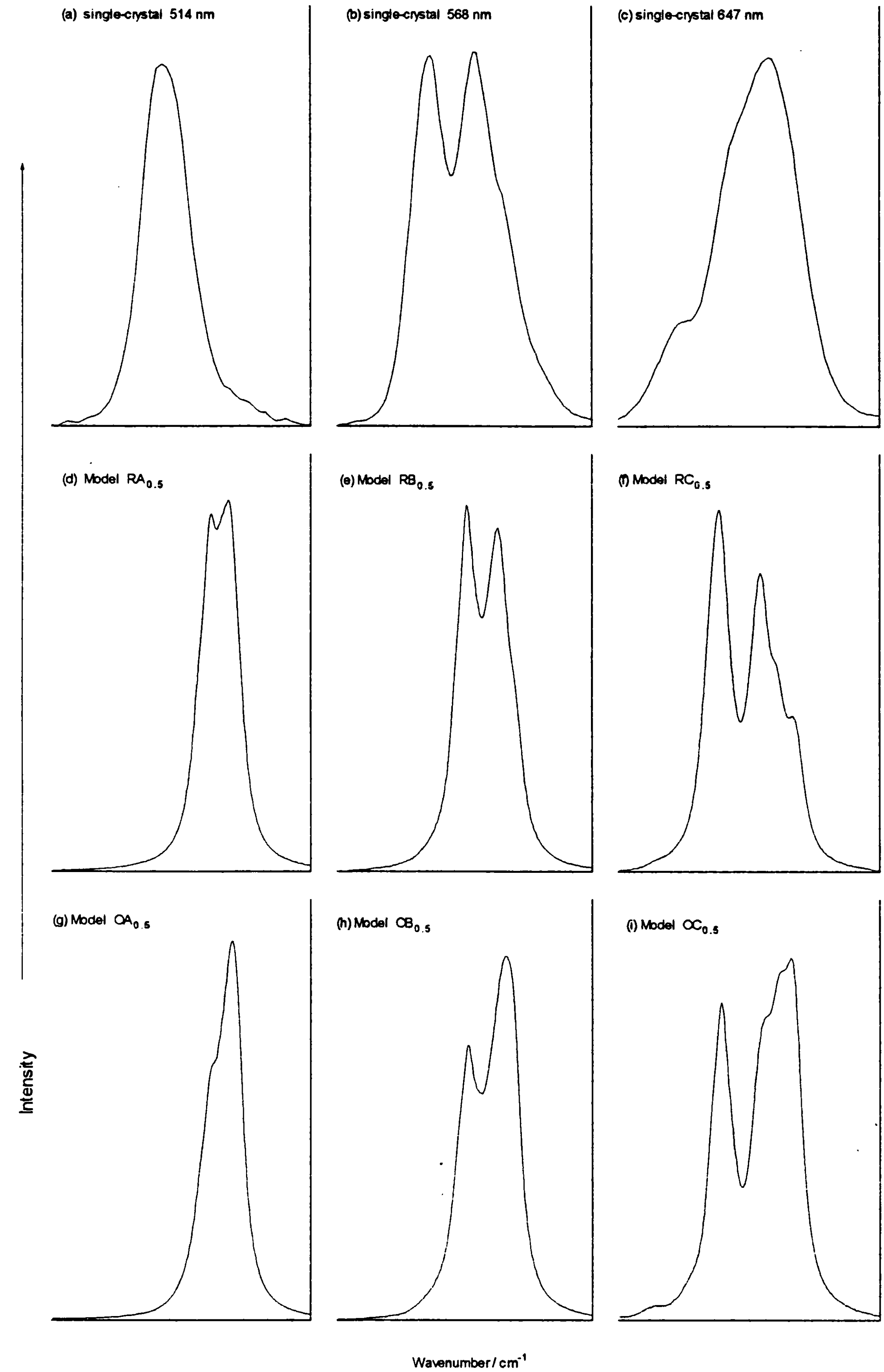

Figure 4.5.12 *Comparison of ν_{1b} Raman signals over a 25 cm^{-1} range: observed for (a) - (c) PtBr$_{0.5}$ and predicted for (d) RA$_{0.5}$, (e) RB$_{0.5}$, (f) RC$_{0.5}$, (g) OA$_{0.5}$, (h) OB$_{0.5}$ and (i) OC$_{0.5}$.*

The ν_{1m} signal for $PtBr_{0.5}$ is a simple solitary peak, but it is not broad enough for a k_2 value as large as 0.6 N m^{-1} (*i.e.* set C) to be considered (see Figure 4.5.13). The resonances predicted by the models $RZ_{0.5}$ and $OZ_{0.5}$ do not differ sufficiently from each other for the superior model to be determined.

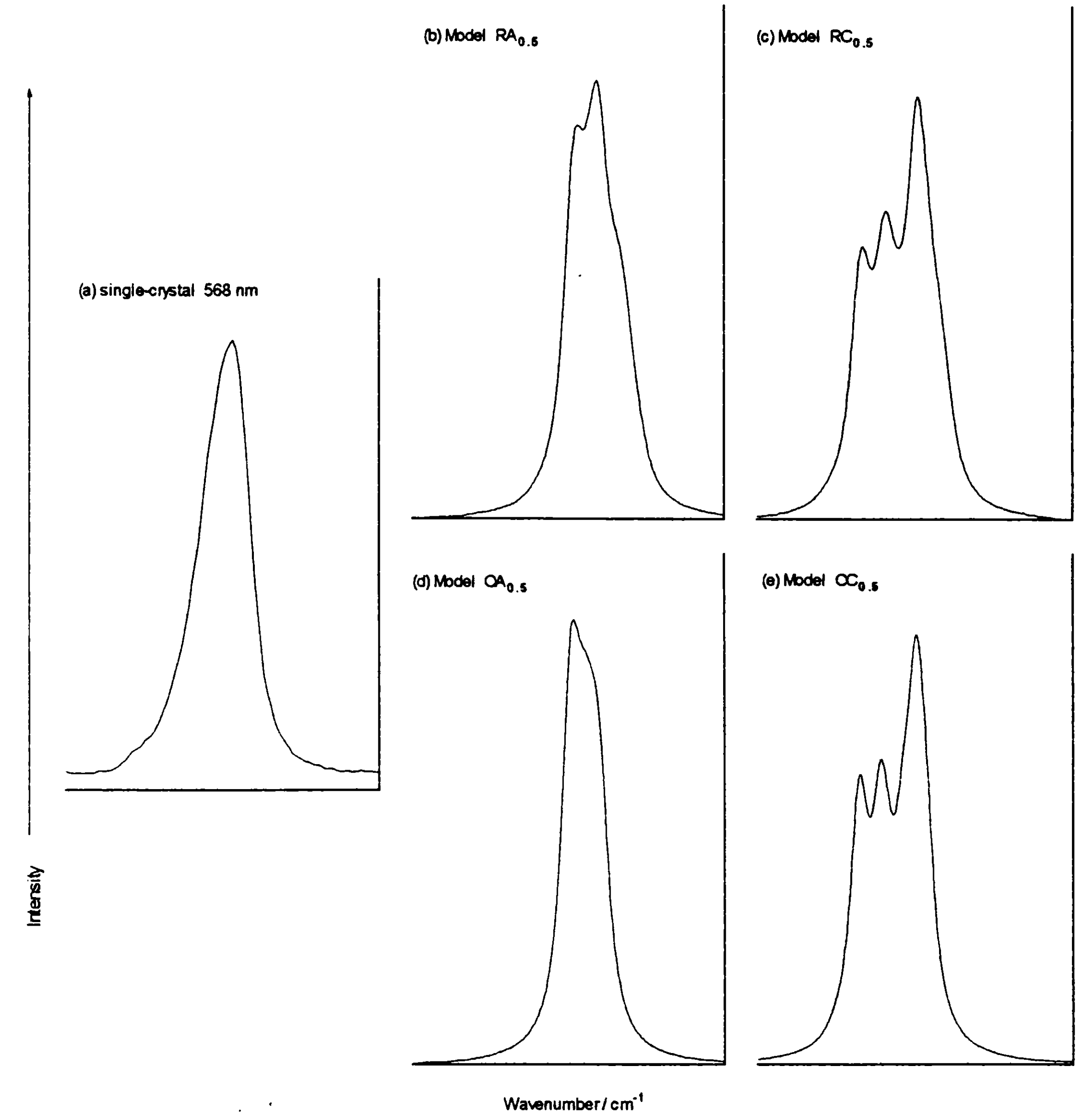

Figure 4.5.13 Comparison of ν_{1m} Raman signals over a 25 cm^{-1} range: (a) observed for $PtBr_{0.5}$ and predicted for (b) $RA_{0.5}$, (c) $RC_{0.5}$, (d) $OA_{0.5}$ and (e) $OC_{0.5}$.

Of the three asymmetric stretches, only ν_{2m} has much intensity in Raman spectra, and even then it is not always clearly defined (see Figure 4.5.14). The simulated spectra show two peaks for the ν_{2m} mode; the larger is due to $\nu_2[^{35}Cl\text{-}Pt^{IV}\text{-}Br]$, the smaller is due to $\nu_2[^{37}Cl\text{-}Pt^{IV}\text{-}Br]$. The experimental results do not match the theoretical ones very closely. $\nu_2[^{35}Cl\text{-}Pt^{IV}\text{-}Br]$ is observed, but the peak for the other chlorine isotope cannot be identified. It may be hidden within the contour of the ν_{1c} signal or the vibration itself may involve much less motion of the chlorine atoms than was predicted in section **4.5.4**. $RC_{0.5}$ is probably the more accurate model because the narrow main peak is unlikely to consist of the two peaks that model $OC_{0.5}$ predicts. The shape of the observed resonance indicates that there may be more modes than just ν_{2m} contributing to the intensity. Possibilities include the asymmetric stretch of an edge defect, or the breathing mode of some point charge defect sited on a [ClPt^{IV}Cl] unit.

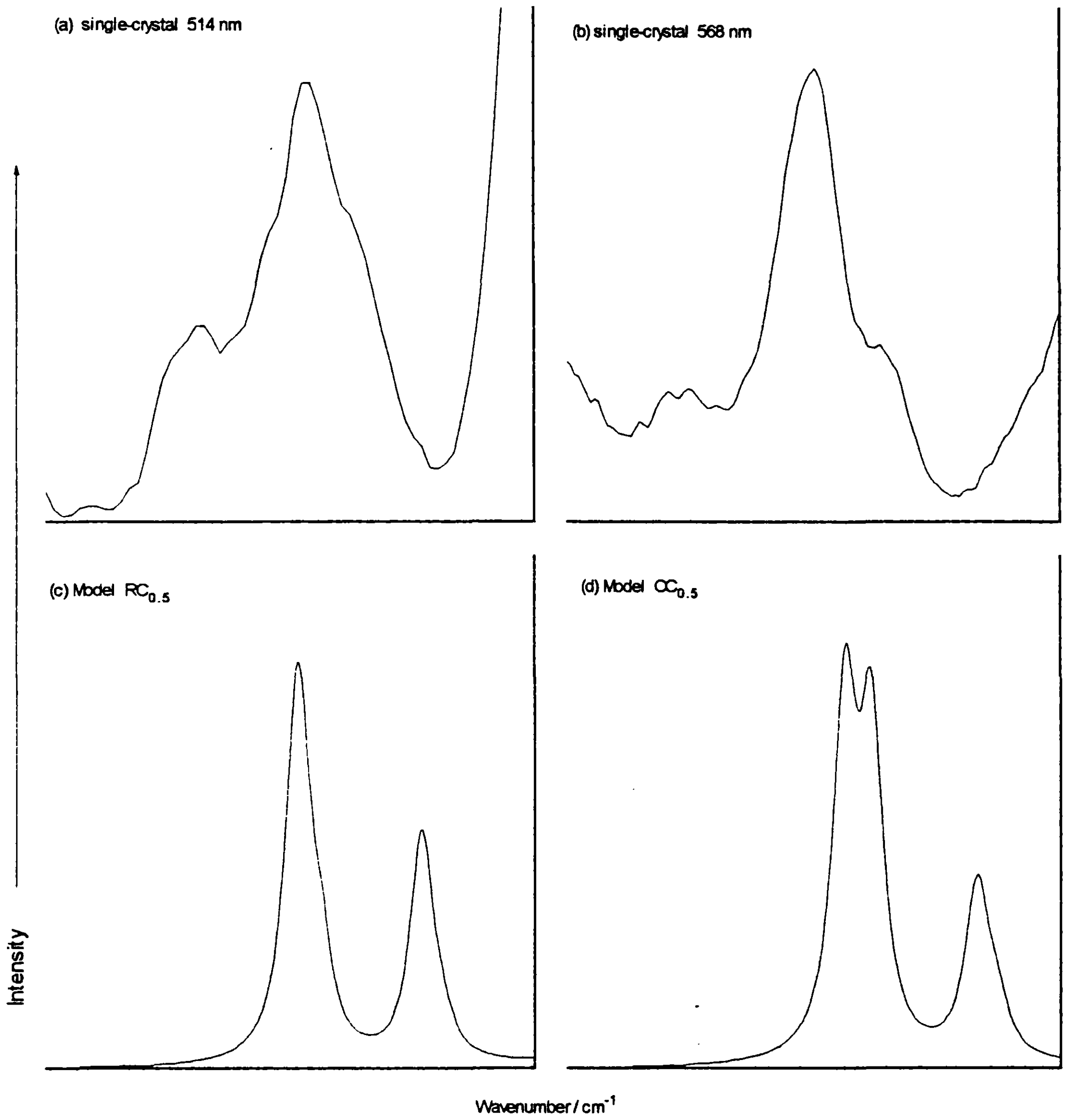

Figure 4.5.14 Comparison of ν_{2m} Raman signals over a 30 cm^{-1} range: observed for (a), (b) $PtBr_{0.5}$ and predicted for (c) $RC_{0.5}$ and (d) $OC_{0.5}$.

The third model to be analysed was $RZ_{0.25}$ (Z = A, B or C). The corresponding $OZ_{0.25}$ models were not investigated because the results for the complex $PtBr_{0.5}$ showed that spectra for the R and O models are either similar or imply that the R model is more accurate. The

Raman spectra for $PtBr_{0.25}$ are compared with those predicted by $RZ_{0.25}$ in Figures 4.5.15-17. The ν_{1c} signal is shown in Figure 4.5.15 next to that for $RC_{0.25}$ ($RA_{0.25}$ and $RB_{0.25}$ are similar); there is reasonable agreement between them.

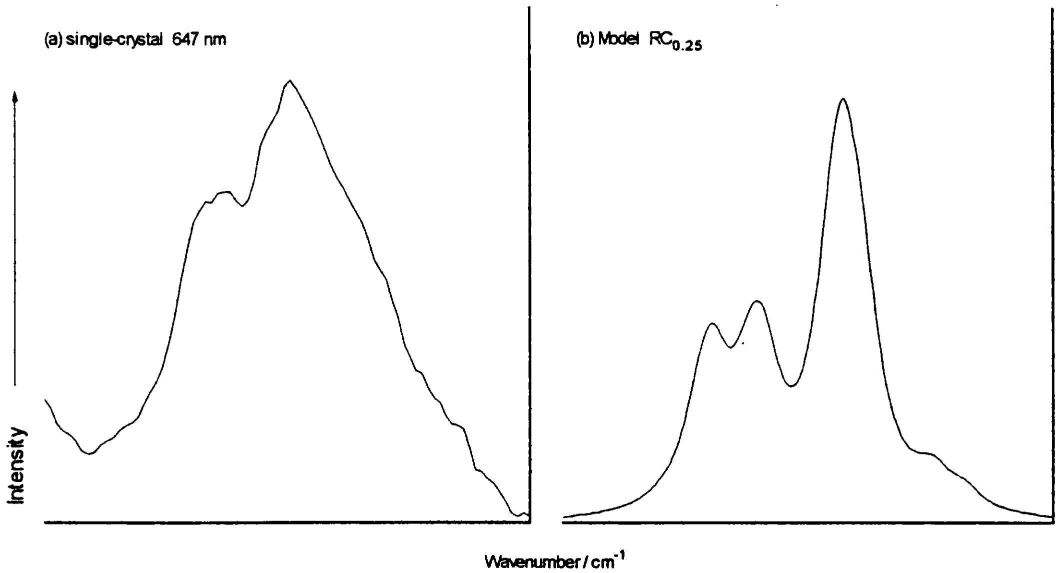

Figure 4.5.15 Comparison of ν_{1c} Raman signals over a 20 cm^{-1} range: (a) observed for $PtBr_{0.25}$ and (b) predicted for $RC_{0.25}$.

The ν_{1b} signal for $PtBr_{0.25}$ has a complicated relationship with excitation energy that makes the determination of the best set of force constants difficult (see Figure 4.5.16); this mirrors the results for $PtBr_{0.5}$. In addition, the correlations between modelled and observed ν_{1b} signals match those for $PtBr_{0.5}$. $RA_{0.25}$ is similar to the spectrum at 514 nm excitation, while $RB_{0.25}$ is similar to that at 568 nm excitation. The spectrum for 647 nm excitation again defies explanation in terms of conventional modes, and appears to contain substantial defect mode intensity. On the basis of the wavenumber of the peak alone, suggested defects are the hole polaron for $[BrPt^{IV}Br]$ or the electron polaron for $[ClPt^{IV}Br]$. The model $RA_{0.25}$ is rejected because it cannot account for any spectra, save for that at 514 nm excitation. Therefore k_2 must be bigger than 0.2 N m^{-1}.

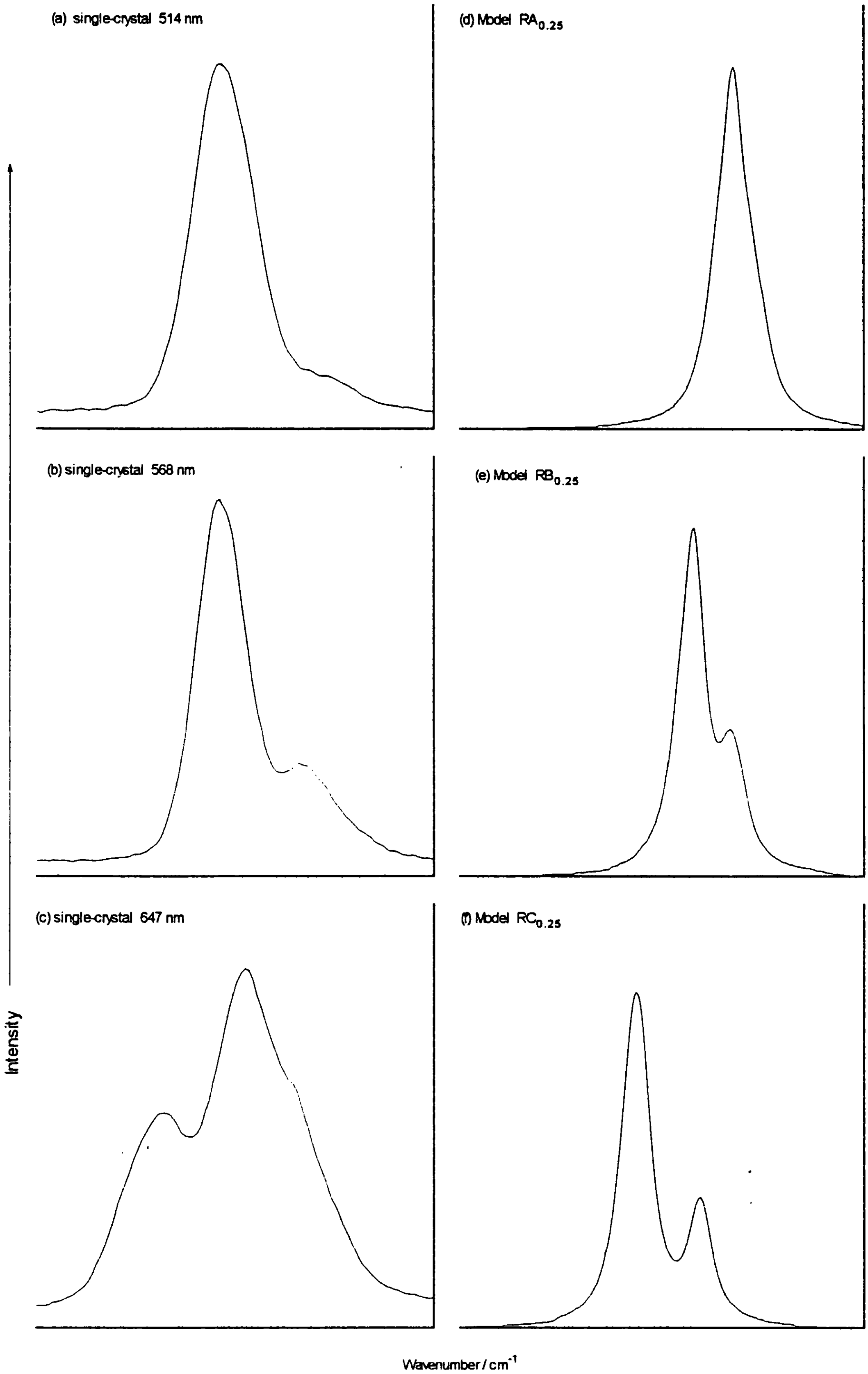

Figure 4.5.16 *Comparison of ν_{1b} Raman signals over a 25 cm^{-1} range: observed for (a) - (c) $PtBr_{0.25}$ and predicted for (d) $RA_{0.25}$, (e) $RB_{0.25}$ and (f) $RC_{0.25}$.*

The ν_{1m} signal is a single broad peak for $PtBr_{0.25}$. Model $RC_{0.25}$ does not reproduce it well (see Figure 4.5.17), which confirms the findings of the analysis into $PtBr_{0.5}$. This establishes that there is an upper limit for the value of k_2 in the vibrational models, so that k_2 probably lies in the region of 0.4 - 0.5 N m^{-1}.

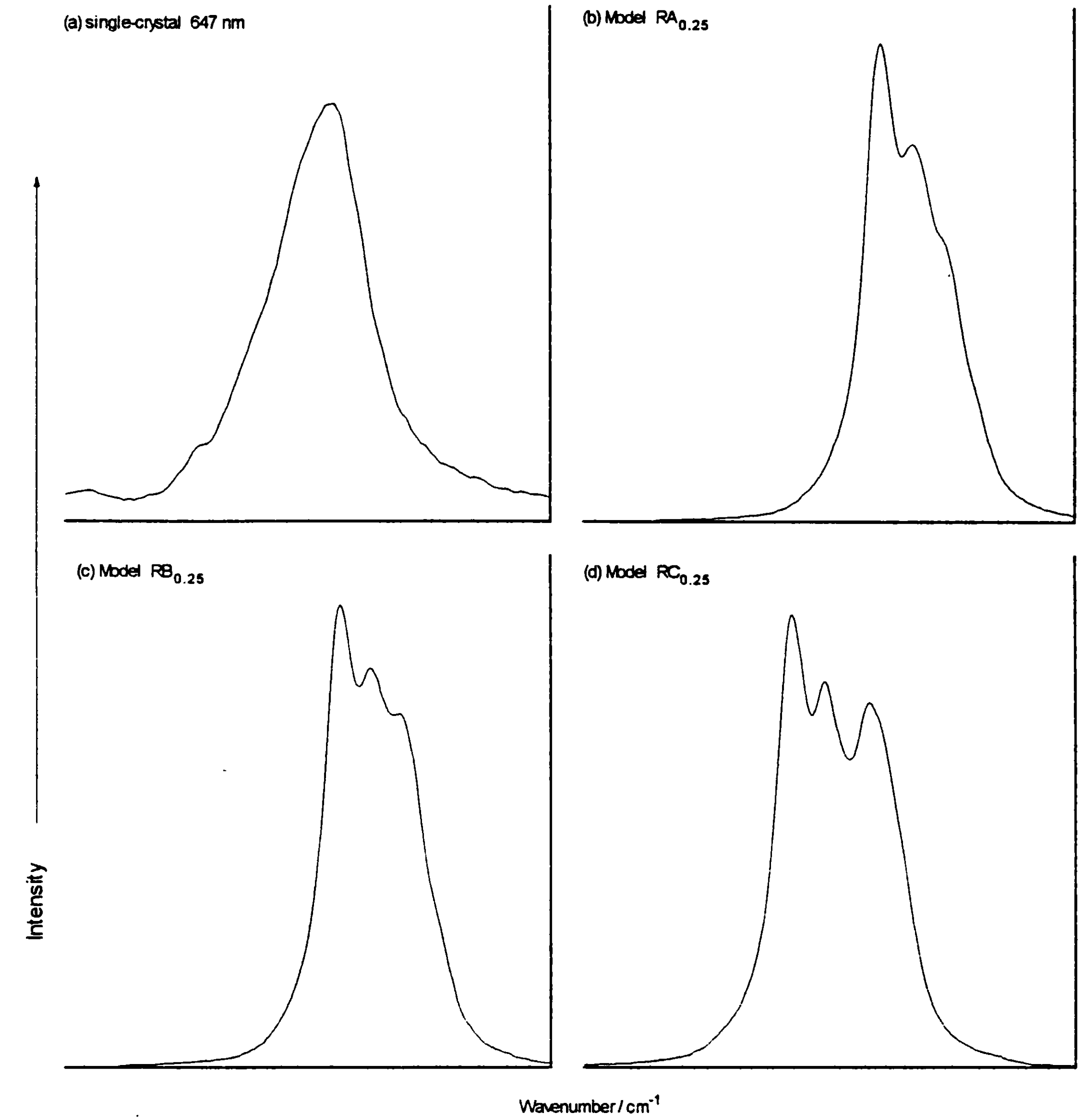

Figure 4.5.17 Comparison of ν_{1m} Raman signals over a 25 cm^{-1} range: (a) observed for $PtBr_{0.25}$ and predicted for (b) $RA_{0.25}$, (c) $RB_{0.25}$ and (d) $RC_{0.25}$.

4.6 Studies of other mixed systems

4.6.1 Mixed-halide HMMCs $[Pt(en)_2][Pt(en)_2Cl_{2-2\alpha}Br_{2\alpha}](BF_4)_4$

If the solid-state ^{15}N NMR results for the mixed-halide perchlorate HMMCs are subject to concern because of the phase changes exhibited, then they can be dispelled by analysis of the corresponding fluoroborate HMMCs, which only have one crystalline form. Unfortunately, the BF_4^- ions broaden the peaks in the solid-state ^{15}N NMR spectra so that they cannot be deconvoluted to the same level of accuracy as the ClO_4^- salts. Previous work has shown that crystals of $[Pt(en)_2][Pt(en)_2X_{2-2\alpha}X'_{2\alpha}](BF_4)_4$ can be grown epitaxially with distinct segments of chloride and bromide chains.[255] The samples in this study were crystallised from solutions containing the desired amounts of $[Pt(en)_2][Pt(en)_2Cl_2](BF_4)_4$ and $[Pt(en)_2][Pt(en)_2Br_2](BF_4)_4$. Only two complexes were made because quantities of the single-halide species were limited. Solutions were prepared to produce HMMCs with theoretical α values of 0.25 or 0.5. Solid-state ^{15}N NMR spectra were recorded for both species (see Figure 4.6.1). The most prominent peaks and their assignments are listed in Table 4.6.1.

Table 4.6.1. ^{15}N chemical shifts and probable assignments for the mixed-halide HMMCs $[Pt(en)_2][Pt(en)_2Cl_{2-2\alpha}Br_{2\alpha}](BF_4)_4$ [a]

Chemical shifts / ppm				Peak assignments
α = 0	α = 0.25	α = 0.5	α = 1	(S = satellite, U = unsplit peak, X-X' = neighbouring halogens)
422	**427a**	**427b**	**423**	
-372.0	-372.0	-372.4		U^{IV}_{Cl-Cl}, S^{IV}_{Cl-Br}
	-375.7	-375.9	-375.4	S^{IV}_{Cl-Cl}, U^{IV}_{Cl-Br}, S^{IV}_{Br-Br}
		-379.1	-379.4	S^{IV}_{Cl-Br}, U^{IV}_{Br-Br}
		-383.7	-383.3	S^{IV}_{Br-Br}, S^{II}_{Br-Br}
	-386.2	-385.4		S^{II}_{Cl-Br}
-387.1				S^{II}_{Cl-Cl}
-391.8	-391.5	-390.1	-388.8	U^{II}_{Cl-Cl}, U^{II}_{Cl-Br}, U^{II}_{Br-Br}
-396.6		-395.1	-394.1	S^{II}_{Cl-Cl}, S^{II}_{Cl-Br}, S^{II}_{Br-Br}

[a] *Chemical shift positions are accurate to ± 0.5 ppm.*

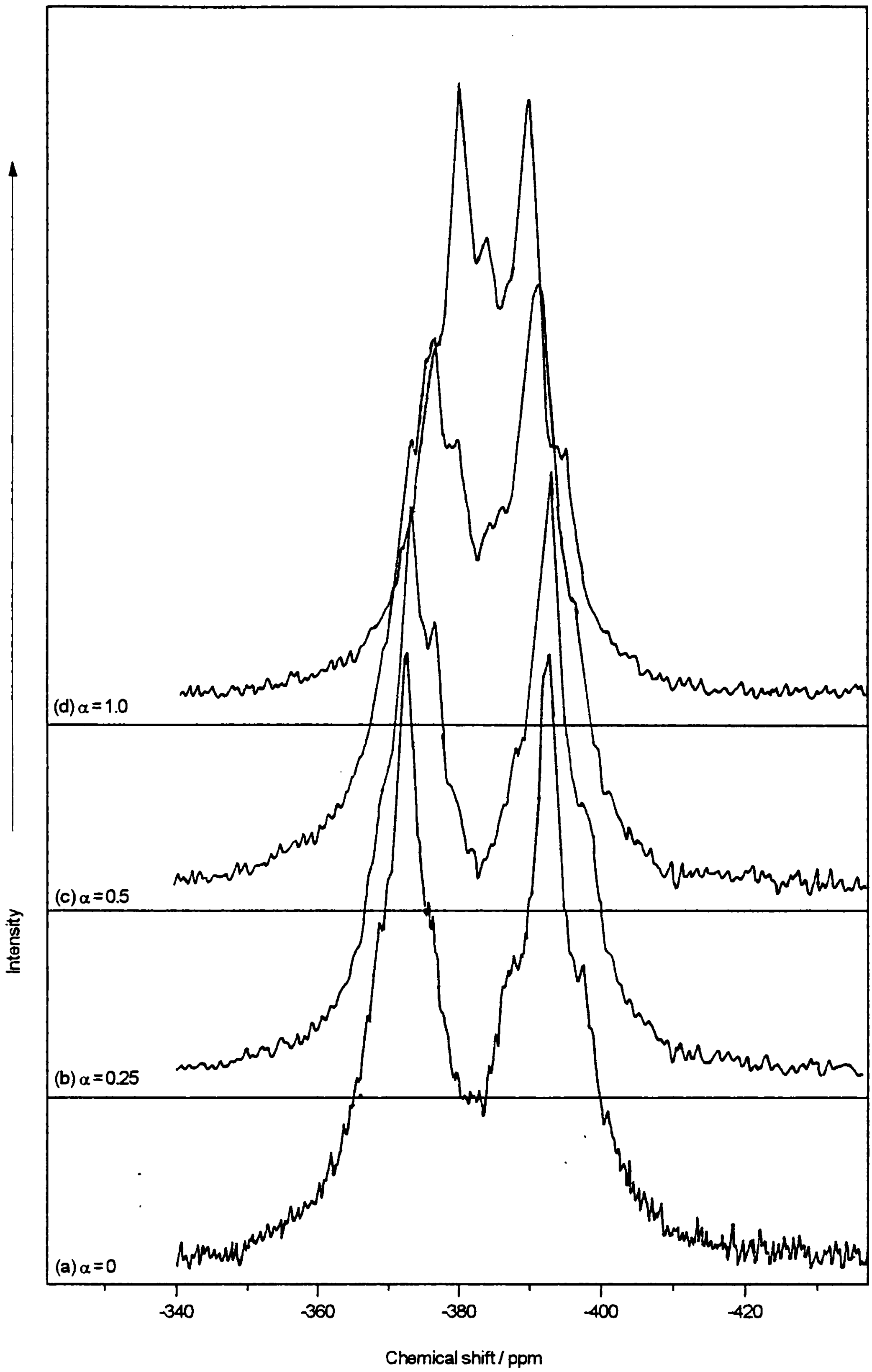

Figure 4.6.1 *Solid-state* ^{15}N *NMR spectra of* $[Pt(en)_2][Pt(en)_2Cl_{2-2\alpha}Br_{2\alpha}](BF_4)_4$, *where (a)* $\alpha = 0$, *(b)* $\alpha = 0.25$, *(c)* $\alpha = 0.5$, *and (d)* $\alpha = 1.0$.

The chemical shifts and intensities of the resonances that comprise the observed peaks are not clearly defined because the signals in the spectra of the BF_4^- complexes are so broad. The proportions of the three types of Pt^{IV} unit cannot be evaluated as they have been in the perchlorate HMMCs, so comparisons with the spectra in Figure 4.4.1 are restricted to general observations. The significant points established in the perchlorate systems are equally true for the fluoroborates. Each spectrum is formed by peaks or satellites (due to particular Pt^{II} or Pt^{IV} units) that have fixed positions but have intensities that depend on the Cl : Br ratio in the chain. In the compound **427b**, the strongest N-Pt^{IV} signal is attributed to [$ClPt^{IV}Br$] units. The position of the N-Pt^{II} resonance appears to vary continuously with bromine content, but this merely reflects which Pt^{II} unit has the largest population.

Raman spectra were recorded for all four fluoroborate HMMCs (see Figures 4.6.2 - 3); peak positions and intensities are listed in Tables 4.6.2-4. Three excitation wavelengths were used. Strong signals were obtained for all samples at 568 nm or 647 nm, but only for **422** and **427a** at 476 nm; the blue light is reflected by the samples with a higher proportion of bromine. Superficially, the results resemble those of the perchlorate complexes and so the same assignments are made where applicable. Closer examination reveals that there are differences in the position, structure or intensity of particular modes. The ν_{1c} signal for PtCl has three main isotopic components that are well resolved, but in ν_{1c} for $[Pt(en)_2][Pt(en)_2Cl_2](BF_4)_4$ the overlap between them is much greater. The -cc- signals appear as a shoulder on the main -cC- peak, but the -CC- resonance cannot be distinguished. This is because the differences between the mean wavenumbers associated with each type of unit are approximately 0.5 cm^{-1} smaller. In the simple vibrational model, the spacings are related directly to the zone centre-defect separation, which can best be controlled by adjusting k_5 (see Tables 4.5.1 - 3). k_1 and k_3 also influence the isotopic dispersion, but they affect other values more, notably the absolute zone centre wavenumbers. The form of the ν_{1c} signal in $[Pt(en)_2][Pt(en)_2Cl_2](BF_4)_4$ corresponds to a value of k_5 that is smaller than that found in the perchlorate. k_5 is a long range force constant and reflects the ligand-counterion structure rather than the electronic properties of the MX chain. The spectra of the mixed-halide species contain signals due to ν_{1c} and ν_{1b}, and some peaks that are absent from those of the starting materials. The mixed-halide modes ν_{1m}

and ν_{2m}, and the polaron signal ν_{dc}, are all observed. Most of the peak positions for the perchlorates are reproduced closely by the fluoroborates, with corresponding vibrations differing by less than 2 cm^{-1}. The discrepancies that are observed between the spectra of the two systems do not challenge the way in which halogen distribution is portrayed in this thesis. There are significant differences between the intensities of both ν_{2m} and the electronic defect modes. In the BF_4^- species, ν_{2m} and ν_{dc} are more enhanced relative to ν_{1c}, but the bromide defect modes are barely visible. The absence of defects on $[BrPt^{IV}Br]$ units is reflected in the structure of the ν_{1b} mode, which has fewer distinguishable peaks when Y = BF_4^-.

Table 4.6.2 Wavenumbers / cm^{-1}, relative intensities and assignments for the bands in the Raman spectra of $[Pt(en)_2][Pt(en)_2Cl_2](BF_4)_4$ [a]

476 nm	568 nm	647 nm	Assignment
185.0 $^{0.03}$	178.0 $^{0.01}$	175.0 ^{wk}	ν_{3c}, ν_T or bend
	184.5 $^{0.01}$	181.0 ^{wk}	ν_{3c}, ν_T or bend
220.5 $^{0.03}$	214.5 $^{0.10}$	212.5 $^{0.02}$	$\delta(PtN_2)$ or ν_T
	286.5 $^{0.02}$	285.0 $^{0.01}$	ν_{dc}
	306.0 $^{0.72}$	304.0 $^{0.75}$	ν_{1c}
312.0 $^{1.00}$	309.5 $^{0.28}$	307.5 $^{0.25}$	ν_{1c}
338.0 $^{0.01}$	333.0 $^{0.02}$	330.5 ^{wk}	ν_a
361.5 $^{0.03}$	358.0 ^{wk}	353.0 ^{wk}	ν_{2c}
	422.0 $^{0.01}$		
496.5 $^{0.06}$	428.5 $^{0.01}$		
526.5 $^{0.02}$	523.5 $^{0.02}$		
585.5 ^{wk}	583.0 $^{0.01}$	580.5 $^{0.01}$	ν(Pt-N)
	607.5 $^{0.01}$	605.5 ^{wk}	$2\nu_{1c}$
618.0 $^{0.61}$	614.0 $^{0.04}$	612.0 $^{0.01}$	$2\nu_{1c}$
	620.0 $^{0.03}$	618.5 ^{wk}	$2\nu_{1c}$

Table 4.6.3 Wavenumbers / cm^{-1}, relative intensities and assignments for the bands in the Raman spectra of $[Pt(en)_2][Pt(en)_2Cl_{2-2\alpha}Br_{2\alpha}](BF_4)_4$ (α = 0.25 or 0.5) [a]

α = 0.25 (**427a**)			α = 0.5 (**427b**)		
476 nm	568 nm	647 nm	568 nm	647 nm	Assignment
		$158.5^{0.01}$			ν_{db}
$184.5^{0.12}$		$172.0^{1.36}$		$172.5^{2.32}$	ν_{1b}
$189.5^{0.06}$	$183.0^{0.56}$	$178.0^{1.51}$	$182.0^{1.76}$	$178.0^{1.61}$	ν_{1b}
$220.0^{1.00}$	$209.5^{1.00}$	$205.0^{1.00}$	$209.5^{1.00}$	$205.5^{1.00}$	ν_{1m}
		229.5^{wk}			ν_{2b}
$293.0^{0.18}$	$285.5^{0.16}$	$283.0^{0.11}$	$285.5^{0.09}$	$284.0^{0.11}$	ν_{dc}
$314.0^{1.86}$	$307.0^{0.30}$	$304.0^{0.37}$	$308.5^{0.21}$	$301.5^{0.12}$	ν_{1c}
	$309.5^{0.26}$				ν_{1c}
$329.0^{0.07}$	$323.5^{0.11}$	$319.5^{0.23}$	$323.0^{0.12}$	$320.0^{0.22}$	ν_a
$338.0^{0.20}$	$330.0^{0.26}$	$326.0^{0.26}$	$329.5^{0.21}$	$326.5^{0.15}$	ν_{2m}
$363.5^{0.06}$	$353.5^{0.03}$	$347.5^{0.53}$	$355.5^{0.18}$	$346.5^{1.27}$	$2\nu_{1b}$
	$367.0^{0.10}$	$358.5^{0.40}$	$363.0^{0.25}$	$357.5^{0.46}$	$2\nu_{1b}$
	$394.5^{0.10}$	$388.0^{0.37}$	$393.0^{0.21}$	$387.5^{0.73}$	$(\nu_{1b} + \nu_{1m})$
$434.0^{0.16}$	$419.0^{0.28}$	$414.0^{0.16}$	$421.0^{0.19}$	$414.0^{0.12}$	$2\nu_{1m}$

Table 4.6.4 Wavenumbers / cm^{-1}, relative intensities and assignments for the bands in the Raman spectra of $[Pt(en)_2][Pt(en)_2Br_2](BF_4)_4$ [a]

568 nm	647 nm	Assignment
$167.0^{1.00}$	$164.0^{1.00}$	ν_{1b}
208.0^{wk}	205.0^{wk}	$\delta(PtN_2)$ or ν_T
$328.0^{0.05}$		$2\nu_{1b}$
$348.5^{0.29}$	$333.0^{0.65}$	$2\nu_{1b}$

[a] *the figures in bold type are the intensities (wk = < 0.01) corrected for spectral response and are relative to ν_{1c} (422), ν_{1m} (**427a** and **427b**) or ν_{1b} (423).*

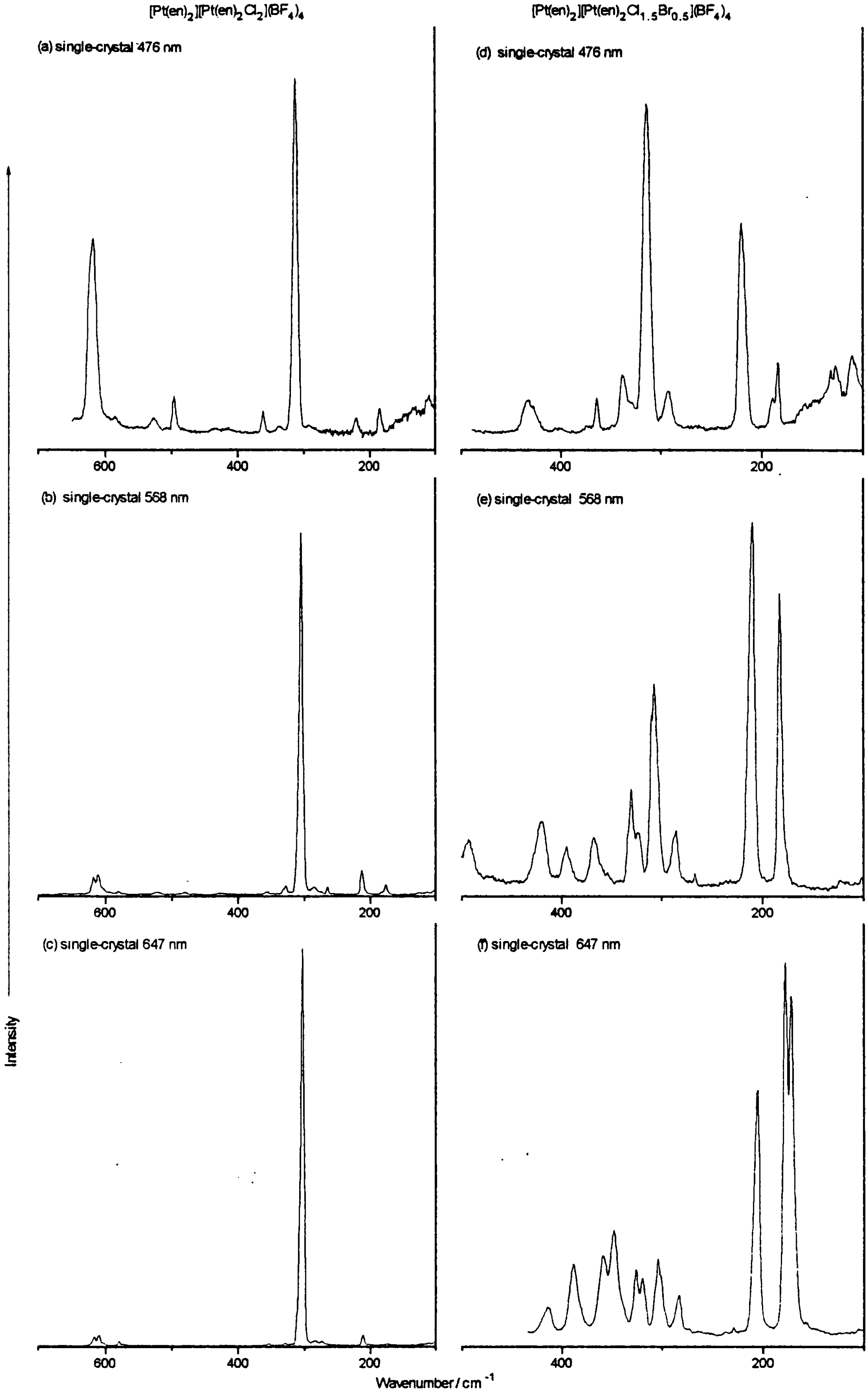

Figure 4.6.2 *Raman spectra of [Pt(en)$_2$][Pt(en)$_2$Cl$_2$](BF$_4$)$_4$ at (a) 476 nm, (b) 568 nm and (c) 647 nm and of [Pt(en)$_2$][Pt(en)$_2$Cl$_{1.5}$Br$_{0.5}$](BF$_4$)$_4$ at (d) 476 nm, (e) 568 nm and (f) 647 nm.*

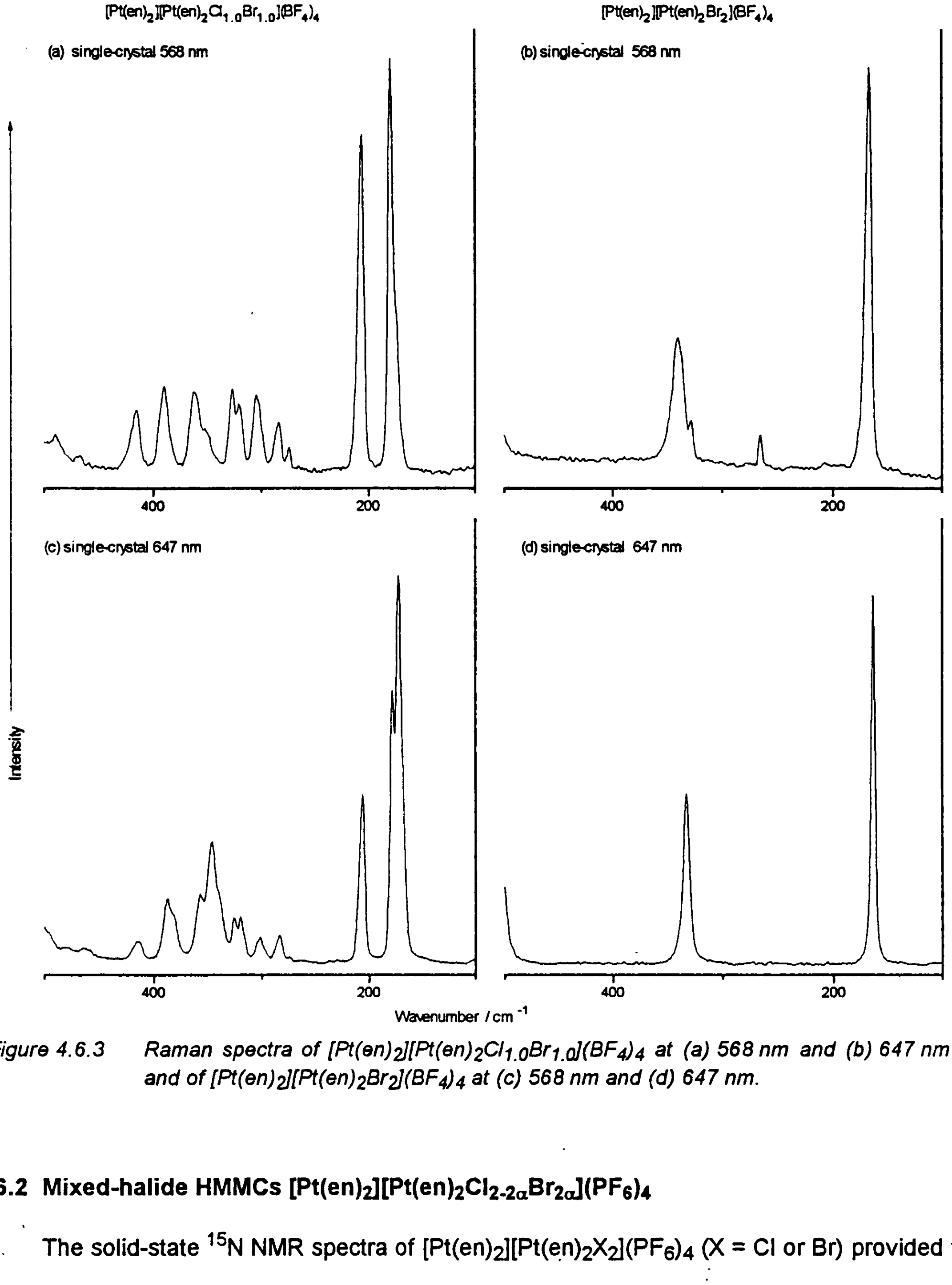

Figure 4.6.3 Raman spectra of $[Pt(en)_2][Pt(en)_2Cl_{1.0}Br_{1.0}](BF_4)_4$ at (a) 568 nm and (b) 647 nm and of $[Pt(en)_2][Pt(en)_2Br_2](BF_4)_4$ at (c) 568 nm and (d) 647 nm.

4.6.2 Mixed-halide HMMCs $[Pt(en)_2][Pt(en)_2Cl_{2-2\alpha}Br_{2\alpha}](PF_6)_4$

The solid-state ^{15}N NMR spectra of $[Pt(en)_2][Pt(en)_2X_2](PF_6)_4$ (X = Cl or Br) provided the most puzzling results of all the analyses carried out on single-halide HMMCs (see section **4.3**). Opaque pale blue crystals of $[Pt(en)_2][Pt(en)_2Cl_{1.0}Br_{1.0}](PF_6)_4$ (**428a**) are produced by mixing these two complexes in equimolar proportions. The solid-state ^{15}N NMR spectra of all three hexafluorophosphate HMMCs are shown in Figure 4.6.4, with the ^{15}N chemical shifts of the observed peaks listed in Table 4.6.5. The spectrum of the mixed-halide complex obeys none of the rules established empirically in the studies of ClO_4^- and BF_4^- species. It is not surprising that anomalous behaviour is observed in the spectrum of the mixed-halide because there is no explanation for the relationship of the peaks in **424** to those in **425**. Peak assignment is limited to the division of the spectrum into regions that contain N-Pt^{II} or N-Pt^{IV} resonances. None of the signals can be attributed to individual unit types because there is little relation between the single- and mixed-halide plots. The solid-state ^{15}N NMR results indicate that the hybrid compound has taken on some of the properties of each starting material. The N-Pt^{II} chemical shifts for **428a** are similar to those for $[Pt(en)_2][Pt(en)_2Cl_2](PF_6)_4$, but the difference between the N-Pt^{IV} and N-Pt^{II} chemical shifts is close to that for $[Pt(en)_2][Pt(en)_2Br_2](PF_6)_4$. The N-$Pt^{IV}$ chemical shifts for **428a** are > 6 ppm upfield of those for **424** or **425**.

Table 4.6.5. ^{15}N chemical shifts and possible assignments for the mixed-halide HMMCs $[Pt(en)_2][Pt(en)_2Cl_{2-2\alpha}Br_{2\alpha}](PF_6)_4$ [a]

α = 0 (424)		α = 0.5 (428a)		α = 1 (425)	
δ_N / ppm	Assignment	δ_N / ppm	Assignment	δ_N / ppm	Assignment
-373.6	U^{IV}_{Cl-Cl}	-379.9	N-Pt^{IV}	-370.9	U^{IV}_{Br-Br}
-386.3	S^{II}_{Cl-Cl}	-381.3		-375.2	S^{II}_{Br-Br}
-391.3	U^{II}_{Cl-Cl}	-389.1	N-Pt^{II}	-379.3	U^{II}_{Br-Br}
-394.3	U^{II}_{Cl-Cl}	-391.7		-383.5	S^{II}_{Br-Br}
-399.7	S^{II}_{Cl-Cl}				

[a] *Chemical shift positions are accurate to ± 0.5 ppm. S = satellite, U = unsplit peak, X-X' = neighbouring halogens.*

Raman spectra were collected for all three HMMCs, using the excitation wavelengths 476, 568 or 647 nm. The spectrum of $[Pt(en)_2][Pt(en)_2Cl_{1.0}Br_{1.0}](PF_6)_4$ has almost no intensity in the region associated with ν_{1c}. This was confirmed by further studies using larger samples of **428a** produced from equimolar mixtures of **424** and **425** made with naturally abundant ^{15}N. A complex with theoretical formula $[Pt(en)_2][Pt(en)_2Cl_{1.33}Br_{0.67}](PF_6)_4$ (**428b**) was also prepared with naturally abundant ^{15}N, so that spectra with some ν_{1c} intensity might be obtained. The Raman spectra of **424**, **425**, **428a** and **428b** are shown in Figures 4.6.5 - 6; peak positions and assignments given in Tables 4.6.6 - 8.

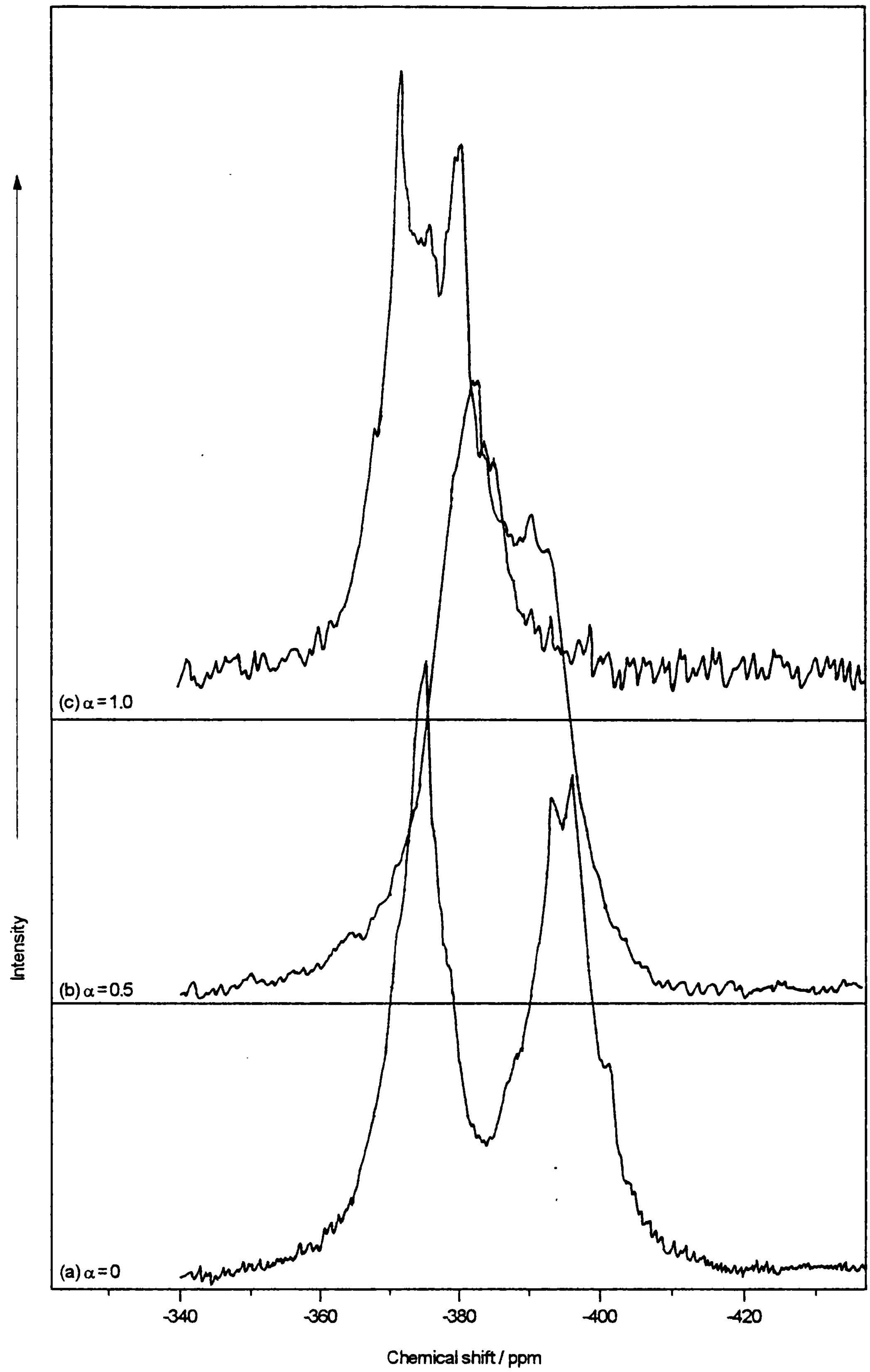

Figure 4.6.4 Solid-state ^{15}N NMR spectra of $[Pt(en)_2][Pt(en)_2Cl_{2-2\alpha}Br_{2\alpha}](PF_6)_4$, where (a) $\alpha = 0$, (b) $\alpha = 0.5$ and (c) $\alpha = 1.0$.

The Raman spectra of $[Pt(en)_2][Pt(en)_2X_2](PF_6)_4$ (X = Cl or Br) are typical of those for cationic chain HMMCs in that they are dominated by a strong ν_{1x} mode but also exhibit weaker signals. The wavenumber of ν_{1b} is similar to ν_{1b} for $[Pt(en)_2][Pt(en)_2Br_2]Y_4$ (Y = ClO_4^- or BF_4^-), but the mean wavenumber of ν_{1c} is appreciably larger than that in the other chloride chains. The properties of the mixed-halide spectra are far more important since they confirm the unusual nature of the hexafluorophosphate HMMCs. The ν_{1c} mode has little intensity in **428b**, and is not observed at all in **428a**. The Raman spectrum of $[Pt(en)_2][Pt(en)_2Cl_{1.0}Br_{1.0}](PF_6)_4$ is very similar to that of $[Pt(en)_2][Pt(en)_2Br_2](PF_6)_4$, even though their solid-state ^{15}N NMR spectra are distinct with almost no coincident intensity. **428b** exhibits more Raman bands than **428a**, but their positions and intensities do not match those for the other mixed-halide species. The most intense signal is ν_{1b}, with both ν_{1c} and ν_{1m} being weaker than expected. The intensity of the polaron mode ν_{dc} relative to ν_{1c} is very large, although this may be due to the weakness of ν_{1c} rather than the strength of ν_{dc}. The difference between the mean wavenumbers of ν_{1c} and ν_{dc} is *ca.* 35 cm^{-1}, which is more than 50 % larger than the values found for the other two systems. The ratio of the intensity of ν_{2m} to that of ν_{1m} is much bigger than it is in related compounds. This might be due to variation in the Raman activities of the modes that stem from changes to the atomic motions in these two vibrations.

Table 4.6.6 Wavenumbers / cm^{-1}, relative intensities and assignments for the bands in the Raman spectra of $[Pt(en)_2][Pt(en)_2Cl_2](PF_6)_4$ [a]

476 nm	568 nm	647 nm	Assignment
185.5 ^{wk}	182.5 ^{wk}	178.0 $^{0.01}$	ν_{3c}, ν_T or bend
224.5 $^{0.01}$	219.5 ^{wk}	216.0 ^{wk}	$\delta(PtN_2)$ or ν_T
292.5 ^{wk}			ν_{dc}
		311.0 ^{sh}	ν_{1c}
323.5 $^{0.58}$	319.5 $^{0.61}$	314.5 $^{0.64}$	ν_{1c}
328.5 $^{0.42}$	323.5 $^{0.39}$	318.5 $^{0.36}$	ν_{1c}
340.0 ^{wk}	337.0 ^{wk}	332.0 ^{wk}	ν_a
364.5 ^{wk}	360.5 ^{wk}	356.5 ^{wk}	ν_{2c}
586.0 $^{0.01}$	582.5 $^{0.01}$	578.5 $^{0.01}$	ν(Pt-N)
	629.5 ^{wk}	624.0 ^{wk}	$2\nu_{1c}$
641.0 $^{0.09}$	637.5 $^{0.02}$	632.0 $^{0.01}$	$2\nu_{1c}$
648.0 $^{0.11}$	645.5 $^{0.02}$	640.0 $^{0.01}$	$2\nu_{1c}$

Table 4.6.7 Wavenumbers / cm^{-1}, relative intensities and assignments for the bands in the Raman spectra of [Pt(en)$_2$][Pt(en)$_2$Cl$_{2-2\alpha}$Br$_{2\alpha}$](PF$_6$)$_4$ (α = 0.33 or 0.5) [a]

α = 0.33 (**428b**)		α = 0.5 (**428a**)			
568 nm	647 nm	476 nm	568 nm	647 nm	Assignment
156.0 ^{wk}	154.0 ^{wk}			148.0 ^{sh}	ν_{db}
180.5 $^{1.00}$	176.5 $^{0.83}$	179.0 $^{0.15}$		163.0 $^{0.60}$	ν_{1b}
	184.0 $^{0.17}$	185.5 $^{0.85}$	173.5 $^{1.00}$	166.0 $^{0.40}$	ν_{1b}
212.5 $^{0.33}$	205.5 $^{0.29}$	217.5 $^{0.04}$	217.5 ^{wk}		ν_{1m}
238.0 ^{wk}		243.0 $^{0.02}$	238.0 ^{wk}		ν_{2b}
275.0 $^{0.01}$					
280.5 $^{0.04}$	278.0 $^{0.04}$				ν_{dc}
313.0 $^{0.12}$	314.0 $^{0.23}$				ν_{1c}
327.0 $^{0.15}$	327.5 $^{0.12}$	331.5 $^{0.01}$	330.0 $^{0.26}$		ν_{2m}
355.5 $^{0.39}$	347.0 $^{0.30}$	357.5 $^{0.22}$	348.0 $^{0.38}$	331.0 $^{0.19}$	$2\nu_{1b}$
360.5 $^{0.32}$		370.5 $^{0.15}$		338.5 $^{0.11}$	$2\nu_{1b}$
394.0 $^{0.20}$	389.0 $^{0.03}$	395.0 $^{0.02}$			$(\nu_{1b} + \nu_{1m})$

Table 4.6.8 Wavenumbers / cm^{-1}, relative intensities and assignments for the bands in the Raman spectra of [Pt(en)$_2$][Pt(en)$_2$Br$_2$](PF$_6$)$_4$ [a]

568 nm	647 nm	Assignment
175.5 $^{1.00}$	166.5 $^{1.00}$	ν_{1b}
215.0 ^{wk}	208.0 ^{wk}	δ(PtN$_2$) or ν_T
354.0 $^{0.46}$	338.0 $^{0.48}$	$2\nu_{1b}$

[a] *the figures in bold type are the intensities (wk = < 0.01) corrected for spectral response and are relative to ν_{1c} (**424**) or ν_{1b} (**428a**, **428b** and **425**).*

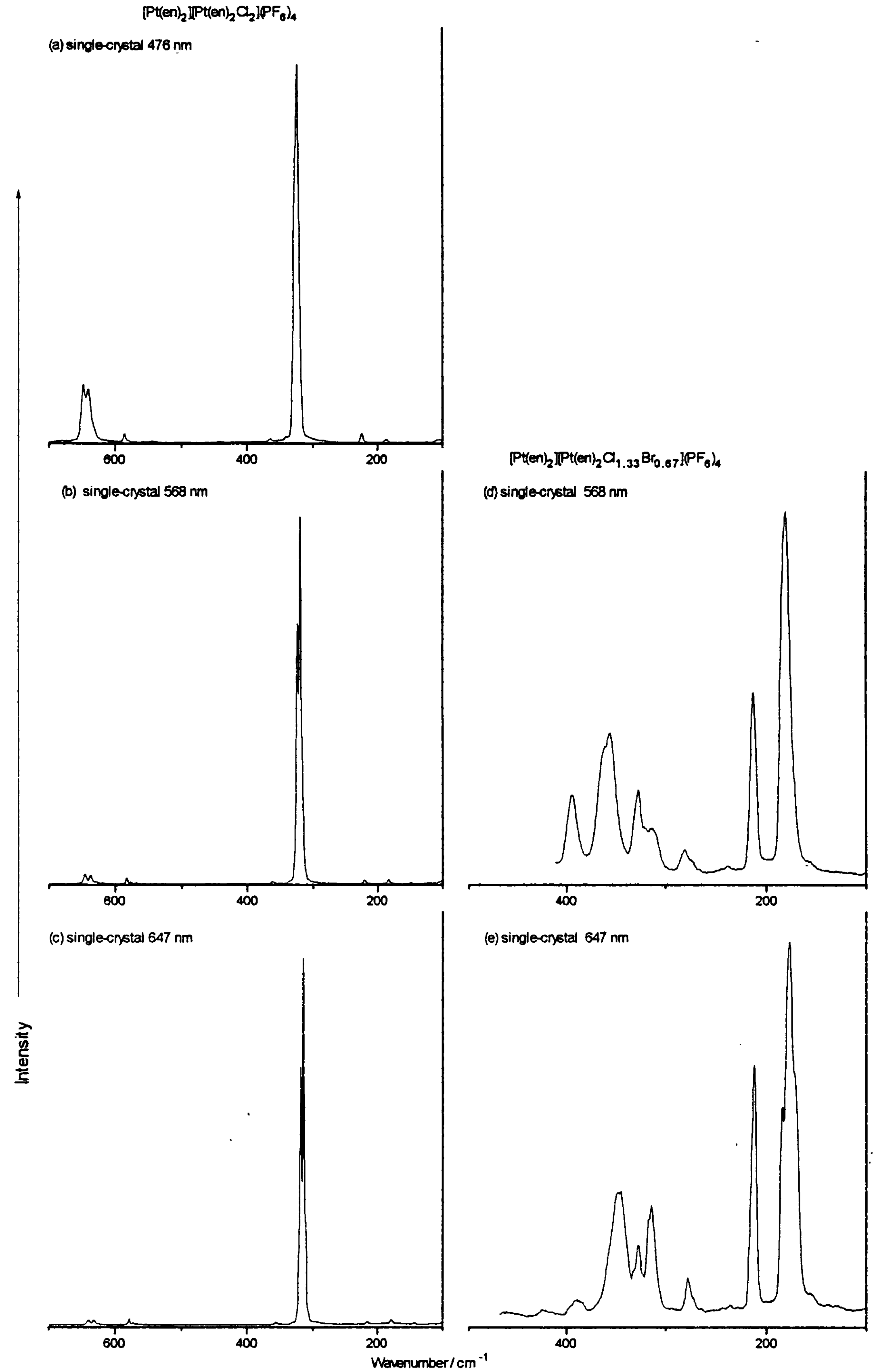

Figure 4.6.5 *Raman spectra of $[Pt(en)_2][Pt(en)_2Cl_2](PP_6)_4$ at (a) 476 nm, (b) 568 nm and (c) 647 nm and of $[Pt(en)_2][Pt(en)_2Cl_{1.33}Br_{0.67}](PF_6)_4$ at (d) 568 nm and (e) 647 nm.*

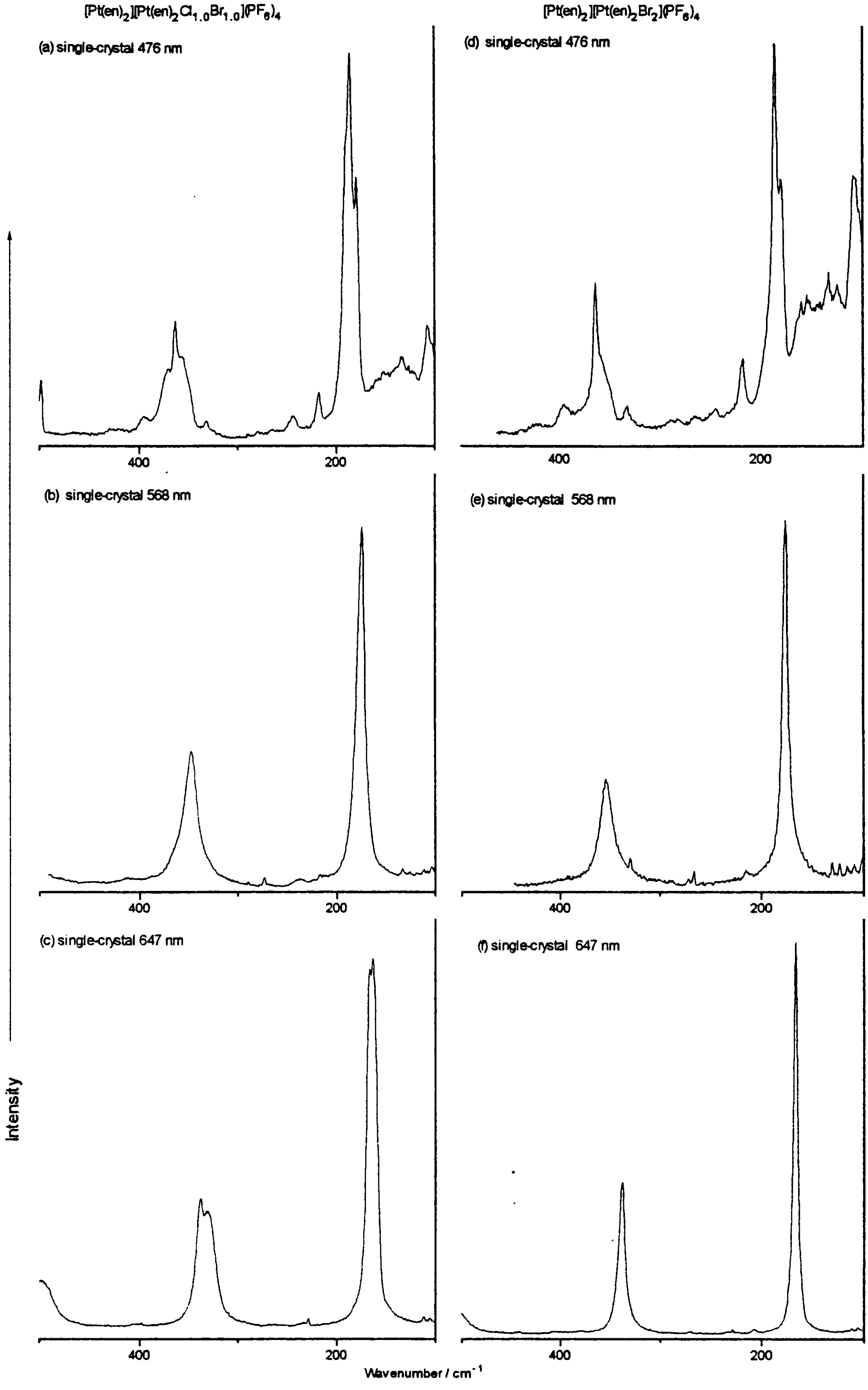

Figure 4.6.6 *Raman spectra of $[Pt(en)_2][Pt(en)_2Cl_{1.0}Br_{1.0}](PF_6)_4$ at (a) 476 nm, (b) 568 nm and (c) 647 nm and of $[Pt(en)_2][Pt(en)_2Br_2](BF_6)_4$ at (d) 476 nm, (e) 568 nm and (f) 647 nm.*

4.6.3 Discussion of the mixed-halide complexes with Y = BF_4^- or PF_6^-

Solid-state ^{15}N NMR and Raman spectroscopic studies were carried out on the species $[Pt(en)_2][Pt(en)_2Cl_{2-2\alpha}Br_{2\alpha}]Y_4$ (Y = BF_4^- or PF_6^-) to provide supporting evidence for the halogen distribution model proposed in section **4.4**. In addition, some results serve to highlight the influence of the counterion on the structure of the HMMCs. For instance, the composition of the ν_{1c} signal in the Raman spectra of $[Pt(en)_2][Pt(en)_2Cl_2]Y_4$ (Y = ClO_4^-, BF_4^- or PF_6^-) is greatly affected by the identity of the counterion. The ν_{1c} profiles recorded for each complex at 568 nm and 647 nm are shown in Figure 4.6.7. Each one is composed of three signals that correspond to the vibrations of the three types of isotopic unit. The shape of ν_{1c} reflects the amount of overlap between these signals. ν_{1c} for PtCl has been simulated and it would be equally simple to do the same for the ν_{1c} modes of the other two chloride HMMCs. For a chain in which all but one chlorine atom is ^{35}Cl, the wavenumber difference between $\nu_1[^{37}Cl\text{-}Pt\text{-}^{35}Cl]$ and $\nu_1[^{35}Cl\text{-}Pt\text{-}^{35}Cl]$ is controlled most effectively by k_5. The force constant k_5 acts between adjacent metal centres across two bonds, *i.e.* $Pt^{IV}\text{-}X\text{-}Pt^{II}$, and has a value of -0.02 N m^{-1} in the models of $[Pt(en)_2][Pt(en)_2Cl_2](ClO_4)_4$. The separation of the ν_{1c} components increases as k_5 decreases and so the counterions can be listed in order of decreasing k_5 value:

$$BF_4^- > ClO_4^- > PF_6^-$$

k_5 may relate to the strength of the ligand-counterion interaction or some manifestation of it, such as the $Pt^{II}\text{-}Pt^{IV}$ distance. The $Pt^{II}\text{-}Pt^{IV}$ distance in $[Pt(en)_2][Pt(en)_2Cl_2](PF_6)_4$ is *ca.* 5.51 Å, which compares with *ca.* 5.43 Å in $[Pt(en)_2][Pt(en)_2Cl_2](ClO_4)_4$; no value has been recorded for $[Pt(en)_2][Pt(en)_2Cl_2](BF_4)_4$.

The distribution of halogens in mixed-halide chains cannot be determined precisely from the solid-state ^{15}N NMR results of $[Pt(en)_2][Pt(en)_2Cl_{2-2\alpha}Br_{2\alpha}](BF_4)_4$, but the shapes of the spectra indicate that it is governed by similar principles to that in the related perchlorates. Furthermore, there are few discrepancies between the Raman spectra of the corresponding BF_4^- and ClO_4^- HMMCs. The results imply that the fluoroborate and perchlorate species are fundamentally the same. However, the mixed-halide hexafluorophosphate complexes show substantially different behaviour.

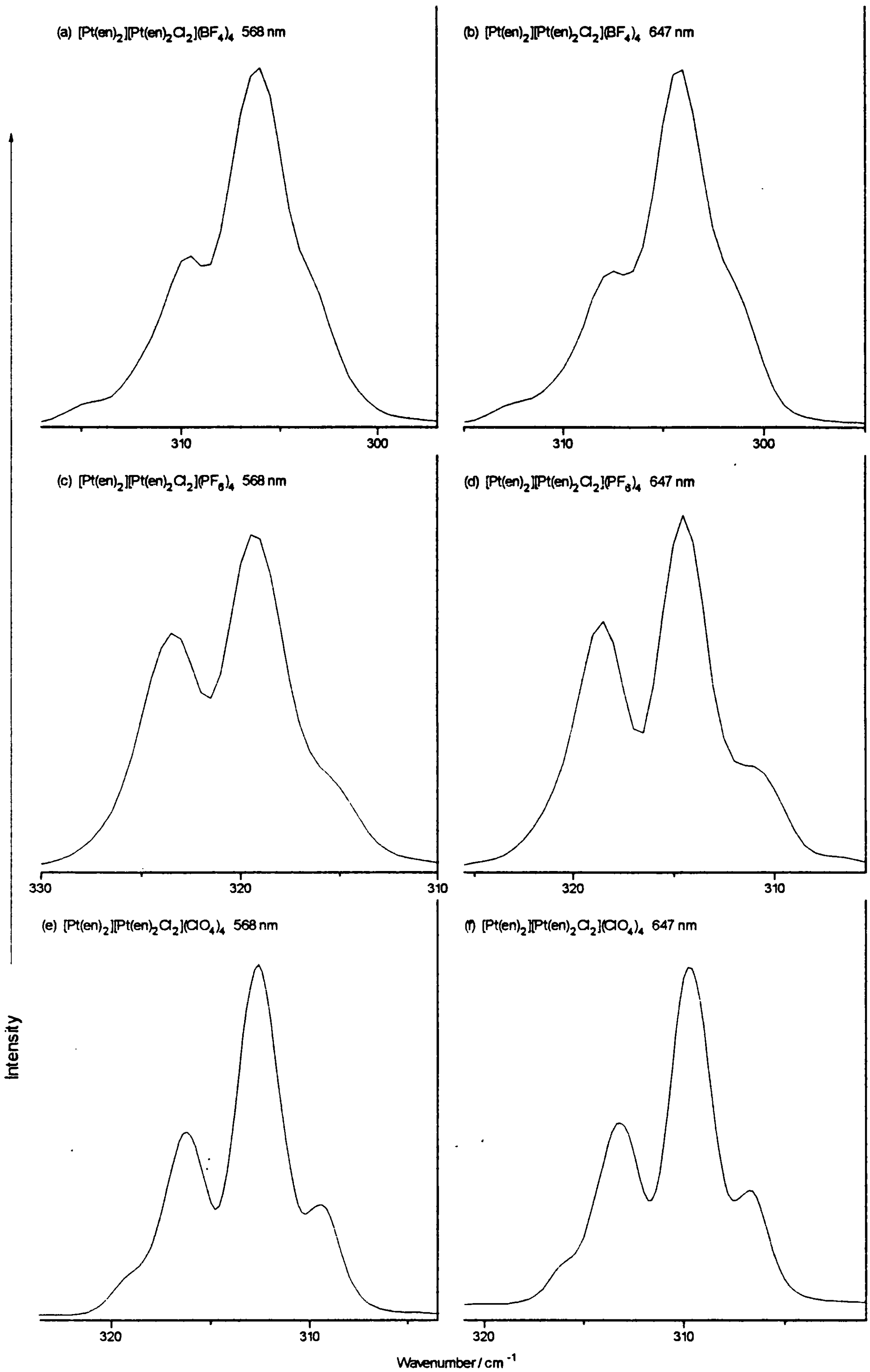

Figure 4.6.7 ν_{1c} signals observed for [Pt(en)$_2$][Pt(en)$_2$Cl$_2$](BF$_4$)$_4$ at (a) 568 nm and (b) 647 nm, for [Pt(en)$_2$][Pt(en)$_2$Cl$_2$](PF$_6$)$_4$ at (c) 568 nm and (d) 647 nm and for [Pt(en)$_2$][Pt(en)$_2$Cl$_2$](ClO$_4$)$_4$ at (e) 568 nm and (f) 647 nm.

The vibrational data for $[Pt(en)_2][Pt(en)_2Cl_{2-2\alpha}Br_{2\alpha}](PF_6)_4$ are very unusual. The ν_{1c} mode has almost no intensity in the Raman spectra of the $[Pt(en)_2][Pt(en)_2Cl_{1.0}Br_{1.0}](PF_6)_4$. There are three possible reasons for this: there are no chlorine atoms present in the complex, or ν_{1c} is not Raman active, or the motion of $[ClPt^{IV}Cl]$ units is strongly coupled to other vibrations. The first suggestion can be discounted because the solid-state ^{15}N NMR spectrum of $[Pt(en)_2][Pt(en)_2Cl_{1.0}Br_{1.0}](PF_6)_4$ does not match that of $[Pt(en)_2][Pt(en)_2Br_2](PF_6)_4$, and because its FT-IR spectrum contains a ν_{2c} signal (see Figure 4.6.8). A simple model that gives the ν_{1c} mode little Raman intensity can be proposed. If the platinum-chlorine segments are vibrationally decoupled from the rest of the chain and then have an effective centre of symmetry, it is possible that the ν_{1c} mode will not be strongly Raman-active. This may mean that the chlorine atoms are midway between the metal centres. This would give a single Pt_{Cl-Cl} signal in the solid-state ^{15}N NMR spectrum, probably at *ca.* -383 ppm, *i.e.* roughly equal to the mean shift of the $N-Pt^{II}$ and $N-Pt^{IV}$ chemical shifts for $[Pt(en)_2][Pt(en)_2Cl_2](PF_6)_4$. The coupling of ν_{1c} to other modes such as ν_{1b} is plausible, although it does not give a clear reason for the small amplitude of the chlorine atom motion that would be required.

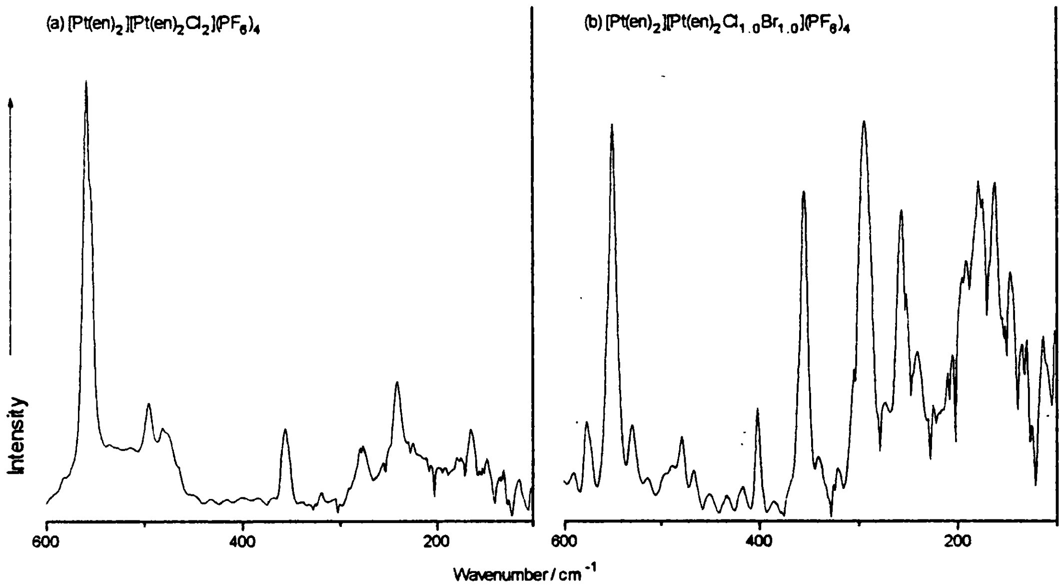

Figure 4.6.8 FT-IR spectra of (a) $[Pt(en)_2][Pt(en)_2Cl_2](PF_6)_4$ and (b) $[Pt(en)_2][Pt(en)_2Cl_{1.0}Br_{1.0}](PF_6)_4$.

4.6.4 Mixed-metal complexes $[M^{II}(en)_2][Pt^{IV}(en)_2X_2](ClO_4)_4$

The optical properties of the mixed-metal linear-chains $[M^{II}(en)_2][Pt^{IV}(en)_2X_2](ClO_4)_4$ (M = Ni or Pd, X = Cl, Br or I) have been studied previously.[35,49-52] The molecular structures that have been resolved for individual crystals show that chains contain alternating M^{II} and Pt^{IV} centres.[34,53] Solid-state ^{15}N NMR spectroscopy can be used to analyse bulk samples to determine whether there is any deviation from this behaviour. The syntheses of the ions $[M^{II}(en)_2]^{2+}$ (M = Ni or Pd) require a large excess of ethylenediamine, so ^{15}N-enriched ligand is used to make the Pt^{IV} monomers alone. $[M^{II}(en)_2](ClO_4)_2$ (M = Ni or Pd) containing ^{15}N nuclei in natural abundance was prepared and then treated with an equimolar amount of ^{15}N-enriched $[Pt^{IV}(en)_2X_2](ClO_4)_2$ (X = Cl or Br) in the presence of $NaClO_4$. Four crystalline products were isolated; $[Ni(en)_2][Pt(en)_2X_2](ClO_4)_4$ forms red or green crystals for X = Cl (**429**) or X = Br (**430**), while $[Pd(en)_2][Pt(en)_2X_2](ClO_4)_4$ forms yellow or red crystals for X = Cl (**431**) or X = Br (**432**). All four complexes were analysed by solid-state ^{15}N NMR spectroscopy. The spectra are shown in Figure 4.6.9 and chemical shifts and coupling constants derived from them are listed in Table 4.6.9. Only one main resonance is observed in each case, with satellites due to ^{15}N-^{195}Pt coupling. Not one of the $J_{N\text{-}Pt}$ coupling constants is greater than 250 Hz, so all signals are attributed to N-Pt^{IV} nuclei; there are no peaks due to N-Pt^{II} nuclei. The N-Pt^{IV} chemical shift is not very sensitive to the identity of the M^{II} centre, or indeed its presence. Amongst the HMMCs, the chemical shift is furthest upfield when the r(M^{II}-Pt) or r(M^{II}-X) distance is largest.

Table 4.6.9 **^{15}N chemical shifts and $J_{N\text{-}Pt}$ values for N-Pt^{IV} in $[M(en)_2][Pt(en)_2X_2](ClO_4)_4$ [a]**

M^{II}	X = Cl				X = Br			
	Label	Crystal colour	δ / ppm	$J_{N\text{-}Pt}$ / Hz	Label	Crystal colour	δ / ppm	$J_{N\text{-}Pt}$ / Hz
none	**414**	yellow	-367.6	235	**417**	yellow	-374.9	250
Ni	**429**	red	-367.9	235	**430**	green	-374.5	240
Pd	**431**	yellow	-368.5	230	**432**	red	-376.0	230
Pt	**419**	red	-369.5	245	**420**	green	-377.6	230

[a] *Chemical shifts are accurate to ± 0.4 ppm. Coupling constants are accurate to ± 40 Hz.*

A mixed-halide variety was made for each mixed-metal complex by preparing a solution with equimolar amounts of $[M(en)_2][Pt(en)_2Cl_2](ClO_4)_4$ and $[M(en)_2][Pt(en)_2Br_2](ClO_4)_4$ and allowing it to crystallise in the presence of $NaClO_4$. Brown crystals were isolated for M = Ni (**433**), and orange crystals for M = Pd (**434**). Solid-state ^{15}N NMR spectra were recorded for each sample; ^{15}N chemical shifts and probable assignments of the prominent signals are given in Table 4.6.10. The spectra show that there are significant populations of the $[ClPt^{IV}Br]$ unit present in the mixed-halide species.

Table 4.6.10 ^{15}N chemical shifts and probable assignments for the mixed-halide HMMCs $[M(en)_2][Pt(en)_2Cl_{2-2\alpha}Br_{2\alpha}](ClO_4)_4$ [a]

Chemical shifts / ppm						Peak assignments
M = Ni			M = Pd			(S = satellite, U = unsplit peak, X-X' = neighbouring halogens)
429	**430**	**433**	**431**	**432**	**434**	
-363.9			-365.0			$S^{IV}_{Cl\text{-}Cl}$
-367.9	-367.6		-368.5	-368.5		$U^{IV}_{Cl\text{-}Cl}$, $S^{IV}_{Cl\text{-}Br}$
-371.8	-371.4	-370.6	-372.6	-371.4		$S^{IV}_{Cl\text{-}Cl}$, $U^{IV}_{Cl\text{-}Br}$, $S^{IV}_{Br\text{-}Br}$
	-374.4	-374.5		-375.3	-376.0	$S^{IV}_{Cl\text{-}Br}$, $U^{IV}_{Br\text{-}Br}$
		-378.5				$S^{IV}_{Br\text{-}Br}$

[a] *Chemical shift positions are accurate to ± 0.5 ppm.*

4.6.5 Discussion

The study of the mixed-metal complexes demonstrates two important results. Firstly, all the platinum sites in the species $[M(en)_2][Pt(en)_2X_2](ClO_4)_4$ (M = Ni or Pd, X = Cl or Br) are in an oxidation state of +4. If it assumed that the oxidation of $[M^{II}(en)_2]^{2+}$ to $[M^{IV}(en)_2X_2]^{2+}$ will only occur through a redox reaction with $[Pt(en)_2X_2]^{2+}$ ions, then it is also possible to say that the number of $[M^{IV}(en)_2X_2]$ units present in the chain is negligibly small. The second result concerns the formation of mixed-halide species. It has been shown already (see section **4.4**) that the scrambling of axial halogens on Pt^{IV} sites can occur in the absence of Pt^{II} ions. The mixed-halide units $[ClPt^{IV}Br]$ may also be produced when the only M^{II} species present in solution are Ni^{II} or Pd^{II} ions. It is unlikely that the M^{II} species (M = Ni or Pd) play any part in the reaction, because if they did one would expect some of the Pt^{IV} ions to be reduced.

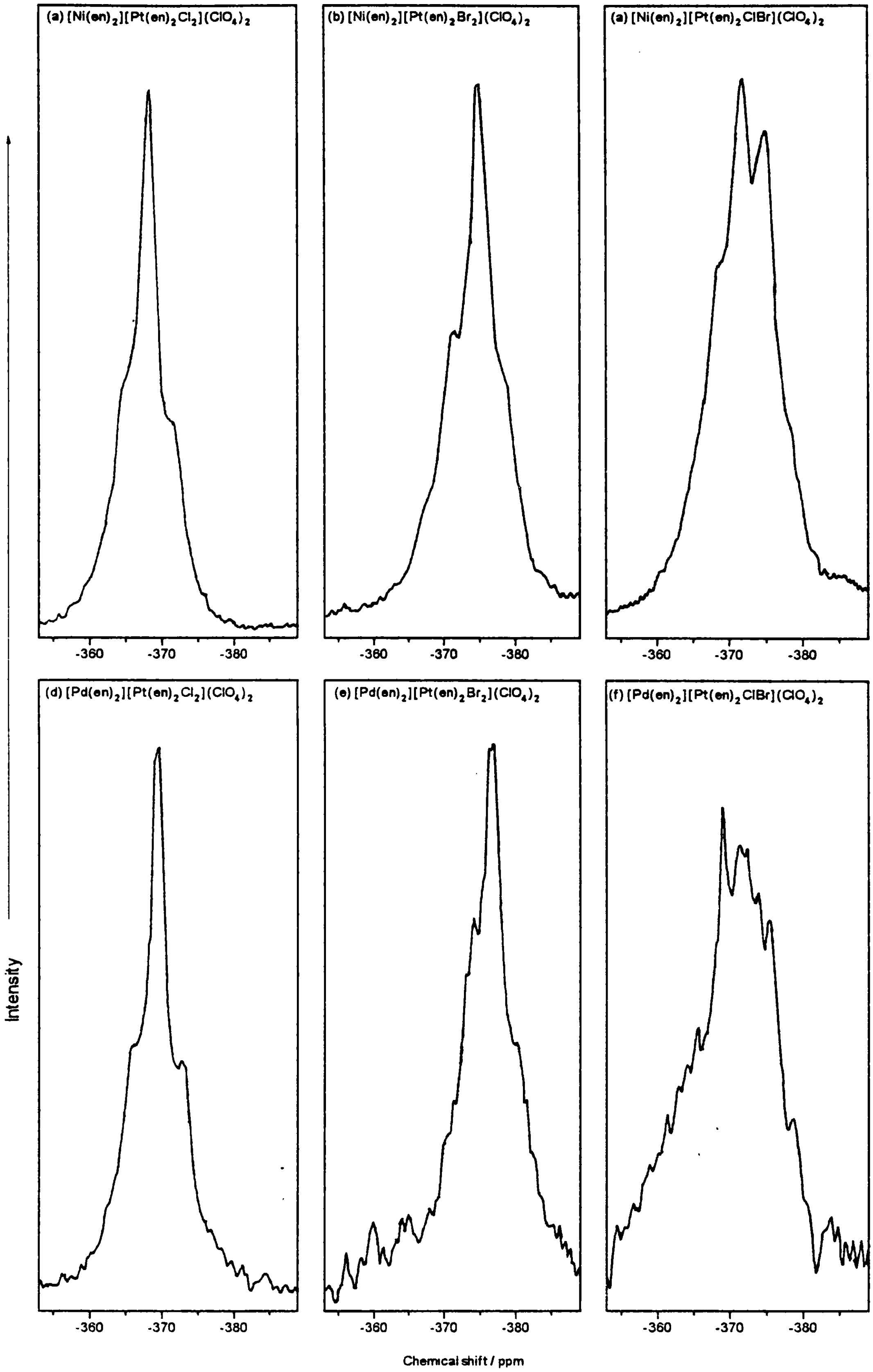

Figure 4.6.9 *Solid-state ^{15}N NMR spectra of $[M(en)_2][Pt(en)_2Cl_{2-2\alpha}Br_{2\alpha}](ClO_4)_4$ where M = Ni and (a) $\alpha = 0$, (b) $\alpha = 0.5$ and (c) $\alpha = 1.0$ and M = Pd and (d) $\alpha = 0$, (e) $\alpha = 0.5$ and (f) $\alpha = 1.0$.*

4.7 Conclusions

The work in this chapter covers a number of areas and, as in Chapter **3**, the significant results may be divided into those which relate to the application of techniques to HMMCs and those which concern some property of the HMMCs themselves. Data from three types of spectroscopic analysis (solid-state ^{15}N NMR, Raman and FT-infrared) are reported and the results from the vibrational studies are simulated using the modelling program Vibra90. More of the useful features of solid-state ^{15}N NMR spectroscopy are demonstrated. It is shown to be an excellent technique for analysing the composition (and hence the purity) of ionic salts. This property is utilised extensively for following the progress of reactions or recrystallisations, *e.g.* the treatment of $[Pt(en)_2]Cl_2$ with $HClO_4$. Just as important is its ability to differentiate between the units $[ClPt^{IV}Cl]$, $[ClPt^{IV}Br]$ and $[BrPt^{IV}Br]$ when they are in an HMMC. Signal intensities are proportional to the number of ^{15}N nuclei present, so it is possible to determine the amounts of each unit in the mixed-halide species $[Pt(en)_2][Pt(en)_2Cl_{2-2\alpha}Br_{2\alpha}](ClO_4)_4$, and therefore the Cl : Br ratio for the whole chain. The values derived are more accurate than those found by elemental analysis, especially for HMMCs that have Cl or Br atoms present in their counterions. However, accuracy is reduced for samples containing BF_4^- or PF_6^- ions because the NMR signals are broadened by residual dipole coupling.

The vibrational modelling experiment has both successes and failures. The Raman spectra are of more analytical use than the infrared spectra because the latter were recorded at room temperature and contain many intense ligand modes in important regions of the spectrum. The modelling experiment shows that with the use of six force constants it is possible to match the wavenumbers of ν_1 and ν_2 simultaneously for $[Pt(en)_2][Pt(en)_2X_2](ClO_4)_4$ (X = Cl or Br). Furthermore, the simulation of the structure of the ν_{1c} signal is very accurate, not only for PtCl but also for the mixed-halide species $PtBr_{0.25}$ and $PtBr_{0.5}$. The ν_{1b} resonance is more difficult to model for the mixed-halide HMMCs, although its simulation does provide a reason for the unusual structure of the signal. The peaks labelled ν_{1m} and ν_{2m} are reproduced qualitatively, although the wavenumbers calculated for them are wrong (however, the value of $\nu_{1m} + \nu_{2m}$ is correct). A description of the motion involved in ν_{1m} or ν_{2m} is derived from the vibrational data and this supplies an explanation for the isotopic structure observed for each mode. Special models were adapted as possible explanations for the weak signals that are observed in some spectra (particularly those of PtCl). The most notable failures of the vibrational modelling technique relate to the electronic defects. Simple point charge models are not able to account for the wavenumber assigned to the hole polaron in PtCl. Furthermore, the ratio of the intensities of ν_{1c}, ν_{1b}, ν_{1m} and ν_{2m} is never accurate because the model derives them simply from bond distance changes and does not make any allowances for resonant enhancement.

Many results are derived from the solid-state ^{15}N NMR and vibrational spectroscopic studies. Some of them relate to individual problems, such as the composition of mixed-metal HMMCs, a suggested cause for blue $[Pt(en)_2]Br_2$, and the reaction of $[Pt(en)_2]I_2$ with iodine. However, the majority are more general. For the ionic monomers and the cationic HMMCs the ^{15}N chemical shifts are related to the hydrogen-bonding strength of the counterion. The data for the HMMCs show that there is no correlation between the structural parameter ρ and the difference between the chemical shifts for the N-Pt^{II} and N-Pt^{IV} nuclei. Despite the presence of counterions, the effect of chain formation is shown to be small for the species $[Pt(en)_2][Pt(en)_2X_2]Y_4$ (X = Cl or Br, Y = ClO_4^- or BF_4^-). This confirms the findings of Chapter 3 and shows that the environments of the nuclei in HMMCs are similar to those in the constituent monomers. This is true for both perchlorate and fluoroborate species, but HMMCs with Y = PF_6^- are shown to have entirely different spectroscopic properties. The extensive solid-state ^{15}N NMR studies of mixed-halide HMMCs show that the amount of mixed-halide unit [$ClPt^{IV}Br$] present in them is much larger than previously thought, and approaches the proportion predicted on the basis of purely random distribution. This conclusion is supported by the evidence gathered from the comparisons between the Raman spectra collected and those predicted by vibrational modelling.

4.8 Experimental details

4.8.1 Syntheses

Platinum (II) monomers

[Pt^{II}(en)$_2$][PtCl$_4$] (404) a solution containing equimolar amounts of potassium tetrachloroplatinate (K_2PtCl_4) and fully ^{15}N-enriched en.2HCl was held under reflux at 90 °C and treated with two molar equiv. of NaOH. The hot, pale yellow solution was then treated with sufficient free unenriched en to decolourise it. The $[Pt(en)_2]^{2+}$ ions this created were extracted by addition of a solution containing $[PtCl_4]^{2-}$ ions, to form the pink solid [Pt(en)$_2$][PtCl$_4$]. This was filtered and washed.

[Pt^{II}(en)$_2$][PtBr$_4$] (405) was prepared by a method similar to that for [Pt(en)$_2$][PtCl$_4$], except that potassium tetrabromoplatinate (K_2PtBr_4) was used instead of K_2PtCl_4 in all instances.

[Pt^{II}(en)$_2$][PtI$_4$] (406) was prepared by an analogous method to that for [Pt(en)$_2$][PtCl$_4$], except that freshly prepared tetraiodoplatinate ions were used instead of tetrachloroplatinate ones. $[PtI_4]^{2-}$ ions were made by warming a stirred solution containing K_2PtCl_4 and five molar equivalents of KI.

[Pt^{II}(en)$_2$]X$_2$ (X = Cl (401), Br (402a) or I (403)) was synthesised by treating a suspension of the corresponding Magnus salt-type complex, [Pt(en)$_2$][PtX$_4$], with free unenriched ethylenediamine under reflux at 90 °C. This resulted in a colourless solution, which was reduced in volume and cooled to remove any insoluble impurities. The filtrate was reduced further, and the desired product was extracted with the addition of ethanol, with recrystallisation from an ethanol / water mixture.

[Pt^{II}(en)$_2$]Br$_2$ (blue complex) (402b) developed (unintentionally) from a solid mixture of [Pt(en)$_2$]Br$_2$ and en.2HBr.

[Pt^{II}(en)$_2$]Y$_2$ (Y = ClO$_4$ (410), BF$_4$ (411) or PF$_6$ (412)) was produced from [Pt(en)$_2$]Cl$_2$ by successively treating with five molar equiv. of the relevant acid and then extracting until the solid-state ^{15}N NMR spectrum showed only [Pt(en)$_2$]Y$_2$ to be present. Generally, three recrystallisations were required to ensure complete conversion. Unwanted oxidation to the respective linear-chain complex was found to occur if too much acid was used, or if the reagent solution was left to stand for too long. In the case of Y = ClO_4^-, the solid-state ^{15}N NMR spectrum of an intermediate product suggested the presence of $[Pt(en)_2](Cl)(ClO_4)$ **(418)**.

$[Pt^{II}(en)_2](Cl)(ClO_4)$ (418) this was not isolated, but was shown to be produced in the synthesis of $[Pt(en)_2](ClO_4)_2$ from $[Pt(en)_2]Cl_2$.

Platinum (IV) monomers

$[Pt^{IV}(en)_2Cl_2]Cl_2$ (407) was prepared from $[Pt(en)_2]Cl_2$ by a standard oxidation method.[218]

$[Pt^{IV}(en)_2Br_2]Br_2$ (408) was prepared by treating a heated solution of $[Pt(en)_2]Br_2$ with an excess of an ethanolic solution of bromine.

"$[Pt^{IV}(en)_2I_2]I_2$" (409) was prepared by reacting a heated solution of $[Pt(en)_2]I_2$ with an excess of an ethanolic solution of iodine. The resulting dark blue / grey material was shown by solid-state NMR most likely to be a matrix of platinum (II) complex with iodine.

$[Pt^{IV}(en)_2Cl_2]Y_2$ (Y = ClO_4 (413), BF_4 (414) or PF_6 (415)) was produced reliably by the oxidation with chlorine of a solution of the corresponding platinum (II) species in dilute HY acid. An alternative preparative route involved treatment of $[Pt(en)_2Cl_2]Cl_2$ with successive amounts of the relevant acid (five molar equiv.). This was found to give some linear-chain complex, in addition to the desired product. Further oxidation was then required to give pure platinum (IV) compound.

$[Pt^{IV}(en)_2Br_2]Y_2$ (Y = ClO_4 (416) or BF_4 (417)) was harder to make than $[Pt^{IV}(en)_2Cl_2]Y_2$; impossible in the case of Y = PF_6^-. Direct bromination of the corresponding $[Pt^{II}(en)_2]Y_2$ was employed, but with stronger reaction conditions (heat, reaction time) than for the analogous chlorination. Careful recrystallisation was required to ensure a pure product.

Normal platinum linear-chain complexes

$[Pt^{II}(en)_2][Pt^{IV}(en)_2X_2](ClO_4)_4$ (X = Cl (419) or Br (420)) was synthesised by mixing a solution of $[Pt(en)_2](ClO_4)_2$ with a solution containing an equimolar amount of the relevant platinum (IV) complex, $[Pt(en)_2X_2](ClO_4)_2$, in the presence of dilute perchloric acid. The linear-chain product was crystallised out of this mixture, and washed with cold water.

[Pt^{II}(en)$_2$][Pt^{IV}(en)$_2$I$_2$](ClO$_4$)$_4$ (421) was made by a similar method to the controlled iodine oxidation described in the literature,[106] except that [Pt(en)$_2$](ClO$_4$)$_2$ was used as the starting material.

[Pt^{II}(en)$_2$][Pt^{IV}(en)$_2$X$_2$](BF$_4$)$_4$ (X = Cl (422) or Br (423)) was made by methods analogous to those used to make the perchlorate HMMCs, except that fluoroborate salts were used.

[Pt^{II}(en)$_2$][Pt^{IV}(en)$_2$Cl$_2$](PF$_6$)$_4$ (424) was synthesised by a method analogous to that used to make [Pt(en)$_2$][Pt(en)$_2$Cl$_2$](ClO$_4$)$_4$, using [Pt(en)$_2$](PF$_6$)$_2$ and [Pt(en)$_2$Cl$_2$](PF$_6$)$_2$ as starting materials.

[Pt^{II}(en)$_2$][Pt^{IV}(en)$_2$Br$_2$](PF$_6$)$_4$ (425) was made by treating [Pt(en)$_2$][Pt(en)$_2$Cl$_2$](PF$_6$)$_4$ with an excess of hydrobromic acid.

Mixed-halide platinum linear-chain complexes (None of the products was recrystallised, since this might have altered the halogen ratio within the chain).

[Pt^{II}(en)$_2$][Pt^{IV}(en)$_2$Cl$_{2-2\alpha}$Br$_{2\alpha}$](ClO$_4$)$_4$ (α = 0.25 (426a), 0.50 (426b) or 0.75 (426c)) were synthesised by mixing solutions containing the required molar quantities of the two linear-chain species, [Pt(en)$_2$][Pt(en)$_2$Cl$_2$](ClO$_4$)$_4$ and [Pt(en)$_2$][Pt(en)$_2$Br$_2$](ClO$_4$)$_4$.

Table 4.8.1 Chemical analyses of the complexes 426a - 426c

Label	Percentage by mass / %					Chain halogens / %	
	C	H	N	Cl	Br	Cl	Br
426a	8.94	2.67	9.96	17.18	4.07	73	27
426b	8.63	2.54	9.75	15.71	7.04	50	50
426c	8.43	2.42	9.52	14.08	10.40	26	74

[Pt^{II}(en)$_2$][Pt^{IV}(en)$_2$Cl$_{2-2\alpha}$Br$_{2\alpha}$](BF$_4$)$_4$ (α = 0.25 (427a), 0.50 (427b)) were synthesised by mixing solutions containing the required molar quantities of the two linear-chain species, [Pt(en)$_2$][Pt(en)$_2$Cl$_2$](BF$_4$)$_4$ and [Pt(en)$_2$][Pt(en)$_2$Br$_2$](BF$_4$)$_4$.

[Pt^{II}(en)$_2$][Pt^{IV}(en)$_2$Cl$_{2-2\alpha}$Br$_{2\alpha}$](PF$_6$)$_4$ (α = 0.33 (428b), 0.50 (428a)) were synthesised by mixing solutions containing the required molar quantities of the two linear-chain species, [Pt(en)$_2$][Pt(en)$_2$Cl$_2$](PF$_6$)$_4$ and [Pt(en)$_2$][Pt(en)$_2$Br$_2$](PF$_6$)$_4$.

Mixed-metal platinum linear-chain complexes

$[M^{II}(en)_2][Pt^{IV}(en)_2X_2](ClO_4)_4$ (M = Ni, X = Cl (429), M = Ni, X = Br (430), M = Pd, X = Cl (431) or M = Pd, X = Br (432)) were synthesised from a solution containing equimolar amounts of $[M(en)_2](ClO_4)_2$ and $[Pt(en)_2X_2](ClO_4)_2$, in the presence of $NaClO_4$.

$[M^{II}(en)_2][Pt^{IV}(en)_2ClBr](ClO_4)_4$ (M = Ni (433), or Pd (434)) crystallised from a solution containing equimolar amounts of $[M(en)_2][Pt(en)_2Cl_2](ClO_4)_4$ and $[M(en)_2][Pt(en)_2Br_2](ClO_4)_4$.

4.8.2 Solid-State ^{15}N NMR spectroscopy

Solid-state ^{15}N NMR spectra were recorded using a Bruker MSL-300 spectrometer at 30.42 MHz using cross-polarisation, proton dipolar decoupling, and magic-angle spinning. The CP condition was set on a sample of doubly ^{15}N-enriched ammonium nitrate. Spinning speeds of 3.7-4.6 kHz were employed, sufficient to eliminate virtually all spinning sidebands for these complexes. The contact time was 0.5 ms, acquisition times were 25-65 ms and the recycle delay between scans was 2-8 s. The typical 90 ° pulse length for protons was 7 µs. All spectra were recorded at room temperature (296 K). Typically, measurements were carried out on sample sizes of 40-60 mg of 25-50 % enriched material. Total scan times varied from 1 h up to 40 h, depending on the number of different nitrogen sites and the identity of the counterion, as well as sample size and quality. Chemical shifts are quoted relative to external liquid nitromethane using solid NH_4NO_3 as a secondary reference: the ammonium peak was taken to resonate at -358.4 ppm.[199] Observed chemical shifts were not corrected for the change in magnetic susceptibility between samples.

4.8.3 Resonance Raman spectroscopy

Spectra were recorded on one of the two scanning spectrometers. The Spex 14018/R6 (usually abbreviated as R6) double monochromator, with Jobin-Yvon holographic gratings (1800 line mm^{-1}), was used with 406.7 nm excitation, provided by a Kr^+ (CR-3000K) laser. All other spectra were recorded on the Spex 1401 double monochromator, with Bausch and Lomb gratings (1200 line mm^{-1}). Appropriate exciting lines were provided by Kr^+ (CR-3000K) or Ar^+ lasers (I-70). All studies were at liquid-nitrogen temperature. Perchlorate complexes were analysed initially as pressed discs. All other Raman studies, both on them and other complexes, were carried out on single crystals. Alignment was achieved with the aid of a Charged Coupled Device (CCD) camera, fitted to the 1401 spectrometer.

4.8.4 Vibrational modelling

Vibra90 technical details

Computer system. The Vibra90 program is supported by the supercomputing service run by the University of London Computer Centre (ULCC). The ULCC has two main machines. The centrepiece is the Convex C3840 known as Neptune, to which most programming jobs are submitted. Neptune is accessed *via* a Convex C3200 known as Pluto, which itself can be used for running less time-consuming programmes. All the vibrational modelling experiments were small enough to be run on Pluto, with no need for submission to Neptune. The Vibra90 program is mounted on the $CHEM directory of Pluto. Pluto was accessed remotely from the UCL computing service, with input and output files being transferred between the two sites. The IP addresses are pluto.ulcc.ac.uk and ts.bcc.ac.uk, respectively. Connections were made using either of the PAD or the telnet services.

Vibra90. The program executes a named input file that contains a sequence of commands and measurements, and delivers an output file to a named destination. The program has a large number of options within it that allow the calculation of various parameters. However, the use of a linear-chain model means that many of these, in particular those relating to intensities, cannot be carried out successfully. Instead, the main purpose of the experiment was the calculation of the frequencies and atomic displacements relating to the vibrations of the model. To do this, the input files had to contain the components listed in Table 4.8.2.

Table 4.8.2 Required components of input file for Vibra90

Program commands	Data required	Purpose of command
TITLE	None.	For reference.
ATOMS	The number of atoms, their atomic masses and Cartesian coordinates.	To set up the structure of the model
BFORM	The number of internal coordinates, the atoms that define them, and the type of motion they describe.	To set up an internal coordinate matrix (B).
FFORM	The number of different force constants and their values. The number of different forces, the combination of internal coordinates that define them, and the force constants to which they correspond	To set up a force matrix (F).
EVALUATE	None.	Uses data from ATOMS and the B and F matrices to form a new matrix (H). The eigenvalues and eigenvectors of H are needed to calculate the vibrational frequencies.
CART	None.	Prints out the Cartesian displacements calculated by EVALUATE.
FINISH	None.	End of file indicator.

Of these commands, only TITLE and FINISH are limited to one usage per file. There are other reusable commands which were implemented at different stages of the development of the model. MASSES allows the substitution of particular atomic masses with new ones. Likewise, FORCES allows the alteration of any of the defined force constants. There is a symmetry coordinate option which can simplify the calculation. This was left in its default condition, since no true symmetry can be applied to a cyclic model such as this.

Limitations. The Vibra90 program can only deal with molecular models up to a certain size. The maximum number of atoms is 50. These can be used to define up to 150 internal coordinates, which in turn means that the largest force field that can be employed is 150 x 150. The F matrix can contain a maximum of 1024 elements; each one can relate to a different force constant. In the files used for the majority of the experiments, the models were chains of

48 atoms (*i.e.* 12 unit cells). 108 internal coordinates were needed to define all the required forces. The largest number of different force constants in any model was ten.

Procedure. For the bulk of the experimental work, which involved the analysis of chains with differing distributions of isotopes and / or halogens, the files that were submitted contained the details of five different chains. The amount of data that these involved was too great to be entered manually, either in the Pluto environment (through the unfriendly emacs editor), or off-site using a word processor or text editor. Therefore a FORTRAN77 program was written which could be used in the off-site generation of files ready for input into Vibra90 (*vide infra*). These files were converted to Unix format using the **dos2unix** command, and sent to Pluto *via* **ftp** transfer, where the output files were generated using Vibra90. The output files often contained more than 2.5 Mb of information, which is too much to be transferred directly to the home address at UCL, where the permanent file space is much less than 2 Mb. Instead, the output files were brought back to the hard drive on the local site, where they were stored temporarily. The files were too big to be saved directly onto floppy disc, so for each file the vibrational frequencies and atomic displacements were extracted to create new files about 125 kb in size. These data were then processed by a second FORTRAN77 program, which calculated approximate intensities of the various vibrations and then constructed a spectrum by imposing a defined degree of broadening.

Fortran77 programs

File generation. The generating program (GENERA) followed simple steps to create the files needed to run Vibra90. In most cases this could be done automatically, with no need for editing. The major exceptions were the chains used to model edge defects, which had no boundary condition and so had different internal coordinates and force constants. When population distributions were modelled, a random number generator was required. The spreadsheet package Origin was found to have a suitable one, with the distribution of the random function checked graphically over many thousands of runs. The details of the program GENERA are given in Table 4.8.3.

Table 4.8.3 Procedure of data generation program GENERA

Step	Details
Set up halogen properties.	Define the number of halogen types (1 or 2), and the number of isotopes for each. For each halogen, each isotope is given a label, a mass and relative proportion.
Set up unit distribution.	The proportions of each Pt^{IV} unit type are defined, as derived from the solid-state ^{15}N NMR spectra. Within these units isotopic distributions are random.
Chain type definition.	Either "random" (R) or "favoured" (F).
Unit probability calculation.	The unit cells are assigned a segment of normalised probability. For the F chains this sectioning is dependent on the identity of the previous unit.
Chain construction.	A "manual" (M) chain can be selected to override the earlier chain definition. This involves simple sequential selection of individual units. Otherwise, a data file containing the random numbers generated by Origin is read in, and these are used to determine successive units in the chain. The number of chains may be varied, but is usually five.
Bond length assignment.	Define the lengths for all types of bond, including those involving defects.
Defect assignments.	Chains may be assigned as "normal" or may be given specific site charge defects by a manual process.
File generation.	A DOS file is written, which includes all the required Vibra90 commands (see Table 4.8.2). The only details omitted are the values of the force constants, which are added on site.

It is important to note that it is the proportions of the **units**, rather than of the halogens themselves, that are used as the basis of chain formation. This is because the distribution of unit populations cannot be calculated from the amounts of halogens present in the mixed-halide complexes, since it does not follow a completely random behaviour. However, all isotopic distributions are taken as random.

Data extraction. The output files recovered from the ULCC are stripped down to leave the vibrational frequencies and the atomic displacements for each vibration. These results are used to help understand the motions of the atoms that contribute to any particular mode. In addition, an approximate theoretical spectrum can be assembled from these data files. The results from many chains are needed in some cases to get a more accurate simulation, and this can be time-consuming. A data extraction program was written in FORTRAN77 to process the files accumulated. The program calculates infrared and Raman intensities from the changes in dipole moments and bond lengths respectively. This is obviously not very accurate, and relative intensities can only really be reliable for single halogen systems. For each vibration in each chain, two calculations are made. The dipole moment change is found by summing the squares of the product of the designated point charge of each atom with its displacement vector. The polarisability is approximated by summing the squares of all the changes in Pt^{IV}-X bond distance. To convert these into a spectral plot, the wavenumber is rounded to the nearest 0.1 cm^{-1}. The total intensity at each point in the spectrum is found over all the chains processed. The intensity at each point is then broadened across neighbouring points by a defined amount by assuming a Gaussian distribution. These results can then be shown as a line graph.

4.8.5 Differential Scanning Calorimetry

DSC experiments were carried out using a Perkin-Elmer DSC7 on approximately 10 mg of sample placed on an aluminium crucible in a nitrogen atmosphere using a heating rate of 5 °C min^{-1}. $[Pt(en)_2][Pt(en)_2Cl_2](ClO_4)_4$ and $[Pt(en)_2][Pt(en)_2Br_2](ClO_4)_4$ were analysed, along with the mixed-halide complexes $[Pt(en)_2][Pt(en)_2X_{2-2\alpha}X'_{2\alpha}](ClO_4)_4$ (**427a - 427c**). The onset of the transition varies roughly linearly with bromine concentration, which agrees with the results reported previously.[38] $PtBr_{0.0}$ has the smallest onset temperature (18.5 °C) and $PtBr_{1.0}$ has the largest (27.2 °C). All enthalpy changes lie in the range 9.0 - 11.6 kJ mol^{-1}.

CHAPTER 5

LINEAR-CHAIN COMPLEXES CONTAINING PLATINUM AMMINES

5.1 Introduction

5.1.1 Platinum ammine linear-chain complexes

In terms of the amount of analytical and spectroscopic work reported, HMMCs containing the ligand ammonia are very much the poor relation of those containing ethylenediamine.[14] This may seem surprising, given that linear-chain ammines have been known for some time,[9] and it is probably not through any lack of effort directed towards them. The chemistry of platinum ammine complexes has long been of interest, independent of the extensive biological studies stemming from the antitumour activity of the compound "cisplatin" (a.k.a. Peyrone's chloride), *cis*-$Pt(NH_3)_2Cl_2$.[256] For just as long, it has also been an area of controversy. Confusion as to the correct formulation of the neutral diammine isomers [257] has given way to disagreement over their relative stabilities in solution.[258-262] There have been conflicting HMMC crystal structures,[6,20,21] and different interpretations of the oxidation of Magnus' Green Salt (MGS), $[Pt(NH_3)_4][PtCl_4]$.[10-13] It appears that the amount of assumed knowledge greatly outweighs that proven.[229] This is no less true of the HMMC complexes than it is of any other. The actual number of linear-chain species that can be reliably and reproducibly synthesised is small. For example, the syntheses of the platinum tetraammine derivatives, which are analogues of $[Pt(en)_2][Pt(en)_2X_2](ClO_4)_4$, involve high concentrations of strong acids and tend to produce non-stoichiometric chains.[11,12]

5.1.2 Solid-state ^{15}N NMR analysis of platinum ammines

Extending the solid-state NMR study to include ^{15}N nuclei in platinum-bonded ammonia is a logical step. Of the ligands contained in HMMCs, only a few are commercially available in an ^{15}N-enriched state, and most of them are very similar chemically to ethylenediamine. Solid-state NMR analysis of the compounds these ligands form would have little purpose other than to confirm the conclusions already reached. Ammine complexes offer a more interesting set of results because there are many structural anomalies to investigate (*vide infra*). However, unlike the ethylenediamine compounds examined in Chapters **3-4**, there are certain synthetic problems surrounding the production of ^{15}N-enriched samples of the HMMCs of diammine or tetraammine platinum. In most of the methods published for the synthesis of platinum ammine complexes, the platinum starting material is treated with a large excess of the base. For instance, $[Pt(NH_3)_4]Cl_2$ is routinely prepared by treating $[PtCl_4]^{2-}$ ions with an excess of concentrated ammonia.[263] The cost of ^{15}N-enrichment prohibits the use of such large amounts of ammonia, and so alternative synthetic routes that consume less ligand are sought. Even after the monomeric ammine complexes have been isolated, there are still considerable difficulties in producing the ammine linear-chains in high yield or purity. This does not necessarily hinder studies using techniques in which single crystals are examined, but successful solid-state NMR spectroscopic analysis requires samples of good quality and of a reasonable size. Therefore, one of the more important aspects of the work on HMMCs containing ammonia involves establishing suitable preparative routes. Some complexes that can usually be synthesised without difficulty with naturally abundant ^{15}N have not been analysed because they could not be produced in sufficient quantity or quality.

5.2 Solid-State ^{15}N NMR of *cis*-diammine platinum complexes

5.2.1 Introduction

The *cis*-diammine complexes are of interest because they can be compared with the related ethylenediamine complexes [Pt(en)X_a] (X = Cl, Br or I; a = 2, 3 or 4). All six monomeric complexes are well known, and their syntheses well established. The method originally used for the production of *cis*-$Pt(NH_3)_2Cl_2$ (cisplatin) can result in many impurities.[264] Because of the biochemical importance of cisplatin, effort has gone into improving its synthesis, and it is now more often prepared using the Dhara method.[265] The crystal structure of *cis*-$Pt(NH_3)_2Cl_2$ has been determined,[266] but because it was derived from the only fragment neither twinned nor disordered out of the large number of crystals examined, it may not be truly representative of the bulk sample. The structure contains two Pt-N distances for each molecule (1.95 and 2.05 Å) and two Pt-Pt distances for the crystal (3.372 and 3.409 Å). The difference in r(Pt-N) is larger than that for $[Pt(en)_2]Cl_2$, which has two distinct peaks in its solid-state ^{15}N NMR spectrum (see section **4.2**). *cis*-$Pt(NH_3)_2Cl_2$ is yellow, but the depth of colour varies from sample to sample, just as it does for $Pt(en)Cl_2$. $Pt(en)Br_2$ is also yellow, but *cis*-$Pt(NH_3)_2Br_2$ can form crystals of one of two different colours. *cis*-$Pt(NH_3)_2Br_2$ was first prepared by Cleve,[267] who isolated a yellow solid only after recrystallisation of the initial red product. There was no further mention of the red compound, until Palkin *et al.* confirmed the existence of the two types of bromide, and reported some analyses of them in a brief article in 1972.[268] The two forms were distinguished by three types of measurement: their molar heat capacities, their X-ray line diagrams and their IR spectra, in which the wavenumbers of both the ν(Pt-N) and the $\rho(NH_3)$ vibrations were found to differ. No significant work has been carried out on these complexes since, and so their differences have not been satisfactorily explained. Keller has suggested that the red solid is a form of the polymeric $[Pt(NH_3)_4][PtBr_4]$,[229] but there are too many similarities in the infrared spectra of the red and yellow forms for this to be true. The third platinum (II) compound, *cis*-$Pt(NH_3)_2I_2$, is yellow and is produced at the first stage of the Dhara synthesis of *cis*-$Pt(NH_3)_2Cl_2$.[265]

Not one of the platinum (IV) complexes shows unusual behaviour. *cis*-$Pt(NH_3)_2Cl_4$ or *cis*-$Pt(NH_3)_2Br_4$ can be prepared by simple oxidation of the corresponding Pt^{II} complex with the appropriate halogen, X_2. Iodine is a weaker oxidising agent than chlorine or bromine, and so *cis*-$Pt(NH_3)_2I_4$ is usually made *via* PtI_4.[223] The best method for preparing the HMMCs $[Pt(en)X_2][Pt(en)X_4]$ involves the mixing equimolar amounts of Pt^{IV} and Pt^{II} monomers, but none of the species *cis*-$[Pt(NH_3)_2X_2][Pt(NH_3)_2X_4]$ has been produced by this method. In fact, only *cis*-$[Pt(NH_3)_2Cl_2][Pt(NH_3)_2Cl_4]$ has been reported at all, and it resulted from the partial oxidation of *cis*-$Pt(NH_3)_2Cl_2$.[9] Even then, doubts have been cast as to its true composition.[229] A significant part of the study of the *cis*-diammines involves the assessment of the factors that inhibit the formation of HMMCs.

5.2.2 *cis*-diammine platinum bromide complexes

The yellow complex (**501a**) was formed by the rapid addition of KBr to a solution containing *cis*-$[Pt(NH_3)_2(OH_2)_2]^{2+}$ ions, which are produced by the action of silver ions on any of the complexes *cis*-$Pt(NH_3)_2X_2$ (X = Cl, Br or I). The red bromide (**501b**) was made by the slow recrystallisation of a solution of **501a**. These observations are consistent with those of Palkin *et al.*,[268] but are in contrast to those of Cleve's original synthetic work.[267] The red complex can be made directly from the diaquo ion as Cleve suggests, but only when the addition of KBr is slow enough to prevent precipitation of the yellow species. The yellow compound is formed more readily and so most of the reported work on *cis*-$Pt(NH_3)_2Br_2$ is concerned with it, while the red bromide has been neglected. The solid-state ^{15}N NMR spectra of the two complexes are shown in Figure 5.2.1, and they exhibit remarkable differences. The spectrum of **501a** contains a single main peak at -408.7 ppm, but no satellites can be resolved because the resonance is so broad. It may be composed of two (or more) closely spaced signals since the resonance is broader than that found for *cis*-$Pt(NH_3)_2I_2$ (*vide infra*), which should be affected more by dipolar broadening. By contrast, the spectrum of the red species exhibits two main peaks, separated by some 13 ppm. This large chemical shift difference is bigger than that between $Pt^{II}(en)Br_2$ and $Pt^{IV}(en)Br_4$ (see section **3.2**). The peaks are at -400.3 and -413.8 ppm, *i.e.* one on either side of the signal for the yellow form. Coupling constants can be determined for both signals in the spectrum of **501b** by increasing the resolution at the expense of extra noise. $J_{N\text{-}Pt}$ values are 355 and 350 Hz for the peaks at high and low field, respectively. Both couplings are typical of $J_{N\text{-}Pt^{II}}$ values and they differ by an amount smaller than the experimental error, which rules out the possibility that the red species is mixed-valent. The vibrational spectra of **501b** confirm that there are none of the chain vibrations normally associated with HMMCs. There is no signal in its Raman spectrum due to ν_1, nor in its infrared spectrum due to ν_2. An orange form (**501c**) of *cis*-$Pt(NH_3)_2Br_2$ was made on one occasion, but its solid-state NMR spectrum reveals that it is simply a mixture of the red and yellow complexes; it has three resolvable peaks, which are at -400.5 , -409.4 and -413.6 ppm.

All three complexes can be oxidised fully with bromine to make the same orange compound, *cis*-$Pt(NH_3)_2Br_4$ (**502a**). Its solid-state ^{15}N NMR spectrum consists of a single main resonance at -392.4 ppm that has a $J_{^{15}N\text{-}Pt}$ coupling value of less than 270 Hz. Oxidation is effected with an ethanol/water solution of bromine, but the temperature required to produce *cis*-$Pt(NH_3)_2Br_4$ depends on the starting material. **501a** is fully oxidised when the solution is warmed, **501b** is only converted under reflux and **501c** may be oxidised in two stages; a red solid (**502b**) is isolated after warming. The solid-state ^{15}N NMR spectrum of **502b** has three peaks, but two of them match the signals in the spectrum of **501b**. The other resonance is at -393.8 ppm, which corresponds to the N-Pt^{IV} peak in *cis*-$Pt(NH_3)_2Br_4$, and it replaces the peak at -409.4 ppm in the spectrum of **501b**. These observations imply that all of the yellow form of *cis*-$Pt(NH_3)_2Br_2$ present in **501c** is oxidised, while the red species is unaffected. The ^{15}N chemical shift positions of all the bromide monomers are summarised in Table 5.2.1.

Table 5.2.1 ^{15}N chemical shifts for *cis*-diammine platinum bromide monomers [a]

Complex	Label	Assigned peak positions / ppm			
		N-Pt^{IV}	N-Pt^{II} (A)	N-Pt^{II} (B)	N-Pt^{II} (C)
Yellow *cis*-$Pt(NH_3)_2Br_2$	**501a**			-408.7	-408.7
Red *cis*-$Pt(NH_3)_2Br_2$	**501b**		-400.3		-413.5
Orange *cis*-$Pt(NH_3)_2Br_2$	**501c**		-400.5	-409.4	-413.6
cis-$Pt(NH_3)_2Br_4$	**502a**	-392.4			
Partially oxidised **501c**	**502b**	-393.8	-400.4		-413.6

[a] *Chemical shifts are accurate to ± 0.4 ppm. Assignments are explained in the discussion.*

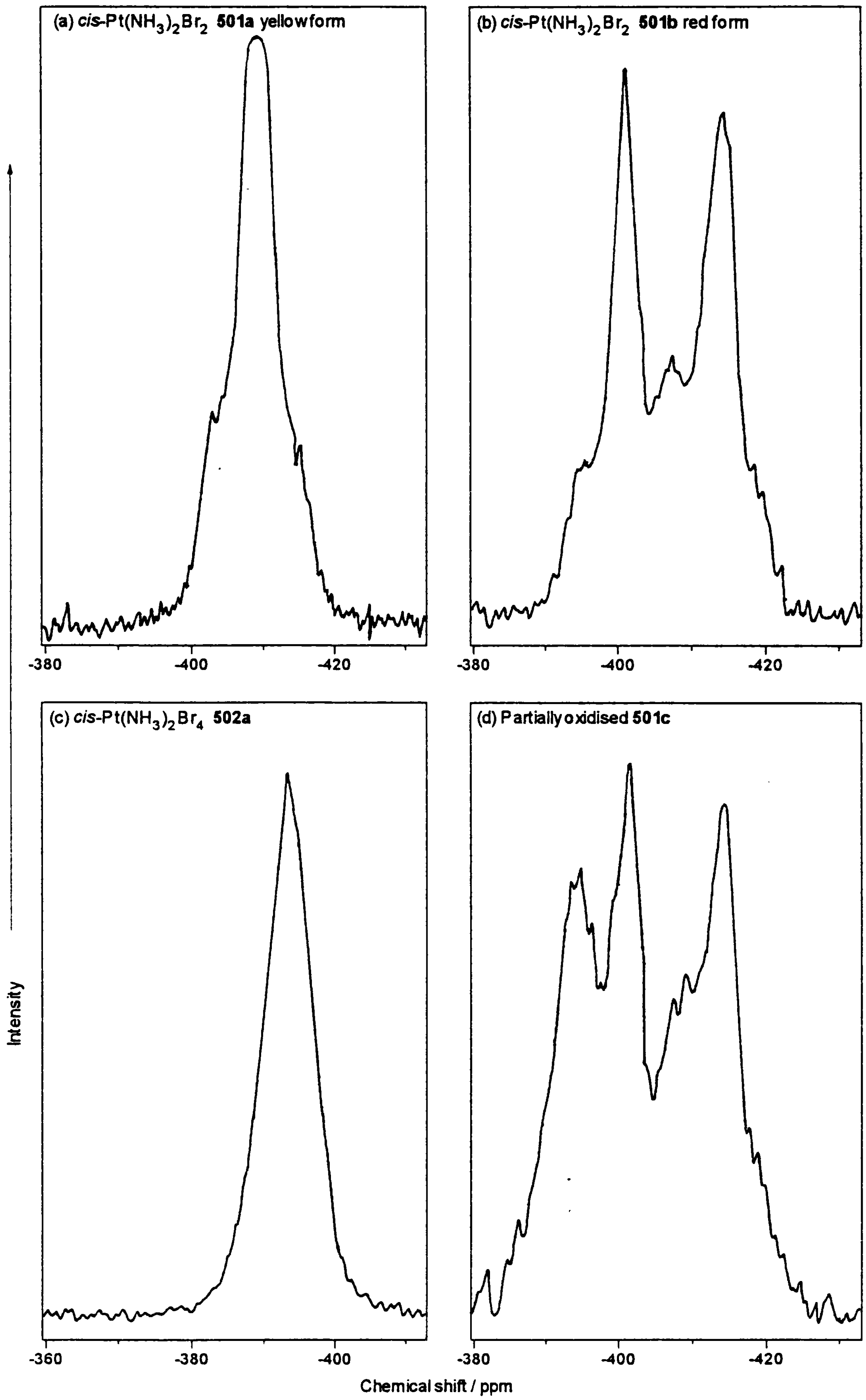

Figure 5.2.1 *Solid-state* ^{15}N *NMR spectra of (a) yellow* cis-$Pt(NH_3)_2Br_2$, *(b) red* cis-$Pt(NH_3)_2Br_2$, *(c)* cis-$Pt(NH_3)_2Br_4$ *and (d) a partially oxidised mixture of the red and yellow forms.*

The HMMC *cis*-[$Pt(NH_3)_2Br_2$][$Pt(NH_3)_2Br_4$] has not been reported previously. Oxidation of yellow *cis*-$Pt(NH_3)_2Br_2$ with ammonium persulphate in the presence of KBr results in a green solid of poor crystallinity (**503a**). Its solid-state ^{15}N NMR spectrum reflects the quality of the sample. It is composed of two peaks that are so broad that no satellite signals can be resolved at all (see Figure 5.2.2). The chemical shifts of the peaks are roughly the same as those in the respective monomers, which reiterates the relationship between [Pt(en)Br_2][Pt(en)Br_4] and its constituents. A second sample of *cis*-[$Pt(NH_3)_2Br_2$][$Pt(NH_3)_2Br_4$] was made by adding water to a dimethylformamide solution containing equimolar amounts of *cis*-$Pt(NH_3)_2Br_2$ and *cis*-$Pt(NH_3)_2Br_4$. The green product (**503b**) which was isolated is more crystalline than **503a**, and its solid-state ^{15}N NMR spectrum is much better resolved (see Figure 5.2.2). The chemical shifts for the two signals in the spectrum of **503b** differ by *ca.* 18 ppm, as they do for **503a**. Both resonances for **503b** have a pair of clearly defined satellites, which are used to determine $J_{N\text{-}Pt}$ values; they are 305 and 245 Hz for the peaks at -414.2 and -396.0 ppm, respectively. Although both complexes have mixed-valence character, the absolute chemical shifts of corresponding signals differ by some 5 ppm. ^{15}N chemical shifts and $J_{N\text{-}Pt}$ values for all the bromide complexes are listed in Table 5.2.2.

Table 5.2.2 ^{15}N chemical shifts and $J_{N\text{-}Pt}$ coupling constants for *cis*-diammine platinum bromide complexes [a]

cis-diammine complex	Colour	Label	$H_3N\text{-}Pt^{II}$		$H_3N\text{-}Pt^{IV}$	
			δ / ppm	$J_{N\text{-}Pt}$ / Hz	δ / ppm	$J_{N\text{-}Pt}$ / Hz
$Pt(NH_3)_2Br_2$	yellow	**501a**	-408.7	-		
$Pt(NH_3)_2Br_2$	red	**501b**	-400.3 -413.5	350 355		
$Pt(NH_3)_2Br_4$	orange	**502a**			-392.4	260
[$Pt(NH_3)_2Br_2$][$Pt(NH_3)_2Br_4$]	green	**503a**	-409.0	-	-391.2	-
[$Pt(NH_3)_2Br_2$][$Pt(NH_3)_2Br_4$]	green	**503b**	-414.2	305	-396.0	245

[a] *Chemical shifts are accurate to ± 0.4 ppm, coupling constants to ± 30 Hz.*

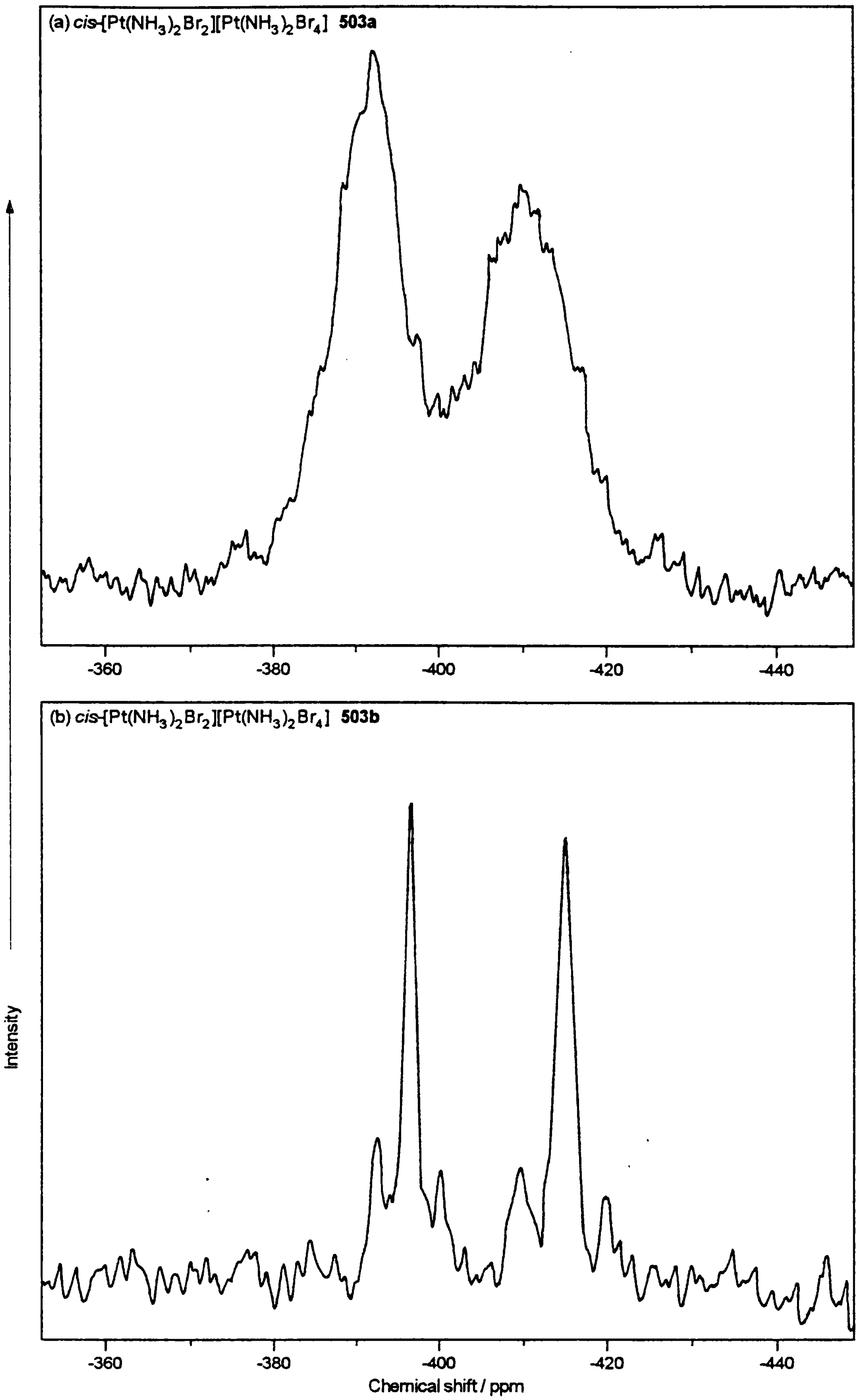

Figure 5.2.2 *Solid-state ^{15}N NMR spectra of cis-[$Pt(NH_3)_2Br_2$][$Pt(NH_3)_2Br_4$] crystallised from (a) water and (b) dimethylformamide.*

The complex **503b** was of sufficient quality for single-crystal Raman spectra to be recorded (see Figure 5.2.3). ν_1 is 172.0 and 167.5 cm^{-1} at excitation wavelengths of 568 and 676 nm, respectively. In addition, at 676 nm excitation there is a signal at 140 cm^{-1}, which is attributed to the localised stretching mode of an electron polaron. ν_1 for *trans*-$[Pt(NH_3)_2Br_2][Pt(NH_3)_2Br_4]$ is 165.4 cm^{-1} for 676 nm excitation.[14]

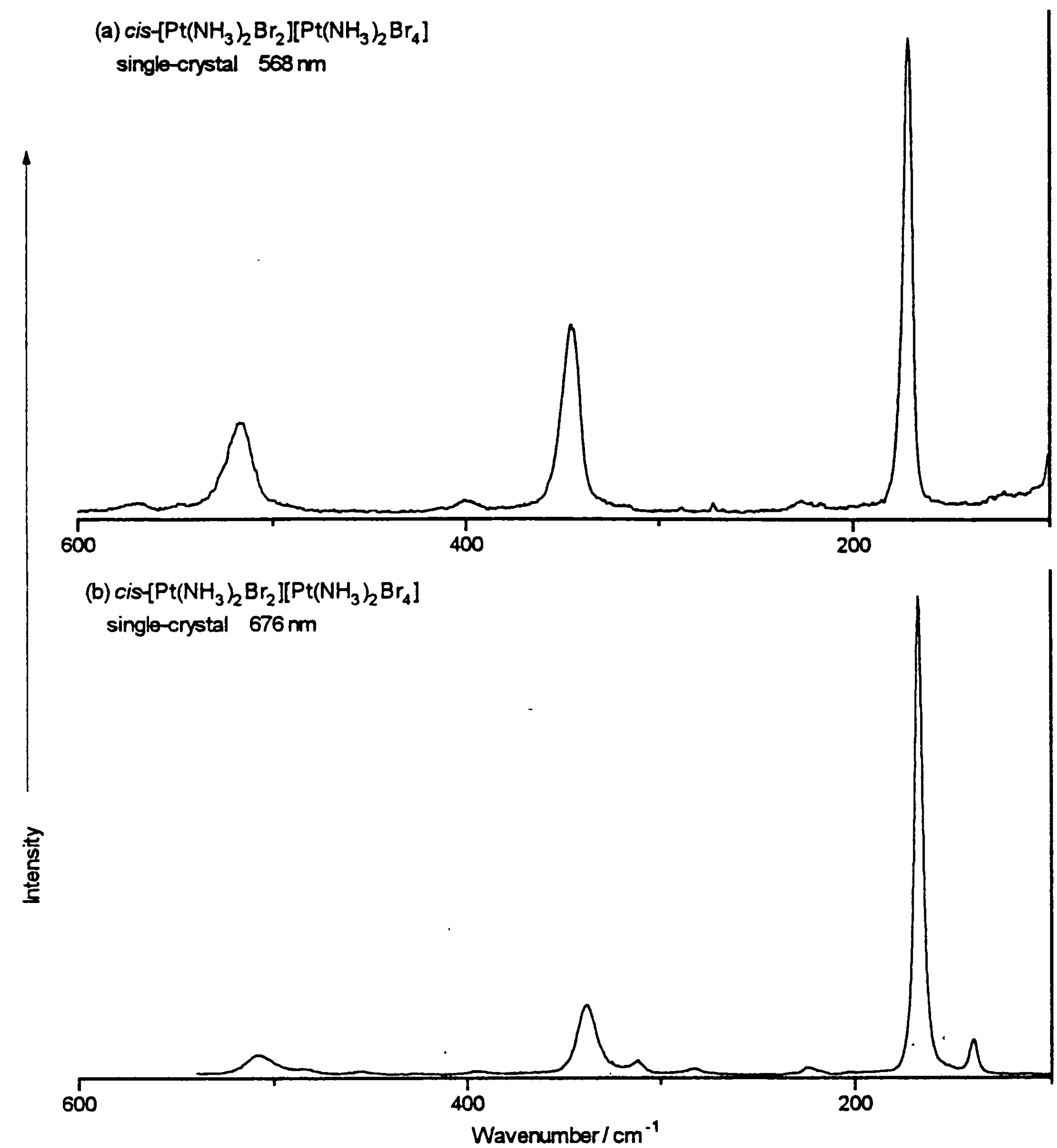

Figure 5.2.3 *Raman spectra of* cis-$[Pt(NH_3)_2Br_2][Pt(NH_3)_2Br_4]$ *with excitation lines (a) 568 nm and (b) 676 nm.*

5.2.3 *cis*-diammine platinum chloride complexes

Two types of *cis*-$Pt(NH_3)_2Cl_2$ can be distinguished by solid-state ^{15}N NMR spectroscopy. The difference between them is not as great as that between the two bromide complexes nor is there an equivalent chloride form of the red *cis*-$Pt(NH_3)_2Br_2$. Both kinds of *cis*-$Pt(NH_3)_2Cl_2$ are yellow and give solid-state NMR spectra that consist of a single main resonance with satellites due to ^{15}N-^{195}Pt coupling. Although two Pt-N distances are observed in the X-ray crystal structure,[266] none of the samples of *cis*-$Pt(NH_3)_2Cl_2$ gave a solid-state ^{15}N NMR spectrum composed of two main signals of equal intensity. The species isolated depends on the synthetic route. *cis*-$Pt(NH_3)_2Cl_2$ made by the standard method (**504a**) [264] has δ_N = -416.5 ppm, but δ_N = -413.5 ppm for *cis*-$Pt(NH_3)_2Cl_2$ made by the Dhara method (**504b**) [265]; $J_{N\text{-}Pt}$ for both species is *ca.* 350 Hz (see Figure 5.2.4). Full oxidation of either form of *cis*-$Pt(NH_3)_2Cl_2$ gives the Pt^{IV} complex, *cis*-$Pt(NH_3)_2Cl_4$ (**505a**), a yellow crystalline solid whose solid-state ^{15}N NMR spectrum contains shows a single peak at -387.7 ppm with a $J_{N\text{-}Pt}$ coupling of 245 Hz.

The partial oxidation of **504a** with persulphate ions has been reported,[9] and by following the same procedure a red complex (**506a**) was isolated. The solid-state ^{15}N NMR spectrum of **506a** is very complicated and consists of peaks as broad and noisy as those for the *ex aquo* sample of *cis*-$[Pt(NH_3)_2Br_2][Pt(NH_3)_2Br_4]$. Four main signals can be distinguished, a pair of large peaks at -416.2 and -387.6 ppm, and a pair of small peaks at -394.4 and -408.5 ppm. Two of them are absent from the spectrum of the yellow solid (**505b**) produced by oxidation of the red complex with chlorine; the two that remain are at -386.6 and -393.1 ppm. The $J_{^{15}N\text{-}Pt}$ values for both resonances are in the range associated with N-Pt^{IV} signals. While these spectra indicate that **506a** probably contains some *cis*-$[Pt(NH_3)_2Cl_2][Pt(NH_3)_2Cl_4]$, there is a significant amount of impurity present, the nature of which is discussed in section **5.2.5**. The mixing of equimolar amounts of Pt^{II} and Pt^{IV} monomers failed to give any red product, resulting instead resulting in a crystalline yellow solid (**506b**). The solid-state ^{15}N NMR spectrum of **506b** has three main peaks, which are at -387.7, -414.3 and -416.4 ppm. The first contributes about half of the total intensity, and its $J_{^{15}N\text{-}Pt}$ coupling is 250 Hz. The remaining intensity is split equally between the second and third peaks, both of which have coupling constants larger than 310 Hz. The vibrational spectra recorded for the yellow complex show no HMMC character; there is no ν_1 signal in its Raman spectrum, nor a ν_2 signal in its infrared spectrum. The results are consistent with a sample containing equal populations of N-Pt^{II} and N-Pt^{IV} sites in which there are two types of N-Pt^{II} nuclei present in a 1 : 1 ratio, but they do not indicate that there is any HMMC complex in the sample. The oxidation of **506b** with chlorine resulted in a crystalline yellow product that has a solid-state NMR spectrum indistinguishable from that of *cis*-$Pt(NH_3)_2Cl_4$. The spectra of **506a** and **506b** are shown in Figure 5.2.5, and the data taken from them are summarised in Table 5.2.3.

Table 5.2.3 ^{15}N **chemical shifts and** $J_{N\text{-}Pt}$ **coupling constants for** ***cis*****-diammine platinum chloride complexes** [a]

cis-diammine complex	Crystal colour	Label	$H_3N\text{-}Pt^{II}$		$H_3N\text{-}Pt^{IV}$	
			δ / ppm	$J_{N\text{-}Pt}$ / Hz	δ / ppm	$J_{N\text{-}Pt}$ / Hz
$Pt(NH_3)_2Cl_2$	yellow	**504a**	-416.5	340		
$Pt(NH_3)_2Cl_2$	yellow	**504b**	-413.5	330		
$Pt(NH_3)_2Cl_4$ (*ex* **504a**, **504b** or **506b**)	yellow	**505a**			-387.7	245
$Pt(NH_3)_2Cl_4$ (*ex* **506a**)	yellow	**505b**			-386.6 -393.1[b]	240 -
$[Pt(NH_3)_2Cl_2][Pt(NH_3)_2Cl_4]$ (*ex* **504a**)	red	**506a**	-416.2 -408.5[b]	- -	-387.6 -394.4[b]	250 -
$[Pt(NH_3)_2Cl_2][Pt(NH_3)_2Cl_4]$ (*ex* **504b**)	yellow	**506b**	-414.3 -416.4	315 325	-387.7	250

[a] *Chemical shifts are accurate to ± 0.3 ppm, coupling constants to ± 20 Hz.*

[b] *Peaks due to impurities.*

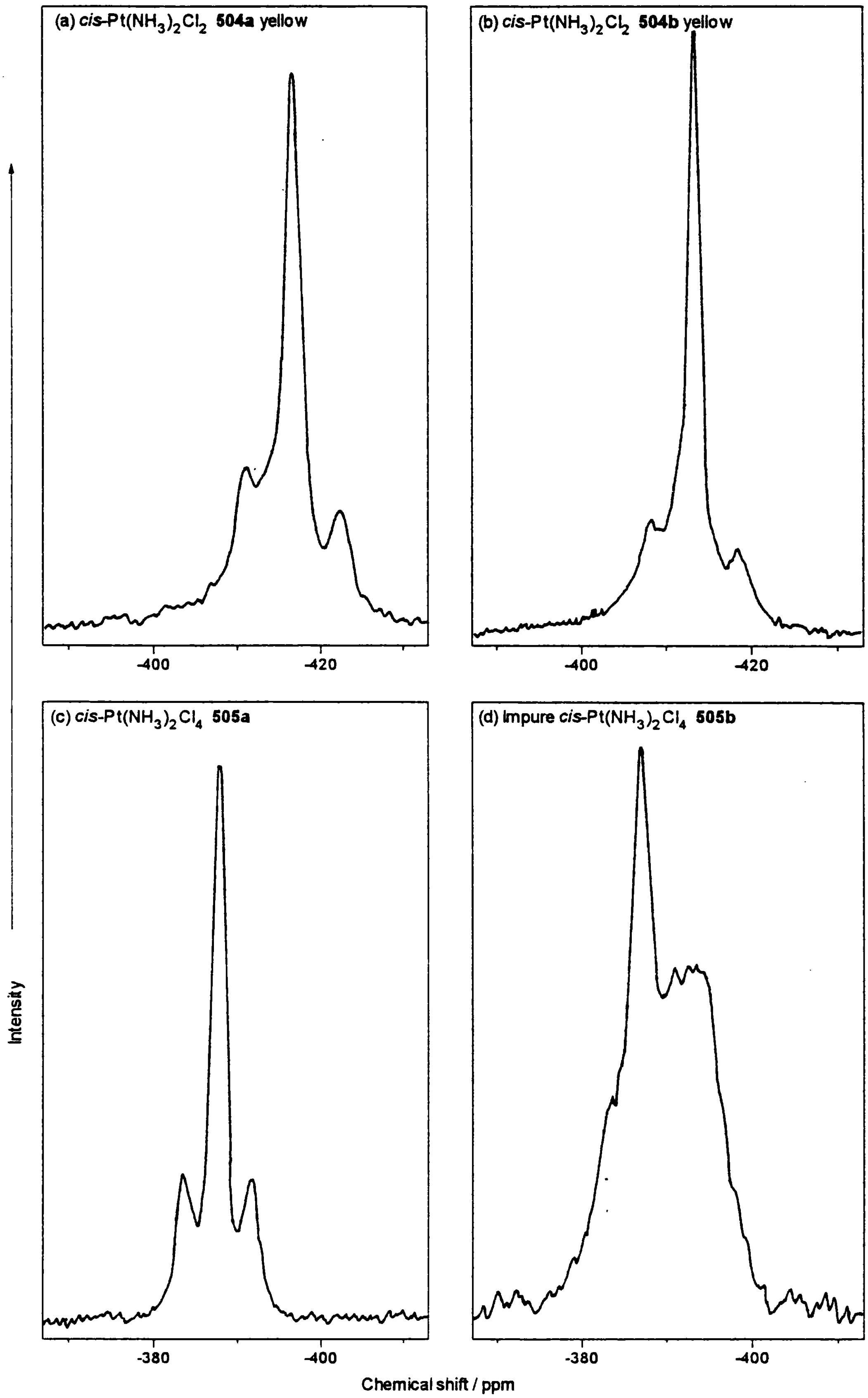

Figure 5.2.4 *Solid-state ^{15}N NMR spectra of (a), (b) two forms of yellow* cis-*$Pt(NH_3)_2Cl_2$, (c)* cis-*$Pt(NH_3)_2Cl_4$ and (d) the product of oxidation of **506a**.*

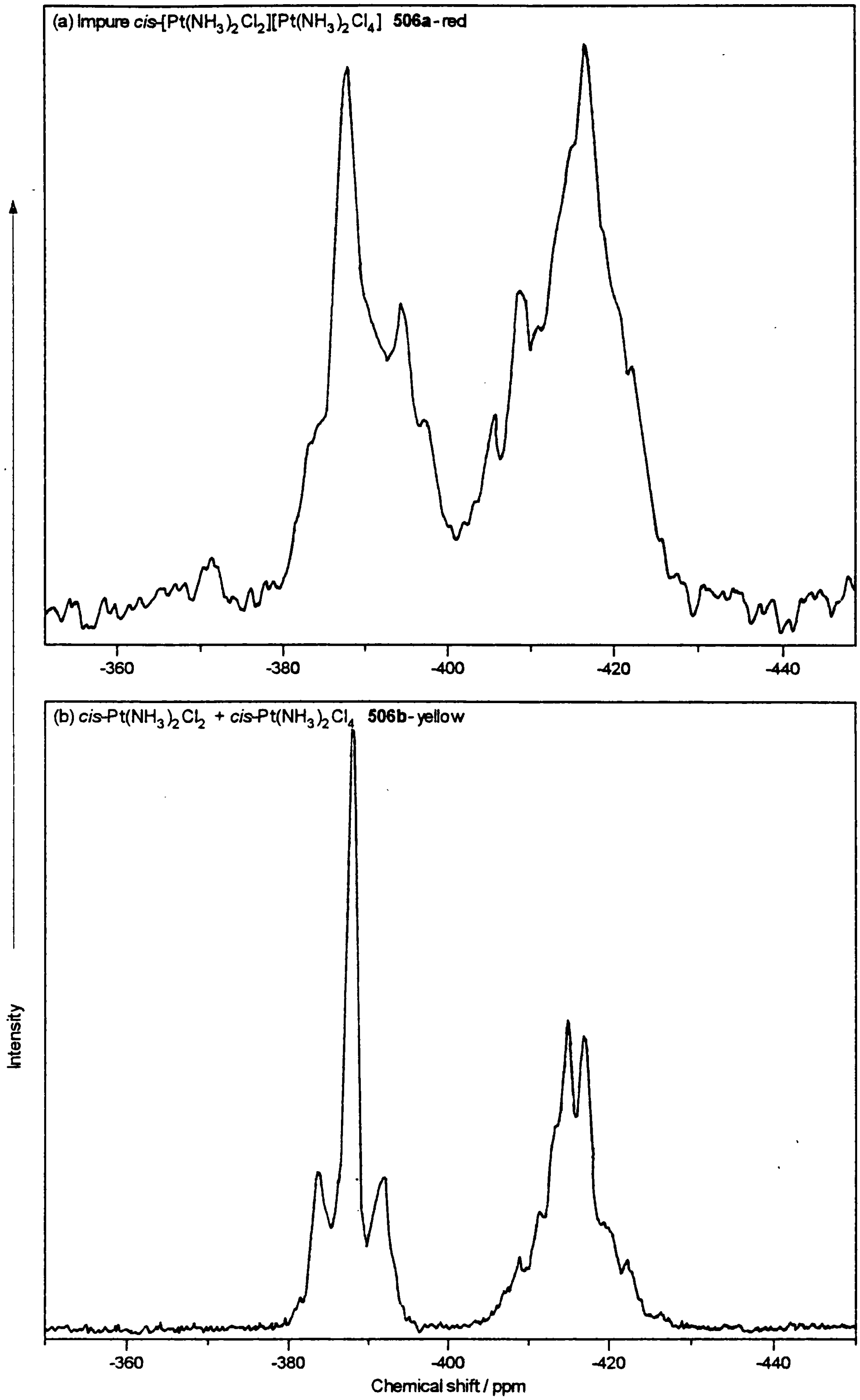

Figure 5.2.5 *Solid-state ^{15}N NMR spectra of the products of attempted syntheses of cis-[Pt(NH_3)$_2$$Cl_2$][Pt($NH_3$)$_2$$Cl_4$], (a) red complex and (b) yellow complex.*

5.2.4 *cis*-diammine platinum iodide complexes

Iodine is the only halogen to form *cis*-diammine complexes that exhibit straightforward behaviour in their solid-state ^{15}N NMR spectra (see Figure 5.2.6). *cis*-$Pt(NH_3)_2I_2$ (**507**) is yellow and it is made at the first stage of the Dhara synthesis of *cis*-$Pt(NH_3)_2Cl_2$.[265] Its solid-state ^{15}N NMR spectrum consists of a single resonance at -393.8 ppm with well-defined satellites due to ^{15}N-^{195}Pt coupling. The signal is reproducible and independent of the method of preparation; *cis*-$Pt(NH_3)_2I_2$ can also be made by converting *cis*-$Pt(NH_3)_2X_2$ (X = Cl or Br) with iodide ions. *cis*-$Pt(NH_3)_2I_4$ (**508**) is a mauve solid that is best prepared by treating PtI_4 with a solution of ammonia. Its solid-state ^{15}N NMR spectrum has a single main peak at -401.7 ppm, which is at higher field than that of *cis*-$Pt(NH_3)_2I_2$. This mirrors the chemical shift relationship between $Pt(en)I_2$ and $Pt(en)I_4$. The HMMC *cis*-$[Pt(NH_3)_2I_2][Pt(NH_3)_2I_4]$ (**509**) is made by adding an excess of water to a dimethylformamide solution containing equimolar amounts of *cis*-$Pt(NH_3)_2I_2$ and *cis*-$Pt(NH_3)_2I_4$. The solid-state ^{15}N NMR spectrum of the bronze product appears to exhibit three distinct peaks, but the central one arises from the overlap of the satellites of the outer two. ^{15}N chemical shifts and J_{N-Pt} coupling constants of the iodide complexes are listed in Table 5.2.4.

Table 5.2.4 **^{15}N chemical shifts and J_{N-Pt} coupling constants for *cis*-diammine platinum iodide complexes** [a]

cis-diammine complex	Colour	Label	H_3N-Pt^{II}		H_3N-Pt^{IV}	
			δ / ppm	J_{N-Pt} / Hz	δ / ppm	J_{N-Pt} / Hz
$Pt(NH_3)_2I_2$	yellow	**507**	-393.9	290		
$Pt(NH_3)_2I_4$	mauve	**508**			-401.7	-
$[Pt(NH_3)_2I_2][Pt(NH_3)_2I_4]$	bronze	**509**	-393.9	315	-401.6	-

[a] *Chemical shifts are accurate to ± 0.3 ppm, coupling constants to ± 20 Hz.*

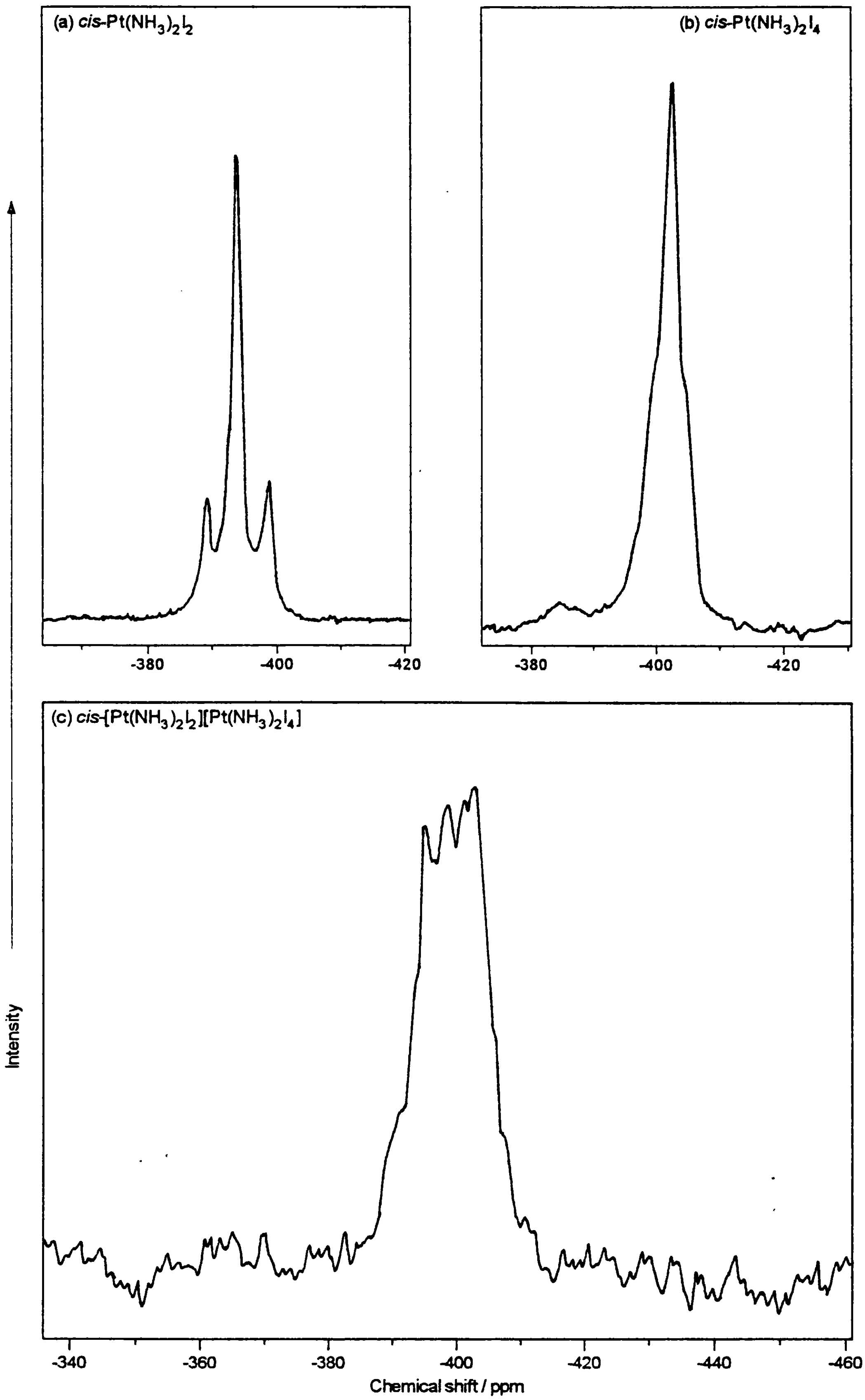

Figure 5.2.6 *Solid-state ^{15}N NMR spectra of (a)* cis-*$Pt(NH_3)_2I_2$, (b)* cis-*$Pt(NH_3)_2I_4$ and (c)* cis-*$[Pt(NH_3)_2I_2][Pt(NH_3)_2I_4]$.*

5.2.5 Comparison of *cis*-[Pt(NH_3)$_2$$X_a$] with [Pt(en)$X_a$] complexes

The most significant result uncovered in the solid-state ^{15}N NMR study of the [Pt(en)X_a] species is that the spectra of the HMMCs can be constructed from the superimposed spectra of the constituent monomers to which a small upfield shift has been applied. At first sight, there appears to be no obvious pattern to the solid-state ^{15}N NMR spectra of the *cis*-diammine species, but it is possible to select from them a set of results in which the established relationship between chain and monomers is maintained. On this basis, the spectra of the following complexes are chosen: **507**, **508** and **509** (X = I), **501a**, **502a** and **503a** (X = Br), and **504a**, **505a** and the pair of large signals in **506a** (X = Cl). The data taken from them are plotted in Figure 5.2.7.

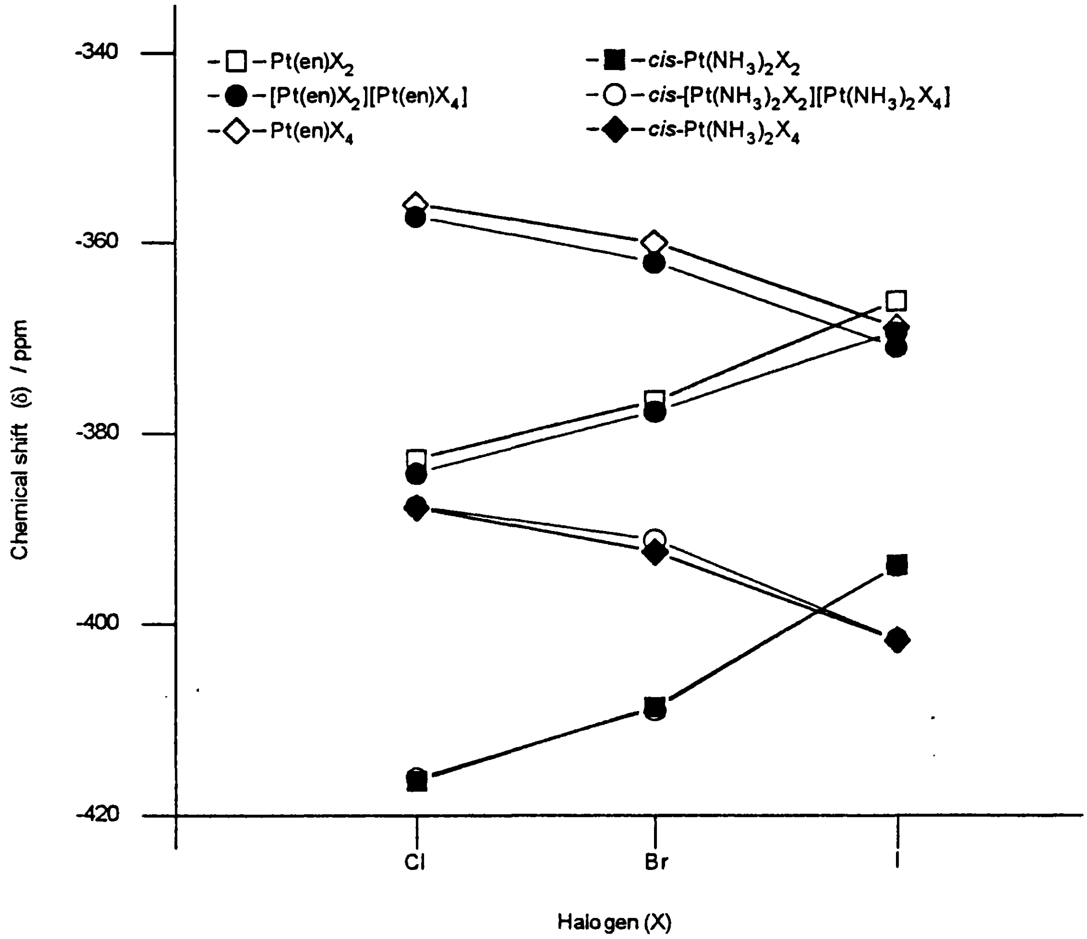

Figure 5.2.7 *Comparison of the chemical shifts for the complexes cis-[Pt(NH_3)$_2$$X_a$] and [Pt(en)$X_a$] (X = Cl, Br or I; a = 2, 3 or 4).*

The only notable difference between the two sets of compounds is in the influence of the halogen on the N-Pt^{II} chemical shift. The rate at which the $\delta_{N\text{-}Pt^{II}}$ value moves to higher field as the halogen is changed from Cl $\rightarrow$ Br $\rightarrow$ I is some 25-50 % larger in the *cis*-diammine species. The consequence of this is that the resonance for *cis*-$Pt(NH_3)_2I_2$ is *significantly* downfield of that for *cis*-$Pt(NH_3)_2I_4$.

5.2.6 Discussion

(a) Normal spectra

The nine spectra selected in the previous section can be discussed in the same way that those for the [Pt(en)X_a] species are in Chapter **3**, *i.e.* by drawing comparisons with the solution ^{15}N NMR spectra of *cis*-$Pt^{II}(NH_3)_2X_2$ and *cis*-$Pt^{IV}(NH_3)_2X_2(OH)_2$. The discussion is mostly limited to consideration of the chemical shifts because accurate coupling constants are known only for chloride species; $J_{N\text{-}Pt}$ is 345 Hz for *cis*-$Pt(NH_3)_2Cl_2$ and 240 Hz for *cis*-$Pt(NH_3)_2Cl_4$. The ratio of these values fits the s-orbital contribution model (Equation [3.2.1]), which predicts that $J_{N\text{-}Pt^{II}}$ should be about one and a half times the size of $J_{N\text{-}Pt^{IV}}$. Chemical shifts are determined by the contributions of two types of substituents: the axial atoms, and the atoms coplanar with the ammines. The electronic structure defined by the axial atoms is overlaid with the effects of substituents *cis* and *trans* to the ammines. The equatorial ligands affect the ^{15}N chemical shifts in two ways. They control the d-orbital contribution of the platinum-ligand bond, and the extent of the splitting of the metal energy levels by the ligand field. In *cis*-$Pt(NH_3)_2X_2$, the atom *trans* to each ammine has the dominant influence, so that the nitrogen nuclei become more deshielded as the halogen is changed from Cl $\rightarrow$ Br $\rightarrow$ I. Solution NMR studies have shown that changing *cis*-$Pt^{II}(NH_3)_2X_2$ to *cis*-$Pt^{IV}(NH_3)_2X_2(OH)_2$ deshields the nitrogens by roughly the same amount, independent of X. The trend in chemical shift is reversed for *cis*-$Pt(NH_3)_2X_4$, because the axial atoms exert a greater influence than the equatorial ones. Axial chlorine atoms deshield the nitrogen nuclei indirectly by drawing electron density from the metal. Axial iodine atoms appear to push electron density on to the nitrogen nuclei *via* the platinum nuclei because the N-Pt^{IV} nuclei in *cis*-$Pt(NH_3)_2I_4$ are actually more shielded than the N-Pt^{II} ones in *cis*-$Pt(NH_3)_2I_2$.

(b) Anomalous spectra

The *cis*-diammine complex of greatest interest is the red form of *cis*-$Pt(NH_3)_2Br_2$. Studies have shown that it is thermodynamically more stable than the yellow form.[260] This is confirmed by the red Pt^{II} complex being the more difficult to oxidise. The solid-state ^{15}N NMR spectrum of red *cis*-$Pt(NH_3)_2Br_2$ consists of two main peaks of roughly equal intensity, which indicates that there are two types of nitrogen atom in the species. The difference between their chemical shifts ($\Delta\delta_N$) is far larger than any seen in a single molecule (*e.g.* $[Pt(en)_2]Cl_2$ or $[Pt(en)_2][PtCl_4]$) or between two forms of a complex (*e.g.* *cis*-$Pt(NH_3)_2Cl_2$). The red form of *cis*-$Pt(NH_3)_2Br_2$ is not mixed-valent because the $J_{N\text{-}Pt}$ coupling constants of both peaks are typical of those for N-Pt^{II} nuclei. There cannot be any charge disproportionation in red *cis*-$Pt(NH_3)_2Br_2$ because the NMR signal would not be as strong unless the sample was almost totally diamagnetic. The vibrational spectra of the red complex show none of the modes characteristic of an HMMC species. Therefore, although $\Delta\delta_N$ is roughly the same size as that found for HMMCs (*e.g.* about two-thirds of that for either *cis*-$[Pt(NH_3)_2Br_2][Pt(NH_3)_2Br_4]$) and the red colour may suggest an IVCT band, there is no evidence that the red form is an HMMC. The infrared spectrum of red *cis*-$Pt(NH_3)_2Br_2$ shows that its structure is similar to that of the yellow species. The only bands that distinguish the two types of *cis*-$Pt(NH_3)_2Br_2$ are ν(Pt-N) and $\rho(NH_3)$,[268] which are the two modes most affected by oxidation of the yellow complex to *cis*-$Pt(NH_3)_2Br_4$.[269,270] Any model proposed for the structure of red *cis*-$Pt(NH_3)_2Br_2$ must satisfy certain general criteria. It must contain two distinguishable nitrogen sites, half more shielded, and half less shielded, than the nitrogen nuclei in yellow *cis*-$Pt(NH_3)_2Br_2$. The infrared data suggest that differences in axial coordination are key to the problem. The structure must be similar to that of the yellow complex, because both red and yellow species can exist in the same sample. The planar molecules in *cis*-$Pt(NH_3)_2Cl_2$ are stacked in parallel columns,[246] but contain only one type of nitrogen nucleus. The simplest modification to this structure that creates two types of nitrogen involves every second molecule being rotated by an angle (θ) (see Figure 5.2.8). θ can take any value between 0 and 180 °, but the more likely rotations are ones of 45 or 90 °. If there is an accompanying change to the Pt^{II}-Pt^{II} distance, it may account for the differences between the infrared spectra of the red and yellow forms of *cis*-$Pt(NH_3)_2Br_2$. However, there are two features of the red complex that await explanation: its colour, and the size of the difference between its two nitrogen types. The colour of the green polymeric Magnus salts, $[Pt(NH_3)_4][PtX_4]$ (X = Cl or Br), is thought to arise from changes to the metal d - d transitions due to the strong Pt - Pt interactions.[271] Such interactions would be much weaker for non-ionic species, but the Pt - Pt distance might be reduced significantly if the angle θ is 45 °. This would bring the ligands closer together, which might magnify the difference between the two types of nitrogen nuclei.

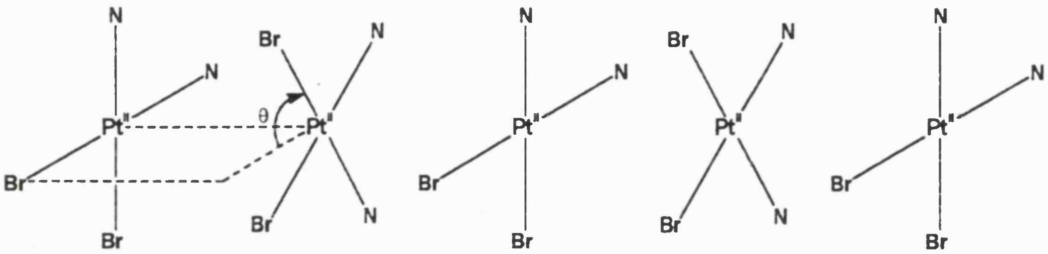

Figure 5.2.8 A depiction of a possible structure for the red form of cis-*$Pt(NH_3)_2Br_2$, where **N** represents an ammonia ligand.*

An equally important consideration is why neither *cis*-$Pt(NH_3)_2Cl_2$ nor *cis*-$Pt(NH_3)_2I_2$ appear to exhibits an analogous form of the red complex. The reason may be connected to steric crowding, and how it determines the rotational angle (θ) of the most stable form. There are two forms of *cis*-$Pt(NH_3)_2Cl_2$, but their ^{15}N chemical shifts differ by only 3 ppm, and their infrared spectra are nearly identical. In the crystal structure resolved for *cis*-$Pt(NH_3)_2Cl_2$, θ = 180 °,[266] and the second form is made from stacks in which θ = 0 °. By contrast, there is only one type of *cis*-$Pt(NH_3)_2I_2$. The bulky iodine atoms may prevent formation of stacks with θ = 0 °, and allow only the complex with θ = 180 ° to form. Yellow *cis*-$Pt(NH_3)_2Br_2$ may also consist of stacks with θ = 180 °. In this scenario, the red complex is intermediate between the systems with θ = 0 ° and θ = 180 °.

The behaviour shown by the supposed HMMCs of the *cis*-diammine species is no less complicated than that of the Pt^{II} monomers. *cis*-$[Pt(NH_3)_2Cl_2][Pt(NH_3)_2Cl_4]$ is difficult to synthesise. The red solid (**506a**) prepared by the published method [9] is known to be impure from its solid-state ^{15}N NMR spectrum, as is the product of its oxidation with chlorine. The impurity in the Pt^{IV} complex **505b** is identified as *trans*-$Pt(NH_3)_2Cl_4$, and comparison with the spectra of the *trans*-diammines (see section **5.4**) reveals that **506a** contains *trans*-[$Pt(NH_3)_2Cl_2$] and *trans*-[$Pt(NH_3)_2Cl_4$] chain units in addition to *cis*-[$Pt(NH_3)_2Cl_2$] and *cis*-[$Pt(NH_3)_2Cl_4$] units. **506a** may be a mixture of *cis*- and *trans*-[$Pt(NH_3)_2Cl_2$][$Pt(NH_3)_2Cl_4$], but the arrangement of the *cis* and *trans* units cannot be determined. The oxidation of *cis*-$Pt(NH_3)_2Cl_2$ by persulphate ions in the presence of KCl appears to involve some *cis*$\rightarrow$*trans* isomerisation. The exchange of chloride ions with Pt^{II} *cis*- complexes is not thought to cause isomerisation, but it has been suggested that there is isomerisation of *cis*-$Pt(NH_3)_2Cl_2$ on activated carbon,[260] although this was later refuted.[272] Chloride ions are known to facilitate exchange of axial halogens between Pt^{IV} and Pt^{II} centres, and some configuration change may be possible during this process. The *trans* units seem to be needed in the formation of the HMMC, because equimolar mixtures of *cis*-$Pt(NH_3)_2Cl_2$ and *cis*-$Pt(NH_3)_2Cl_4$ fail to give any of the desired linear-chain product. The yellow solid **506b** is merely a co-crystallisation of Pt^{II} and Pt^{IV} species with one interesting property; it contains two different types of N-Pt^{II} sites. It is not clear whether they have any connection with the two types of *cis*-$Pt(NH_3)_2Cl_2$, or whether there are two different N-Pt^{II} nuclei because of the presence of Pt^{IV} sites.

The oxidation of yellow *cis*-$Pt(NH_3)_2Br_2$ by persulphate ions also produces a sample with the characteristics of an HMMC. The solid-state ^{15}N NMR spectrum of complex (**503a**) is very noisy, and it is not possible to tell whether it contains any signals due to *trans* impurities. The spectrum of the product extracted from DMF (**503b**) is much better resolved. The two species do not differ significantly in their vibrational spectra, in their elemental analyses or in the difference between their N-Pt^{II} and N-Pt^{IV} chemical shifts, but the peaks for **503b** are some 5 ppm upfield of those for **503a**. The cause of this discrepancy is not clear. Although the presence of dimethylformamide in only one reaction solution may be significant, it does not seem to influence the solid-state ^{15}N NMR spectra of any other complex.

5.3 Solid-State ^{15}N NMR analysis of tetraammine platinum complexes

5.3.1 Introduction

The tetraammine complexes are of interest because they can be compared with the related *bis*-ethylenediamine species, which were examined in see Chapter 4. HMMCs of the formula $[Pt(NH_3)_4][Pt(NH_3)_4X_2]Y_4$, where X = Cl or Br, and Y = HSO_4^-, ClO_4^- or BF_4^-, have been prepared and characterised.[10-13] Few HMMCs with platinum-iodine chains are known,[14] and they are not considered here. Preparations of tetraammine HMMCs involve very severe reaction conditions. Typically, the halide salt $[Pt(NH_3)_4]X_2$ is oxidised with X_2 in hot acid (HY) to make $[Pt(NH_3)_4][Pt(NH_3)_4X_2]Y_4$. Such syntheses yield little product, which is often of poor quality, and are not reliably reproducible. On occasion, single crystals can be isolated from which structural or vibrational data are generated, but techniques that require a bulk sample of homogenous material (such as solid-state NMR spectroscopy) are less favoured. A further complication is that the routine synthesis of the most common HMMC precursor, $[Pt(NH_3)_4]Cl_2$, involves the use of a large excess of ammonia. The source of the ^{15}N-enriched ammine ligands is $^{15}NH_4Cl$, but there was only a limited amount of this compound available, and so it was necessary to find an alternative preparation of the tetraammine complex.

5.3.2 Platinum monomeric complexes

To limit the amount of ^{15}N-enriched starting material used, the platinum tetraammine halide salts, $[Pt(NH_3)_4]X_2$ (X = Cl (**510**) or Br (**511**)), were synthesised in two stages. In the first part of the preparation a solution containing K_2PtX_4 and a six-fold excess of 10 % $^{15}NH_4Cl$ was treated with aqueous NaOH while under reflux. The reaction flask was fitted with a condenser cooled with a dry ice/acetone mixture to reduce the loss of ammonia through evaporation. When the solution was almost colourless, a further aliquot of K_2PtX_4 was added, causing the precipitation of the green Magnus Salt $[Pt(NH_3)_4][PtX_4]$ (X = Cl (**512**) or Br (**513**)). The Magnus salt was then refluxed with a buffered excess of ^{15}N-natural abundance ammonia to form a colourless solution, from which the white halide salt was obtained. Solid-state ^{15}N NMR spectra were recorded for the Magnus Salts and halide complexes (see Figure 5.3.1). The data extracted from them are listed in Table 5.3.1. The most striking difference between the spectra of corresponding $[Pt(NH_3)_4]^{2+}$ and $[Pt(en)_2]^{2+}$ species is in the number of peaks they contain. Most tetraammine salts have only one type of nitrogen site, whereas the $[Pt(en)_2]^{2+}$ compounds appear to have two types. Other features that distinguish the two species are the ^{15}N chemical shifts, which are at much higher field for the $[Pt(NH_3)_4]^{2+}$ salts, and the associated $J_{N\text{-}Pt}$ coupling constants, which are slightly larger for the $[Pt(en)_2]^{2+}$ salts. Oxidation of $[Pt(NH_3)_4]Cl_2$ with chlorine gives the yellow solid $[Pt(NH_3)_4Cl_2]Cl_2$ (**514**). The solid-state ^{15}N NMR spectrum of this Pt^{IV} species consists of a single main peak at -394.4 ppm (with satellites), which is *ca.* 19 ppm downfield of that for the starting material. $J_{N\text{-}Pt^{IV}}$ is 220 Hz, which is about 20 % less than $J_{N\text{-}Pt^{II}}$ for $[Pt(NH_3)_4]Cl_2$. The corresponding bromide complex $[Pt(NH_3)_4Br_2]Br_2$ (**415**) is also yellow and is made by oxidising $[Pt(NH_3)_4]Br_2$ with bromine. It is more difficult to prepare than $[Pt(NH_3)_4Cl_2]Cl_2$, and its solid-state ^{15}N NMR spectrum has two broad signals, which are at -397.1 and -401.4 ppm.

Table 5.3.1 **^{15}N chemical shifts and $J_{N\text{-}Pt}$ coupling constants for halide complexes and Magnus salt-type compounds, (X = Halogen) [a]**

X	$[Pt^{II}(NH_3)_4]X_2$			$[Pt^{II}(NH_3)_4][PtX_4]$			$[Pt^{IV}(NH_3)_4X_2]X_2$		
	Label	δ / ppm	$J_{N\text{-}Pt}$ / Hz	Label	δ / ppm	$J_{N\text{-}Pt}$ / Hz	Label	δ / ppm	$J_{N\text{-}Pt}$ / Hz
Cl	**510**	-413.4	290	**512**	-412.1	300	**514**	-394.4	220
Br	**511**	-413.7	290	**513**	-406.5	300	**515**	-397.1 -401.4	- -

[a] *Chemical shifts are accurate to ± 0.4 ppm. Coupling constants are accurate to ± 20 Hz.*

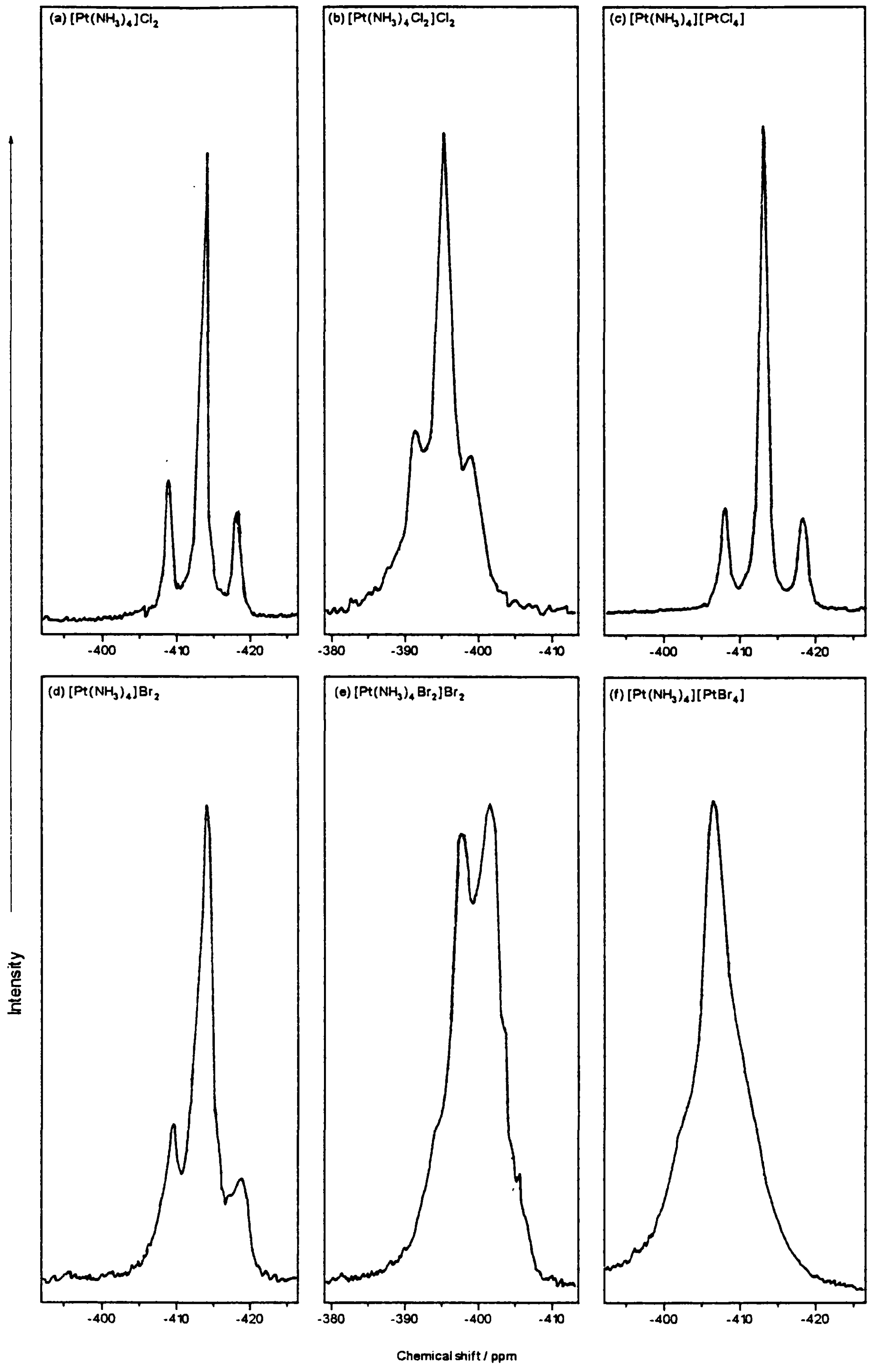

Figure 5.3.1 Solid-state ^{15}N NMR spectra of (a) $[Pt(NH_3)_4]Cl_2$, (b) $[Pt(NH_3)_4Cl_2]Cl_2$, (c) $[Pt(NH_3)_4][PtCl_4]$, (d) $[Pt(NH_3)_4]Br_2$, (e) $[Pt(NH_3)_4Br_2]Br_2$ and (f) $[Pt(NH_3)_4][PtBr_4]$.

On treating $[Pt(NH_3)_4]Cl_2$ with dilute acid HY, where Y = HSO_4^-, BF_4^- or ClO_4^-, the Pt^{II} salts $[Pt^{II}(NH_3)_4]Y_2$ were isolated. The progress of these ion exchange reactions was followed by recording the solid-state ^{15}N NMR spectrum of the solid extracted at each stage. As with the equivalent $[Pt(en)_2]^{2+}$ complexes, recrystallisation was necessary for most of the tetraammine salts. Ion exchange was completed successfully for Y = HSO_4^- (**516**) or BF_4^- (**517**), but not for Y = ClO_4^-. The solid-state ^{15}N NMR spectrum of recrystallised $[Pt(NH_3)_4](ClO_4)_2$ (**518b**) bears little relation to that of the crude material (**518a**). The ^{15}N chemical shifts for **516**, **517** or **518a** are all *ca.* 10 ppm upfield of those for the halide salts, but those for **518b** are *ca.* 15 ppm downfield. The corresponding Pt^{IV} species were synthesised in a similar manner by treating $[Pt(NH_3)_4Cl_2]Cl_2$ with HY. The anion has much less influence on the shielding of ^{15}N-Pt^{IV} nuclei than it does on that of ^{15}N-Pt^{II} nuclei, so ^{15}N chemical shifts for $[Pt(NH_3)_4Cl_2]Y_2$ (Y = HSO_4^- (**519**), BF_4^- (**520**)) are similar to those for $[Pt(NH_3)_4X_2]X_2$ (X = Cl or Br). The same is true for the crude perchlorate salt (**521a**), but the ^{15}N chemical shifts for the recrystallised solid (**521b**) are significantly upfield of those for the halide species. The solid-state ^{15}N NMR spectra for the six recrystallised complexes are shown in Figure 5.3.2; ^{15}N chemical shifts and $J_{N\text{-}Pt}$ values are listed in Table 5.3.2. The $J_{N\text{-}Pt}$ coupling constants are reasonably constant for a given oxidation state. The ranges are 210 - 240 Hz for $J_{N\text{-}Pt^{IV}}$ and 250 - 285 Hz for $J_{N\text{-}Pt^{II}}$. These values are smaller than those for the corresponding $[Pt(en)_2]^{2+}$ or $[Pt(en)_2Cl_2]^{2+}$ species.

Table 5.3.2 **^{15}N chemical shifts and $J_{N\text{-}Pt}$ coupling constants for $[Pt(NH_3)_4]^{2+}$ and $[Pt(NH_3)_4Cl_2]^{2+}$ compounds [a]**

Anion (Y)	$[Pt(NH_3)_4]Y_2$			$[Pt(NH_3)_4Cl_2]Y_2$		
	Label	δ / ppm	$J_{N\text{-}Pt}$ / Hz	Label	δ / ppm	$J_{N\text{-}Pt}$ / Hz
HSO_4^-	**516**	-417.7 -422.1	280 285	**519**	-398.1 -400.0	- -
BF_4^-	**517**	-422.3	-	**520**	-393.2	230
ClO_4^-	**518a**	-418.3 -423.1	270 270	**521a**	-392.8	210
	518b	-397.3 -400.4	250 270	**521b**	-403.3 -405.7	225 240

[a] *Chemical shifts are accurate to ± 0.3 ppm, coupling constants to ± 30 Hz.*

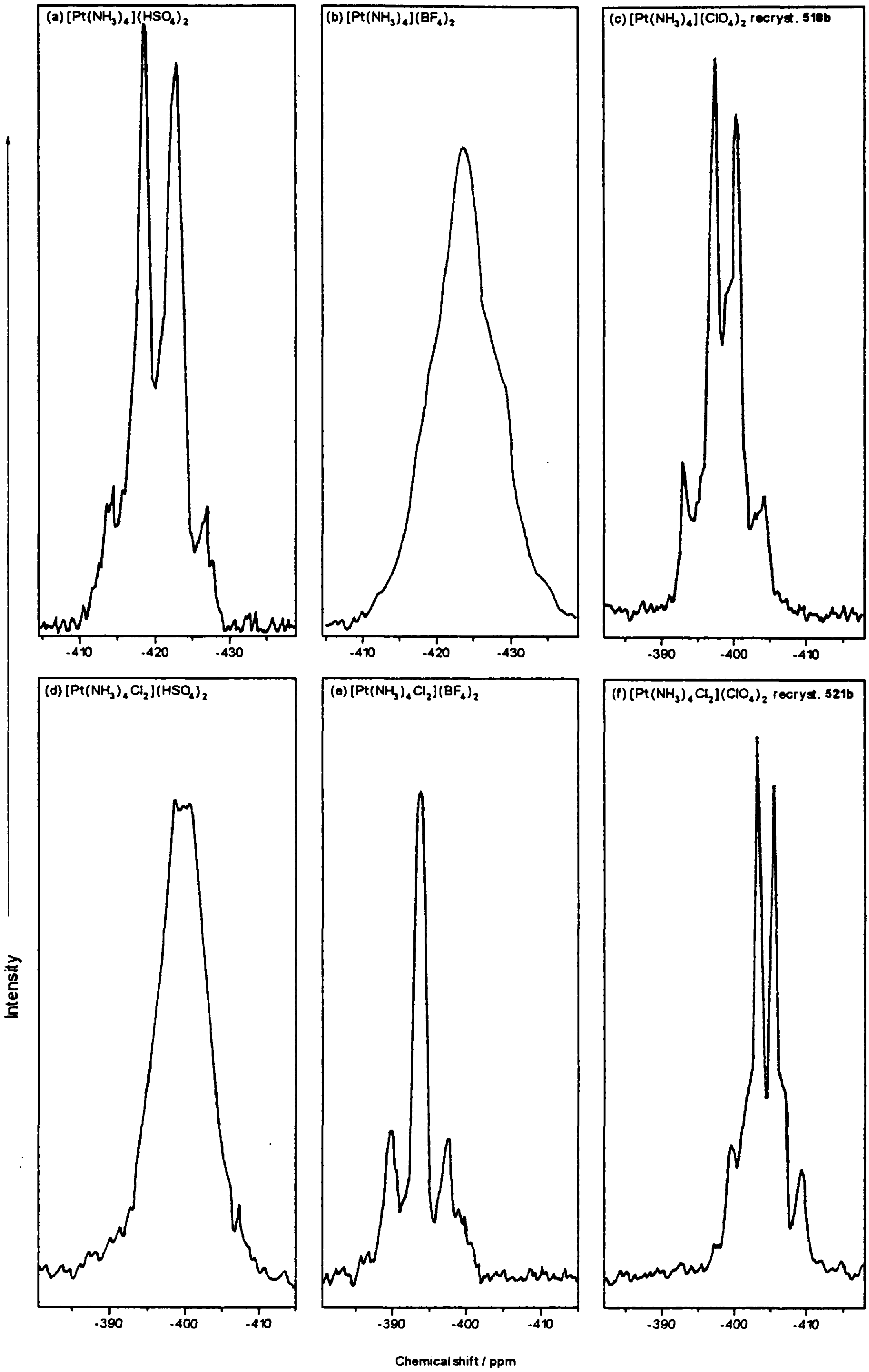

Figure 5.3.2 *Solid-state ^{15}N NMR spectra of (a) $[Pt(NH_3)_4](HSO_4)_2$, (b) $[Pt(NH_3)_4](BF_4)_2$ (c) $[Pt(NH_3)_4](ClO_4)_2$, (d) $[Pt(NH_3)_4Cl_2](HSO_4)_2$, (e) $[Pt(NH_3)_4Cl_2](BF_4)_2$, and (f) $[Pt(NH_3)_4Cl_2](ClO_4)_2$.*

5.3.3 ^{15}N analysis of HMMC complexes

The tetraammine HMMCs are not suited to study by solid-state ^{15}N NMR spectroscopy. Of the three counterions, only HSO_4^- forms monomeric complexes whose spectra are of good quality and are reproduced reliably. The spectra of the BF_4^- salts are very broad and poorly resolved, while those of the ClO_4^- salts are too dependent on the number of recrystallisations carried out. In any case, the HMMCs with ClO_4^- or BF_4^- counterions are difficult to synthesise in the quantities required for solid-state NMR analysis. Synthetic work was mostly limited to the preparation of HMMCs with hydrogensulphate counterions. $[Pt(NH_3)_4][Pt(NH_3)_4Cl_2](HSO_4)_4$ was made from an equimolar mixture of $[Pt(NH_3)_4](HSO_4)_2$ and $[Pt(NH_3)_4Cl_2](HSO_4)_2$. Its solid-state ^{15}N NMR spectrum has a single peak relating to each oxidation state, whereas the spectra of the monomers have two (see Figure 5.3.3). The difference between the chemical shifts of the N-Pt^{II} and N-Pt^{IV} nuclei is *ca.* 18 ppm, which is similar to that between the mean chemical shifts for the two monomers. The bromide linear-chain could not be isolated reproducibly or in sufficient quantities. Some samples of $[Pt(NH_3)_4][Pt(NH_3)_4Br_2](HSO_4)_4$ with ^{15}N in natural abundance had been prepared in a previous unrelated study,[273] and although some of them gave good solid-state NMR signals, their spectra were not consistent.

Table 5.3.3 **^{15}N chemical shifts and J_{N-Pt} coupling constants for tetraammine complexes with HSO_4^- as counterion [a]**

Complex	Colour	Label	$H_3{}^{15}N$-Pt^{II}		$H_3{}^{15}N$-Pt^{IV}	
			δ / ppm	J_{N-Pt} / Hz	δ / ppm	J_{N-Pt} / Hz
$[Pt(NH_3)_4](HSO_4)_2$	white	**516**	-417.7 -422.1	280 285		
$[Pt(NH_3)_4Cl_2](HSO_4)_4$	yellow	**519**			-398.1 -400.0	- -
$[Pt(NH_3)_4][Pt(NH_3)_4Cl_2](HSO_4)_4$	red	**522**	-425.2	270	-407.4	250

[a] *Chemical shifts are accurate to ± 0.3 ppm, coupling constants to ± 30 Hz.*

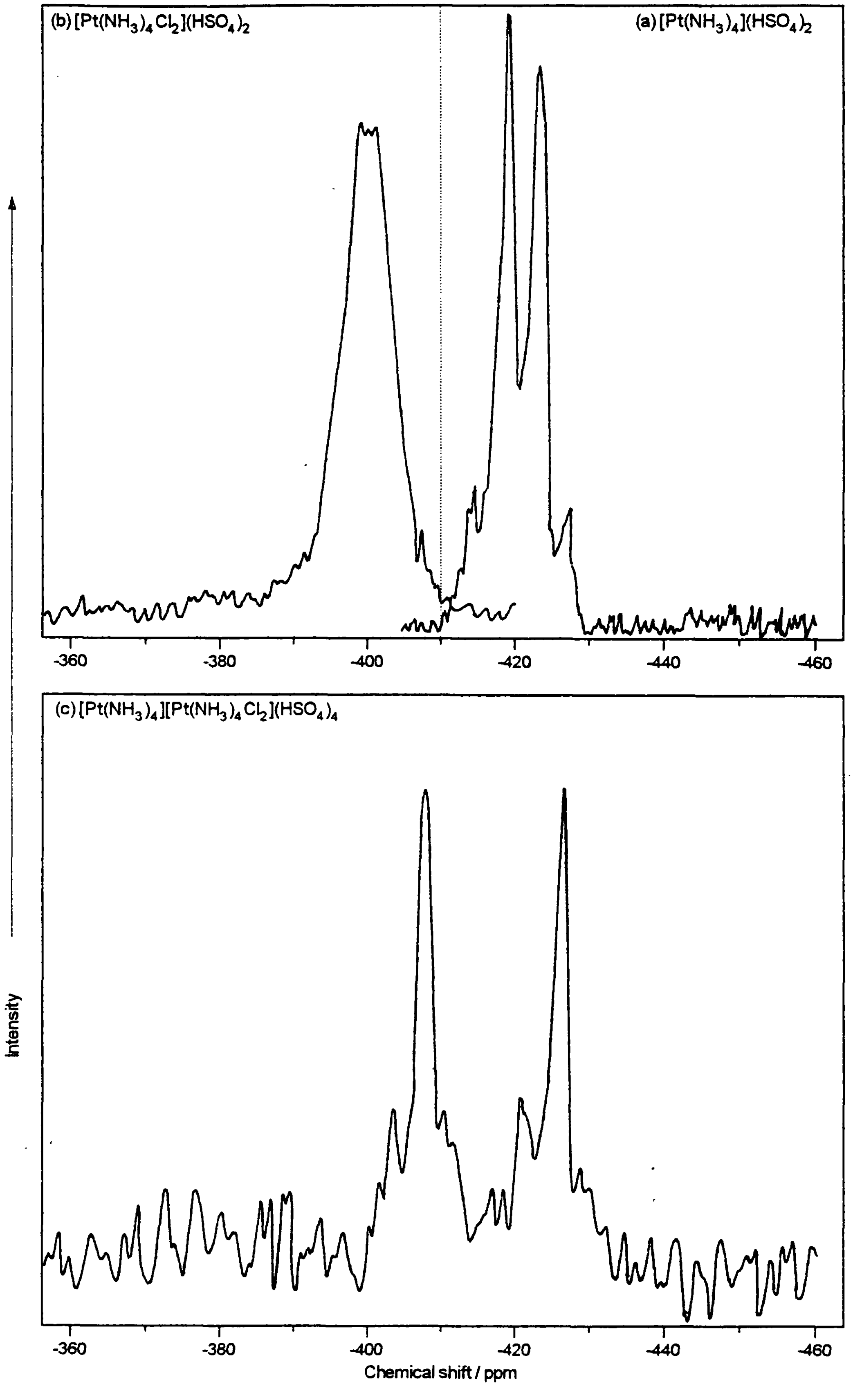

Figure 5.3.3 Solid-state ^{15}N NMR spectra of (a) $[Pt(NH_3)_4](HSO_4)_2$, (b) $[Pt(NH_3)_4Cl_2](HSO_4)_2$ and (c) $[Pt(NH_3)_4][Pt(NH_3)_4Cl_2](HSO_4)_2$.

5.3.4 Discussion

One of the main objectives of the solid-state ^{15}N NMR study is find an explanation for the difficulties encountered in the syntheses of tetraammine HMMCs, particularly in comparison to the corresponding *bis*-ethylenediamine species. Only one tetraammine HMMC was analysed successfully by solid-state ^{15}N NMR spectroscopy, so no general conclusions can be drawn about the effect of chain formation upon nuclear environments. The chemical shifts for $[Pt(NH_3)_4][Pt(NH_3)_4Cl_2](HSO_4)_2$ are roughly 6-8 ppm upfield of the mean values in the respective monomers. This is much larger change than is observed for $[Pt(en)Cl_2][Pt(en)Cl_4]$ or for $[Pt(en)_2][Pt(en)_2Cl_2]Y_4$ ($Y = ClO_4^-$ or BF_4^-), where chemical shift differences between monomer and chain are usually about 2 ppm. This probably means that the hydrogen bonding of the HSO_4^- ions in the HMMCs differs substantially from that in the monomers. Further evidence for this comes from the number of types of nitrogen nuclei that are observed; there are two in each of the constituent monomers, $[Pt(NH_3)_4](HSO_4)_2$ and $[Pt(NH_3)_4Cl_2](HSO_4)_2$, but only one for each oxidation state in the HMMC. Samples of $[Pt(NH_3)_4][Pt(NH_3)_4Br_2](HSO_4)_2$ were prepared, but although they contained sufficient HMMC to give intense resonance Raman signals, their solid-state ^{15}N NMR spectra are neither of good quality nor reproducible.

There is little correlation between the number of different nitrogen types exhibited by the platinum *bis*-en compounds and by the platinum tetraammines. There are two types of nitrogen for $[Pt(en)_2]Cl_2$, which were accounted for in Chapter **4** by examining the Pt-N and Pt-Cl^- distances, but only one type for $[Pt(NH_3)_4]Cl_2$. Changing the anion from a halide to one of the tetrahedral ions makes all the nitrogen nuclei in the $[Pt(en)_2]^{2+}$ salts identical, but the counterion salts of the tetraammines have two types of nitrogen nucleus. There must be a fundamental difference between the $[Pt(en)_2]^{2+}$ and $[Pt(NH_3)_4]^{2+}$ cations in the way that they bond with the anions in the crystal lattice, particularly when the anion is ClO_4^-. The solid-state ^{15}N NMR spectrum of $[Pt(en)_2](ClO_4)_2$ contains a single reproducible peak, but that of $[Pt(NH_3)_4](ClO_4)_2$ has two peaks whose chemical shifts depend on the recrystallisation process, although their coupling constants are invariant. This is no simple explanation for these observations. Possible influences on the spectrum of $[Pt(NH_3)_4](ClO_4)_2$ are the amount of ClO_4^- present in the crystal lattice and its coordination. If the Pt : ClO_4^- ratio does not have a fixed value, then synthesis of the HMMC may be hard to control, and HMMCs that are produced might be of variable character.

The ^{15}N chemical shifts for most of the tetraammine complexes, $[Pt(^{II}NH_3)_4]Y_2$, follow the same anion dependence shown by those for $[Pt^{II}(en)_2]Y_2$. The mean shifts for each Pt^{II} complex are compared graphically in Figure 5.3.4, where the value for $[Pt(NH_3)_4](ClO_4)_2$ is taken from the spectrum of the crude complex.

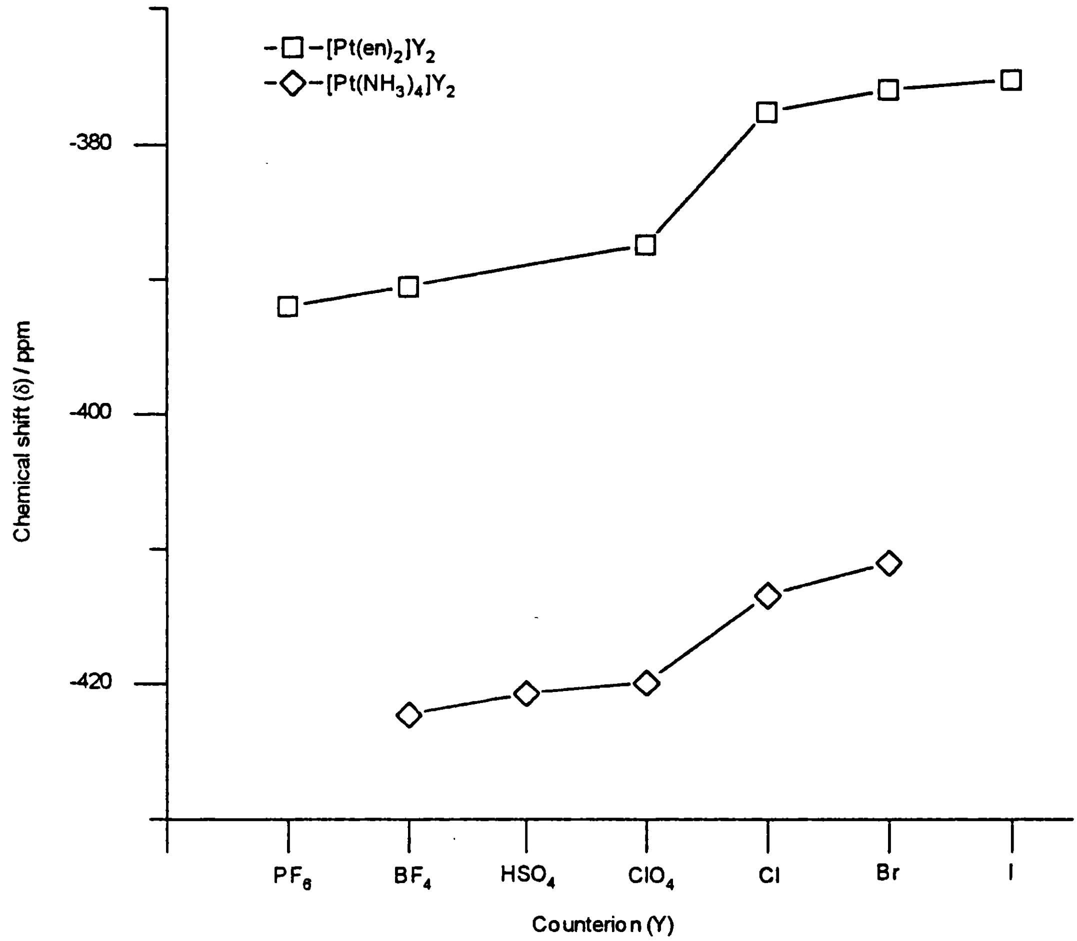

Figure 5.3.4 *Comparison of ^{15}N chemical shifts for $[Pt(en)_2]Y_2$ and $[Pt(NH_3)_4]Y_2$. Where two peaks are observed, the mean shift value is displayed.*

The ^{15}N chemical shifts reflect the hydrogen-bonding strength of the ion, which are in order :

$$Br^- < Cl^- < ClO_4^- < HSO_4^- < BF_4^- \qquad [5.3.1]$$

The relative positions of Br^-, Cl^-, ClO_4^- and BF_4^- in this series are the same as they are in Equation [4.2.1], which lists the hydrogen-bonding strength of these counterions in $[Pt(en)_2]Y_2$.

δ_N values for the halide salts are 5 - 10 ppm downfield of those for the salts with tetrahedral anions. The relationships between the spectra of $[Pt^{II}(NH_3)_4]Y_2$ and $[Pt^{IV}(NH_3)_4Cl_2]Y_2$ are similar to those between $[Pt(en)_2]Y_2$ and $[Pt(en)_2Cl_2]Y_2$. For a corresponding pair of complexes, $J_{N\text{-}Pt^{IV}}$ is generally about 80 % the size of $J_{N\text{-}Pt^{II}}$, while the chemical shifts for the N-Pt^{IV} nuclei are *ca.* 20 - 30 ppm downfield of those for the N-Pt^{II} nuclei. The reduction in coupling constant that occurs on oxidation is attributed to the smaller amount of s-orbital contribution to the Pt-N bond.[211] The contraction of the metal 5d orbital that accompanies oxidation is thought to be responsible for the increase in shielding around the metal, and around the nitrogen nuclei.

5.4 Solid-State ^{15}N NMR analysis of *trans*-diammine platinum complexes

5.4.1 Introduction

Trans-diammine complexes have not been studied as extensively as the *cis*-isomers, presumably because they are much less effective as anti-tumour agents. Most of them are made indirectly from *trans*-$Pt(NH_3)_2Cl_2$.[272] The syntheses of *trans*-$Pt(NH_3)_2Cl_2$ that are used more commonly give products of poor quality or low purified yield. There are no practical alternative methods for preparing *trans*-diammines. There is no synthetic equivalent of the Dhara synthesis of *cis*-$Pt(NH_3)_2I_2$ or *cis*-$Pt(NH_3)_2Cl_2$,[265] nor of the preparation of $Pt(en)I_4$ carried out by Watt and McCarley.[223] Several synthetic methods have been reported for *trans*-$Pt(NH_3)_2Cl_2$, but many of them are very vague.[264,274-279] Typically, $[Pt(NH_3)_4]Cl_2$ is used as the starting material, and it is either heated to decomposition,[275,277] or boiled in 6 M hydrochloric acid.[264,276] Babaeva *et al.* have modified the second method by allowing the reaction to proceed in a stream of carbon dioxide to prevent oxidation.[274] In addition, the slow precipitation of *trans*-$Pt(NH_3)_2Cl_2$ from a solution of $[Pt(NH_3)_4]Cl_2$ in dilute hydrochloric acid has been investigated.[279] The yellow crystalline product is a distinct form of *trans*-$Pt(NH_3)_2Cl_2$; its Raman spectrum differs from those for samples prepared by the other routes. Although thermal decomposition avoids the creation of Pt^{IV} impurities, the technique is unreliable; there is wide variation in the values reported for the most effective temperature and / or heating time. The problems associated with the preparation of ^{15}N-enriched $[Pt(NH_3)_4]Cl_2$ are outlined in section **5.3**, and they are a further hindrance to the synthesis of *trans*-diammines. The only *trans*-diammine HMMC that has been reported is *trans*-$[Pt(NH_3)_2Br_2][Pt(NH_3)_2Br_4]$.[6,22,23] Its crystal structure has been resolved on more than one occasion, and its resonance Raman spectrum has been recorded.[278] The mixed-metal chloride *trans*-$[Pd(NH_3)_2Cl_2][Pt(NH_3)_2Cl_4]$ has been isolated,[280] but only once has a synthesis of *trans*-$[Pt(NH_3)_2Cl_2][Pt(NH_3)_2Cl_4]$ been reported,[281] and its validity has not been confirmed. Therefore, there are several factors that make *trans*-diammines less suited to a study such as this, where both platinum and ligand are in limited supply.

5.4.2 Synthesis of *trans*-$Pt(NH_3)_2Cl_2$

Three different approaches were tried to secure a good quality sample of ^{15}N-enriched *trans*-$Pt(NH_3)_2Cl_2$. The first and most successful is the thermal decomposition of $[Pt(NH_3)_4]Cl_2$. The original method was described by Reiset,[282] but the difficulties encountered in repeating this work have led to reinvestigation of the reaction.[277] Reiset suggested that the tetraammine should be heated to 250 °C, but the accuracy of this value has been questioned because even at *ca.* 200 °C small fluctuations in temperature can result in total decomposition to platinum metal.[277] The most important practical problem to be overcome in the synthesis of *trans*-$Pt(NH_3)_2Cl_2$ from $[Pt(NH_3)_4]Cl_2$ is the prevention of hot spots on the surface of the tetraammine, since reduction of the sample to the metal will quickly follow their creation. In initial attempts, the tetraammine was heated in a thermostatically controlled oven, but uniform and consistent heating of the sample could not be achieved. To overcome this problem, a simple set of apparatus was assembled. $[Pt(NH_3)_4]Cl_2$ was mounted in an insulated glass tube, and it was heated with a Bunsen flame while a stream of nitrogen gas was passed over it (see section **5.6**). Temperature readings were taken from a thermometer in contact with the sample. $[Pt(NH_3)_4]Cl_2$ was heated slowly to 180 °C and the temperature kept constant for ten minutes, until the solid was pale yellow. The sample of *trans*-$Pt(NH_3)_2Cl_2$ (**523a**) isolated in this manner was of good quality. Its solid-state ^{15}N NMR spectrum consists of a single peak at -407.7 ppm, which has a coupling constant of 280 Hz (see Figure 5.4.1b). The ^{15}N chemical shift of *trans*-$Pt(NH_3)_2Cl_2$ is some 6 ppm downfield of that for $[Pt(NH_3)_4]Cl_2$.

The second approach to the synthesis of *trans*-$Pt(NH_3)_2Cl_2$ follows the route outlined by Kauffman *et al.*,[264] which involves boiling a solution of $[Pt(NH_3)_4]Cl_2$ in 6M HCl. A yellow solid was recovered from this reaction, but its solid-state ^{15}N NMR spectrum is not consistent with that of *trans*-$Pt(NH_3)_2Cl_2$. It contains a single main peak at *ca.* -394 ppm, which has a coupling constant of *ca.* 230 Hz, which is too small to be a $J_{N\text{-}Pt^{II}}$ value, even for a *trans*-diammine complex. Products recovered from repetitions of this reaction with weaker concentrations of acid, or without as much heating, have the peak at *ca.* -394 ppm in their solid-state ^{15}N NMR spectra, but they also have a second signal. It is at *ca.* -407 ppm and its $J_{N\text{-}Pt}$ value is close to 300 Hz, so it matches the signal found for *trans*-$Pt(NH_3)_2Cl_2$ (**523a**). When any of these samples is oxidised with chlorine, a yellow solid is isolated which has a solid-state ^{15}N NMR spectrum identical to that of *trans*-$Pt(NH_3)_2Cl_4$ (*vide infra*). The Kauffman method is prone to produce *trans*-$Pt(NH_3)_2Cl_4$ instead of the Pt^{II} species, which explains why Babaeva *et al.* revised the method in their work.[274]

The final preparative method is simply the slow decomposition of $[Pt(NH_3)_4]Cl_2$ in dilute hydrochloric acid. Previous work has suggested that there is a second distinct crystalline form of *trans*-$Pt(NH_3)_2Cl_2$ that is produced by the action of dilute HCl on $[Pt(NH_3)_4]Cl_2$.[279] When an acidified solution of the tetraammine was left to evaporate for a week, a crystalline yellow product (**523b**) formed. Its solid-state ^{15}N NMR spectrum is sharply defined and contains four peaks (see Figure 5.4.1c). The signals at highest or lowest field are the satellites of the two central resonances, which are at -406.9 and -411.5 ppm. The two coupling constants are both close to 280 Hz, and so are typical of N-Pt^{II} nuclei.

5.4.3 Other *trans*-complexes

Trans-$Pt(NH_3)_2Cl_2$ was oxidised fully with chlorine to produce yellow crystals of *trans*-$Pt(NH_3)_2Cl_4$ (**524**). The solid-state ^{15}N NMR spectrum of the Pt^{IV} complex contains a single peak at -394.6 ppm with $J_{N\text{-}Pt}$ = 235 Hz (see Figure 5.4.1d). The chloride HMMC could not be isolated. Partial oxidation of *trans*-$Pt(NH_3)_2Cl_2$ was attempted, and equimolar mixtures of *trans*-$Pt(NH_3)_2Cl_2$ and *trans*-$Pt(NH_3)_2Cl_4$ were prepared, but no linear-chain product was observed. The only reported synthesis for *trans*-$[Pt(NH_3)_2Cl_2][Pt(NH_3)_2Cl_4]$ is lacking in detail and it has not been followed by more explicit work.[281] It is supposed to involve the reaction of $[Pt(NH_3)_4]Cl_2$ with K_2PtCl_6, but the red solid that is isolated when these compounds are treated with each other has an infrared spectrum identical to that of K_2PtCl_4. The ^{15}N chemical shifts of the HMMC are known, but only through the analysis of impure *cis*-$[Pt(NH_3)_2Cl_2][Pt(NH_3)_2Cl_4]$ (see section **5.2**).

trans-$[Pt(NH_3)_2Br_2][Pt(NH_3)_2Br_4]$ (**525**) is the only *trans* HMMC for which reliable reports have appeared in the literature. A large sample of ^{15}N-unenriched HMMC was obtained from a previous study,[273] but its solid-state ^{15}N NMR spectrum was of poor quality. HMMC containing ^{15}N-enriched ammine was prepared freshly, albeit on a smaller scale, by treating an equimolar mixture of *trans*-$Pt(NH_3)_2Cl_2$ and *trans*-$Pt(NH_3)_2Cl_4$ with hydrobromic acid, but the quality of its spectrum was no greater than that of the older sample. Both solid-state NMR spectra contain two broad resonances, at *ca.* -401 and *ca.* -407 ppm, respectively. *trans*-$Pt(NH_3)_2Br_4$ was made by oxidising the HMMC with bromine. The solid-state ^{15}N NMR spectrum of the orange solid (**526**) has a strong peak at -395.3 ppm, which is significantly downfield of the N-Pt^{IV} resonance in *trans*-$[Pt(NH_3)_2Br_2][Pt(NH_3)_2Br_4]$. No iodide complexes were synthesised, nor was *trans*-$Pt(NH_3)_2Br_2$. ^{15}N chemical shifts and coupling constants for the ammine complexes are listed in Table 5.4.1.

Table 5.4.1 ^{15}N chemical shifts and $J_{N\text{-}Pt}$ coupling constants for various *trans*-diammine complexes [a,b]

trans-diammine complex	Colour	Label	H_3N-Pt^{II}		H_3N-Pt^{IV}	
			δ / ppm	$J_{N\text{-}Pt}$ / Hz	δ / ppm	$J_{N\text{-}Pt}$ / Hz
$Pt(NH_3)_2Cl_2$	yellow	**523a**	-407.7	280		
$Pt(NH_3)_2Cl_2$	yellow	**523b**	-407.0* -411.5	275 285		
$Pt(NH_3)_2Cl_4$	yellow	**524**			-394.6	235
$[Pt(NH_3)_2Cl_2][Pt(NH_3)_2Cl_4]$	*red*	***506a***	*-409.0*	-	*-391.2*	-
$Pt(NH_3)_2Br_4$	orange	**526**			-395.3	230
$[Pt(NH_3)_2Br_2][Pt(NH_3)_2Br_4]$	brown	**525**	-407	-	-401	-

[a] *For the monomeric complexes, chemical shifts are accurate to ± 0.3 ppm, and coupling constants to ± 30 Hz. For the HMMCs, chemical shifts are accurate to ± 0.5 ppm.*

[b] *Italics denote results taken from* cis-*$[Pt(NH_3)_2Cl_2][Pt(NH_3)_2Cl_4]$ (see Table 5.2.3).*

* *Signal due to an impurity.*

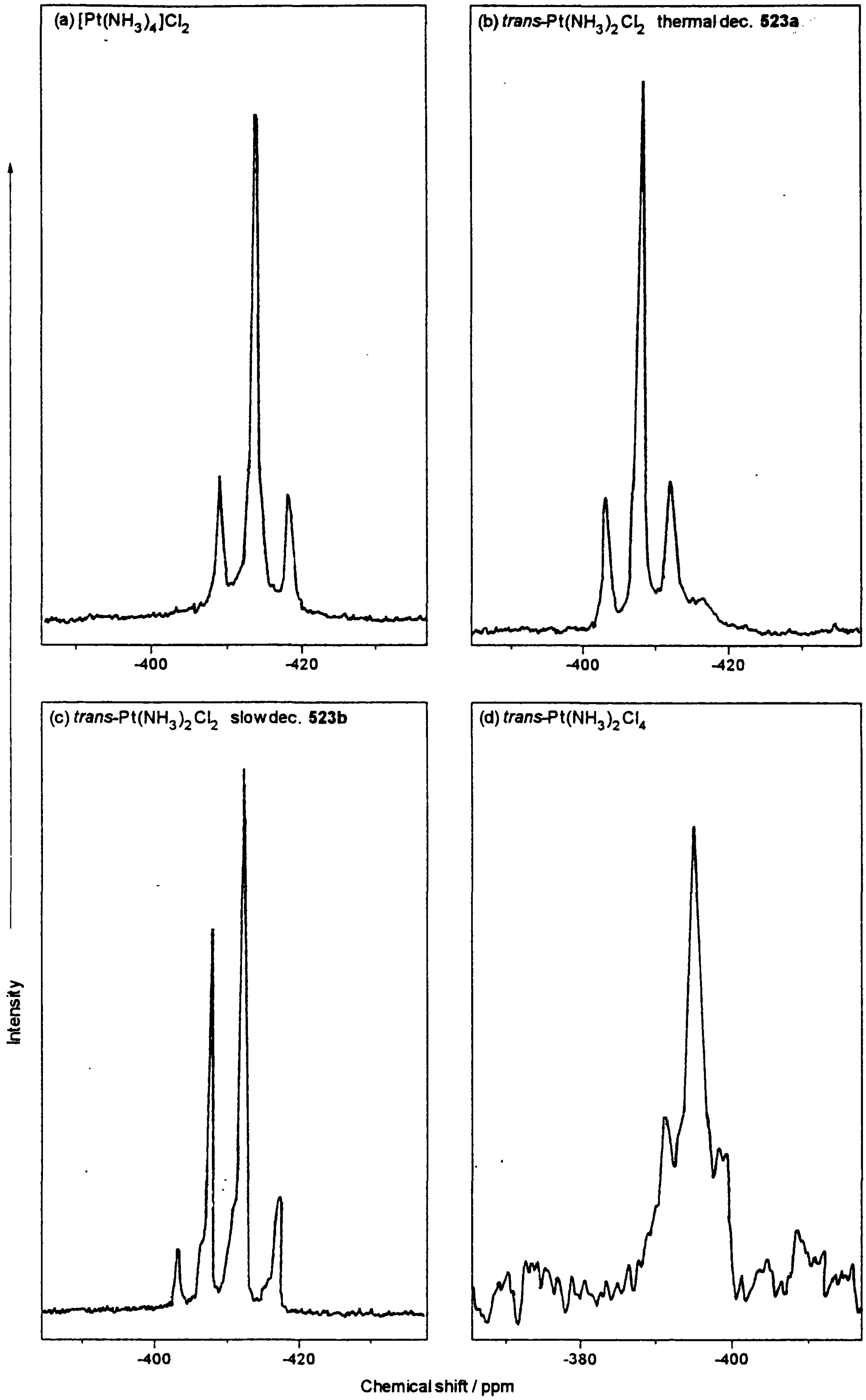

Figure 5.4.1 *Solid-state ^{15}N NMR spectra of (a) $[Pt(NH_3)_4]Cl_2$, (b)* trans-*$Pt(NH_3)_2Cl_2$ from thermal decomposition of $[Pt(NH_3)_4]Cl_2$, (c)* trans-*$Pt(NH_3)_2Cl_2$ from slow decomposition of $[Pt(NH_3)_4]Cl_2$ and (d)* trans-*$Pt(NH_3)_2Cl_4$.*

5.4.4 Discussion

Very few solid-state ^{15}N NMR spectra have been recorded for the *trans*-diammine complexes, and most of them concern the synthesis of *trans*-$Pt(NH_3)_2Cl_2$. The results show that thermal decomposition of $[Pt(NH_3)_4]Cl_2$ is a more effective way of making the Pt^{II} complex than that of heating a solution of the tetraammine in acid. The latter method is more likely to produce *trans*-$Pt(NH_3)_2Cl_4$, which may help to explain the broad ν(PtCl) signals seen in some of the reported infrared spectra for *trans*-$Pt(NH_3)_2Cl_2$ made by this route.[269,283] The decomposition of $[Pt(NH_3)_4]Cl_2$ in dilute hydrochloric acid provides spectrum of most interest, since it contains two main resonances of differing intensities. The ^{15}N chemical shift for the signal at lower field corresponds to that for *trans*-$Pt(NH_3)_2Cl_2$, but this is the minor product. The larger peak is at -411.5 ppm, but none of the chloride complexes analysed previously have a chemical shift that matches it. Even though -411.5 ppm is midway between the chemical shifts for $[Pt(NH_3)_4]Cl_2$ and *trans*-$Pt(NH_3)_2Cl_2$, it would be a mistake to assign this signal to $[Pt(NH_3)_3Cl]Cl$. There are two distinct types of nitrogen in $[Pt(NH_3)_3Cl]Cl$; in each cation there are two N nuclei *cis* to the chlorine atom, and one N nucleus *trans* to it. Solution ^{15}N NMR results for $[Pt(NH_3)_3Cl]^+$ show that relative to $[Pt(NH_3)_4]Cl_2$ the chemical shifts for the nuclei *cis* or *trans* to the chlorine are *ca.* 3 ppm upfield or *ca.* 1 ppm downfield, respectively (see Table 3.2.4).[213] On this basis, the solid-state ^{15}N chemical shifts for $[Pt(NH_3)_3Cl]Cl$ should be roughly -417 and -413 ppm, *i.e.* different from both signals in **523b**. The peak at -411.5 ppm is assigned to the second form of *trans*-$Pt(NH_3)_2Cl_2$. The difference between the chemical shifts of the two forms is large, but such variation is common for platinum ammine complexes. The confirmation of two types of *trans*-$Pt(NH_3)_2Cl_2$ is significant since it provides an explanation for the results obtained by Drew *et al.* in their investigation into the diammines.[257] When they treated *trans*-$Pt(NH_3)_2Cl_2$ (their "α-diammine") with alkali hydroxide or silver oxide, and then neutralised it with HCl, they isolated a complex which they termed "γ-diammine". It is almost certain that the α- and γ-diammines are the two forms of *trans*-$Pt(NH_3)_2Cl_2$.

The main objective of this work has remained unresolved. No convincing argument can be put forward to explain why there has been no unambiguous proof of the existence of *trans*-$[Pt(NH_3)_2Cl_2][Pt(NH_3)_2Cl_4]$ while *trans*-$[Pt(NH_3)_2Br_2][Pt(NH_3)_2Br_4]$ has been known for over fifty years. Samples of *trans*-$[Pt(NH_3)_2Br_2][Pt(NH_3)_2Br_4]$ were synthesised for this study, but they failed to give a good NMR signal. There is no obvious cause for this. Although bromine atoms cause residual dipolar coupling, reasonable results were obtained for both *cis*- and *trans*-$Pt(NH_3)_2Br_4$. The weakness of the signal may be the result of heterogeneity in the sample, or the presence of a significant number of unpaired electrons in the complex. The only reported preparation for *trans*-$[Pt(NH_3)_2Cl_2][Pt(NH_3)_2Cl_4]$ is possibly mistaken;[281] it is more likely to be a mixture of K_2PtCl_4 and $[Pt(NH_3)_4Cl_2]Cl_2$. *trans*-$Pt(NH_3)_2Cl_2$ is oxidised very easily to form *trans*-$Pt(NH_3)_2Cl_4$, but partial oxidation to the HMMC cannot be effected. In terms of their solid-state ^{15}N NMR spectra, *trans*-$Pt(NH_3)_2Cl_2$ and *trans*-$Pt(NH_3)_2Cl_4$ are much more similar than their *cis* counterparts. Their ^{15}N chemical shifts differ by *ca.* 13 or 17 ppm (depending on which Pt^{II} complex is chosen), which is roughly half that for the *cis* species. The solution ^{15}N NMR results for the ions $[Pt(NH_3)_3X]^+$ and $[Pt(NH_3)_3X(OH)_2]^+$ (X = Cl, Br or I) show that the peak for the ammine *trans* to X is upfield of that for the ammines *cis* to X in all cases except $[Pt(NH_3)_3Cl]^+$, where it is downfield.[213] Consequently, in all the species $[Pt(NH_3)_2X_2]$ and $[Pt(NH_3)_2X_2(OH)_2]$ except for $[Pt(NH_3)_2Cl_2]$ the chemical shift for the *trans* isomer will be upfield of that for the *cis* isomer. This is precisely what is observed in the solid-state ^{15}N NMR spectra of $[Pt(NH_3)_2Cl_2]$ and $[Pt(NH_3)_2Cl_4]$. The $J_{N\text{-}Pt}$ coupling constants provide additional information about the differences between *cis* and *trans* isomers. The value of $J_{N\text{-}Pt^{IV}}$ for *trans*-$Pt(NH_3)_2Cl_4$ is 235 Hz, which is similar to that for *cis*-$Pt(NH_3)_2Cl_4$. $J_{N\text{-}Pt^{II}}$ for *trans*-$Pt(NH_3)_2Cl_2$ is *ca.* 280-Hz, but for *cis*-$Pt(NH_3)_2Cl_2$ it is *ca.* 330 Hz. Therefore for the *trans* complexes, $J_{N\text{-}Pt^{II}}$ is 1.2 times the size of $J_{N\text{-}Pt^{IV}}$; the factor predicted on the basis of s-orbital contribution is 1.5 times.[211] Solution NMR studies have shown that $J_{N\text{-}Pt^{II}}$ for *trans*-PtA_2Cl_2 (A = dodecylamine) is *ca.* 85 % the size of that for *cis*-PtA_2Cl_2.[211] This has led to the conclusion that isomerisation in these species is accompanied by significant rehybridisation due to σ effects. A similar kind of rehybridisation in *trans*-$Pt(NH_3)_2Cl_2$ is a possible cause for the difficulty encountered in HMMC formation.

5.5 Conclusions

The results in this chapter have shown that many of the platinum ammine complexes have unusual properties in the solid state. This has prevented any conclusions being made about the general nature of the ammine HMMCs. The solid-state NMR study provides evidence that suggests that the tetraammine complexes are not as closely related to the *bis*-diamine species as might have been supposed. In particular, the process of chain formation, which is straightforward for mixtures of the ions $[Pt(en)_2]^{2+}$ and $[Pt(en)_2Cl_2]^{2+}$, cannot be guaranteed for $[Pt(NH_3)_4]^{2+}$ and $[Pt(NH_3)_4Cl_2]^{2+}$ ions, even in the presence of a large excess of counterion. There are surprising observations for compounds that are supposedly well understood, such as *cis*-$Pt(NH_3)_2Cl_2$, *cis*-$Pt(NH_3)_2Br_2$ or *trans*-$Pt(NH_3)_2Cl_2$. All three exhibit two different forms that can be distinguished easily from their solid-state ^{15}N NMR spectra. Although some properties of the two types of *trans*-$Pt(NH_3)_2Cl_2$ have been compared,[279] as have those of *cis*-$Pt(NH_3)_2Br_2$,[268] the sum of knowledge is not great for two reasons. Firstly, in each case one type is formed less readily than the other and so has escaped the notice of many workers. Secondly, it is difficult to determine how much of each form of a complex is present in a given sample by any means save solid-state ^{15}N NMR spectroscopy. Generally, one form of each species is isolated by rapid precipitation while the other results from slow crystallisation. It is possible that during slow crystal formation the molecules orientate themselves so that there are strong interactions between them, and that the ^{15}N chemical shifts are altered accordingly. The shielding around the nitrogen nuclei may be changed indirectly, due to some overlap between the metal orbitals or directly, through the influence of ammine ligands on neighbouring molecules.

The factors that determine the stability and ease of formation of a diammine HMMC have not been established. Two previously unknown HMMCs, *cis*-$[Pt(NH_3)_2Br_2][Pt(NH_3)_2Br_4]$ and *cis*-$[Pt(NH_3)_2I_2][Pt(NH_3)_2I_4]$, have been synthesised. The third *cis* linear-chain species, *cis*-$[Pt(NH_3)_2Cl_2][Pt(NH_3)_2Cl_4]$, was shown to have significant *trans* impurities. No useful spectra were recorded for any of the *trans* analogues. It is possible that there is some connection between the instability of *trans*-$[Pt(NH_3)_2Cl_2][Pt(NH_3)_2Cl_4]$ and the nature of the hybrid orbitals thought to be present in *trans*-$Pt(NH_3)_2Cl_2$. *trans*-$[Pt(NH_3)_2Br_2][Pt(NH_3)_2Br_4]$

was isolated, but the signals in its solid-state ^{15}N NMR spectrum are very weak and the chemical shifts obtained from them are liable to be inaccurate. Similarly, many tetraammine HMMCs gave poor solid-state NMR spectra; the only complex to yield clearly defined peaks is $[Pt(NH_3)_4][Pt(NH_3)_4Cl_2](HSO_4)_2$. The problems encountered may be linked to a tendency to form non-stoichiometric chains that is shown by tetraammine complexes,[11,13] and by Wolffram's Red.[284] It is possible that such species contain a greater number of unpaired electrons, which reduces the intensity of the NMR signal. It is difficult to gauge the potential of the platinum ammines for further solid-state NMR study. ^{15}N analysis has proved to be much harder than for comparable *bis*-ethylenediamine species. Although many of the spectra could be bettered, it would involve a large investment (in terms of spectrometer time, platinum and ^{15}N-enriched ligands) which may not be justified by the end results. No concerted effort was put into ^{195}Pt analysis, partly because the amount of sample required is large, and partly because the complexes that exhibit the most interesting properties are anisotropic, and will therefore give spectra that contain many spinning sidebands.

The work on the platinum ammines highlights the strengths and weaknesses of the technique of solid-state ^{15}N NMR spectroscopy. It is probably the most effective method for determining the purity and composition of samples, particularly in cases where there are two distinct forms of the complex present. However, it has failed to give strong signals for samples of HMMCs that have good resonance Raman spectra. This indicates that either the quality of Raman spectra is not greatly dependent on sample purity, or certain HMMCs cannot be analysed successfully by solid-state ^{15}N NMR spectroscopy.

5.6 Experimental Details

5.6.1 Syntheses

The source of the ^{15}N-enriched ammine ligands was 10 % ^{15}N-enriched ammonium chloride, obtained from Aldrich Chemical Co.; it is referred to as 10 % $^{15}NH_4Cl$ in the text.

cis-diammine platinum bromide complexes

***cis*-$Pt(NH_3)_2Br_2$**

yellow complex (501a) was made by the rapid addition of KBr solution to a freshly prepared solution of *cis*-$[Pt(NH_3)_2(H_2O)_2]^{2+}$ ions. Diaquo ions are made routinely by treating *cis*-$Pt(NH_3)_2I_2$ **(507)** with silver nitrate in a 1 : 2 molar ratio.

red complex (501b) was made either by careful recrystallisation of **501a**, or by slow addition of KBr solution to *cis*-$[Pt(NH_3)_2(H_2O)_2]^{2+}$ ions.

orange complex (501c) resulted from one preparation of **501a**, where the addition of bromide ions was slow enough to allow some red species to be produced.

***cis*-$Pt(NH_3)_2Br_4$**

orange complex (502a) was produced by the full oxidation of any form of *cis*-$Pt(NH_3)_2Br_2$. For **501a**, this involved warming a slurry of the yellow solid with an excess of bromine dissolved in a water/ethanol mixture. Analogous reaction mixtures were used for **501b** or **501c**, but they were heated and stirred for several hours.

red complex (502b) was a result of the oxidation of **501c** under milder conditions.

***cis*-$[Pt(NH_3)_2Br_2][Pt(NH_3)_2Br_4]$**

Ex-aquo complex (503a) was prepared by an adaptation of the method employed by Chugayev and Chernyaev,[9] using half the specified amount of persulphate.

Ex-DMF complex (503b) was made by adding water to a dimethylformamide (DMF) solution containing equimolar amounts of *cis*-$Pt(NH_3)_2Br_2$ **(501a)** and *cis*-$Pt(NH_3)_2Br_4$ **(502a)**.

cis-diammine platinum chloride complexes

***cis*-Pt$(NH_3)_2Cl_2$**

Standard complex (504a) was synthesised by the published method,[264] except that 10 % $^{15}NH_4Cl$ was used instead of NH_4Cl.

Dhara complex (504b) was made by the published method,[265] with one small alteration. The freshly prepared ammonia was made by adding a solution of NaOH to an equimolar amount of aqueous $^{15}NH_4Cl$.

***cis*-Pt$(NH_3)_2Cl_4$**

Standard complex (505a) was synthesised by the oxidation of **504a**, **504b** or **506b**, using the method of Kauffman and Cowan.[264]

Impure complex (505b) was made by the same oxidation method as the standard complex, but using **506a** as the starting material.

***cis*-[Pt$(NH_3)_2Cl_2$][Pt$(NH_3)_2Cl_4$]**

Red complex (506a) was prepared by an adaptation of the method employed by Chugayev and Chernyaev,[9] using half the specified amount of persulphate, and with **504a** as the starting material.

Yellow complex (506b) was synthesised by first mixing equimolar amounts of *cis*-Pt$(NH_3)_2Cl_2$ (**504a** or **504b**) and *cis*-Pt$(NH_3)_2Cl_4$ (**505a**) (each dissolved in a minimum of hot water) and then allowing the solution to cool *in vacuo*.

cis-diammine platinum iodide complexes

***cis*-Pt$(NH_3)_2I_2$ (507)** was made by a method similar to that employed by Dhara in the preparation of *cis*-Pt$(NH_3)_2Cl_2$.[265] The freshly prepared ammonia was made by adding a solution of NaOH to an equimolar amount of aqueous $^{15}NH_4Cl$.

***cis*-Pt$(NH_3)_2I_4$ (508)** was made oxidising **507** with an excess of persulphate ions and then adding two equiv. of potassium iodide. Alternatively, **505a** was treated with an excess of iodide ions to effect a simple halide exchange reaction.

***cis*-[Pt(NH_3)$_2$$I_2$][Pt($NH_3$)$_2$$I_4$] (509)** was made by mixing DMF solutions containing equimolar amounts of **507** and **508**, followed by immediate addition of water, to precipitate the bronze crystalline product.

tetraammine platinum complexes

[Pt(NH_3)$_4$]Cl_2 (510) was synthesised in stages that were designed to minimise the amount of NH_3 used. A solution containing potassium tetrachloroplatinate (K_2PtCl_4) and 6 equiv. of $^{15}NH_4Cl$ was stirred and heated to 90 °C in a 3-necked flask. A Quickfit coldfinger, chilled with a dry ice/acetone mixture, was fitted to the central neck. A solution containing 4 equiv. of NaOH was added dropwise to the reaction mixture over a period of about 2 h. Once the solution was nearly clear, it was cooled and filtered, and the [Pt(NH_3)$_4$]$^{2+}$ ions extracted in the form of Magnus' Green salt (MGS), [Pt(NH_3)$_4$][$PtCl_4$] (**512**), by addition of K_2PtCl_4. A slurry of MGS, buffered with NH_4Cl, was then treated with an excess of concentrated ammonia in the standard fashion. This resulted in a sample of [Pt(NH_3)$_4$]Cl_2 in which ^{15}N-enrichment is approximately 5 %.

[Pt(NH_3)$_4$]Br_2 (511) was prepared by a method analogous with that of **510**, except that potassium tetrabromoplatinate (K_2PtBr_4) was used instead of K_2PtCl_4 in all cases.

[Pt(NH_3)$_4$][$PtCl_4$] (512) was prepared by the addition of $PtCl_4^{2-}$ ions to **510**. Alternatively, 10 % ^{15}N-enriched samples were collected during the synthesis of **510**.

[Pt(NH_3)$_4$][$PtBr_4$] (513) was prepared by the addition of $PtBr_4^{2-}$ ions to **511**. Alternatively, 10 % ^{15}N-enriched samples were collected during the synthesis of **511**.

[Pt(NH_3)$_4$$Cl_2$]$Cl_2$ (514) was prepared from **510** by a standard oxidation method.[218]

[Pt(NH_3)$_4$$Br_2$]$Br_2$ (515) was prepared by treating a heated solution of **511** with an excess of an ethanolic solution of bromine.

[Pt(NH_3)$_4$]Y_2 (Y = HSO_4^- (516) or BF_4^- (517)) was prepared by the addition of HX to **510**. Each complex was recrystallised from an ethanol/water mixtures.

[Pt(NH_3)$_4$](ClO_4)$_2$ (518a) was prepared by the addition of the perchloric acid to **510**. Recrystallisation of **518a** with $HClO_4$ in an ethanol/water mixture gave product **518b**.

$[Pt(NH_3)_4Cl_2]Y_2$ ($Y = HSO_4^-$ (**519**) or BF_4^- (**520**)) was prepared by the addition HX to **514**. Each complex was recrystallised from ethanol / water mixtures.

$[Pt(NH_3)_4Cl_2](ClO_4)_2$ (**521a**) was prepared by the addition of the perchloric acid to **514**. Recrystallisation of **521a** with $HClO_4$ in an ethanol / water mixture gave product **521b**.

$[Pt(NH_3)_4][Pt(NH_3)_4X_2](HSO_4)_2$ ($X = Cl^-$ (**522**) or Br^-) was prepared by a standard method.[12]

trans-diammine platinum complexes

***trans*-$Pt(NH_3)_2Cl_2$**

Standard complex (**523a**) was made by heating to 180 °C a sample of $[Pt(NH_3)_4]Cl_2$ under a stream of nitrogen until a yellow solid was formed.

Second form (**523b**) was recovered from the evaporated residue of a solution of $[Pt(NH_3)_4]Cl_2$ in dilute hydrochloric acid.

***trans*-$Pt(NH_3)_2Cl_4$** (**524**) was synthesised by a standard oxidation method.[285]

***trans*-$[Pt(NH_3)_2Br_2][Pt(NH_3)_2Br_4]$** (**525**) was recovered from a solution containing equimolar amounts of *trans*-$Pt(NH_3)_2Cl_2$ and *trans*-$Pt(NH_3)_2Cl_4$ by treating it with HBr. A sample with ^{15}N-unenriched ligands was obtained from a previous study.[273]

***trans*-$Pt(NH_3)_2Br_4$** (**526**) was made by oxidising *trans*-$[Pt(NH_3)_2Br_2][Pt(NH_3)_2Br_4]$ (**525**) with an excess of bromine dissolved in a water / ethanol mixture.

5.6.2 Solid-State ^{15}N NMR spectroscopy

Solid-state ^{15}N NMR spectra were recorded using a Bruker MSL-300 spectrometer at 30.42 MHz using cross-polarisation, proton dipolar decoupling, and magic-angle spinning. The CP condition was set on a sample of doubly ^{15}N-enriched ammonium nitrate. Spinning speeds of 2.8-4.5 kHz were employed, sufficient to eliminate virtually all spinning sidebands for these complexes. The contact time was 0.5 ms, acquisition times were 20-75 ms and the recycle delay between scans was 2-5 s. The typical 90 ° pulse length for protons was 7 μs. All spectra were recorded at room temperature (296 K). Typically, measurements were carried out on sample sizes of 50-150 mg of 5-10 % enriched material. Total scan times varied from 1 h up to 40 h, depending on the number of different nitrogen sites and the identity of the counterion, as well as sample size and quality. Chemical shifts are quoted relative to external liquid nitromethane using solid NH_4NO_3 as a secondary reference: the ammonium peak was taken to resonate at -358.4 ppm.[217] Observed chemical shifts were not corrected for the change in magnetic susceptibility between samples.

5.6.3 Resonance Raman spectroscopy

Spectra were recorded on the Spex 1401 double monochromator, with Bausch and Lomb gratings (1200 line mm^{-1}). Appropriate exciting lines were provided by a Kr^+ laser (CR-3000K). All complexes were analysed as single crystals at liquid-nitrogen temperature. Alignment was achieved with the aid of a Charged Coupled Device (CCD) camera, fitted to the spectrometer.

CHAPTER 6

PLATINUM LINEAR-CHAIN COMPLEXES CONTAINING AROMATIC LIGANDS

6.1 Introduction

6.1.1 Purpose of study

An important part of the work currently undertaken on HMMC complexes concerns the chain defects described in section **1.4**. There are several methods for increasing the number of defects in a chain, either temporarily or permanently. Intrinsic defects can be created by chemical doping, either by partial substitution of the metals [46-53] or the halogens,[54-63] or by infusing the crystal lattice with halogen gas.[64] Photolysis can induce temporary defects, which decompose on warming ("annealing"). None of these processes reproduces accurately the intrinsic defects that occur naturally in undoped complexes. Metal or halogen substitution will impose a large mass and/or force defect, independent of any change to the electronic structure of the system. Halogen gas infusion places extra molecules into the lattice, which will cause small vibrational defects. Photoexcitation can alter charge densities and electronic structures in a drastic and imprecise manner, producing many different defects. Consequently, the resonance Raman spectra of photolysed samples contain broad unresolved signals. In this investigation the electronic densities along the MX chain of a template molecule are altered by replacing some of the equatorial ligands. Two templates were chosen, one each for the neutral and cationic chain systems. $[Pt(en)X_2][Pt(en)X_4]$ and $[Pt(en)_2][Pt(en)_2X_2](ClO_4)_4$ (X = Cl or Br) were selected because of the large amount of data available for them, and because they are known to support charge defects. Most of the work was carried out on the chloride complexes, because the defect modes in the bromide complexes are not as well defined and are enhanced mostly at wavelengths longer than those available (see section **2.2**). Enhancement of the defects in chloride-chain species occurs mainly in the yellow or red part of the visible spectrum.

6.1.2 Complexes containing *ortho*-phenylenediamine

In the species that have been reported, the identity of the amine ligand does not usually have a large influence on the spectroscopic properties of cationic-chain platinum HMMCs. This is because most of these ligands are primary amines and they tend to differ from each other in their interaction with the counterions rather than their effect on the electronic structure of the MX chain. The platinum complexes of aromatic amines are not known to form HMMCs, but the behaviour of certain compounds of *ortho*-phenylenediamine (opd) ($C_6H_8N_2$, see Figure 6.1.1) suggests that if such species could be introduced into linear-chains then the products would be worth examining. *Ortho*-phenylenediamine can act as monodentate ligand when bonding to nickel,[286,287] but in its most interesting monomeric complex, [Ni(opd)$_2$] it is solely bidentate. Treatment of [Ni(opd)$_2$] with different amounts of iodine gives species that have the formula [Ni(opd)$_2$]I$_x$ (x = 0.97, 2.57 or 5.79) and form one-dimensional stacks;[288] the products of bromine oxidation have not be characterised.

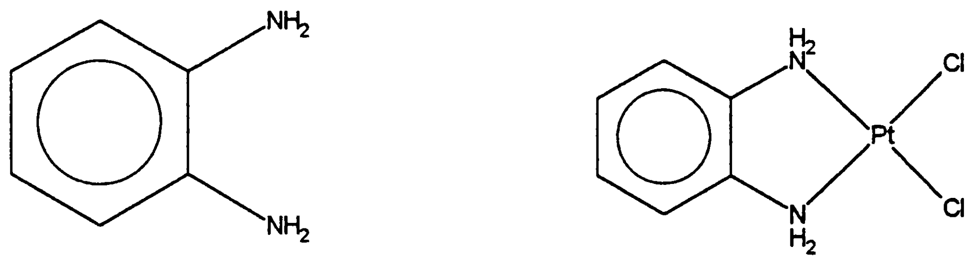

ortho-phenylenediamine (opd) Pt(opd)Cl$_2$

Figure 6.1.1 Representation of the ligand ortho-phenylenediamine (opd) and the cisplatin-type complex it forms with platinum, Pt(opd)Cl$_2$.

[Ni(opd)$_2$] has both a palladium and a platinum analogue.[289] The platinum species is a dark blue solid formed by the reaction of ligand with K_2PtCl_4 at high pH. It is not clear how many hydrogen atoms are bound to each nitrogen atom in [Pt(opd)$_2$]. The ν(N-H) region of its infrared spectrum is very complicated in the solid state, but its solution infrared spectrum shows that $[Pt(opd)_2]^0$ contains NH groups, but not NH_2 ones.[289] Each ligand must therefore lose two or three protons on coordination. It is more likely that two protons are removed, because $[Pt(opd)_2]^0$ can gain or lose up to two units of charge in electrochemical reactions (see Figure 6.1.2). For simplicity, *ortho*-phenylenediamine is still abbreviated as opd for $[Pt(opd)_2]^0$ even though its composition differs from that of the free ligand. If the amine loses two protons, then the platinum centre will have a formal oxidation state of +2. A predicted structure for $[Pt^{II}(opd)_2]^0$ is shown in Figure 6.1.2, along with the products of its reversible two-stage oxidation or reduction in solution. In none of these species is the charge distribution known. The premise for the work in section **6.2** is that the effective oxidation state of the platinum nucleus in $[Pt(opd)_2]^0$ differs significantly from that in $[Pt(en)_2]Y_2$ (Y = counterion), and so the doping of $[Pt(opd)_2]^0$ into the HMMCs $[Pt(en)_2][Pt(en)_2X_2](ClO_4)_4$ (X = Cl or Br) will produce species with interesting spectroscopic features.

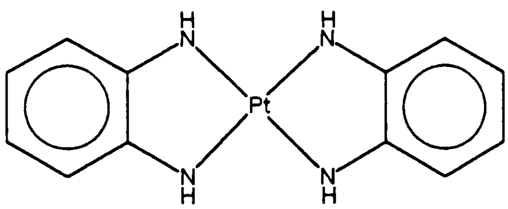

"$[Pt(opd)_2]^0$"

$$[Pt(opd)_2]^{-2} \underset{+e^-}{\overset{-e^-}{\rightleftharpoons}} [Pt(opd)_2]^{-1} \underset{+e^-}{\overset{-e^-}{\rightleftharpoons}} [Pt(opd)_2]^{0} \underset{+e^-}{\overset{-e^-}{\rightleftharpoons}} [Pt(opd)_2]^{+1} \underset{+e^-}{\overset{-e^-}{\rightleftharpoons}} [Pt(opd)_2]^{+2}$$

Figure 6.1.2 *Predicted structure for* $[Pt(opd)_2]^0$*, and the various oxidised and reduced species that can be produced from it electrochemically.*

In common with many amine ligands, opd forms a "cisplatin" analogue $Pt(opd)Cl_2$ (see Figure 6.1.1) which has been analysed to determine its biomedical properties.[290,291] No oxidised form of $Pt(opd)Cl_2$ has been reported, nor has the related bromide or iodide form been investigated. Attempts to produce neutral-chain HMMCs in which the molecules $Pt(opd)X_2$ (or $Pt(opd)X_4$) feature are outlined in section **6.3**.

6.2 Cationic chain HMMC complexes containing $[Pt(LL)_2]^0$ (LL = aromatic diamine)

6.2.1 Reagent systems

The complex $[Pt(opd)_2]^0$ (**601**) was made by a method similar to that in the literature.[289] The preparation is simple and involves the reaction of free amine with $[PtCl_4]^{2-}$ ions in a basic solution. It results in a number of impurities, which makes purification essential. $Pt(opd)Cl_2$ is expected to be the major by-product of the reaction, but other possibilities include Magnus salt type species or compounds in which some of the ligands are monodentate. The crude blue-purple product was purified by Soxhlet extraction into acetone. The first extracts were green and were discarded; crystallisation was only allowed to proceed once the extracts were deep blue. It was possible to produce about 50 mg of blue crystals per day using this method. Purification is very slow because $[Pt(opd)_2]^0$ is only slightly soluble in acetone or methanol, and it is virtually insoluble in water. Therefore, the synthesis of the HMMCs containing opd is difficult for two reasons. Pure starting materials are available in limited quantities and reaction solutions are awkward to prepare.

The oxidation of $[Pt(opd)_2]^0$ was investigated briefly. The blue complex can be dissolved in methanol or 2-methoxyethanol to give a blue solution. Treatment with chlorine gas (in a stream of N_2) changes the colour of either solution from blue through green to yellow, and finally to red. It is very unusual for any solid to be precipitated during this reaction, but it is not unknown; jet black crystals were isolated on occasion, but they defied analysis. The changes in the solution colour are consistent with two single-electron oxidations that produce $[Pt(opd)_2]^{+1}$ and $[Pt(opd)_2]^{+2}$ in succession (see Figure 6.1.2). Neither ion can be isolated, so $[Pt(opd)_2]^0$ was used in all the doping reactions. Each product was analysed by single-crystal Raman spectroscopy, and the results were compared with those for $[Pt(en)_2][Pt(en)_2Cl_2](ClO_4)_4$ recorded under the same conditions. The defect modes in PtCl are enhanced at wavelengths shorter than 550 nm, so most comparisons were made at 568, 647 or 676 nm excitation.

Five reagent mixtures were tested (see Table 6.2.1), but the only product that has possible defect modes in its Raman spectra is compound (**602**), which was isolated as small bluish-red crystals from the reaction of $[Pt(opd)_2]^0$ with $[Pt(en)_2Cl_2](ClO_4)_2$. The vibrational spectra of **602** are considered in section **6.2.2**. The most unusual sample (**603a**) is made by treating $[Pt(opd)_2]^0$ with $[Pt(en)_2](ClO_4)_2$. The Raman spectra of the green-red crystals have no peaks that can be assigned to the ν_1 mode, but displays an overtone progression whose fundamental mode is at 179 or 167 cm^{-1} (514 nm or 647 nm excitation), *i.e.* only a few wavenumbers larger than ν_1(Br-Pt-Br) in PtBr. The Raman spectra of the other three products (**603b - d**) are indistinguishable from those of $[Pt(en)_2][Pt(en)_2Cl_2](ClO_4)_4$, even though the samples made by mixing $[Pt(en)_2Cl_2](ClO_4)_2$ with different proportions of $[Pt(opd)_2]^0$ and $[Pt(en)_2](ClO_4)_2$ have a very unusual physical appearance. They are scarlet needles that are flaky and twisted, without any obvious flat or shiny surfaces.

Table 6.2.1 Summary of the proportions of reagents used to synthesise the $[Pt(opd)_2]^0$ doped analogues of $[Pt(en)_2][Pt(en)_2Cl_2](ClO_4)_4$

Label	$[Pt(opd)_2]^0$	$[Pt(en)_2](ClO_4)_2$	$[Pt(en)_2Cl_2](ClO_4)_2$	$[Pt(en)_2][Pt(en)_2Cl_2](ClO_4)_4$	Colour	Crystal	Raman
602	$^1/_2$		$^1/_2$		Red with blue tints	Small	see **6.2.2**
603a	$^1/_2$	$^1/_2$			Greenish red	Small	Normal
603b	$^1/_8$	$^3/_8$	$^1/_2$		Scarlet	Crooked, dull	Normal
603c	$^1/_4$	$^1/_4$	$^1/_2$		As for **603c**	As for **603c**	As for **603c**
603d	$^1/_2$			$^1/_2$	Red	Normal	Normal

6.2.2 Vibrational spectroscopy

Raman spectra were recorded for complex **602** at excitation wavelengths ranging from 407 to 676 nm. Those collected at 568 or 676 nm excitation are compared with spectra of $[Pt(en)_2][Pt(en)_2Cl_2](ClO_4)_4$ recorded under similar conditions over the range 100 - 700 cm^{-1} (see Figures 6.2.1 - 2). Wavenumbers, relative intensities and possible assignments are given in Table 6.2.2. At all excitation wavelengths, the spectrum of $[Pt(en)_2][Pt(en)_2Cl_2](ClO_4)_4$ is dominated by the ν_1 signal; none of the other modes (*e.g.* ν_2) is strongly Raman-active. The spectra of the doped complex are very unusual and contain a large number of bands. Although the ν_1 signal contributes the most intensity to the Raman spectra of **602**, there are other modes that are strongly Raman-active. The fundamental modes of interest may be split into four regions: (A) the ν_1 region, (B) 275 - 290 cm^{-1}, (C) 200 - 220 cm^{-1} and (D) 145 - 180 cm^{-1}. The signals for **602** are compared explicitly with those for PtCl in Figures 6.2.3 - 4 (regions A and B) and in Figures 6.2.5 - 6 (regions C and D). The wavenumbers of the largest peaks in the ν_1 resonance are nearly identical for both species, but there are significant differences in the lower energy part of the ν_1 signal. For instance when the exciting line is 568 nm the spectrum of **602** contains a peak at 302.5 cm^{-1} that is absent from the spectrum of PtCl, while the signals at *ca.* 305 and 309 cm^{-1} are more intense relative to the peak at *ca.* 312 cm^{-1} than they are in the undoped complex. The spectra of the doped complex show considerable enhancement in region B, particularly at 568 nm, which is typical of an electronic defect mode. The ν_2 mode is not observed in the Raman spectrum of **602** because there are some moderately intense overtone peaks that occur at equivalent wavenumber. The fundamental modes related to these overtones appear in region D and comprise three signals that are labelled ν_p, ν_q and ν_r in order of increasing wavenumber. ν_p has the least intensity of the three, but shows the most dispersion; it occurs at 163.0 and 156.5 cm^{-1} at 568 and 676 nm, respectively. ν_q and ν_r are dispersed equally, and differ in wavenumber by *ca.* 7 cm^{-1} at both excitation wavelengths. There is a fourth signal (ν_n) in region D, but it is only observed at 676 nm excitation. Region C contains one peak of interest, labelled ν_u. Two signals are seen at 676 nm excitation; ν_u is at 205.5 cm^{-1} while the peak at 211.5 cm^{-1} is at the same wavenumber as that observed in the spectrum of PtCl and so is probably due to a mode such as $\delta(PtN_2)$. At 568 nm excitation the two signals are coincident.

Table 6.2.2 Wavenumbers / cm^{-1}, relative intensities and possible assignments for bands in the Raman spectra of $[Pt(en)_2][Pt(en)_2Cl_2](ClO_4)_4$ and complex 602 [a]

$[Pt(en)_2][Pt(en)_2Cl_2](ClO_4)_4$		Complex **602**		Assignment
568 nm	676 nm	568 nm	676 nm	
			149.5 **0.09**	ν_n
		163.0 **0.02**	156.5 **0.03**	ν_p
		171.5 **0.19**	168.0 **0.16**	ν_q
177.0 **wk**	173.0 **wk**	178.0 **0.39**	174.5 **0.11**	ν_a, ν_r
183.5 **wk**				ν_a
			205.5 **0.02**	ν_u
214.5 **0.02**	210.0 **wk**	211.5 **0.14**	211.5 **0.02**	$\delta(PtN_2)$, ν_u
		279.0 **0.05**	274.0 **0.02**	ν_d
288.5 **0.01**	282.0 **wk**	288.5 **0.17**	282.5 **0.04**	ν_d
		302.5 **0.12**	298.0 **0.08**	
305.0 **0.10**	302.5 **0.14**	305.5 **0.29**	303.0 **0.18**	ν_1
309.0 **0.67**	305.5 **0.58**	309.5 **0.49**	306.0 **0.51**	ν_1
313.0 **0.23**	309.5 **0.28**	313.5 **0.10**	310.5 **0.22**	ν_1
329.5 **wk**		328.0 **wk**	293.5 **0.04**	$2\nu_p$
		339.0 **wk**	336.0 **0.03**	$2\nu_q$
356.5 **0.01**	352.5 **wk**	353.0 **0.05**	353.0 **wk**	ν_{2c}, $2\nu_r$
		389.0 **0.02**		(ν_u + ν_p, ν_q or ν_r)
		419.0 **0.02**		$2\nu_u$
		455.0 **0.03**		
		464.0 **0.05**	444.0 **0.02**	(ν_d + ν_p, ν_q or ν_r)
		482.5 **0.14**		(ν_1 + ν_p, ν_q or ν_r), $2\nu_d$
581.0 **0.01**	579.0 **wk**	584.0 **0.02**	578.0 **wk**	ν(Pt-N)
		594.5 **0.05**	594.0 **wk**	(ν_1 + ν_d)
611.5 **wk**	610.0 **wk**	609.5 **0.06**		$2\nu_1$
617.5 **0.02**	614.5 **0.01**	617.0 **0.11**	615.0 **wk**	$2\nu_1$
625.0 **0.02**	621.5 **0.01**	626.0 **0.02**	623.0 **wk**	$2\nu_1$

[a] *the figures in bold type are the intensities (wk = < 0.01) relative to ν_1 corrected for spectral response.*

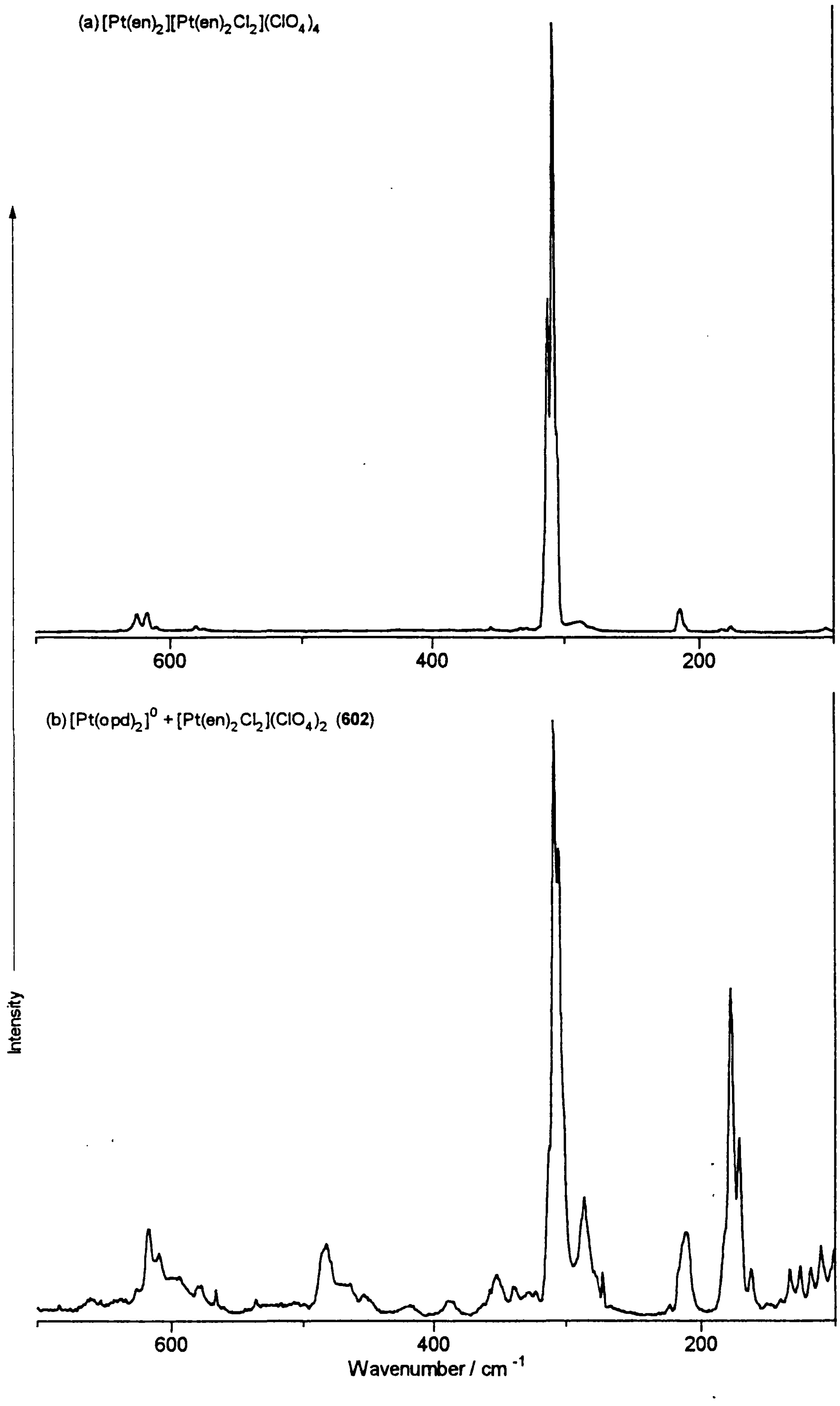

Figure 6.2.1 *Raman spectra for (a)* $[Pt(en)_2][Pt(en)_2Cl_2](ClO_4)_4$ *and (b)* ***602*** *recorded at an excitation wavelength of 568 nm.*

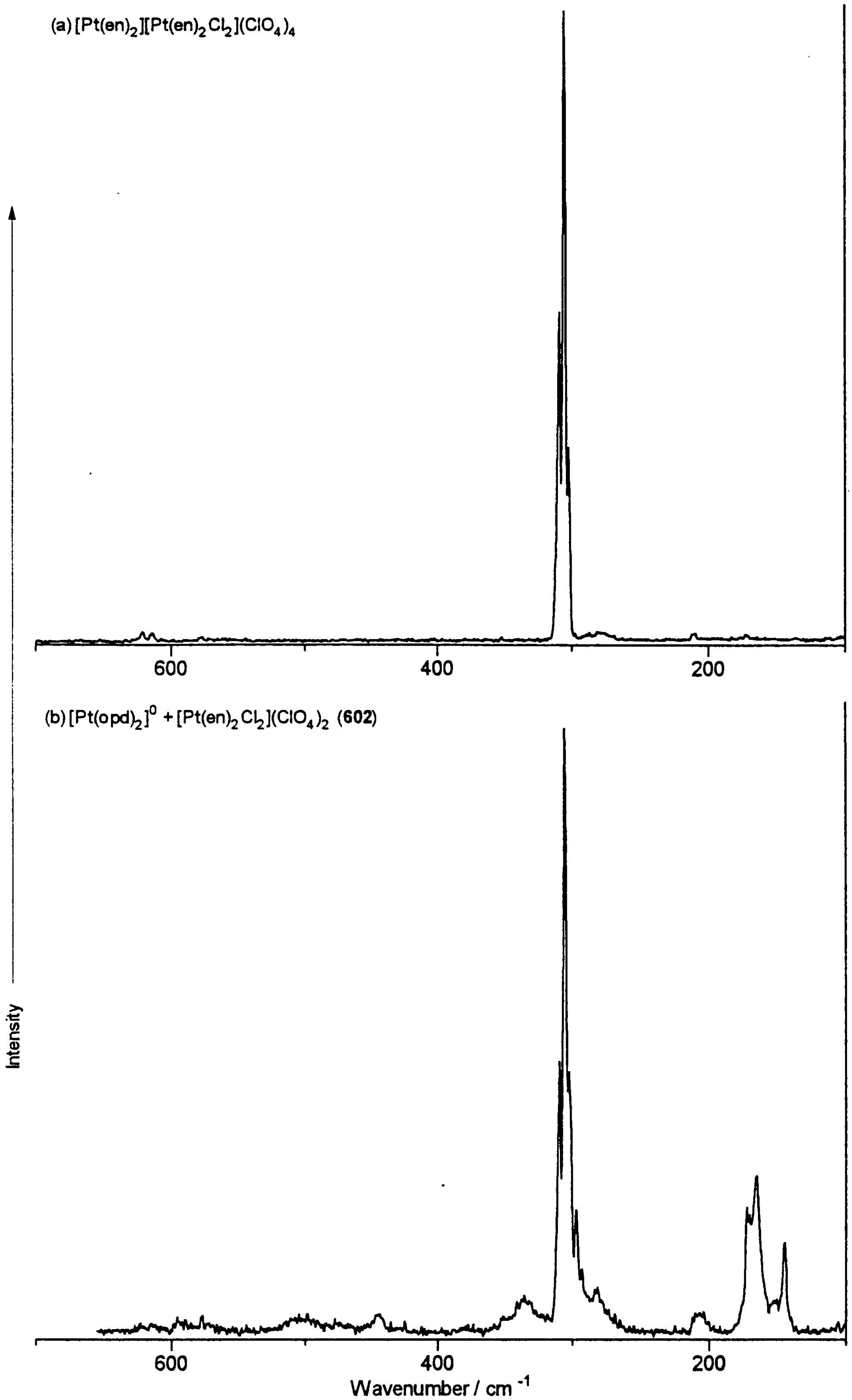

Figure 6.2.2 *Raman spectra for (a) $[Pt(en)_2][Pt(en)_2Cl_2](ClO_4)_4$ and (b)* ***602*** *recorded at an excitation wavelength of 676 nm.*

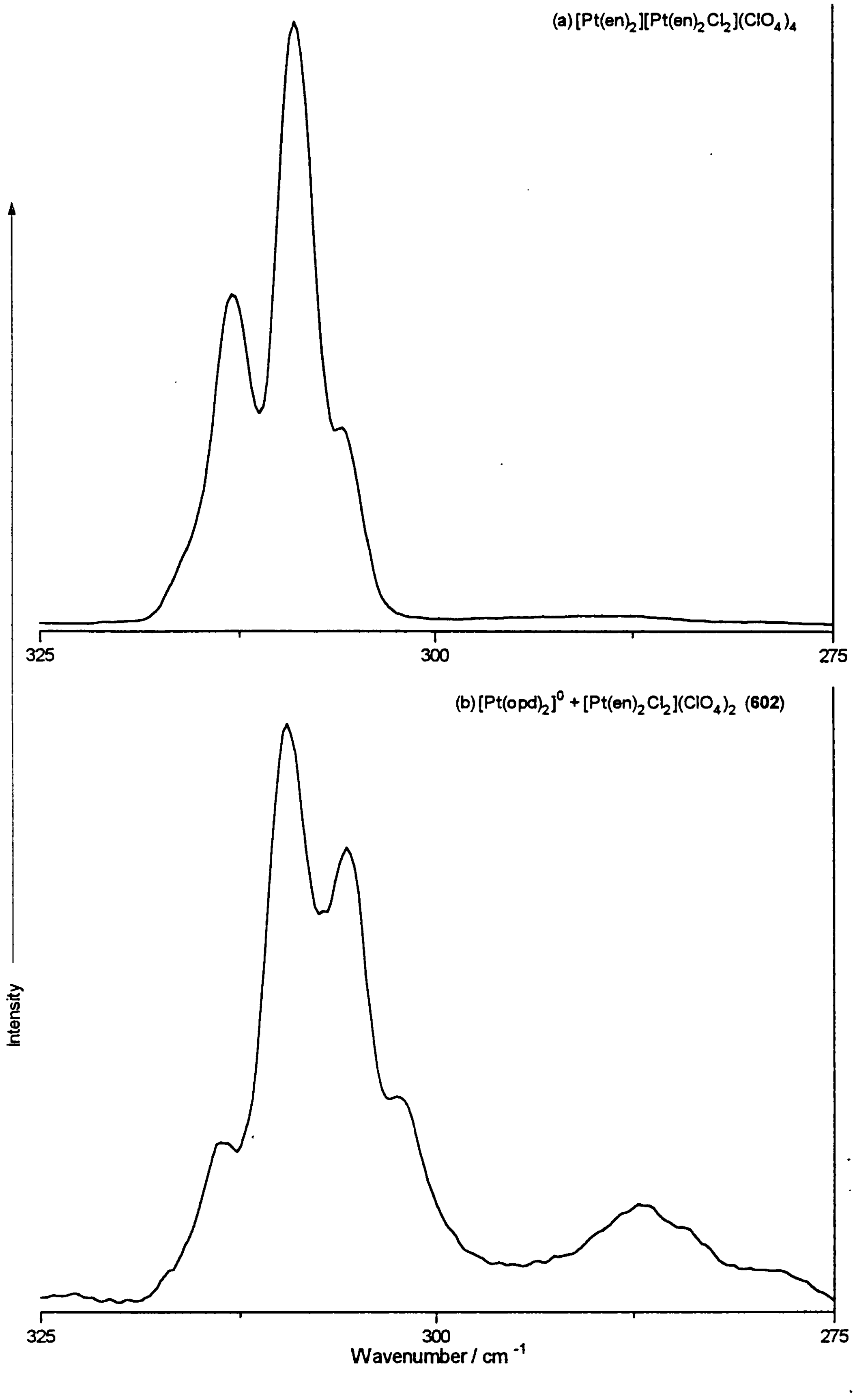

Figure 6.2.3 *The v_1 region of the Raman spectra for (a) $[Pt(en)_2][Pt(en)_2Cl_2](ClO_4)_4$ and (b)* ***602*** *recorded at an excitation wavelength of 568 nm.*

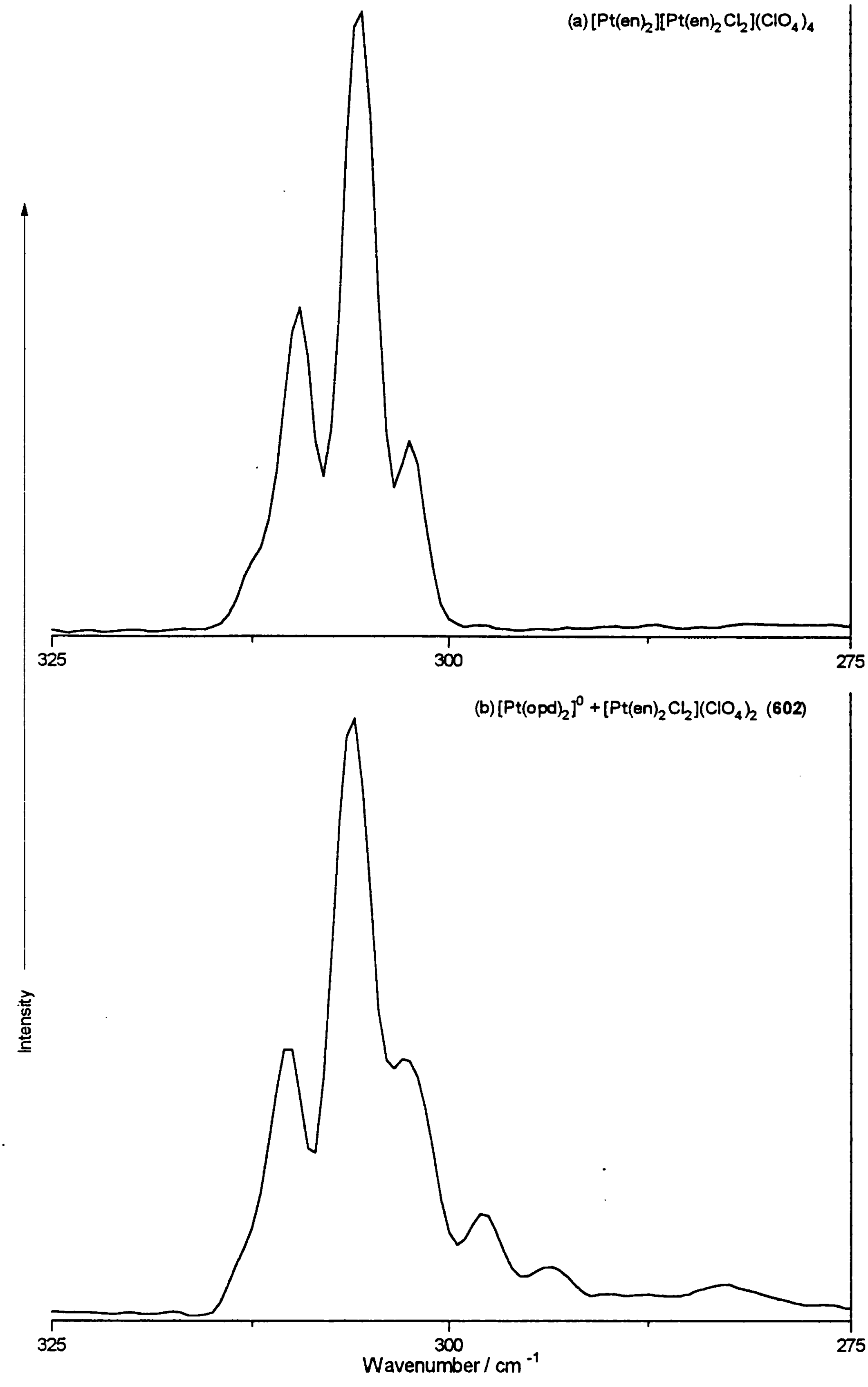

Figure 6.2.4 *The ν_1 region of the Raman spectra for (a) $[Pt(en)_2][Pt(en)_2Cl_2](ClO_4)_4$ and (b)* ***602*** *recorded at an excitation wavelength of 676 nm.*

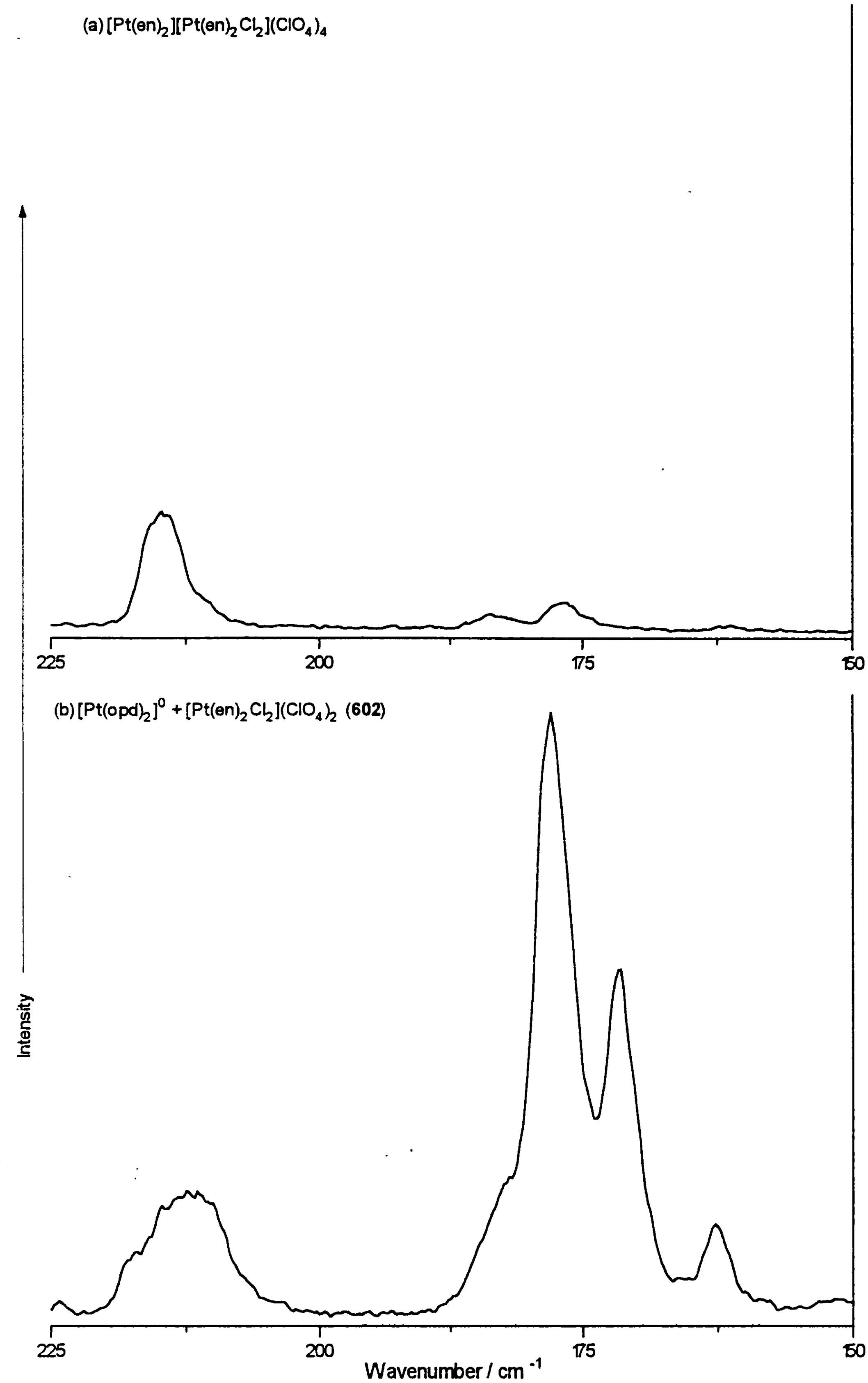

Figure 6.2.5 *Raman spectra for (a) $[Pt(en)_2][Pt(en)_2Cl_2](ClO_4)_4$ and (b)* ***602*** *recorded at an excitation wavelength of 568 nm over the range 150 - 225 cm^{-1}.*

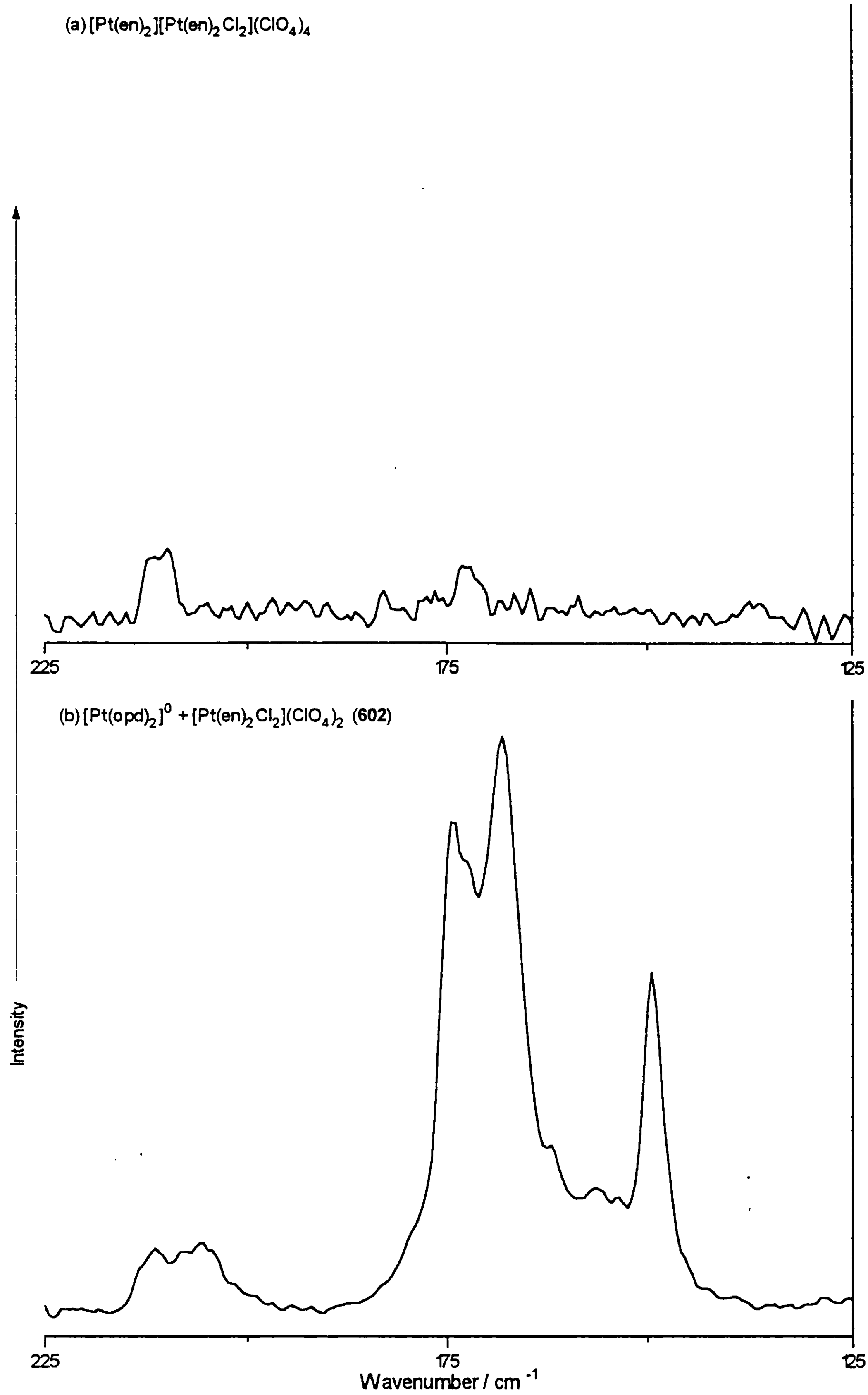

Figure 6.2.6 *Raman spectra for (a) $[Pt(en)_2][Pt(en)_2Cl_2](ClO_4)_4$ and (b)* ***602*** *recorded at an excitation wavelength of 676 nm over the range 150 - 225 cm^{-1}.*

A pressed polythene disc of complex **602** was analysed by FT-infrared spectroscopy at room temperature. The spectrum is compared with that for $[Pt(en)_2][Pt(en)_2Cl_2](ClO_4)_4$ (see Figure 6.2.7); the wavenumbers and intensities of the peaks are listed in Table 6.2.3. The infrared spectra of the two species are very similar, unlike their Raman spectra (*vide supra*). The differences between them are accounted for by motions involving the aromatic ligand or by the presence of $[Pt(en)_2Cl_2](ClO_4)_2$ molecules, as well as by new chain modes. All the ligand-related vibrations occur at greater than 400 cm^{-1}, and are at similar wavenumbers to those of the equivalent modes in $[Pt(opd)_2]^0$ or $Pt(opd)Cl_2$. The $[Pt(en)_2Cl_2](ClO_4)_2$ impurity may have been created during the grinding process, or may be present in the material from which sample was taken to prepare the disc for FTIR analysis. The Pt^{IV} complex is probably responsible for three of the weak infrared peaks, and for the increased intensity of the signal at *ca.* 290 cm^{-1}. Therefore only two clearly resolved resonances can be related to new chain vibrations, and they are at 216.0 and 410.8 cm^{-1}, respectively. The former may be the asymmetric form of the more symmetric vibration is responsible for the peaks in region D of the Raman spectra of **602**. It is possible that there are other chain modes but that they are smothered by more intense ligand modes.

Table 6.2.3 Wavenumbers / cm^{-1}, and relative intensities of the bands in the FTIR spectra of $[Pt(en)_2][Pt(en)_2Cl_2](ClO_4)_4$ and complex 602

420	**604**	Assignment	**420**	**604**	Assignment
138.1 m	136.0 m			410.8 vw	
153.8 m	152.4 m			432.0 m	$[Pt(opd)_2]^0$
165.1 m	165.4 m	ν_3, PtCl bend		461.9 wm	$[Pt(opd)_2]^0$
180.0 m	179.4 m			472.5 wm	Pt^{IV} impurity
	200.6 vw	Pt^{IV} impurity		500.9 vw	
	216.0 w		538.6 m	539.0 sh	
253.3 s	252.6 s	in plane $\delta(PtN_2)$		544.8 m	
290.2 s	291.7 vs	in plane $\delta(PtN_2)$	555.9 s	555.9 s	
325.5 w	325.9 w	ring bends	565.6 sh		
357.8 vs	357.4 s	ν_2, ligand mode		579.5 w	$[Pt(opd)_2]^0$
	372.2 w	Pt^{IV} impurity	584.4 w		
393.0 vw	391.5 vw		594.5 w	595.0 w	

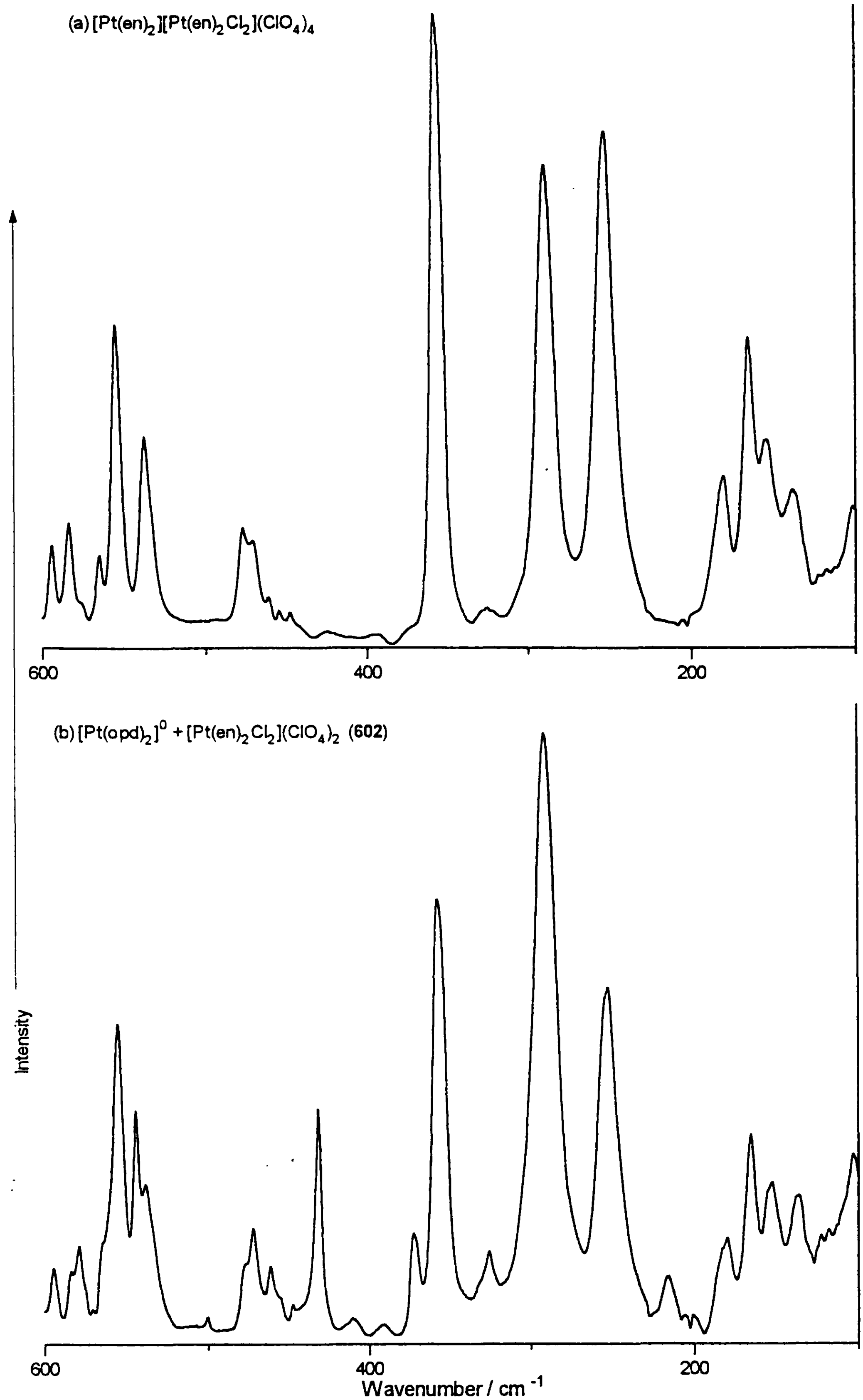

Figure 6.2.7 FT infrared spectra for (a) $[Pt(en)_2][Pt(en)_2Cl_2](ClO_4)_4$ and (b) ***602***.

6.2.3 Discussion and extension of study

The Raman spectra of complex **602** contain several bands that are absent from those of normal PtCl. It would be helpful to know more accurately the structure of the doped complex, but the crystals that were isolated were too small for crystallographic analysis, and so their exact composition is not known. Elemental analysis of the bluish-red crystals shows that the amounts of carbon, hydrogen and nitrogen are between those expected for $[Pt(en)_2][Pt(en)_2Cl_2](ClO_4)_4$ and $[Pt(opd)_2][Pt(en)_2Cl_2](ClO_4)_4$ (see Table 6.2.4). A formula consistent with the carbon data is $[Pt(opd)_2]_{0.8}[Pt(en)_2]_{0.2}[Pt(en)_2Cl_2](ClO_4)_4$. Therefore there appear to be significant numbers of $[Pt(opd)_2]^0$ units in the MX chain.

Table 6.2.4 Elemental analysis of doped complex 602

Complex	C / %	H / %	N / %
$[Pt(en)_2][Pt(en)_2Cl_2](ClO_4)_4$ (calc.)	8.7	2.9	10.2
602	14.6	2.7	9.4
$[Pt(opd)_2][Pt(en)_2Cl_2](ClO_4)_4$ (calc.)	16.1	2.7	9.4

The ν_1 signal in the doped species is very complicated. A difference Raman spectrum can be calculated using the spectra collected at 568 nm for **602** and PtCl (see Figure 6.2.8). It contains three prominent peaks in the ν_1 region, which are at *ca.* 302, 305 and 309 cm^{-1}. Their collective shape resembles that due to the distribution of chlorine isotopes, such as for ν_1 in PtCl. The signals almost certainly relate to some kind of ν_1-type vibration, but its origin is uncertain. In the simple vibrational models of section **4.5**, a small reduction in a force constant such k_1 or k_2 would be enough to lower the wavenumber of the main ν_1 mode sufficiently. If the source of the difference is thought to be the $[Pt(opd)_2]$ sites, then it is probably k_2 that is reduced. This could be effected by alterations to the ligand-counterion interactions, or by changes in the electron density in the bonds in the chain. The peaks are much more enhanced relative to the ν_1 signal at 568 nm than at 676 nm excitation, which may indicate that they are localised defects with only a short enhancement range.

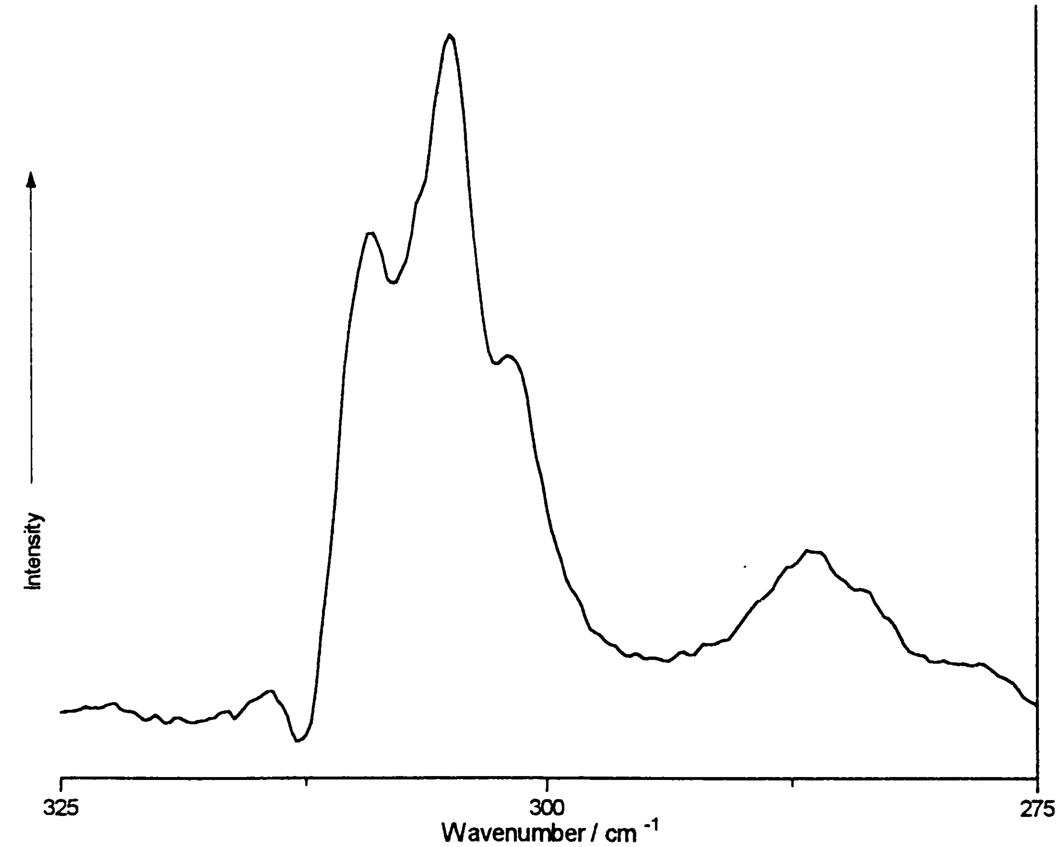

Figure 6.2.8 *Theoretical Raman spectrum showing the differences between the spectra of* ***604*** *and [Pt(en)$_2$][Pt(en)$_2$Cl$_2$](ClO$_4$)$_4$.*

One of the objectives of this study was to generate stable electronic defects on an HMMC by simply altering the ligands. It has been established in several studies that the hole polaron defect is found at *ca.* 285 cm^{-1}.[57,60,100] The Raman spectrum of **602** contains a strong signal in this region at 568 nm excitation; it is considerably weaker when the excitation wavelength is 676 nm. There are two regions on enhancement for the hole defect; 676 nm is on the edge of the low energy band, while 568 nm is within the higher energy region. If the peaks are due to hole polaron modes, then a significant proportion of the Pt^{II} sites must be replaced by Pt^{III} centres. The doped complex is synthesised with the use of only two starting materials: [Pt(en)$_2$Cl$_2$](ClO$_4$)$_2$ and [Pt(opd)$_2$]^0. Elemental analysis indicates that it contains the ligands en and opd in a ratio of roughly 1.5 : 1. If [Pt(en)$_2$] units are present in the HMMC, then they may result from a simple redox reaction in solution between [Pt(en)$_2$Cl$_2$]$^{2+}$ ions and [Pt(opd)$_2$]^0 molecules, which produces [Pt(en)$_2$]$^{2+}$ ions. Alternatively, the presence of [Pt(opd)$_2$]^0 units in an existing segment of chain may stabilise the addition of a unit in a high oxidation state. A suggested path for such a mechanism is given in Equation [6.2.1] where the numbers in circles represent the platinum oxidation state. The chain marked with an asterisk contains unspecified $[Pt(opd)_2]^0$ units at the Pt^{II} sites and can react with free $[Pt(en)_2Cl_2]^{2+}$ ions to produce a chain in which there is a Pt^{IV} site out of phase with the other metal centres. The charge on the new Pt^{IV} site can be dissipated through the chain to minimise the energy of the system. The presence of hole polarons means that it probably gains one electron, which may be drawn from the aromatic ligands on a nearby $[Pt(opd)_2]^0$ unit.

[②④②④②④]* + $[Pt(en)_2Cl_2]^{2+}$ → [②④②④②④❹] + 2 Cl^- [6.2.1]

The most intriguing part of the Raman spectra of **602** is region D, which covers a range of 145 - 180 cm^{-1}. When the exciting line is 568 nm, the peaks are marginally stronger relative to the ν_1 mode, and peaks due to overtone modes are observed in the range 300 - 400 cm^{-1}. If the motions related to these bands are largely symmetrical, then the peak at *ca.* 215 cm^{-1} in the infrared spectrum may be due to the corresponding asymmetric vibrations. It is important to establish that these modes do not result from bromide impurities; normally peaks observed in the range 145 - 180 cm^{-1} in the Raman spectra of HMMCs are due to ν_{1b} vibrations. A number of factors discount this possibility. The spectra of **602** are not consistent with the general form of those for mixed-halide complexes. The peaks in region C are very weak, whereas the ν_{1m} for $[Pt(en)_2][Pt(en)_2Cl_{2-2\alpha}Br_{2\alpha}]Y_4$ is never substantially smaller than both ν_{1c} and ν_{1b} in the same spectrum, nor do the Raman spectra of **602** exhibit any intensity due to the ν_{2m} signal. Thus, the number of $[ClPt^{IV}Br]$ units present is negligible, which is important because they normally accompany $[BrPt^{IV}Br]$ units in HMMCs (see sections **4.4** and **4.6**). The absence of $[BrPt^{IV}Br]$ units in **602** is confirmed by the fact that there is no ν_{2b} signal in its infrared spectrum, and because the modes in region D have no first overtone at 676 nm excitation whereas $2\nu_{1b}$ for PtBr has significant intensity. A simple model that may account for the observed signals involves the fragmentation of the MX chains into segments caused by the $[Pt(opd)_2]$ units. Although $[Pt(opd)_2]^0$ can be oxidised or reduced electrochemically, no species of the form $[Pt(opd)_2Cl_2]^0$ has been isolated. If the platinum centre does not support axial halogen ligands in its free state, then it may not be favourable for a $[Pt(opd)_2]$ unit at the end of a chain segment to bond with a free $[Pt(en)_2Cl_2]^{2+}$ ion. Alternatively, the reaction of free

$[Pt(opd)_2]$ with a chain segment may be slow, and the chain may terminate naturally in the absence of suitable Pt^{II} ions. In either case, it is possible that vibrations at the chain termini are responsible for the signals seen in region D.

Most of the work was carried out on $[Pt(opd)_2]^0$, but analogous complexes were also investigated. In particular, the compounds of two related aromatic diamines were analysed. 4,5-dimethyl-*o*-phenylenediamine (dmpd) contains electron-donating methyl groups, while 4,5-dichloro-*o*-phenylenediamine (dcpd) has electron-withdrawing chlorine atoms (see Figure 6.2.9). The species $[Pt(dmpd)_2]^0$ (**604**) and $[Pt(dcpd)_2]^0$ (**605**) were prepared by methods similar to that used to make $[Pt(opd)_2]^0$.[289] Purification by Soxhlet extraction was only successful for $[Pt(dcpd)_2]^0$; $[Pt(dmpd)_2]^0$ is virtually insoluble in acetone or methanol. $[Pt(dcpd)_2]^0$ is a darker blue than $[Pt(opd)_2]^0$, whereas $[Pt(dmpd)_2]^0$ is purple coloured.

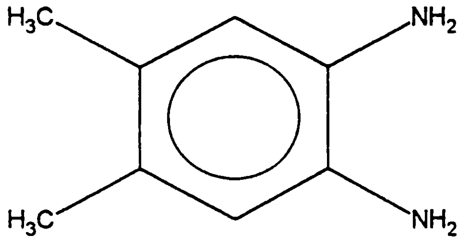

4,5-dimethyl-*ortho*-phenylenediamine
(dmpd)

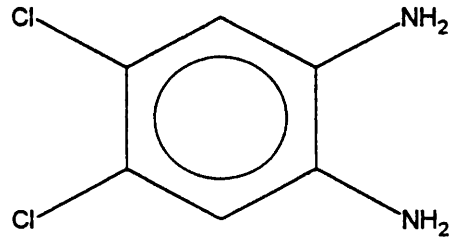

4,5-dichloro-*ortho*-phenylenediamine
(dcpd)

Figure 6.2.9 Representations of the two 4,5-substituted variants of opd: dimethyl- (dmpd) and dichloro- (dcpd).

The reaction between $[Pt(dmpd)_2]^0$ and $[Pt(en)_2Cl_2](ClO_4)_2$ gave some red crystals but the Raman spectra of the sample were similar to those for PtCl. However, a reaction between $[Pt(dcpd)_2]^0$ and the Pt^{IV} species produced red crystals (**606**) with more interesting properties. Its Raman spectrum at 568 nm excitation does not resemble the spectrum of **602** recorded at the same excitation wavelength, especially in the region around 180 cm^{-1}. It is similar to that for PtCl except that it has a large broad signal centred at *ca.* 293 cm^{-1} (see Figure 6.2.10). The wavenumber of this peak is too high for the hole polaron mode. There is no precedent amongst experimental data to help in its assignment, but theoretical studies predict a value of 290 cm^{-1} for the hole bipolaron breathing mode (*i.e.* higher wavenumber than the equivalent vibration for the single polaron). This is certainly a possible argument, given the nature of the ligand and the mechanism proposed in Equation [6.2.1]. The chlorine atoms in dcpd are electron withdrawing, and may prevent the donation of an electron to the stabilised Pt^{IV} sites, which will then remain as bipolarons.

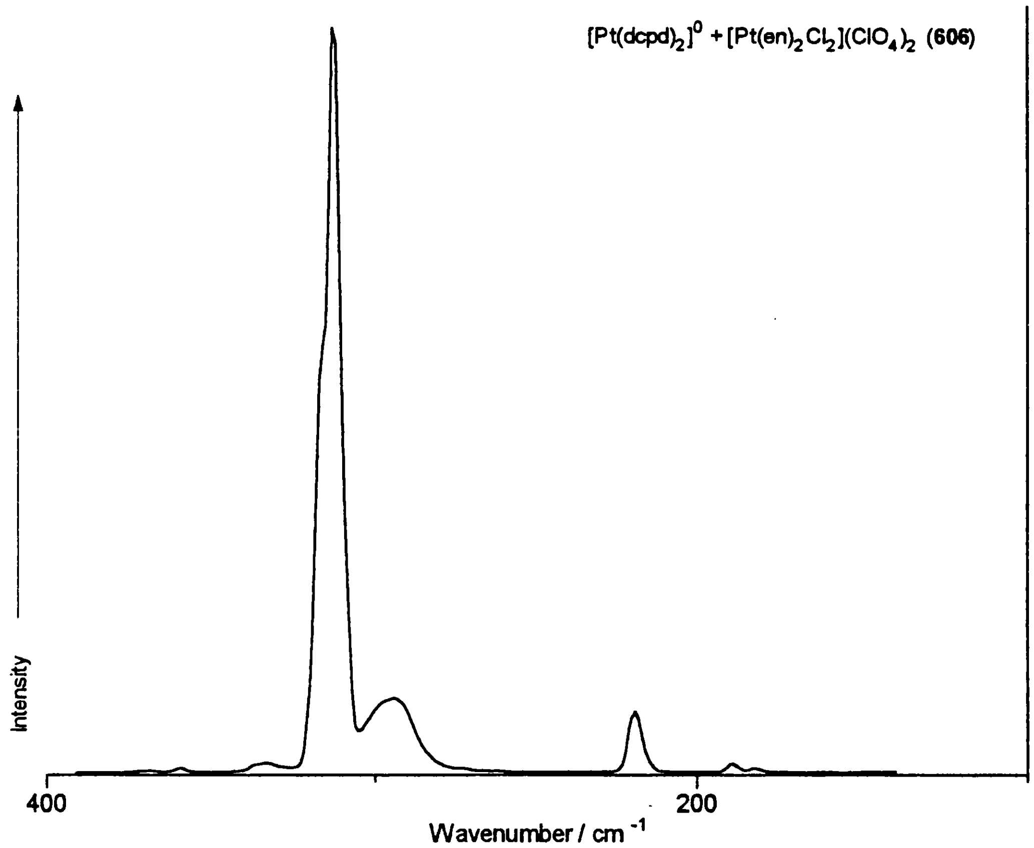

*Figure 6.2.10 Raman spectrum for **606** recorded at an excitation wavelength of 568 nm.*

Although the study was expanded to the reaction of $[Pt(LL)_2]^0$ with $[Pt(en)_2Br_2](ClO_4)_2$, and green crystals were isolated in each case, none of the products showed clear evidence of defect modes at the excitation wavelengths available.

6.3 Neutral chain HMMC complexes containing $Pt(LL)Cl_2$

6.3.1 Reagent systems

$Pt(opd)Cl_2$ (**607**) was made by a method similar to that published,[290] which itself is an adaptation of the route formerly used for the synthesis of *cis*-$Pt(NH_3)_2Cl_2$.[263] It is isolated from the reaction of K_2PtCl_4 with an excess of opd in a solution buffered with HCl. The purified product is yellow, but it can vary in colour or crystallinity, as $Pt(en)Cl_2$ and *cis*-$Pt(NH_3)_2Cl_2$ do. There are two main by-products in the synthesis of $Pt(opd)Cl_2$: the blue complex $[Pt(opd)_2]^0$ and the amorphous green solid that also contaminates $[Pt(opd)_2]^0$. These impurities can give $Pt(opd)Cl_2$ a green or muddied appearance, but they can be removed gradually by washing with an alcohol / acetone mixture. Because this type of preparation is not very efficient, *cis*-$Pt(NH_3)_2Cl_2$ is made preferentially by the Dhara method, which involves the synthesis of *cis*-$Pt(NH_3)_2I_2$ as its first step.[265] Similarly, the treatment of $[PtI_4]^{2-}$ ions with free opd gives the yellow complex $Pt(opd)I_2$ (**608**). However, the reaction of $Pt(opd)I_2$ with $AgNO_3$ does not lead to the formation of $[Pt(opd)(H_2O)_2]^{2+}$ and insoluble yellow AgI, but yields instead a muddy brown precipitate and a filtrate on which halide ions have no effect. There is a similar outcome when $Pt(opd)Cl_2$ is used in place of $Pt(opd)I_2$. The failure of the Dhara method for $Pt(opd)Cl_2$ has no obvious cause, but it is probably related to a redox reaction, possibly between the Ag^+ ions and the aromatic ligands.

$Pt(opd)Cl_2$ was treated in a number of ways to secure an HMMC-type product. No linear-chain material was obtained when $Pt(opd)Cl_2$ was oxidised by chlorine, while other oxidants such as potassium persulphate merely gave amorphous brown solids like those made with $AgNO_3$. The reaction between equimolar amounts of $Pt(opd)Cl_2$ and $Pt(en)Cl_4$ in the presence of chloride ions did give a red crystalline product, but its Raman spectra do not differ significantly from those of $[Pt(en)Cl_2][Pt(en)Cl_4]$. $Pt(opd)Cl_2$ was also treated with an equimolar quantity of $Pt(en)Br_4$ in dilute HBr. A green crystalline sample (**609**) was isolated; its Raman spectra contain signals attributable to defect modes (see section **6.3.2**).

$Pt(opd)I_2$ can be oxidised with persulphate ions, unlike $Pt(opd)Cl_2$. When it was treated with one half the molar equivalent of $S_2O_8^{2-}$ ions and the molar equivalent of iodide ions, a bronze microcrystalline material (**610**) was produced. If double the quantities are used, or **610** is oxidised, a blue-purple solid results (**611**). By analogy with oxidation reactions of $Pt(en)I_2$, these were identified as $[Pt(opd)I_2][Pt(opd)I_4]$ and $Pt(opd)I_4$, respectively. The HMMC can also be made by adding water to a DMF solution containing equimolar amounts of $Pt(opd)I_2$ and $Pt(opd)I_4$. It is reasonably simple to synthesise other species $Pt(LL)I_2$, where LL is an aromatic diamine, and to oxidise them in a similar manner. Examples of such ligands include dmpd, dcpd, 1,8-diaminonaphthalene (dan) and 1,10-phenanthroline (phen). Unfortunately, the syntheses of iodides HMMC is not of any great value to the current study. They cannot be converted to either bromide- or chloride-chain species by treatment with silver ions, and their vibrational spectra contain little useful information.

6.3.2 Raman spectroscopy

The green complex **609** is thought to be $[Pt(opd)Br_2][Pt(en)Br_4]$. Its single-crystal Raman spectrum collected at 647 nm excitation is compared with that for $[Pt(en)Br_2][Pt(en)Br_4]$ recorded under similar conditions (see Figure 6.3.1). Wavenumbers and relative intensities for the observed peaks are given in Table 6.3.1. The spectra differ in two significant ways. Firstly, the spectrum of **609** contains a strong signal at 142.0 cm^{-1}, which is labelled ν_d, and its first overtone ($2\nu_d$) as well as the combination mode ($\nu_1 + \nu_d$). Secondly, the wavenumber of ν_1 for **609** is *ca.* 3 cm^{-1} bigger than that for $[Pt(en)Br_2][Pt(en)Br_4]$.

Table 6.3.1 Wavenumbers / cm^{-1}, relative intensities and possible assignments for the bands in the Raman spectra of $[Pt(LL)Br_2][Pt(en)Br_4]$ (LL = en or opd) [a]

$[Pt(en)Br_2][Pt(en)Br_4]$	$[Pt(opd)Br_2][Pt(en)Br_4]$	Assignment
146.5 **0.01**	142.0 **0.20**	ν_d
164.0 **1.00**	167.0 **1.00**	ν_1
	203.0 **0.01**	
	223.0 **0.02**	
	285.0 **0.07**	$2\nu_d$
313.0 **wk**	311.0 **0.10**	$(\nu_1 + \nu_d)$
334.0 **0.39**	337.0 **0.26**	$2\nu_1$

[a] *The figures in bold type are the intensities (wk = < 0.01) relative to ν_1 corrected for spectral response.*

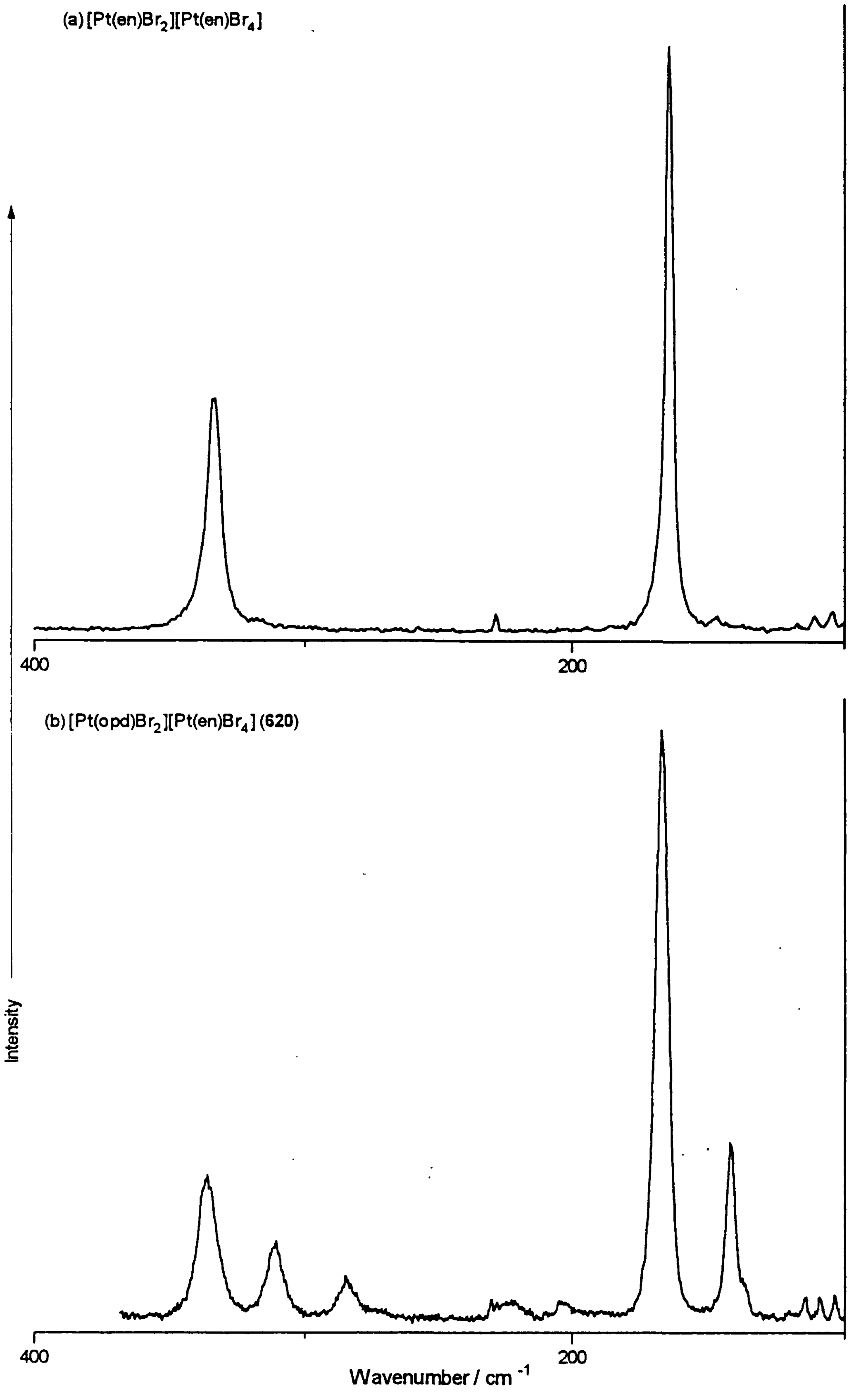

Figure 6.3.1 *Raman spectra collected at 647 nm excitation for (a) [Pt(en)Br$_2$][Pt(en)Br$_4$] and (b) [Pt(opd)Br$_2$][Pt(en)Br$_4$].*

The only linear-chain complexes that contain aromatic diamines alone are those with platinum-iodide chains. This is unfortunate because the vibrational spectra of iodide-chain HMMCs generally are not very rich in detail. Raman spectra were recorded for the iodides with an excitation wavelength of 752 nm. Samples were analysed as polycrystalline pellets since the crystals are too small to be examined. Some examples of spectra are given in Figure 6.3.2; the wavenumbers and intensities of the few peaks that are observed are listed in Table 6.3.2. The wavenumber of ν_1 depends on the identity of the ligand, varying from 111.0 cm^{-1} for $[Pt(en)I_2][Pt(en)I_4]$ to 135 cm^{-1} for $[Pt(opd)I_2][Pt(opd)I_4]$.

Table 6.3.2 Wavenumbers / cm^{-1}, and intensities of peaks found in the Raman spectra of $[Pt(LL)I_2][Pt(LL)I_4]$ (LL = en, opd or dan) at 752 nm excitation [a]

$[Pt(en)I_2][Pt(en)I_4]$	$[Pt(opd)I_2][Pt(opd)I_4]$	$[Pt(dan)I_2][Pt(dan)I_4]$	Assignment
111.0 **1.00**	135.0 **1.00**	117.0 **1.00**	ν_1
	147.5 **0.06**		
177.0 **wk**		173.0 **0.02**	
226.5 **0.31**	275.0 **0.09**	237.0 **0.21**	$2\nu_1$
341.0 **0.15**		358.0 **wk**	$3\nu_1$

[a] *the figures in bold type are the intensities (wk = <0.01) relative to ν_1 corrected for spectral response.*

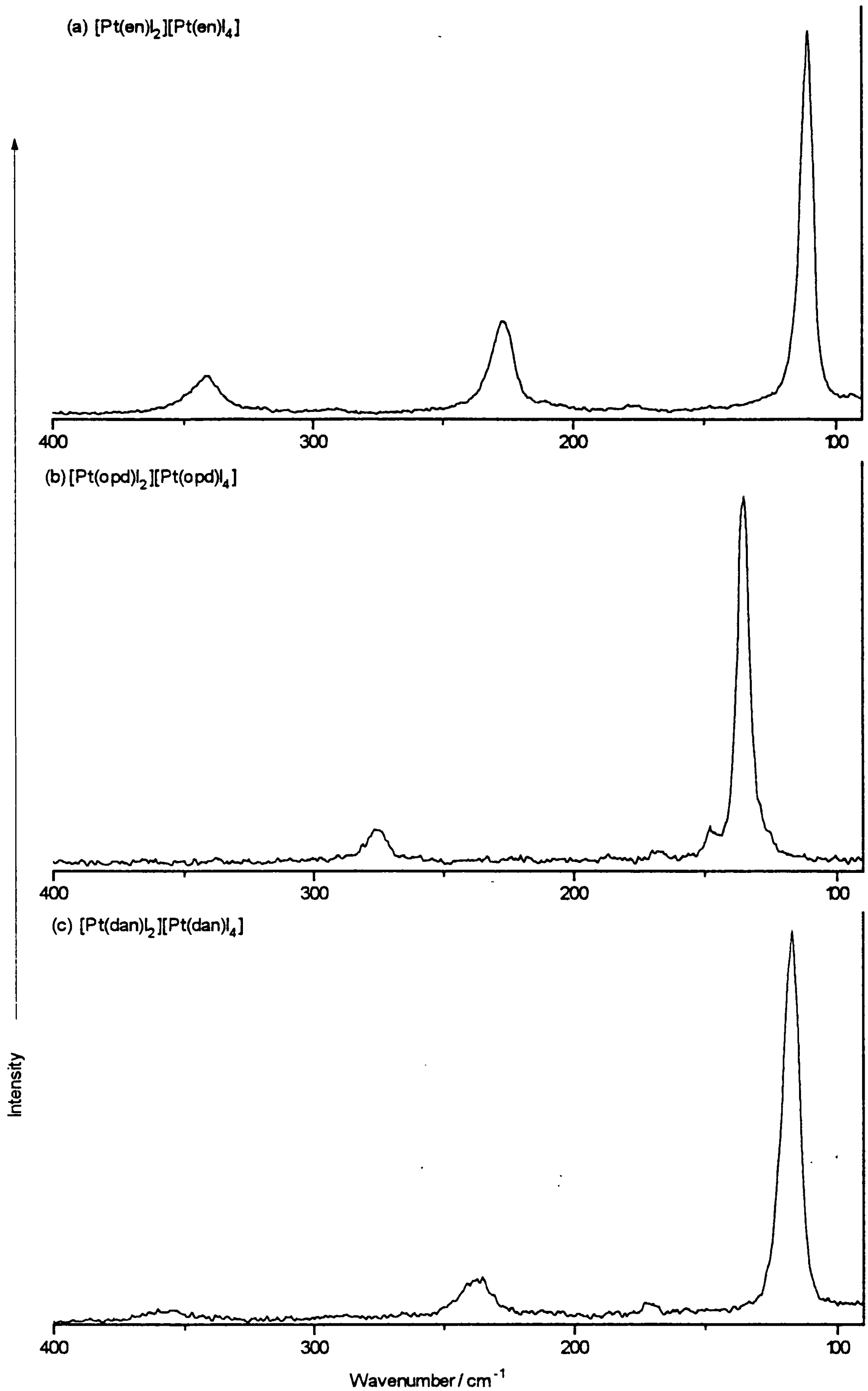

Figure 6.3.2 *Raman spectra recorded at 752 nm excitation for (a) [Pt(en)I_2][Pt(en)I_4], (b) [Pt(opd)I_2][Pt(opd)I_4] and (c) [Pt(dan)I_2][Pt(dan)I_4].*

6.3.3 Discussion

The only neutral-chain complex to contain sufficient electronic defects to produce a significant peak in its Raman spectrum is $[Pt(opd)Br_2][Pt(en)Br_4]$. The vibrational modes associated with polaron defects in $[Pt(en)_2][Pt(en)_2Br_2](ClO_4)_4$ have not been assigned unambiguously. There is some evidence to support a value of *ca.* 150 cm^{-1} for the electron polaron defect,[105] but this is less than the 161 cm^{-1} predicted theoretically.[100] A value of 155 cm^{-1} has been calculated for the hole polaron mode, but no band has been identified for it with certainty in any Raman spectra.[100] The electron bipolaron mode has been assigned in $[Pt(en)_2][Pt(en)_2Br_2](ClO_4)_4$ at 130 cm^{-1}. The defect peak in $[Pt(opd)Br_2][Pt(en)Br_4]$ is at 142 cm^{-1}, which is between the values assigned for electron polaron and bipolaron modes. A simple mechanism for the creation of such defects in the chain involves the donation of electrons from the aromatic ligands to the Pt^{IV} sites. It is impossible to determine from this data alone whether one or two electrons are donated, but bipolaron defects are observed more rarely, so ν_d is assigned provisionally as the breathing mode for an electron polaron defect.

Although the iodide-chain HMMCs appear to be easy to synthesise, they are not species of any great interest. It is noted that ν_1 found in this work for $[Pt(en)I_2][Pt(en)I_4]$ is significantly smaller than the value reported for it previously.[243] In the earlier study, the sample was examined as a pressed disc made from $[Pt(en)I_2][Pt(en)I_4]$ and K_2SO_4; the presence of the sulphate may have affected the HMMC in some way. ν_1 for $[Pt(opd)I_2][Pt(opd)I_4]$ is very large, which may mean that the sample has decomposed into its constituent monomers during analysis and that the ν_1 band for $Pt(opd)I_4$ is observed. ν_1 for $[Pt(dan)I_2][Pt(dan)I_4]$ is 117.0 cm^{-1}, while it is *ca.* 122 cm^{-1} for $[Pt(phen)I_2][Pt(phen)I_4]$ (phen = 1,10-phenanthroline, spectrum not shown). These values are more typical of ν_1 for neutral-chain iodide HMMCs. It is difficult to find any definite evidence of any electronic defects in the iodide chains since most of the spectra are dominated by the ν_1 mode. There is a weak signal at 148.0 cm^{-1} in the spectrum of $[Pt(opd)I_2][Pt(opd)I_4]$, but its origin is not known.

6.4 Conclusions

The purpose of this study was to see if HMMCs could be produced with unusual electronic structures in their MX chains by using aromatic diamine ligands (LL). This has not met with consistent success, but some interesting species have been isolated. The studies show that the only HMMCs composed solely of platinum-aromatic units are the iodide-chain complexes $[Pt(LL)I_2][Pt(LL)I_4]$. Unfortunately, these HMMCs are not of great interest because their vibrational spectra have very few peaks, and not much is known about their electronic defects. Other neutral-chain species were created by treating $Pt(LL)Cl_2$ with $Pt(en)X_4$ in the presence of HX (X = Cl, Br or I). The Raman spectra of the bromide species show clear evidence of electron polarons, which are thought to be stabilised by the aromatic ligands.

The most intriguing results concern the products of the reaction of $[Pt(en)_2Cl_2](ClO_4)_2$ with $[Pt(opd)_2]^0$ or $[Pt(dcpd)_2]^0$. The Raman spectra of the HMMC formed with $[Pt(dcpd)_2]^0$ contains a large defect signal, which because of its wavenumber is assigned to the breathing mode of hole bipolarons. The spectra of the species made with $[Pt(opd)_2]^0$ are much more complicated. They have a signal due to the hole polaron mode, but they also exhibit a cluster of peaks near 180 cm^{-1}, which are thought to arise from vibrations of the chain termini. In addition, the structure of the ν_1 band differs from that found for $[Pt(en)_2][Pt(en)_2Cl_2](ClO_4)_4$.

There is scope for further work in this area. It would be useful to examine the properties of the platinum compounds of a larger variety of aromatic ligands, in order to test the influence of their electronic structure or their interaction with the counterions (where applicable). With the use of longer excitation wavelengths it should be possible to probe more successfully the Raman-active defect modes of the bromide species.

6.5 Experimental Details

6.5.1 Syntheses

Monomeric species

$[Pt(LL)_2]^0$ (LL = opd (601), dmpd (604) or dcpd (605)) a solution containing potassium tetrachloroplatinate was made basic by the addition of a couple of drops of ammonia before treatment with two molar equivalents of free ligand LL dissolved in ethanol.[289] The blue-purple solid that precipitated was purified by Soxhlet extraction from acetone.

$Pt(LL)Cl_2$ (LL = opd (607), dmpd or dcpd) was made by a method analogous to that used for the preparation of *cis*-$Pt(NH_3)_2Cl_2$.[263,290] A solution containing K_2PtCl_4, four molar equivalents of ligand LL, and buffered by six molar equivalents of the dihydrochloride LL.2HCl, was left at 0 °C in darkness to allow the yellow solid $Pt(LL)Cl_2$ to precipitate slowly. Any green contaminant was washed from the sample with methanol.

$Pt(LL)I_2$ (LL = opd (608), dmpd, dcpd, dan or phen) was made by a route analogous to the Dhara preparation for *cis*-$Pt(NH_3)_2I_2$.[264]

$Pt(LL)I_4$ (LL = opd (611)) was made by oxidising $Pt(LL)I_2$ with an excess of potassium persulphate in the presence of KI.

HMMC species

$[Pt(LL)_2]^0$ + $[Pt(en)_2Cl_2](ClO_4)_2$ (LL = opd (602) or dcpd (606)) the Pt^{IV} species was dissolved in a small volume of water. An equimolar amount of $[Pt(LL)_2]^0$ was dissolved slowly in an acetone-water mixture to give a blue solution, which was then added gradually to the yellow $[Pt(en)_2Cl_2]^{2+}$ solution. The solution colour changed from yellow through to red or reddish-brown once the addition was complete. The solution was then allowed to reduce in volume until crystals formed; sometimes an insoluble black deposit was also formed. Care had to be taken in washing the product because it is soluble in acetone as well as water. Cold dilute $HClO_4$ and cold ethanol were generally used instead.

$[Pt(LL)I_2][Pt(LL)I_4]$ (LL = opd (610) was prepared by oxidising $Pt(LL)I_2$ with half the equimolar amount of potassium persulphate in the presence of an equimolar amount of KI. It was also made by adding water to a DMF solution containing equimolar amounts of $Pt(opd)I_2$ and $Pt(opd)I_4$.

$Pt(opd)Cl_2$ + $Pt(en)X_4$ (X = Cl, Br (608) or I) was carried out by allowing a hot aqueous solution containing equimolar amounts of $Pt(opd)Cl_2$ and $Pt(en)X_4$, and a slight excess of HX to cool (X = Cl or Br), or by a method analogous to the second method for $[Pt(opd)I_2][Pt(opd)I_4]$ (X = I).

6.5.2 Resonance Raman spectroscopy

Spectra were recorded on one of the two scanning spectrometers. All spectra were recorded on the Spex 1401 double monochromator, with Bausch and Lomb gratings (1200 line mm^{-1}). Appropriate exciting lines were provided by Kr^+ (CR-3000K) or Ar^+ lasers (I-70). All studies were at liquid-nitrogen temperature. All studies were carried out on single crystals. Alignment was achieved with the aid of a Charged Coupled Device (CCD) camera, fitted to the 1401 spectrometer.

References

1. M. B. Robin, P. Day, Adv. Inorg. Chem. Radiochem., 1967, 10, 247.
2. K. A. Hofmann, F. Resenscheck, *Ann. Chem.*, 1905, **342**, 364.
3. K. A. Hofmann, K. Höschele, *Ber. Deut. Chem. Ges.*, 1915, **48**, 20.
4. H. L. Wells, *Am. J. Sci.,* 1922, **3**, 417.
5. H. Wolffram, *Dissertation*, Königsberg, 1900.
6 C. Brosset, *Arkiv För Kemi, Mineralogi och Geologi*, 1948, **25A**, 19.
7. B. M. Craven, D. Hall, *Acta Crystallogr.*, 1961, **14**, 475.
8. R. J. H. Clark, W. R. Trumble, *Inorg. Chem.*, 1976, **15**, 1030.
9. L. Chugayev, J. Chernayev, *Z. Anorg. Allgem. Chem.*, 1929, **182**, 159.
10. R. J. H. Clark, M. Kurmoo, *J. Chem. Soc. Dalton Trans.*, 1982, 2505.
11. G. C. Papavassiliou, T. Theophanides, *Z. Naturforsch.*, 1979, **34b**, 986.
12. D. Layek, G. C. Papavassiliou, *Z. Naturforsch.*, 1981, **36b**, 83.
13. R. J. H. Clark, M. Kurmoo, *J. Chem. Soc. Dalton Trans.*, 1982, 2515.
14. R. J. H. Clark, in *Advances in Infrared and Raman Spectroscopy*, eds. R. J. H. Clark and R. E. Hester, Wiley, Chichester, 1984, vol **11**, p. 95.
15. J. B. Weinrach, S. A. Ekberg, S. D. Conradson, B. I. Swanson, H. D. Hochheimer, *Inorg. Chem.*, 1990, **29**, 981.
16. F. H. Long, S. P. Love, B. I. Swanson, R. H. McKenzie, *Phys. Rev. Lett.*, 1993, **71**, 762.
17. T. D. Ryan, R. E. Rundle, *J. Am. Chem. Soc.*, 1961, **83**, 2814.
18. A. L. Beauchamp, D. Layek, T. Theophanides, *Acta Crystallogr.*, *Sect. B*, 1982, **B38**, 1158.
19. M. Yamashita, M. Ito, K. Toriumi, T. Ito, *Inorg. Chem.*, 1983, **22**, 1566.
20. K. Toriumi, M. Yamashita, M. Ito, T. Ito, *Acta Crystallogr.*, *Sect. C*, 1986, **C42**, 963.
21. N. Matsushita, *Synth. Met.*, 1993, **56**, 3401.
22. D. Hall, P. P. Williams, *Acta Crystallogr.*, 1958, **11**, 624.
23. H. J. Keller, B. Keppler, G. Ledezma-Sanchez, W. Steiger, *Acta Crystallogr.*, *Sect. B*, 1981, **B37**, 674.
24. H. Endres, H. J. Keller, R. Martin, H. N. Gang, U. Traeger, *Acta Crystallogr.*, *Sect. B*, 1979, **B35**, 1885.
25. N. Matsumoto, M. Yamashita, S. Kida, I. Ueda, *Acta Crystallogr.*, *Sect. B*, 1979, **B35**, 1458.
26. M. Yamashita, K. Toriumi, T. Ito, *Acta Crystallogr.*, *Sect. C*, 1985, **C41**, 876.
27. H. J. Keller, B. Müller, G. Ledzma, R. Martin, *Acta Crystallogr.*, *Sect. C*, 1985, **C41**, 16.
28. M. Tanaka, I. Tsujikawa, K. Toriumi, T. Ito, *Acta Crystallogr.*, *Sect. B*, 1982, **B38**, 2793.
29. H. Okamoto, K. Toriumi, T. Mitani, M. Yamashita, *Phys. Rev. B*, 1990, **42**, 10381.
30. M. Yamashita, E. Tsurata, K. Inoue, T. Furata, H. Okamoto, T. Mitani, K. Toriumi, H. Ohki, R. Ikeda, *Synth. Met.*, 1993, **56**, 3461.
31. A. Hazell, *Acta Crystallogr.*, *Sect. C*, 1991, **C47**, 962.
32. K. P. Larsen, H. Toftlund, *Acta Chem. Scand.*, 1977, **A31**, 182.

33. B. L. Scott, R. J. Donohoe, S. P. Love, S. R. Johnson, M. P. Wilkerson, B. I. Swanson, *Synth. Met.*, 1993, **56**, 3426.

34. R. J. H. Clark, V. B. Croud, R. J. Wills, P. A. Bates, H. M. Dawes, M. B. Hursthouse, *Acta Crystallogr., Sect. B*, 1989, **B45**, 147.

35. K. Toriumi, M. Yamashita, I. Murase, *Chem. Lett.*, 1986, **10**, 1753.

36. K. Toriumi, M. Yamashita, S. Kurita, I. Murase, T. Ito, *Acta Crystallogr., Sect. B*, 1993, **B49**, 497.

37. S. C. Huckett, B. L. Scott, S. P. Love, R. J. Donohoe, C. J. Burns, E. Garcia, T. M. Frankcom, B. I. Swanson, *Inorg. Chem.*, 1993, **32**, 2137.

38. S. C. Huckett, R. J. Donohoe, L. A. Worl, A. D. F. Bulou, C. J. Burns, J. R. Laia, D. Carroll, B. I. Swanson, *Chem. Mater.*, 1991, **3**, 123.

39. M. Kuroda, M. Sakai, Y. Nishina, K. Sasaki, *Phys. Rev. Lett.*, 1992, **68**, 3056.

40. K. Nasu, *J. Phys. Soc. Jpn.*, 1984, **53**, 427.

41. K. Nasu, A. Mishima, *Rev. Solid State Sci.*, 1988, **2**, 539.

42. A. Mishima, K. Nasu, *Phys. Rev. B*, 1989, **39**, 5758.

43. A. Mishima, K. Nasu, *Phys. Rev. B*, 1989, **39**, 5763.

44. A. Kawamori, R. Aoki, M. Yamashita, *J. Phys. C*, 1985, **18**, 5487.

45. N. Matsushita, N. Kojima, T. Ban, I. Tsujikawa, *J. Phys. Soc. Jpn.*, 1987, **56**, 3808.

46. H. Oschio, K. Toriumi, S. Bandow, *Chem. Lett.*, 1988, **12**, 1713.

47. R. J. H. Clark, D. J. Michael, M. Yamashita, *J. Chem. Soc. Dalton Trans.*, 1991, 3447.

48. H. Oshio, K. Toriumi, S. Bandow, K. Miyagawa, S. Kurita, *J. Chem. Soc. Dalton Trans.*, 1990, 1013.

49. Y. Wada, T. Mitani, K. Toriumi, M. Yamashita, *J. Phys. Soc. Jpn.*, 1989, **58**, 3013.

50. G. C. Papavassiliou, D. Layek, *Z. Naturforsch.*, 1982, **37b**, 1406.

51. R. J. H. Clark, V. B. Croud, R. J. Wills, *Inorg. Chem.*, 1988, **27**, 2096.

52. R. J. H. Clark, V. B. Croud, *Inorg. Chem.*, 1985, **24**, 588.

53. R. J. H. Clark, V. B. Croud, *Inorg. Chem.*, 1986, **25**, 1751.

54. B. I. Swanson, R. J. Donohoe, L. A. Worl, J. Tinka Gammel, A. Saxena, I. Batistic, A. R. Bishop, *Synth. Met.*, 1991, **42**, 2733.

55. B. I. Swanson, R. J. Donohoe, L. A. Worl, A. D. F. Bulou, C. A. Arrington, J. Tinka Gammel, A. Saxena, A. R. Bishop, *Mol. Cryst. Liq. Cryst.*, 1991, **194**, 43.

56. A. R. Bishop, I. Batistic, J. Tinka Gammel, A. Saxena, *Synth. Met.*, 1992, **49**, 117.

57. L. A. Worl, S. C. Huckett, B. I. Swanson, A. Saxena, A. R. Bishop, J. Tinka Gammel, *J. Phys.: Condens. Matter*, 1992, **4**, 10237.

58. A. Saxena, A. R. Bishop, L. A. Worl, B. I. Swanson, *Synth. Met.*, 1993, **51**, 431.

59. J. Tinka Gammel, A. Saxena, A. R. Bishop, *Synth. Met.*, 1993, **56**, 3347.

60. A. Saxena, X. Z. Huang, J. Tinka Gammel, A. R. Bishop, L. A. Worl, S. P. Love, B. I. Swanson, *Synth. Met.*, 1993, **56**, 3413.

61. A. Saxena, X. Z. Huang, A. R. Bishop, L. A. Worl, S. P. Love, B. I. Swanson, J. Tinka Gammel, *Synth. Met.*, 1993, **54**, 385.

62. B. L. Scott, S. R. Johnson, B. I. Swanson, *Synth. Met.*, 1993, **56**, 3432.

63. X. Z. Huang, A. Saxena, A. R. Bishop, B. L. Scott, B. I. Swanson, *Synth. Met.*, 1993, **56**, 3449.

64. M. Haruki, S. Kurita, *Phys. Rev. B*, 1989, **39**, 5706.

65. L. Degiorgi, P. Wachter, M. Haruki, S. Kurita, *Phys. Rev. B*, 1989, **40**, 3285.

66. M. Tanaka, S. Kurita, T. Kojima, Y. Yamada, *Chem. Phys.*, 1984, **91**, 257.

67. N. Matsumoto, M. Yamashita, S. Kida, *Bull. Chem. Soc. Jpn.*, 1978, **51**, 2334.

68. R. J. H. Clark, *Chem. Soc. Rev.*, 1990, **19**, 107.

69. H. Tanino, K. Kobayashi, *J. Phys. Soc. Jpn.*, 1983, **52**, 1447.

70. K. Nasu, *J. Phys. Soc. Jpn.*, 1984, **53**, 302.

71. N. Matsushita, N. Kojima, T. Ban, I. Tsujikawa, *Bull. Chem. Soc. Jpn.*, 1989, **62**, 1785.

72. N. Matsushita, N. Kojima, T. Ban, I. Tsujikawa, *Bull. Chem. Soc. Jpn.*, 1989, **62**, 3906.

73. N. Matsushita, N. Kojima, N. Watanabe, T. Ban, *Solid State Commun.*, 1989, **71**, 253.

74. S. Kurita, M. Haruki, K. Miyagawa, *J. Phys. Soc. Jpn.*, 1988, **57**, 1789.

75. S. Kurita, M. Haruki, *Synth. Met.*, 1989, **29**, F129.

76. H. Okamoto, T. Mitani, *Prog. Theor. Phys.*, 1993, **Suppl. No. 113**, 191.

77. J. Tinka Gammel, R. J. Donohoe, A. R. Bishop, B. I. Swanson, *Phys. Rev. B*, 1990, **42**, 10566.

78. S. Kurita, S. Eguchi, S. Ohta, C. A. Arrington, B. I. Swanson, Synth. Met., 1993, **56**, 3341.

79. Y. Wada, N. Matsushita, M. Yamashita, *Synth. Met.*, 1993, **56**, 3391.

80. M. Kuroda, M. Sakai, Y. Nishina, M. Tanaka, S. Kurita, *Phys. Rev. Lett.*, 1987, **58**, 2123.

81. M. Sakai, M. Kuroda, Y. Nishina, *Phys. Rev. B*, 1989, **40**, 3066.

82. H. Ooi, M. Yamashita, K. Kobayashi, *Solid State Commun.*, 1993, **86**, 789.

83. Y. Wada, T. Mitani, M. Yamashita, T. Koda, *Synth. Met.*, 1987, **19**, 907.

84. Y. Wada, M. Yamashita, *Phys. Rev. B*, 1990, **42**, 7399.

85 Y. Hamaue, R. Aoki, M. Yamashita, S. Kida, *Inorg. Chim. Acta*, 1981, **54**, L13.

86. L. V. Interrante, K. W. Browall, F. P. Brundy, *Inorg. Chem.*, 1974, **13**, 1158.

87. S. Kurita, J. Ishikura, M. Haruki, *Synth. Met.*, 1991, **42**, 2785.

88. Y. Wada, T. Mitani, M. Yamashita, T. Koda, *J. Phys. Soc. Jpn.*, 1985, **54**, 3143.

89. H. Tanino, N. Koshizuka, K. Kobayashi, M. Yamashita, K. Hoh, *J. Phys. Soc. Jpn.*, 1985, **54**, 483.

90. K. Aida, J. Takeda, S. Kurita, *Synth. Met.*, 1992, **49**, 109.

91. H. Tanino, W. W. Rüble, K. Takahashi, *Phys. Rev B*, 1988, **38**, 12716.

92. Y. Wada, K. Era, M. Yamashita, *Solid State Commun.*, 1988, **67**, 953.

93. R. J. H. Clark, T. J. Dines, *Angew. Chem. Int. Ed. Engl.*, 1986, **25**, 131.

94. M. Tanaka, S. Kurita, *J. Phys. C*, 1986, **19**, 3019.

95. R. J. H. Clark, M. Kurmoo, *J. Chem. Soc. Faraday Trans. II*, 1983, **79**, 519.

96. S. D. Conradson, R. F. Dallinger, B. I. Swanson, R. J. H. Clark, V. B. Croud, *Chem. Phys. Lett.*, 1987, **135**, 463.

97. R. J. H. Clark, T. J. Dines, *Chem. Phys. Lett.*, 1991, **185**, 490.

98. R. J. H. Clark, V. B. Croud, in *Organic and Inorganic Low-Dimensional Crystalline Materials*, eds. P.Delhaes and M.Drillon, NATO Advanced Research Workshop, Plenum, 1987, p. 341.

99. R. J. H. Clark, D. J. Michael, *J. Mol. Struct.*, 1988, **189**, 173.

100. A. R. Bishop, I. Batistic, X. Z. Huang, A. Saxena, *Prog. Theor. Phys.*, 1993, **Suppl. No. 113**, 133.

101. R. J. Donohoe, R. B. Dyer, B. I. Swanson, *Solid State Commun.*, 1990, **73**, 521.

102. R. J. Donohoe, C. D. Tait, B. I. Swanson, *Chem. Mater.*, 1990, **2**, 315.

103. R. J. Donohoe, L. A. Worl, A. D. F. Bulou, B. I. Swanson, J. Tinka Gammel, A. R. Bishop, *Synth. Met.*, 1991, **42**, 2745.

104. R. J. Donohoe, L. A. Worl, B. I. Swanson, A. D. F. Bulou, *Synth. Met.*, 1991, **42**, 2749.

105. R. J. Donohoe, L. A. Worl, C. A. Arrington, A. D. F. Bulou, B. I. Swanson, *Phys. Rev. B*, 1992, **45**, 13185.

106. R. J. Donohoe, C. A. Arrington, B. I. Swanson, *Synth. Met.*, 1992, **49**, 99.

107. S. C. Huckett, R. J. Donohoe, L. A. Worl, A. D. F. Bulou, C. J. Burns, B. I. Swanson, *Synth. Met.*, 1991, **42**, 2773.

108. X. Z. Huang, A. Saxena, A. R. Bishop, L. A. Worl, S. P. Love, B. I. Swanson, *Solid State Commun.*, 1992, **84**, 957.

109. S. P. Love, L. A. Worl, R. J. Donohoe, S. C. Huckett, S. R. Johnson, B. I. Swanson, *Synth. Met.*, 1993, **56**, 3456.

110. S. P. Love, L. A. Worl, R. J. Donohoe, S. C. Huckett, B. I. Swanson, *Phys. Rev. B*, 1992, **46**, 813.

111. S. P. Love, L. A. Worl, R. J. Donohoe, S. C. Huckett, A. Saxena, X. Z. Huang, A. R. Bishop, B. I. Swanson, *Synth. Met.*, 1993, **56**, 3335.

112. S. P. Love, S. C. Huckett, L. A. Worl, T. M. Frankcom, S. A. Ekberg, B. I. Swanson, *Phys. Rev. B*, 1993, **47**, 11107.

113. M. Sakai, M. Hayakawa, M. Kuroda, Y. Nishina, M. Yamashita, *J. Phys. Soc. Jpn.*, 1991, **60**, 1619.

114. K. Okaniwa, H. Okamoto, T. Mitani, K. Toriumi, M. Yamashita, *J. Phys. Soc. Jpn.*, 1991, **60**, 997.

115. M. Kuroda, T. Ito, Y. Nishina, M. Yamashita, *J. Phys. Soc. Jpn.*, 1993, **62**, 2237.

116. R. J. Donohoe, S. A. Ekberg, C. D. Tait, B. I. Swanson, *Solid State Commun.*, 1989, **71**, 49.

117. L. Degiorgi, P. Wachter, M. Haruki, S. Kurita, *Phys. Rev. B*, 1990, **42**, 4341.

118. L. Degiorgi, P. Wachter, M. Haruki, S. Kurita, *Synth. Met.*, 1989, **29**, F137.

119. M. Kuroda, M. Sakai, M. Suezawa, Y. Nishina, K. Sumino, *J. Phys. Soc. Jpn.*, 1990, **59**, 3049.

120. C. A. Arrington, C. J. Unkefer, R. J. Donohoe, S. C. Huckett, S. Kurita, B. I. Swanson, *Solid State Commun.*, 1992, **84**, 979.

121. A. Kawamori, R. Aoki, M. Yamashita, *J. Phys. C*, 1985, **18**, 5487.

122. M. Sakai, M. Kuroda, M. Suezawa, Y. Nishina, K. Sumino, M. Yamashita, *J. Phys. Soc. Jpn.*, 1992, **61**, 1326.

123. J.-M. Bret, P. Castan, G. Commenges, J.-P. Laurent, D. Muller, *Chem. Commun.*, 1983, 1273.

124. R. Ikeda, T. Tamura, M. Yamashita, *Chem. Phys. Lett.*, 1990, **173**, 466.

125. E. J. W. Austin, P. J. Barrie, R. J. H. Clark, *Inorg. Chem.*, 1992, **31**, 4281.

126. E. J. W. Austin, P. J. Barrie, R. J. H. Clark, *Chem. Commun.*, 1993, 1405.

127. E. J. W. Austin, P. J. Barrie, R. J. H. Clark, *Inorg. Chem.*, 1995, **34**, 3859.

128. C. Halvorson, T. W. Hagler, D. Moses, Y. Cao, A. J. Heeger, *Chem. Phys. Lett.*, 1992, **200**, 364.

129. Y. Iwasa, E. Funatsu, T. Masegawa, T. Koda, M. Yamashita, *Appl. Phys. Lett.*, 1991, **59**, 2219.

130. Y. Wada, M. Yamashita, *Jap. J. Appl. Phys. (I)*, 1990, **29**, 2744.

131. M. Yamashita, I. Murase, T. Ito, Y. Wada, T. Mitani, T. Ikemoto, *Bull. Chem. Soc. Jpn.*, 1985, **58**, 2336.

132. M. Yamashita, I. Murase, T. Ikemoto, *Bull. Chem. Soc. Jpn.*, 1985, **58**, 2697.

133. M. Yamashita, N. Matsumoto, S. Kida, *Inorg. Chim. Acta*, 1978, **31**, L381.

134. I. Ikemoto, K. Kikuchi, K. Iwai, M. Yamashita, M. Nomura, K. Asakura, N. Kosugi, K. Yakushi, M. Kuroda, *Bull. Chem. Soc. Jpn.*, 1986, **59**, 3271.

135. S. C. Huckett, E. Garcia, J. R. Laia, D. Carroll, B. I. Swanson, *Synth. Met.*, 1991, **42**, 2777.

136. A. D. F. Bulou, S. C. Huckett, E. Garcia, B. I. Swanson, G. H. Kwei, J. Eckert, *Ferroelectrics*, 1992, **125**, 45.

137. S. Piepho, E. R. Krausz. P. N. Schatz, *J. Am. Chem. Soc.*, 1978, **100**, 2996.

138. K. Y. Wong, P. N. Schatz, *Chem. Phys. Lett.*, 1980, **73**, 456.

139. M.-H. Whangbo, in *Extended Linear-Chain Compounds*, ed. J. S. Miller, Plenum, New York, 1982, vol **2**, p. 127.

140. M.-H. Whango, M. J. Foshee, *Inorg. Chem.*, 1981, **20**, 113.

141. K. Nasu, Y. Toyazawa, *J. Phys. Soc. Jpn.*, 1982, **51**, 2098.

142. D. K. Campbell, J. Tinka Gammel, E. Y. Loh Jr., *Phys. Rev. B*, 1988, **38**, 12043.

143. S. Kivelson, W.-P. Su, J. R. Schrieffer, A. J. Heeger, *Phys. Rev. Lett.*, 1988, **60**, 71.

144. K. Nasu, Y. Toyazawa, *J. Phys. Soc. Jpn.*, 1982, **51**, 3111.

145. K. Nasu, *J. Phys. Soc. Jpn.*, 1984, **52**, 3865.

146. M. Suzuki, K. Nasu, *Phys. Rev. B*, 1992, **45**, 1605.

147. A. Mishima, K. Nasu, *Synth. Met.*, 1989, **29**, F175.

148. K. Iwano, K. Nasu, *J. Phys. Soc. Jpn.*, 1992, **61**, 1380.

149. K. Iwano, K. Nasu, *Synth. Met.*, 1991, **42**, 2781.

150. D. Baeriswyl, A. R. Bishop, *Phys. Scr.*, 1987, **T19**, 239.

151. J. Tinka Gammel, I. Batistic, A. R. Bishop, E. Y. Loh Jr., S. Marianer, *Physica B*, 1990, **163**, 458.

152. J. Tinka Gammel, A. Saxena, I. Batistic, A. R. Bishop, S. R. Phillpot, *Phys. Rev. B*, 1992, **45**, 6408.

153. D. Baeriswyl, A. R. Bishop, *J. Phys. C*, 1988, **21**, 339.

154. J. Tinka Gammel, S. M. Weber-Milbrodt, E. Y. Loh Jr., A. R. Bishop, *Synth. Met.*, 1989, **29**, F161.

155. A. R. Bishop, J. Tinka Gammel, S. R. Phillpot, *Synth. Met.*, 1989, **29**, F151.

156. J. Tinka Gammel, S. M. Weber-Milbrodt, A. R. Bishop, S. Marianer, E. Y. Loh Jr., J. Reichl, *Synth. Met.*, 1991, **42**, 2755.

157. I. Batistic, J. Tinka Gammel, A. R. Bishop, *Synth. Met.*, 1991, **42**, 2727.

158. I. Batistic, J. Tinka Gammel, A. R. Bishop, *Phys. Rev. B*, 1991, **44**, 13228.

159. I. Batistic, A. R. Bishop, J. Tinka Gammel, A. Saxena, *Synth. Met.*, 1991, **42**, 2715.

160. S. M. Weber-Milbrodt, J. Tinka Gammel, A. R. Bishop, E. Y. Loh Jr., *Phys. Rev. B*, 1992, **45**, 6435.

161. J. Tinka Gammel, A. Saxena, A. R. Bishop, *Synth. Met.*, 1991, **42**, 2761.

162. X. Z. Huang, I. Batistic, A. R. Bishop, *Synth. Met.*, 1993, **56**, 3443.

163. I. Batistic, X. Z. Huang, A. R. Bishop, A. Saxena, *Phys. Rev. B*, 1993, **48**, 6065.

164. X. Z. Huang, A. R. Bishop, *Phys. Rev. B*, 1993, **48**, 16148.

165. R. C. Albers, *Synth. Met.*, 1989, **29**, F169.

166. M. Alouani, R. C. Albers, J. M. Wills, M. Springborg, *Phys. Rev. Lett.*, 1992, **69**, 3104.

167. M. Alouani, R. C. Albers, *Synth. Met.*, 1993, **56**, 3352.

168. M. Alouani, R. C. Albers, J. M. Wills, *Synth. Met.*, 1993, **56**, 3358.

169. M. Alouani, R. C. Albers, J. M. Wills, M. Springborg, *Synth. Met.*, 1993, **56**, 3364.

170. R. C. Albers, M. Alouani, J. M. Wills, M. Springborg, *Synth. Met.*, 1991, **42**, 2739.

171. C. G. Barraclough, R. J. H. Clark, M. Kurmoo, *J. Mol. Struct.*, 1982, **79**, 239.

172. C. E. Pavaskeraidis, C. Papatriantafillou, G. C. Papavassiliou, *Lect. Notes Phys.*, 1979, **96**, 224.

173. S. D. Allen, R. J. H. Clark, V. B. Croud, M. Kurmoo, *Phil. Trans. Roy. Soc. London*, 1985, **A314**, 131.

174. T. Hori, T. Asahi, *Prog. Theor. Phys.*, 1957, **17**, 523.

175. P. Dean, *Proc. Phys. Soc.*, 1959, **73**, 413.

176. P. Dean, *Proc. Roy. Soc. (A)*, 1960, **254**, 507.

177. P. Dean, *Proc. Roy. Soc. (A)*, 1961, **260**, 263.

178. P. Dean, M. D. Bacon, *Proc. Phys. Soc.*, 1963, **81**, 642.

179. P. Dean, *Proc. Phys. Soc.*, 1967, **90**, 479.

180. U. Schmidt, *Phys. Rev.*, 1957, **105**, 425.

181. F. J. Dyson, *Phys. Rev.*, 1953, **92**, 1331.

182. P. Dean, *J. Inst. Maths. Applics.*, 1967, **3**, 98.

183. A. S. Barker, A. J. Sievers, *Rev. Modern Phys.*, 1975, **47**, Suppl. No. 2, S1.

184. I. F. Chang, S. S. Mitra, *Adv. Phys.*, 1971, **20**, 359.

185. J. J. Sinai, S.-Y. Wu, *Phys. Rev. B*, 1979, **19**, 1800.

186. J. J. Sinai, S.-Y. Wu, *Phys. Rev. B*, 1979, **19**, 6267.

187. H. W. Diehl, P. L. Leath, T. Kaplan, *Phys. Rev. B*, 1979, **19**, 5044.

188. A. D. F. Bulou, R. J. Donohoe, B. I. Swanson, *J. Phys.: Condens. Matter*, 1991, **3**, 1727.

189. L. D. Barton, *Mol. Phys.*, 1976, **31**, 129.

190. H. A. Kramers, W. Heisenberg, *Z. Physik*, 1925, **31**, 681.

191. W. Heisenberg, *Ann. Physik*, 1931, **9**, 338.

192. P. A. M. Dirac, *Proc. Roy. Soc. (London)*, 1927, **A114**, 710.

193. M. Born, R. J. Oppenheimer, *Ann. Physik*, 1927, **89**, 457.

194. G. Herzberg, E. Teller, *Z. Phys. Chem.*, 1933, **21**, 410.

195. T. G. Spiro, T. M. Loehr, in *Advances in Infrared and Raman Spectroscopy*, eds. R. J. H. Clark and R. E. Hester, Wiley, Chichester, 1975, vol **1**, p. 98.

196. J. Behringer, in *Raman Spectroscopy*, eds. H. A. Szymanski, Plenum, New York, 1967, vol **1**, p. 168.

197. R. J. H. Clark, in *Advances in Infrared and Raman Spectroscopy*, eds. R. J. H. Clark and R. E. Hester, Wiley, Chichester, 1975, vol **1**, p. 143.

198. R. J. H. Clark, B. Stewart, in *Structure and Bonding*, Springer, Berlin, 1979, vol **36**, p. 1.

199. W. Siebrand, M. Z. Zgierski, in *Excited States*, ed. E. C. Lim, Academic Press, New York, 1979, vol **4**, p. 1.

200. R. J. H Clark, in *Inorganic Chemistry Toward the 21st Century*, A. C. S. Symposium Series, No. **211**, ed. M. H. Chisholm, 1983, p. 509.

201. R. J. H. Clark, *J. Mol. Struct.*, 1984, **113**, 117.

202. J.-M. Bret, P. Castan, G. Commenges, J.-P. Laurent, *Polyhedron*, 1983, **2**, 901.

203. E. R. Andrew, *Int. Rev. Phys. Chem.*, 1981, **1**, 195.

204. R. J. Abraham, J. Fisher, P. Loftus, in *Introduction to NMR Spectroscopy*, Wiley, Chichester, 1988, p. 5.

205. S. W. Sparks, P. D. Ellis, *J. Am. Chem. Soc.*, 1986, **108**, 3215.

206. R. K. Harris, P. Reams, K. J. Packer, *J. Chem. Soc. Dalton Trans.*, 1986, 1015.

207. T. G. Appleton, K. J. Barnham, J. R. Hall, M. T. Mathieson, *Inorg. Chem.*, 1991, **30**, 2751.

208. StJ. S. Kerrison, P. J. Sadler, *J. Chem. Soc. Dalton Trans.*, 1982, 2363.

209. M. Brémond, G. J. Martin, G. A. Webb, D. J. Reynolds, *Org. Magnet. Res.*, 1984, **22**, 640.

210. R. Hagen, J. P. Warren, D. H. Hunter, J. D. Roberts, *J. Am. Chem. Soc.*, 1973, **95**, 5712.

211. P. S. Pregosin, H. Omura, L. M. Venanzi, *J. Am. Chem. Soc.*, 1973, **95**, 2047.

212. StJ. S. Kerrison, P. J. Sadler, *Chem. Commun.*, 1977, 861.

213. T. G. Appleton, J. R. Hall, S. F. Ralph, *Inorg. Chem.*, 1985, **24**, 4685.

214. P. Pregosin, *Annu. Rep. NMR Spectrosc.*, 1986, **17**, 285.

215. R. J. H. Clark, D. J. Michael, M. Yamashita, *J. Chem. Soc. Dalton Trans.*, 1991, 725.

216. R. J. H. Clark, D. J. Michael, M. Yamashita, *J. Chem. Soc. Dalton Trans.*, 1991, 3447.

217. M. Witanowski, L. Stefaniak, G. A. Webb, *Annu. Rep. NMR Spectrosc.*, 1986, **18**, 1.

218. F. Basolo, J. C. Bailar, B. R. Tarr, *J. Am. Chem. Soc.*, 1957, **72**, 2433.

219. D. J. Michael, *Ph. D. Thesis*, London, 1992.

220. Ö. Bekaroglu, H. Breer, H. Endres, H. J. Keller, H. N. Gang, *Inorg. Chim. Acta*, 1977, **21**, 183.

221. G. W. Kabalka, K. A. R. Sastry, G. W. McCollum, C. A. Lane, *Chem. Commun.*, 1982, 62.

222. G. W. Kabalka, K. A. R. Sastry, G. W. McCollum, H. Yoshiaki, *J. Org. Chem.*, 1981, **46**, 4296.

223. G. W. Watt, R. E. McCarley, *J. Am. Chem. Soc.*, 1957, **79**, 3315.

224. G. L. Johnson, *Inorg. Synth.*, 1966, **8**, 242.

225. H. D. K. Drew, H. J. Tress, *J. Chem. Soc.*, 1933, 1335.

226. H. D. K. Drew, H. J. Tress, *J. Chem. Soc.*, 1935, 1251.
227. G. W. Watt, R. E. McCarley, *J. Am. Chem. Soc.*, 1957, **79**, 4585.
228. K. W. Browall, J. S. Kasper, L. V. Interrante, *Acta Crystallogr., Sect. B*, 1974, **B30**, 1649.
229. H.-J. Keller, in *Extended Linear-Chain Compounds*, ed. J. S. Miller, Plenum, New York, 1981, vol **1**, p. 357.
230. J. Iball, M. MacDougall, S. Scringeour, *Acta Crystallogr., Sect. B*, 1975, **B31**, 1672.
231. E. M. Menger, *J. Magn. Reson.*, 1982, **46**, 257.
232. S. Hayashi, K. Hayamizu, *Magn. Reson. Chem.*, 1992, **30**, 658.
233. J. G. Hexem, M. H. Frey, S. J. Opella, *J. Chem. Phys.*, 1982, **77**, 3847.
234. J. Mason, *J. Chem. Soc. Faraday Trans.*, 1977, 1464.
235. W.McFarlane, *J. Chem. Soc. Dalton Trans.*, 1974, 1959.
236. J. D. Kennedy, W.McFarlane, R. J. Puddephatt, P. J. Thompson, *J. Chem. Soc. Dalton Trans.*, 1976, 874.
237. R. R. Dean, J. C. Green, *J. Chem. Soc. A*, 1968, 3047.
238. A. D. Buckingham, P. J. Stephens, *J. Chem. Soc.*, 1964, 2747.
239. A. D. Buckingham, P. J. Stephens, *J. Chem. Soc.*, 1964, 4583.
240. M. Comeau, M.-T. Béraldin, E. C. Vauthier, S. Fliszár, *Can. J. Chem.*, 1985, **63**, 3266.
241. M. Takasuka, Y. Terui, *J. Chem. Soc. Perkin Trans. II*, 1984, 1545.
242. J. R. Campbell, R. J. H. Clark, P. C. Turtle, *Inorg. Chem.*, 1978, **17**, 3622.
243. R. J. H. Clark, M. Kurmoo, *J. Chem. Soc. Dalton Trans.*, 1981, 524.
244. A. J. Poë, *J. Chem. Soc.*, 1963, 183.
245. A. Hantzsch, F. Rosenblatt, *Z. Anorg. Chem.*, 1930, **187**, 241.
246. S. Sato, M. Haruki, S. Kurita, *Acta Crystallogr., Sect. C*, 1990, **C46**, 1107.
247. S. Sato, M. Haruki, P. Wachter, S. Kurita, *Acta Crystallogr., Sect. C*, 1990, **C46**, 1812.
248. N. F. Ramsey, *Phys. Rev.*, 1950, **78**, 699.
249. C. F. Liu, J. A. Ibers, *Inorg. Chem.*, 1970, **9**, 773.
250. A. Saxena, X. Z. Huang, A. R. Bishop, *Synth. Met.*, 1993, **56**, 3421.
251. H. Tanino, D. Schäfer-Siebert, K. Takahashi, M. Tajima, *Synth. Met.*, 1991, **42**, 2797.
252. A. J. Poë, D. H. Vaughan, *J. Am. Chem. Soc.*, 1970, **92**, 7537.
253. R. J. H. Clark, V. B. Croud, *J. Phys. C*, 1986, **19**, 3467.
254. R. G. Pearson, F. Basolo, *Mechanisms of Inorganic Reactions*, 2nd ed., Wiley, Chichester, 1967.
255. H. Tanino, K. Takahashi, T. Yao, *Jap. J. Appl. Phys. (II)*, 1987, **26**, L983.
256. B. Rosenberg, L. VanCamp, T. Krigas, *Nature*, 1965, **205**, 698.
257. H. D. K. Drew, F. W. Pinkard, W. Wardlaw, E. G. Cox, *J. Chem. Soc.*, 1932, 988.
258. A. A. Grinberg, A. I. Dobrovskaya, *Russ. J. Inorg. Chem.*, 1967, **12**, 141.
259. A. A. Grinberg, M. I. Gel'fman, S. I. Pechenyuk, *Russ. J. Inorg. Chem.*, 1970, **15**, 252.
260. V. A. Palkin, T. A. Kuzina, *Russ. J. Inorg. Chem.*, 1973, **18**, 247.
261. V. A. Palkin, T. A. Kuzina, N. N. Kuz'mina, R. N. Shchelokov, *Russ. J. Inorg. Chem.*, 1980, **25**, 122.

262. V. A. Palkin, T. A. Kuzina, N. N. Kuz'mina, R. N. Shchelokov, *Russ. J. Inorg. Chem.*, 1980, **25**, 573.

263. R. N. Keller, *Inorg. Synth.*, 1946, **2**, 250.

264. G. B. Kaufmann, D. O. Cowan, *Inorg. Synth.*, 1963, **7**, 239.

265. S. C. Dhara, *Ind. J. Chem.*, 1970, **8**, 193.

266. G. H. W. Milbum, M. R. Truter, *J. Chem. Soc. A*, 1966, 1609.

267. P. T. Cleve, *Ofvers. Akad. Stockholm*, 1870, **27**, 783.

268. V. A. Palkin, N. N. Kuz'mina, V. E. Gorbunov, O. N. Evstafeva, *Russ. J. Inorg. Chem.*, 1972, **17**, 291.

269. K. Nakamoto, P. J. McCarthy, J. Fujita, R. A. Condrate, G. T. Behnke, *Inorg. Chem.*, 1965, **4**, 37.

270. D. W. James, M. J. Nolan, *Aust. J. Chem*, 1973, **26**, 271.

271. M. L. Rodgers, D. S. Martin Jr., *Polyhedron*, 1987, **6**, 225.

272. K. P. Beaumont, C. A. McAuliffe, *Inorg. Chim. Acta*, 1974, **8**, 105.

273. V. B. Croud, *Ph. D. Thesis*, London, 1986.

274. A. V. Babaeva, O. N. Evstafeva, *Russ. J. Inorg. Chem.*, 1961, **6**, 28.

275. L. Ramberg, *Z. Anorg. Allgem. Chem.*, 1913, **63**, 33.

276. M. M. Singh, Z. Svafrom, R. M. Pike, *J. Chem. Educ.*, 1990, **67**, A261.

277. B. P. Block, E. S. Roth, J. Simkin, *J. Inorg. Nucl. Chem.*, 1960, **16**, 48.

278. R. J. H. Clark, P. C. Turtle, *J. Chem. Soc. Dalton Trans.*, 1979, 1622.

279. V. E. Volkov, I. I. Smirnov, *Russ. J. Inorg. Chem.*, 1981, **26**, 1174.

280. R. J. H. Clark, W. P. Trumble, *Inorg. Chem.*, 1975, **15**, 1031.

281. G. M. Summa, B. A. Scott, *Inorg. Chem.*, 1980, **19**, 1079.

282. J. Reiset, *Compt. Rend. Acad. Sci. Paris*, 1844, **18**, 1103.

283. J. Hiraishi, I. Nakagawa, T. Shimanouchi, *Spectrochim. Acta*, 1968, **24A**, 819.

284. Y. S. Varshavskii, M. I. Gel'fman, S. C. Dkhara, N. V. Ivannikova, *Russ. J. Inorg. Chem.*, 1968, **13**, 1409.

285. G. B. Kaufmann, *Inorg. Synth.*, 1963, **7**, 236.

286. S. Prasad, V. Krishnan, *J. Ind. Chem. Soc.*, 1958, **35**, 352.

287. D. R. Harks, D. J. Phillips, J. P. Redfem, *J. Chem. Soc. A*, 1967, 1465.

288. Y.-M. Wuu, S.-M. Peng, *J. Inorg. Nucl. Chem.*, 1980, **42**, 205.

289. A. L. Basch, R. C. Holm, *J. Am. Chem. Soc.*, 1966, **88**, 5201.

290. B. A. Howell, E. M. Walles, *Inorg. Chim. Acta*, 1988, **142**, 185.

291. C. Hansch, B. H. Venger, A. Panthananickal, *J. Med. Chem.*, 1980, **23**, 459.